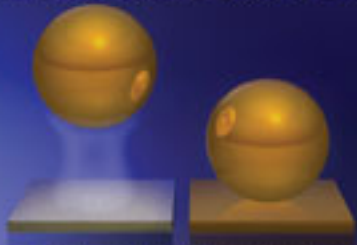


# nature



## QUANTUM LEVITATION

Demonstration of the elusive Casimir-Lifshitz repulsion

### CARBON OFFSETS

Market forces: lost in the forest

### BEING HUMAN

What love's got to do with it

### PROTEIN SYNTHESIS

Proof-reading in the ribosome

### NATUREJOBS

Find a career  
that's right  
for you

# Data for the masses

Initiatives for digital research infrastructure should focus more on making standardized data openly available, and less on developing new portals.

**T**he flood of digital research data that scientists are generating through genomics, sensor and other technologies has made it imperative to create an infrastructure to use, repurpose and preserve those data. Some such efforts are already under way, notably the US National Science Foundation's \$100-million, five-year DataNet programme, and Europe's Alliance for Permanent Access (see Big Data special, <http://tinyurl.com/5hh2rq>). But how should the responsibilities be divided between governments and the private sector?

A series of events in December highlights the complexities of this issue. One was a pioneering move by Amazon to host large scientific data sets for free, starting with GenBank and other widely used sequence and chemical-structure databases

Amazon's move is not altogether altruistic. Although researchers will be able to download the data to their own computers, the company is betting that many will instead use its 'cloud computing' technology, which makes the company's vast server infrastructure available to process the data sets on a pay-as-you-go basis.

Such services could offer immense benefits to research. By giving scientific data a permanent home online, Amazon could help to ease the long-running problem of databases that are abandoned when, for example, funding dries up at the end of a research grant. Its cloud-computing approach could liberate smaller labs from the cost of running data centres of their own. And it should facilitate the sharing of data and analysis tools between widely dispersed research teams.

Also in December, however, came a reminder of the risks of

depending on the public or private sector alone to create such infrastructure: Google announced it was abandoning its plans to host large scientific data sets for free, apparently because of the economic downturn. In November, the European Union, in collaboration with research organizations, libraries and museums, launched the Europeana online digital library as its much-touted alternative to Google Books. Europeana has scanned valuable historical collections, but its computing infrastructure crashed within hours, not clunking back into service until more than a month later. A similar fate met Géoportail, a service created by the French government as a competitor to Google Earth, and launched with great fanfare in 2006 by President Jacques Chirac.

In creating such public offerings, governments address valid concerns that private companies will exercise monopolies over significant cultural and scientific heritage. But their focus on creating their own digital libraries and databases too often means that other, perhaps more important, ways to address such concerns are neglected. Making standardized data openly available to both commercial and not-for-profit organizations, for instance, could spur innovation of superior information services. And to avoid embarrassing crashes, public efforts might well consider partnerships with private firms to tap into the economies of scale and expertise of the Googles and Amazons of the world. ■

**"Making standardized data openly available could spur innovation of superior information services."**

## Culture clash

Samuel Huntington will be remembered for his ideas, controversial as they might have been.

**"**It is my hypothesis that the fundamental source of conflict in this new world will not be primarily ideological or primarily economic. The great divisions among humankind and the dominating source of conflict will be cultural ... The fault lines of civilizations will be the battle lines of the future."

With newspaper headlines dominated by the conflict between Israel and the Palestinians, as well as by the confrontation between Pakistan and India, these early lines in Samuel Huntington's 1993 *Foreign Affairs* essay, 'The Clash of Civilizations', seem more resonant than ever. Huntington, who died on 24 December 2008, aged 81, was a controversial giant among public intellectuals in the United States. He taught at Harvard University for 58 years, founded *Foreign Policy* magazine and worked in the White House under Presi-

dent Jimmy Carter. Yet he attracted strong criticism from scientists.

In the 1980s, for example, members of the US National Academy of Sciences voted twice to deny him membership. At the heart of the dispute was Huntington's use of mathematical notation as a shorthand summary of complex political ideas, such as his use of equations to claim that apartheid South Africa was a "satisfied society". As mathematician and academy member Serge Lang of Yale University in New Haven, Connecticut, declared, this gave "the illusion of science without any of its substance".

That quarrel paled, however, next to the controversy over Huntington's essay. Speculating on conflicts to come in the post-cold-war era, he argued that people ought to be classified as being members of distinct cultures, and asserted that wars can be better understood as conflicts among these 'civilizations', rather than between nations. Most controversial, however, was his suggestion that Chinese and Islamic 'civilizations' posed the biggest potential risks to Western nations.

For many people, including senior policymakers in Europe and the United States, Huntington was saying aloud what they had already

# Data for the masses

Initiatives for digital research infrastructure should focus more on making standardized data openly available, and less on developing new portals.

**T**he flood of digital research data that scientists are generating through genomics, sensor and other technologies has made it imperative to create an infrastructure to use, repurpose and preserve those data. Some such efforts are already under way, notably the US National Science Foundation's \$100-million, five-year DataNet programme, and Europe's Alliance for Permanent Access (see Big Data special, <http://tinyurl.com/5hh2rq>). But how should the responsibilities be divided between governments and the private sector?

A series of events in December highlights the complexities of this issue. One was a pioneering move by Amazon to host large scientific data sets for free, starting with GenBank and other widely used sequence and chemical-structure databases

Amazon's move is not altogether altruistic. Although researchers will be able to download the data to their own computers, the company is betting that many will instead use its 'cloud computing' technology, which makes the company's vast server infrastructure available to process the data sets on a pay-as-you-go basis.

Such services could offer immense benefits to research. By giving scientific data a permanent home online, Amazon could help to ease the long-running problem of databases that are abandoned when, for example, funding dries up at the end of a research grant. Its cloud-computing approach could liberate smaller labs from the cost of running data centres of their own. And it should facilitate the sharing of data and analysis tools between widely dispersed research teams.

Also in December, however, came a reminder of the risks of

depending on the public or private sector alone to create such infrastructure: Google announced it was abandoning its plans to host large scientific data sets for free, apparently because of the economic downturn. In November, the European Union, in collaboration with research organizations, libraries and museums, launched the Europeana online digital library as its much-touted alternative to Google Books. Europeana has scanned valuable historical collections, but its computing infrastructure crashed within hours, not clunking back into service until more than a month later. A similar fate met Géoportail, a service created by the French government as a competitor to Google Earth, and launched with great fanfare in 2006 by President Jacques Chirac.

In creating such public offerings, governments address valid concerns that private companies will exercise monopolies over significant cultural and scientific heritage. But their focus on creating their own digital libraries and databases too often means that other, perhaps more important, ways to address such concerns are neglected. Making standardized data openly available to both commercial and not-for-profit organizations, for instance, could spur innovation of superior information services. And to avoid embarrassing crashes, public efforts might well consider partnerships with private firms to tap into the economies of scale and expertise of the Googles and Amazons of the world. ■

**"Making standardized data openly available could spur innovation of superior information services."**

## Culture clash

Samuel Huntington will be remembered for his ideas, controversial as they might have been.

**"**It is my hypothesis that the fundamental source of conflict in this new world will not be primarily ideological or primarily economic. The great divisions among humankind and the dominating source of conflict will be cultural ... The fault lines of civilizations will be the battle lines of the future."

With newspaper headlines dominated by the conflict between Israel and the Palestinians, as well as by the confrontation between Pakistan and India, these early lines in Samuel Huntington's 1993 *Foreign Affairs* essay, 'The Clash of Civilizations', seem more resonant than ever. Huntington, who died on 24 December 2008, aged 81, was a controversial giant among public intellectuals in the United States. He taught at Harvard University for 58 years, founded *Foreign Policy* magazine and worked in the White House under Presi-

dent Jimmy Carter. Yet he attracted strong criticism from scientists.

In the 1980s, for example, members of the US National Academy of Sciences voted twice to deny him membership. At the heart of the dispute was Huntington's use of mathematical notation as a shorthand summary of complex political ideas, such as his use of equations to claim that apartheid South Africa was a "satisfied society". As mathematician and academy member Serge Lang of Yale University in New Haven, Connecticut, declared, this gave "the illusion of science without any of its substance".

That quarrel paled, however, next to the controversy over Huntington's essay. Speculating on conflicts to come in the post-cold-war era, he argued that people ought to be classified as being members of distinct cultures, and asserted that wars can be better understood as conflicts among these 'civilizations', rather than between nations. Most controversial, however, was his suggestion that Chinese and Islamic 'civilizations' posed the biggest potential risks to Western nations.

For many people, including senior policymakers in Europe and the United States, Huntington was saying aloud what they had already

begun to believe privately: that to survive and continue to prosper, Western nations need to consider the people of China and the Islamic countries as adversaries. The terrorist attacks of 11 September 2001 strengthened this view, and won Huntington many more converts.

To others, however, Huntington was simply giving academic respectability to the views of ultra-nationalists and religious extremists. The Nobel-prizewinning economist Amartya Sen of Harvard University spoke for many when he argued that classifying humans using a single metric — whether religion or civilization — was not just factually wrong, but also an untested predictor of future conflict. Looking at the historical data, moreover, Malcolm Chalmers of the Royal United Services Institute, a London-based defence think-tank, has found that the proportion of people dying in wars and conflicts has actually declined since the end of the Second World War. And looking at archaeological records of even older conflicts, the economist Samuel Bowles of the Santa Fe Institute in New Mexico suggests that the public-spiritedness and generosity of people today may have come about in part because of a bloodier history of hostility towards outsiders (see *Nature* **456**, 326–327; 2008).

Elsewhere, anthropologist Arjun Appadurai of the New School in New York says that today's tensions and conflicts are characterized less by a 'clash of civilizations', than by larger groups feeling threatened

by smaller ones. This is certainly the case with China's fears on Tibet; India's worries over Pakistan; Israel's dispute with the Palestinians; and the fears among host societies of much smaller immigrant communities. At King's College London, Christoph Meyer and his colleagues in the Department of War Studies have just begun a three-year project that will use this idea to search for ways to provide advanced warning that hostility or antipathy will boil over into violence.

Still, Huntington's clash-of-civilizations idea has had staying power, if only because few, if any, of his critics could match the simplicity and scope of his original concept. Scientists these days often work in highly specialized fields, and tend to be reluctant to propose over-arching theories. Yet policymakers are more likely to respond to people who seem to give the bigger picture, and are able to synthesize it and communicate it clearly.

This is a skill that Huntington had in spades and it poses both a lesson and a dilemma for scientists. Huntington wasn't always right, but his ability to occupy and exploit the space between researchers and its end-users meant that his ideas carried more influence than might otherwise have been the case. ■

**"Few, if any, of Huntington's critics could match the simplicity and scope of his original concept."**

## Cuba's biotech boom

The United States would do well to end restrictions on collaborations with the island nation's scientists.

For a week after Cuba marked the 50th anniversary of its revolution on 1 January, a celebratory 'Caravan of Liberty' carried 50 people, including many university students and scientists, along the triumphal route that Fidel Castro had taken half a century earlier. These people represented the health-care and educational systems of which Cubans are proud, however much they bemoan their other privations behind closed doors. And in no small measure the scientists in the caravan symbolize the foundation of that health-care system in the developing world's most established biotechnology industry, which has grown rapidly even though it eschewed the venture-capital funding model that rich countries consider a prerequisite.

This growth in biotech has been a top-down affair, like most of the changes in Castro's Cuba. At the president's personal instigation, the island nation's half-dozen university centres from before the revolution expanded to at least 35 in the decades that followed. But the growth also owes a great deal to individual researchers' desire to make a contribution. Ask a Cuban scientist why he or she works long hours to earn little more than the US\$20-per-month average wage, and the answer is often that they want to make sick people better, with the kudos of having done so. The venture-capital model's promise of riches is nice, it seems, but not essential.

But despite many constraints on interaction between Cuban and US scientists, biotech has prospered in the nation. In 1980, with a scientifically literate workforce at hand and the biotech boom ready to take off,

Castro's interest in the fledgling industry was sparked by a meeting with Randolph Lee Clark, the former president of the M. D. Anderson Cancer Center in Houston, Texas. Castro accordingly sent six scientists to a lab in Finland to learn how to make interferon from white blood cells. The knowledge gleaned from this project has been ploughed into an industry that developed the first vaccine against meningitis B in 1985, and subsequently a vaccine against *Haemophilus influenzae* type B — the world's first human vaccine to contain a synthetic antigen.

Unfortunately, Cuba's biotech industry has also begun to feel the limitations of the top-down model. Since the early 1990s, when the Soviet Union fell apart and had to cease its generous funding of Castro's ambitions, Cuba's research institutes have become more bureaucratic and politically expedient, which has slowly pushed many of the country's best minds abroad. Meanwhile, Raúl Castro, Cuba's leader for the past two years, has allowed the country's citizens to buy previously prohibited electronic devices — but has not allowed them unfettered access to the Internet.

Still, Raúl Castro is 77 years old; the regime will not last much longer in its current form. And America's cold-war perspective on Cuba does seem to be thawing. In August, the state of Florida overturned a 2004 law that stopped researchers at its universities from using private funds to travel to the island. And President-elect Barack Obama has stated his willingness to talk to his country's enemies.

Obama's administration would be wise to start that conversation with Cuba as soon after his 20 January inauguration as possible. The reasons go well beyond biotech, of course, and the advantages could be substantial for both sides. As the global centre of biotech, and with some of its marine ecosystems contiguous with Cuba's, the United States is surely the country with which cross-fertilization of ideas makes the most sense. ■



begun to believe privately: that to survive and continue to prosper, Western nations need to consider the people of China and the Islamic countries as adversaries. The terrorist attacks of 11 September 2001 strengthened this view, and won Huntington many more converts.

To others, however, Huntington was simply giving academic respectability to the views of ultra-nationalists and religious extremists. The Nobel-prizewinning economist Amartya Sen of Harvard University spoke for many when he argued that classifying humans using a single metric — whether religion or civilization — was not just factually wrong, but also an untested predictor of future conflict. Looking at the historical data, moreover, Malcolm Chalmers of the Royal United Services Institute, a London-based defence think-tank, has found that the proportion of people dying in wars and conflicts has actually declined since the end of the Second World War. And looking at archaeological records of even older conflicts, the economist Samuel Bowles of the Santa Fe Institute in New Mexico suggests that the public-spiritedness and generosity of people today may have come about in part because of a bloodier history of hostility towards outsiders (see *Nature* **456**, 326–327; 2008).

Elsewhere, anthropologist Arjun Appadurai of the New School in New York says that today's tensions and conflicts are characterized less by a 'clash of civilizations', than by larger groups feeling threatened

by smaller ones. This is certainly the case with China's fears on Tibet; India's worries over Pakistan; Israel's dispute with the Palestinians; and the fears among host societies of much smaller immigrant communities. At King's College London, Christoph Meyer and his colleagues in the Department of War Studies have just begun a three-year project that will use this idea to search for ways to provide advanced warning that hostility or antipathy will boil over into violence.

Still, Huntington's clash-of-civilizations idea has had staying power, if only because few, if any, of his critics could match the simplicity and scope of his original concept. Scientists these days often work in highly specialized fields, and tend to be reluctant to propose over-arching theories. Yet policymakers are more likely to respond to people who seem to give the bigger picture, and are able to synthesize it and communicate it clearly.

This is a skill that Huntington had in spades and it poses both a lesson and a dilemma for scientists. Huntington wasn't always right, but his ability to occupy and exploit the space between researchers and its end-users meant that his ideas carried more influence than might otherwise have been the case. ■

**"Few, if any, of Huntington's critics could match the simplicity and scope of his original concept."**

## Cuba's biotech boom

The United States would do well to end restrictions on collaborations with the island nation's scientists.

For a week after Cuba marked the 50th anniversary of its revolution on 1 January, a celebratory 'Caravan of Liberty' carried 50 people, including many university students and scientists, along the triumphal route that Fidel Castro had taken half a century earlier. These people represented the health-care and educational systems of which Cubans are proud, however much they bemoan their other privations behind closed doors. And in no small measure the scientists in the caravan symbolize the foundation of that health-care system in the developing world's most established biotechnology industry, which has grown rapidly even though it eschewed the venture-capital funding model that rich countries consider a prerequisite.

This growth in biotech has been a top-down affair, like most of the changes in Castro's Cuba. At the president's personal instigation, the island nation's half-dozen university centres from before the revolution expanded to at least 35 in the decades that followed. But the growth also owes a great deal to individual researchers' desire to make a contribution. Ask a Cuban scientist why he or she works long hours to earn little more than the US\$20-per-month average wage, and the answer is often that they want to make sick people better, with the kudos of having done so. The venture-capital model's promise of riches is nice, it seems, but not essential.

But despite many constraints on interaction between Cuban and US scientists, biotech has prospered in the nation. In 1980, with a scientifically literate workforce at hand and the biotech boom ready to take off,

Castro's interest in the fledgling industry was sparked by a meeting with Randolph Lee Clark, the former president of the M. D. Anderson Cancer Center in Houston, Texas. Castro accordingly sent six scientists to a lab in Finland to learn how to make interferon from white blood cells. The knowledge gleaned from this project has been ploughed into an industry that developed the first vaccine against meningitis B in 1985, and subsequently a vaccine against *Haemophilus influenzae* type B — the world's first human vaccine to contain a synthetic antigen.

Unfortunately, Cuba's biotech industry has also begun to feel the limitations of the top-down model. Since the early 1990s, when the Soviet Union fell apart and had to cease its generous funding of Castro's ambitions, Cuba's research institutes have become more bureaucratic and politically expedient, which has slowly pushed many of the country's best minds abroad. Meanwhile, Raúl Castro, Cuba's leader for the past two years, has allowed the country's citizens to buy previously prohibited electronic devices — but has not allowed them unfettered access to the Internet.

Still, Raúl Castro is 77 years old; the regime will not last much longer in its current form. And America's cold-war perspective on Cuba does seem to be thawing. In August, the state of Florida overturned a 2004 law that stopped researchers at its universities from using private funds to travel to the island. And President-elect Barack Obama has stated his willingness to talk to his country's enemies.

Obama's administration would be wise to start that conversation with Cuba as soon after his 20 January inauguration as possible. The reasons go well beyond biotech, of course, and the advantages could be substantial for both sides. As the global centre of biotech, and with some of its marine ecosystems contiguous with Cuba's, the United States is surely the country with which cross-fertilization of ideas makes the most sense. ■

## RESEARCH HIGHLIGHTS

## Aloha Mohoidae

*Curr. Biol.* doi:10.1016/j.cub.2008.10.051 (2008)  
Since their discovery by explorer James Cook, five species of Hawaiian bird have been lumped in with Australasian honeyeaters, of the family Meliphagidae, by classifiers. Robert Fleischer and his team at the Smithsonian Institution in Washington DC report that none of the five now-extinct Hawaiian honeyeaters belongs there.

Using DNA sequences from museum specimens, the researchers report that the birds are actually members of the Passerida, the group of well-known songbirds that includes birds such as sparrows, warblers,

wrens and waxwings. Analysis of nuclear DNA indicated that these birds may have diverged from their nearest living mainland ancestor at about the same

time bird-pollinated plants took root on the islands 14 million–17 million years ago. They propose reclassifying them as a unique family, the Mohoidae.



## ENVIRONMENTAL SCIENCE

### It's in the water

*Environ. Sci. Technol.* doi:10.1021/es801845a (2008)  
US drinking water is drugged. Shane Snyder and his colleagues at the Southern Nevada Water Authority in Las Vegas tested the water at 19 treatment facilities across the nation for a selection of compounds that disrupt body function, including pharmaceuticals.

Of the 51 compounds the team tested for, 34 were detected in at least one sample, although none at levels deemed unsafe. The herbicide atrazine and the drugs meprobamate and phenytoin were present in more than half of the samples collected from tap water distributed to homes and businesses.

## CANCER

### Interfering with cancer

*N. Engl. J. Med.* 359, 2641–2650 (2008)  
RNA interference, in which cells use short stretches of RNA to block the translation of genetic recipes into proteins, has been linked to survival in the largest study yet to examine the effect of this phenomenon on human cancers.

A team led by Anil Sood of the University of Texas M. D. Anderson Cancer Center in Houston measured gene expression levels of

Dicer and Drosha, proteins involved in the interference pathway, in 111 invasive ovarian tumours. Women with high levels of both proteins survived for a median of more than 11 years — more than four times longer than those with low levels.

The findings were verified using a second set of 132 ovarian cancer samples. For lung cancer and breast cancer, only Dicer levels affected survival. The findings could lead to the development of better prognostic tests and therapies.

## NEUROBIOLOGY

### Crossing the barrier

*Nature Biotechnol.* doi:10.1038/nbt1515 (2008)

A virus has been found that can shuttle genes across the blood–brain barrier. The discovery raises hopes that gene therapy could one day be used to treat neurodegenerative diseases.

Although a variety of viruses have been harnessed as vectors to carry genes into cells, none has been able to enter the brain from the bloodstream. Brian Kaspar of Nationwide Children's Hospital in Columbus, Ohio, and his co-workers have found that adeno-associated-virus 9 (AAV9) carrying a fluorescent 'reporter' gene enters neurons in the brain and spinal cord when injected intravenously into newborn mouse pups, in

which the blood–brain barrier is not fully formed.

AAV9 also entered the central nervous system of adult mice, but primarily targeted support cells called astrocytes.

## MATHEMATICAL BIOLOGY

### Sensible swarming

*Curr. Biol.* doi:10.1016/j.cub.2008.10.070

Locusts live two lives. Usually solitary, something in them stirs when the density of their fellows reaches a certain threshold. They then change their markings and exhibit an intense desire to swarm together.

Using a mathematical model called percolation theory, Andy Reynolds of Rothamsted Research in Harpenden, UK, and three colleagues explain why this behaviour might have evolved. If a landscape is divided into patches — clumps of plants, say — then each patch has a density of locusts below which it is not worth a predator expending the effort to look for them. So at low densities, locusts are relatively safe. With increasing density, they would become worth hunting, a smorgasbord of crunchy treats allowing well-fed predators to move around the landscape. Before this happens, locusts flip into a highly bunched distribution in which most patches are locust-free and only a few patches are full, so fewer predators are on hand to menace the entire swarm.

## BIOMECHANICS

### Wobble mystery solved

*Proc. R. Soc. A* doi:10.1098/rspa.2008.0367 (2008)  
It's the way people balance themselves rather than the timing of their steps that makes certain bridges wobble, John Macdonald of the University of Bristol, UK, has found.

The Millennium Bridge (pictured below), a footbridge straddling the Thames in London, closed just days after it opened in June 2000 because it was wobbling sideways. It looked as if pedestrians were synchronizing their steps in time with the wobble, and that this was exacerbating the movement.



J. C. ANDERTON

P. GREENHALGH (UKPIX.COM)/ALAMY



## RESEARCH HIGHLIGHTS

## Aloha Mohoidae

*Curr. Biol.* doi:10.1016/j.cub.2008.10.051 (2008)  
Since their discovery by explorer James Cook, five species of Hawaiian bird have been lumped in with Australasian honeyeaters, of the family Meliphagidae, by classifiers. Robert Fleischer and his team at the Smithsonian Institution in Washington DC report that none of the five now-extinct Hawaiian honeyeaters belongs there.

Using DNA sequences from museum specimens, the researchers report that the birds are actually members of the Passerida, the group of well-known songbirds that includes birds such as sparrows, warblers,

wrens and waxwings. Analysis of nuclear DNA indicated that these birds may have diverged from their nearest living mainland ancestor at about the same

time bird-pollinated plants took root on the islands 14 million–17 million years ago. They propose reclassifying them as a unique family, the Mohoidae.



## ENVIRONMENTAL SCIENCE

### It's in the water

*Environ. Sci. Technol.* doi:10.1021/es801845a (2008)  
US drinking water is drugged. Shane Snyder and his colleagues at the Southern Nevada Water Authority in Las Vegas tested the water at 19 treatment facilities across the nation for a selection of compounds that disrupt body function, including pharmaceuticals.

Of the 51 compounds the team tested for, 34 were detected in at least one sample, although none at levels deemed unsafe. The herbicide atrazine and the drugs meprobamate and phenytoin were present in more than half of the samples collected from tap water distributed to homes and businesses.

## CANCER

### Interfering with cancer

*N. Engl. J. Med.* 359, 2641–2650 (2008)  
RNA interference, in which cells use short stretches of RNA to block the translation of genetic recipes into proteins, has been linked to survival in the largest study yet to examine the effect of this phenomenon on human cancers.

A team led by Anil Sood of the University of Texas M. D. Anderson Cancer Center in Houston measured gene expression levels of

Dicer and Drosha, proteins involved in the interference pathway, in 111 invasive ovarian tumours. Women with high levels of both proteins survived for a median of more than 11 years — more than four times longer than those with low levels.

The findings were verified using a second set of 132 ovarian cancer samples. For lung cancer and breast cancer, only Dicer levels affected survival. The findings could lead to the development of better prognostic tests and therapies.

## NEUROBIOLOGY

### Crossing the barrier

*Nature Biotechnol.* doi:10.1038/nbt1515 (2008)

A virus has been found that can shuttle genes across the blood–brain barrier. The discovery raises hopes that gene therapy could one day be used to treat neurodegenerative diseases.

Although a variety of viruses have been harnessed as vectors to carry genes into cells, none has been able to enter the brain from the bloodstream. Brian Kaspar of Nationwide Children's Hospital in Columbus, Ohio, and his co-workers have found that adeno-associated-virus 9 (AAV9) carrying a fluorescent 'reporter' gene enters neurons in the brain and spinal cord when injected intravenously into newborn mouse pups, in

which the blood–brain barrier is not fully formed.

AAV9 also entered the central nervous system of adult mice, but primarily targeted support cells called astrocytes.

## MATHEMATICAL BIOLOGY

### Sensible swarming

*Curr. Biol.* doi:10.1016/j.cub.2008.10.070

Locusts live two lives. Usually solitary, something in them stirs when the density of their fellows reaches a certain threshold. They then change their markings and exhibit an intense desire to swarm together.

Using a mathematical model called percolation theory, Andy Reynolds of Rothamsted Research in Harpenden, UK, and three colleagues explain why this behaviour might have evolved. If a landscape is divided into patches — clumps of plants, say — then each patch has a density of locusts below which it is not worth a predator expending the effort to look for them. So at low densities, locusts are relatively safe. With increasing density, they would become worth hunting, a smorgasbord of crunchy treats allowing well-fed predators to move around the landscape. Before this happens, locusts flip into a highly bunched distribution in which most patches are locust-free and only a few patches are full, so fewer predators are on hand to menace the entire swarm.

## BIOMECHANICS

### Wobble mystery solved

*Proc. R. Soc. A* doi:10.1098/rspa.2008.0367 (2008)  
It's the way people balance themselves rather than the timing of their steps that makes certain bridges wobble, John Macdonald of the University of Bristol, UK, has found.

The Millennium Bridge (pictured below), a footbridge straddling the Thames in London, closed just days after it opened in June 2000 because it was wobbling sideways. It looked as if pedestrians were synchronizing their steps in time with the wobble, and that this was exacerbating the movement.



J. C. ANDERTON

P. GREENHALGH (UKPIX.COM)/ALAMY

## RESEARCH HIGHLIGHTS

## Aloha Mohoidae

*Curr. Biol.* doi:10.1016/j.cub.2008.10.051 (2008)  
Since their discovery by explorer James Cook, five species of Hawaiian bird have been lumped in with Australasian honeyeaters, of the family Meliphagidae, by classifiers. Robert Fleischer and his team at the Smithsonian Institution in Washington DC report that none of the five now-extinct Hawaiian honeyeaters belongs there.

Using DNA sequences from museum specimens, the researchers report that the birds are actually members of the Passerida, the group of well-known songbirds that includes birds such as sparrows, warblers,



wrens and waxwings. Analysis of nuclear DNA indicated that these birds may have diverged from their nearest living mainland ancestor at about the same

time bird-pollinated plants took root on the islands 14 million–17 million years ago. They propose reclassifying them as a unique family, the Mohoidae.

## ENVIRONMENTAL SCIENCE

### It's in the water

*Environ. Sci. Technol.* doi:10.1021/es801845a (2008)  
US drinking water is drugged. Shane Snyder and his colleagues at the Southern Nevada Water Authority in Las Vegas tested the water at 19 treatment facilities across the nation for a selection of compounds that disrupt body function, including pharmaceuticals.

Of the 51 compounds the team tested for, 34 were detected in at least one sample, although none at levels deemed unsafe. The herbicide atrazine and the drugs meprobamate and phenytoin were present in more than half of the samples collected from tap water distributed to homes and businesses.

## CANCER

### Interfering with cancer

*N. Engl. J. Med.* 359, 2641–2650 (2008)  
RNA interference, in which cells use short stretches of RNA to block the translation of genetic recipes into proteins, has been linked to survival in the largest study yet to examine the effect of this phenomenon on human cancers.

A team led by Anil Sood of the University of Texas M. D. Anderson Cancer Center in Houston measured gene expression levels of

Dicer and Drosha, proteins involved in the interference pathway, in 111 invasive ovarian tumours. Women with high levels of both proteins survived for a median of more than 11 years — more than four times longer than those with low levels.

The findings were verified using a second set of 132 ovarian cancer samples. For lung cancer and breast cancer, only Dicer levels affected survival. The findings could lead to the development of better prognostic tests and therapies.

## NEUROBIOLOGY

### Crossing the barrier

*Nature Biotechnol.* doi:10.1038/nbt1515 (2008)

A virus has been found that can shuttle genes across the blood–brain barrier. The discovery raises hopes that gene therapy could one day be used to treat neurodegenerative diseases.

Although a variety of viruses have been harnessed as vectors to carry genes into cells, none has been able to enter the brain from the bloodstream. Brian Kaspar of Nationwide Children's Hospital in Columbus, Ohio, and his co-workers have found that adeno-associated-virus 9 (AAV9) carrying a fluorescent 'reporter' gene enters neurons in the brain and spinal cord when injected intravenously into newborn mouse pups, in

which the blood–brain barrier is not fully formed.

AAV9 also entered the central nervous system of adult mice, but primarily targeted support cells called astrocytes.

## MATHEMATICAL BIOLOGY

### Sensible swarming

*Curr. Biol.* doi:10.1016/j.cub.2008.10.070

Locusts live two lives. Usually solitary, something in them stirs when the density of their fellows reaches a certain threshold. They then change their markings and exhibit an intense desire to swarm together.

Using a mathematical model called percolation theory, Andy Reynolds of Rothamsted Research in Harpenden, UK, and three colleagues explain why this behaviour might have evolved. If a landscape is divided into patches — clumps of plants, say — then each patch has a density of locusts below which it is not worth a predator expending the effort to look for them. So at low densities, locusts are relatively safe. With increasing density, they would become worth hunting, a smorgasbord of crunchy treats allowing well-fed predators to move around the landscape. Before this happens, locusts flip into a highly bunched distribution in which most patches are locust-free and only a few patches are full, so fewer predators are on hand to menace the entire swarm.

## BIOMECHANICS

### Wobble mystery solved

*Proc. R. Soc. A* doi:10.1098/rspa.2008.0367 (2008)  
It's the way people balance themselves rather than the timing of their steps that makes certain bridges wobble, John Macdonald of the University of Bristol, UK, has found.

The Millennium Bridge (pictured below), a footbridge straddling the Thames in London, closed just days after it opened in June 2000 because it was wobbling sideways. It looked as if pedestrians were synchronizing their steps in time with the wobble, and that this was exacerbating the movement.



J. C. ANDERTON

P. GREENHALGH (UKPIX.COM)/ALAMY



## RESEARCH HIGHLIGHTS

## Aloha Mohoidae

*Curr. Biol.* doi:10.1016/j.cub.2008.10.051 (2008)  
Since their discovery by explorer James Cook, five species of Hawaiian bird have been lumped in with Australasian honeyeaters, of the family Meliphagidae, by classifiers. Robert Fleischer and his team at the Smithsonian Institution in Washington DC report that none of the five now-extinct Hawaiian honeyeaters belongs there.

Using DNA sequences from museum specimens, the researchers report that the birds are actually members of the Passerida, the group of well-known songbirds that includes birds such as sparrows, warblers,

wrens and waxwings. Analysis of nuclear DNA indicated that these birds may have diverged from their nearest living mainland ancestor at about the same

time bird-pollinated plants took root on the islands 14 million–17 million years ago. They propose reclassifying them as a unique family, the Mohoidae.



## ENVIRONMENTAL SCIENCE

### It's in the water

*Environ. Sci. Technol.* doi:10.1021/es801845a (2008)  
US drinking water is drugged. Shane Snyder and his colleagues at the Southern Nevada Water Authority in Las Vegas tested the water at 19 treatment facilities across the nation for a selection of compounds that disrupt body function, including pharmaceuticals.

Of the 51 compounds the team tested for, 34 were detected in at least one sample, although none at levels deemed unsafe. The herbicide atrazine and the drugs meprobamate and phenytoin were present in more than half of the samples collected from tap water distributed to homes and businesses.

## CANCER

### Interfering with cancer

*N. Engl. J. Med.* 359, 2641–2650 (2008)  
RNA interference, in which cells use short stretches of RNA to block the translation of genetic recipes into proteins, has been linked to survival in the largest study yet to examine the effect of this phenomenon on human cancers.

A team led by Anil Sood of the University of Texas M. D. Anderson Cancer Center in Houston measured gene expression levels of

Dicer and Drosha, proteins involved in the interference pathway, in 111 invasive ovarian tumours. Women with high levels of both proteins survived for a median of more than 11 years — more than four times longer than those with low levels.

The findings were verified using a second set of 132 ovarian cancer samples. For lung cancer and breast cancer, only Dicer levels affected survival. The findings could lead to the development of better prognostic tests and therapies.

## NEUROBIOLOGY

### Crossing the barrier

*Nature Biotechnol.* doi:10.1038/nbt1515 (2008)

A virus has been found that can shuttle genes across the blood–brain barrier. The discovery raises hopes that gene therapy could one day be used to treat neurodegenerative diseases.

Although a variety of viruses have been harnessed as vectors to carry genes into cells, none has been able to enter the brain from the bloodstream. Brian Kaspar of Nationwide Children's Hospital in Columbus, Ohio, and his co-workers have found that adeno-associated-virus 9 (AAV9) carrying a fluorescent 'reporter' gene enters neurons in the brain and spinal cord when injected intravenously into newborn mouse pups, in

which the blood–brain barrier is not fully formed.

AAV9 also entered the central nervous system of adult mice, but primarily targeted support cells called astrocytes.

## MATHEMATICAL BIOLOGY

### Sensible swarming

*Curr. Biol.* doi:10.1016/j.cub.2008.10.070

Locusts live two lives. Usually solitary, something in them stirs when the density of their fellows reaches a certain threshold. They then change their markings and exhibit an intense desire to swarm together.

Using a mathematical model called percolation theory, Andy Reynolds of Rothamsted Research in Harpenden, UK, and three colleagues explain why this behaviour might have evolved. If a landscape is divided into patches — clumps of plants, say — then each patch has a density of locusts below which it is not worth a predator expending the effort to look for them. So at low densities, locusts are relatively safe. With increasing density, they would become worth hunting, a smorgasbord of crunchy treats allowing well-fed predators to move around the landscape. Before this happens, locusts flip into a highly bunched distribution in which most patches are locust-free and only a few patches are full, so fewer predators are on hand to menace the entire swarm.

## BIOMECHANICS

### Wobble mystery solved

*Proc. R. Soc. A* doi:10.1098/rspa.2008.0367 (2008)  
It's the way people balance themselves rather than the timing of their steps that makes certain bridges wobble, John Macdonald of the University of Bristol, UK, has found.

The Millennium Bridge (pictured below), a footbridge straddling the Thames in London, closed just days after it opened in June 2000 because it was wobbling sideways. It looked as if pedestrians were synchronizing their steps in time with the wobble, and that this was exacerbating the movement.



J. C. ANDERTON

P. GREENHALGH (UKPIX.COM)/ALAMY

## RESEARCH HIGHLIGHTS

## Aloha Mohoidae

*Curr. Biol.* doi:10.1016/j.cub.2008.10.051 (2008)  
Since their discovery by explorer James Cook, five species of Hawaiian bird have been lumped in with Australasian honeyeaters, of the family Meliphagidae, by classifiers. Robert Fleischer and his team at the Smithsonian Institution in Washington DC report that none of the five now-extinct Hawaiian honeyeaters belongs there.

Using DNA sequences from museum specimens, the researchers report that the birds are actually members of the Passerida, the group of well-known songbirds that includes birds such as sparrows, warblers,

wrens and waxwings. Analysis of nuclear DNA indicated that these birds may have diverged from their nearest living mainland ancestor at about the same

time bird-pollinated plants took root on the islands 14 million–17 million years ago. They propose reclassifying them as a unique family, the Mohoidae.



## ENVIRONMENTAL SCIENCE

### It's in the water

*Environ. Sci. Technol.* doi:10.1021/es801845a (2008)  
US drinking water is drugged. Shane Snyder and his colleagues at the Southern Nevada Water Authority in Las Vegas tested the water at 19 treatment facilities across the nation for a selection of compounds that disrupt body function, including pharmaceuticals.

Of the 51 compounds the team tested for, 34 were detected in at least one sample, although none at levels deemed unsafe. The herbicide atrazine and the drugs meprobamate and phenytoin were present in more than half of the samples collected from tap water distributed to homes and businesses.

## CANCER

### Interfering with cancer

*N. Engl. J. Med.* 359, 2641–2650 (2008)  
RNA interference, in which cells use short stretches of RNA to block the translation of genetic recipes into proteins, has been linked to survival in the largest study yet to examine the effect of this phenomenon on human cancers.

A team led by Anil Sood of the University of Texas M. D. Anderson Cancer Center in Houston measured gene expression levels of

Dicer and Drosha, proteins involved in the interference pathway, in 111 invasive ovarian tumours. Women with high levels of both proteins survived for a median of more than 11 years — more than four times longer than those with low levels.

The findings were verified using a second set of 132 ovarian cancer samples. For lung cancer and breast cancer, only Dicer levels affected survival. The findings could lead to the development of better prognostic tests and therapies.

## NEUROBIOLOGY

### Crossing the barrier

*Nature Biotechnol.* doi:10.1038/nbt1515 (2008)

A virus has been found that can shuttle genes across the blood–brain barrier. The discovery raises hopes that gene therapy could one day be used to treat neurodegenerative diseases.

Although a variety of viruses have been harnessed as vectors to carry genes into cells, none has been able to enter the brain from the bloodstream. Brian Kaspar of Nationwide Children's Hospital in Columbus, Ohio, and his co-workers have found that adeno-associated-virus 9 (AAV9) carrying a fluorescent 'reporter' gene enters neurons in the brain and spinal cord when injected intravenously into newborn mouse pups, in

which the blood–brain barrier is not fully formed.

AAV9 also entered the central nervous system of adult mice, but primarily targeted support cells called astrocytes.

## MATHEMATICAL BIOLOGY

### Sensible swarming

*Curr. Biol.* doi:10.1016/j.cub.2008.10.070

Locusts live two lives. Usually solitary, something in them stirs when the density of their fellows reaches a certain threshold. They then change their markings and exhibit an intense desire to swarm together.

Using a mathematical model called percolation theory, Andy Reynolds of Rothamsted Research in Harpenden, UK, and three colleagues explain why this behaviour might have evolved. If a landscape is divided into patches — clumps of plants, say — then each patch has a density of locusts below which it is not worth a predator expending the effort to look for them. So at low densities, locusts are relatively safe. With increasing density, they would become worth hunting, a smorgasbord of crunchy treats allowing well-fed predators to move around the landscape. Before this happens, locusts flip into a highly bunched distribution in which most patches are locust-free and only a few patches are full, so fewer predators are on hand to menace the entire swarm.

## BIOMECHANICS

### Wobble mystery solved

*Proc. R. Soc. A* doi:10.1098/rspa.2008.0367 (2008)  
It's the way people balance themselves rather than the timing of their steps that makes certain bridges wobble, John Macdonald of the University of Bristol, UK, has found.

The Millennium Bridge (pictured below), a footbridge straddling the Thames in London, closed just days after it opened in June 2000 because it was wobbling sideways. It looked as if pedestrians were synchronizing their steps in time with the wobble, and that this was exacerbating the movement.



J. C. ANDERTON

P. GREENHALGH (UKPIX.COM)/ALAMY



## RESEARCH HIGHLIGHTS

**Aloha  
Mohoidae**

*Curr. Biol.* doi:10.1016/j.cub.2008.10.051 (2008)  
Since their discovery by explorer James Cook, five species of Hawaiian bird have been lumped in with Australasian honeyeaters, of the family Meliphagidae, by classifiers. Robert Fleischer and his team at the Smithsonian Institution in Washington DC report that none of the five now-extinct Hawaiian honeyeaters belongs there.

Using DNA sequences from museum specimens, the researchers report that the birds are actually members of the Passerida, the group of well-known songbirds that includes birds such as sparrows, warblers,



wrens and waxwings. Analysis of nuclear DNA indicated that these birds may have diverged from their nearest living mainland ancestor at about the same

time bird-pollinated plants took root on the islands 14 million–17 million years ago. They propose reclassifying them as a unique family, the Mohoidae.

**ENVIRONMENTAL SCIENCE****It's in the water**

*Environ. Sci. Technol.* doi:10.1021/es801845a (2008)  
US drinking water is drugged. Shane Snyder and his colleagues at the Southern Nevada Water Authority in Las Vegas tested the water at 19 treatment facilities across the nation for a selection of compounds that disrupt body function, including pharmaceuticals.

Of the 51 compounds the team tested for, 34 were detected in at least one sample, although none at levels deemed unsafe. The herbicide atrazine and the drugs meprobamate and phenytoin were present in more than half of the samples collected from tap water distributed to homes and businesses.

**CANCER****Interfering with cancer**

*N. Engl. J. Med.* 359, 2641–2650 (2008)  
RNA interference, in which cells use short stretches of RNA to block the translation of genetic recipes into proteins, has been linked to survival in the largest study yet to examine the effect of this phenomenon on human cancers.

A team led by Anil Sood of the University of Texas M. D. Anderson Cancer Center in Houston measured gene expression levels of

Dicer and Drosha, proteins involved in the interference pathway, in 111 invasive ovarian tumours. Women with high levels of both proteins survived for a median of more than 11 years — more than four times longer than those with low levels.

The findings were verified using a second set of 132 ovarian cancer samples. For lung cancer and breast cancer, only Dicer levels affected survival. The findings could lead to the development of better prognostic tests and therapies.

**NEUROBIOLOGY****Crossing the barrier**

*Nature Biotechnol.* doi:10.1038/nbt1515 (2008)

A virus has been found that can shuttle genes across the blood–brain barrier. The discovery raises hopes that gene therapy could one day be used to treat neurodegenerative diseases.

Although a variety of viruses have been harnessed as vectors to carry genes into cells, none has been able to enter the brain from the bloodstream. Brian Kaspar of Nationwide Children's Hospital in Columbus, Ohio, and his co-workers have found that adeno-associated-virus 9 (AAV9) carrying a fluorescent 'reporter' gene enters neurons in the brain and spinal cord when injected intravenously into newborn mouse pups, in

which the blood–brain barrier is not fully formed.

AAV9 also entered the central nervous system of adult mice, but primarily targeted support cells called astrocytes.

**MATHEMATICAL BIOLOGY****Sensible swarming**

*Curr. Biol.* doi:10.1016/j.cub.2008.10.070

Locusts live two lives. Usually solitary, something in them stirs when the density of their fellows reaches a certain threshold. They then change their markings and exhibit an intense desire to swarm together.

Using a mathematical model called percolation theory, Andy Reynolds of Rothamsted Research in Harpenden, UK, and three colleagues explain why this behaviour might have evolved. If a landscape is divided into patches — clumps of plants, say — then each patch has a density of locusts below which it is not worth a predator expending the effort to look for them. So at low densities, locusts are relatively safe. With increasing density, they would become worth hunting, a smorgasbord of crunchy treats allowing well-fed predators to move around the landscape. Before this happens, locusts flip into a highly bunched distribution in which most patches are locust-free and only a few patches are full, so fewer predators are on hand to menace the entire swarm.

**BIOMECHANICS****Wobble mystery solved**

*Proc. R. Soc. A* doi:10.1098/rspa.2008.0367 (2008)  
It's the way people balance themselves rather than the timing of their steps that makes certain bridges wobble, John Macdonald of the University of Bristol, UK, has found.

The Millennium Bridge (pictured below), a footbridge straddling the Thames in London, closed just days after it opened in June 2000 because it was wobbling sideways. It looked as if pedestrians were synchronizing their steps in time with the wobble, and that this was exacerbating the movement.



J. C. ANDERTON

P. GREENHALGH (UKPIX.COM)/ALAMY

But Macdonald's model says that wasn't what was happening at all. By looking at the biomechanics of how humans balance, Macdonald has revealed the effects of the adjustments people make to keep their balance, by sticking one foot further out to the left or right. These add energy to the bridge's natural wobble. Once a critical number of people start trying to balance in this way, that extra energy becomes significant, and increases the bridge's sway.

## GEOCHEMISTRY

### Oh molybdenum!

*Nature Geosci.* doi:10.1038/ngeo366 (2008)

A lack of the silvery metal molybdenum limits nitrogen fixation in tropical soils. The finding comes from the work of Lars Hedin at Princeton University in New Jersey and his colleagues, and calls into question the role phosphorus was thought to have in the process.

Hedin and his team looked at the activity of nitrogenase — the enzyme that converts atmospheric nitrogen into ammonium, which plants can use — in the top layer of soil in a tropical forest floor in Panama. The plots had been given fertilizers rich in nitrogen, phosphorus or micronutrients including molybdenum over a period of seven years. The researchers also measured the short-term effects of molybdenum and phosphorus on nitrogenase activity.

Results from both experiments suggest that molybdenum alone can trigger nitrogenase activity, and that contamination by this element might underlie the efficacy of commercial phosphorus fertilizers, Hedin says.

## MATERIALS SCIENCE

### Hitting a nerve gas

*Angew. Chem. Int. Edn* doi:10.1002/anie.200802932 (2008)

Protective clothing can provide a first line of defence against chemical-warfare agents such as mustard gas, but the relief is limited if the perilous substance remains on the fabric.

Valérie Keller of Louis Pasteur University in Strasbourg, France, and her colleagues have a solution. They show that cotton textiles coated by dipping or spraying with photocatalytic particles can burn up simulants of blistering and nerve agents within minutes when irradiated with artificial solar-like light. The particles consist of titanate nanotubes encrusted with crystals of tungsten trioxide, and their light-induced degradation of organic molecules resembles that of self-cleaning tiles and glass coated with titanium dioxide.

## GENOMICS

### 25 to life

*Proc. Natl Acad. Sci. USA* 105, 20404–20409 (2008)

Edging their way towards the construction of a synthetic organism, Daniel Gibson at the J. Craig Venter Institute in Rockville, Maryland, and his colleagues have performed a one-step assembly of an entire bacterial genome inside yeast.

In early 2008, the team reported that they had manufactured the 592-kilobase genome of *Mycoplasma genitalium* using several steps to sew together chemically synthesized DNA fragments (D. G. Gibson *et al. Science* 319, 1215–1220; 2008). In the new simplified version, they show that yeast can take up 25 DNA fragments and splice them together correctly on its own. The technique could make it easier to assemble 'designer' genomes.



B. MILLER

## ZOOLOGY

### Breathing deep

*Proc. R. Soc. B* doi:10.1098/rspb.2008.1489 (2008)

Antarctic sea spiders (pictured above), some up to 90 centimetres long, are giants compared with their 1–10-millimetre-long tropical cousins. Researchers have had a simple hypothesis for this 'polar gigantism', but results from a research team co-led by Arthur Woods of the University of Montana, Missoula, have complicated the picture.

Polar water has a higher level of dissolved oxygen, and cold-water arthropods have lower metabolic rates than their warm-water counterparts. The big spiders were thus expected to perform worse in low-oxygen environments.

Woods's team repeatedly flipped over spiders from 12 species that encompassed the small, medium and large varieties for an hour each, to see how long they took to right themselves. Overall, the giants were no more sluggish than the tiny ones. This result suggests that scientists must search for other possible evolutionary or ecological mechanisms for polar gigantism.

## JOURNAL CLUB

Stephen Curry, Imperial College, London

### A crystallographer takes a jaunt into immunology.

Although I spend most of my time exploring a landscape formed by atoms and bonds, I know it is healthy to make occasional journeys into less familiar territories, and I was intrigued to spot a paper on the curious interplay between infection and immunity in cattle with foot-and-mouth disease virus (FMDV).

FMDV, a highly contagious pathogen that can cause lameness, low weight and decreased milk production, is a scourge of agricultural livestock around the world. Although the acute phase of infection is rarely fatal, infection may persist in animals that have apparently recovered, creating a viral reservoir that some fear could contribute to the spread of disease. Nicholas Juleff and colleagues, from the United Kingdom's Institute for Animal Health, report a fascinating discovery that may have unlocked the secret of FMDV persistence.

They used an array of molecular techniques to search for traces of virus in tissues from the mouths and throats of infected cattle (N. Juleff *et al. PLoS ONE* 3, e3434; 2008). In a carefully controlled study, they found evidence of intact, non-replicating virus particles trapped by immune cells called follicular dendritic cells within the germinal centres of lymph nodes. Strikingly, virus was present for at least 38 days post infection, even though it was undetectable in surrounding tissues.

The retention of intact virus within germinal centres is likely to have a role in stimulating the long-lasting immune response of white blood cells that is characteristic of viral infections (but not current vaccine preparations) and echoes a pattern previously seen for HIV infection. The authors suggest that this capture may inadvertently also be responsible for preserving intact viruses capable of infecting susceptible cells as they come into contact with germinal centres. A causal relationship has yet to be firmly established but the paper illuminates a clear pathway by which to check this out.

Discuss this paper at <http://blogs.nature.com/nature/journalclub>



But Macdonald's model says that wasn't what was happening at all. By looking at the biomechanics of how humans balance, Macdonald has revealed the effects of the adjustments people make to keep their balance, by sticking one foot further out to the left or right. These add energy to the bridge's natural wobble. Once a critical number of people start trying to balance in this way, that extra energy becomes significant, and increases the bridge's sway.

## GEOCHEMISTRY

### Oh molybdenum!

*Nature Geosci.* doi:10.1038/ngeo366 (2008)

A lack of the silvery metal molybdenum limits nitrogen fixation in tropical soils. The finding comes from the work of Lars Hedin at Princeton University in New Jersey and his colleagues, and calls into question the role phosphorus was thought to have in the process.

Hedin and his team looked at the activity of nitrogenase — the enzyme that converts atmospheric nitrogen into ammonium, which plants can use — in the top layer of soil in a tropical forest floor in Panama. The plots had been given fertilizers rich in nitrogen, phosphorus or micronutrients including molybdenum over a period of seven years. The researchers also measured the short-term effects of molybdenum and phosphorus on nitrogenase activity.

Results from both experiments suggest that molybdenum alone can trigger nitrogenase activity, and that contamination by this element might underlie the efficacy of commercial phosphorus fertilizers, Hedin says.

## MATERIALS SCIENCE

### Hitting a nerve gas

*Angew. Chem. Int. Edn* doi:10.1002/anie.200802932 (2008)

Protective clothing can provide a first line of defence against chemical-warfare agents such as mustard gas, but the relief is limited if the perilous substance remains on the fabric.

Valérie Keller of Louis Pasteur University in Strasbourg, France, and her colleagues have a solution. They show that cotton textiles coated by dipping or spraying with photocatalytic particles can burn up simulants of blistering and nerve agents within minutes when irradiated with artificial solar-like light. The particles consist of titanate nanotubes encrusted with crystals of tungsten trioxide, and their light-induced degradation of organic molecules resembles that of self-cleaning tiles and glass coated with titanium dioxide.

## GENOMICS

### 25 to life

*Proc. Natl Acad. Sci. USA* 105, 20404–20409 (2008)

Edging their way towards the construction of a synthetic organism, Daniel Gibson at the J. Craig Venter Institute in Rockville, Maryland, and his colleagues have performed a one-step assembly of an entire bacterial genome inside yeast.

In early 2008, the team reported that they had manufactured the 592-kilobase genome of *Mycoplasma genitalium* using several steps to sew together chemically synthesized DNA fragments (D. G. Gibson *et al. Science* 319, 1215–1220; 2008). In the new simplified version, they show that yeast can take up 25 DNA fragments and splice them together correctly on its own. The technique could make it easier to assemble 'designer' genomes.



B. MILLER

## ZOOLOGY

### Breathing deep

*Proc. R. Soc. B* doi:10.1098/rspb.2008.1489 (2008)

Antarctic sea spiders (pictured above), some up to 90 centimetres long, are giants compared with their 1–10-millimetre-long tropical cousins. Researchers have had a simple hypothesis for this 'polar gigantism', but results from a research team co-led by Arthur Woods of the University of Montana, Missoula, have complicated the picture.

Polar water has a higher level of dissolved oxygen, and cold-water arthropods have lower metabolic rates than their warm-water counterparts. The big spiders were thus expected to perform worse in low-oxygen environments.

Woods's team repeatedly flipped over spiders from 12 species that encompassed the small, medium and large varieties for an hour each, to see how long they took to right themselves. Overall, the giants were no more sluggish than the tiny ones. This result suggests that scientists must search for other possible evolutionary or ecological mechanisms for polar gigantism.

## JOURNAL CLUB

Stephen Curry, Imperial College, London

### A crystallographer takes a jaunt into immunology.

Although I spend most of my time exploring a landscape formed by atoms and bonds, I know it is healthy to make occasional journeys into less familiar territories, and I was intrigued to spot a paper on the curious interplay between infection and immunity in cattle with foot-and-mouth disease virus (FMDV).

FMDV, a highly contagious pathogen that can cause lameness, low weight and decreased milk production, is a scourge of agricultural livestock around the world. Although the acute phase of infection is rarely fatal, infection may persist in animals that have apparently recovered, creating a viral reservoir that some fear could contribute to the spread of disease. Nicholas Juleff and colleagues, from the United Kingdom's Institute for Animal Health, report a fascinating discovery that may have unlocked the secret of FMDV persistence.

They used an array of molecular techniques to search for traces of virus in tissues from the mouths and throats of infected cattle (N. Juleff *et al. PLoS ONE* 3, e3434; 2008). In a carefully controlled study, they found evidence of intact, non-replicating virus particles trapped by immune cells called follicular dendritic cells within the germinal centres of lymph nodes. Strikingly, virus was present for at least 38 days post infection, even though it was undetectable in surrounding tissues.

The retention of intact virus within germinal centres is likely to have a role in stimulating the long-lasting immune response of white blood cells that is characteristic of viral infections (but not current vaccine preparations) and echoes a pattern previously seen for HIV infection. The authors suggest that this capture may inadvertently also be responsible for preserving intact viruses capable of infecting susceptible cells as they come into contact with germinal centres. A causal relationship has yet to be firmly established but the paper illuminates a clear pathway by which to check this out.

Discuss this paper at <http://blogs.nature.com/nature/journalclub>

But Macdonald's model says that wasn't what was happening at all. By looking at the biomechanics of how humans balance, Macdonald has revealed the effects of the adjustments people make to keep their balance, by sticking one foot further out to the left or right. These add energy to the bridge's natural wobble. Once a critical number of people start trying to balance in this way, that extra energy becomes significant, and increases the bridge's sway.

## GEOCHEMISTRY

### Oh molybdenum!

*Nature Geosci.* doi:10.1038/ngeo366 (2008)

A lack of the silvery metal molybdenum limits nitrogen fixation in tropical soils. The finding comes from the work of Lars Hedin at Princeton University in New Jersey and his colleagues, and calls into question the role phosphorus was thought to have in the process.

Hedin and his team looked at the activity of nitrogenase — the enzyme that converts atmospheric nitrogen into ammonium, which plants can use — in the top layer of soil in a tropical forest floor in Panama. The plots had been given fertilizers rich in nitrogen, phosphorus or micronutrients including molybdenum over a period of seven years. The researchers also measured the short-term effects of molybdenum and phosphorus on nitrogenase activity.

Results from both experiments suggest that molybdenum alone can trigger nitrogenase activity, and that contamination by this element might underlie the efficacy of commercial phosphorus fertilizers, Hedin says.

## MATERIALS SCIENCE

### Hitting a nerve gas

*Angew. Chem. Int. Edn* doi:10.1002/anie.200802932 (2008)

Protective clothing can provide a first line of defence against chemical-warfare agents such as mustard gas, but the relief is limited if the perilous substance remains on the fabric.

Valérie Keller of Louis Pasteur University in Strasbourg, France, and her colleagues have a solution. They show that cotton textiles coated by dipping or spraying with photocatalytic particles can burn up simulants of blistering and nerve agents within minutes when irradiated with artificial solar-like light. The particles consist of titanate nanotubes encrusted with crystals of tungsten trioxide, and their light-induced degradation of organic molecules resembles that of self-cleaning tiles and glass coated with titanium dioxide.

## GENOMICS

### 25 to life

*Proc. Natl Acad. Sci. USA* 105, 20404–20409 (2008)

Edging their way towards the construction of a synthetic organism, Daniel Gibson at the J. Craig Venter Institute in Rockville, Maryland, and his colleagues have performed a one-step assembly of an entire bacterial genome inside yeast.

In early 2008, the team reported that they had manufactured the 592-kilobase genome of *Mycoplasma genitalium* using several steps to sew together chemically synthesized DNA fragments (D. G. Gibson *et al. Science* 319, 1215–1220; 2008). In the new simplified version, they show that yeast can take up 25 DNA fragments and splice them together correctly on its own. The technique could make it easier to assemble 'designer' genomes.



B. MILLER

## ZOOLOGY

### Breathing deep

*Proc. R. Soc. B* doi:10.1098/rspb.2008.1489 (2008)

Antarctic sea spiders (pictured above), some up to 90 centimetres long, are giants compared with their 1–10-millimetre-long tropical cousins. Researchers have had a simple hypothesis for this 'polar gigantism', but results from a research team co-led by Arthur Woods of the University of Montana, Missoula, have complicated the picture.

Polar water has a higher level of dissolved oxygen, and cold-water arthropods have lower metabolic rates than their warm-water counterparts. The big spiders were thus expected to perform worse in low-oxygen environments.

Woods's team repeatedly flipped over spiders from 12 species that encompassed the small, medium and large varieties for an hour each, to see how long they took to right themselves. Overall, the giants were no more sluggish than the tiny ones. This result suggests that scientists must search for other possible evolutionary or ecological mechanisms for polar gigantism.

## JOURNAL CLUB

Stephen Curry, Imperial College, London

### A crystallographer takes a jaunt into immunology.

Although I spend most of my time exploring a landscape formed by atoms and bonds, I know it is healthy to make occasional journeys into less familiar territories, and I was intrigued to spot a paper on the curious interplay between infection and immunity in cattle with foot-and-mouth disease virus (FMDV).

FMDV, a highly contagious pathogen that can cause lameness, low weight and decreased milk production, is a scourge of agricultural livestock around the world. Although the acute phase of infection is rarely fatal, infection may persist in animals that have apparently recovered, creating a viral reservoir that some fear could contribute to the spread of disease. Nicholas Juleff and colleagues, from the United Kingdom's Institute for Animal Health, report a fascinating discovery that may have unlocked the secret of FMDV persistence.

They used an array of molecular techniques to search for traces of virus in tissues from the mouths and throats of infected cattle (N. Juleff *et al. PLoS ONE* 3, e3434; 2008). In a carefully controlled study, they found evidence of intact, non-replicating virus particles trapped by immune cells called follicular dendritic cells within the germinal centres of lymph nodes. Strikingly, virus was present for at least 38 days post infection, even though it was undetectable in surrounding tissues.

The retention of intact virus within germinal centres is likely to have a role in stimulating the long-lasting immune response of white blood cells that is characteristic of viral infections (but not current vaccine preparations) and echoes a pattern previously seen for HIV infection. The authors suggest that this capture may inadvertently also be responsible for preserving intact viruses capable of infecting susceptible cells as they come into contact with germinal centres. A causal relationship has yet to be firmly established but the paper illuminates a clear pathway by which to check this out.

Discuss this paper at <http://blogs.nature.com/nature/journalclub>



But Macdonald's model says that wasn't what was happening at all. By looking at the biomechanics of how humans balance, Macdonald has revealed the effects of the adjustments people make to keep their balance, by sticking one foot further out to the left or right. These add energy to the bridge's natural wobble. Once a critical number of people start trying to balance in this way, that extra energy becomes significant, and increases the bridge's sway.

## GEOCHEMISTRY

### Oh molybdenum!

*Nature Geosci.* doi:10.1038/ngeo366 (2008)

A lack of the silvery metal molybdenum limits nitrogen fixation in tropical soils. The finding comes from the work of Lars Hedin at Princeton University in New Jersey and his colleagues, and calls into question the role phosphorus was thought to have in the process.

Hedin and his team looked at the activity of nitrogenase — the enzyme that converts atmospheric nitrogen into ammonium, which plants can use — in the top layer of soil in a tropical forest floor in Panama. The plots had been given fertilizers rich in nitrogen, phosphorus or micronutrients including molybdenum over a period of seven years. The researchers also measured the short-term effects of molybdenum and phosphorus on nitrogenase activity.

Results from both experiments suggest that molybdenum alone can trigger nitrogenase activity, and that contamination by this element might underlie the efficacy of commercial phosphorus fertilizers, Hedin says.

## MATERIALS SCIENCE

### Hitting a nerve gas

*Angew. Chem. Int. Edn* doi:10.1002/anie.200802932 (2008)

Protective clothing can provide a first line of defence against chemical-warfare agents such as mustard gas, but the relief is limited if the perilous substance remains on the fabric.

Valérie Keller of Louis Pasteur University in Strasbourg, France, and her colleagues have a solution. They show that cotton textiles coated by dipping or spraying with photocatalytic particles can burn up simulants of blistering and nerve agents within minutes when irradiated with artificial solar-like light. The particles consist of titanate nanotubes encrusted with crystals of tungsten trioxide, and their light-induced degradation of organic molecules resembles that of self-cleaning tiles and glass coated with titanium dioxide.

## GENOMICS

### 25 to life

*Proc. Natl Acad. Sci. USA* 105, 20404–20409 (2008)

Edging their way towards the construction of a synthetic organism, Daniel Gibson at the J. Craig Venter Institute in Rockville, Maryland, and his colleagues have performed a one-step assembly of an entire bacterial genome inside yeast.

In early 2008, the team reported that they had manufactured the 592-kilobase genome of *Mycoplasma genitalium* using several steps to sew together chemically synthesized DNA fragments (D. G. Gibson *et al. Science* 319, 1215–1220; 2008). In the new simplified version, they show that yeast can take up 25 DNA fragments and splice them together correctly on its own. The technique could make it easier to assemble 'designer' genomes.



B. MILLER

## ZOOLOGY

### Breathing deep

*Proc. R. Soc. B* doi:10.1098/rspb.2008.1489 (2008)

Antarctic sea spiders (pictured above), some up to 90 centimetres long, are giants compared with their 1–10-millimetre-long tropical cousins. Researchers have had a simple hypothesis for this 'polar gigantism', but results from a research team co-led by Arthur Woods of the University of Montana, Missoula, have complicated the picture.

Polar water has a higher level of dissolved oxygen, and cold-water arthropods have lower metabolic rates than their warm-water counterparts. The big spiders were thus expected to perform worse in low-oxygen environments.

Woods's team repeatedly flipped over spiders from 12 species that encompassed the small, medium and large varieties for an hour each, to see how long they took to right themselves. Overall, the giants were no more sluggish than the tiny ones. This result suggests that scientists must search for other possible evolutionary or ecological mechanisms for polar gigantism.

## JOURNAL CLUB

Stephen Curry, Imperial College, London

### A crystallographer takes a jaunt into immunology.

Although I spend most of my time exploring a landscape formed by atoms and bonds, I know it is healthy to make occasional journeys into less familiar territories, and I was intrigued to spot a paper on the curious interplay between infection and immunity in cattle with foot-and-mouth disease virus (FMDV).

FMDV, a highly contagious pathogen that can cause lameness, low weight and decreased milk production, is a scourge of agricultural livestock around the world. Although the acute phase of infection is rarely fatal, infection may persist in animals that have apparently recovered, creating a viral reservoir that some fear could contribute to the spread of disease. Nicholas Juleff and colleagues, from the United Kingdom's Institute for Animal Health, report a fascinating discovery that may have unlocked the secret of FMDV persistence.

They used an array of molecular techniques to search for traces of virus in tissues from the mouths and throats of infected cattle (N. Juleff *et al. PLoS ONE* 3, e3434; 2008). In a carefully controlled study, they found evidence of intact, non-replicating virus particles trapped by immune cells called follicular dendritic cells within the germinal centres of lymph nodes. Strikingly, virus was present for at least 38 days post infection, even though it was undetectable in surrounding tissues.

The retention of intact virus within germinal centres is likely to have a role in stimulating the long-lasting immune response of white blood cells that is characteristic of viral infections (but not current vaccine preparations) and echoes a pattern previously seen for HIV infection. The authors suggest that this capture may inadvertently also be responsible for preserving intact viruses capable of infecting susceptible cells as they come into contact with germinal centres. A causal relationship has yet to be firmly established but the paper illuminates a clear pathway by which to check this out.

Discuss this paper at <http://blogs.nature.com/nature/journalclub>

But Macdonald's model says that wasn't what was happening at all. By looking at the biomechanics of how humans balance, Macdonald has revealed the effects of the adjustments people make to keep their balance, by sticking one foot further out to the left or right. These add energy to the bridge's natural wobble. Once a critical number of people start trying to balance in this way, that extra energy becomes significant, and increases the bridge's sway.

## GEOCHEMISTRY

### Oh molybdenum!

*Nature Geosci.* doi:10.1038/ngeo366 (2008)

A lack of the silvery metal molybdenum limits nitrogen fixation in tropical soils. The finding comes from the work of Lars Hedin at Princeton University in New Jersey and his colleagues, and calls into question the role phosphorus was thought to have in the process.

Hedin and his team looked at the activity of nitrogenase — the enzyme that converts atmospheric nitrogen into ammonium, which plants can use — in the top layer of soil in a tropical forest floor in Panama. The plots had been given fertilizers rich in nitrogen, phosphorus or micronutrients including molybdenum over a period of seven years. The researchers also measured the short-term effects of molybdenum and phosphorus on nitrogenase activity.

Results from both experiments suggest that molybdenum alone can trigger nitrogenase activity, and that contamination by this element might underlie the efficacy of commercial phosphorus fertilizers, Hedin says.

## MATERIALS SCIENCE

### Hitting a nerve gas

*Angew. Chem. Int. Edn* doi:10.1002/anie.200802932 (2008)

Protective clothing can provide a first line of defence against chemical-warfare agents such as mustard gas, but the relief is limited if the perilous substance remains on the fabric.

Valérie Keller of Louis Pasteur University in Strasbourg, France, and her colleagues have a solution. They show that cotton textiles coated by dipping or spraying with photocatalytic particles can burn up simulants of blistering and nerve agents within minutes when irradiated with artificial solar-like light. The particles consist of titanate nanotubes encrusted with crystals of tungsten trioxide, and their light-induced degradation of organic molecules resembles that of self-cleaning tiles and glass coated with titanium dioxide.

## GENOMICS

### 25 to life

*Proc. Natl Acad. Sci. USA* 105, 20404–20409 (2008)

Edging their way towards the construction of a synthetic organism, Daniel Gibson at the J. Craig Venter Institute in Rockville, Maryland, and his colleagues have performed a one-step assembly of an entire bacterial genome inside yeast.

In early 2008, the team reported that they had manufactured the 592-kilobase genome of *Mycoplasma genitalium* using several steps to sew together chemically synthesized DNA fragments (D. G. Gibson *et al. Science* 319, 1215–1220; 2008). In the new simplified version, they show that yeast can take up 25 DNA fragments and splice them together correctly on its own. The technique could make it easier to assemble 'designer' genomes.



B. MILLER

## ZOOLOGY

### Breathing deep

*Proc. R. Soc. B* doi:10.1098/rspb.2008.1489 (2008)

Antarctic sea spiders (pictured above), some up to 90 centimetres long, are giants compared with their 1–10-millimetre-long tropical cousins. Researchers have had a simple hypothesis for this 'polar gigantism', but results from a research team co-led by Arthur Woods of the University of Montana, Missoula, have complicated the picture.

Polar water has a higher level of dissolved oxygen, and cold-water arthropods have lower metabolic rates than their warm-water counterparts. The big spiders were thus expected to perform worse in low-oxygen environments.

Woods's team repeatedly flipped over spiders from 12 species that encompassed the small, medium and large varieties for an hour each, to see how long they took to right themselves. Overall, the giants were no more sluggish than the tiny ones. This result suggests that scientists must search for other possible evolutionary or ecological mechanisms for polar gigantism.

## JOURNAL CLUB

Stephen Curry, Imperial College, London

### A crystallographer takes a jaunt into immunology.

Although I spend most of my time exploring a landscape formed by atoms and bonds, I know it is healthy to make occasional journeys into less familiar territories, and I was intrigued to spot a paper on the curious interplay between infection and immunity in cattle with foot-and-mouth disease virus (FMDV).

FMDV, a highly contagious pathogen that can cause lameness, low weight and decreased milk production, is a scourge of agricultural livestock around the world. Although the acute phase of infection is rarely fatal, infection may persist in animals that have apparently recovered, creating a viral reservoir that some fear could contribute to the spread of disease. Nicholas Juleff and colleagues, from the United Kingdom's Institute for Animal Health, report a fascinating discovery that may have unlocked the secret of FMDV persistence.

They used an array of molecular techniques to search for traces of virus in tissues from the mouths and throats of infected cattle (N. Juleff *et al. PLoS ONE* 3, e3434; 2008). In a carefully controlled study, they found evidence of intact, non-replicating virus particles trapped by immune cells called follicular dendritic cells within the germinal centres of lymph nodes. Strikingly, virus was present for at least 38 days post infection, even though it was undetectable in surrounding tissues.

The retention of intact virus within germinal centres is likely to have a role in stimulating the long-lasting immune response of white blood cells that is characteristic of viral infections (but not current vaccine preparations) and echoes a pattern previously seen for HIV infection. The authors suggest that this capture may inadvertently also be responsible for preserving intact viruses capable of infecting susceptible cells as they come into contact with germinal centres. A causal relationship has yet to be firmly established but the paper illuminates a clear pathway by which to check this out.

Discuss this paper at <http://blogs.nature.com/nature/journalclub>



But Macdonald's model says that wasn't what was happening at all. By looking at the biomechanics of how humans balance, Macdonald has revealed the effects of the adjustments people make to keep their balance, by sticking one foot further out to the left or right. These add energy to the bridge's natural wobble. Once a critical number of people start trying to balance in this way, that extra energy becomes significant, and increases the bridge's sway.

## GEOCHEMISTRY

### Oh molybdenum!

*Nature Geosci.* doi:10.1038/ngeo366 (2008)

A lack of the silvery metal molybdenum limits nitrogen fixation in tropical soils. The finding comes from the work of Lars Hedin at Princeton University in New Jersey and his colleagues, and calls into question the role phosphorus was thought to have in the process.

Hedin and his team looked at the activity of nitrogenase — the enzyme that converts atmospheric nitrogen into ammonium, which plants can use — in the top layer of soil in a tropical forest floor in Panama. The plots had been given fertilizers rich in nitrogen, phosphorus or micronutrients including molybdenum over a period of seven years. The researchers also measured the short-term effects of molybdenum and phosphorus on nitrogenase activity.

Results from both experiments suggest that molybdenum alone can trigger nitrogenase activity, and that contamination by this element might underlie the efficacy of commercial phosphorus fertilizers, Hedin says.

## MATERIALS SCIENCE

### Hitting a nerve gas

*Angew. Chem. Int. Edn* doi:10.1002/anie.200802932 (2008)

Protective clothing can provide a first line of defence against chemical-warfare agents such as mustard gas, but the relief is limited if the perilous substance remains on the fabric.

Valérie Keller of Louis Pasteur University in Strasbourg, France, and her colleagues have a solution. They show that cotton textiles coated by dipping or spraying with photocatalytic particles can burn up simulants of blistering and nerve agents within minutes when irradiated with artificial solar-like light. The particles consist of titanate nanotubes encrusted with crystals of tungsten trioxide, and their light-induced degradation of organic molecules resembles that of self-cleaning tiles and glass coated with titanium dioxide.

## GENOMICS

### 25 to life

*Proc. Natl Acad. Sci. USA* 105, 20404–20409 (2008)

Edging their way towards the construction of a synthetic organism, Daniel Gibson at the J. Craig Venter Institute in Rockville, Maryland, and his colleagues have performed a one-step assembly of an entire bacterial genome inside yeast.

In early 2008, the team reported that they had manufactured the 592-kilobase genome of *Mycoplasma genitalium* using several steps to sew together chemically synthesized DNA fragments (D. G. Gibson *et al. Science* 319, 1215–1220; 2008). In the new simplified version, they show that yeast can take up 25 DNA fragments and splice them together correctly on its own. The technique could make it easier to assemble 'designer' genomes.



B. MILLER

## ZOOLOGY

### Breathing deep

*Proc. R. Soc. B* doi:10.1098/rspb.2008.1489 (2008)

Antarctic sea spiders (pictured above), some up to 90 centimetres long, are giants compared with their 1–10-millimetre-long tropical cousins. Researchers have had a simple hypothesis for this 'polar gigantism', but results from a research team co-led by Arthur Woods of the University of Montana, Missoula, have complicated the picture.

Polar water has a higher level of dissolved oxygen, and cold-water arthropods have lower metabolic rates than their warm-water counterparts. The big spiders were thus expected to perform worse in low-oxygen environments.

Woods's team repeatedly flipped over spiders from 12 species that encompassed the small, medium and large varieties for an hour each, to see how long they took to right themselves. Overall, the giants were no more sluggish than the tiny ones. This result suggests that scientists must search for other possible evolutionary or ecological mechanisms for polar gigantism.

## JOURNAL CLUB

Stephen Curry, Imperial College, London

### A crystallographer takes a jaunt into immunology.

Although I spend most of my time exploring a landscape formed by atoms and bonds, I know it is healthy to make occasional journeys into less familiar territories, and I was intrigued to spot a paper on the curious interplay between infection and immunity in cattle with foot-and-mouth disease virus (FMDV).

FMDV, a highly contagious pathogen that can cause lameness, low weight and decreased milk production, is a scourge of agricultural livestock around the world. Although the acute phase of infection is rarely fatal, infection may persist in animals that have apparently recovered, creating a viral reservoir that some fear could contribute to the spread of disease. Nicholas Juleff and colleagues, from the United Kingdom's Institute for Animal Health, report a fascinating discovery that may have unlocked the secret of FMDV persistence.

They used an array of molecular techniques to search for traces of virus in tissues from the mouths and throats of infected cattle (N. Juleff *et al. PLoS ONE* 3, e3434; 2008). In a carefully controlled study, they found evidence of intact, non-replicating virus particles trapped by immune cells called follicular dendritic cells within the germinal centres of lymph nodes. Strikingly, virus was present for at least 38 days post infection, even though it was undetectable in surrounding tissues.

The retention of intact virus within germinal centres is likely to have a role in stimulating the long-lasting immune response of white blood cells that is characteristic of viral infections (but not current vaccine preparations) and echoes a pattern previously seen for HIV infection. The authors suggest that this capture may inadvertently also be responsible for preserving intact viruses capable of infecting susceptible cells as they come into contact with germinal centres. A causal relationship has yet to be firmly established but the paper illuminates a clear pathway by which to check this out.

Discuss this paper at <http://blogs.nature.com/nature/journalclub>

## NEWS

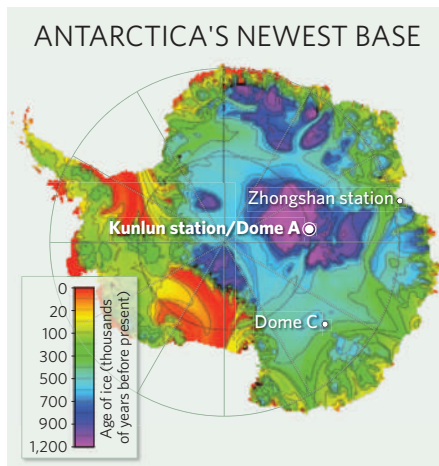
# China builds inland Antarctic base

Kunlun station to open later this month atop the frozen continent's oldest ice.

After a three-week crawl carrying 625 tonnes of cargo towards the highest ice in Antarctica, a Chinese expedition is expected this week to begin building a research base at Dome Argus, or 'Dome A', 4,093 metres above sea level. The station, called Kunlun and scheduled to open on 28 January, will gather data in fields ranging from global climate change to the origin of the Universe.

The 250-million-renminbi (US\$37-million) Kunlun will be China's third Antarctic station, joining the Great Wall station in the South Shetland Islands and the Zhongshan station in east Antarctica. "The Kunlun station will be a major legacy of the International Polar Year and will propel China to the heart of the Antarctic map," says Jean de Pomereu, a photographer who followed the expedition to Zhongshan for the Brussels-based International Polar Foundation. "It is absolutely fantastic to have a station there," adds Eric Wolff, an ice-core specialist at the British Antarctic Survey in Cambridge, UK.

On 20 October, the Chinese Arctic and Antarctic Administration (CAA) sent its expedition team from Shanghai aboard the icebreaker *Xue Long* ('Snow Dragon' in English) to the coastal Zhongshan station.



Bad ice conditions delayed their arrival, but on 18 December — two weeks behind schedule — a 28-man 'inland team' began the nearly 1,300-kilometre traverse to Dome A. On arriving at Dome A this week, the expeditioners will have just 20 days to build the station before temperatures drop sharply to below  $-50^{\circ}\text{C}$  in early February.

At the end of this year's first phase of construction, Kunlun is expected to have a main building of 230 square metres, with 11 units

for sleeping, eating and working. It will have space for up to 25 people, says Qu Tanzhou, director of the CAA. Six more units are expected to be added next year, for a total area of 327 square metres.

Over the next decade, China hopes to add more facilities to Kunlun, including a large fuel tank and a solar-panel array to provide additional power, and to eventually be able to operate year round. The CAA also plans to have its own aircraft in Antarctica to shuttle researchers between Zhongshan and Kunlun, increasing the research capacity at both stations. "Only with these logistics in place will we be able to make the most out of the station," says Qu.

A key focus of research is finding sites where ice cores stretching back further in time than any others could be drilled. A core obtained at a site known as Dome C — about 1,000 kilometres from Dome A (see map) — reached 3,200 metres deep and helped to reconstruct past climate going back 800,000 years. Many believe that Dome A promises older ice because it is higher and has less snow, meaning that researchers can get more years of climate records in a given thickness of ice.

"Our radar studies show that the ice

SOURCE: P. HUYBRECHTS, VRIJE UNIVERSITEIT BRUSSEL

## Companies racing into India's nuclear market

Russia, France and other countries are rushing to capitalize on India's nuclear-power programme, four months after the United States pressured the 45-nation Nuclear Suppliers Group to end India's nuclear isolation. Arms-control experts strongly criticize the Indo-US nuclear deal that set off the rush, saying it undermines the Nuclear Non-Proliferation Treaty. India, a nuclear-armed state, has not signed the treaty; those seeking to sell to it have.

India wants to increase the proportion of its electricity generated from nuclear sources from 2.8% to 25% by 2050. That would mean building 30 or more new reactors to join the 17 existing ones and the 6 that are under construction.

The Nuclear Power Corporation of India Limited (NPCIL) in Mumbai expects this month to finalize a total of US\$15 billion in contracts with France's Areva group and Russia's nuclear-energy conglomerate Rosatom, says NPCIL chairman Shreyans Kumar Jain. The US companies Westinghouse and General Electric have not signed contracts, but are due this month to visit India and scout out possible locations for reactors. The NPCIL has readied four sites — one for each vendor — each capable of accepting eight to ten imported reactors.

On 5 December, Russian president Dmitry Medvedev signed a deal in New Delhi that paves the way for four more 1-gigawatt reactors over the next decade, in

addition to the two that Russia is already building at Kudankulam in the southern state of Tamil Nadu. In November, the United Kingdom lifted its six-year-old blanket ban on exporting 'trigger list' items, including nuclear materials, to India. And in September, France signed an agreement similar to the US one to share nuclear technology and know-how with India.

Some formalities remain before the US and French agreements can be declared operational, says Ravi Bhushan Grover, director of strategic planning in India's Department of Atomic Energy (DAE) and a key negotiator of the Indo-US



Russian President Dmitry Medvedev and Indian Prime Minister Manmohan Singh.

nuclear deal. The countries will have to exchange diplomatic notes confirming that all requirements have been met. The DAE must also file a declaration with the International Atomic Energy Agency (IAEA) listing civilian facilities to

RAVEENDRAN/AFP/GETTY IMAGES



**HAVE YOUR SAY**

Comment on any of our news stories, online.

[www.nature.com/news](http://www.nature.com/news)



CAA **A base at Antarctica's Dome A could provide access to the oldest ice-core samples yet.**

underneath Dome A is over 3,000 metres thick," says Sun Bo, a glaciologist at the Polar Research Institute of China, based in Shanghai. "This could push the climate record back to 1.5 million years."

What ice-core researchers have to decide

first is where exactly to place their drills. "Ideally, the ice has to be deep and unfolded and not melting at the bottom," says Sun. To locate such ice, they are looking for help from Antarctica's Gamburtsev Province Project, an international initiative that is collecting data

over a vast area of east Antarctica, including the buried Gamburtsev mountain range.

For the past several weeks, low-flying aircraft have been sweeping over the area, gathering gravity and magnetic readings as well as radar information to illuminate the thickness and internal layers of the ice sheet. The group has made at least seven data flights over Dome A, which will be fed into ice models to predict the best places to drill a core. Meanwhile, the Polar Research Institute of China will continue to gather data from the ground and will start test-drilling as early as next year.

Until then, researchers are pursuing other work they can do at Dome A: astronomical observing. "The seeing conditions on Dome A are just phenomenal," says Cui Xiangqun, director of the Nanjing Institute of Astronomical Optics & Technology. Last year the Chinese team installed a remotely operated observatory called PLATO built by the University of New South Wales in Sydney, Australia. Two of its four 14.5-centimetre optical telescopes broke down halfway through the winter, whereas the other two operated for more than 130 days before the last engine gave out. Early results from another PLATO telescope suggest that Dome A is an excellent spot to observe at sub-millimetre wavelengths.

Gong Xuefei, of the Nanjing institute, will repair parts of PLATO and calibrate its instruments this month — as well as adding an instrument to measure the transparency of the sky. ■

**Jane Qiu**

be placed under its safeguards; as part of the US deal, India agreed to separate civilian nuclear facilities from military ones and open to IAEA inspectors its present and future civilian facilities.

That is far from sufficient, say arms-control experts who argue that India should sign and ratify the Comprehensive Nuclear-Test-Ban Treaty, as well as cap the amount of fissile weapons material it produces. "India retains, deal or no deal, the capability to produce weapons-grade material at a far higher rate than it is believed to have ever done or to be likely to do," says Paul Nelson at the Nuclear Security Science and Policy Institute of Texas A&M University in College Station. The United States unilaterally brought India in from the nuclear cold without requiring it to make significant concessions, says Rebecca Johnson,

director of the Acronym Institute for Disarmament Diplomacy in London.

Within India, DAE employees are concerned that an influx of proposed new reactors could lead to quality standards being compromised. The country's Atomic Energy Regulatory Board will have to inspect and clear several new reactors of different designs as they are approved. "Our primary concern is over safety," says A. Sathasivam, president of the National Federation of Atomic Energy Employees. Om Pal Singh, the board's secretary, says the problem is simply a lack of manpower. To deal with the new applications, the board intends to double its number of regulators within the next five years, he says.

And the NPCIL is losing staff, because many of its employees have been enticed into more lucrative jobs as consultants in the new nuclear rush. "Almost all our directors who

have retired or who are going to retire in a few years have been grabbed by private companies at ten times my salary," says Jain. For instance, his predecessor, V. K. Chaturvedi, now heads the nuclear group at Reliance Infrastructure in Mumbai, and some present and former NPCIL engineers are in the process of forming nuclear-consultancy companies.

Meanwhile, domestic critics such as Annaswamy Narayana Prasad, retired director of the Bhabha Atomic Research Centre, and Padmanabha Krishnagopala Iyengar, former DAE secretary, claim that Indian nuclear scientists are giving up prematurely on their thorium research programme in exchange for a few uranium reactors from abroad. India has very little domestic uranium but one-quarter of the world's thorium reserves; its thorium research programme focuses on turning the material into fissile

uranium-233 for use as reactor fuel. Fast breeder reactors, of the type under construction in Kalpakkam, would breed uranium-233 in thorium blankets surrounding a plutonium core. Recovering plutonium and uranium-233 from spent fuel is key to India's thorium programme, but, under the Indo-US deal, this has to be done in a dedicated plant under IAEA safeguards and with US permission.

Still, at least one overseas company is betting on thorium. Last month, Thorium Power in McLean, Virginia, with a market capitalization of about \$40 million, established a joint venture with Punj Lloyd, an engineering company in Gurgaon. The two companies plan to set up an investment fund and to act as consultants to other companies looking to get in on the rush. ■

K. S. Jayaraman, with additional reporting by Declan Butler.

## SPECIAL REPORT

# Biotechs feel the pain

The biotechnology industry is weathering the financial crisis better than some. That doesn't mean it's in great shape, reports **Heidi Ledford**.

For the past decade, the annual MassBio Investors Forum has been the place for Massachusetts biotechnology companies to network and woo new investors. But although the courtship continued last month at the Sheraton Boston hotel, the meeting rooms were also filled with investors and executives taking a crash course in how to survive the current economic climate.

The 9 December meeting, organized by the Massachusetts Biotechnology Council, included new sessions about alternative sources of funding, such as non-profit foundations and under-used government programmes. The council has also organized 'pharma days' during which local biotechnology executives can speak with business-development leaders at pharmaceutical firms, in the hope of facilitating partnerships. Robert Coughlin, the council's president, advises struggling local biotechs: "Just get out there and raise money," he says. "You've got to flip over every rock that's out there."

## Survival of the fittest

There's no question that the biotechnology industry is facing turbulent times. The cash-hungry industry has long struggled to meet exorbitant research-and-development costs in the decade-long quest to produce a marketable drug — and perhaps only then turn a profit. Several biotech companies have already filed for bankruptcy since the onset of the economic crisis, among them Introgen Therapeutics in Houston, Texas; Chemokine Therapeutics in Vancouver, Canada; and Orchestra Therapeutics in Carlsbad, California.



Some industry observers worry that worthwhile therapies will get lost in the shuffle. "At the moment, nobody can raise money," says Aisling Burnand, chief executive of the BioIndustry Association, a trade organization for UK biotechnology firms. "I think there's a real possibility that some really good companies will go to the wall, and that's very worrying." This could be a particular problem for companies that haven't acquired venture-capital financing recently and had planned to knock on doors early in 2009.

Others argue that culling weaker companies will ultimately benefit the industry. "Getting rid of some of the weak ones will help focus attention on some of the remaining stocks that are pretty strong," says Paul Cuddon, a life-sciences analyst at the investment bank KBC Peel Hunt in London. "That's what I'm hoping for." He and others argue that investors will continue to support the stronger biotechs no matter what the financial climate.

Thus far, the biotech sector has fared relatively well in the financial storm, although many small companies have been hard hit. Overall, the industry outperformed broader markets in 2008; for instance, whereas the NASDAQ declined by 41% during the year, the NASDAQ Biotech Index — which tracks 136 companies — lost only 12% (see chart). "People have to invest somewhere, and if you compare the biotech index to most of the other industries, it's looking pretty attractive," says Jens Eckstein, a Boston-based venture capitalist at TVM Capital. "People who had their money in large-, mid- and small-biotech mixed portfolios



The path to a marketable drug is long and expensive.

lost less money than many other people."

But picking apart those portfolios shows that smaller companies have borne the brunt of the damage. According to the Burrill Biotechnology Indices, compiled by life-science investment specialists Burrill & Company in San Francisco, California, large biotech firms lost 13% of their market value in 2008, medium-sized firms lost 31% and small companies lost 43%. "Effectively you're losing part of the food chain," says Burnand.

Meanwhile, there has been an inevitable knock-on effect for researchers. Matt Gardner, president and chief executive of BayBio, an association of life-sciences companies in northern California, says that hiring freezes at small companies have lengthened the job hunt for unemployed scientists in the region. "Normally there's so much demand for talent, they would be placed in a new position in 30 to 60 days," he says. "But now there aren't as many smaller companies ready to swallow them up."

As investors tighten their purse strings, survival may boil down to how much cash a company had squirrelled away before the crisis hit. By that measure, many biotechs are in bad shape. According to BIO, a biotechnology trade organization based in Washington DC, roughly a third of small public biotechnology companies in the United States have insufficient cash

NASDAQ versus NASDAQ Biotech Index (NBI)







**BIOCONTROL**  
Dengue fever tackled by  
mosquito-busting bacteria.  
[www.nature.com/news](http://www.nature.com/news)

S. GOULD  
SIRTRIS, GLAXOSMITHKLINE



— a former venture capitalist and co-founder of Sirtris, a biotechnology company that was purchased by GlaxoSmithKline in June 2008 — predicted that venture capitalists will increasingly fund individual projects rather than entire companies.

Some have looked to the pharmaceutical industry for salvation. Large pharmaceutical companies were already snapping up biotechnology companies to replenish dwindling product pipelines even before the market crashed late last year. When stock values plunged, executives of several large pharmaceutical companies vowed to go on a shopping spree while prices were low. The Swiss pharmaceutical company Roche, for example, recently purchased Memory Pharmaceuticals, based in Montvale, New Jersey, after the company's stock plummeted to \$0.15 per share. More acquisitions are expected. But researching and assimilating a biotechnology company can be expensive, and there are limits to how much pharmaceutical companies, many of which are downsizing themselves, are willing to buy. "It is widely acknowledged that Big Pharma is increasingly reliant on biotech for new product development," wrote Cuddon in a 25 November report, "but we doubt Big Pharma will be UK biotech's knight in shining armour."

Partnerships between big pharma and biotechnology companies, though, are expected to accelerate. On 12 December, New York-based Bristol-Myers Squibb entered into a partnership with San Francisco's Exelixis, providing a welcome influx of cash to the mid-sized biotechnology company that had outgrown the option of renewed venture-capital funding. However, Tibor Papp, head of consulting at PharmaVentures, a UK-based business consultancy for pharmaceutical firms, notes that licensing deals with pharmaceutical companies declined by nearly 30% in October 2008 compared with the same month in 2007.

What all this means for the future of biotech remains to be seen. Eckstein predicts that scientists and investors may wait longer and gather more preliminary data before launching a company. Coughlin expects widespread mergers and partnerships to leave the field with fewer, larger companies. And Papp says investors will emphasize business acumen over scientific prowess among biotech executives. Biotechs, he says, "will resemble corporate-finance-oriented companies with stronger business strategies and a deal maker at the top. Biotech companies will not just be pure science companies going into the future."

to survive the next six months. In a 14 October report on European biotechnology firms, analysts at the investment bank Goldman Sachs concluded that half of such companies would face funding difficulties in 2009 or 2010: "In our view, companies that need to raise additional capital will either fail to do so ... or may be forced to raise cash at an exorbitant cost, diluting existing shareholders significantly."

### Mergers and acquisitions

So it is no surprise that many companies are cutting payrolls and shelving projects in an attempt to conserve cash. Last month, Emisphere Technologies announced that it would change its business model, lay off employees and close a facility in Tarrytown, New York, to focus efforts at its headquarters in Cedar Knolls, New Jersey. And Peptimmune in Cambridge, Massachusetts, has cut staff by more than 50% and put a hold on research into potential therapies for Alzheimer's disease and Parkinson's disease. Others are trying new avenues to raise money. Vernalis of Berkshire, UK, has sold the rights to some of its projected future royalty income. And Trancept Pharmaceuticals, a privately held firm in Point Richmond, California, has gone public by performing a reverse merger with the publicly traded company Novacea based in South San Francisco; the merger allows Trancept access to public financing without having to launch a lengthy and expensive initial public offering.

Meanwhile, conventional funding sources have not dried up entirely. The crisis had little immediate impact on venture-capital investment, says Gardner. "We're still seeing plenty of venture capital happening," he says. "But in the longer run, if private equity doesn't keep moving, venture capitalists won't be able to raise the next round of funding." In a recent survey of more than 400 US venture capitalists, 92% predicted that venture investment would slow this year relative to 2008, and 61% predicted that the decline would exceed 10%. But the life sciences were viewed as the second safest investment — after clean technology — and a quarter of respondents thought that investment in the life sciences would increase in 2009.

Venture capitalists have become increasingly conservative during the past few years, and the financial crisis is likely to exacerbate that trend. Although it was once standard to keep a few 'high risk' companies in a firm's biotechnology portfolio, "today you have to work much harder to convince people that this is worth taking the risk," says Eckstein. Investors will probably also push harder to ensure that companies are efficient and focused, and that company executives initiate early discussions with potential partners in the pharmaceutical industry. At the recent MassBio forum, Christoph Westphal

**"If private equity doesn't keep moving, venture capitalists won't be able to raise the next round of funding."**

— Matt Gardner

**GOT A NEWS TIP?**

Send any article ideas for Nature's News section to [newstips@nature.com](mailto:newstips@nature.com)

K. CAMPBELL/GETTY

# European boost for particle therapy

Treatment centres poised to use carbon-ion beams to tackle cancer.

The first European clinical centre offering carbon-ion therapy to treat cancer is set to open early this year in Heidelberg, Germany, followed by a second facility in Pavia, Italy, by 2010.

Proponents of the technique — which uses beams of ions to kill tumour cells — say the new centres mark a significant watershed for a field that has been slowly gaining ground for more than 60 years.

In 1946, Robert Wilson, a physicist on the Manhattan Project and later head of the Fermi National Accelerator Laboratory in Illinois, proposed using charged particles to treat cancer. Since then, there has been growing evidence that beams of protons and carbon ions — known collectively as hadron therapy — may offer an important alternative to X-rays for treating cancer.

Unlike X-rays, which deposit most of their energy near the skin's surface, hadron beams are more effective at reaching tumour cells in deeper tissue. The particles release the bulk of their energy as they slow down in the last few millimetres of their journey, a point called the Bragg peak. The beams also scatter very little, allowing the maximum radiation dose to be precisely targeted to tumour cells, and thus minimizing damage to surrounding healthy tissue, explains biologist Manjit Dosanjh, director of the European Network for Research in Light Ion Hadron Therapy at CERN.

Neutron beams share many of these properties but are more difficult to guide because of their lack of charge, necessitating higher doses that can cause severe side effects. Today, only a handful of clinics offer neutron therapy.

Proton therapy is in regular use at medical centres around the world, whereas carbon-ion therapy is at a much more experimental stage. But researchers believe that it may offer even greater accuracy in targeting tumour cells, which, combined with carbon ions' greater mass, gives the beams a much sharper Bragg peak.

Carbon ions also produce a different type of cellular damage from protons or photons, explains Ugo Amaldi, a medical physicist at the University of Milan-Bicocca, Italy, and CERN, the European particle-physics centre near Geneva in Switzerland. "Conventional radiation damages DNA indirectly through the production of free radicals, which requires

oxygen to work," says Amaldi. Carbon ions directly cleave double-stranded DNA at multiple sites without the need for oxygen, so they can tackle hypoxic areas of tumours that are resistant to radiotherapy. "About 10% of all tumours are resistant to X-rays and protons," says Amaldi. "Such tumours — in the brain, liver and lung — have a greater chance of responding to bombardment with carbon ions."

Japan, a pioneer in the field, began testing carbon-ion therapy in 1994, and opened the world's first dual-therapy facility at the Hyogo



Particle-beam therapy can target cancers that are resistant to X-rays.

Ion Beam Medical Center in 2001. A pilot carbon-ion therapy centre at the Society for Heavy Ion Research (GSI) in Darmstadt, Germany, has treated about 450 patients since 1997.

But critics say that there are not enough data to show that carbon-ion therapy is any more effective than conventional treatments. A systematic literature review in 2007, led by the Cochrane Cancer Network, based in Oxford, UK, argued that although early results have been promising, most studies have been done in physics facilities, which did not run randomized, controlled clinical trials (M. Lodge *et al. Radiother. Oncol.* **83**, 110–122; 2007).

It is hoped that the two new facilities — the Heidelberg Ion Therapy Centre (HIT) and Pavia's National Centre for Oncological Hadron Therapy (CNAO) — will rectify that deficit with much more extensive clinical trials. The facilities aim to compare protons and carbon ions, used separately and in combination, with X-rays and surgery, and will be the first in Europe to offer both therapies to treat a range of tumours, including spinal-cord and ocular tumours, and lung, prostate and liver cancer.

Only one comparable dual-particle facility

is planned for the near future in the United States: at Touro University near San Francisco, California. The facility expects to have its \$75-million proton accelerator in place by 2010 — its carbon-ion capability will follow by 2012 at an additional cost of \$121 million. But most cancer centres — and the National Institutes of Health — say that they are not ready to invest in expensive carbon-ion-therapy centres without further clinical data.

"Carbon-ion beams may have an advantage in certain tumour types, but that has not yet been proven," says Herman Suit, chief of radiation oncology at the Dana-Farber/Harvard Cancer Center in Boston, Massachusetts, who has conducted proton-therapy research since 1973. Even if carbon ions damage tumours more effectively, he says, it is an open question whether they cause longer-term problems, such as triggering the formation of secondary tumours.

In contrast to the situation in the United States, carbon-ion therapy is attracting growing funding in Europe. Half of the HIT's start-up funding has come from a German government loan, whereas the creation of the CNAO will be funded entirely by the Italian government. Five other European carbon-ion or dual-particle centres are planned: in Wiener Neustadt, Austria; Lyon, France; Marburg and Kiel in Germany; and Stockholm. Like the HIT, the two German facilities will be operated by Siemens, the engineering conglomerate.

The field still faces significant hurdles, though. The HIT's accelerator system has been ready for more than six months, says Thomas Haberer, the centre's scientific director, but problems with the software that controls the ion beams have delayed the centre's opening. And researchers at both the HIT and CNAO expect that it will take years to refine their beam-scanning techniques to allow them to treat highly mobile organs such as the lungs.

But pioneers in ion therapy are bullish. "Europe is at the frontier of this research," says Gerhard Kraft, who oversaw the GSI's ion-therapy programme for many years before his retirement. "Carbon ions are sometimes considered potentially dangerous — but that's because they are extremely effective."

**Vicki Brower**

SIEMENS



## Geophysicists accused of breach of publishing ethics

Scientists at the Institute of Geophysics in Paris (IPGP) have been accused of acting as editors for dozens of papers by IPGP colleagues published from 1992 to 2008 in the journal *Earth and Planetary Science Letters* while they were members of the editorial board. The allegations follow a joint investigation by science journalists at the French newspapers *Le Monde* and *Libération*.

Among the authors of the articles involved is Claude Allègre, a former research and education minister in the French government and former IPGP head, whom French President Nicolas Sarkozy has been rumoured to be wooing to take up a ministerial position; and Vincent Courtillot, the institute's current head and a member of the journal's editorial board from 2003 to 2005.

Courtillot has dismissed the allegations, pointing out in *Le Monde* that all editors of papers submitted to the journal by the IPGP were openly identified. Allègre has described the allegations as "ridiculous". But Friso Veenstra, publisher of the Elsevier journal, maintains that reviewing papers from one's own institution runs against the journal's ethics policy.

## UK revises visa rules to help visiting scientists

The UK government is to reform aspects of immigration rules implemented in November 2008, after universities warned that the system would prevent up to 2,000 overseas researchers a year from entering the country. Previously, overseas academics coming to the United Kingdom to carry out research for two to three years could enter the country on a 'sponsored researcher visa'. But under the new points-based immigration system, the visa was scrapped, leaving researchers with no clear entry route. Researchers will now be included under a 'tier 5' entry route, reserved for sponsored temporary workers.

## US National Academies suspend visits to Iran

The US National Academies are advising American scientists to avoid travelling to Iran, following the detention in December of one of the academies' top officials.

Glenn Schweitzer, a veteran physicist who manages scientific visits and exchanges in Eurasia for the National Academy of Sciences, was in Iran as part of a long-running programme between the academy

## Dinosaur graveyard promises clues to extinction

More than 7,600 fossilized dinosaur bones have been unearthed since March 2008 at what Chinese palaeontologists now claim is the largest dinosaur graveyard in the world.

Most of the bones date back to the Late Cretaceous period more than 100 million years ago, raising speculation that the finds could offer clues about why the creatures died out. The discoveries, made by researchers from the Chinese Academy of Sciences, include bones from what might be the largest duck-billed dinosaur discovered to date. The site consists of 15 separate areas in Zhucheng, Shandong province, which has yielded more than 50 tonnes of dinosaur bones since the 1960s.



XINHUA/ZHU ZHENG

and Iranian scientific organizations. The programme promotes collaboration and aims to keep scientific diplomatic channels open between the two countries despite the continuing political confrontation.

Schweitzer was detained on two occasions by three men claiming to be from the Iranian security services, who threatened to prevent him from leaving the country if he did not cooperate, he says. The academies say that visits will resume only if the Iranian government provides firm assurances that US scientists can visit the country safely.

For a longer version of this story, see <http://tinyurl.com/7ajyfc>.

## California sues in bid to preserve wildlife laws

The state of California has filed a lawsuit against the US government to block recent changes to the Endangered Species Act that conservationists say threaten animals and their habitats.

The changes to the act, finalized by the Bush administration on 16 December 2008, allow federal agencies to undertake commercial activities, such as logging and

mining, without getting external wildlife biologists to assess the environmental consequences of new projects. The rules also bypass the need to consider the effects of greenhouse gases on species and ecosystems.

Three US environmental groups — the Natural Resources Defense Council, the National Wildlife Federation and the Center for Biological Diversity — have filed similar lawsuits. President-elect Barack Obama has said that he opposes the last-minute changes to the act.

## Nigeria finally appoints its health ministers

Nine months after the health minister and a minister of state resigned over corruption charges, the Nigerian government has at last filled the vacant posts.

Pathologist Babatunde Osotimehin, who until last month was the director-general of Nigeria's National Agency for the Control of AIDS, was sworn in on 17 December 2008 as health minister alongside his new minister of state, Aliyu Idi Hong. Osotimehin told *Nature* that he sees research into infectious diseases as a priority for the country.

Former minister Adenike Grange and her minister of state, Gabriel Aduku, stepped down after a plot to share 300 million Nigerian naira (US\$2.2 million) from the ministry's 2007 budget among staff was leaked to the country's anticorruption watchdog. The two, together with more than ten other officials, are now on trial facing 56 counts of fraud between them.

K. SCHAFER/NHPA



The sea otter may be adversely affected by changes to the US Endangered Species Act.

### Correction

The reference list and citations in the News Feature 'Let's make a mammoth' (*Nature* **456**, 310–314; 2008) are in the incorrect order. The html version of this article has been amended to give the correct citations, and a corrected PDF can be downloaded from <http://tinyurl.com/86hmp2>.



## Geophysicists accused of breach of publishing ethics

Scientists at the Institute of Geophysics in Paris (IPGP) have been accused of acting as editors for dozens of papers by IPGP colleagues published from 1992 to 2008 in the journal *Earth and Planetary Science Letters* while they were members of the editorial board. The allegations follow a joint investigation by science journalists at the French newspapers *Le Monde* and *Libération*.

Among the authors of the articles involved is Claude Allègre, a former research and education minister in the French government and former IPGP head, whom French President Nicolas Sarkozy has been rumoured to be wooing to take up a ministerial position; and Vincent Courtillot, the institute's current head and a member of the journal's editorial board from 2003 to 2005.

Courtillot has dismissed the allegations, pointing out in *Le Monde* that all editors of papers submitted to the journal by the IPGP were openly identified. Allègre has described the allegations as "ridiculous". But Friso Veenstra, publisher of the Elsevier journal, maintains that reviewing papers from one's own institution runs against the journal's ethics policy.

## UK revises visa rules to help visiting scientists

The UK government is to reform aspects of immigration rules implemented in November 2008, after universities warned that the system would prevent up to 2,000 overseas researchers a year from entering the country. Previously, overseas academics coming to the United Kingdom to carry out research for two to three years could enter the country on a 'sponsored researcher visa'. But under the new points-based immigration system, the visa was scrapped, leaving researchers with no clear entry route. Researchers will now be included under a 'tier 5' entry route, reserved for sponsored temporary workers.

## US National Academies suspend visits to Iran

The US National Academies are advising American scientists to avoid travelling to Iran, following the detention in December of one of the academies' top officials.

Glenn Schweitzer, a veteran physicist who manages scientific visits and exchanges in Eurasia for the National Academy of Sciences, was in Iran as part of a long-running programme between the academy

## Dinosaur graveyard promises clues to extinction

More than 7,600 fossilized dinosaur bones have been unearthed since March 2008 at what Chinese palaeontologists now claim is the largest dinosaur graveyard in the world.

Most of the bones date back to the Late Cretaceous period more than 100 million years ago, raising speculation that the finds could offer clues about why the creatures died out. The discoveries, made by researchers from the Chinese Academy of Sciences, include bones from what might be the largest duck-billed dinosaur discovered to date. The site consists of 15 separate areas in Zhucheng, Shandong province, which has yielded more than 50 tonnes of dinosaur bones since the 1960s.



XINHUA/ZHU ZHENG

and Iranian scientific organizations. The programme promotes collaboration and aims to keep scientific diplomatic channels open between the two countries despite the continuing political confrontation.

Schweitzer was detained on two occasions by three men claiming to be from the Iranian security services, who threatened to prevent him from leaving the country if he did not cooperate, he says. The academies say that visits will resume only if the Iranian government provides firm assurances that US scientists can visit the country safely.

For a longer version of this story, see <http://tinyurl.com/7ajyfc>.

## California sues in bid to preserve wildlife laws

The state of California has filed a lawsuit against the US government to block recent changes to the Endangered Species Act that conservationists say threaten animals and their habitats.

The changes to the act, finalized by the Bush administration on 16 December 2008, allow federal agencies to undertake commercial activities, such as logging and

mining, without getting external wildlife biologists to assess the environmental consequences of new projects. The rules also bypass the need to consider the effects of greenhouse gases on species and ecosystems.

Three US environmental groups — the Natural Resources Defense Council, the National Wildlife Federation and the Center for Biological Diversity — have filed similar lawsuits. President-elect Barack Obama has said that he opposes the last-minute changes to the act.

## Nigeria finally appoints its health ministers

Nine months after the health minister and a minister of state resigned over corruption charges, the Nigerian government has at last filled the vacant posts.

Pathologist Babatunde Osotimehin, who until last month was the director-general of Nigeria's National Agency for the Control of AIDS, was sworn in on 17 December 2008 as health minister alongside his new minister of state, Aliyu Idi Hong. Osotimehin told *Nature* that he sees research into infectious diseases as a priority for the country.

Former minister Adenike Grange and her minister of state, Gabriel Aduku, stepped down after a plot to share 300 million Nigerian naira (US\$2.2 million) from the ministry's 2007 budget among staff was leaked to the country's anticorruption watchdog. The two, together with more than ten other officials, are now on trial facing 56 counts of fraud between them.

K. SCHAFER/NHPA



The sea otter may be adversely affected by changes to the US Endangered Species Act.

### Correction

The reference list and citations in the News Feature 'Let's make a mammoth' (*Nature* **456**, 310–314; 2008) are in the incorrect order. The html version of this article has been amended to give the correct citations, and a corrected PDF can be downloaded from <http://tinyurl.com/86hmp2>.

## Geophysicists accused of breach of publishing ethics

Scientists at the Institute of Geophysics in Paris (IPGP) have been accused of acting as editors for dozens of papers by IPGP colleagues published from 1992 to 2008 in the journal *Earth and Planetary Science Letters* while they were members of the editorial board. The allegations follow a joint investigation by science journalists at the French newspapers *Le Monde* and *Libération*.

Among the authors of the articles involved is Claude Allègre, a former research and education minister in the French government and former IPGP head, whom French President Nicolas Sarkozy has been rumoured to be wooing to take up a ministerial position; and Vincent Courtillot, the institute's current head and a member of the journal's editorial board from 2003 to 2005.

Courtillot has dismissed the allegations, pointing out in *Le Monde* that all editors of papers submitted to the journal by the IPGP were openly identified. Allègre has described the allegations as "ridiculous". But Friso Veenstra, publisher of the Elsevier journal, maintains that reviewing papers from one's own institution runs against the journal's ethics policy.

## UK revises visa rules to help visiting scientists

The UK government is to reform aspects of immigration rules implemented in November 2008, after universities warned that the system would prevent up to 2,000 overseas researchers a year from entering the country. Previously, overseas academics coming to the United Kingdom to carry out research for two to three years could enter the country on a 'sponsored researcher visa'. But under the new points-based immigration system, the visa was scrapped, leaving researchers with no clear entry route. Researchers will now be included under a 'tier 5' entry route, reserved for sponsored temporary workers.

## US National Academies suspend visits to Iran

The US National Academies are advising American scientists to avoid travelling to Iran, following the detention in December of one of the academies' top officials.

Glenn Schweitzer, a veteran physicist who manages scientific visits and exchanges in Eurasia for the National Academy of Sciences, was in Iran as part of a long-running programme between the academy

## Dinosaur graveyard promises clues to extinction

More than 7,600 fossilized dinosaur bones have been unearthed since March 2008 at what Chinese palaeontologists now claim is the largest dinosaur graveyard in the world.

Most of the bones date back to the Late Cretaceous period more than 100 million years ago, raising speculation that the finds could offer clues about why the creatures died out. The discoveries, made by researchers from the Chinese Academy of Sciences, include bones from what might be the largest duck-billed dinosaur discovered to date. The site consists of 15 separate areas in Zhucheng, Shandong province, which has yielded more than 50 tonnes of dinosaur bones since the 1960s.



XINHUA/ZHU ZHENG

and Iranian scientific organizations. The programme promotes collaboration and aims to keep scientific diplomatic channels open between the two countries despite the continuing political confrontation.

Schweitzer was detained on two occasions by three men claiming to be from the Iranian security services, who threatened to prevent him from leaving the country if he did not cooperate, he says. The academies say that visits will resume only if the Iranian government provides firm assurances that US scientists can visit the country safely.

For a longer version of this story, see <http://tinyurl.com/7ajyfc>.

## California sues in bid to preserve wildlife laws

The state of California has filed a lawsuit against the US government to block recent changes to the Endangered Species Act that conservationists say threaten animals and their habitats.

The changes to the act, finalized by the Bush administration on 16 December 2008, allow federal agencies to undertake commercial activities, such as logging and

mining, without getting external wildlife biologists to assess the environmental consequences of new projects. The rules also bypass the need to consider the effects of greenhouse gases on species and ecosystems.

Three US environmental groups — the Natural Resources Defense Council, the National Wildlife Federation and the Center for Biological Diversity — have filed similar lawsuits. President-elect Barack Obama has said that he opposes the last-minute changes to the act.

## Nigeria finally appoints its health ministers

Nine months after the health minister and a minister of state resigned over corruption charges, the Nigerian government has at last filled the vacant posts.

Pathologist Babatunde Osotimehin, who until last month was the director-general of Nigeria's National Agency for the Control of AIDS, was sworn in on 17 December 2008 as health minister alongside his new minister of state, Aliyu Idi Hong. Osotimehin told *Nature* that he sees research into infectious diseases as a priority for the country.

Former minister Adenike Grange and her minister of state, Gabriel Aduku, stepped down after a plot to share 300 million Nigerian naira (US\$2.2 million) from the ministry's 2007 budget among staff was leaked to the country's anticorruption watchdog. The two, together with more than ten other officials, are now on trial facing 56 counts of fraud between them.

K. SCHAFER/NHPA



The sea otter may be adversely affected by changes to the US Endangered Species Act.

### Correction

The reference list and citations in the News Feature 'Let's make a mammoth' (*Nature* **456**, 310–314; 2008) are in the incorrect order. The html version of this article has been amended to give the correct citations, and a corrected PDF can be downloaded from <http://tinyurl.com/86hmp2>.



## Geophysicists accused of breach of publishing ethics

Scientists at the Institute of Geophysics in Paris (IPGP) have been accused of acting as editors for dozens of papers by IPGP colleagues published from 1992 to 2008 in the journal *Earth and Planetary Science Letters* while they were members of the editorial board. The allegations follow a joint investigation by science journalists at the French newspapers *Le Monde* and *Libération*.

Among the authors of the articles involved is Claude Allègre, a former research and education minister in the French government and former IPGP head, whom French President Nicolas Sarkozy has been rumoured to be wooing to take up a ministerial position; and Vincent Courtillot, the institute's current head and a member of the journal's editorial board from 2003 to 2005.

Courtillot has dismissed the allegations, pointing out in *Le Monde* that all editors of papers submitted to the journal by the IPGP were openly identified. Allègre has described the allegations as "ridiculous". But Friso Veenstra, publisher of the Elsevier journal, maintains that reviewing papers from one's own institution runs against the journal's ethics policy.

## UK revises visa rules to help visiting scientists

The UK government is to reform aspects of immigration rules implemented in November 2008, after universities warned that the system would prevent up to 2,000 overseas researchers a year from entering the country. Previously, overseas academics coming to the United Kingdom to carry out research for two to three years could enter the country on a 'sponsored researcher visa'. But under the new points-based immigration system, the visa was scrapped, leaving researchers with no clear entry route. Researchers will now be included under a 'tier 5' entry route, reserved for sponsored temporary workers.

## US National Academies suspend visits to Iran

The US National Academies are advising American scientists to avoid travelling to Iran, following the detention in December of one of the academies' top officials.

Glenn Schweitzer, a veteran physicist who manages scientific visits and exchanges in Eurasia for the National Academy of Sciences, was in Iran as part of a long-running programme between the academy

## Dinosaur graveyard promises clues to extinction

More than 7,600 fossilized dinosaur bones have been unearthed since March 2008 at what Chinese palaeontologists now claim is the largest dinosaur graveyard in the world.

Most of the bones date back to the Late Cretaceous period more than 100 million years ago, raising speculation that the finds could offer clues about why the creatures died out. The discoveries, made by researchers from the Chinese Academy of Sciences, include bones from what might be the largest duck-billed dinosaur discovered to date. The site consists of 15 separate areas in Zhucheng, Shandong province, which has yielded more than 50 tonnes of dinosaur bones since the 1960s.



XINHUA/ZHU ZHENG

and Iranian scientific organizations. The programme promotes collaboration and aims to keep scientific diplomatic channels open between the two countries despite the continuing political confrontation.

Schweitzer was detained on two occasions by three men claiming to be from the Iranian security services, who threatened to prevent him from leaving the country if he did not cooperate, he says. The academies say that visits will resume only if the Iranian government provides firm assurances that US scientists can visit the country safely.

For a longer version of this story, see <http://tinyurl.com/7ajyfc>.

## California sues in bid to preserve wildlife laws

The state of California has filed a lawsuit against the US government to block recent changes to the Endangered Species Act that conservationists say threaten animals and their habitats.

The changes to the act, finalized by the Bush administration on 16 December 2008, allow federal agencies to undertake commercial activities, such as logging and

mining, without getting external wildlife biologists to assess the environmental consequences of new projects. The rules also bypass the need to consider the effects of greenhouse gases on species and ecosystems.

Three US environmental groups — the Natural Resources Defense Council, the National Wildlife Federation and the Center for Biological Diversity — have filed similar lawsuits. President-elect Barack Obama has said that he opposes the last-minute changes to the act.

## Nigeria finally appoints its health ministers

Nine months after the health minister and a minister of state resigned over corruption charges, the Nigerian government has at last filled the vacant posts.

Pathologist Babatunde Osotimehin, who until last month was the director-general of Nigeria's National Agency for the Control of AIDS, was sworn in on 17 December 2008 as health minister alongside his new minister of state, Aliyu Idi Hong. Osotimehin told *Nature* that he sees research into infectious diseases as a priority for the country.

Former minister Adenike Grange and her minister of state, Gabriel Aduku, stepped down after a plot to share 300 million Nigerian naira (US\$2.2 million) from the ministry's 2007 budget among staff was leaked to the country's anticorruption watchdog. The two, together with more than ten other officials, are now on trial facing 56 counts of fraud between them.

K. SCHAFER/NHPA



The sea otter may be adversely affected by changes to the US Endangered Species Act.

### Correction

The reference list and citations in the News Feature 'Let's make a mammoth' (*Nature* **456**, 310–314; 2008) are in the incorrect order. The html version of this article has been amended to give the correct citations, and a corrected PDF can be downloaded from <http://tinyurl.com/86hmp2>.



## Geophysicists accused of breach of publishing ethics

Scientists at the Institute of Geophysics in Paris (IPGP) have been accused of acting as editors for dozens of papers by IPGP colleagues published from 1992 to 2008 in the journal *Earth and Planetary Science Letters* while they were members of the editorial board. The allegations follow a joint investigation by science journalists at the French newspapers *Le Monde* and *Libération*.

Among the authors of the articles involved is Claude Allègre, a former research and education minister in the French government and former IPGP head, whom French President Nicolas Sarkozy has been rumoured to be wooing to take up a ministerial position; and Vincent Courtillot, the institute's current head and a member of the journal's editorial board from 2003 to 2005.

Courtillot has dismissed the allegations, pointing out in *Le Monde* that all editors of papers submitted to the journal by the IPGP were openly identified. Allègre has described the allegations as "ridiculous". But Friso Veenstra, publisher of the Elsevier journal, maintains that reviewing papers from one's own institution runs against the journal's ethics policy.

## UK revises visa rules to help visiting scientists

The UK government is to reform aspects of immigration rules implemented in November 2008, after universities warned that the system would prevent up to 2,000 overseas researchers a year from entering the country. Previously, overseas academics coming to the United Kingdom to carry out research for two to three years could enter the country on a 'sponsored researcher visa'. But under the new points-based immigration system, the visa was scrapped, leaving researchers with no clear entry route. Researchers will now be included under a 'tier 5' entry route, reserved for sponsored temporary workers.

## US National Academies suspend visits to Iran

The US National Academies are advising American scientists to avoid travelling to Iran, following the detention in December of one of the academies' top officials.

Glenn Schweitzer, a veteran physicist who manages scientific visits and exchanges in Eurasia for the National Academy of Sciences, was in Iran as part of a long-running programme between the academy

## Dinosaur graveyard promises clues to extinction

More than 7,600 fossilized dinosaur bones have been unearthed since March 2008 at what Chinese palaeontologists now claim is the largest dinosaur graveyard in the world.

Most of the bones date back to the Late Cretaceous period more than 100 million years ago, raising speculation that the finds could offer clues about why the creatures died out. The discoveries, made by researchers from the Chinese Academy of Sciences, include bones from what might be the largest duck-billed dinosaur discovered to date. The site consists of 15 separate areas in Zhucheng, Shandong province, which has yielded more than 50 tonnes of dinosaur bones since the 1960s.



XINHUA/ZHU ZHENG

and Iranian scientific organizations. The programme promotes collaboration and aims to keep scientific diplomatic channels open between the two countries despite the continuing political confrontation.

Schweitzer was detained on two occasions by three men claiming to be from the Iranian security services, who threatened to prevent him from leaving the country if he did not cooperate, he says. The academies say that visits will resume only if the Iranian government provides firm assurances that US scientists can visit the country safely.

For a longer version of this story, see <http://tinyurl.com/7ajyfc>.

## California sues in bid to preserve wildlife laws

The state of California has filed a lawsuit against the US government to block recent changes to the Endangered Species Act that conservationists say threaten animals and their habitats.

The changes to the act, finalized by the Bush administration on 16 December 2008, allow federal agencies to undertake commercial activities, such as logging and

mining, without getting external wildlife biologists to assess the environmental consequences of new projects. The rules also bypass the need to consider the effects of greenhouse gases on species and ecosystems.

Three US environmental groups — the Natural Resources Defense Council, the National Wildlife Federation and the Center for Biological Diversity — have filed similar lawsuits. President-elect Barack Obama has said that he opposes the last-minute changes to the act.

## Nigeria finally appoints its health ministers

Nine months after the health minister and a minister of state resigned over corruption charges, the Nigerian government has at last filled the vacant posts.

Pathologist Babatunde Osotimehin, who until last month was the director-general of Nigeria's National Agency for the Control of AIDS, was sworn in on 17 December 2008 as health minister alongside his new minister of state, Aliyu Idi Hong. Osotimehin told *Nature* that he sees research into infectious diseases as a priority for the country.

Former minister Adenike Grange and her minister of state, Gabriel Aduku, stepped down after a plot to share 300 million Nigerian naira (US\$2.2 million) from the ministry's 2007 budget among staff was leaked to the country's anticorruption watchdog. The two, together with more than ten other officials, are now on trial facing 56 counts of fraud between them.

K. SCHAFER/NHPA



The sea otter may be adversely affected by changes to the US Endangered Species Act.

### Correction

The reference list and citations in the News Feature 'Let's make a mammoth' (*Nature* **456**, 310–314; 2008) are in the incorrect order. The html version of this article has been amended to give the correct citations, and a corrected PDF can be downloaded from <http://tinyurl.com/86hmp2>.

## Geophysicists accused of breach of publishing ethics

Scientists at the Institute of Geophysics in Paris (IPGP) have been accused of acting as editors for dozens of papers by IPGP colleagues published from 1992 to 2008 in the journal *Earth and Planetary Science Letters* while they were members of the editorial board. The allegations follow a joint investigation by science journalists at the French newspapers *Le Monde* and *Libération*.

Among the authors of the articles involved is Claude Allègre, a former research and education minister in the French government and former IPGP head, whom French President Nicolas Sarkozy has been rumoured to be wooing to take up a ministerial position; and Vincent Courtillot, the institute's current head and a member of the journal's editorial board from 2003 to 2005.

Courtillot has dismissed the allegations, pointing out in *Le Monde* that all editors of papers submitted to the journal by the IPGP were openly identified. Allègre has described the allegations as "ridiculous". But Friso Veenstra, publisher of the Elsevier journal, maintains that reviewing papers from one's own institution runs against the journal's ethics policy.

## UK revises visa rules to help visiting scientists

The UK government is to reform aspects of immigration rules implemented in November 2008, after universities warned that the system would prevent up to 2,000 overseas researchers a year from entering the country. Previously, overseas academics coming to the United Kingdom to carry out research for two to three years could enter the country on a 'sponsored researcher visa'. But under the new points-based immigration system, the visa was scrapped, leaving researchers with no clear entry route. Researchers will now be included under a 'tier 5' entry route, reserved for sponsored temporary workers.

## US National Academies suspend visits to Iran

The US National Academies are advising American scientists to avoid travelling to Iran, following the detention in December of one of the academies' top officials.

Glenn Schweitzer, a veteran physicist who manages scientific visits and exchanges in Eurasia for the National Academy of Sciences, was in Iran as part of a long-running programme between the academy

## Dinosaur graveyard promises clues to extinction

More than 7,600 fossilized dinosaur bones have been unearthed since March 2008 at what Chinese palaeontologists now claim is the largest dinosaur graveyard in the world.

Most of the bones date back to the Late Cretaceous period more than 100 million years ago, raising speculation that the finds could offer clues about why the creatures died out. The discoveries, made by researchers from the Chinese Academy of Sciences, include bones from what might be the largest duck-billed dinosaur discovered to date. The site consists of 15 separate areas in Zhucheng, Shandong province, which has yielded more than 50 tonnes of dinosaur bones since the 1960s.



XINHUA/ZHU ZHENG

and Iranian scientific organizations. The programme promotes collaboration and aims to keep scientific diplomatic channels open between the two countries despite the continuing political confrontation.

Schweitzer was detained on two occasions by three men claiming to be from the Iranian security services, who threatened to prevent him from leaving the country if he did not cooperate, he says. The academies say that visits will resume only if the Iranian government provides firm assurances that US scientists can visit the country safely.

For a longer version of this story, see <http://tinyurl.com/7ajyfc>.

## California sues in bid to preserve wildlife laws

The state of California has filed a lawsuit against the US government to block recent changes to the Endangered Species Act that conservationists say threaten animals and their habitats.

The changes to the act, finalized by the Bush administration on 16 December 2008, allow federal agencies to undertake commercial activities, such as logging and

mining, without getting external wildlife biologists to assess the environmental consequences of new projects. The rules also bypass the need to consider the effects of greenhouse gases on species and ecosystems.

Three US environmental groups — the Natural Resources Defense Council, the National Wildlife Federation and the Center for Biological Diversity — have filed similar lawsuits. President-elect Barack Obama has said that he opposes the last-minute changes to the act.

## Nigeria finally appoints its health ministers

Nine months after the health minister and a minister of state resigned over corruption charges, the Nigerian government has at last filled the vacant posts.

Pathologist Babatunde Osotimehin, who until last month was the director-general of Nigeria's National Agency for the Control of AIDS, was sworn in on 17 December 2008 as health minister alongside his new minister of state, Aliyu Idi Hong. Osotimehin told *Nature* that he sees research into infectious diseases as a priority for the country.

Former minister Adenike Grange and her minister of state, Gabriel Aduku, stepped down after a plot to share 300 million Nigerian naira (US\$2.2 million) from the ministry's 2007 budget among staff was leaked to the country's anticorruption watchdog. The two, together with more than ten other officials, are now on trial facing 56 counts of fraud between them.

K. SCHAFER/NHPA



The sea otter may be adversely affected by changes to the US Endangered Species Act.

### Correction

The reference list and citations in the News Feature 'Let's make a mammoth' (*Nature* **456**, 310–314; 2008) are in the incorrect order. The html version of this article has been amended to give the correct citations, and a corrected PDF can be downloaded from <http://tinyurl.com/86hmp2>.



## Geophysicists accused of breach of publishing ethics

Scientists at the Institute of Geophysics in Paris (IPGP) have been accused of acting as editors for dozens of papers by IPGP colleagues published from 1992 to 2008 in the journal *Earth and Planetary Science Letters* while they were members of the editorial board. The allegations follow a joint investigation by science journalists at the French newspapers *Le Monde* and *Libération*.

Among the authors of the articles involved is Claude Allègre, a former research and education minister in the French government and former IPGP head, whom French President Nicolas Sarkozy has been rumoured to be wooing to take up a ministerial position; and Vincent Courtillot, the institute's current head and a member of the journal's editorial board from 2003 to 2005.

Courtillot has dismissed the allegations, pointing out in *Le Monde* that all editors of papers submitted to the journal by the IPGP were openly identified. Allègre has described the allegations as "ridiculous". But Friso Veenstra, publisher of the Elsevier journal, maintains that reviewing papers from one's own institution runs against the journal's ethics policy.

## UK revises visa rules to help visiting scientists

The UK government is to reform aspects of immigration rules implemented in November 2008, after universities warned that the system would prevent up to 2,000 overseas researchers a year from entering the country. Previously, overseas academics coming to the United Kingdom to carry out research for two to three years could enter the country on a 'sponsored researcher visa'. But under the new points-based immigration system, the visa was scrapped, leaving researchers with no clear entry route. Researchers will now be included under a 'tier 5' entry route, reserved for sponsored temporary workers.

## US National Academies suspend visits to Iran

The US National Academies are advising American scientists to avoid travelling to Iran, following the detention in December of one of the academies' top officials.

Glenn Schweitzer, a veteran physicist who manages scientific visits and exchanges in Eurasia for the National Academy of Sciences, was in Iran as part of a long-running programme between the academy

## Dinosaur graveyard promises clues to extinction

More than 7,600 fossilized dinosaur bones have been unearthed since March 2008 at what Chinese palaeontologists now claim is the largest dinosaur graveyard in the world.

Most of the bones date back to the Late Cretaceous period more than 100 million years ago, raising speculation that the finds could offer clues about why the creatures died out. The discoveries, made by researchers from the Chinese Academy of Sciences, include bones from what might be the largest duck-billed dinosaur discovered to date. The site consists of 15 separate areas in Zhucheng, Shandong province, which has yielded more than 50 tonnes of dinosaur bones since the 1960s.



XINHUA/ZHU ZHENG

and Iranian scientific organizations. The programme promotes collaboration and aims to keep scientific diplomatic channels open between the two countries despite the continuing political confrontation.

Schweitzer was detained on two occasions by three men claiming to be from the Iranian security services, who threatened to prevent him from leaving the country if he did not cooperate, he says. The academies say that visits will resume only if the Iranian government provides firm assurances that US scientists can visit the country safely.

For a longer version of this story, see <http://tinyurl.com/7ajyfc>.

## California sues in bid to preserve wildlife laws

The state of California has filed a lawsuit against the US government to block recent changes to the Endangered Species Act that conservationists say threaten animals and their habitats.

The changes to the act, finalized by the Bush administration on 16 December 2008, allow federal agencies to undertake commercial activities, such as logging and

mining, without getting external wildlife biologists to assess the environmental consequences of new projects. The rules also bypass the need to consider the effects of greenhouse gases on species and ecosystems.

Three US environmental groups — the Natural Resources Defense Council, the National Wildlife Federation and the Center for Biological Diversity — have filed similar lawsuits. President-elect Barack Obama has said that he opposes the last-minute changes to the act.

## Nigeria finally appoints its health ministers

Nine months after the health minister and a minister of state resigned over corruption charges, the Nigerian government has at last filled the vacant posts.

Pathologist Babatunde Osotimehin, who until last month was the director-general of Nigeria's National Agency for the Control of AIDS, was sworn in on 17 December 2008 as health minister alongside his new minister of state, Aliyu Idi Hong. Osotimehin told *Nature* that he sees research into infectious diseases as a priority for the country.

Former minister Adenike Grange and her minister of state, Gabriel Aduku, stepped down after a plot to share 300 million Nigerian naira (US\$2.2 million) from the ministry's 2007 budget among staff was leaked to the country's anticorruption watchdog. The two, together with more than ten other officials, are now on trial facing 56 counts of fraud between them.

K. SCHAFER/NHPA



The sea otter may be adversely affected by changes to the US Endangered Species Act.

### Correction

The reference list and citations in the News Feature 'Let's make a mammoth' (*Nature* **456**, 310–314; 2008) are in the incorrect order. The html version of this article has been amended to give the correct citations, and a corrected PDF can be downloaded from <http://tinyurl.com/86hmp2>.





# The lab at the bottom of the sea

The best way to study life beneath the waves is to live there. **Mark Schrope** describes his experiences in the world's longest-running undersea laboratory.

It is night on Conch Reef in the Florida Keys, and Niels Lindquist is running a thin green plane of laser light through a lone sponge. The psychedelic display captures the attention of a rather large, green moray eel. As Lindquist watches, the eel inspects the laser light, decides it doesn't approve and finds another way around, swimming right down the side of Lindquist's leg. It is only when the eel has vanished into the night that Lindquist notices that his dive buddy has risen to a safe distance with the wariness most divers accord such beasts. Lindquist, though, had been completely at ease.

Lindquist's sangfroid comes from the sort of experience and familiarity most divers can't even dream of. A chemical ecologist from the University of North Carolina in Chapel Hill, he has spent the past ten days underwater, living and working at the world's only underwater long-term research station — the Aquarius Undersea Laboratory, which sits next to Conch Reef. Aquarius is roughly the size of a school

bus, 15 metres under the waves and 6.5 kilometres off the Florida coast. Managed by the University of North Carolina in Wilmington for the US National Oceanic and Atmospheric Administration (NOAA), the laboratory began operating in 1993. Over the years, according to its director, Andrew Shepard, it has sometimes been hard to convince people that the facility is worth its annual operating budget, currently about US\$2 million. Since 2007, in part to provide clearer justification, Aquarius's chief scientist, Ellen Prager, and her colleagues have been working to better define the facility's mission. One research focus she and her colleagues are highlighting is technology development for long-term ocean observing — an established priority for NOAA. The laser that was illuminating that sponge is one such technology.

But there is more to the sponge work than a technological shakedown cruise. It is the latest part of a set of Aquarius-based studies of the roles that sponges play in reef ecology. Sponges have long been known to be prodigious

pumpers of water<sup>1</sup>, but these expeditions have provided the first precise figures on quite how prodigious the pumping powers are — findings that could have implications for reef research worldwide. Such work can be done without a home under the waves, but it takes a lot longer, and it might not lead to the same insights and achievements. An 'aquanaut' in Aquarius can spend 12 hours a day diving, a tally that could take weeks to accomplish with regular scuba dives from the surface. The sustained access that Aquarius offers also makes researchers much more responsive to anything untoward.

Aquarius is not just about convenience, though. Most scuba divers will tell you that when you pause to really watch a section of a coral reef you are sure to spot subtle details you would have missed if you had kept swimming. Researchers who have lived in Aquarius say that experience is magnified many times over. "You're looking at the complete ecosystem if you're working from Aquarius," says

M. SCHROPE



Chris Martens of the University of North Carolina in Wilmington. "You gain so much, so fast."

Aquarius is not just a home for aquanauts — and the occasional astronaut who comes for some zero-g simulation time and experience of cramped conditions. There are plenty of snapper and other fish living in the waters below the coral and algae-bedecked lab, utterly at ease with the human residents. Divers making their way into the hole at the end of the lab that leads into the 'wet porch' entryway are often greeted by chub fish swimming between their legs. The lab is filled with normal air under enough pressure to keep water from entering. Burps of air periodically escape the entrance hole, resonating inside the wet porch like the sound of a draining tub.

From the wet porch, visitors enter a small workroom that houses research equipment and a curtained toilet. Every other room is visible to the world via webcams, creating a sort of human fishbowl effect. "You get used to it," says Lindquist, with a laugh and in a voice of slightly higher pitch than normal, due to the extra atmosphere-and-a-bit of pressure.

The next chamber is known as the main lock. On one side is a bank of monitors and controls for the lab's life-support system, and a computer. On the other is a simple kitchen where aquanauts prepare mainly freeze-dried meals, and a table that sits next to one of the portholes. "We get friends coming to the view ports all the time, especially at night," says Lindquist. Soon after, a large barracuda swims by. The final space is the kind that someone seeking to make a sale might describe as cosy: triple-decker bunks on either side of the structure for four researchers and two technicians. "There's



Niels Lindquist, safe from eels inside Aquarius.

not a lot of personal space," says Jim Hench, a veteran aquanaut from Stanford University in California. "Unless you're outside — then it's great."

The North Carolina team's sponge-studying mission last September lasted eight working days — a typical length for the facility's eight or so missions a year — largely devoted to just four individual star sponges on Conch Reef. Like patients in an emergency department, each sponge was wired up at one time or another with a full complement of monitors and sampling devices that linked back to Aquarius: a device for measuring water flow, a mass spectrometer to calculate the isotopic signatures of nitrogen and other compounds going into and coming out of the sponge, and an autoanalyser to record nutrient concentrations.

### Pump it up

The team's most startling results have been on the sheer amount of water that the sponges pump. Below the waves and away from fairly

well understood upwellings, ocean water tends to move only horizontally. "A few millimetres of vertical velocity gets people's attention," says Hench. That's why, on a previous mission, the team had been astonished to measure a vertical-flow rate of 25 centimetres per second from a single giant barrel sponge "When I first saw that I couldn't believe it," says Hench, "because you just don't see that in nature."

More measurements, though, proved that the rates were real. In fact, some vase sponges can pump more than 100,000 times their own volume in a single day. A modest-sized giant barrel sponge can pump 15,000 litres per hour, giving a weekly volume roughly equal to that of an Olympic-sized swimming pool. Some sponges have since proved less siphontastic; but in terms of flow for a given body size, some were even more vigorous in their pumping than the giant barrel sponges.

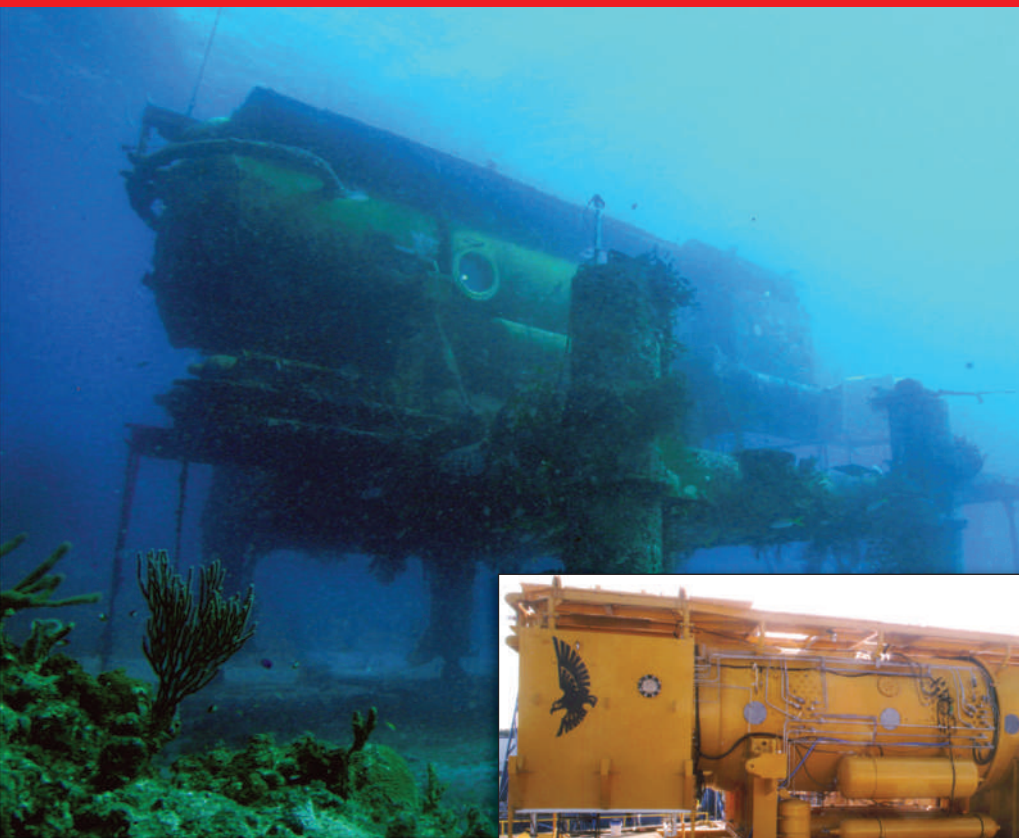
The plumbing that enables the sponges to work at these impressive rates consists of a system of channels and chambers spread throughout the sponges' bodies. Cells known as choanocytes, which line the pumping chambers, are equipped with waving flagella that move water past filter-feeding components and out of the sponge. For decades, researchers thought that water currents assisted the sponge's pumping action. But work on Conch Reef suggests that the choanocytes work alone to establish those impressive rates.

More surprising still is that barrel sponges in various parts of the reef will occasionally stop pumping in unison for periods of up to several hours for no apparent reason. "There's a rhythm out there nobody has ever seen before," says Lindquist. What triggers this synchronized action is not clear. In the September mission, the team recorded that synchronized slow-downs, but not complete stoppages, seemed to be happening in the reef's stinker sponges — so called because of the sulphurous smell they exude when brought to the surface.

The ways of the sponge are important because what comes out is not what goes in. Sponges are remarkably efficient at pulling particles and plankton out of the water during the few seconds that the water remains in their bodies<sup>2</sup>. This means that they are crucial for cleaning the water and helping to create the clear conditions that many reefs require to thrive. But they don't just change the particulate content of the water — they also change its chemical content. Much of the responsibility for these changes can be laid at the door not of the sponges but of the microbes that live within them — high-microbial-abundance (HMA) sponges can be 50% bacterial by mass.



Measuring how fast water is pumped out by sponges provides clues about the health of a reef.



A sea change: Aquarius as it was originally built (right) and as it is now.

In past research, the team has showed that the microbes in HMA sponges process massive quantities of nitrogen from plankton and dissolved organic matter<sup>3</sup>. And researchers in the Netherlands have similarly found large nitrogen contributions from sponges in the cracks and crevices of coral reefs<sup>4</sup>. The nitrates and ammonia that these microbes churn out can serve as fertilizer for some types of seaweed. “This definitely shifts the whole way that ecosystems function,” says Martens.

On many reefs in the Florida Keys, and around the world, seaweeds are increasingly smothering coral, with devastating effects. Whether the nitrogen that fuels this growth comes from the ocean itself or from the land, in the form of run-off and sewage, remains a topic of intense debate. Although they don’t have a firm answer, the Aquarius researchers have shown that the sponges and the seaweed on Conch Reef often have similar nitrogen isotopic signatures. This serves as circumstantial evidence that wherever the nitrogen is coming from, the processing done by sponges to liberate nitrogen from other components of dissolved organic matter is important for the subsequent growth of algae. The team is now looking for direct evidence of the role of sponges in enhancing that growth.

Martens and Lindquist believe that by increasing nitrogen fertilization, growing sponge populations could change the basic ecology of some reefs in a way that favours sea-

weed at the expense of corals. Unfortunately, there is relatively little solid evidence of historical sponge populations to test this hypothesis against — although Martens, who lived in the Keys for several years while growing up, thinks that sponges were less common in the 1960s.

But more sponges might not always be bad news. Preliminary studies from Aquarius suggest that some sponges and their microbes have a denitrifying effect, changing nitrate into nitrogen gas and thereby making what used to be a fertilizer into something that can then escape into the atmosphere. This could counteract some of the fertilizing tendency and

thus possibly help to maintain the health of the reef. This side of the work began when the researchers realized that the nitrate and ammonium concentrations they were measuring amounted to only about half of what would be predicted given how much

oxygen the sponges were taking up to process organic matter. For four years the team has been working to find this ‘missing’ nitrogen.

### Bagging data

In 2008 the North Carolina group finally established a way to clearly measure the conversion to nitrogen gas. Aquanauts wrestled a plastic bag over individual sponges to temporarily cut them off from the surrounding water, and the sponges were then exposed to ammonium ions with unnaturally high levels of a heavy nitrogen isotope. The team found that this ‘labelled’

ammonium was converted to nitrogen gas in one HMA species, but not in a low-microbial-abundance species. “This is the most exciting discovery we could have made because of the potential to actually get rid of some nitrogen from reefs,” says Martens.

A second variation on the enclosed sponge experiment helped to answer another crucial question. Conversion to nitrogen gas was once thought to take place only through conventional denitrification, in which ammonium and nitrite are converted into nitrate and then

to nitrogen gas. But in the past two decades scientists have found that in the ocean, most of this conversion involves a sort of shortcut known as anaerobic ammonium oxidation, or anammox<sup>5,6</sup>. To determine the type of conversion at play in the sponges, the team also exposed the sponges to labelled nitrate. The team found that the sponges missed out the step of conversion of nitrate to nitrogen gas, supporting the idea that anammox is the denitrifying process that goes on in the low-oxygen microenvironments

within the sponges.

The researchers hope to run additional experiments to confirm this, then move on to determine rates and, by extension, how important sponge denitrification is to reefs. “I think we’ve got the tiger by the tail, but we’ll have to see if it turns out to be a big tiger or a little tiger,” says Martens. If the group can show that anammox is occurring widely, he says, it could change people’s views of how important sponges are on reefs.

Cristina Diaz, a sponge expert at the Margarita Marine Museum in Venezuela, says that the group’s research is reviving interest in sponges and their environmental impacts on reefs. “I’m really excited,” she says, “I think it’s fantastic work.” Nonetheless, she says there is still much to be learned: “We are still in diapers.” Martens and Lindquist agree, and hope that Aquarius will remain available to support their own research and that of a growing number of other groups. Shepard says the lab is designed to last for at least another ten years, and that he is encouraged by growing support inside and outside NOAA. “I think we’re going in the right direction.”

**Mark Schroppe is a writer in Melbourne, Florida.**

**“You’re looking at the complete ecosystem if you’re working from Aquarius.”**

— Chris Martens

1. Reyswig, H. M. *Marine Biol.* **9**, 38–50 (1971).
2. Reyswig, H. M. *J. Exp. Mar. Biol. Ecol.* **14**, 231–249 (1974).
3. Southwell, M. W., Weisz, J. B., Martens, C. S. & Lindquist, N. *Limnol. Oceanogr.* **53**, 986–996 (2008).
4. van Duyl, F. C., Scheffers, S. R., Thomas, F. I. M. & Driscoll, M. *Coral Reefs* **25**, 23–36 (2006).
5. Dalsgaard, T., Canfield, D. E., Petersen, J., Thamdrup, B. & Acuña-González, J. *Nature* **422**, 606–608 (2003).
6. Devol, A. H. *Nature* **422**, 575–576 (2003).



# A GREEN INVESTMENT

If growing forests in India can generate lucrative carbon credits, then why isn't everyone planting trees? **Paroma Basu** reports.

**O**n a humid morning in August 2008, Harshkumar Kulkarni strolled through a thicket of young eucalyptus trees, surveying their slender forms. Stroking each silver trunk as he passed, Kulkarni, the general manager for plantations at the conglomerate Indian Tobacco Corporation (ITC), seemed like a concerned father checking on his children — albeit more than 3 million of them.

Kulkarni has spent the better part of two decades breeding fast-growing, disease-tolerant varieties of eucalyptus, leucaena and casuarina trees that can survive in the swampy, inhospitable soils of Khammam district, in India's southeastern state of Andhra Pradesh. Farmers who had struggled to grow traditional crops such as cotton can now earn up to US\$500 per hectare from timber that they sell to paper mills, including the one owned by the ITC.

But for the past few years, Kulkarni has been grooming some of his trees for a new role: carbon offsetting. Kulkarni and his colleagues realized that they might benefit from the global carbon market established in 2001 as part of the Kyoto Protocol. The Clean Development Mechanism (CDM) is a system by which participating countries can meet some of their greenhouse-gas reductions by buying certified carbon credits from projects in developing countries that reduce emissions. Kulkarni decided to devote a portion of the ITC's plantations to supplying those credits.

Seven years, mountains of paperwork and almost \$70,000 of the company's funds later, the project is set to become one of only two forest-based CDM projects in India — and one of only a handful in the world — to win the necessary approval from the United Nations Framework Convention on Climate Change (UNFCCC). If it is approved as expected in the next few months, families will be paid \$65 per year for each hectare they commit to grow for four years rather than logging every year. The owners still get money from timber sales when the trees are logged, as long as they immediately replant the plot. Kulkarni considers the project one of his biggest triumphs — but the past seven years have been difficult. "I lost 11 kilos and ruined my health trying to get this CDM project registered," he says.

**"I lost 11 kilos and ruined my health trying to get this project off the ground."**

**— Harshkumar Kulkarni**

India should be thick with forestry carbon-offset schemes: it was one of the first nations to move aggressively into carbon offsetting, has robust forestry policies and has vast swaths of land that could be planted. The challenge for Kulkarni and others trying to establish CDM forestry projects has come from the convoluted, expensive and bureaucratic approval process. Some of the biggest difficulties lie in documenting how much carbon the growing trees will absorb. Piecing together the patchwork of land involved is hard too; the 3,070 hectares in Kulkarni's project is owned by around 3,000 local tribal families. "Forest-based CDM has not yielded the desired results so far," says a high-ranking forestry official in India's Ministry

of Environment and Forests, who did not want to be named. "The required methodologies and calculations are too complex and the costs are too high to justify. There is certainly huge scope to simplify the whole business."

Despite the complex system, India and other countries are keen to grow more forests for carbon credits. Those efforts that plant native trees could aid biodiversity conservation, and all such schemes can provide a potential source of income for impoverished families who depend on forests for their livelihoods. Soyam Nagamani, a community leader of the Koya tribe in Khammam district's Bhimavaram village, says that ever since she switched from growing traditional cotton crops to the ITC's eucalyptus trees, a lot more money has come in from the sale of timber. Now the promise of additional income has convinced her to devote a portion of her land to carbon offsetting. "We don't understand that much [about global warming]," says Nagamani, "but before we ate only two small meals a day whereas now we eat three full meals of rice."

## Grand potential

India is among the most densely forested countries in the world and already has robust conservation policies requiring that trees are replanted as they are removed. Some 24% of the country's land mass is now forested, with the government aiming to reach up to 33% by 2012. India also has vast stretches of land degraded by agriculture, development and pollution, plus remote and uncultivable lands, all of which could be planted with trees. It is here that the CDM could make a big difference. Project developers and forest-dependent

A. VITALE/PANOS



communities now have an economic reason to plant and preserve trees. "Through the CDM, we need to create situations in which a standing tree makes more business sense than a felled tree, for only then will poor communities retain the tree," says Mohit Gera, a government forestry officer who has carried out research at the Energy and Resources Institute in New Delhi. "In developing countries such as India, carbon sequestration and poverty alleviation must happen side by side."

Trees can only ever be a temporary carbon sink. They will eventually release all their carbon when they die from old age, if not before, because of logging, fires, pests, floods or cyclones. "I feel that in forestry projects you are not actually mitigating climate change but just 'buying' time, or postponing the problem, because of the non-permanence issue," says José Domingos Miguez, a member of the UN's CDM executive board and an adviser on climate change in Brazil's ministry of science and technology. But forestry projects are still considered to be valuable as temporary 'carbon banks' that soak up greenhouse gases until researchers work out ways to make longer-lasting emissions cuts.

When the CDM was formally established, some expected forestry schemes to thrive because tree-planting is a relatively cheap and easy way to mitigate emissions compared with establishing a wind farm or hydropower plant. But although the incentives are there, few projects have materialized. Only one, in China's Pearl River basin, has received the green light from the UNFCCC. Around 25 more are awaiting final approval, according to UNFCCC figures: six in India (see map, overleaf), five in China and the rest scattered through Asia, Africa and South America. By contrast, the organization has approved 1,270 schemes worldwide — including 378 in India, more than any other country — to offset carbon in other sectors, ranging from wind farms to the destruction of non-CO<sub>2</sub> greenhouse gases.

China's Pearl River project aims to reforest 4,000 hectares of watershed areas along the Pearl River basin in Guangxi province and to generate around 600,000 carbon credits by 2036. It was an inspiration for the Indian forestry community, but it also exposed serious bottlenecks in the system, says Promode Kant, a former forestry official and director of the Institute of Climate Change and Ecology in New Delhi. Kant learned this first-hand as a technical adviser to a small, 370-hectare reforestation project in the north Indian state of Haryana that is, along with Kulkarni's project, on the brink of getting UNFCCC approval for carbon offsetting.

### Contrasting fortunes

Where the Pearl River project enjoyed full government support — including a multi-million-dollar budget and the contribution of its mostly government-owned land — the Haryana scheme received none. The project was funded with less than \$75,000 by the state's cash-strapped forestry department, and Kant and his colleagues had to corral together 227 farmers across many villages, each owning tiny patches of a hectare or less. State forest departments ought to be the most enthusiastic proponents of India's forest-based carbon offsetting, but they lack financial resources and the experience to compile complicated project applications, says Jagdish Kishwan, director-general of the government's Indian Council of Forestry Research and Education.

There are a number of bureaucratic hurdles to forest-based carbon offsetting. Many of them arise from the UNFCCC's stringent approval process. Before they can sell carbon credits, potential CDM projects have to pass through three rounds of evaluation: a government task force in the home nation, an audit of methodologies, finances and documentation

by a UN-accredited body, and a final review by a CDM executive board staffed by scientists and officials.

After the CDM executive board was established in 2001, Indian entrepreneurs moved aggressively into the carbon-trade business and an industry of domestic and international carbon-consulting firms soon emerged to help Indian clients prepare technically sound projects in renewable energies and other areas. But the same is not true for forestry. The CDM guidelines for the forestry sector weren't figured out until 2003, two years after other emissions-reducing sectors, says Martin Schröder, lead auditor for forestry projects at TÜV SÜD Industrie Service in Munich, Germany, a UN-accredited firm that evaluates CDM projects. "Very few consultants are actually experienced in the field, so there are more project developers who are trying to make a go of it on their own," says Schröder. "They are discovering the hard way that the process is not so easy,

because UNFCCC rules [for forest-based schemes] are rather complex, maybe even more complex than regular CDM projects."

One of the complexities lies in documenting — to the UNFCCC's satisfaction — how much carbon

a forest will actually store for the duration of a project. Different tree species take up carbon at different rates and store it for varying amounts of time, depending on lifespans and harvesting cycles. Although researchers have fairly good estimates for these figures, it has been challenging for people such as Kulkarni, who are going it alone, to apply the CDM's methods on the ground. To ensure he made all of his calculations accurately, Kulkarni spent a lot of time travelling to conferences, reading scientific papers and consulting with CDM specialists, climate scientists and forestry researchers. But Miguez says that such an involved approval

**"In developing countries, carbon sequestration and poverty alleviation must happen side by side."**

— Mohit Gera



process is unavoidable. "The complexity of this type of project is necessary to guarantee that uptake of CO<sub>2</sub> from the atmosphere is real and measurable," he says.

Managers of carbon-offset ventures must also meticulously account for 'leakage' — greenhouse gases that will be released into the atmosphere in the process of setting up the project. For example, a World Bank-funded reforestation project in the north Indian state of Himachal Pradesh had to account for emissions that would have been released by resident cattle, and would continue to be released when the cattle were moved elsewhere, along with those caused by land preparation, clearing bushes, petrol-burning trucks, water pumps and labourers.

More challenging, say proponents, is

demonstrating that projects meet the crucial 'additionality' concept, meaning that the greenhouse-gas reductions will be more than those that would have occurred anyway. As part of his application, Kulkarni had to prove that the land he wanted to plant on stood no chance of being otherwise reforested — by locals who own the land or by government 'social forestry' programmes — because the cost was too high and the soil so poor that it could support nothing but eucalyptus and other specially bred trees. Offset projects also have to describe the exact Global Positioning System coordinates for each of the land patches included, a job that, in India, must be contracted out to the only government agency that can produce such maps. This can cost thousands of dollars.

Even if Kulkarni and others do get approval for their projects, they cannot be sure of getting a good price for their carbon credits — or of finding buyers for them at all. This comes back to Miguez's 'non-permanence issue', the fact that the carbon in the forest will eventually be released, however many times it is logged and replanted. Because of their uncertain environmental value, forest-generated credits are expected to fetch only \$4–\$5 apiece in the global markets, compared with the \$20–\$23 fetched by carbon credits from other offset schemes. So far, only a few buyers, including Japan, Canada, Spain and the World Bank's BioCarbon Fund have expressed interest in buying these credits, and China's Pearl River project is yet to sell a single one.

### On the way to market

Demand for forestry credits also remains low because the European Union does not yet allow their sale on its emissions trading system, or carbon stock exchange, ostensibly fearing that cheap forest credits would swamp the market and bring down prices. Miguez says this exclusion may be reconsidered during the next review by the system's governing committee, although it is still uncertain when that will be.

Kulkarni and other forestry managers are hoping that pricing issues and the other problems they have encountered will be ironed out in the post-Kyoto negotiations, so all eyes are on the 2009 Copenhagen talks, when discussions are expected to begin in earnest. Kant says he would like to see a simplification of the rules and regulations for forest-based CDM projects so that "the process becomes accessible to larger numbers of poor communities across the

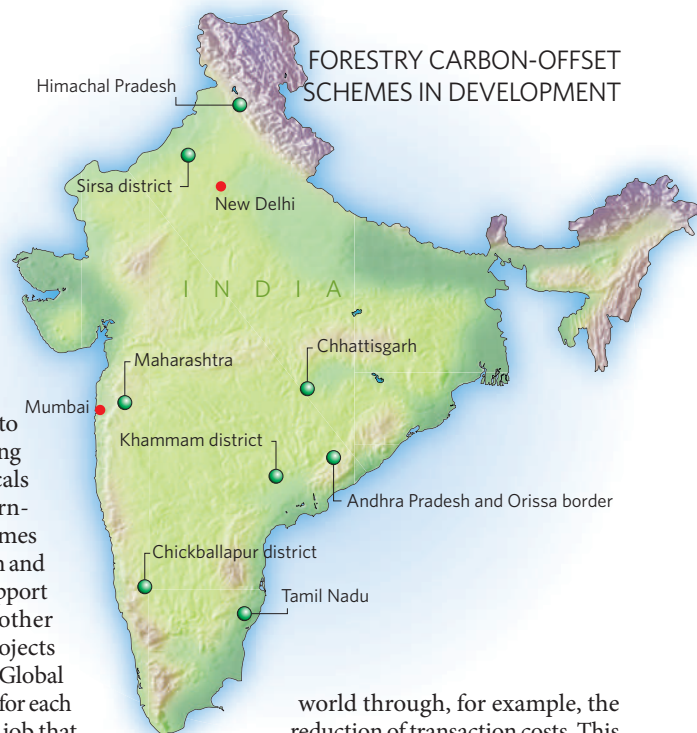
world through, for example, the reduction of transaction costs. This is one area that has to be tackled and will be tackled."

Kant now conducts CDM training workshops for forestry officers in several developing countries and says that the situation is already improving. "I constantly used to hear that the CDM just can't be done," he says. "But now awareness and actual training efforts are growing, so there is increased understanding and confidence about the process." As many as six groups around India are currently in the early stages of planning forest offset schemes. Forestry managers still think that such ventures, with their UNFCCC stamp of approval, will provide an international, reputable business for the long term, says N. H. Ravindranath, an ecologist at the Indian Institute of Science, Bangalore, who serves on the government's CDM task force. "The whole CDM process is maybe a bit too rigorous, but it is generally the right way of doing projects as it is introducing accountability, encouraging community participation and trying to set good standards."

Kulkarni's experience in meeting those standards means that he is now in regular contact with others in the CDM community and has come to be known as something of an expert on forest-based carbon offsetting. "I still say the future [of forest offsetting] is bright in India," he says, "provided we line up simpler methods and practices."

On the ITC plantations, more and more farmers are agreeing to grow eucalyptus trees for carbon storage, persuaded by the additional income. But as for Kulkarni, he says that his motivations have changed. "By this point, earning money [from carbon credits] is not even the issue," he says. "We just want others to feel that if we can succeed, they can too." ■

**Paroma Basu is a freelance writer based in New Delhi, India.**



Harshkumar Kulkarni (top) is helping farmers in Khammam district to grow trees for carbon credits.

## CORRESPONDENCE

## Replacement of animals in research will never be possible

SIR — Your Editorial ‘Call to action’ (*Nature* **456**, 281–282; 2008), concerning the draft of the new European directive on the use of animals in scientific research, correctly points out the risk of severely limiting the use of non-human primates in invasive studies of brain function. Performing such experiments requires humane treatment of animals and painless experimental procedures. This ‘refinement’ of procedure is the first of the 3Rs, the philosophy underlying the European Union (EU) directive. During the past 20 years, technical improvements have significantly reduced both the time and the number of animals used in a project, while increasing the data yield. Thus, the second of the 3Rs, ‘reduction’, is already firmly established.

What needs to be clearly appreciated is that ‘replacement’ (the third R) of this type of research will never be possible. The current draft of the EU directive, in confining the use of non-human primates as far as possible to projects aimed at understanding life-threatening diseases, takes a direction that is both incorrect and illusory, towards a future ban that it considers desirable. As stated in your Editorial, this is a real threat. We must combat it with strength and without compromise. A ban could be justified only if and when all brain function is understood, and if no further challenge is posed to neuroscience by the evolution of modern societies and their pathologies. Obviously, neither of these conditions will ever be realized.

From my privileged observatory as chair of the Programme of European Neuroscience Schools (<http://fens.mdc-berlin.de/pens>), I can testify to the increasing interest among the younger generation in the integrative study of brain function. At the

same time, I stress the dramatic negative consequences that a severe limitation or ban on the use of non-human primates will have on education, in a discipline that currently places Europe at the forefront of modern research in neuroscience.

Behavioural studies have the power to shed light on some of the most common neurological syndromes that affect our societies. They have already provided encouraging first answers about Parkinson’s disease and the principles underlying neural prosthetics and brain-machine interface devices, among other examples. The enforced abandonment of research on great apes has phased out experimental studies on, for example, brain evolution, malaria, hepatitis C and respiratory syncytial virus infection. Prohibiting studies on primates will confine Europe to the periphery of the neuroscience and biomedical arena, with negative consequences for the quality of life of future generations.

**Roberto Caminiti** Department of Physiology and Pharmacology, Sapienza University of Rome, Piazzale Aldo Moro 5, 00185 Rome, Italy

## Western prosperity is based on resources that are running out

SIR — In response to the lack of a flagship achievement by economics, as noted by Jean-Philippe Bouchaud in his Essay ‘Economics needs a scientific revolution’ (*Nature* **455**, 1181; 2008), Jesper Stage proposes in Correspondence that the prosperity of western societies is one such achievement (‘Speaking up for economic-sciences modelling’ *Nature* **456**, 570; 2008). However, this prosperity is mainly based on the use of non-renewable resources and therefore is probably spurious.

Several hundred million years were needed to form

the fossil energy that will be exhausted during a few hundred years. This is roughly equivalent to spending all one’s annual income during the first 30 seconds of a year. In particular, the frenzy to automate processes in order to increase competitiveness leads to rapid exhaustion of available resources, for example through over-fishing or degradation of soils.

All current growth-based economic models imply massive use of non-renewable resources and environmental degradation. These models are not sustainable, even in the short term.

As early as 160 years ago, John Stuart Mill affirmed that “the richest and most prosperous countries would very soon attain the stationary state” (*Principles of Political Economy* Longmans, 1848). In contrast to that time, when resources were being used up at a rate that was several orders of magnitude slower than today, a phase of economic degrowth is necessary before a stationary state can be reached. It would be a major achievement of economics to achieve such a degrowth without social and political disasters.

**Hervé Philippe** Département de Biochimie, Université de Montréal, 2900 Édouard Montpetit, H3C 3J7 Montréal, Québec, Canada  
e-mail: [hervé.philippe@umontreal.ca](mailto:hervé.philippe@umontreal.ca)

## ‘Subspecies’ and ‘race’ should not be used as synonyms

SIR — Your News Feature ‘Disputed definition’ looks at the pitfalls of discussing race with regard to humans (*Nature* **455**, 1025–1026; 2008). Social norms now effectively prohibit, with good cause, the assumption that there are biological distinctions among human races. Thankfully, too, the heyday of eugenics has long since passed.

You do not mention, however, that the term ‘race’ is often treated as a synonym for the taxonomic

rank of subspecies (for example, see E. Mayr *Principles of Systematic Zoology* 44, McGraw-Hill, 1969). An unwitting reader might infer that the term ‘subspecies’ is equally problematic and should therefore be equally eschewed. Some, indeed, would argue as much (for example, E. O. Wilson and W. L. Brown *Syst. Zool.* **2**, 97–111; 1953; and R. M. Zink *Proc. R. Soc. B* **271**, 561–564; 2004).

However, ‘subspecies’ remains a useful taxonomic division that enriches our understanding of evolution and biogeography. It provides a handle for identifiable units of geographic variation and, therefore, frequently acts as impetus for investigations into the evolution of particular species.

Subspecies can be defined as “a collection of populations occupying a distinct breeding range and diagnosably distinct from other such populations” (M. A. Patten and P. Unitt *Auk* **119**, 26–35; 2002), representing a level of biological organization below that of species. This definition is not arbitrary, as there are clear ways of describing a subspecies objectively.

Given the problems associated with the term ‘race’, conflating ‘race’ and ‘subspecies’ is potentially misleading and unnecessarily undermines the proper definition of subspecies. So stop the common practice of using ‘race’ as a synonym for ‘subspecies’ (as, for example, in *Field Guide to the Birds of North America* National Geographic, 5th edn, 2006). Let us relegate that murky term for use by sociologists and politicians enamoured of purported differences among humans.

**Michael A. Patten** Oklahoma Biological Survey, University of Oklahoma, Norman, Oklahoma 73019, USA  
e-mail: [mpatten@ou.edu](mailto:mpatten@ou.edu)

Contributions may be submitted to [correspondence@nature.com](mailto:correspondence@nature.com); please see the Guide to Authors at <http://tinyurl.com/373jsv>. Comments and debate are also welcomed at <http://blogs.nature.com/nautilus>.



## CORRESPONDENCE

## Replacement of animals in research will never be possible

SIR — Your Editorial ‘Call to action’ (*Nature* **456**, 281–282; 2008), concerning the draft of the new European directive on the use of animals in scientific research, correctly points out the risk of severely limiting the use of non-human primates in invasive studies of brain function. Performing such experiments requires humane treatment of animals and painless experimental procedures. This ‘refinement’ of procedure is the first of the 3Rs, the philosophy underlying the European Union (EU) directive. During the past 20 years, technical improvements have significantly reduced both the time and the number of animals used in a project, while increasing the data yield. Thus, the second of the 3Rs, ‘reduction’, is already firmly established.

What needs to be clearly appreciated is that ‘replacement’ (the third R) of this type of research will never be possible. The current draft of the EU directive, in confining the use of non-human primates as far as possible to projects aimed at understanding life-threatening diseases, takes a direction that is both incorrect and illusory, towards a future ban that it considers desirable. As stated in your Editorial, this is a real threat. We must combat it with strength and without compromise. A ban could be justified only if and when all brain function is understood, and if no further challenge is posed to neuroscience by the evolution of modern societies and their pathologies. Obviously, neither of these conditions will ever be realized.

From my privileged observatory as chair of the Programme of European Neuroscience Schools (<http://fens.mdc-berlin.de/pens>), I can testify to the increasing interest among the younger generation in the integrative study of brain function. At the

same time, I stress the dramatic negative consequences that a severe limitation or ban on the use of non-human primates will have on education, in a discipline that currently places Europe at the forefront of modern research in neuroscience.

Behavioural studies have the power to shed light on some of the most common neurological syndromes that affect our societies. They have already provided encouraging first answers about Parkinson’s disease and the principles underlying neural prosthetics and brain-machine interface devices, among other examples. The enforced abandonment of research on great apes has phased out experimental studies on, for example, brain evolution, malaria, hepatitis C and respiratory syncytial virus infection. Prohibiting studies on primates will confine Europe to the periphery of the neuroscience and biomedical arena, with negative consequences for the quality of life of future generations.

**Roberto Caminiti** Department of Physiology and Pharmacology, Sapienza University of Rome, Piazzale Aldo Moro 5, 00185 Rome, Italy

## Western prosperity is based on resources that are running out

SIR — In response to the lack of a flagship achievement by economics, as noted by Jean-Philippe Bouchaud in his Essay ‘Economics needs a scientific revolution’ (*Nature* **455**, 1181; 2008), Jesper Stage proposes in Correspondence that the prosperity of western societies is one such achievement (‘Speaking up for economic-sciences modelling’ *Nature* **456**, 570; 2008). However, this prosperity is mainly based on the use of non-renewable resources and therefore is probably spurious.

Several hundred million years were needed to form

the fossil energy that will be exhausted during a few hundred years. This is roughly equivalent to spending all one’s annual income during the first 30 seconds of a year. In particular, the frenzy to automate processes in order to increase competitiveness leads to rapid exhaustion of available resources, for example through over-fishing or degradation of soils.

All current growth-based economic models imply massive use of non-renewable resources and environmental degradation. These models are not sustainable, even in the short term.

As early as 160 years ago, John Stuart Mill affirmed that “the richest and most prosperous countries would very soon attain the stationary state” (*Principles of Political Economy* Longmans, 1848). In contrast to that time, when resources were being used up at a rate that was several orders of magnitude slower than today, a phase of economic degrowth is necessary before a stationary state can be reached. It would be a major achievement of economics to achieve such a degrowth without social and political disasters.

**Hervé Philippe** Département de Biochimie, Université de Montréal, 2900 Édouard Montpetit, H3C 3J7 Montréal, Québec, Canada  
e-mail: [hervé.philippe@umontreal.ca](mailto:hervé.philippe@umontreal.ca)

## ‘Subspecies’ and ‘race’ should not be used as synonyms

SIR — Your News Feature ‘Disputed definition’ looks at the pitfalls of discussing race with regard to humans (*Nature* **455**, 1025–1026; 2008). Social norms now effectively prohibit, with good cause, the assumption that there are biological distinctions among human races. Thankfully, too, the heyday of eugenics has long since passed.

You do not mention, however, that the term ‘race’ is often treated as a synonym for the taxonomic

rank of subspecies (for example, see E. Mayr *Principles of Systematic Zoology* 44, McGraw-Hill, 1969). An unwitting reader might infer that the term ‘subspecies’ is equally problematic and should therefore be equally eschewed. Some, indeed, would argue as much (for example, E. O. Wilson and W. L. Brown *Syst. Zool.* **2**, 97–111; 1953; and R. M. Zink *Proc. R. Soc. B* **271**, 561–564; 2004).

However, ‘subspecies’ remains a useful taxonomic division that enriches our understanding of evolution and biogeography. It provides a handle for identifiable units of geographic variation and, therefore, frequently acts as impetus for investigations into the evolution of particular species.

Subspecies can be defined as “a collection of populations occupying a distinct breeding range and diagnosably distinct from other such populations” (M. A. Patten and P. Unitt *Auk* **119**, 26–35; 2002), representing a level of biological organization below that of species. This definition is not arbitrary, as there are clear ways of describing a subspecies objectively.

Given the problems associated with the term ‘race’, conflating ‘race’ and ‘subspecies’ is potentially misleading and unnecessarily undermines the proper definition of subspecies. So stop the common practice of using ‘race’ as a synonym for ‘subspecies’ (as, for example, in *Field Guide to the Birds of North America* National Geographic, 5th edn, 2006). Let us relegate that murky term for use by sociologists and politicians enamoured of purported differences among humans.

**Michael A. Patten** Oklahoma Biological Survey, University of Oklahoma, Norman, Oklahoma 73019, USA  
e-mail: [mpatten@ou.edu](mailto:mpatten@ou.edu)

Contributions may be submitted to [correspondence@nature.com](mailto:correspondence@nature.com); please see the Guide to Authors at <http://tinyurl.com/373jsv>. Comments and debate are also welcomed at <http://blogs.nature.com/nautilus>.

## CORRESPONDENCE

## Replacement of animals in research will never be possible

SIR — Your Editorial ‘Call to action’ (*Nature* **456**, 281–282; 2008), concerning the draft of the new European directive on the use of animals in scientific research, correctly points out the risk of severely limiting the use of non-human primates in invasive studies of brain function. Performing such experiments requires humane treatment of animals and painless experimental procedures. This ‘refinement’ of procedure is the first of the 3Rs, the philosophy underlying the European Union (EU) directive. During the past 20 years, technical improvements have significantly reduced both the time and the number of animals used in a project, while increasing the data yield. Thus, the second of the 3Rs, ‘reduction’, is already firmly established.

What needs to be clearly appreciated is that ‘replacement’ (the third R) of this type of research will never be possible. The current draft of the EU directive, in confining the use of non-human primates as far as possible to projects aimed at understanding life-threatening diseases, takes a direction that is both incorrect and illusory, towards a future ban that it considers desirable. As stated in your Editorial, this is a real threat. We must combat it with strength and without compromise. A ban could be justified only if and when all brain function is understood, and if no further challenge is posed to neuroscience by the evolution of modern societies and their pathologies. Obviously, neither of these conditions will ever be realized.

From my privileged observatory as chair of the Programme of European Neuroscience Schools (<http://fens.mdc-berlin.de/pens>), I can testify to the increasing interest among the younger generation in the integrative study of brain function. At the

same time, I stress the dramatic negative consequences that a severe limitation or ban on the use of non-human primates will have on education, in a discipline that currently places Europe at the forefront of modern research in neuroscience.

Behavioural studies have the power to shed light on some of the most common neurological syndromes that affect our societies. They have already provided encouraging first answers about Parkinson’s disease and the principles underlying neural prosthetics and brain-machine interface devices, among other examples. The enforced abandonment of research on great apes has phased out experimental studies on, for example, brain evolution, malaria, hepatitis C and respiratory syncytial virus infection. Prohibiting studies on primates will confine Europe to the periphery of the neuroscience and biomedical arena, with negative consequences for the quality of life of future generations.

**Roberto Caminiti** Department of Physiology and Pharmacology, Sapienza University of Rome, Piazzale Aldo Moro 5, 00185 Rome, Italy

## Western prosperity is based on resources that are running out

SIR — In response to the lack of a flagship achievement by economics, as noted by Jean-Philippe Bouchaud in his Essay ‘Economics needs a scientific revolution’ (*Nature* **455**, 1181; 2008), Jesper Stage proposes in Correspondence that the prosperity of western societies is one such achievement (‘Speaking up for economic-sciences modelling’ *Nature* **456**, 570; 2008). However, this prosperity is mainly based on the use of non-renewable resources and therefore is probably spurious.

Several hundred million years were needed to form

the fossil energy that will be exhausted during a few hundred years. This is roughly equivalent to spending all one’s annual income during the first 30 seconds of a year. In particular, the frenzy to automate processes in order to increase competitiveness leads to rapid exhaustion of available resources, for example through over-fishing or degradation of soils.

All current growth-based economic models imply massive use of non-renewable resources and environmental degradation. These models are not sustainable, even in the short term.

As early as 160 years ago, John Stuart Mill affirmed that “the richest and most prosperous countries would very soon attain the stationary state” (*Principles of Political Economy* Longmans, 1848). In contrast to that time, when resources were being used up at a rate that was several orders of magnitude slower than today, a phase of economic degrowth is necessary before a stationary state can be reached. It would be a major achievement of economics to achieve such a degrowth without social and political disasters.

**Hervé Philippe** Département de Biochimie, Université de Montréal, 2900 Édouard Montpetit, H3C 3J7 Montréal, Québec, Canada  
e-mail: [hervé.philippe@umontreal.ca](mailto:hervé.philippe@umontreal.ca)

## ‘Subspecies’ and ‘race’ should not be used as synonyms

SIR — Your News Feature ‘Disputed definition’ looks at the pitfalls of discussing race with regard to humans (*Nature* **455**, 1025–1026; 2008). Social norms now effectively prohibit, with good cause, the assumption that there are biological distinctions among human races. Thankfully, too, the heyday of eugenics has long since passed.

You do not mention, however, that the term ‘race’ is often treated as a synonym for the taxonomic

rank of subspecies (for example, see E. Mayr *Principles of Systematic Zoology* 44, McGraw-Hill, 1969). An unwitting reader might infer that the term ‘subspecies’ is equally problematic and should therefore be equally eschewed. Some, indeed, would argue as much (for example, E. O. Wilson and W. L. Brown *Syst. Zool.* **2**, 97–111; 1953; and R. M. Zink *Proc. R. Soc. B* **271**, 561–564; 2004).

However, ‘subspecies’ remains a useful taxonomic division that enriches our understanding of evolution and biogeography. It provides a handle for identifiable units of geographic variation and, therefore, frequently acts as impetus for investigations into the evolution of particular species.

Subspecies can be defined as “a collection of populations occupying a distinct breeding range and diagnosably distinct from other such populations” (M. A. Patten and P. Unitt *Auk* **119**, 26–35; 2002), representing a level of biological organization below that of species. This definition is not arbitrary, as there are clear ways of describing a subspecies objectively.

Given the problems associated with the term ‘race’, conflating ‘race’ and ‘subspecies’ is potentially misleading and unnecessarily undermines the proper definition of subspecies. So stop the common practice of using ‘race’ as a synonym for ‘subspecies’ (as, for example, in *Field Guide to the Birds of North America* National Geographic, 5th edn, 2006). Let us relegate that murky term for use by sociologists and politicians enamoured of purported differences among humans.

**Michael A. Patten** Oklahoma Biological Survey, University of Oklahoma, Norman, Oklahoma 73019, USA  
e-mail: [mpatten@ou.edu](mailto:mpatten@ou.edu)

Contributions may be submitted to [correspondence@nature.com](mailto:correspondence@nature.com); please see the Guide to Authors at <http://tinyurl.com/373jsv>. Comments and debate are also welcomed at <http://blogs.nature.com/nautilus>.



# ESSAY

## Love: Neuroscience reveals all

Poetry it is not. Nor is it particularly romantic. But reducing love to its component parts helps us to understand human sexuality, and may lead to drugs that enhance or diminish our love for another, says **Larry J. Young**.

In his *Love's Trinity*, the Victorian poet laureate Alfred Austin sums up the holistic view of love that has long held sway:

*Soul, heart, and body, we thus singly name,  
Are not in love divisible and distinct,  
But each with each inseparably link'd.*

Now researchers are attempting to isolate and identify the neural and genetic components underlying this seemingly uniquely human emotion. Indeed, biologists may soon be able to reduce certain mental states associated with love to a biochemical chain of events. This has implications for the evolution of human sexuality, and raises important societal issues given our increasing use of genetic tests to screen for certain behaviours, and of drugs to modulate mental processes.

Animal models have greatly aided our understanding of the mechanisms that regulate emotions — particularly for evolutionarily conserved states such as fear and anxiety. These advances have led to pharmaceutical therapies for anxiety, phobias and post-traumatic stress disorders. Such models are also beginning to shed light on love.

We are not alone in being able to form intense and enduring social ties. Take the mother-infant bond. Whether or not the emotional connection between a ewe and her lamb, or a female macaque and her offspring, is qualitatively similar to human motherly love, it is highly likely that these relationships share evolutionarily conserved brain mechanisms. In humans, rats and sheep, the hormone oxytocin is released during labour, delivery and nursing. In ewes, an infusion of oxytocin into the brain results in rapid bonding with a foreign lamb.

Long-term bonding between mates is rare in mammals. It may be regulated by the same brain mechanisms as those involved in maternal bonding. For instance, pair bonding in the female monogamous prairie vole is stimulated by oxytocin released in the brain during mating. A female prairie vole rapidly becomes attached to the nearest male if her brain is infused with oxytocin. The hormone interacts with the reward and reinforcement system driven by the neurotransmitter dopamine

— the same circuitry that drugs such as nicotine, cocaine and heroine act on in humans to produce euphoria and addiction.

There is intriguing overlap between the brain areas involved in vole pair bonding and those associated with human love. Dopamine-related reward regions of the human brain are active in mothers viewing images of their child. Similar activation patterns are seen in people looking at photographs of their lovers.

The notion that pair bonding in humans may have evolved through a tweaking of the brain mechanisms underlying maternal bonding could explain certain unique characteristics

relationships than do those of men lacking it. For both voles and humans, *AVPR1A* genetic polymorphisms predict how much vasopressin receptor is expressed in the brain.

The view of love as an emergent property of a cocktail of ancient neuropeptides and neurotransmitters raises important issues for society. For one thing, drugs that manipulate brain systems at whim to enhance or diminish our love for another may not be far away. Experiments have shown that a nasal squirt of oxytocin enhances trust and tunes people into others' emotions. Internet entrepreneurs are already marketing products such as Enhanced Liquid

Trust, a cologne-like mixture of oxytocin and pheromones "designed to boost the dating and relationship area of your life".

Although such products are unlikely to do anything other than boost users' confidence, studies are under way in Australia to determine whether an oxytocin spray might aid traditional

marital therapy.

We don't yet know whether the drugs commonly used to treat disorders from depression to sexual dysfunction affect people's relationships by altering neurochemistry. But both Prozac and Viagra influence the oxytocin system. The quality of patients' relationships should be included in the list of variables assessed in controlled psychiatric drug studies.

The possibility that genetic variation may influence the quality of our romantic relationships also has intriguing implications. Perhaps genetic tests for the suitability of potential partners will one day become available, the results of which could accompany, and even override, our gut instincts in selecting the perfect partner. Either way, recent advances in the biology of pair bonding mean it won't be long before an unscrupulous suitor could slip a pharmaceutical 'love potion' in our drink. And if they did, would we care? After all, love is insanity. ■

**Larry Young** is at 954 Gatewood Road, Yerkes National Primate Research Center, Emory University, Atlanta, Georgia 30322, USA. e-mail: lyoun03@emory.edu

See <http://tinyurl.com/6quanw> for further reading. For more on Being Human, see [www.nature.com/nature/focus/beinghuman](http://www.nature.com/nature/focus/beinghuman).



G. BECKER

of human sexuality. For example, female sexual desire may have become decoupled from fertility, and the female breast may have become an erotic stimulus for males, to activate ancient maternal-bonding systems. The stimulation of the cervix and nipples during sexual intimacy are potent releasers of brain oxytocin, and may function to strengthen the emotional tie between partners.

Pair bonding in males involves similar brain circuitry to that in females, but different neurochemical pathways. In male prairie voles, for example, vasopressin — a hormone related to oxytocin — stimulates pair bonding, aggression towards potential rivals, and paternal instincts, such as grooming offspring in the nest. Variation in a regulatory region of the vasopressin receptor gene, *avpr1a*, predicts the likelihood that a male vole will bond with a female.

Similarly, in humans, different forms of the *AVPR1A* gene are associated with variation in pair bonding and relationship quality. A recent study shows that men with a particular *AVPR1A* variant are twice as likely as men without it to remain unmarried, or when married, twice as likely to report a recent crisis in their marriage. Spouses of men with the variant also express more dissatisfaction in their

## BOOKS &amp; ARTS

# Future tigers of innovation

Manufacturing in China and India has seen huge expansion, but California's Silicon Valley can breathe easy — the countries are still some way from becoming world innovation leaders, explains **Ming-Wei Wang**.

**The Venturesome Economy:  
How Innovation Sustains Prosperity in a  
More Connected World**

by Amar Bhidé

Princeton University Press: 2008. 520 pp.  
\$35, £19.95

Written during these times of economic instability and job insecurity, *The Venturesome Economy* by Amar Bhidé examines innovation and its market in an era of rapid globalization. Bhidé, a professor of business at Columbia University, New York, provides an analysis of the nature and mechanism of innovation.

He examines the relationships between know-how and products to stress that innovation can materialize only when there is a benefit to the public. Ownership of intellectual-property rights and practical use of innovation dictate the economic return to inventors and to those who financed or participated in its development, regardless of where the innovation originated.

Innovation is divided into three layers: ground-, mid- and high-level. Bhidé clearly lays out the importance of mid-level innovation: the capability to develop products. It bridges high-level creativity and ground-level production, allowing the formation of novel products or services. Outsourcing research and manufacturing activities to poorer countries does not affect this capability, as innovation proves to be a dynamic ecosystem that involves many participants and aspects of society. "The different forms of innovation interact in complicated ways, and it is these interconnected, multilevel advances that create economic value," he says.

Using many interviews with business executives and reliable statistics, Bhidé points out how venture-capital participation is crucial in pushing innovation into the market. Many discoveries that are later developed to benefit the public are supported in their infancy by venture-capital funds. This mechanism is a key vehicle among Western nations for transforming creative ideas into commercially viable products or services.

*The Venturesome Economy* also explains that cutting-edge research performed overseas can ultimately help production and consumption for domestic users. Sending research and development (R&D) activities offshore to China and India, for example, is good for the United States and Europe. In a persuasive analysis from historical and scholarly perspectives, Bhidé convinces us that this outward activity frees innovators in



China's manufacturing power turns innovations from other countries into consumer products.

the United States and Europe, allowing them to pursue more intellectual endeavours, as long as they retain ownership of the inventions and have a dominant role in sales and marketing — both crucial to realizing the value of innovations.

Bhidé recognizes concerns that outsourcing research activities will challenge the supremacy of the United States and other developed countries in terms of technological innovation, and hence their national interests. In reality, this is unlikely to happen at present. Although the United States is facing huge financial problems, its economy is the largest in the world, around four times larger than China's and almost twelve times that of India, according to World Bank data. The United States has a tradition and culture of innovation and has the largest consumer market, which is very receptive to new products and services. Although China is the largest producer of modern goods for the international market, its capacity for consumption has yet to catch up, providing no immediate competition to US consumers. In addition, lower tolerance to failure, a need for more cohesive teamwork, insufficient development experience — that is, mid-level innovation — and deficient venture-capital mechanisms continuously hinder China's attempts to become a major leader in the global innovation arena.

Bhidé agrees that concerns about China taking over US scientific supremacy are unsubstantiated, and "arise from a failure to appreciate the complex nature of the modern innovation system and its interactions with globalization". It took more than 50 years to develop California's

Silicon Valley, and one cannot expect it to be reproduced overnight in China or India, despite massive infrastructure expansion in both countries and booming outsourcing businesses. An essential spirit of Silicon Valley is respect for entrepreneurship — risk-taking and accepting failure have become part of the unique culture that continues to exalt innovations from generation to generation. It also attracts many immigrants from all over the world, forming a pool of talent that is indispensable to its success and fervour. Innovation is not only about science and technology, but extends to management, finance and culture.

A venturesome economy relies on what Bhidé calls 'venturesome consumption', without which the benefits of innovation cannot be realized: "the willingness and ability of intermediate producers and individual consumers to take a chance on and effectively use new know-how and products is at least as important as, if not more important than, its capacity to undertake high-level research," he writes. Becoming an innovative nation requires scientific and technological superiority, and mastery of the commercialization of innovation to benefit from it.

However, the current financial climate has caused significant difficulties in raising venture-capital funds. The economic gloom has resulted in dwindling resources for R&D as venturesome business has become less attractive to wary investors. There is also a lack of funding for early-stage research compared with the disproportionate amount being spent on late-stage product development. Without

W. WEN/EPA/CORBIS





Gary Hall argues for the importance of free, worldwide and perpetual access to scientific research results in *Digitize this Book!* (Univ. Minnesota Press, 2008). He focuses on the benefits and problems of open access for academic and research purposes, discusses the global effects of new media and asks to what extent increasing Internet use has changed political decision-making.

Two new books discuss the effects of technology on society. *Beyond: Business and Society in Transformation* (Palgrave Macmillan, 2008) looks at how it is



influencing areas such as science, religion, art and politics — and what we can expect in the future. Studying how technologies have altered education has led Mario Raich and Simon L. Dolan to predict the rise of a 'virtual culture' in business and society, in which physically distant individuals are linked by shared purposes online.

William E. Halal's *Technology's Promise* (Palgrave Macmillan, 2008) uses data gathered by the TechCast Project at George Washington University in Washington DC to predict how current problems, such as food shortages or the energy crisis, could lead to future opportunities. Assessing developments in genetics, energy and space travel, Halal speculates on how greater access to global information will provide opportunities for developing nations.

*Innovative India Rises* (Medialand, 2008), edited by veteran science writer and political journalist L. K. Sharma, presents a broad view of India's innovation. Scientists, policy makers and businessmen, justifiably proud of what India has achieved, assess the problems it faces and the future it may attain. Authors discuss India's aspirations in space and the potential benefits of space technology on the ground. Energy, defence and biotechnology also get an in-depth look. The volume updates a previous version written a decade ago.

Jenny Meyer

such crucial resources, innovation faces obstacles in getting off the ground.

In *The Venturesome Economy*, Bhidé provides a thorough discussion of the relationship between venture-backed business and globalization. Asserting the global influence of the United States, he explores the complex synthesis of innovation in an increasingly open international market. He also emphasizes the importance of embracing the ever-changing market and not fearing the false alarms and paranoia that strike an unpredictable economy. Fortune can be invited only by discourse with other countries

and by encouraging their advancement and development. The venturesome economy will establish itself on such frankness to innovation in a constantly changing world. ■

**Ming-Wei Wang** is director of the Chinese National Center for Drug Screening and professor of pharmacology at the Shanghai Institute of Materia Medica, Chinese Academy of Sciences, Shanghai 201203, China.

e-mail: wangmw@mail.shcnc.ac.cn

For more on innovation, see [www.nature.com/nature/focus/innovation/index.html](http://www.nature.com/nature/focus/innovation/index.html).

## India's scientific legacy

**Technology at the Core:  
Science and Technology with Indira Gandhi**  
by Ashok Parthasarathi  
Addison-Wesley Professional: 2008.  
348 pp. \$29.99

The end of the Second World War saw the beginning of decolonization in many countries. Among the nations that became free, India is unique in having a firm science and technology base. This exists because the nation was led by a visionary prime minister, Jawaharlal Nehru, who strongly believed in directing science and technology for the development of the emerging nation. Nehru's dialogue with high-ranking scientists, such as Shanti Swarup Bhatnagar, Homi Bhabha and Daulat Singh Kothari, led to practical solutions for how to achieve it. Another fortunate circumstance was that Nehru had a long tenure of 17 years at the helm, during which India enjoyed political stability.

It is against this background that one should read *Technology at the Core*. The author's father, the late G. Parthasarathi, was a senior diplomat and close confidant of prime minister Indira Gandhi, Nehru's daughter. And author Ashok Parthasarathi worked for several years in her secretariat, making him eminently qualified to write an account of how she handled issues relating to science and technology. Indeed, in several places he cites instances showing the informality of her interaction with him.

Mrs Gandhi, as she was widely known, succeeded her father two years after his demise, and like him, she had a soft spot for science and technology. "It was Indira Gandhi who brought scientists, engineers and technocrats into policy-making and managerial positions," explains Parthasarathi. Nehru, by contrast, saw them more as laboratory workers and thinkers.

This book focuses on the years 1967 to 1977

and 1980 to 1984, when Mrs Gandhi was in power and when Parthasarathi was able to observe, report on and somewhat influence the events that were important enough for the prime minister's intervention. Since Nehru's time, major science and technology issues in India, such as space and atomic energy, have been handled by the prime minister. Parthasarathi was initially appointed special assistant to Vikram Sarabhai, the Chairman of the Atomic Energy Commission. In 1970 he was moved to the prime minister's secretariat, where his job was administrative in nature but required good scientific knowledge. His varied roles included briefing the prime minister, preparing drafts of her speeches, acquainting her with the progress of meetings — including complaints about bureaucratic delay — and reminding her of previous enabling decisions of the cabinet.

One might imagine that science-related decisions would be taken rationally. That image receives a knock if one reads the accounts in this book. One learns that Sarabhai gave an unrealistic future estimate of nuclear power generation without consulting his second-in-command at the Atomic Energy Commission, Homi Sethna, who had the engineering experience. The Department of Atomic Energy continued to have internal quarrels between engineers and scientists. The book also describes controversies from the Council of Scientific and Industrial Research, with one director-general reportedly victimizing the favoured staff of his predecessor.

There are hints of bigger controversies. When the Indian National Satellite System was being constructed, Mrs Gandhi insisted on finding out who was involved in the tendering procedure. She suspected that one of her senior ministerial colleagues was trying to influence the bids. Advance payments were reportedly sent to suppliers of defence equipment in the United States shortly before the US government was



Gary Hall argues for the importance of free, worldwide and perpetual access to scientific research results in *Digitize this Book!* (Univ. Minnesota Press, 2008). He focuses on the benefits and problems of open access for academic and research purposes, discusses the global effects of new media and asks to what extent increasing Internet use has changed political decision-making.

Two new books discuss the effects of technology on society. *Beyond: Business and Society in Transformation* (Palgrave Macmillan, 2008) looks at how it is



influencing areas such as science, religion, art and politics — and what we can expect in the future. Studying how technologies have altered education has led Mario Raich and Simon L. Dolan to predict the rise of a 'virtual culture' in business and society, in which physically distant individuals are linked by shared purposes online.

William E. Halal's *Technology's Promise* (Palgrave Macmillan, 2008) uses data gathered by the TechCast Project at George Washington University in Washington DC to predict how current problems, such as food shortages or the energy crisis, could lead to future opportunities. Assessing developments in genetics, energy and space travel, Halal speculates on how greater access to global information will provide opportunities for developing nations.

*Innovative India Rises* (Medialand, 2008), edited by veteran science writer and political journalist L. K. Sharma, presents a broad view of India's innovation. Scientists, policy makers and businessmen, justifiably proud of what India has achieved, assess the problems it faces and the future it may attain. Authors discuss India's aspirations in space and the potential benefits of space technology on the ground. Energy, defence and biotechnology also get an in-depth look. The volume updates a previous version written a decade ago.

Jenny Meyer

such crucial resources, innovation faces obstacles in getting off the ground.

In *The Venturesome Economy*, Bhidé provides a thorough discussion of the relationship between venture-backed business and globalization. Asserting the global influence of the United States, he explores the complex synthesis of innovation in an increasingly open international market. He also emphasizes the importance of embracing the ever-changing market and not fearing the false alarms and paranoia that strike an unpredictable economy. Fortune can be invited only by discourse with other countries

and by encouraging their advancement and development. The venturesome economy will establish itself on such frankness to innovation in a constantly changing world. ■

**Ming-Wei Wang** is director of the Chinese National Center for Drug Screening and professor of pharmacology at the Shanghai Institute of Materia Medica, Chinese Academy of Sciences, Shanghai 201203, China.

e-mail: wangmw@mail.shcnc.ac.cn

For more on innovation, see [www.nature.com/nature/focus/innovation/index.html](http://www.nature.com/nature/focus/innovation/index.html).

## India's scientific legacy

**Technology at the Core:  
Science and Technology with Indira Gandhi**  
by Ashok Parthasarathi  
Addison-Wesley Professional: 2008.  
348 pp. \$29.99

The end of the Second World War saw the beginning of decolonization in many countries. Among the nations that became free, India is unique in having a firm science and technology base. This exists because the nation was led by a visionary prime minister, Jawaharlal Nehru, who strongly believed in directing science and technology for the development of the emerging nation. Nehru's dialogue with high-ranking scientists, such as Shanti Swarup Bhatnagar, Homi Bhabha and Daulat Singh Kothari, led to practical solutions for how to achieve it. Another fortunate circumstance was that Nehru had a long tenure of 17 years at the helm, during which India enjoyed political stability.

It is against this background that one should read *Technology at the Core*. The author's father, the late G. Parthasarathi, was a senior diplomat and close confidant of prime minister Indira Gandhi, Nehru's daughter. And author Ashok Parthasarathi worked for several years in her secretariat, making him eminently qualified to write an account of how she handled issues relating to science and technology. Indeed, in several places he cites instances showing the informality of her interaction with him.

Mrs Gandhi, as she was widely known, succeeded her father two years after his demise, and like him, she had a soft spot for science and technology. "It was Indira Gandhi who brought scientists, engineers and technocrats into policy-making and managerial positions," explains Parthasarathi. Nehru, by contrast, saw them more as laboratory workers and thinkers.

This book focuses on the years 1967 to 1977

and 1980 to 1984, when Mrs Gandhi was in power and when Parthasarathi was able to observe, report on and somewhat influence the events that were important enough for the prime minister's intervention. Since Nehru's time, major science and technology issues in India, such as space and atomic energy, have been handled by the prime minister. Parthasarathi was initially appointed special assistant to Vikram Sarabhai, the Chairman of the Atomic Energy Commission. In 1970 he was moved to the prime minister's secretariat, where his job was administrative in nature but required good scientific knowledge. His varied roles included briefing the prime minister, preparing drafts of her speeches, acquainting her with the progress of meetings — including complaints about bureaucratic delay — and reminding her of previous enabling decisions of the cabinet.

One might imagine that science-related decisions would be taken rationally. That image receives a knock if one reads the accounts in this book. One learns that Sarabhai gave an unrealistic future estimate of nuclear power generation without consulting his second-in-command at the Atomic Energy Commission, Homi Sethna, who had the engineering experience. The Department of Atomic Energy continued to have internal quarrels between engineers and scientists. The book also describes controversies from the Council of Scientific and Industrial Research, with one director-general reportedly victimizing the favoured staff of his predecessor.

There are hints of bigger controversies. When the Indian National Satellite System was being constructed, Mrs Gandhi insisted on finding out who was involved in the tendering procedure. She suspected that one of her senior ministerial colleagues was trying to influence the bids. Advance payments were reportedly sent to suppliers of defence equipment in the United States shortly before the US government was





Gary Hall argues for the importance of free, worldwide and perpetual access to scientific research results in *Digitize this Book!* (Univ. Minnesota Press, 2008). He focuses on the benefits and problems of open

access for academic and research purposes, discusses the global effects of new media and asks to what extent increasing Internet use has changed political decision-making.

Two new books discuss the effects of technology on society. *Beyond: Business and Society in Transformation* (Palgrave Macmillan, 2008) looks at how it is



influencing areas such as science, religion, art and politics — and what we can expect in the future. Studying how technologies have altered education has led Mario Raich and Simon L. Dolan to predict the rise of a 'virtual culture' in business and society, in

which physically distant individuals are linked by shared purposes online.

William E. Halal's *Technology's Promise* (Palgrave Macmillan, 2008) uses data gathered by the TechCast Project at George Washington University in Washington DC to predict how current problems, such as food shortages or the energy crisis, could lead to future opportunities. Assessing developments in genetics, energy and space travel, Halal speculates on how greater access to global information will provide opportunities for developing nations.

*Innovative India Rises* (Medialand, 2008), edited by veteran science writer and political journalist L. K. Sharma, presents a broad view of India's innovation. Scientists, policy makers and businessmen, justifiably proud of what India has achieved, assess the problems it faces and the future it may attain. Authors discuss India's aspirations in space and the potential benefits of space technology on the ground. Energy, defence and biotechnology also get an in-depth look. The volume updates a previous version written a decade ago.

Jenny Meyer

such crucial resources, innovation faces obstacles in getting off the ground.

In *The Venturesome Economy*, Bhidé provides a thorough discussion of the relationship between venture-backed business and globalization. Asserting the global influence of the United States, he explores the complex synthesis of innovation in an increasingly open international market. He also emphasizes the importance of embracing the ever-changing market and not fearing the false alarms and paranoia that strike an unpredictable economy. Fortune can be invited only by discourse with other countries

and by encouraging their advancement and development. The venturesome economy will establish itself on such frankness to innovation in a constantly changing world. ■

**Ming-Wei Wang** is director of the Chinese National Center for Drug Screening and professor of pharmacology at the Shanghai Institute of Materia Medica, Chinese Academy of Sciences, Shanghai 201203, China.

e-mail: wangmw@mail.shcnc.ac.cn

For more on innovation, see [www.nature.com/nature/focus/innovation/index.html](http://www.nature.com/nature/focus/innovation/index.html).

## India's scientific legacy

**Technology at the Core:  
Science and Technology with Indira Gandhi**  
by Ashok Parthasarathi  
Addison-Wesley Professional: 2008.  
348 pp. \$29.99

The end of the Second World War saw the beginning of decolonization in many countries. Among the nations that became free, India is unique in having a firm science and technology base. This exists because the nation was led by a visionary prime minister, Jawaharlal Nehru, who strongly believed in directing science and technology for the development of the emerging nation. Nehru's dialogue with high-ranking scientists, such as Shanti Swarup Bhatnagar, Homi Bhabha and Daulat Singh Kothari, led to practical solutions for how to achieve it. Another fortunate circumstance was that Nehru had a long tenure of 17 years at the helm, during which India enjoyed political stability.

It is against this background that one should read *Technology at the Core*. The author's father, the late G. Parthasarathi, was a senior diplomat and close confidant of prime minister Indira Gandhi, Nehru's daughter. And author Ashok Parthasarathi worked for several years in her secretariat, making him eminently qualified to write an account of how she handled issues relating to science and technology. Indeed, in several places he cites instances showing the informality of her interaction with him.

Mrs Gandhi, as she was widely known, succeeded her father two years after his demise, and like him, she had a soft spot for science and technology. "It was Indira Gandhi who brought scientists, engineers and technocrats into policy-making and managerial positions," explains Parthasarathi. Nehru, by contrast, saw them more as laboratory workers and thinkers.

This book focuses on the years 1967 to 1977

and 1980 to 1984, when Mrs Gandhi was in power and when Parthasarathi was able to observe, report on and somewhat influence the events that were important enough for the prime minister's intervention. Since Nehru's time, major science and technology issues in India, such as space and atomic energy, have been handled by the prime minister. Parthasarathi was initially appointed special assistant to Vikram Sarabhai, the Chairman of the Atomic Energy Commission. In 1970 he was moved to the prime minister's secretariat, where his job was administrative in nature but required good scientific knowledge. His varied roles included briefing the prime minister, preparing drafts of her speeches, acquainting her with the progress of meetings — including complaints about bureaucratic delay — and reminding her of previous enabling decisions of the cabinet.

One might imagine that science-related decisions would be taken rationally. That image receives a knock if one reads the accounts in this book. One learns that Sarabhai gave an unrealistic future estimate of nuclear power generation without consulting his second-in-command at the Atomic Energy Commission, Homi Sethna, who had the engineering experience. The Department of Atomic Energy continued to have internal quarrels between engineers and scientists. The book also describes controversies from the Council of Scientific and Industrial Research, with one director-general reportedly victimizing the favoured staff of his predecessor.

There are hints of bigger controversies. When the Indian National Satellite System was being constructed, Mrs Gandhi insisted on finding out who was involved in the tendering procedure. She suspected that one of her senior ministerial colleagues was trying to influence the bids. Advance payments were reportedly sent to suppliers of defence equipment in the United States shortly before the US government was

B. KAPOOR/SYGMA/CORBIS



Indira Gandhi at the site of India's first nuclear test, part of her vision for the country's development.

expected to ban the sale of such equipment to India. Parthasarathi also discusses his own role in the investigation of Monkombu Sambasivan Swaminathan, the distinguished agricultural scientist known for developing high-yielding Indian wheat varieties. He describes how Swaminathan was exonerated after being accused of falsifying scientific claims.

Occasionally, there are glimpses reminiscent of the British sitcom *Yes Minister*, when decisions approved by the cabinet or the prime minister were stalled in the corridors of power. The administration was even divided

between the technocrats and those who came through the regular channel of the administrative service. I recall that during my tenure as member of the Science Advisory Council to prime minister Rajiv Gandhi, the exasperated leader once asked the council: "Tell me, how am I to get this recommendation implemented by my administrators?"

Excellent though this account is, there are serious gaps. Important political events such as the war leading to the formation of Bangladesh, the declaration of emergency with draconian powers assumed by Mrs Gandhi,

her loss of the post-emergency election, and her return to power nearly three years later are mentioned only fleetingly. How did science and technology, especially the prime minister's secretariat, fare during these traumatic events? Even in a purely scientific context, there is no discussion of the 1974 peaceful nuclear test. How much did the secretariat staff know of it? There is frequent mention of Purshottam Narayan Haksar as an important decision-maker whose views were greatly respected by Mrs Gandhi. Yet there is no discussion of why and how he was sidelined during the state of emergency declared in 1975.

A comparison with a political biography of Mrs Gandhi, such as the one by Inder Malhotra, would make this book seem a somewhat dry and oversimplified account of how she functioned and how she ran science and technology in a big emerging nation. *Technology at the Core* is eminently readable as an eyewitness account. But it could have been even more so had the political ambience not been filtered out. ■

**Jayant V. Narlikar** is emeritus professor at the Inter-University Centre for Astronomy and Astrophysics at Pune, India.  
e-mail: jvn@iucaa.ernet.in

## The learning revolution

**Opening Up Education:  
The Collective Advancement of Education  
Through Open Technology, Open Content,  
and Open Knowledge**

Edited by Toru Iiyoshi and M. S. Vijay Kumar  
MIT Press: 2008. 500 pp. \$24.95, £16.95

Education is changing. The ethos of openness that increasingly pervades activities from journalism to software to finance is being adopted by the educational community. The series of essays in *Opening Up Education* offers examples, opportunities and thoughts on the use of shared and freely available resources in education. The book is arranged in three sections: software, content and pedagogy.

Educational software, as in other areas serving a specific need, has both open-source and commercial versions that exist in parallel. Learning management systems, which enable teachers to deliver online content to students and to manage the educational process, are no exception. Projects and open-source software described in the book include the Visual Understanding Environment project at Tufts University, Massachusetts; the University of Oxford's adaptation of the Bodington software developed at

the University of Leeds, UK; and iLab and Open-CourseWare from the Massachusetts Institute of Technology (MIT). The book does not compare specific commercial products against open-source alternatives, nor does it give an inventory of common open-source educational software; in its essays, leaders in the field discuss high-level design and implementation issues, such as ease of adoption by teachers and students, and management of user-access policies.

The authors discuss current open resources in education and their possible future. The section on open content, in addition to MIT's OpenCourseWare, covers the Multimedia Educational Resource for Learning and Online Teaching, Connexions and the Open Learning Initiative, all of which offer free, online educational materials in formats ranging from small learning modules to entire courses also taught as traditional lectures. A major theme is the management of intellectual property, such as with Creative Commons licences, investigated in detail by David Wiley. Quality control of the educational materials is important, whether mediated by peer-review or other means. Many essays repeatedly discuss the merits of top-down versus bottom-up approaches to the creation and management of open content.

The growing availability of high-quality open content is colliding with traditional academic business models, particularly textbook publication. Diane Harley explores the barriers preventing the adoption of digital and open content by faculty members. These include time, cost, access to support structures and the nature of current academic culture, raising a need to integrate traditional reward systems with new forms of educational materials and scholarship.

Richard Baraniuk tries to predict the future of open education by extrapolating from the evolution of the Internet. Using the terminology of web-publishing firm O'Reilly, the first open content was disseminated through the direct mechanisms of 'Web 1.0', when creating content was difficult and a broadcast model emerged. With the rise of the more interactive 'Web 2.0', content creation and remixing has become easy using social-networking sites and intuitive interfaces such as blogs and wikis. Now that students can also create content, the role of the teacher is changing. We are currently observing the rise of this phase against a backdrop of traditionally taught courses. Most students can no longer expect a homogenous style of education across the curriculum. The future promises 'Web 3.0', in which the semantic web will allow further opportunities for automation and artificial intelligence. Increased efficiencies in learning and measuring learning might lie ahead, yet what is worth learning could also change significantly.



B. KAPOOR/SYGMA/CORBIS



Indira Gandhi at the site of India's first nuclear test, part of her vision for the country's development.

expected to ban the sale of such equipment to India. Parthasarathi also discusses his own role in the investigation of Monkombu Sambasivan Swaminathan, the distinguished agricultural scientist known for developing high-yielding Indian wheat varieties. He describes how Swaminathan was exonerated after being accused of falsifying scientific claims.

Occasionally, there are glimpses reminiscent of the British sitcom *Yes Minister*, when decisions approved by the cabinet or the prime minister were stalled in the corridors of power. The administration was even divided

between the technocrats and those who came through the regular channel of the administrative service. I recall that during my tenure as member of the Science Advisory Council to prime minister Rajiv Gandhi, the exasperated leader once asked the council: "Tell me, how am I to get this recommendation implemented by my administrators?"

Excellent though this account is, there are serious gaps. Important political events such as the war leading to the formation of Bangladesh, the declaration of emergency with draconian powers assumed by Mrs Gandhi,

her loss of the post-emergency election, and her return to power nearly three years later are mentioned only fleetingly. How did science and technology, especially the prime minister's secretariat, fare during these traumatic events? Even in a purely scientific context, there is no discussion of the 1974 peaceful nuclear test. How much did the secretariat staff know of it? There is frequent mention of Purshottam Narayan Haksar as an important decision-maker whose views were greatly respected by Mrs Gandhi. Yet there is no discussion of why and how he was sidelined during the state of emergency declared in 1975.

A comparison with a political biography of Mrs Gandhi, such as the one by Inder Malhotra, would make this book seem a somewhat dry and oversimplified account of how she functioned and how she ran science and technology in a big emerging nation. *Technology at the Core* is eminently readable as an eyewitness account. But it could have been even more so had the political ambience not been filtered out. ■

**Jayant V. Narlikar** is emeritus professor at the Inter-University Centre for Astronomy and Astrophysics at Pune, India.  
e-mail: jvn@iucaa.ernet.in

## The learning revolution

**Opening Up Education:  
The Collective Advancement of Education  
Through Open Technology, Open Content,  
and Open Knowledge**

Edited by Toru Iiyoshi and M. S. Vijay Kumar  
MIT Press: 2008. 500 pp. \$24.95, £16.95

Education is changing. The ethos of openness that increasingly pervades activities from journalism to software to finance is being adopted by the educational community. The series of essays in *Opening Up Education* offers examples, opportunities and thoughts on the use of shared and freely available resources in education. The book is arranged in three sections: software, content and pedagogy.

Educational software, as in other areas serving a specific need, has both open-source and commercial versions that exist in parallel. Learning management systems, which enable teachers to deliver online content to students and to manage the educational process, are no exception. Projects and open-source software described in the book include the Visual Understanding Environment project at Tufts University, Massachusetts; the University of Oxford's adaptation of the Bodington software developed at

the University of Leeds, UK; and iLab and OpenCourseWare from the Massachusetts Institute of Technology (MIT). The book does not compare specific commercial products against open-source alternatives, nor does it give an inventory of common open-source educational software; in its essays, leaders in the field discuss high-level design and implementation issues, such as ease of adoption by teachers and students, and management of user-access policies.

The authors discuss current open resources in education and their possible future. The section on open content, in addition to MIT's OpenCourseWare, covers the Multimedia Educational Resource for Learning and Online Teaching, Connexions and the Open Learning Initiative, all of which offer free, online educational materials in formats ranging from small learning modules to entire courses also taught as traditional lectures. A major theme is the management of intellectual property, such as with Creative Commons licences, investigated in detail by David Wiley. Quality control of the educational materials is important, whether mediated by peer-review or other means. Many essays repeatedly discuss the merits of top-down versus bottom-up approaches to the creation and management of open content.

The growing availability of high-quality open content is colliding with traditional academic business models, particularly textbook publication. Diane Harley explores the barriers preventing the adoption of digital and open content by faculty members. These include time, cost, access to support structures and the nature of current academic culture, raising a need to integrate traditional reward systems with new forms of educational materials and scholarship.

Richard Baraniuk tries to predict the future of open education by extrapolating from the evolution of the Internet. Using the terminology of web-publishing firm O'Reilly, the first open content was disseminated through the direct mechanisms of 'Web 1.0', when creating content was difficult and a broadcast model emerged. With the rise of the more interactive 'Web 2.0', content creation and remixing has become easy using social-networking sites and intuitive interfaces such as blogs and wikis. Now that students can also create content, the role of the teacher is changing. We are currently observing the rise of this phase against a backdrop of traditionally taught courses. Most students can no longer expect a homogenous style of education across the curriculum. The future promises 'Web 3.0', in which the semantic web will allow further opportunities for automation and artificial intelligence. Increased efficiencies in learning and measuring learning might lie ahead, yet what is worth learning could also change significantly.

The book's final section examines initiatives that explore how learning happens. The Carnegie Academy for the Scholarship of Teaching and Learning, the Visible Knowledge Project, the KEEP toolkit and the Learning Activity Management System are cited as examples. They do not necessarily involve much technology but use alternatives to the standard lecture format, such as discussions in small student groups. Peer review of research is standard practice, and some argue that teaching should also undergo this process. As these activities require time and effort, new teaching methods need to be given

greater priority in the academic reward system before we can expect their widespread adoption. Bernadine Chuck Fong, a former president of Foothill College, California, describes the college's pioneering work in online and open education. She says that leadership is key to supporting such new initiatives: it must be made clear to faculty members that honesty, trust, integrity and forgiveness are highly valued across the institution. Many authors mention that a strong sense of community is important for the sustained sharing of teaching experiences.

For anyone interested in the openness

movement or in changes to the educational system, *Opening Up Education* is worth perusing. The book is freely available online with links to individual chapters, making it easy to cite and share. It is not an exhaustive review of the field — more examples can be found in the blogosphere — but this valuable book highlights the leading authors on openness in education who we should follow as the field evolves. ■

**Jean-Claude Bradley** is an associate professor in the Department of Chemistry, Drexel University, Philadelphia, Pennsylvania 19104, USA.  
e-mail: jean-claude.bradley@drexel.edu

## Rare books in the flesh

**Beautiful Science:  
Ideas that Changed the World**  
Huntington Library, San Marino, California  
Permanent exhibition

Authentic books, documents and models provide an inspirational introduction to the development of science. One of the world's major rare-book collections is held by the Huntington Library in San Marino, California, which has set up its first permanent exhibition about the history of science.

*Beautiful Science*, which opened in November, displays classic manuscripts and other artefacts relating to astronomy, biology, medicine and physics in four rooms. The original Huntington collection, which now includes the astronomy holdings of the Observatories of the Carnegie Institution of Washington, was bolstered in 2006 by the addition of 67,000 books from the Dibner family's Burndy Library. Curator Dan Lewis has selected about 100 major scientific works from the hundreds of thousands in the collection.

The astronomy room opens with two thirteenth-century manuscripts: *Almagest*, Ptolemy's astronomical treatise originally written in the second century AD, and an Arabic manuscript covering similar material. Edwin Hubble's own copy of Nicolaus Copernicus's *De Revolutionibus*, alas only the second edition from 1566 instead of the first (1543), is on show. Censored by order of the Inquisition in the early seventeenth century, the book reveals the original Sun-centred diagram. Isaac Newton's *Principia Mathematica* (1687) is alongside, a copy that was owned by first Newton himself and then Edmond Halley. The exhibition combines the new with the old: computer animations contrast the Ptolemaic and Copernican views of planetary orbits, and an audio stream quotes from a letter from Hubble explaining the expanding Universe. Also here is Hubble's 1923 logbook that he used at the 2.5-metre Mount



Unravelling the fabric of the body using Andreas Vesalius's drawings from 1543.

Wilson telescope near Pasadena, California. A mark shows his discovery in the Andromeda galaxy of the variable star — later found to be a supernova — that sparked our understanding of the Universe's expansion.

In the biology and natural history section lies a first edition of Charles Darwin's *On the Origin of Species*, with 251 editions of the book in various languages along the wall. Robert Hooke's detailed engraving of a flea in his *Micrographia* (1665) is accompanied by a replica microscope of the time, through which visitors can look at a real flea. Similarly displayed are Antonie von Leeuwenhoek's complete works from 1664 to 1718. Diagrams of the human body in Andreas Vesalius's oversized anatomy book from 1543 are paired with hands-on plastic versions. An unusual, small ivory model from 1540, about 15 centimetres long, shows a pregnant woman with a removable front torso.

The room devoted to physics and light hosts a collection of strangely shaped light bulbs and filaments, three labelled in Thomas Edison's handwriting. Newton's own copy of the second edition of his *Opticks* (1717) is accompanied by

a metre-square display of his 1664 experiment: one prism breaks up white light into a rainbow of colours, and a second prism, which can be moved with a lever, recomposes it. Three spectral atlases are displayed, including Josef Fraunhofer's own from 1816, with his labelling of the strongest absorption lines in the solar spectrum with capital letters, a notation still used today. This atlas belonged to George Ellery Hale, founder of the California Institute of Technology in Pasadena and the Palomar and Mount Wilson Observatories, and who encouraged Henry Huntington to buy the extensive grounds in which the Huntington Library now stands.

The exhibition is a delight. The Huntington's botanical gardens, which are resplendent during the Californian winter, provide the ideal setting to reflect on the great moments of science collected in this fascinating exhibition. ■

**Jay M. Pasachoff** is an astronomer at the California Institute of Technology, Pasadena, California 91125, on sabbatical leave from Williams College, Williamstown, Massachusetts 01267, USA.  
e-mail: jay@gps.caltech.edu



The book's final section examines initiatives that explore how learning happens. The Carnegie Academy for the Scholarship of Teaching and Learning, the Visible Knowledge Project, the KEEP toolkit and the Learning Activity Management System are cited as examples. They do not necessarily involve much technology but use alternatives to the standard lecture format, such as discussions in small student groups. Peer review of research is standard practice, and some argue that teaching should also undergo this process. As these activities require time and effort, new teaching methods need to be given

greater priority in the academic reward system before we can expect their widespread adoption. Bernadine Chuck Fong, a former president of Foothill College, California, describes the college's pioneering work in online and open education. She says that leadership is key to supporting such new initiatives: it must be made clear to faculty members that honesty, trust, integrity and forgiveness are highly valued across the institution. Many authors mention that a strong sense of community is important for the sustained sharing of teaching experiences.

For anyone interested in the openness

movement or in changes to the educational system, *Opening Up Education* is worth perusing. The book is freely available online with links to individual chapters, making it easy to cite and share. It is not an exhaustive review of the field — more examples can be found in the blogosphere — but this valuable book highlights the leading authors on openness in education who we should follow as the field evolves. ■

**Jean-Claude Bradley** is an associate professor in the Department of Chemistry, Drexel University, Philadelphia, Pennsylvania 19104, USA. e-mail: jean-claude.bradley@drexel.edu

## Rare books in the flesh

**Beautiful Science:  
Ideas that Changed the World**  
Huntington Library, San Marino, California  
Permanent exhibition

Authentic books, documents and models provide an inspirational introduction to the development of science. One of the world's major rare-book collections is held by the Huntington Library in San Marino, California, which has set up its first permanent exhibition about the history of science.

*Beautiful Science*, which opened in November, displays classic manuscripts and other artefacts relating to astronomy, biology, medicine and physics in four rooms. The original Huntington collection, which now includes the astronomy holdings of the Observatories of the Carnegie Institution of Washington, was bolstered in 2006 by the addition of 67,000 books from the Dibner family's Burndy Library. Curator Dan Lewis has selected about 100 major scientific works from the hundreds of thousands in the collection.

The astronomy room opens with two thirteenth-century manuscripts: *Almagest*, Ptolemy's astronomical treatise originally written in the second century AD, and an Arabic manuscript covering similar material. Edwin Hubble's own copy of Nicolaus Copernicus's *De Revolutionibus*, alas only the second edition from 1566 instead of the first (1543), is on show. Censored by order of the Inquisition in the early seventeenth century, the book reveals the original Sun-centred diagram. Isaac Newton's *Principia Mathematica* (1687) is alongside, a copy that was owned by first Newton himself and then Edmond Halley. The exhibition combines the new with the old: computer animations contrast the Ptolemaic and Copernican views of planetary orbits, and an audio stream quotes from a letter from Hubble explaining the expanding Universe. Also here is Hubble's 1923 logbook that he used at the 2.5-metre Mount



Unravelling the fabric of the body using Andreas Vesalius's drawings from 1543.

Wilson telescope near Pasadena, California. A mark shows his discovery in the Andromeda galaxy of the variable star — later found to be a supernova — that sparked our understanding of the Universe's expansion.

In the biology and natural history section lies a first edition of Charles Darwin's *On the Origin of Species*, with 251 editions of the book in various languages along the wall. Robert Hooke's detailed engraving of a flea in his *Micrographia* (1665) is accompanied by a replica microscope of the time, through which visitors can look at a real flea. Similarly displayed are Antonie van Leeuwenhoek's complete works from 1664 to 1718. Diagrams of the human body in Andreas Vesalius's oversized anatomy book from 1543 are paired with hands-on plastic versions. An unusual, small ivory model from 1540, about 15 centimetres long, shows a pregnant woman with a removable front torso.

The room devoted to physics and light hosts a collection of strangely shaped light bulbs and filaments, three labelled in Thomas Edison's handwriting. Newton's own copy of the second edition of his *Opticks* (1717) is accompanied by

a metre-square display of his 1664 experiment: one prism breaks up white light into a rainbow of colours, and a second prism, which can be moved with a lever, recomposes it. Three spectral atlases are displayed, including Josef Fraunhofer's own from 1816, with his labelling of the strongest absorption lines in the solar spectrum with capital letters, a notation still used today. This atlas belonged to George Ellery Hale, founder of the California Institute of Technology in Pasadena and the Palomar and Mount Wilson Observatories, and who encouraged Henry Huntington to buy the extensive grounds in which the Huntington Library now stands.

The exhibition is a delight. The Huntington's botanical gardens, which are resplendent during the Californian winter, provide the ideal setting to reflect on the great moments of science collected in this fascinating exhibition. ■

**Jay M. Pasachoff** is an astronomer at the California Institute of Technology, Pasadena, California 91125, on sabbatical leave from Williams College, Williamstown, Massachusetts 01267, USA. e-mail: jay@gps.caltech.edu

## ORGANIC CHEMISTRY

## Molecular diversity by design

Stuart L. Schreiber

Many organic syntheses are target-oriented — each multi-step route is designed to make just one compound. But now a diversity-oriented synthesis can make 80 different molecular skeletons in just a few steps.

Genome biology is shining a bright light on the origins of human disease. Unfortunately, the biological targets emerging as ideal points for therapeutic intervention are often viewed as being extremely difficult, if not impossible, to modulate with small molecules — which is a problem, because most drugs are small molecules. But is this view justified? Drug hunters search for candidates for drug-discovery programmes by screening large numbers of compounds in biological assays. Perhaps these collections simply lack compounds from structural classes that would modulate the targets identified by genomics studies<sup>1</sup>. Reporting in *Angewandte Chemie*, Morton *et al.*<sup>2</sup> describe an ingenious synthetic pathway that will help to populate screening collections with structurally diverse compounds.

For many decades, organic chemists have searched for ways of making naturally occurring small molecules (known in the field as natural products). These objects of affection pose strategic challenges: can sequences of reactions be devised that turn simple, readily available compounds into more complex target compounds<sup>3</sup>? In the more-notable successes, the resulting syntheses have provided insights into such fundamental areas as conformational analysis<sup>4,5</sup> (the study of the dynamic shapes of molecules), general principles of reactivity<sup>6</sup>, and biosynthesis and life's prebiotic origins<sup>7</sup>. Natural-product syntheses have on several occasions served as starting points for drug development<sup>8</sup>, and they have revealed gaps in the methods of organic synthesis, providing motivation to fill them<sup>9</sup>.

But in recent years, synthetic targets have changed. Modern biology is gradually discovering how molecules such as transcription factors and regulatory RNAs are involved in disease. Such molecules are considered to be 'undruggable' targets, because they bear little resemblance to the approximately 500 targets of the current pharmacopoeia. In addition, as the functions of disease genes have been uncovered, they have suggested other processes (such as the changing of one type of cell in the body into another) or interactions (such as those between proteins, or between proteins and DNA) that might be targeted and/or

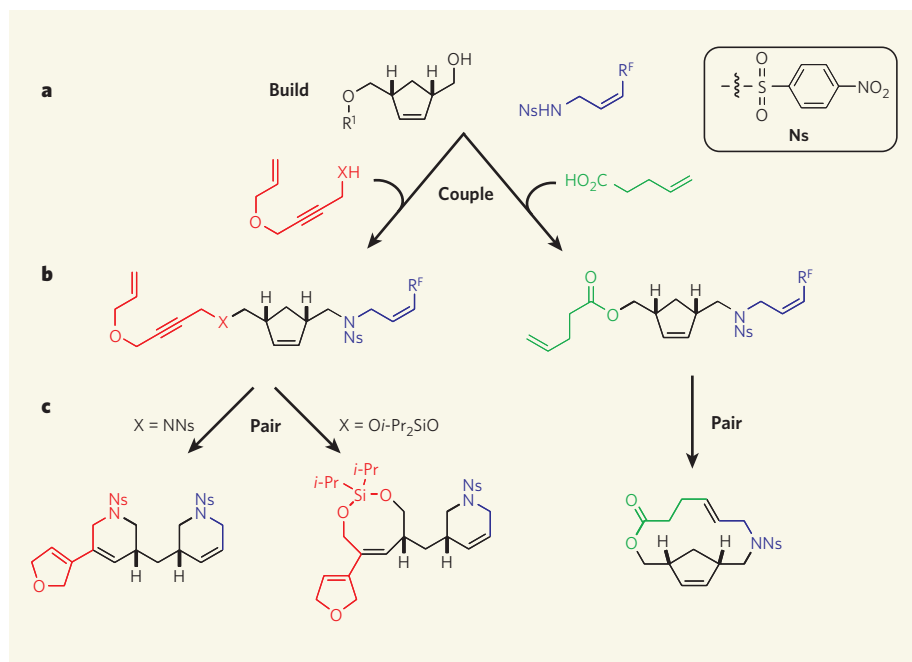


**Figure 1 | Diversity-oriented synthesis.** Morton *et al.*<sup>2</sup> have devised a general 'build-couple-pair' synthetic strategy, and have used it to make 80 different structural classes of compounds rapidly. **a**, The first step is to build a set of molecular building blocks, of which four are shown here, each in a different colour.  $R^1$  is any hydrocarbon;  $R^F$  is a fluorocarbon attached through a linker molecule; and  $X$  is a variable structural element. **b**, In the second step, the building blocks are coupled together in various combinations to create intermediate molecules. **c**, Finally, pairs of groups within the intermediates react to form a structurally diverse set of final compounds.  $i\text{-Pr}$  is an isopropyl group,  $\text{C}(\text{CH}_3)_2$ .

disrupted by drugs. But these also fall into the 'undruggable' category. Natural products tend to modulate a limited set of targets that have general functions — cytoskeletal proteins that define the shapes of cells are common examples — but do not seem to modulate these other, more-specialized targets and processes. Chemists are therefore stepping in to make compounds that do.

It is impossible to design such compounds from scratch. Instead, it is best to make a 'super-set' of compounds of such structural diversity that, for any given aspect of a biological process, members can be found that can modulate that aspect. When the super-set is screened in biological assays, compounds would thus be found that modulate even undruggable biological targets. Experience shows that

successful programmes for drug discovery, or for finding molecular probes of biological processes, require that many thousands of compounds be available for screening. This makes it impractical to prepare each member of a super-set using its own, target-based synthesis pathway. Instead, flexible, modular syntheses must be devised that allow many structurally diverse compounds to be prepared efficiently. So which compounds should be prepared, and how should such a diversity-oriented synthesis be planned?

The best, but most difficult, strategy is to make compounds in a way that anticipates problems at each step of the drug-discovery process in which organic synthesis is involved. As described above, the first such step involves finding a molecule that modulates a disease





## 50 YEARS AGO

The final stage of a Russian multi-stage rocket, launched at about 17.00 hr. U.T. on January 2, flew past the Moon to become the first artificial planet of the Sun. The final-stage rocket is stated to have weighed 1,472 kgm ... after all its fuel was burnt, and its pay-load of scientific instruments, together with the container, weighed 361.3 kgm ... The instruments were intended to measure the Moon's magnetic field, the intensity and composition of cosmic rays, lunar radioactivity, the impact of meteors and the composition of the Moon's atmosphere ... The programme of scientific measurements is stated to have been successfully accomplished before radio contact was lost on January 5 ... Since the Moon was near last quarter at the time of the launching, the rocket's path was nearly tangential to the Earth's orbit; the rocket's orbit around the Sun, therefore, has almost the same perihelion distance as the Earth's orbit, though the aphelion distance is greater because of the rocket's greater speed at perihelion.

From *Nature* 10 January 1959.

## 100 YEARS AGO

Never had earthquake taken such toll of human life as that which has just devastated Calabria ... [T]he Yeddo — now Tokio — earthquake of 1703, with its death-roll of 200,000, had stood in a class by itself; yet even this great number seems insufficient to count the deaths on the morning of December 28, 1908, and if to those whose lives were ended by the immediate effects of the earthquake we add the subsequent deaths from injury, exposure, and sickness, the loss will amount to well over a quarter of a million lives ... From Pizzo the band of destruction extends southwards for about 50 miles through ill-starred Monteleone, which no earthquake seems to spare, Palmi, and Bagnara, to Reggio di Calabria.

From *Nature* 7 January 1909.

target or process. This requires thousands of structurally diverse compounds to be made for screening. The next step is to optimize the biological properties of the compounds found during screening. This involves making analogues of the compounds, each containing slightly different structural modifications — ideally, every atom in the compound should be modified, without an overwhelming synthetic effort. The final step involves synthesizing the optimal compound, either for use as a biochemical probe for research or as a drug in medicine, efficiently, at low cost and in large quantities.

Historically, the pharmaceutical industry has dealt with each of these steps in a serial fashion, and the associated problems have been addressed independently. Each step is challenging and can create bottlenecks in the overall process. Diversity-oriented synthesis aims to address, if not overcome, all of these challenges before the first compounds have even been screened.

Morton *et al.*<sup>2</sup> implement a strategy for a diversity-oriented synthesis that might advance each of the above steps of the drug-discovery process. Their approach yields structurally novel and diverse products in high yields and of excellent purity — impressively, the authors made 80 different molecular 'skeletons'. Because the synthetic route is modular, many modifications can in principle be made to each skeleton simply by using different variants of the reactants at the first step. This is ideal for the optimization stage of drug discovery. Finally, the route contains only a small number of steps, which should make it adaptable for large-scale synthesis.

The authors use the 'build-couple-pair' strategy of organic synthesis<sup>9</sup>, which entails preparing molecular building blocks that contain several chemical groups (Fig. 1). Some of these groups react in the first step of the synthesis to couple the building blocks together. Once all the different blocks have been coupled, the remaining groups react with others found in the same intermediate molecule. The build-couple-pair strategy precisely mimics that used by nature in the biosynthesis of nearly all natural products, where it also allows structurally diverse products to be formed. Helpfully, Morton *et al.* have designed the protocol of their diversity-oriented synthesis with a particular eye to making it simple to purify the compounds — this is a boon, because purification is usually the most labour-intensive part of any chemical reaction.

The resulting products<sup>2</sup> differ from the compounds found in most small-molecule screening collections. Typically purchased from commercial vendors, the compounds in such collections frequently lack chirality and are structurally simple. This means that they can bind to only a small number of biological targets. The compounds in commercial libraries also tend to be structurally similar — their 'diversity' is limited to variations in appendages attached to a small number of common

skeletons. This undesirable combination of properties means that, although enormous numbers of compounds (often more than a million) are frequently tested in screenings, at great expense, in the case of undruggable targets relatively few biologically active 'hits' are found. In principle, a smaller library of compounds that contains a more diverse range of molecular shapes, such as those made by Morton *et al.*, would provide both more hits for less money, and hits for the more challenging biological targets.

The structural complexity of natural products enables them to perform demanding biological tasks, and their structural diversity allows them to perform different tasks. The same is true of non-natural compounds produced using diversity-oriented synthesis and subsequently identified as small-molecule probes of protein-DNA interactions<sup>10</sup>, protein-protein interactions<sup>11</sup>, transcription-factor activity<sup>12</sup>, multi-drug resistance in pathogens<sup>13</sup> and many other processes often imagined to be impervious to modulation by small molecules. These results suggest that Morton and colleagues' synthetic pathway might also yield molecular probes of many aspects of disease.

Diversity-oriented syntheses are growing in number and sophistication, and this study<sup>2</sup> will probably inspire even more advances in the area. The tremendous growth of small-molecule screening for biological research and drug discovery will provide additional clues to the contrasting biological activities of small molecules derived from diversity-oriented syntheses, from commercial libraries, and from nature. There remains an urgent need to understand better both the relationship of structural features of small molecules to screening outcomes and, more generally, the relationship of synthetic strategies to success in discovering probes for biological research and drugs for therapeutic interventions. ■

Stuart L. Schreiber is at the Howard Hughes Medical Institute, Broad Institute of Harvard and MIT, Cambridge, Massachusetts 02142, USA.  
e-mail: stuart\_schreiber@harvard.edu

- Payne, D. J., Gwynn, M. N., Holmes, D. J. & Pompliano, D. L. *Nature Rev. Drug Discov.* **6**, 29–40 (2007).
- Morton, D., Leach, S., Cordier, C., Warriner, S. & Nelson, A. *Angew. Chem. Int. Edn* **48**, 104–109 (2008).
- Corey, E. J. & Cheng, X.-M. *The Logic of Chemical Synthesis* (Wiley, 1989).
- Barton, D. H. *Science* **169**, 539–544 (1970).
- Vovack, V. J. & Still, W. C. *J. Am. Chem. Soc.* **106**, 1148–1149 (1984).
- Woodward, R. B. & Hoffmann, R. *Angew. Chem. Int. Edn* **8**, 781–853 (1969).
- Eschenmoser, A. & Wintner, C. E. *Science* **196**, 1410–1420 (1977).
- Yu, M., Kishi, Y. & Littlefield, B. in *Anticancer Agents from Natural Products* (eds Cragg, G., Kingston, D. & Newman, D.) 241–265 (Taylor & Francis, 2005).
- Nielsen, T. E. & Schreiber, S. L. *Angew. Chem. Int. Edn* **47**, 48–56 (2008).
- Ng, P. Y. *et al.* *Angew. Chem. Int. Edn* **46**, 5352–5355 (2007).
- Kuruvilla, F. G., Shamji, A. F., Sternson, S. M., Hergenrother, P. J. & Schreiber, S. L. *Nature* **416**, 653–657 (2002).
- Koehler, A. N., Shamji, A. F. & Schreiber, S. L. *J. Am. Chem. Soc.* **125**, 8420–8421 (2003).
- Thomas, G. L. *et al.* *Angew. Chem. Int. Edn* **47**, 2808–2812 (2008).



## 50 YEARS AGO

The final stage of a Russian multi-stage rocket, launched at about 17.00 hr. U.T. on January 2, flew past the Moon to become the first artificial planet of the Sun. The final-stage rocket is stated to have weighed 1,472 kgm ... after all its fuel was burnt, and its pay-load of scientific instruments, together with the container, weighed 361.3 kgm ... The instruments were intended to measure the Moon's magnetic field, the intensity and composition of cosmic rays, lunar radioactivity, the impact of meteors and the composition of the Moon's atmosphere ... The programme of scientific measurements is stated to have been successfully accomplished before radio contact was lost on January 5 ... Since the Moon was near last quarter at the time of the launching, the rocket's path was nearly tangential to the Earth's orbit; the rocket's orbit around the Sun, therefore, has almost the same perihelion distance as the Earth's orbit, though the aphelion distance is greater because of the rocket's greater speed at perihelion.

From *Nature* 10 January 1959.

## 100 YEARS AGO

Never had earthquake taken such toll of human life as that which has just devastated Calabria ... [T]he Yeddo — now Tokio — earthquake of 1703, with its death-roll of 200,000, had stood in a class by itself; yet even this great number seems insufficient to count the deaths on the morning of December 28, 1908, and if to those whose lives were ended by the immediate effects of the earthquake we add the subsequent deaths from injury, exposure, and sickness, the loss will amount to well over a quarter of a million lives ... From Pizzo the band of destruction extends southwards for about 50 miles through ill-starred Monteleone, which no earthquake seems to spare, Palmi, and Bagnara, to Reggio di Calabria.

From *Nature* 7 January 1909.

target or process. This requires thousands of structurally diverse compounds to be made for screening. The next step is to optimize the biological properties of the compounds found during screening. This involves making analogues of the compounds, each containing slightly different structural modifications — ideally, every atom in the compound should be modified, without an overwhelming synthetic effort. The final step involves synthesizing the optimal compound, either for use as a biochemical probe for research or as a drug in medicine, efficiently, at low cost and in large quantities.

Historically, the pharmaceutical industry has dealt with each of these steps in a serial fashion, and the associated problems have been addressed independently. Each step is challenging and can create bottlenecks in the overall process. Diversity-oriented synthesis aims to address, if not overcome, all of these challenges before the first compounds have even been screened.

Morton *et al.*<sup>2</sup> implement a strategy for a diversity-oriented synthesis that might advance each of the above steps of the drug-discovery process. Their approach yields structurally novel and diverse products in high yields and of excellent purity — impressively, the authors made 80 different molecular 'skeletons'. Because the synthetic route is modular, many modifications can in principle be made to each skeleton simply by using different variants of the reactants at the first step. This is ideal for the optimization stage of drug discovery. Finally, the route contains only a small number of steps, which should make it adaptable for large-scale synthesis.

The authors use the 'build-couple-pair' strategy of organic synthesis<sup>9</sup>, which entails preparing molecular building blocks that contain several chemical groups (Fig. 1). Some of these groups react in the first step of the synthesis to couple the building blocks together. Once all the different blocks have been coupled, the remaining groups react with others found in the same intermediate molecule. The build-couple-pair strategy precisely mimics that used by nature in the biosynthesis of nearly all natural products, where it also allows structurally diverse products to be formed. Helpfully, Morton *et al.* have designed the protocol of their diversity-oriented synthesis with a particular eye to making it simple to purify the compounds — this is a boon, because purification is usually the most labour-intensive part of any chemical reaction.

The resulting products<sup>2</sup> differ from the compounds found in most small-molecule screening collections. Typically purchased from commercial vendors, the compounds in such collections frequently lack chirality and are structurally simple. This means that they can bind to only a small number of biological targets. The compounds in commercial libraries also tend to be structurally similar — their 'diversity' is limited to variations in appendages attached to a small number of common

skeletons. This undesirable combination of properties means that, although enormous numbers of compounds (often more than a million) are frequently tested in screenings, at great expense, in the case of undruggable targets relatively few biologically active 'hits' are found. In principle, a smaller library of compounds that contains a more diverse range of molecular shapes, such as those made by Morton *et al.*, would provide both more hits for less money, and hits for the more challenging biological targets.

The structural complexity of natural products enables them to perform demanding biological tasks, and their structural diversity allows them to perform different tasks. The same is true of non-natural compounds produced using diversity-oriented synthesis and subsequently identified as small-molecule probes of protein-DNA interactions<sup>10</sup>, protein-protein interactions<sup>11</sup>, transcription-factor activity<sup>12</sup>, multi-drug resistance in pathogens<sup>13</sup> and many other processes often imagined to be impervious to modulation by small molecules. These results suggest that Morton and colleagues' synthetic pathway might also yield molecular probes of many aspects of disease.

Diversity-oriented syntheses are growing in number and sophistication, and this study<sup>2</sup> will probably inspire even more advances in the area. The tremendous growth of small-molecule screening for biological research and drug discovery will provide additional clues to the contrasting biological activities of small molecules derived from diversity-oriented syntheses, from commercial libraries, and from nature. There remains an urgent need to understand better both the relationship of structural features of small molecules to screening outcomes and, more generally, the relationship of synthetic strategies to success in discovering probes for biological research and drugs for therapeutic interventions. ■

Stuart L. Schreiber is at the Howard Hughes Medical Institute, Broad Institute of Harvard and MIT, Cambridge, Massachusetts 02142, USA.  
e-mail: stuart\_schreiber@harvard.edu

- Payne, D. J., Gwynn, M. N., Holmes, D. J. & Pompliano, D. L. *Nature Rev. Drug Discov.* **6**, 29–40 (2007).
- Morton, D., Leach, S., Cordier, C., Warriner, S. & Nelson, A. *Angew. Chem. Int. Edn* **48**, 104–109 (2008).
- Corey, E. J. & Cheng, X.-M. *The Logic of Chemical Synthesis* (Wiley, 1989).
- Barton, D. H. *Science* **169**, 539–544 (1970).
- Vovack, V. J. & Still, W. C. *J. Am. Chem. Soc.* **106**, 1148–1149 (1984).
- Woodward, R. B. & Hoffmann, R. *Angew. Chem. Int. Edn* **8**, 781–853 (1969).
- Eschenmoser, A. & Wintner, C. E. *Science* **196**, 1410–1420 (1977).
- Yu, M., Kishi, Y. & Littlefield, B. in *Anticancer Agents from Natural Products* (eds Cragg, G., Kingston, D. & Newman, D.) 241–265 (Taylor & Francis, 2005).
- Nielsen, T. E. & Schreiber, S. L. *Angew. Chem. Int. Edn* **47**, 48–56 (2008).
- Ng, P. Y. *et al.* *Angew. Chem. Int. Edn* **46**, 5352–5355 (2007).
- Kuruvilla, F. G., Shamji, A. F., Sternson, S. M., Hergenrother, P. J. & Schreiber, S. L. *Nature* **416**, 653–657 (2002).
- Koehler, A. N., Shamji, A. F. & Schreiber, S. L. *J. Am. Chem. Soc.* **125**, 8420–8421 (2003).
- Thomas, G. L. *et al.* *Angew. Chem. Int. Edn* **47**, 2808–2812 (2008).



## IMMUNOLOGY

# Barrier to electrical storms

Richard M. Ransohoff

**Epilepsy is characterized by repetitive seizures due to abnormal electrical activity in the brain. Immune cells promote development of this disorder by mediating the breakdown of the blood–brain barrier.**

It has long been thought that epilepsy is mainly caused by structural changes in the central nervous system, without much input from outside this system. The blood–brain barrier has, however, been a candidate for helping to protect the brain from seizures<sup>1</sup>: it maintains ionic and metabolic homeostasis in the central nervous system, excluding serum and circulating cells while facilitating the passage of essential substances such as glucose. Indeed, several studies have shown that compromising this barrier aids the initiation and progression of epilepsy, even in the absence of structural damage to brain tissue. Two reports<sup>2,3</sup>, including one by Kim *et al.*<sup>2</sup> on page 191 of this issue, now take us a step further by documenting the involvement of inflammatory cells in the leakiness of the blood–brain barrier in mouse models of seizures and epilepsy.

Infection of the mouse central nervous system with lymphocytic choriomeningitis virus (LCMV) results in the breakdown of the blood–brain barrier and fatal seizures. This condition had been believed to occur when T cells expressing the CD8 marker protein (CD8<sup>+</sup> T cells) recognized virus-infected cells, bound to them and killed them. Kim and colleagues<sup>2</sup> tested this hypothesis by performing a detailed dynamic study in the LCMV-mouse model, visualizing fluorescently labelled CD8<sup>+</sup> T cells through the intact skull using two-photon microscopy.

Of the meninges membranes that enclose the brain, the one adjacent to the brain tissue is separated from the membrane that adheres to the skull's inner surface by the subarachnoid space (SAS). This space contains

cerebrospinal fluid and structural connective tissue containing stromal cells. Shortly after LCMV infection, Kim *et al.* did not detect CD8<sup>+</sup> T cells in the brain parenchyma — the functional tissue into which the virus had been inoculated and whence it spreads to the SAS stromal cells. During this time, however, T cells entered the SAS to make short-lived contact with LCMV-infected stromal cells. The transient contact seems to be sufficient for the T cells to recognize the virus and become activated. But the T cells fail to adhere firmly to the infected cells — a step essential for the killing of virus-infected cells — probably because the stromal cells secrete proteins called chemokines, which can impair the special type of adhesiveness involved in immune recognition.

Kim *et al.*<sup>2</sup> also find that, once activated, the CD8<sup>+</sup> T cells secrete additional chemokines, which trigger an enormous influx of inflammatory myeloid cells such as neutrophils and monocytes into the SAS (Fig. 1a). Recruitment of the inflammatory cells was associated with the disruption of the blood–brain barrier within the brain parenchyma, presumably because these cells produce inflammatory immune mediators called cytokines; these small proteins diffuse into the brain tissue and compromise the barrier functions of the endothelial cells lining blood vessels, leading to seizures and death. Depleting LCMV-infected mice of the myeloid cells delayed death, pointing at a causal relation between the inflammatory reaction at the meninges, leakiness of the blood–brain barrier and fatal seizures<sup>2</sup>.

These results vividly demonstrate that CD8<sup>+</sup> T cells initially recognize LCMV through

immune surveillance in the SAS. Intriguingly, within the SAS, immune recognition of antigenic targets by CD4<sup>+</sup> T cells has also been reported<sup>4</sup>. Together, these papers<sup>2,4</sup> highlight the need to understand the versatile immune apparatus that resides within the SAS<sup>5</sup> and supports the notion of surveillance of the central nervous system<sup>5</sup> by both CD4<sup>+</sup> and CD8<sup>+</sup> T cells within the SAS.

Of the previous studies that have convincingly implicated breakdown of the blood–brain barrier in the development of epilepsy, one salient example involved injection of the epilepsy-inducing drug pilocarpine into the systemic circulation of mice<sup>6</sup>. This treatment causes severe seizures followed by the onset of chronic epilepsy. At the molecular level, pilocarpine injection leads to a mild inflammatory reaction with release of the cytokine interleukin-1 $\beta$ , causing a slightly leaky blood–brain barrier<sup>6</sup> and the subsequent entry of low levels of pilocarpine and potassium ions (which lower seizure thresholds) into the central nervous system.

The understanding of how pilocarpine injection leads to breakdown of the blood–brain barrier is extended by Fabene *et al.* in a study published in *Nature Medicine*<sup>3</sup>. The authors propose that pilocarpine injection stimulates white blood cells as well as the endothelial cells of the blood–brain barrier, which then transiently adhere to each other, causing the barrier to become leaky (Fig. 1b). They tested this hypothesis by blocking (using neutralizing antibodies) or genetically eliminating molecules that these two cell types use for adhesion. Remarkably, suppressing interaction between white blood cells and endothelial cells virtually abrogated initiation of seizures. And when adhesion molecules were blocked after a single severe seizure, progression to epilepsy was suppressed.

These findings<sup>3</sup> are in line with several previous reports: seizures disrupt the function of the blood–brain barrier and permit entry of serum albumin into the brain<sup>7</sup>; albumin is taken up into the brain's support cells, the astrocytes, downregulating potassium channels in these cells and impairing their ability to buffer excess

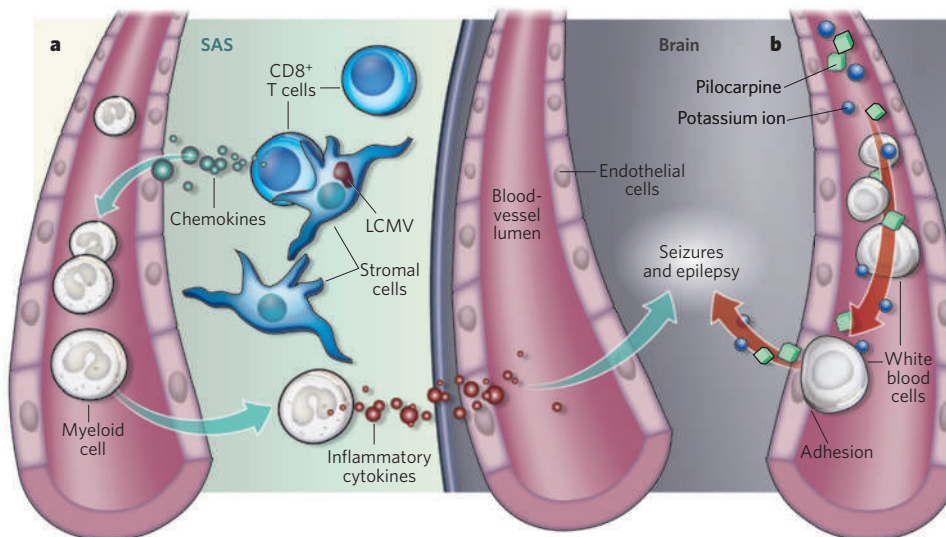


**Figure 1 | Role of the immune system in epilepsy.** **a**, Kim *et al.*<sup>2</sup> show that, while surveying the mouse brain, T cells carrying the CD8 marker (CD8<sup>+</sup> T cells) recognize and bind to stromal cells infected with lymphocytic choriomeningitis virus (LCMV) in the subarachnoid space (SAS). Consequently, the T cells secrete chemoattractants that trigger the influx of myeloid cells into the SAS and their secretion of inflammatory cytokines. The cytokines then enter the brain, breaking down the blood–brain barrier, causing seizures and death. **b**, Fabene *et al.*<sup>3</sup> find that systemic injection of the drug pilocarpine triggers adhesion of white blood cells to endothelial cells. This compromises the blood–brain barrier, allowing the entry of pilocarpine, as well as potassium ions (K<sup>+</sup>) into the brain, which trigger seizures and ultimately chronic epilepsy.

potassium<sup>8</sup>; and chronic seizures induce vessel formation (angiogenesis), increasing vascular surface area and producing a crop of porous, newly formed vascular elements that have poor barrier function<sup>9</sup>. The blood–brain barrier therefore seems to be involved in the initiation, progression and perpetuation of seizures.

These exciting findings<sup>2,3</sup> document two routes to the development of seizures and epilepsy. Kim *et al.* show that meningeal inflammation can signal ‘inwards’ to the brain parenchyma, activating the vasculature there and compromising the blood–brain barrier. Fabene and colleagues confirm that, in the presence of an epilepsy-inducing factor, even mild systemic inflammation leading to minimal disruption of the blood–brain barrier can produce seizures. These authors’ results<sup>3</sup> are

convincing and of potential significance for treatment, as they studied some molecules that could be used to inhibit the adherence of white blood cells to endothelial cells in humans.

But as far as therapeutic application is concerned, these findings are fraught with concerns about how well the animal models reflect epilepsy in humans. What’s more, long-term administration of adhesion-molecule blockers would pose some risk<sup>10</sup>, as they would alter immune function and increase vulnerability to infection. However, short courses of such treatment after brain trauma, for example, which is known to increase liability to seizures, might offer the opportunity both to enhance patients’ chances of recovery and to generate a proof-of-principle for the validity in humans of observations derived from animal models. ■

Richard M. Ransohoff is at the Neuroinflammation Research Center, Department of Neurosciences, Lerner Research Institute, Cleveland Clinic Foundation, Cleveland, Ohio 44195, USA.  
e-mail: ransohr@ccf.org

1. Janigro, D. *Epilepsy Curr.* **7**, 105–107 (2007).
2. Kim, J. V., Kang, S. S., Dustin, M. L. & McGavern, D. B. *Nature* **457**, 191–195 (2009).
3. Fabene, P. F. *et al. Nature Med.* **14**, 1377–1383 (2008).
4. Kivisakk, P. *et al. Ann. Neurol.* doi:10.1002/ana.21379 (2008).
5. Ransohoff, R. M., Kivisakk, P. & Kidd, G. *Nature Rev. Immunol.* **3**, 569–581 (2003).
6. Marchi, N. *et al. Epilepsia* **48**, 732–742 (2007).
7. van Vliet, E. A. *et al. Brain* **130**, 521–534 (2007).
8. Ivens, S. *et al. Brain* **130**, 535–547 (2007).
9. Rigau, V. *et al. Brain* **130**, 1942–1956 (2007).
10. Ransohoff, R. M. *N. Engl. J. Med.* **356**, 2622–2629 (2007).

## QUANTUM PHYSICS

# Quantum force turns repulsive

Steve K. Lamoreaux

**The experimental verification that a bizarre quantum effect — the Casimir force — can manifest itself in its repulsive form is pivotal not only for fundamental physics but also for nanotechnology.**

In 1948, Hendrik Casimir predicted<sup>1</sup> that two uncharged, perfectly conducting plates in a vacuum would be attracted to each other because of quantum fluctuations in the vacuum’s electromagnetic field between the plates. Generalized for real materials by Evgeny Lifshitz<sup>2</sup> in 1956, Casimir’s prediction has been verified many times and is now known as the Casimir–Lifshitz (C–L) force. But for all systems studied experimentally so far, the C–L force is attractive. Writing in this issue (page 170), Munday *et al.*<sup>3</sup> report the first experimental measurement of a repulsive C–L force.

The attractive C–L force has been measured with great precision, and has been taken into account in the design of nanoscale mechanical devices. But in many instances, the attractive nature of the force has led to more problems than solutions. One such problem is that the components in a nanodevice can stick together irreversibly. The desirability of a repulsive C–L force stems from its potential to fix this problem and also to enable objects to be levitated in fluids, which could find applications in nanotechnology. Proposals for the design of ‘metamaterials’ capable of producing such a repulsive force have been put forward, but attempts to achieve this have been unsuccessful<sup>4</sup>.

Munday and colleagues’ experiment<sup>3</sup> is based on a further generalization<sup>5</sup> of Lifshitz’s formulation of the force, which allows the vacuum to be replaced by a material — here, a liquid. One of the most precise tests of Lifshitz’s theory was performed<sup>6</sup> by Edward Sabisky

and Charles Anderson in 1973, when they measured the binding energy of a superfluid helium film to a crystal surface.

But Lifshitz’s theory also asserts that if the properties of the liquid and plates are appropriately chosen, the C–L force can be repulsive. A repulsive C–L force can be generated by judicious choice of the dielectric permittivities of the plates and the liquid, which describe their ability to store electric-field energy. If the dielectric permittivities of the plates are  $\epsilon_1$  and  $\epsilon_2$ , respectively, and that of the liquid in the gap is  $\epsilon_3$ , the force will be repulsive when  $\epsilon_1 > \epsilon_3 > \epsilon_2$ . And because these permittivities depend on the frequency of the electromagnetic field, this relationship must hold over the broad range of frequencies that contribute to the C–L force.

If this relationship is met, the C–L force will cause the liquid to wet the material’s surface. For example, if one plate is replaced by air or a vacuum ( $\epsilon_2 = 1$ ), and if the liquid’s permittivity is less than that of the other plate, the liquid will spread out in a thin film, rather than forming droplets as is the case with water on an oily glass surface. For instance, liquid helium, which has a very small permittivity, readily forms a thin film on almost all surfaces (except caesium films) because it is ‘repelled’ by the vacuum ( $\epsilon_1 > \epsilon_3 > \epsilon_2 = 1$ ), or highly attracted to the surface, and so wets the surface. In contrast, liquid mercury, which has a high permittivity, does not wet glass ( $\epsilon_1 < \epsilon_3 > \epsilon_2 = 1$ ).

Although many liquids can wet surfaces such as glass or silica, only a few sets of materials (plate–liquid–plate) will satisfy the

requirement for a repulsive force between the plates. The set used by Munday *et al.* consisted of silica and gold, with bromobenzene as the liquid separating them. The authors’ experimental set-up (see Fig. 2 on page 171) used an atomic force microscope that was modified to detect average surface forces rather than atomic-scale point forces. A typical atomic force microscope consists of a microcantilever with a sharp tip at its end that is moved above the specimen’s surface. As the tip scans the surface, the cantilever bends in response to the surface force felt by the tip. This bending is monitored by measuring the angular displacement of laser light reflected from the top surface of the cantilever, and allows the force’s topography to be mapped out.

To measure the C–L force, Munday and colleagues replaced the sharp tip by a microsphere (of diameter about 40 micrometres) coated with gold. This served as the gold plate. Using a spherical surface for one plate simplifies the geometry of the system, which is completely defined by the radius of the sphere and the distance of closest approach to the flat silica plate. Although this leads to a significant — but easily calculated — modification of the force, it eliminates the need for angular alignment of the plates.

A problem associated with all C–L force measurements is the calibration of the system. Munday and colleagues have come up with a clever technique to overcome this problem. When the separation between the gold sphere and the silica plate is changed, the fluid produces a hydrodynamic force that changes linearly with the velocity at which the separation is altered. By measuring the total force at two different velocities, the hydrodynamic force can be isolated with high accuracy from the C–L force. Scaled to the appropriate velocity, the hydrodynamic force can then be subtracted from the total force at a given sphere–plate separation, yielding a clean measurement of the C–L force. The measurements spanned a range in separation from 20 nm to several hundred nanometres, with the minimum distance being



potassium<sup>8</sup>; and chronic seizures induce vessel formation (angiogenesis), increasing vascular surface area and producing a crop of porous, newly formed vascular elements that have poor barrier function<sup>9</sup>. The blood–brain barrier therefore seems to be involved in the initiation, progression and perpetuation of seizures.

These exciting findings<sup>2,3</sup> document two routes to the development of seizures and epilepsy. Kim *et al.* show that meningeal inflammation can signal ‘inwards’ to the brain parenchyma, activating the vasculature there and compromising the blood–brain barrier. Fabene and colleagues confirm that, in the presence of an epilepsy-inducing factor, even mild systemic inflammation leading to minimal disruption of the blood–brain barrier can produce seizures. These authors’ results<sup>3</sup> are

convincing and of potential significance for treatment, as they studied some molecules that could be used to inhibit the adherence of white blood cells to endothelial cells in humans.

But as far as therapeutic application is concerned, these findings are fraught with concerns about how well the animal models reflect epilepsy in humans. What’s more, long-term administration of adhesion-molecule blockers would pose some risk<sup>10</sup>, as they would alter immune function and increase vulnerability to infection. However, short courses of such treatment after brain trauma, for example, which is known to increase liability to seizures, might offer the opportunity both to enhance patients’ chances of recovery and to generate a proof-of-principle for the validity in humans of observations derived from animal models. ■

Richard M. Ransohoff is at the Neuroinflammation Research Center, Department of Neurosciences, Lerner Research Institute, Cleveland Clinic Foundation, Cleveland, Ohio 44195, USA.  
e-mail: ransohr@ccf.org

1. Janigro, D. *Epilepsy Curr.* **7**, 105–107 (2007).
2. Kim, J. V., Kang, S. S., Dustin, M. L. & McGavern, D. B. *Nature* **457**, 191–195 (2009).
3. Fabene, P. F. *et al. Nature Med.* **14**, 1377–1383 (2008).
4. Kivisakk, P. *et al. Ann. Neurol.* doi:10.1002/ana.21379 (2008).
5. Ransohoff, R. M., Kivisakk, P. & Kidd, G. *Nature Rev. Immunol.* **3**, 569–581 (2003).
6. Marchi, N. *et al. Epilepsia* **48**, 732–742 (2007).
7. van Vliet, E. A. *et al. Brain* **130**, 521–534 (2007).
8. Ivens, S. *et al. Brain* **130**, 535–547 (2007).
9. Rigau, V. *et al. Brain* **130**, 1942–1956 (2007).
10. Ransohoff, R. M. *N. Engl. J. Med.* **356**, 2622–2629 (2007).

## QUANTUM PHYSICS

# Quantum force turns repulsive

Steve K. Lamoreaux

**The experimental verification that a bizarre quantum effect — the Casimir force — can manifest itself in its repulsive form is pivotal not only for fundamental physics but also for nanotechnology.**

In 1948, Hendrik Casimir predicted<sup>1</sup> that two uncharged, perfectly conducting plates in a vacuum would be attracted to each other because of quantum fluctuations in the vacuum’s electromagnetic field between the plates. Generalized for real materials by Evgeny Lifshitz<sup>2</sup> in 1956, Casimir’s prediction has been verified many times and is now known as the Casimir–Lifshitz (C–L) force. But for all systems studied experimentally so far, the C–L force is attractive. Writing in this issue (page 170), Munday *et al.*<sup>3</sup> report the first experimental measurement of a repulsive C–L force.

The attractive C–L force has been measured with great precision, and has been taken into account in the design of nanoscale mechanical devices. But in many instances, the attractive nature of the force has led to more problems than solutions. One such problem is that the components in a nanodevice can stick together irreversibly. The desirability of a repulsive C–L force stems from its potential to fix this problem and also to enable objects to be levitated in fluids, which could find applications in nanotechnology. Proposals for the design of ‘metamaterials’ capable of producing such a repulsive force have been put forward, but attempts to achieve this have been unsuccessful<sup>4</sup>.

Munday and colleagues’ experiment<sup>3</sup> is based on a further generalization<sup>5</sup> of Lifshitz’s formulation of the force, which allows the vacuum to be replaced by a material — here, a liquid. One of the most precise tests of Lifshitz’s theory was performed<sup>6</sup> by Edward Sabisky

and Charles Anderson in 1973, when they measured the binding energy of a superfluid helium film to a crystal surface.

But Lifshitz’s theory also asserts that if the properties of the liquid and plates are appropriately chosen, the C–L force can be repulsive. A repulsive C–L force can be generated by judicious choice of the dielectric permittivities of the plates and the liquid, which describe their ability to store electric-field energy. If the dielectric permittivities of the plates are  $\epsilon_1$  and  $\epsilon_2$ , respectively, and that of the liquid in the gap is  $\epsilon_3$ , the force will be repulsive when  $\epsilon_1 > \epsilon_3 > \epsilon_2$ . And because these permittivities depend on the frequency of the electromagnetic field, this relationship must hold over the broad range of frequencies that contribute to the C–L force.

If this relationship is met, the C–L force will cause the liquid to wet the material’s surface. For example, if one plate is replaced by air or a vacuum ( $\epsilon_2 = 1$ ), and if the liquid’s permittivity is less than that of the other plate, the liquid will spread out in a thin film, rather than forming droplets as is the case with water on an oily glass surface. For instance, liquid helium, which has a very small permittivity, readily forms a thin film on almost all surfaces (except caesium films) because it is ‘repelled’ by the vacuum ( $\epsilon_1 > \epsilon_3 > \epsilon_2 = 1$ ), or highly attracted to the surface, and so wets the surface. In contrast, liquid mercury, which has a high permittivity, does not wet glass ( $\epsilon_1 < \epsilon_3 > \epsilon_2 = 1$ ).

Although many liquids can wet surfaces such as glass or silica, only a few sets of materials (plate–liquid–plate) will satisfy the

requirement for a repulsive force between the plates. The set used by Munday *et al.* consisted of silica and gold, with bromobenzene as the liquid separating them. The authors’ experimental set-up (see Fig. 2 on page 171) used an atomic force microscope that was modified to detect average surface forces rather than atomic-scale point forces. A typical atomic force microscope consists of a microcantilever with a sharp tip at its end that is moved above the specimen’s surface. As the tip scans the surface, the cantilever bends in response to the surface force felt by the tip. This bending is monitored by measuring the angular displacement of laser light reflected from the top surface of the cantilever, and allows the force’s topography to be mapped out.

To measure the C–L force, Munday and colleagues replaced the sharp tip by a microsphere (of diameter about 40 micrometres) coated with gold. This served as the gold plate. Using a spherical surface for one plate simplifies the geometry of the system, which is completely defined by the radius of the sphere and the distance of closest approach to the flat silica plate. Although this leads to a significant — but easily calculated — modification of the force, it eliminates the need for angular alignment of the plates.

A problem associated with all C–L force measurements is the calibration of the system. Munday and colleagues have come up with a clever technique to overcome this problem. When the separation between the gold sphere and the silica plate is changed, the fluid produces a hydrodynamic force that changes linearly with the velocity at which the separation is altered. By measuring the total force at two different velocities, the hydrodynamic force can be isolated with high accuracy from the C–L force. Scaled to the appropriate velocity, the hydrodynamic force can then be subtracted from the total force at a given sphere–plate separation, yielding a clean measurement of the C–L force. The measurements spanned a range in separation from 20 nm to several hundred nanometres, with the minimum distance being

limited by the roughness of the gold and silica surfaces, and the maximum distance limited by the system's sensitivity.

Munday and colleagues' demonstration of a repulsive C–L force is pivotal for both fundamental physics and nanodevice engineering. For example, it might be possible to 'tune' the liquid (possibly by mixing two or more liquids) so that the force becomes attractive at large separations, but remains repulsive at

short range. This would provide the means for quantum levitation of an object in a fluid at a fixed distance above another object, and so could lead to the design of ultra-low-friction devices. The applications of the C–L force to nanodevices remain to be investigated, but the prospects look exciting.

Steve K. Lamoreaux is in the Department of Physics, Yale University, New Haven, Connecticut 06520–8120, USA.

e-mail: steve.lamoreaux@yale.edu

1. Casimir, H. B. G. *Proc. K. Ned. Akad. Wet.* **51**, 793–795 (1948).
2. Lifshitz, E. M. *Sov. Phys. JETP* **2**, 73–83 (1956).
3. Munday, J. N., Capasso, F. & Parsegian, V. A. *Nature* **457**, 170–173 (2009).
4. Rosa, F. S. S., Dalvit, D. A. R. & Milonni, P. W. *Phys. Rev. Lett.* **100**, 183602 (2008).
5. Dzyaloshinskii, I. E., Lifshitz, E. M. & Pitaevskii, L. P. *Adv. Phys.* **10**, 165–209 (1961).
6. Sabisky, E. S. & Anderson, C. H. *Phys. Rev. A* **7**, 790–806 (1973).

## PROTEIN SYNTHESIS

# Errors rectified in retrospect

Kurt Fredrick and Michael Ibba

**During protein synthesis, mistakes in adding amino acids to the growing polypeptide chain are usually prevented. If they are not, a quality-control mechanism ensures premature termination of erroneous sequences.**

For cells to flourish, the genetic code must be translated with great accuracy into the amino acids that proteins are made from. During translation, the cell's protein-synthesis factory — the ribosome — carefully monitors the process by which new amino acids are added to a growing polypeptide chain. For each one, a specific trinucleotide (a codon) on messenger RNA is paired with a complementary anticodon on a transfer RNA, which at its other end carries the corresponding amino acid. Once codon–anticodon pairs have formed, the amino acid is chemically linked to the polypeptide chain by a peptide bond. At this point, it was thought that the quality-control duties of the ribosome were more or less complete. But Zaher and Green<sup>1</sup> present evidence in this issue (page 161) that, even after peptide-bond formation, the ribosome can detect codon–anticodon mismatches and reacts by bringing the protein's synthesis to a premature end.

The matching of codons and anticodons by the ribosome is a tricky process, involving a certain amount of leeway (Watson–Crick wobble) to allow the reading of all 64 codons that make up the genetic code. So it is not surprising that, despite careful matchmaking, mistakes are sometimes made, resulting in misfolded or non-functional proteins that must be refolded or destroyed after translation is finished. During protein synthesis, mistakes are generally thought to occur at a rate of about 1 in every 20,000 amino acids, although levels can be higher or lower depending on the conditions<sup>2,3</sup>. Studies in different living systems support this estimated rate of error, whereas experiments with individual components of the protein-synthesis machinery *in vitro* have yielded less clear-cut results.

It was one such experiment that piqued Zaher and Green's interest. When looking at the formation of simple two-amino-acid

peptides, they sometimes saw error rates as high as 1 in 2,000 — an order of magnitude higher than they had expected. To further explore these high error rates, they turned to an occasional mistake that is well documented in living systems: the erroneous translation of the AAU codon into the amino acid lysine, rather than asparagine. They also began to look at the formation of longer peptides of up to four amino acids. Much to their surprise, they found that, once a mistake has been made, the ribosome becomes much less efficient at adding amino acids. So rather than continuing to grow, the nascent peptide chain was released from the translational machinery prematurely.

Ribosomes contain three binding sites for their tRNA substrates: the aminoacyl (A) site, the peptidyl (P) site and the exit (E) site. During each round of amino-acid chain elongation, codon–anticodon pairing allows entry of the correct tRNA into the A site (Fig. 1a). The nascent polypeptide chain bound to the tRNA at the P site is then transferred to the tRNA bearing a new amino acid at the A site, thereby lengthening the chain by one residue. This cycle of amino-acid addition is completed when the tRNA originally at the P site moves to the E site and the tRNA at the A site shifts to the P site, freeing up the A site for the next tRNA (Fig. 1a). The tRNA translocations are accompanied by mRNA movement by three

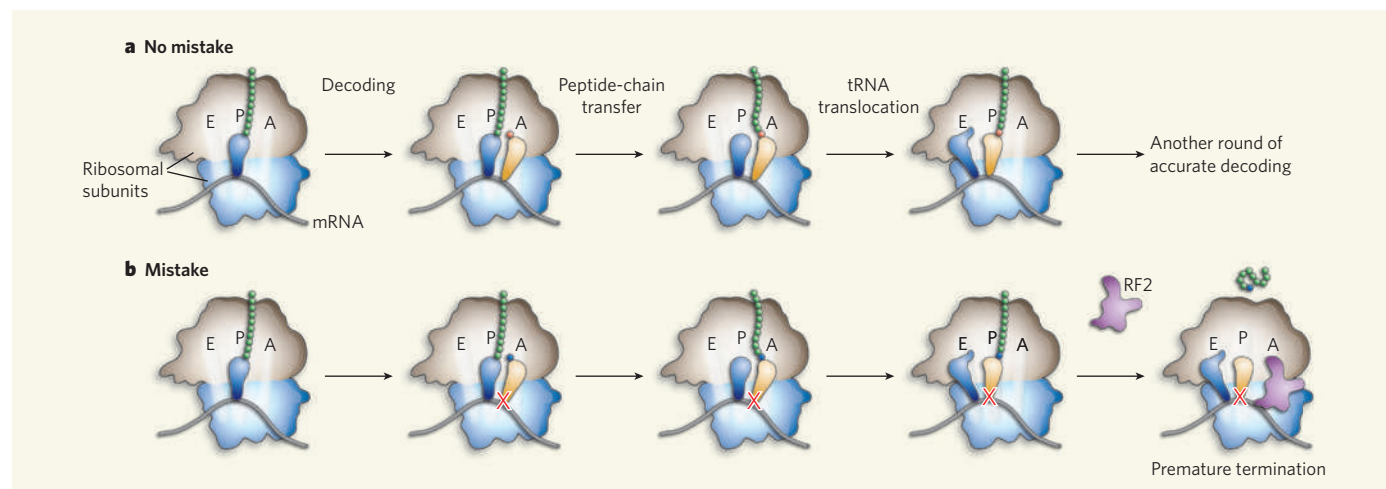


**Figure 1 | Ribosomal matchmaking.** **a**, Normally, the correct tRNA (yellow) enters the A site of the ribosome and the appropriate amino acid (red) is incorporated into the growing peptide chain, which transfers from tRNA in the P site to the tRNA at the A site. Both tRNAs, as well as the mRNA, then shift towards the E site. **b**, When mistakes are made and the mismatched codon–anticodon helix (indicated by a red cross) translocates to the P site, the ribosomal complex becomes susceptible to premature termination by translation factors such as RF2, and the erroneous sequence is prematurely released.



limited by the roughness of the gold and silica surfaces, and the maximum distance limited by the system's sensitivity.

Munday and colleagues' demonstration of a repulsive C–L force is pivotal for both fundamental physics and nanodevice engineering. For example, it might be possible to 'tune' the liquid (possibly by mixing two or more liquids) so that the force becomes attractive at large separations, but remains repulsive at

short range. This would provide the means for quantum levitation of an object in a fluid at a fixed distance above another object, and so could lead to the design of ultra-low-friction devices. The applications of the C–L force to nanodevices remain to be investigated, but the prospects look exciting.

Steve K. Lamoreaux is in the Department of Physics, Yale University, New Haven, Connecticut 06520–8120, USA.

e-mail: steve.lamoreaux@yale.edu

1. Casimir, H. B. G. *Proc. K. Ned. Akad. Wet.* **51**, 793–795 (1948).
2. Lifshitz, E. M. *Sov. Phys. JETP* **2**, 73–83 (1956).
3. Munday, J. N., Capasso, F. & Parsegian, V. A. *Nature* **457**, 170–173 (2009).
4. Rosa, F. S. S., Dalvit, D. A. R. & Milonni, P. W. *Phys. Rev. Lett.* **100**, 183602 (2008).
5. Dzyaloshinskii, I. E., Lifshitz, E. M. & Pitaevskii, L. P. *Adv. Phys.* **10**, 165–209 (1961).
6. Sabisky, E. S. & Anderson, C. H. *Phys. Rev. A* **7**, 790–806 (1973).

## PROTEIN SYNTHESIS

# Errors rectified in retrospect

Kurt Fredrick and Michael Ibba

**During protein synthesis, mistakes in adding amino acids to the growing polypeptide chain are usually prevented. If they are not, a quality-control mechanism ensures premature termination of erroneous sequences.**

For cells to flourish, the genetic code must be translated with great accuracy into the amino acids that proteins are made from. During translation, the cell's protein-synthesis factory — the ribosome — carefully monitors the process by which new amino acids are added to a growing polypeptide chain. For each one, a specific trinucleotide (a codon) on messenger RNA is paired with a complementary anticodon on a transfer RNA, which at its other end carries the corresponding amino acid. Once codon–anticodon pairs have formed, the amino acid is chemically linked to the polypeptide chain by a peptide bond. At this point, it was thought that the quality-control duties of the ribosome were more or less complete. But Zaher and Green<sup>1</sup> present evidence in this issue (page 161) that, even after peptide-bond formation, the ribosome can detect codon–anticodon mismatches and reacts by bringing the protein's synthesis to a premature end.

The matching of codons and anticodons by the ribosome is a tricky process, involving a certain amount of leeway (Watson–Crick wobble) to allow the reading of all 64 codons that make up the genetic code. So it is not surprising that, despite careful matchmaking, mistakes are sometimes made, resulting in misfolded or non-functional proteins that must be refolded or destroyed after translation is finished. During protein synthesis, mistakes are generally thought to occur at a rate of about 1 in every 20,000 amino acids, although levels can be higher or lower depending on the conditions<sup>2,3</sup>. Studies in different living systems support this estimated rate of error, whereas experiments with individual components of the protein-synthesis machinery *in vitro* have yielded less clear-cut results.

It was one such experiment that piqued Zaher and Green's interest. When looking at the formation of simple two-amino-acid

peptides, they sometimes saw error rates as high as 1 in 2,000 — an order of magnitude higher than they had expected. To further explore these high error rates, they turned to an occasional mistake that is well documented in living systems: the erroneous translation of the AAU codon into the amino acid lysine, rather than asparagine. They also began to look at the formation of longer peptides of up to four amino acids. Much to their surprise, they found that, once a mistake has been made, the ribosome becomes much less efficient at adding amino acids. So rather than continuing to grow, the nascent peptide chain was released from the translational machinery prematurely.

Ribosomes contain three binding sites for their tRNA substrates: the aminoacyl (A) site, the peptidyl (P) site and the exit (E) site. During each round of amino-acid chain elongation, codon–anticodon pairing allows entry of the correct tRNA into the A site (Fig. 1a). The nascent polypeptide chain bound to the tRNA at the P site is then transferred to the tRNA bearing a new amino acid at the A site, thereby lengthening the chain by one residue. This cycle of amino-acid addition is completed when the tRNA originally at the P site moves to the E site and the tRNA at the A site shifts to the P site, freeing up the A site for the next tRNA (Fig. 1a). The tRNA translocations are accompanied by mRNA movement by three

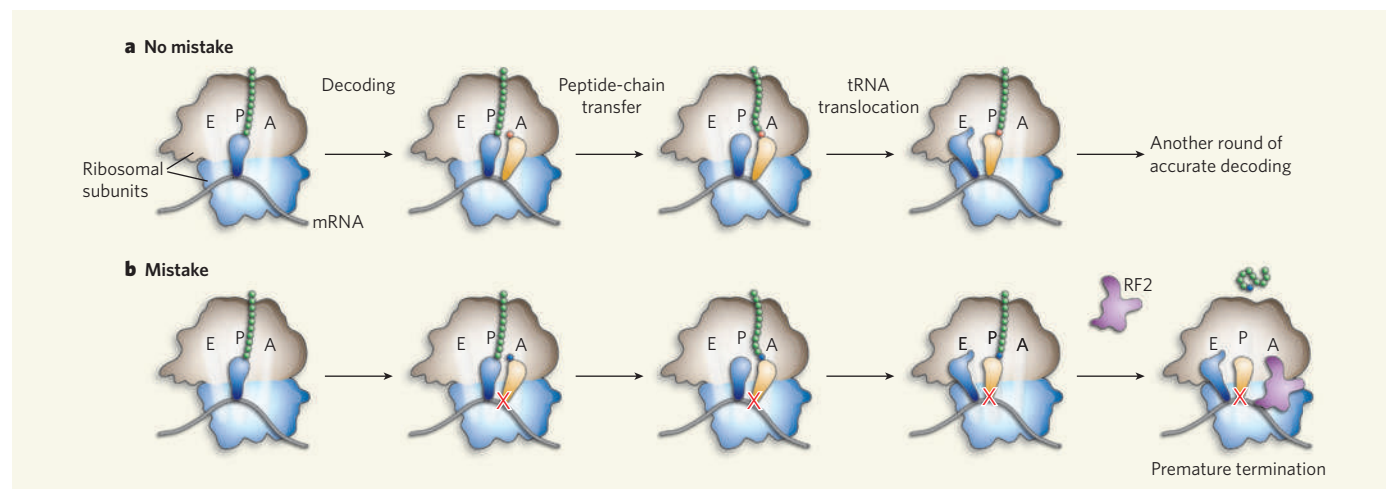


**Figure 1 | Ribosomal matchmaking.** **a**, Normally, the correct tRNA (yellow) enters the A site of the ribosome and the appropriate amino acid (red) is incorporated into the growing peptide chain, which transfers from tRNA in the P site to the tRNA at the A site. Both tRNAs, as well as the mRNA, then shift towards the E site. **b**, When mistakes are made and the mismatched codon–anticodon helix (indicated by a red cross) translocates to the P site, the ribosomal complex becomes susceptible to premature termination by translation factors such as RF2, and the erroneous sequence is prematurely released.

nucleotides — or one codon — towards the E site. Iterative cycles of elongation occur until a stop codon, signalling the end, reaches the A site. Specific recognition of this codon by a primary release factor (known as RF proteins in the bacterium *Escherichia coli*) promotes hydrolysis of the now mature polypeptide from the P-site tRNA, a process called termination<sup>4</sup>.

In an effort to understand their puzzling observations, Zaher and Green<sup>1</sup> studied several defined ribosomal complexes, made from purified components, *in vitro*. They find that complexes containing a mismatch between the anticodon and codon in the P site are susceptible to RF2-mediated peptide release, despite the absence of a stop codon in the A site (Fig. 1b). Although slow, this reaction was stimulated considerably by the secondary release factor RF3, suggesting that it might be relevant *in vivo*, where both RFs are present.

Intriguingly, a sequence containing a mismatched codon–anticodon pair in the P site also stimulated further error — that is, incorporation of an amino acid despite the

absence of correct codon–anticodon pairing<sup>1</sup>. Consequently, complexes containing codon–anticodon mismatches were made in both the E and P sites. Again, the authors observed high rates of RF-dependent peptide release in these complexes, suggesting that termination can efficiently compete with elongation. The net effect is that miscoding errors terminate translation prematurely, which is another means of quality control by the ribosome — retrospectively, following peptide-bond formation — to increase the fraction of functional proteins made.

How codon–anticodon mismatches in the P site (or P and E sites) stimulate further miscoding and peptide release remains unclear. Codon–anticodon pairing in these sites normally helps to maintain the correct reading of codons on mRNA. Mismatches could disrupt such systematic reading of mRNA, potentially allowing various codons to transiently occupy the A site as the mRNA slides through the ribosome unpaired. Another possibility is that mismatches generate a conformational signal in the ribosomal complex that alters the activities

of the translation factors such as RF proteins. Indeed, earlier work<sup>5–7</sup> showed that conformational changes in the ribosome regulate both the decoding of mRNA and its termination. Regardless of the precise mechanism involved, Zaher and Green's work<sup>1</sup> reveals a facet of quality control in protein synthesis that depends on an unanticipated level of complexity in the workings of the ribosome. ■

Kurt Fredrick and Michael Ibba are in the Department of Microbiology, the Ohio State Biochemistry Program and the Center for RNA Biology, Ohio State University, Columbus, Ohio 43210-1292, USA.  
e-mail: [ibba.1@osu.edu](mailto:ibba.1@osu.edu)

1. Zaher, H. S. & Green, R. *Nature* **457**, 161–166 (2009).
2. Kurland, C. G. *Annu. Rev. Genet.* **26**, 29–50 (1992).
3. Kramer, E. B. & Farabaugh, P. J. *RNA* **13**, 87–96 (2007).
4. Ogle, J. M. & Ramakrishnan, V. *Annu. Rev. Biochem.* **74**, 129–177 (2005).
5. Youngman, E. M., He, S. L., Nikstad, L. J. & Green, R. *Mol. Cell* **28**, 533–543 (2007).
6. Laurberg, M. *et al.* *Nature* **454**, 852–857 (2008).
7. Weixlbaumer, A. *et al.* *Science* **322**, 953–956 (2008).

## ASTROPHYSICS

# Magnetic bond

Christopher M. Johns-Krull

**How low-mass stars produce their ubiquitous magnetic fields has long puzzled astronomers. Models of how Earth accomplishes this task could hold the key to understanding the phenomenon on such stars.**

Most of us have probably sprinkled iron filings on a piece of paper laid on top of a bar magnet and seen how they line up in an ordered pattern. The filings trace out the magnetic field produced by the magnet. The strength of the magnetic fields observed in stars and planets, which act like giant bar magnets, varies by several orders of magnitude. Finding the culprit behind this variation has been a challenge. On page 167 of this issue, Christensen *et al.*<sup>1</sup> announce that it is the convective energy flux available that sets the strength of the magnetic field in certain stars.

Like Earth, many — perhaps most — astronomical objects have magnetic fields threading through their interiors and emanating from their surfaces. On the Sun, the magnetic field is known to produce sunspots — regions of intense magnetic activity that are cooler, and hence darker, than the typical surface temperature of the Sun (about 6,000 kelvin). Sunspots were in fact first observed by Galileo, although at the time he was unaware of the role magnetic fields played in creating them. Solar magnetic fields produce a number of other effects, including a very hot ( $10^6$  K), tenuous corona and energetic explosions such as solar flares.

Magnetic fields are now thought to be a common feature of all stars with masses similar to, or lower than, that of the Sun. The evidence comes from observations of the high-energy X-ray emission produced by the hot coronae

surrounding these stars (the X-ray emission and the magnetic-field flux follow a linear relationship<sup>2</sup>). Magnetic fields also seem to be responsible for slowing the rotation of Sun-like stars over time, and are strongly implicated in a range of phenomena that occur during the early and late stages of a star's life.

But how are these magnetic fields produced? The answer seems to lie in some sort of dynamo action. A dynamo is a mechanism that takes a weak, seed magnetic field and amplifies its strength by many orders of magnitude. We have basic ideas about the solar dynamo. Imagine magnetic-field lines drawn on the surface of the Sun starting at its south pole and extending to its north pole (Fig. 1a), and

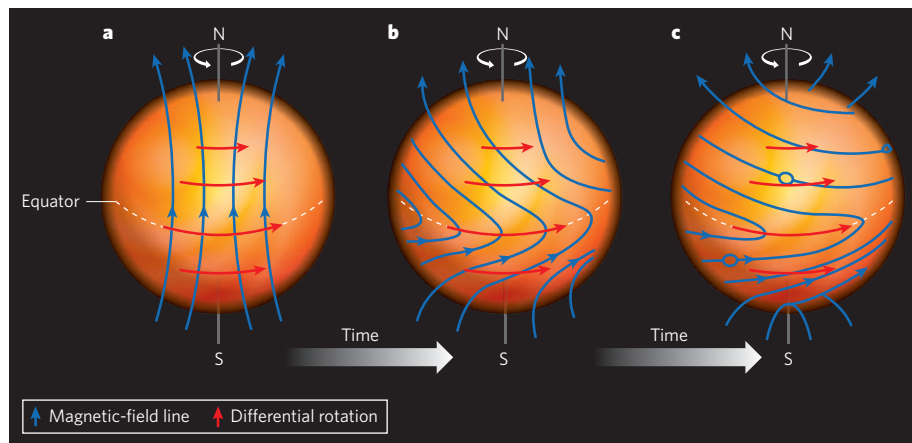


**Figure 1 | The Sun's swirling magnetic field.** Because the Sun is not solid like Earth, but is instead a massive sphere of hot gas, different parts of it rotate at different speeds: the gas at the equator rotates faster than does that at the poles. This differential rotation shears the gas and affects the Sun's magnetic field. As time goes on, the magnetic-field lines become highly distorted and twisted. This process amplifies the strength of the magnetic field. Christensen and colleagues' models<sup>1</sup>, which agree with observations of stars and planets over five orders of magnitude in magnetic-field strength, replace the shear owing to differential rotation with convection-driven shear, but the main principle is the same.



nucleotides — or one codon — towards the E site. Iterative cycles of elongation occur until a stop codon, signalling the end, reaches the A site. Specific recognition of this codon by a primary release factor (known as RF proteins in the bacterium *Escherichia coli*) promotes hydrolysis of the now mature polypeptide from the P-site tRNA, a process called termination<sup>4</sup>.

In an effort to understand their puzzling observations, Zaher and Green<sup>1</sup> studied several defined ribosomal complexes, made from purified components, *in vitro*. They find that complexes containing a mismatch between the anticodon and codon in the P site are susceptible to RF2-mediated peptide release, despite the absence of a stop codon in the A site (Fig. 1b). Although slow, this reaction was stimulated considerably by the secondary release factor RF3, suggesting that it might be relevant *in vivo*, where both RFs are present.

Intriguingly, a sequence containing a mismatched codon–anticodon pair in the P site also stimulated further error — that is, incorporation of an amino acid despite the

absence of correct codon–anticodon pairing<sup>1</sup>. Consequently, complexes containing codon–anticodon mismatches were made in both the E and P sites. Again, the authors observed high rates of RF-dependent peptide release in these complexes, suggesting that termination can efficiently compete with elongation. The net effect is that miscoding errors terminate translation prematurely, which is another means of quality control by the ribosome — retrospectively, following peptide-bond formation — to increase the fraction of functional proteins made.

How codon–anticodon mismatches in the P site (or P and E sites) stimulate further miscoding and peptide release remains unclear. Codon–anticodon pairing in these sites normally helps to maintain the correct reading of codons on mRNA. Mismatches could disrupt such systematic reading of mRNA, potentially allowing various codons to transiently occupy the A site as the mRNA slides through the ribosome unpaired. Another possibility is that mismatches generate a conformational signal in the ribosomal complex that alters the activities

of the translation factors such as RF proteins. Indeed, earlier work<sup>5–7</sup> showed that conformational changes in the ribosome regulate both the decoding of mRNA and its termination. Regardless of the precise mechanism involved, Zaher and Green's work<sup>1</sup> reveals a facet of quality control in protein synthesis that depends on an unanticipated level of complexity in the workings of the ribosome. ■

Kurt Fredrick and Michael Ibba are in the Department of Microbiology, the Ohio State Biochemistry Program and the Center for RNA Biology, Ohio State University, Columbus, Ohio 43210-1292, USA.  
e-mail: [ibba.1@osu.edu](mailto:ibba.1@osu.edu)

1. Zaher, H. S. & Green, R. *Nature* **457**, 161–166 (2009).
2. Kurland, C. G. *Annu. Rev. Genet.* **26**, 29–50 (1992).
3. Kramer, E. B. & Farabaugh, P. J. *RNA* **13**, 87–96 (2007).
4. Ogle, J. M. & Ramakrishnan, V. *Annu. Rev. Biochem.* **74**, 129–177 (2005).
5. Youngman, E. M., He, S. L., Nikstad, L. J. & Green, R. *Mol. Cell* **28**, 533–543 (2007).
6. Laurberg, M. *et al.* *Nature* **454**, 852–857 (2008).
7. Weixlbaumer, A. *et al.* *Science* **322**, 953–956 (2008).

## ASTROPHYSICS

# Magnetic bond

Christopher M. Johns-Krull

**How low-mass stars produce their ubiquitous magnetic fields has long puzzled astronomers. Models of how Earth accomplishes this task could hold the key to understanding the phenomenon on such stars.**

Most of us have probably sprinkled iron filings on a piece of paper laid on top of a bar magnet and seen how they line up in an ordered pattern. The filings trace out the magnetic field produced by the magnet. The strength of the magnetic fields observed in stars and planets, which act like giant bar magnets, varies by several orders of magnitude. Finding the culprit behind this variation has been a challenge. On page 167 of this issue, Christensen *et al.*<sup>1</sup> announce that it is the convective energy flux available that sets the strength of the magnetic field in certain stars.

Like Earth, many — perhaps most — astronomical objects have magnetic fields threading through their interiors and emanating from their surfaces. On the Sun, the magnetic field is known to produce sunspots — regions of intense magnetic activity that are cooler, and hence darker, than the typical surface temperature of the Sun (about 6,000 kelvin). Sunspots were in fact first observed by Galileo, although at the time he was unaware of the role magnetic fields played in creating them. Solar magnetic fields produce a number of other effects, including a very hot (10<sup>6</sup> K), tenuous corona and energetic explosions such as solar flares.

Magnetic fields are now thought to be a common feature of all stars with masses similar to, or lower than, that of the Sun. The evidence comes from observations of the high-energy X-ray emission produced by the hot coronae

surrounding these stars (the X-ray emission and the magnetic-field flux follow a linear relationship<sup>2</sup>). Magnetic fields also seem to be responsible for slowing the rotation of Sun-like stars over time, and are strongly implicated in a range of phenomena that occur during the early and late stages of a star's life.

But how are these magnetic fields produced? The answer seems to lie in some sort of dynamo action. A dynamo is a mechanism that takes a weak, seed magnetic field and amplifies its strength by many orders of magnitude. We have basic ideas about the solar dynamo. Imagine magnetic-field lines drawn on the surface of the Sun starting at its south pole and extending to its north pole (Fig. 1a), and

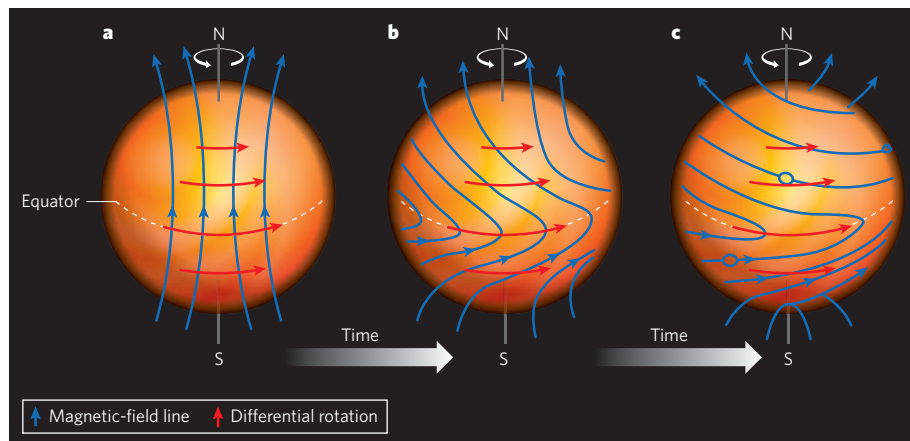


**Figure 1 | The Sun's swirling magnetic field.** Because the Sun is not solid like Earth, but is instead a massive sphere of hot gas, different parts of it rotate at different speeds: the gas at the equator rotates faster than does that at the poles. This differential rotation shears the gas and affects the Sun's magnetic field. As time goes on, the magnetic-field lines become highly distorted and twisted. This process amplifies the strength of the magnetic field. Christensen and colleagues' models<sup>1</sup>, which agree with observations of stars and planets over five orders of magnitude in magnetic-field strength, replace the shear owing to differential rotation with convection-driven shear, but the main principle is the same.

closing back on themselves in large loops above the Sun's surface. The relatively high temperature of the gas in the Sun's atmosphere means that the material is partially ionized (there are free electrons and protons floating around) and the magnetic field lines are anchored to the gas and forced to move with it. Because of differential rotation — the Sun's equator rotates faster than the poles — the gas is sheared and the magnetic field becomes twisted over time (Fig. 1b, c). This process amplifies the strength of the field and thus acts as a dynamo.

Comparison of solar observations with theoretical modelling has led to the conclusion that the solar dynamo is rooted in a region of very strong gas shear called the tachocline. This transition region separates the Sun's radiative interior zone from its convective outer layers, in which energy is transferred by boiling-like gas motions. The intense shear is caused by the difference in the rotation rate between the two zones.

Although the above dynamo theory works well for many stars, there are certain classes — such as mature stars with very low masses (less than about 0.3 solar masses) and young stars with low to moderate masses — for which it fails. Such stars are devoid of a tachocline zone, and the energy is transported throughout their interiors solely by convection. Yet these stars are strongly magnetic, and their observed magnetic fields cover essentially their entire surface<sup>3,4</sup>. Convective motions may themselves be responsible for the dynamo mechanism. Because convection involves gas rising and falling, different regions of ionized gas slip past one another, producing strong shear and, potentially, a dynamo. But previous investigations<sup>5,6</sup> of such a turbulent dynamo have suggested that although relatively strong fields could be produced, they would cover only a small fraction of the stellar surface.

Just like low-mass stars, some planets of our Solar System — such as Earth and Jupiter — also possess magnetic dynamos driven by convection. Intrigued by this common facet, Christensen *et al.*<sup>1</sup> applied existing dynamo models developed for Earth to stars. These models<sup>7</sup> indicate that when the object's rotation rate is high — as it is for Earth — it is the total energy flux from the core to the surface that sets the strength of the magnetic field. Christensen and colleagues translate these geodynamo models to the very different conditions present in fully convective stars and predict their magnetic-field strengths.

Models of convection-driven dynamos have been previously developed for fully convective stars<sup>8,9</sup>. But these models were not able to make specific predictions for the resulting magnetic-field strength. Christensen *et al.* are the first to do so, finding broad agreement between the models and observations both of stars with very low masses and of young stars with low to moderate masses. Until now, it had been believed that the magnetic fields of these stars were too strong<sup>10</sup> to be generated by

the star itself, and it was suggested that they were a by-product of the star-formation process. Although Christensen and colleagues' work suggests that the stars themselves produce the fields, it should be noted that, within their sample of stars, there is still substantial variation that the models do not yet predict.

Considering both stars and planets, the models and observations agree over an impressive five orders of magnitude in magnetic-field strength. But although Christensen and colleagues' result is an impressive step forward in our understanding of magnetic dynamo behaviour in celestial objects, it is far from a complete description of the process. Christensen *et al.* provide a scaling relationship to predict the magnetic fields on stars and planets that satisfy certain conditions. One such condition is that the objects rotate rapidly. There is much left to

be done before a full picture of stellar dynamos can be drawn. However, Christensen and colleagues' result puts researchers on a promising new track.

Christopher M. Johns-Krull is in the Department of Physics and Astronomy, Rice University, 6100 Main Street, Houston, Texas 77005, USA. e-mail: cmj@rice.edu

1. Christensen, U. R., Holzwarth, V. & Reiners, A. *Nature* **457**, 167–169 (2009).
2. Pevtsov, A. A. *et al.* *Astrophys. J.* **598**, 1387–1391 (2003).
3. Reiners, A. & Basri, G. *Astrophys. J.* **656**, 1121–1135 (2007).
4. Johns-Krull, C. M. *Astrophys. J.* **664**, 975–985 (2007).
5. Cattaneo, F. *Astrophys. J.* **515**, L39–L42 (1999).
6. Bercik, D. J. *et al.* *Astrophys. J.* **631**, 529–539 (2005).
7. Christensen, U. R. & Aubert, J. *Geophys. J. Int.* **166**, 97–114 (2006).
8. Dobler, W., Stix, M. & Brandenburg, A. *Astrophys. J.* **638**, 336–347 (2006).
9. Chabrier, G. & Küker, M. *Astron. Astrophys.* **446**, 1027–1037 (2006).
10. Safier, P. N. *Astrophys. J.* **510**, L127–L130 (1999).

## STRUCTURAL BIOLOGY

# Anticancer drug target pictured

Michael R. Waterman

**Not only is the aromatase enzyme implicated in a common form of breast cancer, but it also catalyses an unusual biochemical reaction. Its crystal structure therefore offers both practical and fundamental insights.**

About 75% of breast cancers contain high levels of oestrogens — up to ten times more than is found in the circulatory system. In these cases, tumour cells formed at the early stage of the disease express elevated levels of the gene that encodes aromatase (the key enzyme in the biosynthetic pathway of oestrogen). The resulting increase in aromatase activity explains the observed build-up of oestrogens, which enhance tumour-cell growth. Aromatase inhibitors block oestrogen synthesis, and are used in combination with the anticancer drug tamoxifen (which blocks oestrogen activity) to treat such breast cancers. Reporting on page 219 of this issue, Ghosh *et al.*<sup>1</sup> present a high-resolution X-ray structure of human aromatase. This might aid drug-discovery efforts targeting new aromatase inhibitors for the treatment of breast cancer.

Aromatase belongs to one of the monooxygenase families of enzymes. Monooxygenases metabolize substrates by adding single oxygen atoms to them, usually leading to the formation of hydroxyl (OH) groups. Each of these oxygen atoms is taken from a different oxygen molecule, O<sub>2</sub>; the leftover oxygen atoms from each O<sub>2</sub> molecule are used by the enzymes to produce water<sup>2,3</sup>.

The largest group of monooxygenases is the cytochrome P450 (CYP) superfamily, which is encoded by more than 8,700 genes spread across all biological kingdoms<sup>4</sup>. The exact role of most CYP enzymes is unknown, but those

with known functions fall into two groups: those that participate in the biosynthesis of compounds such as steroid hormones, vitamins or antibiotics; and those that metabolize 'foreign' compounds (such as drugs or environmental toxins). Enzymes from the second group generally oxidize a greater range of substrates than their biosynthetic counterparts. Aromatase belongs to the first group, and oxidizes only a few substrates that are involved in oestrogen biosynthesis.

Many experts consider aromatase to be the most important CYP because of its role in the development of female characteristics, and because it is a target for drugs that fight breast cancer. The enzyme catalyses the direct production of oestrone (the least abundant of the oestrogens, except in post-menopausal women) from a steroid known as androstenedione (Fig. 1, overleaf). This involves three sequential reactions, each requiring one O<sub>2</sub> molecule. In the third reaction, a non-aromatic hydrocarbon ring is converted into an aromatic ring. No other enzymes have been found that can catalyse such aromatization reactions<sup>5</sup>.

Ghosh and colleagues' structure<sup>1</sup> shows aromatase in complex with its substrate androstenedione. The authors reveal that the enzyme folds in a way that is characteristic of CYP enzymes<sup>6</sup>. The substrate fits tightly in the active site, as expected for a CYP that binds specifically to a small number of closely related structures — 'promiscuous' enzymes that bind



closing back on themselves in large loops above the Sun's surface. The relatively high temperature of the gas in the Sun's atmosphere means that the material is partially ionized (there are free electrons and protons floating around) and the magnetic field lines are anchored to the gas and forced to move with it. Because of differential rotation — the Sun's equator rotates faster than the poles — the gas is sheared and the magnetic field becomes twisted over time (Fig. 1b, c). This process amplifies the strength of the field and thus acts as a dynamo.

Comparison of solar observations with theoretical modelling has led to the conclusion that the solar dynamo is rooted in a region of very strong gas shear called the tachocline. This transition region separates the Sun's radiative interior zone from its convective outer layers, in which energy is transferred by boiling-like gas motions. The intense shear is caused by the difference in the rotation rate between the two zones.

Although the above dynamo theory works well for many stars, there are certain classes — such as mature stars with very low masses (less than about 0.3 solar masses) and young stars with low to moderate masses — for which it fails. Such stars are devoid of a tachocline zone, and the energy is transported throughout their interiors solely by convection. Yet these stars are strongly magnetic, and their observed magnetic fields cover essentially their entire surface<sup>3,4</sup>. Convective motions may themselves be responsible for the dynamo mechanism. Because convection involves gas rising and falling, different regions of ionized gas slip past one another, producing strong shear and, potentially, a dynamo. But previous investigations<sup>5,6</sup> of such a turbulent dynamo have suggested that although relatively strong fields could be produced, they would cover only a small fraction of the stellar surface.

Just like low-mass stars, some planets of our Solar System — such as Earth and Jupiter — also possess magnetic dynamos driven by convection. Intrigued by this common facet, Christensen *et al.*<sup>1</sup> applied existing dynamo models developed for Earth to stars. These models<sup>7</sup> indicate that when the object's rotation rate is high — as it is for Earth — it is the total energy flux from the core to the surface that sets the strength of the magnetic field. Christensen and colleagues translate these geodynamo models to the very different conditions present in fully convective stars and predict their magnetic-field strengths.

Models of convection-driven dynamos have been previously developed for fully convective stars<sup>8,9</sup>. But these models were not able to make specific predictions for the resulting magnetic-field strength. Christensen *et al.* are the first to do so, finding broad agreement between the models and observations both of stars with very low masses and of young stars with low to moderate masses. Until now, it had been believed that the magnetic fields of these stars were too strong<sup>10</sup> to be generated by

the star itself, and it was suggested that they were a by-product of the star-formation process. Although Christensen and colleagues' work suggests that the stars themselves produce the fields, it should be noted that, within their sample of stars, there is still substantial variation that the models do not yet predict.

Considering both stars and planets, the models and observations agree over an impressive five orders of magnitude in magnetic-field strength. But although Christensen and colleagues' result is an impressive step forward in our understanding of magnetic dynamo behaviour in celestial objects, it is far from a complete description of the process. Christensen *et al.* provide a scaling relationship to predict the magnetic fields on stars and planets that satisfy certain conditions. One such condition is that the objects rotate rapidly. There is much left to

be done before a full picture of stellar dynamos can be drawn. However, Christensen and colleagues' result puts researchers on a promising new track.

Christopher M. Johns-Krull is in the Department of Physics and Astronomy, Rice University, 6100 Main Street, Houston, Texas 77005, USA. e-mail: cmj@rice.edu

1. Christensen, U. R., Holzwarth, V. & Reiners, A. *Nature* **457**, 167–169 (2009).
2. Pevtsov, A. A. *et al.* *Astrophys. J.* **598**, 1387–1391 (2003).
3. Reiners, A. & Basri, G. *Astrophys. J.* **656**, 1121–1135 (2007).
4. Johns-Krull, C. M. *Astrophys. J.* **664**, 975–985 (2007).
5. Cattaneo, F. *Astrophys. J.* **515**, L39–L42 (1999).
6. Bercik, D. J. *et al.* *Astrophys. J.* **631**, 529–539 (2005).
7. Christensen, U. R. & Aubert, J. *Geophys. J. Int.* **166**, 97–114 (2006).
8. Dobler, W., Stix, M. & Brandenburg, A. *Astrophys. J.* **638**, 336–347 (2006).
9. Chabrier, G. & Küker, M. *Astron. Astrophys.* **446**, 1027–1037 (2006).
10. Safier, P. N. *Astrophys. J.* **510**, L127–L130 (1999).

## STRUCTURAL BIOLOGY

# Anticancer drug target pictured

Michael R. Waterman

**Not only is the aromatase enzyme implicated in a common form of breast cancer, but it also catalyses an unusual biochemical reaction. Its crystal structure therefore offers both practical and fundamental insights.**

About 75% of breast cancers contain high levels of oestrogens — up to ten times more than is found in the circulatory system. In these cases, tumour cells formed at the early stage of the disease express elevated levels of the gene that encodes aromatase (the key enzyme in the biosynthetic pathway of oestrogen). The resulting increase in aromatase activity explains the observed build-up of oestrogens, which enhance tumour-cell growth. Aromatase inhibitors block oestrogen synthesis, and are used in combination with the anticancer drug tamoxifen (which blocks oestrogen activity) to treat such breast cancers. Reporting on page 219 of this issue, Ghosh *et al.*<sup>1</sup> present a high-resolution X-ray structure of human aromatase. This might aid drug-discovery efforts targeting new aromatase inhibitors for the treatment of breast cancer.

Aromatase belongs to one of the monooxygenase families of enzymes. Monooxygenases metabolize substrates by adding single oxygen atoms to them, usually leading to the formation of hydroxyl (OH) groups. Each of these oxygen atoms is taken from a different oxygen molecule, O<sub>2</sub>; the leftover oxygen atoms from each O<sub>2</sub> molecule are used by the enzymes to produce water<sup>2,3</sup>.

The largest group of monooxygenases is the cytochrome P450 (CYP) superfamily, which is encoded by more than 8,700 genes spread across all biological kingdoms<sup>4</sup>. The exact role of most CYP enzymes is unknown, but those

with known functions fall into two groups: those that participate in the biosynthesis of compounds such as steroid hormones, vitamins or antibiotics; and those that metabolize 'foreign' compounds (such as drugs or environmental toxins). Enzymes from the second group generally oxidize a greater range of substrates than their biosynthetic counterparts. Aromatase belongs to the first group, and oxidizes only a few substrates that are involved in oestrogen biosynthesis.

Many experts consider aromatase to be the most important CYP because of its role in the development of female characteristics, and because it is a target for drugs that fight breast cancer. The enzyme catalyses the direct production of oestrone (the least abundant of the oestrogens, except in post-menopausal women) from a steroid known as androstenedione (Fig. 1, overleaf). This involves three sequential reactions, each requiring one O<sub>2</sub> molecule. In the third reaction, a non-aromatic hydrocarbon ring is converted into an aromatic ring. No other enzymes have been found that can catalyse such aromatization reactions<sup>5</sup>.

Ghosh and colleagues' structure<sup>1</sup> shows aromatase in complex with its substrate androstenedione. The authors reveal that the enzyme folds in a way that is characteristic of CYP enzymes<sup>6</sup>. The substrate fits tightly in the active site, as expected for a CYP that binds specifically to a small number of closely related structures — 'promiscuous' enzymes that bind

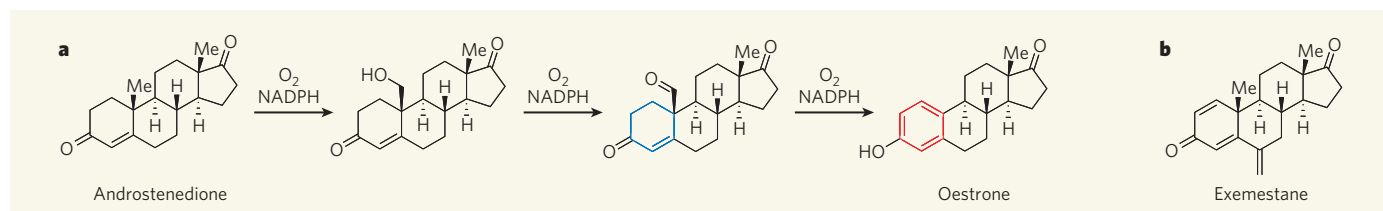


**Figure 1 | Aromatase reactions.** **a**, The aromatase enzyme catalyses a three-step process in which the steroid androstenedione is converted into an oestrogen molecule (oestrone). Each step requires oxygen (O<sub>2</sub>) and a cofactor (NADPH). The final step is an aromatization reaction in which a non-aromatic ring (blue) is converted to an aromatic phenol ring (red). No other enzymes are known to catalyse aromatization

reactions. Ghosh *et al.*<sup>1</sup> report the crystal structure of human aromatase in complex with androstenedione. **b**, Exemestane is an aromatase inhibitor that is used to treat a common form of breast cancer. Ghosh *et al.* show that it binds to aromatase in a slightly different way from the structurally related androstenedione, perhaps accounting for its inhibitory behaviour.

to many different substrates exhibit a looser fit, to accommodate more structural variety.

The structure conclusively reveals which amino acids form the active site, and which of those interact directly with androstenedione — information that previously could only be inferred indirectly. Ghosh *et al.* propose a mechanism for the aromatization reaction (see Fig. 3b on page 221) that is consistent with the observed enzyme–substrate interactions. Future studies to establish the details of the mechanism will require crystal structures for mutated versions of the protein, in which specific amino acids from the active site have been replaced with others. By observing the effect of such mutations on the function of the enzyme and on substrate–enzyme interactions, the precise roles of active-site amino acids in the normal enzyme can be determined.

Several clinical trials have compared the anticancer activity of state-of-the-art aromatase inhibitors (anastrozole, letrozole and exemestane) with that of tamoxifen<sup>7</sup>. The results indicate that aromatase inhibitors are more effective than tamoxifen at increasing the disease-free survival time of patients (the time interval between the initial diagnosis of cancer and recurrence of the disease following therapy) than in increasing their overall survival time (the lifespan after first diagnosis). The structure of exemestane is closely related to that of androstenedione (Fig. 1). Ghosh *et al.*<sup>1</sup> therefore modelled the binding of exemestane in the aromatase active site, and compared it with that of androstenedione. Although the binding of the inhibitor is closely related to that of androstenedione, the models also predict subtle structural differences. Specifically, part of the exemestane molecule becomes clamped in a hydrophobic part of the active site. This effect might lower the ability of a nearby amino-acid residue to initiate the formation of a reactive iron group in the active site. Such information could help to guide the development of a new generation of improved aromatase inhibitors, using existing compounds as a starting point.

One of the most remarkable aspects of the work<sup>1</sup> is that the structure was determined for native aromatase isolated from human placenta, rather than using a recombinant protein that had been artificially constructed

using genetic-engineering techniques<sup>8</sup> (as is usually the case for X-ray studies). This is an advantage, as recombinant proteins are often truncated for practical reasons, so that a complete picture of the structure is lost. Ghosh and colleagues' native aromatase contains the hydrophobic 'tail' of the enzyme — a string of mostly hydrophobic amino acids at the amino terminus of the protein. *In vivo*, the tail extends through the phospholipid bilayer of the intracellular organelle known as the endoplasmic reticulum. Aromatase is the first example of a CYP protein that has been crystallized with its hydrophobic tail intact.

Ghosh and colleagues' structure will be vital for establishing the mechanism of the complex, three-step process catalysed by aromatase, particularly the biochemically unique

aromatization reaction. But perhaps more importantly, it provides a roadmap for future drug-discovery efforts in the battle against the most common form of breast cancer.

Michael R. Waterman is in the Department of Biochemistry, Vanderbilt University School of Medicine, Nashville, Tennessee 37232, USA.  
e-mail: michael.waterman@vanderbilt.edu

1. Ghosh, D., Griswold, J., Erman, M. & Pangborn, W. *Nature* **457**, 219–223 (2009).
2. Hayaishi, O. *Annu. Rev. Biochem.* **31**, 25–46 (1962).
3. Mason, H. S. *Annu. Rev. Biochem.* **34**, 595–634 (1965).
4. <http://drnelson.utmem.edu/CytochromeP450.html>
5. Akhtar, A. *et al. Biochem. J.* **201**, 569–580 (1982).
6. Poulos, T. L. & Johnson, E. F. in *Cytochrome P450: Structure Mechanism and Biochemistry* 3rd edn (ed. Ortiz de Montellano, P.) 87–114 (Kluwer Academic/Plenum, 2004).
7. Eisen, A. *et al. Cancer Treat. Rev.* **34**, 154–174 (2008).
8. Kagawa, N., Hori, H., Waterman, M. R. & Yoshioka, S. *Steroids* **69**, 235–243 (2004).

## MOLECULAR BIOLOGY

### A taste of umami

Of the five basic tastes — bitter, sweet, umami, sour and salty — umami is the least well known and certainly the least romantic. Yet most of us have experienced this savoury flavour, and commonly associate it with oriental cuisine. Xiaodong Li and colleagues now reveal the molecular mechanism behind perception of the umami taste (F. Zhang *et al. Proc. Natl Acad. Sci. USA* doi:10.1073/pnas.0810174106; 2008).

The umami taste comes from the amino acid glutamate, although ribonucleotides such as IMP and GMP greatly enhance its intensity. Like the sweet taste, perception of this taste depends on G-protein-coupled receptors of class C (C-GPCRs), which are found in cell membranes and also include many receptors of

physiological importance. In C-GPCRs, a 'Venus flytrap' (VFT) domain, which binds to ligands on the cell surface, is connected to a transmembrane domain.

Although the receptors for the umami taste (consisting of T1R1–T1R3) and the sweet taste (T1R2–T1R3) share the same transmembrane subunit (T1R3), Li and colleagues show — using different combinations of these three subunits — that, in each case, the unique subunit mediates taste recognition. Moreover, four amino-acid residues deep inside the VFT domain seem to be essential for recognition of glutamate.

Enhancement of the umami taste by IMP/GMP, however, seems to depend on a different set of four amino acids in the opening to the VFT domain. So the authors propose that



IMP binds near glutamate, supporting the ligand-bound, closed conformation of the VFT domain.

Regulatory molecules such as IMP that modulate the activity of GPCRs are of great interest to the drug industry — for example, they are more selective than agonist molecules, which might affect the activity of related receptors. As there are few known naturally occurring examples of IMP-like regulatory molecules, the significance of Li and colleagues' results goes beyond unravelling the mysteries of a curious taste.

**Sadaf Shadan**



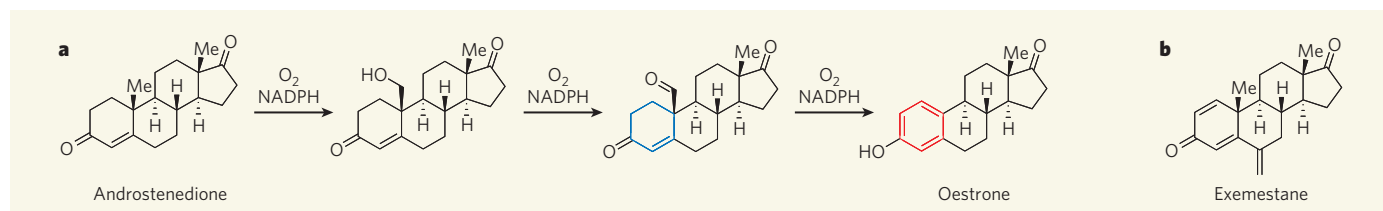


**Figure 1 | Aromatase reactions.** **a**, The aromatase enzyme catalyses a three-step process in which the steroid androstenedione is converted into an oestrogen molecule (oestrone). Each step requires oxygen (O<sub>2</sub>) and a cofactor (NADPH). The final step is an aromatization reaction in which a non-aromatic ring (blue) is converted to an aromatic phenol ring (red). No other enzymes are known to catalyse aromatization

reactions. Ghosh *et al.*<sup>1</sup> report the crystal structure of human aromatase in complex with androstenedione. **b**, Exemestane is an aromatase inhibitor that is used to treat a common form of breast cancer. Ghosh *et al.* show that it binds to aromatase in a slightly different way from the structurally related androstenedione, perhaps accounting for its inhibitory behaviour.

to many different substrates exhibit a looser fit, to accommodate more structural variety.

The structure conclusively reveals which amino acids form the active site, and which of those interact directly with androstenedione — information that previously could only be inferred indirectly. Ghosh *et al.* propose a mechanism for the aromatization reaction (see Fig. 3b on page 221) that is consistent with the observed enzyme–substrate interactions. Future studies to establish the details of the mechanism will require crystal structures for mutated versions of the protein, in which specific amino acids from the active site have been replaced with others. By observing the effect of such mutations on the function of the enzyme and on substrate–enzyme interactions, the precise roles of active-site amino acids in the normal enzyme can be determined.

Several clinical trials have compared the anticancer activity of state-of-the-art aromatase inhibitors (anastrozole, letrozole and exemestane) with that of tamoxifen<sup>7</sup>. The results indicate that aromatase inhibitors are more effective than tamoxifen at increasing the disease-free survival time of patients (the time interval between the initial diagnosis of cancer and recurrence of the disease following therapy) than in increasing their overall survival time (the lifespan after first diagnosis). The structure of exemestane is closely related to that of androstenedione (Fig. 1). Ghosh *et al.*<sup>1</sup> therefore modelled the binding of exemestane in the aromatase active site, and compared it with that of androstenedione. Although the binding of the inhibitor is closely related to that of androstenedione, the models also predict subtle structural differences. Specifically, part of the exemestane molecule becomes clamped in a hydrophobic part of the active site. This effect might lower the ability of a nearby amino-acid residue to initiate the formation of a reactive iron group in the active site. Such information could help to guide the development of a new generation of improved aromatase inhibitors, using existing compounds as a starting point.

One of the most remarkable aspects of the work<sup>1</sup> is that the structure was determined for native aromatase isolated from human placenta, rather than using a recombinant protein that had been artificially constructed

using genetic-engineering techniques<sup>8</sup> (as is usually the case for X-ray studies). This is an advantage, as recombinant proteins are often truncated for practical reasons, so that a complete picture of the structure is lost. Ghosh and colleagues' native aromatase contains the hydrophobic 'tail' of the enzyme — a string of mostly hydrophobic amino acids at the amino terminus of the protein. *In vivo*, the tail extends through the phospholipid bilayer of the intracellular organelle known as the endoplasmic reticulum. Aromatase is the first example of a CYP protein that has been crystallized with its hydrophobic tail intact.

Ghosh and colleagues' structure will be vital for establishing the mechanism of the complex, three-step process catalysed by aromatase, particularly the biochemically unique

aromatization reaction. But perhaps more importantly, it provides a roadmap for future drug-discovery efforts in the battle against the most common form of breast cancer.

Michael R. Waterman is in the Department of Biochemistry, Vanderbilt University School of Medicine, Nashville, Tennessee 37232, USA.  
e-mail: michael.waterman@vanderbilt.edu

1. Ghosh, D., Griswold, J., Erman, M. & Pangborn, W. *Nature* **457**, 219–223 (2009).
2. Hayaishi, O. *Annu. Rev. Biochem.* **31**, 25–46 (1962).
3. Mason, H. S. *Annu. Rev. Biochem.* **34**, 595–634 (1965).
4. <http://drnelson.utmem.edu/CytochromeP450.html>
5. Akhtar, A. *et al. Biochem. J.* **201**, 569–580 (1982).
6. Poulos, T. L. & Johnson, E. F. in *Cytochrome P450: Structure Mechanism and Biochemistry* 3rd edn (ed. Ortiz de Montellano, P.) 87–114 (Kluwer Academic/Plenum, 2004).
7. Eisen, A. *et al. Cancer Treat. Rev.* **34**, 154–174 (2008).
8. Kagawa, N., Hori, H., Waterman, M. R. & Yoshioka, S. *Steroids* **69**, 235–243 (2004).

## MOLECULAR BIOLOGY

### A taste of umami

Of the five basic tastes — bitter, sweet, umami, sour and salty — umami is the least well known and certainly the least romantic. Yet most of us have experienced this savoury flavour, and commonly associate it with oriental cuisine. Xiaodong Li and colleagues now reveal the molecular mechanism behind perception of the umami taste (F. Zhang *et al. Proc. Natl Acad. Sci. USA* doi:10.1073/pnas.0810174106; 2008).

The umami taste comes from the amino acid glutamate, although ribonucleotides such as IMP and GMP greatly enhance its intensity. Like the sweet taste, perception of this taste depends on G-protein-coupled receptors of class C (C-GPCRs), which are found in cell membranes and also include many receptors of

physiological importance. In C-GPCRs, a 'Venus flytrap' (VFT) domain, which binds to ligands on the cell surface, is connected to a transmembrane domain.

Although the receptors for the umami taste (consisting of T1R1–T1R3) and the sweet taste (T1R2–T1R3) share the same transmembrane subunit (T1R3), Li and colleagues show — using different combinations of these three subunits — that, in each case, the unique subunit mediates taste recognition. Moreover, four amino-acid residues deep inside the VFT domain seem to be essential for recognition of glutamate.

Enhancement of the umami taste by IMP/GMP, however, seems to depend on a different set of four amino acids in the opening to the VFT domain. So the authors propose that



IMP binds near glutamate, supporting the ligand-bound, closed conformation of the VFT domain.

Regulatory molecules such as IMP that modulate the activity of GPCRs are of great interest to the drug industry — for example, they are more selective than agonist molecules, which might affect the activity of related receptors. As there are few known naturally occurring examples of IMP-like regulatory molecules, the significance of Li and colleagues' results goes beyond unravelling the mysteries of a curious taste.

**Sadaf Shadan**

# Quality control by the ribosome following peptide bond formation

Hani S. Zaher<sup>1</sup> & Rachel Green<sup>1</sup>

The overall fidelity of protein synthesis has been thought to rely on the combined accuracy of two basic processes: the aminoacylation of transfer RNAs with their cognate amino acid by the aminoacyl-tRNA synthetases, and the selection of cognate aminoacyl-tRNAs by the ribosome in cooperation with the GTPase elongation factor EF-Tu. These two processes, which together ensure the specific acceptance of a correctly charged cognate tRNA into the aminoacyl (A) site, operate before peptide bond formation. Here we report the identification of an additional mechanism that contributes to high fidelity protein synthesis after peptidyl transfer, using a well-defined *in vitro* bacterial translation system. In this retrospective quality control step, the incorporation of an amino acid from a non-cognate tRNA into the growing polypeptide chain leads to a general loss of specificity in the A site of the ribosome, and thus to a propagation of errors that results in abortive termination of protein synthesis.

The overall *in vivo* rate of misincorporation during protein synthesis has been estimated to be in the range of  $6 \times 10^{-4}$  to  $5 \times 10^{-3}$  per amino acid incorporated<sup>1,2</sup>. Current models for the mechanisms governing this level of accuracy focus on the accurate charging of tRNAs with their cognate amino acid by the aminoacyl-tRNA synthetases and correct tRNA selection by the ribosome facilitated by the GTPase elongation factor EF-Tu in bacteria (or eEF1A in eukaryotes). Kinetic discrimination mechanisms, driven by induced fit, have been demonstrated for the synthetases and the ribosome to facilitate accurate selection of amino acids or charged tRNAs, respectively<sup>3,4</sup>. In addition, for both processes, proofreading (or editing) mechanisms have been shown to increase the overall fidelity further<sup>3,5-7</sup>. Experimental measurements of *in vitro* aminoacylation accuracy ( $\sim 10^5$ ) agree well with that observed *in vivo*<sup>8</sup>. *In vitro* protein synthesis systems (generally poly-Phe synthesis on polyU) have been shown to proceed with an overall fidelity (combining the tRNA selection and proofreading steps) of as high as  $10^{-4}$  (refs 3, 9 and 10). However, fidelity measurements in our own laboratory conducted in the full range of published buffer systems with tRNA mixtures on heteropolymeric messenger RNA suggest that *in vitro* protein synthesis proceeds with slower fidelity (an error rate of  $2 \times 10^{-3}$  to  $10 \times 10^{-3}$ ; Supplementary Fig. 1), thus arguing that further quality control mechanisms may exist.

Here we identify a previously uncharacterized ribosome-centred mechanism that contributes to translational quality control, and which may help explain discrepancies between *in vitro* and *in vivo* measured fidelity values. The surprising feature of this pathway is that it monitors the fidelity of protein synthesis after the formation of a peptide bond (retrospectively), in certain ways analogous to the exonucleolytic proofreading step in DNA replication<sup>11</sup>. We provide evidence that the ribosome recognizes errors during synthesis by evaluating the codon-anticodon helix in the peptidyl (P) site of the small subunit of the ribosome, leading first to reduced fidelity during subsequent tRNA selection and ultimately to premature termination by release factors.

## A mismatched P site triggers unusual release behaviour

During the course of reconstituting *in vitro* the translation of ribosome nascent chain complexes (RNCs), with the core elongation

steps shown in Fig. 1a, we identified an abundant miscoding event in which Lys-tRNA<sup>Lys</sup> (anticodon UUU) efficiently decoded an AAU Asn codon in a short peptide sequence, as previously documented *in vivo*<sup>12</sup>. In these reactions, we observed that in miscoded ribosome complexes the peptidyl-tRNA did not efficiently react to incorporate the next amino acid encoded by the mRNA, but instead seemed to be promiscuously hydrolysed. These data suggested the existence of a quality control step that follows peptide bond formation and effectively functions to terminate translation of aberrant protein products, thus enhancing the overall fidelity of protein synthesis.

To characterize this unusual observation, we produced RNCs carrying a dipeptidyl-tRNA in the P site with either a matched or a mismatched codon-anticodon helix and a variety of different codons in the A site. We started with a pair of RNCs containing a stop codon in the A site (mRNAs encoding MKX (AUG AAA UGA) or MNX (AUG AAU UGA)) to check anticipated release factor 2 (RF2) properties on these complexes. Complexes were assembled in a simplified reaction mixture containing initiation factors (IF1-IF3) and fMet-tRNA<sup>fMet</sup>, and were reacted with ternary complex (Lys-tRNA<sup>Lys</sup>-EF-Tu-GTP) in the presence of elongation factor EF-G to yield ribosome complexes with fMet-Lys-tRNA<sup>Lys</sup> in the P site (Fig. 1b and Supplementary Fig. 2), followed by purification over a sucrose cushion. As anticipated, RF2 reacted efficiently with both complexes (MKX and MNX), releasing the dipeptide with a rate constant ( $k_{\text{cat}}$ ) close to that previously reported in buffer A ( $\sim 0.05 \text{ s}^{-1}$ , Fig. 1c)<sup>13,14</sup>. Notably, titration experiments indicated that less RF2 was required to promote the maximal rate of catalysis on the mismatched P site complex than on the matched one ( $K_{1/2}$ , release factor concentration at which half of the maximal rate is observed, values of  $\sim 75 \text{ nM}$  and  $800 \text{ nM}$ , respectively, Fig. 1d). These data suggested that RF2 interacts differently with these two complexes that vary by a single mismatch in the P site. We note that the maximal rate of release on other matched stop-codon-programmed complexes was, as expected, dependent on the buffer used and on the source of RF2 (over- or chromosomally-expressed) reaching a maximum of  $10 \text{ s}^{-1}$ , close to numbers reported previously<sup>15</sup> (Supplementary Fig. 3). Although maximal rates of release are achieved in buffer D, we chose to complete the study in buffer A because background release rates were minimal under these conditions.

<sup>1</sup>Howard Hughes Medical Institute, Department of Molecular Biology and Genetics, Johns Hopkins University School of Medicine, Baltimore, Maryland 21205, USA.



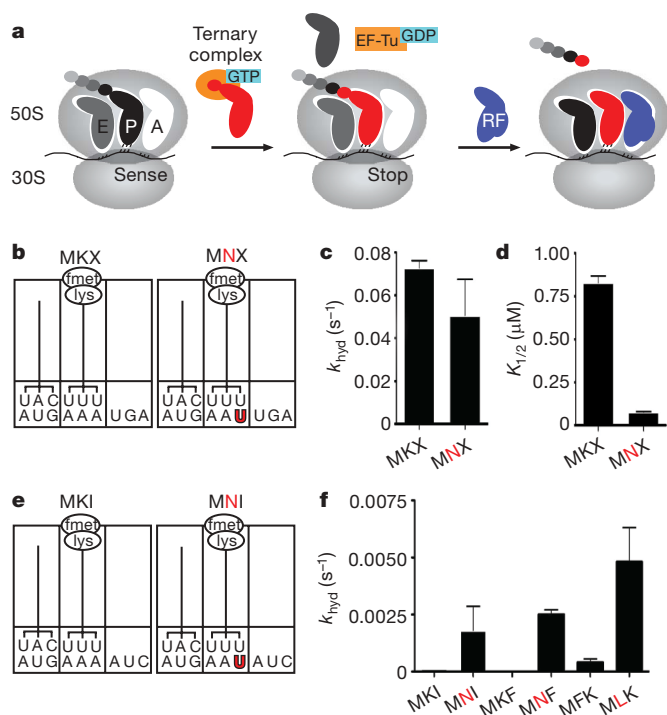


**Figure 1 | Unusual behaviour by RF2 after a miscoding event.** **a**, Schematic of the core steps of elongation and termination on the ribosome. During the elongation cycle, a ternary complex comprising aminoacylated tRNA, EF-Tu and GTP enters the A site, and reacts with the peptidyl-tRNA elongating the nascent peptide by one amino acid. When a stop codon enters the A site, it is recognized by a class I release factor resulting in the hydrolysis of peptidyl-tRNA. **b**, Schematic representation of the matched MKX and mismatched MNX (mismatched base pair shown in red) dipeptidyl-tRNA ribosome complexes (dipeptidyl-RNCs), which have a stop codon in the A site. **c**, Rate constants for release ( $k_{hyd}$ ) measured on the P-site-matched (MKX) and mismatched (MNX) complexes with saturating RF2. **d**,  $K_{1/2}$  values for the same complexes. **e**, An example of matched (MKI) and mismatched (MNI) dipeptidyl-RNCs with a sense codon (I) in the A site. **f**, Rate constants for release ( $k_{hyd}$ ) measured on several matched (MKI, MKF, MFK) or mismatched (MNI, MNF, MLK) RNCs with saturating RF2. Rate constants for MKI and MKF complexes are immeasurably low. Error bars indicate the standard error obtained from the nonlinear regression fit of the data.

We next prepared several dipeptidyl-tRNA ribosomal complexes that instead carried sense codons in the A site and assessed their behaviour in pre-steady state release assays. In the first set, complexes MKI and MNI carrying fMet-Lys-tRNA<sup>Lys</sup> in the P site and the Ile codon AUC in the A site were used (Fig. 1e). RF2-catalysed release on the sense codon was immeasurably slow for the matched (MKI) complex ( $k_{cat} < 0.0002 \text{ s}^{-1}$ ), as expected<sup>16</sup>, but was markedly faster ( $k_{cat} \sim 0.002 \text{ s}^{-1}$ ) for the P-site-mismatched complex (Fig. 1f). We next prepared similar matched and mismatched ribosome complexes, MKF and MNF, carrying a different A-site codon (Phe, UUU). As before, the  $k_{cat}$  of the mismatched P-site complex (MNF) was markedly faster than that of the matched complex (MKF;  $0.0025 \text{ s}^{-1}$  versus  $< 0.0001 \text{ s}^{-1}$ , respectively, Fig. 1f). We note further that the second order rate difference ( $k_{cat}/K_m$ ) was considerably greater for the mismatched complex MNF relative to MKF ( $> 300$ -fold, Supplementary Fig. 4).

To determine whether the increased reactivity of the P-site-mismatched complex depended on particular decoding mistakes or if the phenomenon was more general, we forced a different near-cognate pairing interaction to prepare matched and mismatched dipeptidyl tRNA complexes (MFK and MLK). These complexes contained several differences compared to the previous set (P-site tRNA, P-site mismatch and A-site codon). Again, RF2-catalysed peptide

release was considerably faster for the P-site-mismatched complex than for the matched version ( $0.0048 \text{ s}^{-1}$  versus  $0.0004 \text{ s}^{-1}$ , respectively, Fig. 1f). The related release factor, RF1, showed similar promiscuous release activity (data not shown), but will not be further characterized in this study.

Given the apparent generality of the observed release-factor-promiscuity on sense codons, we performed several experiments to determine whether this phenomenon is an authentic ribosome-based event. One concern was that the mismatch in the P site might destabilize the complex and permit a frameshifting or hopping event on the mRNA<sup>17</sup> that might reposition an authentic stop codon in the A site. Although the mRNAs were designed to avoid this potential complication, we nevertheless examined the positioning of the ribosome on the mRNA in the matched and mismatched ribosome complexes using a primer-extension based toe-printing assay<sup>18</sup>. The primer extension reactions on MKI and MNI have indistinguishable toe-printing patterns, consistent with a 3-nucleotide shift of the complex after a round of elongation (Supplementary Fig. 5). Further controls established that hydrolysis cannot be attributed to P-site tRNA drop-off followed by hydrolysis by potential contaminating peptidyl hydrolase (Supplementary Fig. 6). Furthermore, the promiscuous release activity, like authentic release, was inhibited by paromomycin<sup>14,19</sup> (Supplementary Fig. 7). These experiments together argue that the observed activity on the P-site-mismatched complexes reports on an authentic release-factor-mediated ribosomal event.

### RF3 stimulates promiscuous release by RF2

Although the observed stimulation of premature peptide release on the sense codons of P-site-mismatched complexes was substantial ( $> 20$ -fold), the resulting rate constant for the reaction ( $0.002$ – $0.005 \text{ s}^{-1}$ ) still lagged behind that of authentic peptide release ( $\sim 0.05 \text{ s}^{-1}$ ) and the competing tRNA selection/peptidyl transfer processes ( $\sim 2 \text{ s}^{-1}$ )<sup>20,21</sup>. Class II release factor RF3 is a GTPase that is integrally involved in the removal of the class I release factor after peptide release, but has no effect on the rate constants for peptide release on authentic termination complexes (Fig. 2 and ref. 22). Interestingly, when RF2 and RF3 were added together to a variety of P-site-mismatched complexes (with first, second and third position mismatches in the P site), release activity was substantially accelerated ( $\sim 20$ – $50$ -fold, Fig. 2). We note that the resulting rate constants for the release reaction can be remarkably fast for some complexes ( $\sim 0.1 \text{ s}^{-1}$ ), in a range in which this promiscuity could influence the fidelity of protein synthesis *in vivo*. Notably, it has been

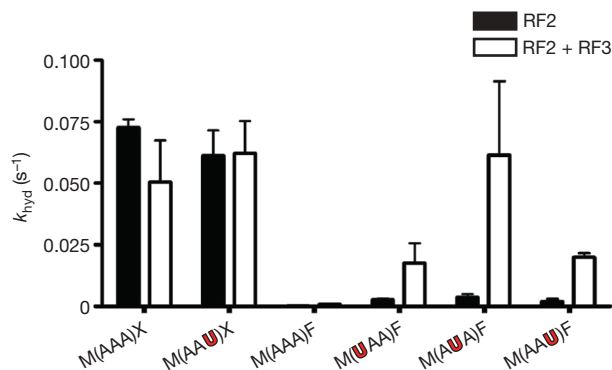


**Figure 2 | Abortive termination reaction is stimulated by the class II RF3 and is general for all P-site mismatches.** Rate constants for release ( $k_{hyd}$ ) for the indicated P-site-matched and mismatched (red) dipeptidyl-RNC complexes with RF2 only or with RF2 and RF3, all at saturating concentrations. fMet-Lys-tRNA<sup>Lys</sup> occupies the P site in each case, either on cognate (AAA) or on first (UAA), second (AUA) or third (AAU) position mismatches. Error bars indicate the standard error obtained from the nonlinear regression fit of the data.

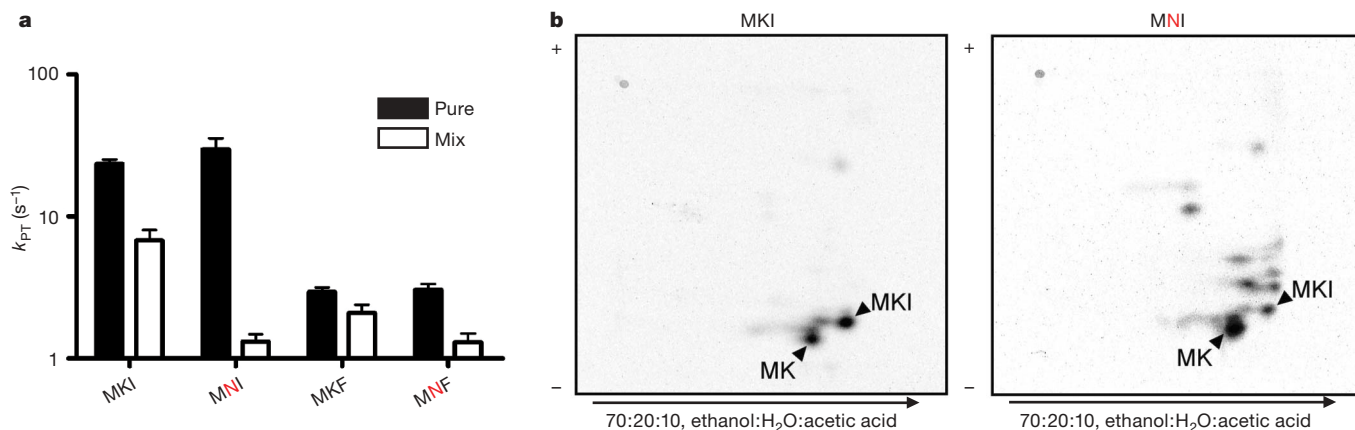


**Figure 3 | A single miscoding event promotes iterated errors in tRNA selection.** **a**, Rate constants for peptidyl transfer ( $k_{PT}$ ) for the indicated dipeptidyl-RNCs with either the cognate aminoacyl-tRNA (for MKI and MNI, total tRNA mix aminoacylated only with isoleucine, and for MKF and MNF, purified Phe-tRNA<sup>Phe</sup>) or with bulk aminoacyl-tRNA. Error bars

indicate the standard error obtained from the nonlinear regression fit of the data. **b**, Two-dimensional TLCs resolve the peptidyl transfer reaction products resulting from reaction of the MKI (left panel) or MNI (right panel) dipeptidyl-RNC with bulk aminoacylated tRNA; the reaction was incubated for 0.5 s, short of its endpoint. Mismatched base pairs are shown in red.

previously shown that RF3 could stimulate release on certain ribosome complexes containing a near-cognate stop codon in the A site<sup>16</sup>.

A related question is whether the mechanism that monitors miscoding is sensitive to the identity of the mismatch found at each of the three positions of the codon. The U•U mismatch and U•G wobble resulted in similar release activity when located at the first or second codon positions; in contrast, at the third codon position, whereas the U•U mismatch strongly stimulated peptide release, the U•G wobble had little consequence (Supplementary Fig. 8). These data are fully consistent with expectations on the basis of the permissivity of the genetic code at the third codon position and argue that the system for monitoring fidelity in the P site can identify a wide range of errors during translation.

### P-site mismatches compromise tRNA selection fidelity

Class I release factors must naturally compete during translation with the cognate and near-cognate tRNA species that sample the same ribosomal A site. Given the apparent substantial effects of the P-site mismatch on release factor activity, we next looked at the peptidyl transfer activity of the P-site-matched and mismatched complexes. In two different examples (MKI versus MNI, and MKF versus MNF), we observed that the rate constant for peptidyl transfer (for cognate Ile-tRNA<sup>Ile</sup> and Phe-tRNA<sup>Phe</sup>, respectively) was unaffected by the mismatch in the P site (Fig. 3a). We did observe, however, that catalysis of peptidyl transfer is diminished by twofold to sixfold for the P-site-mismatched complexes relative to the matched complexes in the presence of a full complement of competitor tRNA (Fig. 3a). We suggest that this reduced overall peptidyl transfer rate results from the increased dwell time of near-cognate tRNAs on the P-site-mismatched complexes with inefficient progression to the irreversible peptidyl transfer reaction.

A more complete understanding of the observed competition from total tRNA mix comes from analysis of the actual peptide products. We compared product purity of two different sets of P-site-matched and mismatched complexes, MKI versus MNI, and MKF versus MNF, using a two-dimensional thin-layer chromatography (TLC) format. As anticipated on the basis of the high fidelity of protein synthesis, the P-site-matched complexes (MKI and MKF) yielded a predominant tripeptide product corresponding to the encoded sequence (Fig. 3b and Supplementary Fig. 9). However, for both mismatched complexes (MNI and MNF) we observed marked losses of fidelity such that a wide range of miscoded products is observed after the initial forced miscoding event. An estimate of partitioning to correct product (relative to partitioning to incorrect products) in the P-site-matched complex is higher than 96%, whereas for the

mismatched complex that same value falls in a range between 10 and 30%. Indeed, we can show that specifically chosen near-cognate tRNAs react more readily with the mismatched complex than with the matched one (Supplementary Fig. 10). The observed losses in fidelity for tRNA selection coupled with the promiscuity of release factors documented earlier, both after a simple miscoding event, suggest that the A site itself is generally perturbed.

### Amplification of errors leads to fast termination

The previous sections have described a series of experiments suggesting that a single misincorporation during translation leads to marked changes in A-site behaviour including increased miscoding and accelerated release of polypeptides on sense codons. Increasing the rate of miscoding is not terminal, but it does serve at a minimum to extend the window of opportunity for release factors to abort translation. We tested whether a second sequential miscoding event might generate a complex with even more unusual properties because it carries a mismatch in both the E- and P-site regions of the small

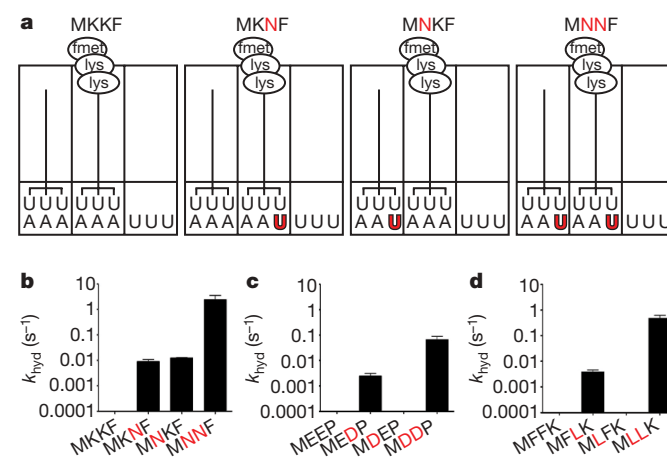
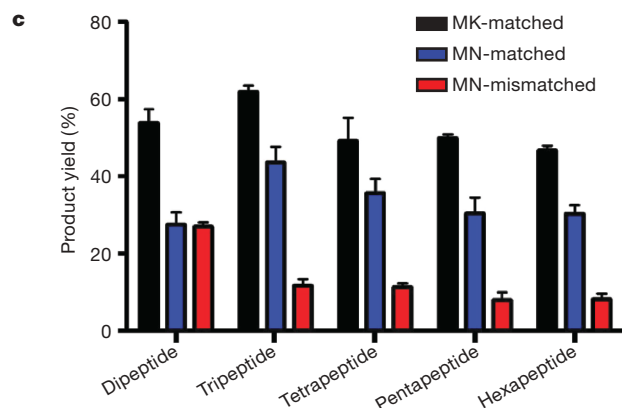
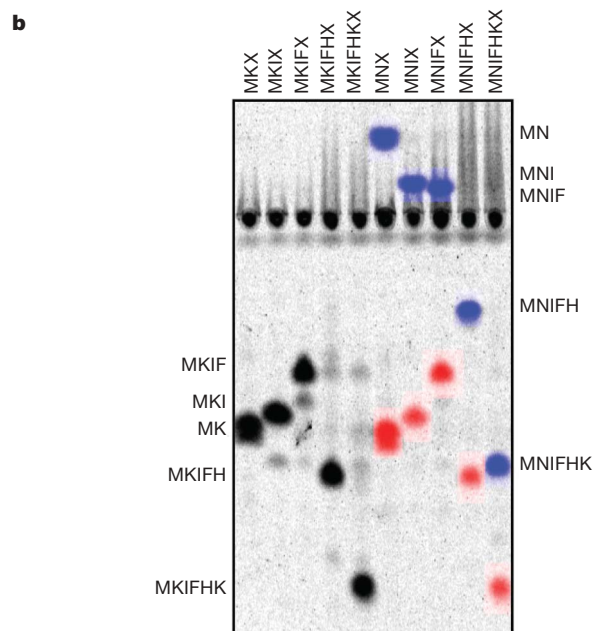
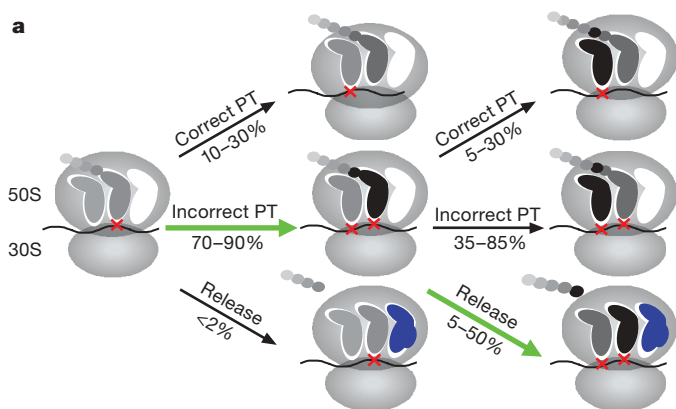


**Figure 4 | Iterated miscoding results in doubly mismatched complexes, where release catalysis is dramatically promoted.** **a**, Schematic representation of one of the tripeptidyl-RNC series used to address E-site effects on release; shown is the MKKF series. The MKKF complex carries no mismatches, MKNF contains a P-site mismatch, MNKF has an E-site mismatch, and MNMF bears both E- and P-site mismatches. Mismatched base pairs are shown in red. **b–d**, Rate constants for release ( $k_{hyd}$ ) on a log scale with saturating RF2 and RF3 for the MKKF series (**b**), MEEP series (**c**) and MFFK series (**d**). Error bars indicate the standard error obtained from the nonlinear regression fit of the data.



ribosomal subunit. We explored the consequences of the iterated miscoding by programming tripeptidyl-tRNA ribosome complexes with a single mismatch in the P site (MKNF, MEDP or MFLK), a single mismatch in the exit (E) site (MNKF, MDEP or MLFK), or a combination of both mismatches (MNNF, MDDP or MLLK) as might result from repeated miscoding events (the MKKF series is depicted in Fig. 4a). As we saw previously, the P-site-mismatched complexes are robust substrates for RF2 and RF3, yielding rate constants for peptide release in the range of 0.005 to 0.01 s<sup>-1</sup>. For the singly mismatched E-site complexes, there was no stimulation of release activity in two of the complexes (MDEP and MLFK), whereas the results were buffer-dependent for the MNKF complex (Fig. 4b



and Supplementary Fig. 11). These differences will be discussed later. Most marked, however, was the increased rate of premature peptide release on each of the doubly mismatched complexes with rate constants for release ranging from 0.07 to 2 s<sup>-1</sup> (Fig. 4b-d). These values are in a range comparable to tRNA selection and thus should compete in the continuing process of protein synthesis. The robust nature of these findings was confirmed by observing very similar relative rates of release on the MKKF RNC series in a different buffer (poly-mix, D) and with chromosomally-expressed (fully methylated) RF2 (Supplementary Fig. 11). Control experiments were also performed to ensure that RNCs carrying a miscoding event that has fully exited the E site are no longer identified by RF2 as aberrant (Supplementary Fig. 12).

To further explore the molecular mechanism responsible for the disparate E-site effects, we performed a toe-printing experiment to determine the positioning of the tripeptidyl-tRNA RNCs on several mRNA species. For the MEEP series, the tripeptidyl-tRNA complexes seem rather uniform and fully extended with a toe-print positioned primarily at +6 relative to their starting position (Supplementary Fig. 13a). Notably, for the MKKF series, whereas the P-site-mismatched complex (MKNF) was positioned as anticipated on the mRNA, for both complexes carrying an E-site mismatch (MNKF and MNNF), a substantial fraction of the complex exhibits a heterogeneous banding pattern (Supplementary Fig. 13b). These latter data are consistent with proposals suggesting that codon-anticodon interactions in the E site can be critical for reading frame maintenance during translation<sup>23</sup>. We can not explain in molecular terms why the E-site mismatch alone typically has no effect on release activity (MDEP, MLFK and MNKF in buffer D) but strongly stimulates release in all cases when combined with a P-site mismatch, although the synthetic E-site effects are reminiscent of E-site allosteric models proposed previously<sup>24</sup>. We suggest that the effects of E-site mismatches on the A site are mostly manifested through structural perturbations of the proximal P-site decoding helix, an idea nicely supported by studies in yeast demonstrating that P-site mismatches can affect frame maintenance<sup>25</sup>.

### In vivo relevance of post-peptidyl quality control

To evaluate the potential contribution of retrospective quality control to the fidelity of translation in the cell, we estimated the partitioning between premature release, inaccurate and accurate peptidyl transfer after a first miscoding event (Fig. 5a) on the basis of rough cellular estimates of tRNA and release-factor concentrations (50–200 μM and 6–25 μM, respectively, ref. 26) and the measured  $k_{cat}/K_m$  values of peptidyl transfer, incorrect peptidyl transfer and release after a single miscoding event (Figs 3, 4 and Supplementary Fig. 3). We predict from these calculations (see Supplementary Information) that the net effect of the iterated partitioning steps (detailed in Fig. 5a) is that a single initial miscoding event results in a marked increase in premature chain termination (highlighted by green arrows).

**Figure 5 | An initial miscoding event results in an overall drop in yield of full-length peptides.** **a**, Proposed model for the events after a miscoding event with the steps contributing to the quality control described here highlighted by green arrows. PT, peptidyl transfer. **b**, Mock *in vivo* experiment recapitulates predictions of model. The indicated series of mRNAs (MKX to MKIFHKX for the matched series and MNX to MNIFHKX for the mismatched series) were used in complete translation reactions to observe the consequences of competition between tRNAs and release factors for peptide synthesis. Peptides initiated with the cognate dipeptide MK from the matched mRNA series are in black (MK-matched), peptides initiated with the cognate MN from the mismatched mRNA series are in blue (MN-matched), whereas peptides resulting from an incorrect decoding by Lys-tRNA<sup>Lys</sup> on the Asn (N) codon are in red (MN-mismatched). **c**, Yield was quantified as the fractional radioactivity in each product band relative to the whole lane. The plot represents the average of three independent experiments, with error bars representing the standard deviation from the mean.

There are two predictions of the proposed model: (1) that the yield of full-length product will diminish after a miscoding event; and (2) that there will be evidence of prematurely truncated, multiply miscoded peptides. To test these predictions under competitive conditions, we evaluated the translation of a heteropolymeric mRNA sequence containing an AAU codon at position two for targeted decoding and miscoding by Asn-tRNA<sup>Asn</sup> and Lys-tRNA<sup>Lys</sup>, respectively, followed by sequence coding for abundant aminoacyl-tRNAs in the mixture. Translation of this mRNA in an S100 extract under limiting concentrations of Asn-tRNA<sup>Asn</sup> allowed us to follow the consequences of cognate and near-cognate decoding during translation in an *in-vivo*-like setting. In this competition experiment (Fig. 5b, c), we observe that the yield of full-length product after an initial miscoding event was decreased nearly fourfold (relative to two different controls). When the experiment was repeated in buffer D, the observed reduction in product after a miscoding event was even more impressive (~tenfold, Supplementary Fig. 15). This overall drop in yield is markedly consistent with the partitioning that we predict in Fig. 5a. Although we see no strong signature of prematurely-released miscoded polypeptides, we expect that such a diffuse set of products would be very difficult to detect in our TLC system. We have also looked directly at partitioning for a defined (biochemically isolated) tripeptidyl tRNA RNC (MNNF) in the presence of S100 and aminoacyl-tRNA mix, and observe an extent of release consistent with estimates from our purified system (Supplementary Fig. 14).

With some hindsight, early *in vivo* studies of translation processivity probably provided evidence for the post-peptidyl transfer editing process described here, although it was not possible at the time to identify the root cause of the premature termination events<sup>27</sup>. Later studies characterized connections between ribosome accuracy and processivity<sup>28</sup>, but did not predict that there might be a direct consequence of miscoding on termination. In these studies, we note that low fidelity ribosome (*ram*) strains showed poor processivity, as would be predicted by our model.

Another intriguing *in vivo* correlation for our studies comes from the known auto-regulation of RF2. Translation of RF2 in the cell depends on a programmed frameshifting event that occurs when a UGA codon encountered in the A site results in a stalled complex due to the low abundance of RF2 (ref. 29). As with many frameshifting events, the decoding helix found in the P site after the programmed frameshifting event is perturbed (with RF2, for example, a G•U mismatch in the first position of the codon) and thus should normally be a prime candidate for recognition by the surveillance system described here. Paradoxically, in this case, RF2 concentration is low and thus is not likely to contribute to substantial premature chain termination until the overall RF2 levels in the cell are increased. We suggest that this feedback loop has evolved to effectively evade the quality control mechanism described here.

## Conclusions

Quality control mechanisms are important throughout the cell in ensuring the faithful replication of the genome and its expression into functional components. Like DNA replication, the quality control system that we describe here for protein synthesis depends on recognition of error after chemical incorporation of the building block into the growing polymer. However, unlike DNA replication, in which extension of the growing strand is completed after the hydrolytic action of the polymerase removes the misincorporated nucleotides, the quality control described here results in termination of protein synthesis.

In light of the competition experiments described earlier, we argue that the post-peptidyl transfer process described here might contribute close to an order of magnitude to fidelity *in vivo* under standard conditions. Moreover, under conditions of starvation, in which amino acids become limiting in the cell and miscoding events are increasingly probable, we suggest that this surveillance system could have an even more substantial role in specifying the fidelity of

translation. We note that the experiments here were conducted on very early stage RNCs (almost initiation complexes) and that premature release might have a distinct role during the elongation phase of translation. Nevertheless, the effects we have measured in this study are notable. To give some perspective, whereas false termination at a sense codon normally occurs with a frequency of less than once per 100,000 codons (measured here and in ref. 30) in fully matched complexes, in one of the doubly mismatched complexes, false termination occurs half the time. These changes in the biochemical activity of the ribosome are triggered by single mismatches positioned in the P and E sites of the small ribosomal subunit, highlighting the existence of another intricate molecular system within the ribosome that precisely dictates perfection in the transmission of the genetic code.

## METHODS SUMMARY

RNCs were essentially prepared as described in ref. 13, and subsequent release or peptidyl transfer assays are described in the Methods.

**Full Methods** and any associated references are available in the online version of the paper at [www.nature.com/nature](http://www.nature.com/nature).

Received 18 July; accepted 24 October 2008.

Published online 17 December 2008.

- Edelmann, P. & Gallant, J. Mistranslation in *E. coli*. *Cell* **10**, 131–137 (1977).
- Boudloun, F., Donner, D. & Kurland, C. G. Codon-specific missense errors *in vivo*. *EMBO J.* **2**, 1351–1356 (1983).
- Gromadski, K. B. & Rodnina, M. V. Kinetic determinants of high-fidelity tRNA discrimination on the ribosome. *Mol. Cell* **13**, 191–200 (2004).
- Guth, E. C. & Francklyn, C. S. Kinetic discrimination of tRNA identity by the conserved motif 2 loop of a class II aminoacyl-tRNA synthetase. *Mol. Cell* **25**, 531–542 (2007).
- Schmidt, E. & Schimmel, P. Mutational isolation of a sieve for editing in a transfer RNA synthetase. *Science* **264**, 265–267 (1994).
- Hopfield, J. J. Kinetic proofreading: a new mechanism for reducing errors in biosynthetic processes requiring high specificity. *Proc. Natl Acad. Sci. USA* **71**, 4135–4139 (1974).
- Ninio, J. Kinetic amplification of enzyme discrimination. *Biochimie* **57**, 587–595 (1975).
- Soll, D. The accuracy of aminoacylation—ensuring the fidelity of the genetic code. *Experientia* **46**, 1089–1096 (1990).
- Szaflarski, W. *et al.* New features of the ribosome and ribosomal inhibitors: non-enzymatic recycling, misreading and back-translocation. *J. Mol. Biol.* **380**, 193–205 (2008).
- Jelenc, P. C. & Kurland, C. G. Nucleoside triphosphate regeneration decreases the frequency of translation errors. *Proc. Natl Acad. Sci. USA* **76**, 3174–3178 (1979).
- Brutlag, D. & Kornberg, A. Enzymatic synthesis of deoxyribonucleic acid. 36. A proofreading function for the 3' leads to 5' exonuclease activity in deoxyribonucleic acid polymerases. *J. Biol. Chem.* **247**, 241–248 (1972).
- Precup, J. & Parker, J. Missense misreading of asparagine codons as a function of codon identity and context. *J. Biol. Chem.* **262**, 11351–11355 (1987).
- Brunelle, J. L., Shaw, J. J., Youngman, E. M. & Green, R. Peptide release on the ribosome depends critically on the 2' OH of the peptidyl-tRNA substrate. *RNA* **14**, 1526–1531 (2008).
- Youngman, E. M., He, S. L., Nikstad, L. J. & Green, R. Stop codon recognition by release factors induces structural rearrangement of the ribosomal decoding center that is productive for peptide release. *Mol. Cell* **28**, 533–543 (2007).
- Dincbas-Renqvist, V. *et al.* A post-translational modification in the GGQ motif of RF2 from *Escherichia coli* stimulates termination of translation. *EMBO J.* **19**, 6900–6907 (2000).
- Freistoffer, D. V., Kwiatkowski, M., Buckingham, R. H. & Ehrenberg, M. The accuracy of codon recognition by polypeptide release factors. *Proc. Natl Acad. Sci. USA* **97**, 2046–2051 (2000).
- Baranov, P. V., Gesteland, R. F. & Atkins, J. F. Recoding: translational bifurcations in gene expression. *Gene* **286**, 187–201 (2002).
- Hartz, D., McPheeters, D. S., Traut, R. & Gold, L. Extension inhibition analysis of translation initiation complexes. *Methods Enzymol.* **164**, 419–425 (1988).
- Brown, C. M., McCaughan, K. K. & Tate, W. P. Two regions of the *Escherichia coli* 16S ribosomal RNA are important for decoding stop signals in polypeptide chain termination. *Nucleic Acids Res.* **21**, 2109–2115 (1993).
- Katunin, V. I., Muth, G. W., Strobel, S. A., Wintermeyer, W. & Rodnina, M. V. Important contribution to catalysis of peptide bond formation by a single ionizing group within the ribosome. *Mol. Cell* **10**, 339–346 (2002).
- Youngman, E. M., Brunelle, J. L., Kochaniak, A. B. & Green, R. The active site of the ribosome is composed of two layers of conserved nucleotides with distinct roles in peptide bond formation and peptide release. *Cell* **117**, 589–599 (2004).



22. Freistroffer, D. V., Pavlov, M. Y., MacDougall, J., Buckingham, R. H. & Ehrenberg, M. Release factor RF3 in *E. coli* accelerates the dissociation of release factors RF1 and RF2 from the ribosome in a GTP-dependent manner. *EMBO J.* **16**, 4126–4133 (1997).
  23. Marquez, V., Wilson, D. N., Tate, W. P., Triana-Alonso, F. & Nierhaus, K. H. Maintaining the ribosomal reading frame: the influence of the E site during translational regulation of release factor 2. *Cell* **118**, 45–55 (2004).
  24. Geigenmuller, U. & Nierhaus, K. H. Significance of the third tRNA binding site, the E site, on *E. coli* ribosomes for the accuracy of translation: an occupied E site prevents the binding of non-cognate aminoacyl-tRNA to the A site. *EMBO J.* **9**, 4527–4533 (1990).
  25. Sundararajan, A., Michaud, W. A., Qian, Q., Stahl, G. & Farabaugh, P. J. Near-cognate peptidyl-tRNAs promote +1 programmed translational frameshifting in yeast. *Mol. Cell* **4**, 1005–1015 (1999).
  26. Dong, H., Nilsson, L. & Kurland, C. G. Co-variation of tRNA abundance and codon usage in *Escherichia coli* at different growth rates. *J. Mol. Biol.* **260**, 649–663 (1996).
  27. Manley, J. L. Synthesis and degradation of termination and premature-termination fragments of  $\beta$ -galactosidase *in vitro* and *in vivo*. *J. Mol. Biol.* **125**, 407–432 (1978).
  28. Dong, H. & Kurland, C. G. Ribosome mutants with altered accuracy translate with reduced processivity. *J. Mol. Biol.* **248**, 551–561 (1995).
  29. Craigen, W. J. & Caskey, C. T. Expression of peptide chain release factor 2 requires high-efficiency frameshift. *Nature* **322**, 273–275 (1986).
  30. Jorgensen, F., Adamski, F. M., Tate, W. P. & Kurland, C. G. Release factor-dependent false stops are infrequent in *Escherichia coli*. *J. Mol. Biol.* **230**, 41–50 (1993).
- Supplementary Information** is linked to the online version of the paper at [www.nature.com/nature](http://www.nature.com/nature).
- Acknowledgements** We thank B. Cormack, A. Nahvi, A. Buskirk and R. Reed for helpful comments on the manuscript and members of the laboratory for useful discussions. This work was supported by the National Institutes of Health with salary support from Howard Hughes Medical Institute.
- Author Contributions** H.S.Z. and R.G. designed the experiments and wrote the manuscript. H.S.Z. performed the experiments.
- Author Information** Reprints and permissions information is available at [www.nature.com/reprints](http://www.nature.com/reprints). Correspondence and requests for materials should be addressed to R.G. ([ragreen@jhmi.edu](mailto:ragreen@jhmi.edu)).

## METHODS

**Materials.** Buffers used were as follows: buffer A (50 mM Tris-HCl, pH 7.5, 70 mM NH<sub>4</sub>Cl, 30 mM KCl, 7 mM MgCl<sub>2</sub>, 1 mM dithiothreitol (DTT))<sup>31</sup>, buffer B (HiFi) (50 mM Tris-HCl, pH 7.5, 70 mM NH<sub>4</sub>Cl, 30 mM KCl, 3.5 mM MgCl<sub>2</sub>, 0.5 mM spermidine, 8 mM putrescine, and 2 mM DTT)<sup>3</sup>, buffer C (polyamine) (20 mM HEPES-potassium-hydroxide, pH 7.6, 150 mM NH<sub>4</sub>Cl, 4.5 mM MgCl<sub>2</sub>, 2 mM spermidine, 0.05 mM spermine, 4 mM β-mercaptoethanol)<sup>32</sup>, buffer D (polymix) (95 mM KCl, 5 mM NH<sub>4</sub>Cl, 5 mM magnesium acetate, 0.5 mM CaCl<sub>2</sub>, 8 mM putrescine, 1 mM spermidine, 5 mM potassium phosphate, pH 7.5, 1 mM DTT)<sup>10</sup>.

*Escherichia coli* MRE600 (ATCC29417) tight couple 70S ribosomes were prepared as described previously<sup>33</sup>. Overexpressed native IF1 and IF3 and His-tagged IF2 were purified as described<sup>34</sup>. Amino-terminally His-tagged RF1 and the 20 aminoacyl-tRNA synthetases were expressed and purified as previously described<sup>35</sup>. His6-tagged EF-Tu and EF-G were purified over Ni-NTA resin, the His tag was later removed by tobacco etch virus protease, which was followed by a second passage over Ni-NTA column<sup>36</sup>. Overexpressed His-tagged RF2 and RF3 were purified as described<sup>15</sup>. Chromosomally-expressed RF2 was purified using a procedure similar to that previously described<sup>15</sup> except for the following modifications. After the ammonium sulphate precipitation following the first gel-filtration step, fractions containing RF2 were resuspended in 25 mM sodium phosphate, buffer pH 6.8, and dialysed against the same buffer overnight. The protein was then applied to a hydroxyapatite column (0.7 cm × 5.2 cm), and eluted with a 50 ml linear phosphate gradient (25–500 mM). The purified protein was finally dialysed in a buffer comprised of 40 mM Tris-HCl, pH 7.5, 10 mM MgCl<sub>2</sub>, 100 mM KCl, 1 mM DTT and 50% glycerol.

tRNA<sup>Lys</sup>, tRNA<sup>Phe</sup>, tRNA<sup>Met</sup> (all from *E. coli*) and rabbit muscle pyruvate kinase were purchased from Sigma-Aldrich. Total *E. coli* tRNA was purchased from Roche. mRNA templates were prepared from double-stranded DNA templates using run-off transcription by T7 RNA polymerase<sup>37</sup>, and purified by PAGE. mRNAs used for dipeptidyl complexes had the following sequence: GGGUGUCUUGCGAGGAUAAGUGCAU AUG (X) (Y) UGA UUUGCCCU-UCUGUAGCCA, in which the initiator Met codon is in bold, whereas X and Y denote codons occupying the P and A site, respectively. The tripeptidyl RNCs were programmed with similar mRNAs that had an extra codon, Z, after the Y codon. The mRNA coding for fMet-Phe (AUG UUC) used for fidelity measurements (Supplementary Fig. 1) was chemically synthesized (Dharmacon).

**tRNA charging.** Aminoacylation and formylation of the initiator tRNA<sup>Met</sup> with radiolabelled [<sup>35</sup>S]-methionine using an S100 extract was performed as described previously<sup>38</sup>. Pure tRNAs were charged by incubating the tRNA at 10 μM with the corresponding aminoacyl-tRNA synthetase (~1 μM) in the presence of the appropriate amino acid and ATP (100 μM and 2 mM, respectively) in the following buffer: 20 mM Tris-HCl, pH 7.5, 20 mM MgCl<sub>2</sub>, 1 mM DTT. After incubation at 37 °C for 30 min, the aminoacylated tRNA was purified by phenol and chloroform extraction followed by ethanol precipitation and resuspended in 20 mM potassium acetate buffer, pH 5.1, with 1 mM DTT. Total tRNA was charged using a similar procedure except that the tRNA concentration was increased to 100 μM and all 20 aminoacyl-tRNA synthetases were added (1 μM each) and all 20 amino acids were added (100 μM each). In cases in which a single tRNA in the complete tRNA mixture was aminoacylated, the same basic reaction was set up, but only the desirable synthetase and amino acid were supplied (for example, for the Ile-tRNA<sup>Ile</sup> in Fig. 3a).

**RNC ribosome complex formation.** Initiation complexes were first prepared by incubating 70S ribosomes (2 μM) with IF1, IF2, IF3, f[<sup>35</sup>S]Met-tRNA<sup>Met</sup> (3 μM each), and mRNA (6 μM) in buffer C (or buffer D for experiments in Supplementary Figs 3, 11 and 15) in the presence of GTP at 2 mM at 37 °C for 45 min. RNCs were then obtained by adding equivalent volumes of initiation complexes and a pre-incubated elongation mixture containing EF-Tu (15 μM), charged tRNA (6 μM for dipeptidyl and 10 μM for tripeptidyl complexes, respectively), EF-G (6 μM), and GTP (2 mM) in buffer C (or buffer D, as above) and incubating at 37 °C for 10 min. Buffer C was used to form RNC complexes that were ultimately assayed in buffer A because of its permissivity in allowing near cognate tRNAs to react. Buffer A was considerably less promiscuous for certain near cognate pairings, thus making RNC complex formation difficult. To purify RNCs away from unincorporated tRNAs and factors, the reaction mixture was layered over a 1,300 μl sucrose cushion (1.1 M sucrose, 20 mM Tris-HCl, pH 7.5, 500 mM NH<sub>4</sub>Cl, 10 mM MgCl<sub>2</sub>, 0.5 mM EDTA) and spun at 258,000g in a TL100.3 rotor for 2 h. The resulting pellet was resuspended in buffer A (or buffer D, as above), aliquoted and stored at -80 °C. Electrophoretic TLC analysis of the complexes (see below) was used to determine the efficiency of dipeptide or tripeptide formation on the matched and mismatched mRNA templates. The typical yield for RNCs was as follows: in dipeptide- and tripeptide-matched complexes >80% of fMet was converted to the appropriate peptide; in mismatched

complexes involving Lys-tRNA<sup>Lys</sup> or Glu-tRNA<sup>Glu</sup> the yield was >60% for dipeptides and >40% for tripeptides; whereas in mismatched complexes involving Phe-tRNA<sup>Phe</sup>, the yields were 40% and 10% for dipeptides and tripeptides, respectively. In addition, the amount of f[<sup>35</sup>S]Met that pellets provides further information about the stability of the RNC complexes. We note that mismatched templates typically yield less radioactivity in pelleting, probably because of the increased off-rates of the peptidyl-tRNA (Supplementary Fig. 4). We can easily follow the particular RNC of interest, despite the range in yield that we observe, because the relevant peptide product is well resolved in our electrophoretic TLC system (for example, Fig. 5b).

**Release assays.** Peptidyl RNCs (both dipeptidyl and tripeptidyl) at 25 to 150 nM were incubated with RF2 at 30 μM (determined to be saturating for mismatched complexes, see Supplementary Fig. 3) in buffer A at 37 °C. Where indicated, RF3 was added to a final concentration of 30 μM with 2 mM GTP. Time points were obtained by taking aliquots at different time intervals and stopping the reaction with one-quarter of the volume of 25% formic acid. Released peptides of various lengths and identity were separated from unreacted peptidyl-tRNA using cellulose TLC plates that were electrophoresed in pyridine-acetate at pH 2.8 (ref. 21). Reactions with relatively fast rate constants (for example, >0.05 s<sup>-1</sup>), such as the doubly mismatched RNCs in Fig. 4, were performed on a quench-flow instrument (RQF-3 quench-flow, KinTek Corporation). The fraction of peptide released at each time point was quantified using ImageQuant v5.2 (Molecular Dynamics) and plotted against time. The data were fit to the first-order rate equation;  $F = F_{\max}(1 - e^{-kt})$ , in which  $F$  is the fraction hydrolysed, to obtain the rate constant ( $k$ ) and the fraction of the population ( $F_{\max}$ ) that could react. In most cases,  $F_{\max}$  was found to be between 60% and 90%. To determine  $K_{1/2}$  values, release time courses were conducted with RNCs (25 nM) at varying concentrations of RF2 (0.025–30 μM). The  $k_{\text{obs}}$  values were obtained from individual fits at a given concentration of RF2 and the  $K_{1/2}$  was derived from the hyperbolic fit of the  $k_{\text{obs}}$  versus [RF2] curve (Michaelis-Menten). The background rate—in the absence of RF2—was determined for all complexes and subtracted from the rate observed in the presence of RF2. For certain P-site-matched complexes, the rate of peptide release was immeasurably low, and so in these cases an upper limit for the rate constant is provided (for example, MKI and MKF complexes in Fig. 1f).

**Peptidyl transferase assays.** EF-Tu at 100 μM was first incubated with 2 mM GTP in buffer A for 15 min to promote exchange of the bound GDP for GTP. The enzyme was then diluted to 20 μM in buffer A containing charged tRNA (10 μM) and 2 mM GTP, and incubated for another 15 min. The mixture was incubated with an equal volume of RNC (final concentration ~100 nM). The reaction was stopped by the addition of potassium hydroxide to a concentration of 100 mM. Reaction products were resolved by electrophoretic TLC as above, and analysed similarly. Reactions performed with total tRNAs were carried out with final concentrations of EF-Tu and tRNA of 100 μM and 80 μM, respectively. The rate constants for these experiments were determined by fitting curves following the fraction of substrate (for example, dipeptide) that disappeared as a function of time.

**Toe-print assay.** Initiated and elongated peptidyl-tRNA complexes were prepared as above, except that the mRNAs used had extra sequence at the 3'-end to allow for an oligonucleotide primer to anneal and be extended by reverse transcriptase. The toe-printing reactions were then carried out essentially as described<sup>39</sup>. The RNCs were resuspended in buffer A that was supplemented with an additional 10 mM MgCl<sub>2</sub>. A trace amount of 5'-radiolabelled reverse transcription primer (5' phosphorylated using polynucleotide kinase and [<sup>32</sup>P]-ATP), and dNTPs (600 μM each) were added. Primer extension was initiated by the addition of AMV reverse transcriptase at a concentration of 1 U μl<sup>-1</sup>. The reaction was incubated at 37 °C for 10 min, followed by the addition of sodium hydroxide at 100 mM and incubation at 90 °C for 10 min to digest the RNA. The reaction was ethanol precipitated before analysis on long format 6% PAGE.

**Two-dimensional TLC separation.** For resolution of complex peptidyl transfer reactions incubated with total tRNA mixtures, the peptidyl transfer reactions were performed essentially as described above. At the end of the reaction, peptidyl-tRNA was hydrolysed with 100 mM KOH before spotting the sample on a 20 × 20 cm cellulose TLC. In the first dimension the mobile phase was composed of ethanol:water:acetic acid at a ratio of 70:20:10. The TLC was then thoroughly dried and run electrophoretically in pyridine-acetate buffer (pH 2.8) for the second dimension.

**S100 *in vitro* translation.** For Fig. 5b, purified initiation complexes, instead of the post-translocation complexes used in previous reactions, were prepared as described above, and then incubated (~50 nM final concentration) with an S100 extract containing 120 μM tRNA (pre-charged with a tRNA synthetase mix lacking asparaginyl-tRNA synthetase (AsnRS), 2 mM GTP, 6 mM PEP and 0.02 mg ml<sup>-1</sup> pyruvate kinase in buffer A at 37 °C for 10 min. For



Supplementary Fig. 14, post-translocation tripeptidyl-RNCs were prepared as above, and reacted in a similar fashion with S100 and aminoacyl-tRNA mixture. The samples were resolved using the electrophoretic TLC system described above. Observed Asn-tRNA<sup>Asn</sup> activity in Fig. 5b probably derives from contaminating reagent that carries through in the bulk tRNA mixture or through impurities in the individual amino acids, as seen for Leu-tRNA<sup>Leu</sup> activity in Supplementary Fig. 1.

31. Pape, T., Wintermeyer, W. & Rodnina, M. Induced fit in initial selection and proofreading of aminoacyl-tRNA on the ribosome. *EMBO J.* **18**, 3800–3807 (1999).
32. Bartetzko, A. & Nierhaus, K. H.  $Mg^{2+}/NH_4^+$ /polyamine system for polyuridine-dependent polyphenylalanine synthesis with near in vivo characteristics. *Methods Enzymol.* **164**, 650–658 (1988).
33. Shaw, J. J. & Green, R. Two distinct components of release factor function uncovered by nucleophile partitioning analysis. *Mol. Cell* **28**, 458–467 (2007).
34. Brunelle, J. L., Youngman, E. M., Sharma, D. & Green, R. The interaction between C75 of tRNA and the A loop of the ribosome stimulates peptidyl transferase activity. *RNA* **12**, 33–39 (2006).
35. Shimizu, Y. *et al.* Cell-free translation reconstituted with purified components. *Nature Biotechnol.* **19**, 751–755 (2001).
36. Blanchard, S. C., Kim, H. D., Gonzalez, R. L. Jr, Puglisi, J. D. & Chu, S. tRNA dynamics on the ribosome during translation. *Proc. Natl Acad. Sci. USA* **101**, 12893–12898 (2004).
37. Zaher, H. S. & Unrau, P. J. T7 RNA polymerase mediates fast promoter-independent extension of unstable nucleic acid complexes. *Biochemistry* **43**, 7873–7880 (2004).
38. Moazed, D. & Noller, H. F. Sites of interaction of the CCA end of peptidyl-tRNA with 23S rRNA. *Proc. Natl Acad. Sci. USA* **88**, 3725–3728 (1991).
39. Dorner, S., Brunelle, J. L., Sharma, D. & Green, R. The hybrid state of tRNA binding is an authentic translation elongation intermediate. *Nature Struct. Mol. Biol.* **13**, 234–241 (2006).

# Energy flux determines magnetic field strength of planets and stars

Ulrich R. Christensen<sup>1</sup>, Volkmar Holzwarth<sup>1</sup> & Ansgar Reiners<sup>2</sup>

The magnetic fields of Earth and Jupiter, along with those of rapidly rotating, low-mass stars, are generated by convection-driven dynamos that may operate similarly<sup>1–4</sup> (the slowly rotating Sun generates its field through a different dynamo mechanism<sup>5</sup>). The field strengths of planets and stars vary over three orders of magnitude, but the critical factor causing that variation has hitherto been unclear<sup>5,6</sup>. Here we report an extension of a scaling law derived from geodynamo models<sup>7</sup> to rapidly rotating stars that have strong density stratification. The unifying principle in the scaling law is that the energy flux available for generating the magnetic field sets the field strength. Our scaling law fits the observed field strengths of Earth, Jupiter, young contracting stars and rapidly rotating low-mass stars, despite vast differences in the physical conditions of the objects. We predict that the field strengths of rapidly rotating brown dwarfs and massive extrasolar planets are high enough to make them observable.

So far, attempts to explain the magnetic field strength of natural dynamos have been largely heuristic and disparate for planets and stars. The field strength in a planetary dynamo is often attributed to the supposed balance between Lorentz (electromagnetic) and Coriolis (rotational) forces, requiring that the Elsasser number  $\Lambda = \sigma B^2 / (\rho \Omega)$  is of the order of one (here  $\sigma$  is electrical conductivity,  $B$  is r.m.s. magnetic field strength in the dynamo,  $\rho$  is density and  $\Omega$  is rotation rate). This is in fair agreement with the observed field strength of Earth and some other planets<sup>6</sup>. However,  $\Lambda$  falls in the range 0.1–100 in different geodynamo models<sup>7</sup>. For stellar dynamos, the equipartitioning of magnetic and kinetic energy is sometimes assumed to be the guiding principle controlling the field strength<sup>5</sup>. The geodynamo probably operates in the whole of the fluid outer core, but in the Sun, much of the magnetic field generation is supposedly localized at the tachocline<sup>5</sup>, a thin layer of intense shear between the convecting outer region and the deeper radiative zone. Fully convective stars, such as mature stars of less than 0.35 solar masses (M dwarfs) and T Tauri stars (very young contracting stars with moderate mass), often have stronger magnetic fields than the Sun and their dynamo may resemble that of planets.

Rotation strongly influences the dynamo. For stars with moderate and low mass, the X-ray luminosity (a proxy for the magnetic flux) increases with rotation rate up to some threshold value, where it saturates<sup>8</sup>. Direct measurements of the field strength by the magnetic broadening of spectral lines confirm the saturation for M dwarfs<sup>9</sup>. The magnetic field topology, which is small-scale at the surface of the slowly rotating Sun, becomes more large-scale with prominent dipole contributions when rotation is fast and the star is fully convective<sup>1,2</sup>. In dynamo simulations of fully convective stars, the scale and strength of the field increase with rotation rate<sup>3</sup>, but the strength levels off in the most rapidly rotating cases. Geodynamo model studies support the existence of two regimes: for slow rotation, the magnetic

field is small-scale and weak; for fast rotation, it is dipole-dominated and its strength is independent of rotation rate<sup>7,10,11</sup>.

In ref. 7, a scaling theory for the field strength of planetary dynamos has been presented which is based on the (thermodynamically) available energy flux; in the case of thermal flux, this is the part that can be converted to magnetic energy to sustain it against ohmic dissipation. To test if the same scaling rule applies to the field strength in stellar dynamos, we generalize it to also cover cases of strong density stratification. We restrict our study to objects in the rapidly rotating regime, where in incompressible geodynamo models<sup>7</sup> the magnetic energy density was found to depend on density and convected energy flux  $q_c$ , but not (or very weakly) on magnetic diffusivity and rotation rate (that is, the field is saturated):

$$B^2 / (2\mu_0) \propto f_{\text{ohm}} \rho^{1/3} (q_c L / H_T)^{2/3} \quad (1)$$

Here  $\mu_0$  is permeability,  $f_{\text{ohm}} \leq 1$  is the ratio of ohmic dissipation to total dissipation,  $L$  is the length scale of the largest convective structures (in the geodynamo, this is the thickness  $D = R - r_i$  of the convective shell with outer radius  $R$  and inner radius  $r_i$ ) and  $H_T = c_p / (\alpha g)$  is the temperature scale height with  $c_p$  the heat capacity,  $\alpha$  the thermal expansivity and  $g$  the acceleration due to gravity. For stars we adopt the common assumption that  $L$  is of the order of the density scale height  $H_\rho$ . To account for the strong variations of density and scale height with radius, we assume that the mean squared magnetic field  $\langle B^2 \rangle$  is obtained by taking the average of equation (1) over the volume  $V$  of the spherical shell. We normalize density with its mean value  $\langle \rho \rangle$  and  $q_c$  with a reference value  $q_0$ , for which we take the bolometric flux at the outer boundary (except for Earth's core, see below):

$$\langle B^2 \rangle / (2\mu_0) = c f_{\text{ohm}} \langle \rho \rangle^{1/3} (F q_0)^{2/3} \quad (2)$$

Here  $c$  is a constant of proportionality, and the averaging of radially varying properties has been condensed into the efficiency factor  $F$ :

$$F^{2/3} = \frac{1}{V} \int_{r_i}^R \left( \frac{q_c(r)}{q_0} \frac{L(r)}{H_T(r)} \right)^{2/3} \left( \frac{\rho(r)}{\langle \rho \rangle} \right)^{1/3} 4\pi r^2 dr \quad (3)$$

where we set  $L = \min(D, H_\rho)$ .

$F$  must be calculated for each object separately. For Earth's core, simplifying approximations are made, such as  $L = D$ , constancy of density and thermodynamic properties, and linear variation of gravity with radius,  $g = g_0 r / R$ . A significant part (perhaps all) of the flux at Earth's core–mantle boundary is transported by conduction. At greater depth, the convected portion is larger and augmented by compositional driving of convection, which we treat as enhanced effective heat flux. We take the effective flux on the inner boundary  $q_{i,c}$  to define the reference flux as  $q_0 = q_{i,c} (r_i / R)^2$ . Two options for the variation of  $q_c$

<sup>1</sup>Max-Planck-Institut für Sonnensystemforschung, Max Planck Strasse 2, 37191 Katlenburg-Lindau, Germany. <sup>2</sup>Institut für Astrophysik, Universität Göttingen, Friedrich Hund Platz 1, 37077 Göttingen, Germany.



with radius are considered: constancy of total flux  $4\pi r^2 q_c$  as used in many geodynamo models, or a decrease to zero on the outer boundary. With these assumptions, equation (3) can be evaluated analytically. Setting  $r_i/R = 0.35$ , we obtain  $F = 0.88\alpha g_o R/c_p$  for constant total flux and  $F = 0.45\alpha g_o R/c_p$  when  $q_c(R) = 0$ . For  $\alpha = 1.35 \times 10^{-5}$ ,  $g_o = 10.7$ ,  $R = 3.48 \times 10^6$  and  $c_p = 840$  in SI units<sup>12</sup>,  $F$  in the Earth's core is obtained as 0.52 or 0.27, respectively.

In Fig. 1 we compare results of geodynamo simulations (ref. 7 and this work) with a non-dimensional form of the scaling equation (2). The spread in the non-dimensional flux  $q^*$  relates to a variation of the rotation rate by a factor of 1,000 and a variation of the flux for fixed rotation rate by a factor of 100. The good agreement confirms the independence of the field strength from the rotation rate and the variation with the  $2/3$  power of the flux. It provides the constant of proportionality as  $c = 0.63$ . Data for zero flux on the outer boundary (Supplementary Information) are collapsed with those for constant total flux when the difference in the efficiency factor  $F$  is accounted for. Results from a stellar dynamo model with moderate density stratification<sup>3</sup> agree with the scaling law, suggesting that it may also be applicable to stars and that the dynamo mechanisms in this model

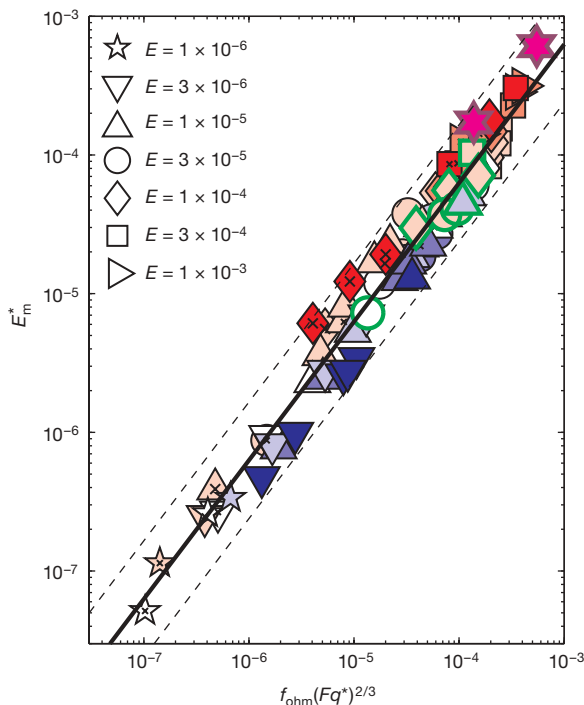


**Figure 1 | Scaling law versus results from dynamo models.** The non-dimensional form of equation (2) is obtained by dividing by  $\langle \rho \rangle \Omega^2 R^2$ , resulting in a non-dimensional energy density  $E_m^* = \langle B^2 \rangle / (2\mu_o \langle \rho \rangle \Omega^2 R^2)$  and flux  $q^* = q_o / (\langle \rho \rangle \Omega^3 R^3)$ ; the non-dimensional mean density is unity. Black-edged symbols are for models with radially constant total flux (ref. 7 and this work), green-edged symbols are for flux decreasing to zero at the outer radius (Supplementary Information).  $F$  is  $0.88\alpha g_o R/c_p$  in the first case and  $0.45\alpha g_o R/c_p$  in the second case. Only results in the strongly rotational regime are included, which requires that the local Rossby number<sup>7,11</sup> be less than 0.12. The Ekman number  $E = \nu / (\Omega D^2)$ , where  $\nu$  is viscosity, varies between  $10^{-3}$  and  $10^{-6}$ . The magnetic Prandtl number  $Pm = \nu / \eta$ , where  $\eta$  is magnetic diffusivity, is colour-coded; white means  $Pm = 1$ , different shades of red indicate values progressively larger than 1, and blue values less than 1. The pink hexagrams are the two most rapidly rotating cases from a set of dynamo models for fully convecting stars with a polytropic equation of state<sup>3</sup> with  $Pm = 1$  and  $E = 1.6 \times 10^{-4}$  and  $0.8 \times 10^{-4}$ , respectively. Here  $F = 1.48$  is calculated by numerically integrating the reference star model (Supplementary Information). The slope of the fitting line is set to one (if unconstrained, the least-squares slope is 1.02). Dashed lines,  $3\sigma$  standard error.

and in our geodynamo models are similar. We note that if the magnetic field strength is strictly independent of rotation rate and of magnetic (and any other) diffusivity, for dimensional reasons the exponents for density and heat flux in equation (2) must necessarily be  $1/3$  and  $2/3$ , respectively.

We numerically integrate equation (3) for structural models of Jupiter and stars. For Jupiter, we use the adiabatic model with gradual metallization<sup>13</sup>, assuming that the top of the dynamo region is at 0.84 planetary radii. With convection as the only means of heat transport and with luminosity varying with radius proportional to  $T dm/dr$ , where  $T$  is temperature and  $m$  is the mass inside radius  $r$ , we obtain  $F = 1.19$ . We use a stellar evolution code<sup>14</sup>, which provides density, temperature, luminosity and convected flux as function of radius, to generate models in the range of 0.25 to 0.7 solar masses for ages between 1.2 and 20 Myr and for masses of 0.25 and 0.30 solar masses up to 4.5 Gyr. The resulting  $F$  factors lie in the range 0.69–1.22.

We compare the predictions of our scaling law with the magnetic fields of Earth, Jupiter and two groups of rapidly rotating stars whose surface field strength has been determined spectroscopically. One is the classical T Tauri stars<sup>15</sup> and the other is a set of old M dwarfs<sup>16</sup>, from which we select those with a projected rotational velocity  $v \sin(i) \geq 3 \text{ km s}^{-1}$  (here  $v$  is the actual velocity, and  $i$  is inclination). To estimate their mean internal field strength  $B$  from the observed mean surface field  $B_s$ , we multiply the latter by a factor of 3.5, the typical ratio found in our geodynamo simulations. Additionally, we include some M stars whose large-scale field has been inferred from Zeeman–Doppler tomography<sup>2</sup>. Here the total surface field  $B_s$  is usually unknown. We use the dipole field strength  $B_{\text{dip}}$  and multiply by factors  $B_s/B_{\text{dip}} \approx 7$  found at EV Lac and YZ CMi (Supplementary Tables 4 and 6) and  $B/B_s = 3.5$  to obtain  $B$ . Also, for planets the total field strength at the top of the dynamo is unknown. The dipole field strengths at the dynamo surface are 0.26 mT and 1.0 mT at Earth<sup>17</sup> and Jupiter<sup>18</sup>, respectively. In our geodynamo simulations, we find a typical ratio  $B/B_{\text{dip}}$  of around seven for dynamos with an Earth-like magnetic power spectrum, which we apply to estimate the internal field strength of the planets.

The agreement with the theoretical prediction is remarkable for the different groups of rapidly rotating objects (Fig. 2), which span more than eight orders of magnitude in (equivalent) bolometric flux. For comparison, we also include stars with radiative cores and slow rotation<sup>19</sup>; as expected they fall below the prediction (green and yellow bars). The validity of some assumptions may be questioned for dynamos with strong density stratification—for example the use of  $H_\rho$  for the length scale  $L$  in equation (3) or the application of scaling factors between internal field and surface field derived from incompressible models. However, the latter are unlikely to differ vastly and even when we assume  $L = D$ , the  $F$  factor for stars increases only from one to five. Hence we consider the scaling law as robust on an order of magnitude scale. We conclude that dynamos in rapidly rotating stars and planets are basically similar, and that a single principle controls their magnetic field strength.

Some T Tauri stars in our sample may have formed a small radiative core. The observations for rapidly rotating old stars that are too massive to be fully convective<sup>19</sup> (orange symbols in Fig. 2) also agree with our field strength scaling law. Thus, the essential condition for its applicability is probably rapid rotation.

Although magnetic fields have been measured at other planets in the Solar System, the scaling law is either hard to test or not applicable at these locations: Mercury is a slow rotator and may hence fall into the non-dipolar dynamo regime<sup>20</sup>, the dynamos in Saturn<sup>21</sup> and Mercury<sup>20</sup> probably lie below a stably stratified conducting layer of unknown thickness, and those in Uranus and Neptune may operate in a thin shell overlying a stable region<sup>22</sup>.

Stars, particularly old M dwarfs, cluster in a narrow range of  $\langle \rho \rangle^{1/3} (F q_o)^{2/3}$  because the decrease in bolometric flux is balanced by an increase in density. This explains why rapidly rotating stars with rather different luminosities all have magnetic surface fields of

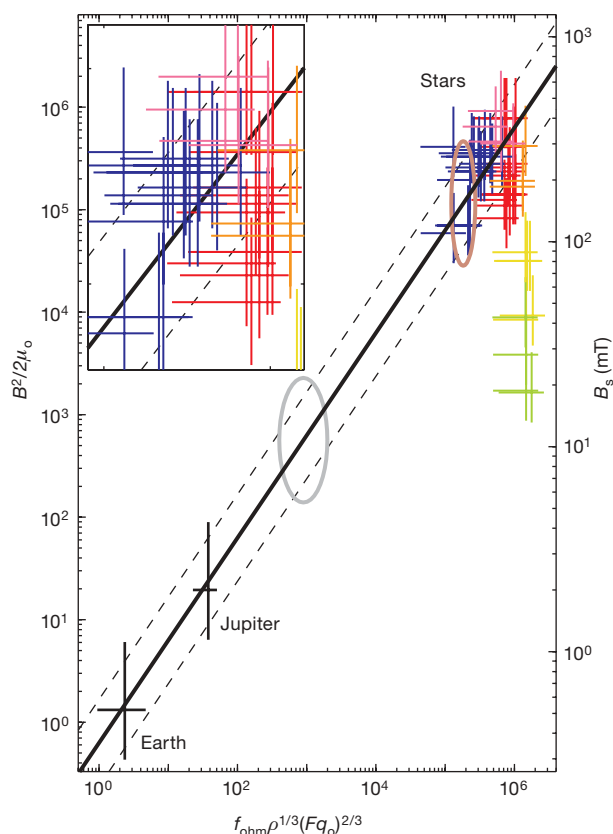


**Figure 2 | Scaling law versus magnetic fields of planets and stars.**

Magnetic energy density in the dynamo versus a function of density and bolometric flux (both in units of  $\text{J m}^{-3}$ ). The scale on the right shows r.m.s. field strength at the dynamo surface. The heat flow from Earth's core is uncertain<sup>12,26</sup> but is in the range  $30\text{--}100\text{ mW m}^{-2}$ . The effective convected flux including compositional convection is about twice as large (Supplementary Information); we use  $q_0 = 100\text{ mW m}^{-2}$ ,  $\langle\rho\rangle = 10^4\text{ kg m}^{-3}$  and  $F = 0.35$ . For Jupiter<sup>27</sup>,  $q_0 = 5.4\text{ W m}^{-2}$  and  $\langle\rho\rangle = 1,330\text{ kg m}^{-3}$ . For stars we assume  $F = 1$ . For T Tauri stars<sup>15</sup> (in blue) and old M dwarfs (in red where data for total field is known<sup>16</sup>, and in pink where the large-scale field was observed<sup>2</sup>),  $q_0$  is obtained from the effective surface temperatures<sup>15,16,28</sup>. Stars of  $0.6\text{--}1.1$  solar masses<sup>19</sup> are shown in green for rotation periods  $P > 10\text{ d}$ , yellow for  $4\text{ d} < P < 10\text{ d}$  and orange for  $P < 4\text{ d}$ . Where relevant stellar data are not quoted, we use model-based relationships between spectral subclass, mass and luminosity<sup>29,30</sup>. We assume  $f_{\text{ohm}} \approx 1$  as a nominal value. The bar lengths show estimated uncertainty rather than formal error (Supplementary Information). Black lines show the rescaled fit from Fig. 1 with  $3\sigma$  uncertainties (solid and dashed lines, respectively). The stellar field is enlarged in the inset. Brown and grey ellipses indicate predicted locations of a brown dwarf with  $1,500\text{ K}$  surface temperature and an extrasolar planet with seven Jupiter masses, respectively.

some tenths of a tesla. Even for a typical 1-Gyr-old brown dwarf of  $0.05$  solar masses<sup>23</sup> with an effective temperature of  $1,500\text{ K}$  and  $\langle\rho\rangle = 90,000\text{ kg m}^{-3}$ , a surface magnetic field of the order of  $0.1\text{ T}$  is expected (brown ellipse in Fig. 2). Magnetic fields have not been detected at brown dwarfs so far, but our estimate suggests that a search might well be productive. For young ( $1\text{--}3\text{ Gyr}$ ) giant extrasolar planets of  $5\text{--}10$  Jupiter masses, which should have  $20\text{--}200$  times Jupiter's intrinsic luminosity at a similar radius<sup>23</sup>, the expected field strength is  $5\text{--}12$  times larger than that at Jupiter's surface (considering also the shallower depth of the dynamo). Another estimate<sup>24</sup> based on the Elsasser number rule arrived at similar maximum values, but only for rotation periods  $< 5\text{ h}$ , which we do not require. The presence of such strong fields improves the prospects for detecting radio emissions from these planets<sup>25</sup>. From the high-frequency cut-off in the radio spectrum, the surface field strength can then be determined<sup>25</sup>.

Received 21 August; accepted 30 October 2008.

- Donati, J.-F. *et al.* The large-scale axisymmetric magnetic topology of a very low-mass fully convective star. *Science* **311**, 633–635 (2006).
- Morin, J. *et al.* Large-scale magnetic topologies of mid-M dwarfs. *Mon. Not. R. Astron. Soc.* **390**, 567–581 (2008).
- Dobler, W., Stix, M. & Brandenburg, A. Magnetic field generation in fully convective rotating spheres. *Astrophys. J.* **638**, 336–347 (2006).
- Browning, M. Simulations of dynamo action in fully convective stars. *Astrophys. J.* **676**, 1262–1280 (2008).
- Charbonneau, P. Dynamo models of the solar cycle. *Living Rev. Sol. Phys.* **2**, 2 (2005); (<http://solarphysics.livingreviews.org/Articles/lrsp-2005-2>) (cited on 13 November 2008).
- Stevenson, D. J. Planetary magnetic fields. *Earth Planet. Sci. Lett.* **208**, 1–11 (2003).
- Christensen, U. R. & Aubert, J. Scaling properties of convection-driven dynamos in rotating spherical shells and applications to planetary magnetic fields. *Geophys. J. Int.* **166**, 97–114 (2006).
- Pizzolato, N., Maggio, A., Micela, G., Sciortino, S. & Ventura, P. The stellar activity-rotation relationship revisited: Dependence of saturated and non-saturated X-ray emission regimes on stellar mass for late-type dwarfs. *Astron. Astrophys.* **397**, 147–157 (2003).
- Reiners, A., Basri, M. & Browning, M. Evidence for magnetic flux saturation in rapidly rotating M stars. *Astrophys. J.* (in the press).
- Sreenivasan, B. & Jones, C. A. The role of inertia in the evolution of spherical dynamos. *Geophys. J. Int.* **164**, 467–476 (2006).
- Olson, P. & Christensen, U. R. Dipole moment scaling for convection-driven planetary dynamos. *Earth Planet. Sci. Lett.* **250**, 561–571 (2006).
- Nimmo, F. in *Treatise on Geophysics* Vol. 8, *Core dynamics* (ed. Olson, P.) 31–66 (Elsevier, 2007).
- Guillot, T. A comparison of the interiors of Jupiter and Saturn. *Planet. Space Sci.* **47**, 1183–1200 (1999).
- Granzler, T., Schüssler, M., Caligari, P. & Strassmeier, K. G. Distribution of star spots on cool stars. II. Pre-main-sequence and ZAMS stars between  $0.4 M_{\text{Sun}}$  and  $1.7 M_{\text{Sun}}$ . *Astron. Astrophys.* **355**, 1087–1095 (2000).
- Johns-Krull, C. M. The magnetic field of classical T Tauri stars. *Astrophys. J.* **664**, 975–985 (2007).
- Reiners, A. & Basri, G. The first direct measurements of surface magnetic fields on very low mass stars. *Astrophys. J.* **656**, 1121–1135 (2007).
- Bloxham, J. & Jackson, A. Time-dependent mapping of the magnetic field at the core-mantle boundary. *J. Geophys. Res.* **97**, 19537–19563 (1992).
- Connerney, J. E. P. Magnetic fields of the outer planets. *J. Geophys. Res.* **98**, 18659–18679 (1993).
- Saari, S. H. in *Magnetodynamic Phenomena in the Solar Atmosphere* (eds Uchida, Y., Kosugi, T. & Hudson, H. S.) 367–374 (Kluwer, 1996).
- Christensen, U. R. A deep dynamo generating Mercury's magnetic field. *Nature* **444**, 1056–1058 (2006).
- Stevenson, D. J. Saturn's luminosity and magnetism. *Science* **208**, 746–748 (1980).
- Stanley, S. & Bloxham, J. Convective region geometry as the cause for Uranus's and Neptune's unusual magnetic fields. *Nature* **428**, 151–153 (2004).
- Burrows, A., Hubbard, W. B., Lunine, J. I. & Liebert, J. The theory of brown dwarfs and extrasolar giant planets. *Rev. Mod. Phys.* **73**, 719–765 (2001).
- Sanchez-Lavega, A. The magnetic field in giant extrasolar planets. *Astrophys. J.* **609**, L87–L90 (2004).
- Zarka, P. Plasma interactions of exoplanets with their parent star and associated radio emissions. *Planet. Space Sci.* **55**, 598–617 (2007).
- Lay, T., Hernlund, J. & Buffett, B. A. Core-mantle boundary heat flow. *Nature Geosci.* **1**, 25–32 (2008).
- Guillot, T., Stevenson, D. J., Hubbard, W. B. & Saumon, D. in *Jupiter* (eds Bagenal, F., Towling, T. E. & McKinnon, W. B.) 39–57 (Cambridge Univ. Press, 2005).
- Neuhäuser, R., Sterzik, M. F., Schmitt, J. H. M. M., Wichmann, R. & Krautter, J. ROSAT survey observations of T Tauri stars in Taurus. *Astron. Astrophys.* **297**, 391–417 (1995).
- Baraffe, I. & Chabrier, G. Mass-spectral class relationship for M-dwarfs. *Astrophys. J.* **461**, L51–L54 (1996).
- Drilling, J. S. & Landolt, A. U. in *Allen's Astrophysical Quantities* (ed. Cox, A. N.) 381–396 (Springer, 2000).

**Supplementary Information** is linked to the online version of the paper at [www.nature.com/nature](http://www.nature.com/nature).

**Acknowledgements** Reviews by C. Johns-Krull helped to sharpen the paper. U.R.C. thanks M. Rempel for prompting this study by asking if planetary scaling laws also apply to stars.

**Author Contributions** U.R.C. suggested the basic concept, performed dynamo simulations and wrote the paper. V.H. calculated stellar models. A.R. provided magnetic field data and other stellar data. All authors discussed results and commented on the manuscript.

**Author Information** Reprints and permissions information is available at [www.nature.com/reprints](http://www.nature.com/reprints). Correspondence and requests for materials should be addressed to U.R.C. ([christensen@mps.mpg.de](mailto:christensen@mps.mpg.de)).



## LETTERS

# Measured long-range repulsive Casimir–Lifshitz forces

J. N. Munday<sup>1</sup>, Federico Capasso<sup>2</sup> & V. Adrian Parsegian<sup>3</sup>

Quantum fluctuations create intermolecular forces that pervade macroscopic bodies<sup>1–3</sup>. At molecular separations of a few nanometres or less, these interactions are the familiar van der Waals forces<sup>4</sup>. However, as recognized in the theories of Casimir, Polder and Lifshitz<sup>5–7</sup>, at larger distances and between macroscopic condensed media they reveal retardation effects associated with the finite speed of light. Although these long-range forces exist within all matter, only attractive interactions have so far been measured between material bodies<sup>8–11</sup>. Here we show experimentally that, in accord with theoretical prediction<sup>12</sup>, the sign of the force can be changed from attractive to repulsive by suitable choice of interacting materials immersed in a fluid. The measured repulsive interaction is found to be weaker than the attractive. However, in both cases the magnitude of the force increases with decreasing surface separation. Repulsive Casimir–Lifshitz forces could allow quantum levitation of objects in a fluid and lead to a new class of switchable nanoscale devices with ultra-low static friction<sup>13–15</sup>.

The van der Waals force between molecules<sup>4</sup> or, more generally, small dielectric particles<sup>16</sup>, results in large part from their quantum mechanical zero-point energy, which induces electromagnetic charge fluctuations that interact at small separations. At larger distances, typically more than a few nanometres, a qualitatively new regime is entered: the interaction is no longer instantaneous owing to the finite speed of light. As first shown by Casimir and Polder<sup>6</sup>, this ‘retardation effect’ causes the force to fall more rapidly with distance than in the short-range van der Waals limit.

Interactions due to quantum fluctuations impinge on fields ranging from fundamental physics to chemistry and biology when surfaces are in contact or in close proximity<sup>2</sup>. Their consequences are felt in phenomena such as adhesion, friction, wetting and stiction<sup>2,17</sup>. Casimir’s formulation for the interaction between ideal metals in vacuum was extended by Lifshitz, Dzyaloshinskii and Pitaevskii to macroscopic bodies made of real materials described by their dielectric response functions. Their formulation included solids or liquids separated by a fluid<sup>7,12</sup>. As between two molecules, one can distinguish a short-range van der Waals regime and a retarded long-range regime characterized by a stronger dependence on separation. Several measurements have confirmed the theoretically predicted attractive forces between electrically neutral surfaces<sup>8,9</sup>.

Recently there has been renewed interest in measuring the Casimir–Lifshitz force with higher precision and in applying it to the design of nanomechanical devices<sup>10,18–20</sup>. So far, however, all measurements of Casimir–Lifshitz forces have revealed attractive interactions. Although repulsive forces have been predicted<sup>12</sup>, no direct measurement of long-range repulsion between material bodies has (to our knowledge) been reported. In the non-retarded van der Waals limit (surface separations up to a few nanometres), evidence for repulsive interactions between solids separated by a liquid has been

presented<sup>15,21–24</sup>. When working at small separations, however, the polarity and orientation of the molecules may influence the force. Measurements at larger separations do not suffer from this problem because solvation forces die out with characteristic decay lengths the size of solvent molecules. Note also that the long-range repulsion addressed here is different from the prediction of a repulsive force associated with the geometry of the boundary conditions, which has been criticized in the literature (see ref. 25 and references therein), or with the use of metamaterials<sup>26</sup>.

In this Letter, we report the direct measurement of long-range repulsive forces between solids separated by a fluid. We compare the results with Lifshitz’s theory and find them to be consistent within the uncertainties of the optical properties of the materials.

Repulsive forces between macroscopic bodies can be qualitatively understood by considering their material polarizabilities or, better, their dielectric response functions:  $\epsilon_1$ ,  $\epsilon_2$  and  $\epsilon_3$  (see Supplementary Information). The interaction of material 1 with material 2 across medium 3 goes as a summation of terms with differences in material permittivities

$$-(\epsilon_1 - \epsilon_3)(\epsilon_2 - \epsilon_3) \quad (1)$$

over frequencies  $\zeta$  that span the entire spectrum<sup>2,12</sup>. Between two like materials,  $\epsilon_1 = \epsilon_2$ , these terms are negative and correspond to attraction. However, when the dielectric response  $\epsilon_3$  of the medium is between  $\epsilon_1$  and  $\epsilon_2$ ,

$$\epsilon_1 > \epsilon_3 > \epsilon_2 \quad (2)$$

then the  $-(\epsilon_1 - \epsilon_3)(\epsilon_2 - \epsilon_3)$  terms are positive; the force is repulsive.

An easy-to-see limit for this repulsion is the case where region 2 is air or vacuum and the polarizability of medium 3 is less than that of substrate 1 (see, for example, ref. 2, pages 27 and 58). As a result, substance 3, rather than form a droplet, spreads out to achieve maximum proximity to substance 1.

Examples of material systems that obey equation (2) are rare but do exist. One of the earliest successes of Lifshitz’s equation was the quantitative explanation of the thickening of a superfluid helium film on the walls of a container<sup>12,27</sup>. In that system, it is energetically more favourable for the liquid to be between the vapour and the container, and the liquid climbs the wall. One set of materials (solid–liquid–solid) that obeys inequality (2) over a large frequency range is gold, bromobenzene and silica (Fig. 1b; see also Supplementary Information for a discussion of the optical properties).

Our measurements are conducted between a large plate and a 39.8  $\mu\text{m}$  diameter polystyrene sphere coated with a 100 nm thick gold film, which is attached to a cantilever and mounted on an atomic force microscope with a fluid-filled cell (Fig. 2a). Light from a superluminescent diode is reflected off the back of the cantilever and is

<sup>1</sup>Department of Physics, <sup>2</sup>School of Engineering and Applied Sciences, Harvard University, Cambridge, Massachusetts 02138, USA. <sup>3</sup>National Institutes of Health, Bethesda, Maryland 20892, USA.

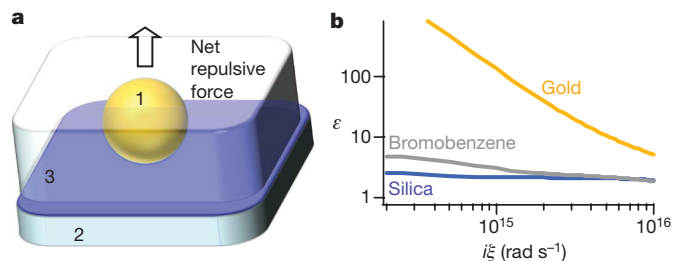


**Figure 1 | Repulsive quantum electrodynamical forces can exist for two materials separated by a fluid.** **a**, The interaction between material 1 and material 2 immersed in a fluid (material 3) is repulsive when  $\varepsilon_1(i\xi) > \varepsilon_3(i\xi) > \varepsilon_2(i\xi)$ , where the  $\varepsilon(i\xi)$  terms are the dielectric functions at imaginary frequency (see Supplementary Information for details about the definition of  $\varepsilon(i\xi)$ ). **b**, The optical properties of gold, bromobenzene and silica are such that  $\varepsilon_{\text{gold}}(i\xi) > \varepsilon_{\text{bromobenzene}}(i\xi) > \varepsilon_{\text{silica}}(i\xi)$  and lead to a repulsive force between the gold and silica surfaces.

used to monitor its bending. To advance the sphere towards the plate, an Asylum Research linear variable differential transformer is used to control a piezo column, which reduces hysteresis and nonlinearities inherent in piezoelectrics. Any interaction between the sphere and the plate will result in a bending of the cantilever and a change in the detector signal that monitors the difference in light intensity between the top half of the detector and the bottom half of the detector. This difference signal is proportional to the force.

Cleaning procedures are performed on all surfaces before measurements. The silica plate, gold plate (consisting of a silica plate

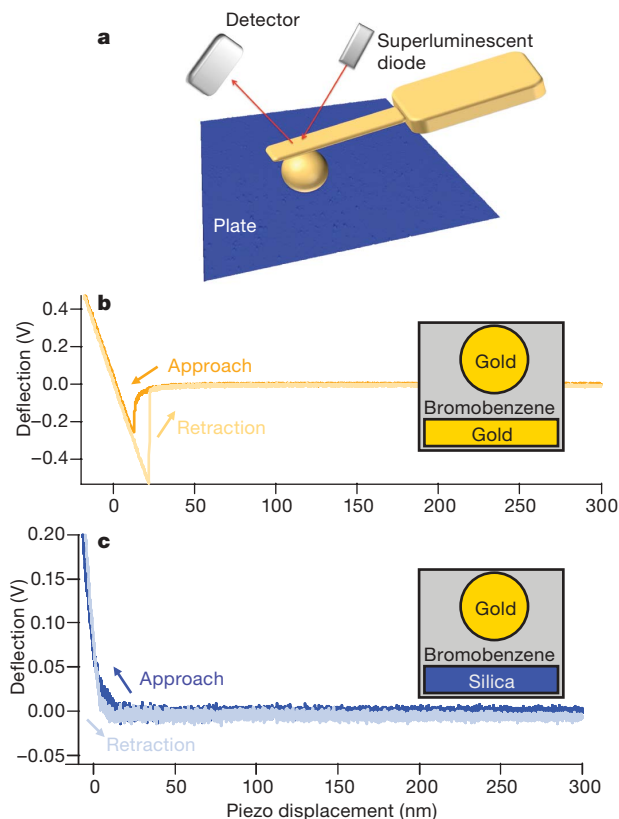


**Figure 2 | Experimental set-up and deflection data.** **a**, A sphere is attached to an atomic force microscope cantilever, which is enclosed within a bromobenzene-filled cell for force measurements. **b**, Deflection data showing attractive interactions between a gold sphere and a gold plate. **c**, For the case of the same gold sphere and a silica plate, deflection data show a repulsive interaction evident during both approach and retraction. Note that the deflection voltage signal is a difference signal obtained from the detector and is proportional to the bending of the cantilever, as discussed in the text.

coated with 200 nm of gold) and fluid cell are ultrasonically cleaned for 30 min in ethanol followed by drying in flowing nitrogen. The cantilever chip is similarly rinsed with ethanol, but without ultrasonic cleaning (to avoid damage).

Electrostatic force microscopy is performed on the samples to ensure that surface charge effects are small and will not mask the Casimir–Lifshitz force (see Supplementary Information). For both the silica and gold plates used in the experiments, no evidence of excess charge accumulation is found. Similarly, no electrostatic double-layer force is expected for clean, uncharged surfaces separated by a fluid of low dielectric constant like bromobenzene<sup>17</sup>.

Force measurements are conducted in a fluid-filled cell containing both the gold and silica plates. The cantilever is completely submerged in bromobenzene (EM Science, Merck), which is filtered through a 0.2  $\mu\text{m}$  PTFE filter before use. The set-up is assembled and allowed to equilibrate for 1 h before measurements. All measurements are performed at room temperature.

Raw deflection versus piezo displacement data show that the force is changed from attractive to repulsive by replacing the gold plate with the silica plate (Fig. 2b, c). The data in Fig. 2b, c were acquired with a piezo speed of 45  $\text{nm s}^{-1}$ . With the gold plate, the cantilever is bent towards the surface during the approach, which corresponds to an attractive force between the sphere and plate until contact (Fig. 2b). Once contact is made, the normal force of the plate pushes against the sphere. Upon retraction, the sphere sticks to the plate for an additional 10 nm, owing to stiction between the two gold surfaces, before losing contact with the surface. When the silica plate is used, the cantilever is bent away from the surface during the approach, corresponding to a repulsive interaction (Fig. 2c). During retraction, the sphere continues to show repulsion. This cannot be a result of the hydrodynamic force, because that force is in a direction that opposes the motion of the sphere and will change sign as the direction is changed. Similarly, the repulsion observed in Fig. 2c cannot be due to charge trapped on silica; any charge that does exist on the surface will induce an image charge of opposite sign on the metal sphere and lead to an attractive interaction.

The detector signal is converted to a force signal by calibration with the hydrodynamic force<sup>28</sup>. By performing measurements at different piezo speeds, we can isolate the hydrodynamic force from the Casimir–Lifshitz force for calibration purposes<sup>28</sup>. Because the hydrodynamic force is linear with velocity, subtracting the total measured force at two different speeds results in only a hydrodynamic force with no contribution from the Casimir–Lifshitz force. A similar scheme can be used to distinguish the Casimir–Lifshitz force. Experimental precautions to minimize electrostatic effects are described in detail in the Supplementary Information and in ref. 28.

The measured forces after calibration show a clear distinction between the attractive and repulsive regimes when the plate is changed from gold to silica (Fig. 3a). The blue (orange) circles correspond to the average force from 50 runs between the gold sphere and the silica (gold) plate. Histograms of the force data at different distances show a Gaussian distribution and no evidence of systematic errors (see Supplementary Information). For clarity, error bars, which represent the standard deviation of the data, are shown for only seven points.

The experiment is repeated with an additional sphere and plate for both configurations. Figure 3b shows the measured force for two different spheres of nominally the same diameter and two different silica plates. Similar measurements for two spheres and gold plates are shown in Fig. 3c. The solid lines are the temperature dependent Lifshitz's theory including surface roughness corrections (see Supplementary Information) for the first sphere–plate pair (circles). Because the second set of measurements are made with spheres and plates of similar surface roughness and size, the corrections are of similar magnitude.

Uncertainties in the optical properties of the materials used are probably responsible for the significant discrepancy between theory and experiment. Previous measurements of attractive forces between



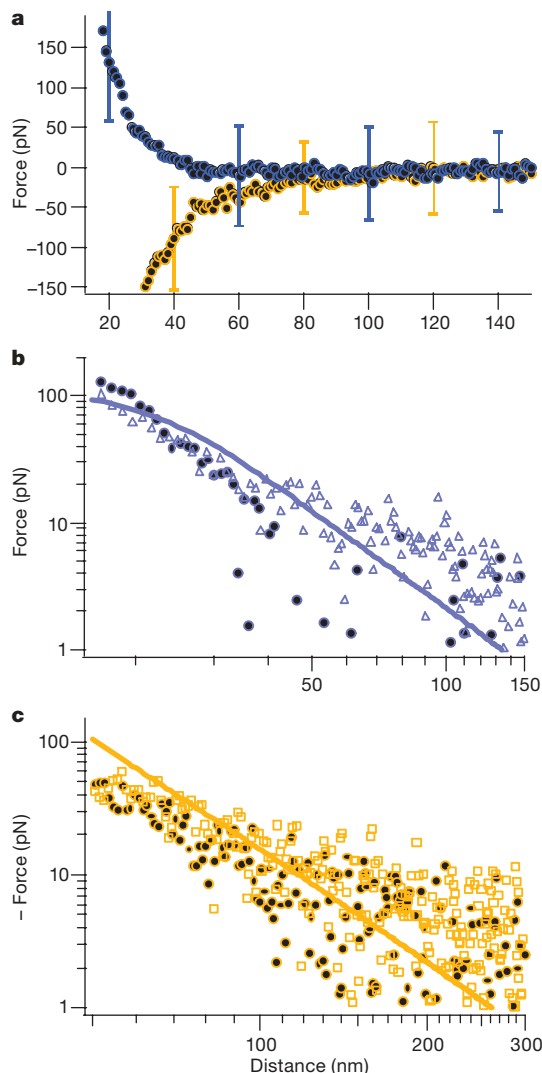


**Figure 3 | Attractive and repulsive Casimir-Lifshitz force measurements.** **a**, Blue (orange) circles represent the average of 50 data sets for the force between a gold sphere and a silica (gold) plate in bromobenzene. For clarity, error bars, which represent the standard deviation of the data, are only shown for seven data points. **b**, Measured repulsive force between a gold sphere and a silica plate in bromobenzene on a log-log scale (blue circles) and calculated force using Lifshitz's theory (solid line) including corrections for the measured surface roughness of the sphere and the plate. Blue triangles are force data for another gold sphere (nominally of the same diameter)/silica plate pair. **c**, Measured attractive force on a log-log scale for two gold sphere/plate pairs (circles and squares) in bromobenzene. The calculated force includes surface roughness corrections corresponding to the data represented by the circles (see Supplementary Information for calculations).

gold surfaces in ethanol<sup>11,28</sup> showed a smaller discrepancy between theory and experiments. This comparison leads us to believe that the two-oscillator model (see Supplementary Information) is insufficient for detailed theoretical analysis using bromobenzene. Besides, measurements of the optical properties over a large spectral range are not available for bromobenzene. It is also possible that the optical properties are modified for very thin films. In addition to the uncertainties in the optical properties of the materials, discrepancies between theory and experiment are expected at small separations. There the surface roughness correction to Lifshitz's theory begins to fail when the surface roughness is of comparable size to the surface separation. Finally, we note that for the largest distances shown in Fig. 3b, c the averaged values for the force magnitude appear to be greater than the predicted value of the force from Lifshitz's theory. However, it should be stressed that this appearance is mostly due to

logarithmic compression of the vertical axis and the fact that negative values are necessarily omitted on the log-log plot. It should further be noted that force magnitudes below 10 pN cannot be accurately determined because of the relatively large spread in the data.

Finally, other effects are sometimes named after Casimir, which are not quantum electrodynamic in origin but rather the result of thermodynamic fluctuations. The critical Casimir effect is one such phenomenon (see, for example, ref. 29 and references therein); however, this effect is not present in our experiment because it occurs only in binary liquid mixtures near a critical point. Away from the critical point, the correlation length is too small to result in a force between macroscopic surfaces separated by tens or hundreds of nanometres. Thermal acoustic pressure fluctuations can also occur between two surfaces separated by a third material and give rise to an attractive force sometimes referred to as the acoustic Casimir effect<sup>30</sup>. For two plates that are perfect reflectors of electromagnetic and acoustic waves, the ratio of the acoustic Casimir force to the quantum electrodynamic Casimir force is about 0.06 at 100 nm and room temperature<sup>30</sup>. The introduction of a fluid results in a decrease of the acoustic impedance mismatch, and hence a reduction in the acoustic Casimir force due to a weaker confinement of pressure fluctuations. Given these results, we expect the acoustic Casimir effect to be similarly small for our system.

We have presented detailed measurements, which unambiguously show that long-range quantum electrodynamic forces between solid bodies can become repulsive when the optical properties of the materials are properly chosen. With such materials, quantum levitation of one surface above another in a fluid should be possible and could lead to the suppression of stiction and to ultra-low friction devices and sensors<sup>13–15</sup>.

Received 6 August; accepted 30 October 2008.

1. Milonni, P. W. *The Quantum Vacuum: An Introduction to Quantum Electrodynamics* (Academic, 1993).
2. Parsegian, V. A. *van der Waals Forces: A Handbook for Biologists, Chemists, Engineers, and Physicists* (Cambridge Univ. Press, 2006).
3. Ball, P. Feel the force. *Nature* **447**, 772–774 (2007).
4. London, F. The general theory of molecular forces. *Trans. Faraday Soc.* **33**, 8–26 (1937).
5. Casimir, H. B. G. On the attraction between two perfectly conducting plates. *Proc. K. Ned. Akad. Wet.* **51**, 793–795 (1948).
6. Casimir, H. B. G. & Polder, D. The influence of retardation on the London-van der Waals forces. *Phys. Rev.* **73**, 360–372 (1948).
7. Lifshitz, E. M. The theory of molecular attractive forces between solids. *Sov. Phys. JETP* **2**, 73–83 (1956).
8. Derjaguin, B. V., Abrikosova, I. I. & Lifshitz, E. M. Direct measurement of molecular attraction between solids separated by a narrow gap. *Q. Rev. Chem. Soc.* **10**, 295–329 (1956).
9. van Blokland, P. H. G. M. & Overbeek, J. T. G. van der Waals forces between objects covered with a chrome layer. *J. Chem. Soc. Faraday Trans. I* **74**, 2637–2651 (1978).
10. Lamoreaux, S. K. Demonstration of the Casimir force in the 0.6 to 6  $\mu\text{m}$  range. *Phys. Rev. Lett.* **78**, 5–8 (1997).
11. Munday, J. N. & Capasso, F. Precision measurement of the Casimir-Lifshitz force in a fluid. *Phys. Rev. A* **75**, 060102(R) (2007).
12. Dzyaloshinskii, I. E., Lifshitz, E. M. & Pitaevskii, L. P. The general theory of van der Waals forces. *Adv. Phys.* **10**, 165–209 (1961).
13. Capasso, F., Munday, J. N., Iannuzzi, D. & Chan, H. B. Casimir forces and quantum electrodynamic torques: Physics and nanomechanics. *IEEE J. Select. Top. Quant. Electron.* **13**, 400–414 (2007).
14. Iannuzzi, D., Munday, J. & Capasso, F. Ultra-low friction configuration. US Patent Application US20070066494 (filed, 19 September 2005).
15. Feiler, A. A., Bergstrom, L. & Rutland, M. W. Superlubricity using repulsive van der Waals forces. *Langmuir* **24**, 2274–2276 (2008).
16. Hamaker, H. C. The London – van Der Waals attraction between spherical particles. *Physica* **4**, 1058–1072 (1937).
17. Israelachvili, J. N. *Intermolecular and Surface Forces* (Academic, 1992).
18. Mohideen, U. & Roy, A. Precision measurement of the Casimir force from 0.1 to 0.9  $\mu\text{m}$ . *Phys. Rev. Lett.* **81**, 4549–4552 (1998).
19. Bressi, G., Carugno, G., Onofrio, R. & Ruoso, G. Measurement of the Casimir force between parallel metallic surfaces. *Phys. Rev. Lett.* **88**, 041804 (2002).
20. Chan, H. B., Aksyuk, V. A., Kleiman, R. N., Bishop, D. J. & Capasso, F. Quantum mechanical actuation of microelectromechanical systems by the Casimir force. *Science* **291**, 1941–1944 (2001).
21. Lee, S. & Sigmund, W. M. Repulsive van der Waals forces for silica and alumina. *J. Colloid Interface Sci.* **243**, 365–369 (2001).

22. Lee, S. & Sigmund, W. AFM study of repulsive van der Waals forces between Teflon AF thin film and silica or alumina. *J. Colloids Surf. A* **204**, 43–50 (2002).
23. Milling, A., Mulvaney, P. & Larson, I. Direct measurement of repulsive van der Waals interactions using an atomic force microscope. *J. Colloid Interface Sci.* **180**, 460–465 (1996).
24. Meurk, A., Luckham, P. F. & Bergstrom, L. Direct measurement of repulsive and attractive van der Waals forces between inorganic materials. *Langmuir* **13**, 3896–3899 (1997).
25. Graham, N. *et al.* The Dirichlet Casimir problem. *Nucl. Phys. B* **677**, 379–404 (2004).
26. Leonhardt, U. & Philbin, T. G. Quantum levitation by left-handed metamaterials. *N. J. Phys.* **9**, 254 (2007).
27. Sabisky, E. S. & Anderson, C. H. Verification of the Lifshitz theory of the van der Waals potential using liquid-helium films. *Phys. Rev. A* **7**, 790–806 (1973).
28. Munday, J. N., Capasso, F., Parsegian, V. A. & Bezrukov, S. M. Measurements of the Casimir-Lifshitz force in fluids: The effect of electrostatic forces and Debye screening. *Phys. Rev. A* **78**, 032109 (2008).
29. Hertlein, C., Helden, L., Gambassi, A., Dietrich, S. & Bechinger, C. Direct measurement of critical Casimir forces. *Nature* **451**, 172–175 (2008).
30. Bschorr, O. The force between two parallel rigid plates due to the radiation pressure of phonons. *J. Acoust. Soc. Am.* **106**, 3730–3731 (1999).

**Supplementary Information** is linked to the online version of the paper at [www.nature.com/nature](http://www.nature.com/nature).

**Acknowledgements** We thank D. Iannuzzi, R. Podgornik, J. Zimmerberg, S. M. Bezrukov and M. B. Romanowsky for discussions. This project was partially supported by the Center for Nanoscale Systems at Harvard University, and by the Intramural Research Program of the NIH, Eunice Kennedy Shriver National Institute of Child Health and Human Development. J.N.M. acknowledges support from the NSF.

**Author Information** Reprints and permissions information is available at [www.nature.com/reprints](http://www.nature.com/reprints). Correspondence and requests for materials should be addressed to F.C. ([capasso@seas.harvard.edu](mailto:capasso@seas.harvard.edu)).



## LETTERS

# Electrically pumped photonic-crystal terahertz lasers controlled by boundary conditions

Y. Chassagneux<sup>1</sup>, R. Colombelli<sup>1</sup>, W. Maineult<sup>2</sup>, S. Barbieri<sup>2</sup>, H. E. Beere<sup>3</sup>, D. A. Ritchie<sup>3</sup>, S. P. Khanna<sup>4</sup>, E. H. Linfield<sup>4</sup> & A. G. Davies<sup>4</sup>

Semiconductor lasers based on two-dimensional photonic crystals<sup>1,2</sup> generally rely on an optically pumped central area, surrounded by un-pumped, and therefore absorbing, regions<sup>3</sup>. This ideal configuration is lost when photonic-crystal lasers are electrically pumped, which is practically more attractive as an external laser source is not required. In this case, in order to avoid lateral spreading of the electrical current, the device active area must be physically defined by appropriate semiconductor processing. This creates an abrupt change in the complex dielectric constant at the device boundaries, especially in the case of lasers operating in the far-infrared, where the large emission wavelengths impose device thicknesses of several micrometres. Here we show that such abrupt boundary conditions can dramatically influence the operation of electrically pumped photonic-crystal lasers. By demonstrating a general technique to implement reflecting or absorbing boundaries, we produce evidence that whispering-gallery-like modes or true photonic-crystal states can be alternatively excited. We illustrate the power of this technique by fabricating photonic-crystal terahertz (THz) semiconductor lasers, where the photonic crystal is implemented via the sole patterning of the device top metallization. Single-mode laser action is obtained in the 2.55–2.88 THz range, and the emission far field exhibits a small angular divergence, thus providing a solution for the quasi-total lack of directionality typical of THz semiconductor lasers based on metal–metal waveguides<sup>4</sup>.

Terahertz radiation—loosely defined as the region of the electromagnetic spectrum between 0.5 THz and 5 THz (ref. 5)—finds promising applications in very different areas of science and technology, such as astronomy, environmental monitoring and security<sup>6</sup>. However, its spectral location—between optical and microwave frequencies—has hindered the development of compact semiconductor sources. A significant breakthrough in this direction took place in 2002<sup>7</sup> with the demonstration of a quantum cascade laser operating at ~4.4 THz. Quantum cascade lasers rely on transitions between quantized conduction band states of a suitably designed semiconductor multi-quantum-well structure<sup>8</sup>. They are in-plane emitters, with the electric-field vector perpendicular to the plane of the layers, and the unnatural surface emission (often desirable) has to be engineered. The advantage of transverse magnetic polarization, however, is the possibility of exploiting surface plasmons for waveguiding<sup>9</sup>. Indeed, surface-plasmon single-metal<sup>7</sup> and metal–metal<sup>10</sup> ridge waveguides proved to be a key ingredient in the extension of the quantum cascade concept from mid-infrared to long-infrared wavelengths ( $\lambda > 19 \mu\text{m}$ ).

In the mid-infrared, photonic-crystal-based quantum cascade structures have been demonstrated for surface emission<sup>11</sup> and normal-incidence detection<sup>12</sup>. The application of photonic-crystal technology to active devices is particularly appealing because it allows

the achievement of simultaneous spectral and spatial (surface emission, beaming and so on) mode engineering. In the above-mentioned mid-infrared structures, the effective index contrast was obtained via a deep etch of the semiconductor material. This approach has been transferred to the THz range to realize devices based on lattices of deeply etched pillars<sup>13,14</sup>. Besides the high degree of technological complexity, these devices did not lead to surface emission, and they did not exploit the possibility of ‘printing’ the photonic structure on the top metal only. First-order<sup>15</sup> and second-order<sup>16</sup> distributed-feedback devices were demonstrated only recently, with one-dimensional metallic gratings implemented on top of standard ridge-waveguide lasers. At shorter mid-infrared wavelengths and for edge emitting devices, a plasmonic collimator was also recently demonstrated<sup>17</sup>.

In this work we demonstrate a new approach to the implementation of a resonator for THz semiconductor lasers, based on a two-dimensional (2D) photonic-crystal structure, lithographically transferred onto the top metallization only of a metal–metal THz quantum cascade laser<sup>18</sup>. In addition, we show that the operation of the photonic crystal is critically dependent on the boundary conditions. This finding is general, and is a key element for the development of any electrically pumped photonic-crystal device. Devices with a similar geometry have been reported in ref. 19. However, the crucial role of boundary conditions was not investigated, and no effect of the photonic crystal on the far-field emission pattern was detected. Our micro-resonators exhibit—when the correct boundary conditions are implemented—lithographically tunable single-mode emission, and an angularly narrow (though not always single-lobed) far-field emission pattern.

The quantum cascade laser used in this work was grown by molecular beam epitaxy in the GaAs/AlGaAs material system. It consists of a 12- $\mu\text{m}$ -thick, bound-to-continuum active region with emission at ~2.7 THz (ref. 20). The active core is sandwiched between 700 nm,  $2 \times 10^{18} \text{ cm}^{-3}$  and 80 nm,  $5 \times 10^{18} \text{ cm}^{-3}$  doped layers, forming the lower and upper contacts. The quantum cascade wafer was thermo-compressively bonded onto an n<sup>+</sup>-GaAs wafer. After selective etching of the GaAs substrate, the 700-nm-thick top doped layer was thinned to 200 nm to reduce free carrier absorption. Hexagonal mesas were etched down to the bottom metal to avoid lateral current dispersion, and the photonic-crystal pattern was implemented in the top metallization only, which acts as a contact and—simultaneously—provides the necessary optical feedback. In Fig. 1a a schematic cross-section of a typical device is displayed, and an optical microscope image taken from the top is shown in Fig. 1b.

Two-dimensional photonic-crystal slab waveguide lasers can be divided in two families: defect mode lasers and band-edge mode lasers. The former operate at frequencies inside the bandgap by intentionally introducing a defect that supports localized modes<sup>21</sup>. Band-edge mode

<sup>1</sup>Institut d'Electronique Fondamentale, Université Paris Sud and CNRS, UMR 8622, 91405 Orsay, France. <sup>2</sup>Laboratoire MPQ, Université Paris7 and CNRS, UMR 7162, 75013 Paris, France. <sup>3</sup>Cavendish Laboratory, University of Cambridge, Cambridge CB3 0HE, UK. <sup>4</sup>School of Electronic and Electrical Engineering, University of Leeds, Leeds LS2 9JT, UK.

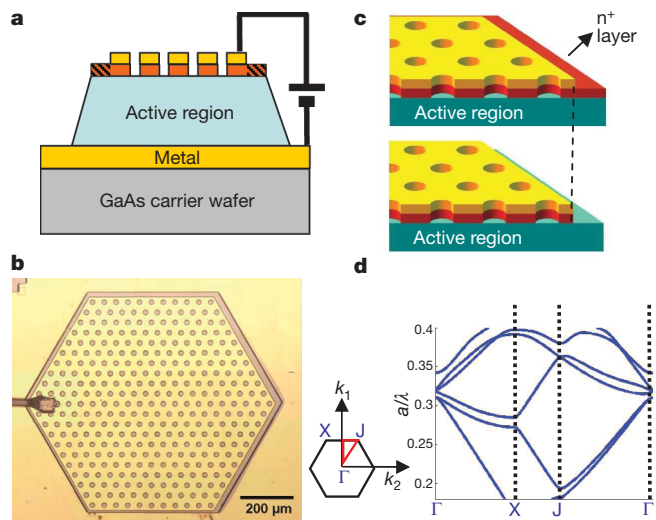


**Figure 1 | Device details and design.** **a**, Schematic cross-section of the device. The laser active region (blue) is sandwiched between two metal Ti/Au contact layers. The top metal is patterned with the desired photonic-crystal design. The top  $n^+$ -GaAs contact layer, approximately 200 nm thick (red) is removed in the photonic-crystal holes in order to reduce the losses. At the edge of the device, the  $n^+$ -GaAs layer (red hatched region) can be removed or left in place, if mirror or absorbing boundary conditions, respectively, need to be implemented. **b**, Optical microscope image of the surface of a typical device. The wire bonding is applied directly on the top metallization. **c**, Detailed scheme of the boundary conditions implementation technique. When the top  $n^+$  contact, represented as a red layer, is left in place between the metal edge and the mesa periphery (top panel), the absorption is high and the boundary behaves like an absorber. When instead it is removed (bottom panel), the mode mismatch at the metal edge introduces a high reflectivity, and therefore mirror boundary conditions. **d**, Transverse-magnetic photonic band structure (around the point  $\Gamma$ ) of the trigonal lattice used for the experiment, for  $r/a = 0.22$ . The calculation is fully 3D and therefore it does not require an effective index for the holes. The distribution of the electromagnetic field is calculated with a finite-element solver for a single lattice unit cell using Bloch-periodic boundary conditions.  $k_1$ ,  $k_2$  indicate axes in reciprocal space.

lasers instead operate in regions of energy–momentum space that have a high photonic density of states and a corresponding small group velocity<sup>22</sup>. We implemented the latter device architecture in order to take advantage of (1) the connected nature of the lattice that greatly simplifies the processing, and (2) the spatial delocalization of band-edge modes<sup>3</sup>, which allows for improved power extraction.

It is intuitively clear that the index contrast induced by the top metal patterning originates from the following effect: the guided mode sees two different effective indexes ( $n_{\text{eff}}$ ) as it propagates, the large  $n_{\text{eff}}$  of the guided surface-plasmon mode where the metal is left intact, and a lower  $n_{\text{eff}}$  corresponding to a more delocalized mode where the metal is removed<sup>18</sup>. However, the photonic-band structure of our devices cannot—in principle—be calculated within a 2D effective-index approximation, as this approach would not take into account the effect of the mode profile in the regions not covered by metal. Therefore we performed 3D photonic-band-structure calculations by solving the Helmholtz equation in a single unit cell of the triangular lattice of Fig. 1, with Bloch periodic boundary conditions applied in the plane. The resulting band structure (Fig. 1d) allows the appropriate photonic-crystal dimensions to be inferred in order to spectrally overlap the material gain with the regions of small group velocity.

We fabricated a series of devices with different photonic-lattice periods ( $a$ ) in order to target the band edge-states at the  $\Gamma$ -point, corresponding to  $a/\lambda = 0.33$ . We also fabricated devices with different  $r/a$  values (where  $r$  is the hole radius) for a fixed period  $a = 36.5 \mu\text{m}$  (including a control sample with unpatterned top metallization).

The boundary conditions represent the last crucial point that needs to be addressed for a correct device design. This issue is often overlooked for optically pumped devices<sup>3</sup>, as the photonic crystal is usually much larger than the laser excitation spot. Absorbing boundary conditions are therefore naturally implemented, owing to the photonic-crystal regions that are not optically pumped. The case of a current injection device is radically different, because in general the photonic crystal must have a finite size. For metal–metal waveguides in particular, it can be shown that the facet reflectivities are extremely high, as the waveguide thickness is much smaller than the lasing wavelength<sup>23</sup>.

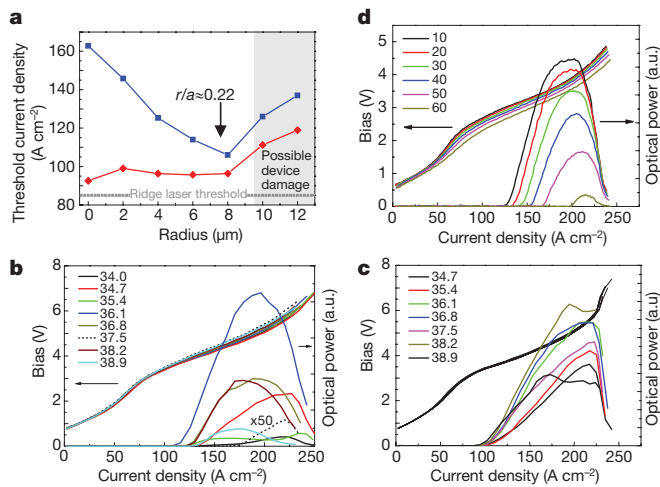
In order to tailor the reflectivity at the device boundary, in our photonic-crystal devices the hexagonal etched mesas are slightly larger than the top metallization. The 200-nm-thick top contact layer—which is removed in the photonic-crystal holes to reduce the losses—can be etched or left in place at the mesa periphery (hatched red region in Fig. 1a). If left in place (Fig. 1c, top panel), absorbing boundary conditions are obtained as the loss ( $\alpha$ ) introduced by the  $n^{++}$ -layer, when not metal-covered, is high ( $\alpha \approx 750 \text{ cm}^{-1}$ ). If instead it is removed (Fig. 1c, bottom panel), mirror boundary conditions are obtained, as exemplified in ref. 24 for micro-disk devices. In this case the losses are at least 50 times lower and equal to  $\sim 8 \text{ cm}^{-1}$ . Details are given in Supplementary Information. For each photonic-crystal design, pairs of devices have been fabricated: one with mirror boundaries (M) and one with absorbing boundaries (A). In the rest of the paper, these will be labelled as M devices and A devices, respectively.

Figure 2a reports the threshold current density ( $J_{\text{th}}$ ) for a set of M and A devices as a function of  $r$ , the hole radius of the photonic lattice, with a constant lattice spacing  $a = 36.5 \mu\text{m}$ . A markedly different behaviour can be observed for the two device families. All M devices lase at approximately the same  $J_{\text{th}}$ ,  $\sim 95 \pm 5 \text{ A cm}^{-2}$ , which is of the same order as what was obtained on metal–metal ridges fabricated from the same epitaxial material. On the contrary, the  $J_{\text{th}}$  of A devices strongly depends on the photonic-crystal characteristics:  $J_{\text{th}}$  is maximum for the ‘control’ sample ( $r = 0$ ) and decreases down to  $J_{\text{th}} \approx 110 \text{ A cm}^{-2}$  for  $r = 8 \mu\text{m}$  (the  $J_{\text{th}}$  increase for  $r \geq 10 \mu\text{m}$  is attributed to device damage when wire-bonding on the top metallization for large values of  $r/a$ ). These results offer an initial indication that different optical modes are active, depending on the applied boundary conditions. M devices, being unaffected by the photonic crystal (Fig. 2a), probably lase on whispering-gallery-like modes<sup>24,25</sup>, while devices with absorbing boundaries are our candidates for photonic-crystal lasing on delocalized band-edge states<sup>22</sup>. The spatial overlap between whispering-gallery-like and photonic-crystal modes is  $\sim 50\%$  (see Supplementary Information). Mode competition therefore causes mode selection, and the lasing mode is the one with the highest Q factor. When the  $n^+$  layer is removed, whispering-gallery-like modes have a high Q factor, and therefore reach lasing before the photonic-crystal modes. When the  $n^+$  layer is instead left in place, the Q factor of the whispering-gallery-like modes decreases by approximately a factor of two and the photonic-crystal modes are now favoured.

To elucidate the origin of lasing, we fabricated a second set of devices with several different photonic-lattice spacings  $a$ , and with  $r/a$  fixed at the most favourable value of 0.22. The values of  $a$  were chosen around  $a/\lambda = 0.33$ , to overlap the quantum cascade material gain peak with the band-edge states at point  $\Gamma$  (Fig. 1c). The corresponding light–current–voltage curves for A- and M-device families are shown in Fig. 2b and c, respectively. M devices exhibit identical  $J_{\text{th}}$ , confirming that they are unaffected by the photonic structure patterned on the top metal. In contrast, the  $J_{\text{th}}$  for the devices with absorbing boundary conditions depend on the lattice spacing, and they roughly follow the active material gain curve.

The clear demonstration that a photonic-crystal mode is active when absorbing boundary conditions are applied comes from the spectral analysis. Figure 3a shows the laser spectra of several M





**Figure 2 | Light-current-voltage characteristics and laser thresholds.** **a**, Threshold current density ( $T = 10$  K) as a function of the photonic-crystal hole radius ( $r$ ) and constant photonic-lattice spacing  $a = 36.5$  μm. Results for devices with absorbing (blue curve) and with mirror (red curve) boundary conditions are shown. A He-cooled Si bolometer was used for detection. **b**, **c**, Light-current-density and voltage-current-density curves as a function of  $a$  (shown in key in μm) for a different set of devices with fixed  $r/a = 0.22$ . The most favourable value of  $r/a$  has been chosen, based on the results reported in **a**. Devices with absorbing boundary conditions (A devices) are reported in **b**, while those with mirror boundary conditions (M devices) are shown in **c**. The A device with  $a = 37.5$  μm is probably damaged (dashed line in **b**), since its output power is 50 times reduced with respect to the others. The M devices exhibit identical  $J_{th}$ , confirming that they are unaffected by the photonic-structure patterned on the top metal, contrary to the A devices. The threshold densities are calculated as follows: when the  $n^+$  layer is present, the whole disk surface is employed, and when the  $n^+$  layer is missing, the metal contact surface only is employed, since the top  $n^+$  layer is responsible for current spreading. Data in **b** and **c** justify this choice *a posteriori*: the voltage-current characteristics plotted in current-density perfectly overlap for the whole set of devices. **d**, Light-current-voltage characteristics (20-kHz repetition rate, 300-ns pulse width) as a function of temperature (shown in key in K) for a typical photonic-crystal (A) device. The maximum operating temperature ( $T_{max}$ ) is 62 K, just 15 K lower than standard ridge waveguides fabricated from the same material.  $T_{max}$  in continuous wave is 44 K (data not shown).

devices as a function of the photonic-lattice spacing. The emission is multimode, and no clear trend with the photonic-crystal characteristic is observed. In contrast, when absorbing boundary conditions are implemented on identical devices, the spectra dramatically clean up (Fig. 3b): almost all the devices become single mode, and the emission is lithographically tuned between 2.55 THz and 2.88 THz ( $\lambda \approx 104 \rightarrow 118$  μm). Single-mode devices show a sideband suppression ratio of more than 30 dB (Fig. 3c), and the typical maximum operating temperature is 60 K (Fig. 2d). These characteristics, together with the continuous-wave operation data (not shown) prove that this technology is viable for applications.

We have established that controlling the boundary conditions allows the device to be operated on the desired mode. We will now show the effect of this mode selection on the far-field emission patterns. Figure 4b–h reports several experimental far fields obtained by scanning a Golay cell detector at constant distance from the lasers (Fig. 4a defines the angles of scanning). Figure 4b shows the results for a control device: the emission is non-directional, as expected since no top-metal patterning is present. Figure 4c and d refers instead to two different photonic-crystal devices with mirror boundary conditions. The emission is non-directional in these cases also, and several hot spots are present. These devices exhibit the same problems, typical of standard metal-metal waveguides<sup>4</sup>. When absorbing boundary conditions are introduced, the far fields dramatically localize in the angular domain (Fig. 4e–h). The angular patterns are mostly bi-lobed, with

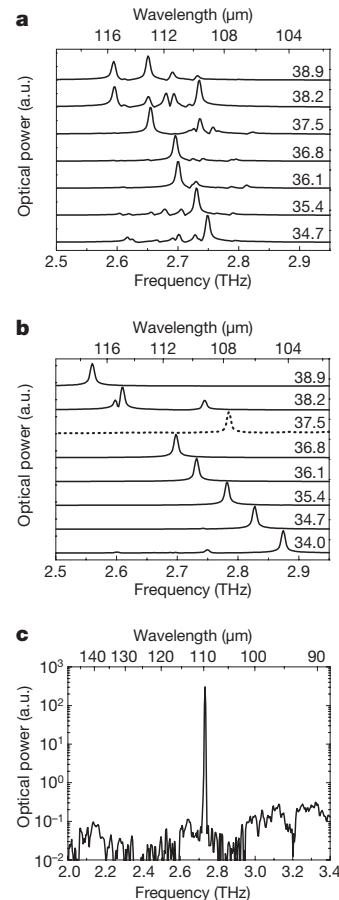


**Figure 3 | Spectral characterizations.** Laser output spectra for several devices with different photonic-lattice periods,  $a$  (shown next to the spectra, in μm). **a**, Devices with mirror boundary conditions; **b**, identical devices with absorbing boundary conditions. In the first case the emission is multimode, while in the second case the spectra clean up, become mostly single-mode, and exhibit a clear frequency shift with  $a$ . The device with  $a = 37.5$  μm in **b** is anomalous, and is probably damaged; its output power is in fact 50 times less than the others (see dashed curve in Fig. 2b). The spectra were acquired in rapid scan mode with a resolution of  $0.125$  cm<sup>-1</sup> using a Bruker IFS66 FTIR and a He-cooled Si-bolometer detector. **c**, Typical single-mode spectrum of a photonic-crystal (A) device with  $a = 36.1$  μm, on a log-linear scale. A side-mode suppression ratio of at least 30 dB is obtained.

one lobe typically dominant. Each lobe is angularly very narrow,  $\leq 10^\circ$ , evidence that the laser mode is spatially more delocalized.

To elucidate the role of the wire bonding (applied directly to the device surface), we performed a series of tests. Figure 4e and f correspond to the same device, bonded first on the periphery (Fig. 4e), then re-bonded in the centre (Fig. 4f). The far fields are very similar, proving that the bonding is not directly involved in the surface emission process. Figure 4g and h corresponds instead to two different devices, wire-bonded in the centre and on all the resonator corners, respectively. The latter device exhibits a single, angularly extremely narrow lobe at ( $\varphi \approx 10^\circ$ ,  $\theta \approx -10^\circ$ ). The former device shows instead a multi-lobed emission, with two dominant lobes, allowing us to propose a hypothesis to explain the device behaviour. The far-field emission pattern is multi-lobed, as observed in band-edge lasers operating at shorter wavelengths<sup>11</sup>, but the position of the metallic wire-bondings—and possible device imperfections—affects the slowly varying components of the device near field. As shown in ref. 26, minute modifications of a photonic-crystal device near-field can yield important far-field changes. As a result of the bonding, the symmetry is broken and one—or more—lobe is enhanced or suppressed. A full understanding of the laser near-field requires 3D finite-difference time-domain (FDTD) simulations which are beyond the

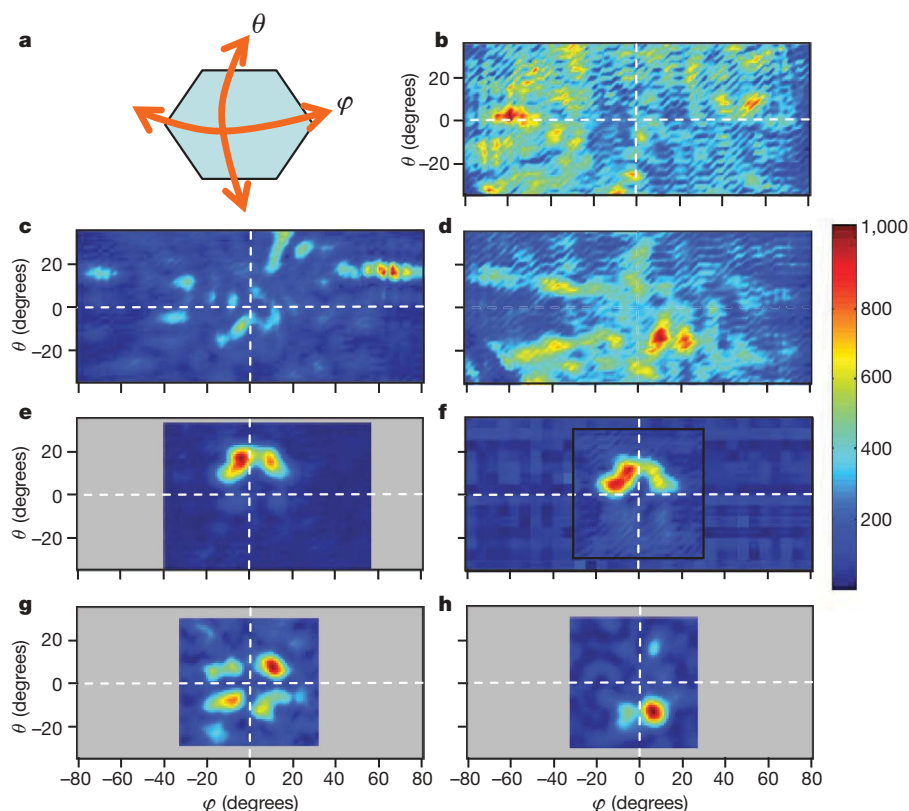


**Figure 4 | Far-field characterizations.** Far-field emission patterns of several devices, obtained by scanning a Golay cell at a distance of 6 cm or 13 cm from the surface of the device. A pinhole of 2 mm in diameter was used to partially shield the detector active element. **a**, Device position and definitions of the angles  $\varphi$  and  $\theta$ . **b**, Far field of a 'control' device, that is, a cavity with no holes in the top metallization and mirror boundary conditions. The emission is non-directional, and it extends up to very large angles of  $\sim 80^\circ$ . **c**, Far field of a device with mirror boundary conditions (an M device), with  $a = 36.8 \mu\text{m}$  and  $r/a = 0.22$ . (See Fig. 3a for the emission spectrum of this device.) The emission is not directional, and a hot spot is present at a very large  $\varphi$  value of  $\sim 80^\circ$ . We believe it might originate from a mesa facet. **d**, Far field of another M device, with  $a = 35.4 \mu\text{m}$  and  $r/a = 0.22$ . (See Fig. 3a for the spectrum of this device.) The emission is highly non-directional, with several hot spots distributed in a very wide angular range. **e**, Far field of a device with absorbing boundary conditions (an A device), with  $a = 35.4 \mu\text{m}$  and  $r/a = 0.22$  (Fig. 3b for the spectrum of this device). Compared with the M devices, the emission dramatically cleans up. It becomes highly directional, with two lobes concentrated in a narrow angular range ( $\pm 10^\circ$ ). The bonding

wire is in this case applied to the top left edge of the device. **f**, Far field of the same device shown in **e**, after the bonding wire is removed from the edge and re-applied in the centre of the device. The far-field is very similar to **e**, suggesting that the bonding is not directly involved in the emission process. The black continuous line marks the region that has been scanned at higher angular resolution. **g**, Far field of an A device, with  $a = 35.4 \mu\text{m}$  and  $r/a = 0.22$  (Fig. 3b for the spectrum of this device), and bonding wire applied in the centre of the device. The emission exhibits four lobes (two of them dominant with respect to the others), within an angular range of  $\sim 20^\circ \times 30^\circ$ . **h**, Far field of another A device, with  $a = 36.1 \mu\text{m}$  and  $r/a = 0.22$  (Fig. 3b for the spectrum of this device), and bonding wires applied at all the six edges of the hexagon. These measurements show that (1) when absorbing boundary conditions are implemented, the system lases on a delocalized photonic-crystal mode, and as a consequence the emission far-field pattern localizes in the angular domain; and (2) the bonding wires are not direct emission sources, rather their presence affects the slowly varying components of the device near field, thus enhancing/suppressing some of the lobes.

scope of this paper. However, initial very encouraging results based on 2D FDTD simulations are reported in the Supplementary Information. With new, better fabricated and more powerful devices, we obtain in fact an unambiguous identification of lasing on the hexapolar and monopolar  $\Gamma$ -point band-edge states (data shown in Supplementary Information).

In conclusion, we have shown that boundary conditions are a key parameter for the effective design and implementation of active, electrically injected photonic devices. The application of this idea to a class of semiconductor THz lasers where the photonic-crystal structure has been 'written' in the top metallization layer yielded lithographically tunable, single-mode operation and—simultaneously—angularly narrow surface emission. The addition of these functionalities comes at almost no detriment to the overall device performance. This demonstration represents an important step in the development of photonic-crystal micro-cavity lasers for practical applications. The remaining issues, namely the increase in output power and full control of the emission far field, can be addressed by using a thin top metallization layer<sup>27</sup>, and by using more advanced photonic-crystal designs, such as graded photonic structures<sup>28</sup>. Finally, a similar approach could

be used to explore systems not only in the weak-coupling regime (lasing), but also active devices in the strong-coupling regime (inter-subband polaritons)<sup>29</sup>. In the THz range particularly, where a novel ultrastrong-coupling regime is expected to arise<sup>30</sup>, the possibility of accurately tuning the frequency position of the photonic-crystal cavity resonance is a valuable experimental tool.

Received 29 March; accepted 5 November 2008.

1. Yablonovitch, E. Inhibited spontaneous emission in solid-state physics and electronics. *Phys. Rev. Lett.* **58**, 2059–2062 (1987).
2. Sajeev, J. Strong localization of photons in certain disordered dielectric superlattices. *Phys. Rev. Lett.* **58**, 2486–2489 (1987).
3. Letarte, X., Monat, C., Seassal, C. & Viktorovitch, P. Analytical modeling and an experimental investigation of two-dimensional photonic crystal microlasers: Defect state (microcavity) versus band-edge state (distributed feedback) structures. *J. Opt. Soc. Am. B* **22**, 2581–2595 (2005).
4. Adam, A. J. L. et al. Beam pattern of terahertz quantum cascade lasers with subwavelength cavity dimensions. *Appl. Phys. Lett.* **88**, 151105 (2006).
5. Sakai, K. *Terahertz Optoelectronics* (Topics in Applied Physics, Vol. 97, Springer, 2005).
6. Mittleman, D. *Sensing with Terahertz Radiation* (Springer Series in Optical Sciences, Vol. 85, Springer, 2004).



7. Kohler, R. *et al.* Terahertz semiconductor-heterostructure laser. *Nature* **417**, 156–159 (2002).
8. Williams, B. S. Terahertz quantum-cascade lasers. *Nature Photon.* **1**, 517–525 (2007).
9. Sirtori, C. *et al.* Long-wavelength ( $\lambda = 8\text{--}11.5\ \mu\text{m}$ ) semiconductor lasers with waveguides based on surface plasmons. *Opt. Lett.* **23**, 1366–1368 (1998).
10. Unterrainer, K. *et al.* Quantum cascade lasers with double metal-semiconductor waveguide resonators. *Appl. Phys. Lett.* **80**, 3060–3062 (2002).
11. Colombelli, R. *et al.* Quantum cascade surface-emitting photonic crystal laser. *Science* **302**, 1374–1377 (2003).
12. Scharfner, S. *et al.* Band structure mapping of photonic crystal intersubband detectors. *Appl. Phys. Lett.* **89**, 151107 (2006).
13. Dunbar, L. A. *et al.* Design, fabrication and optical characterization of quantum cascade lasers at terahertz frequencies using photonic crystal reflectors. *Opt. Express* **13**, 8960–8968 (2005).
14. Zhang, H., Dunbar, A., Scalari, G., Houdré, R. & Faist, J. Terahertz photonic crystal quantum cascade lasers. *Opt. Express* **15**, 16818–16827 (2007).
15. Mahler, L. *et al.* High-performance operation of single-mode terahertz quantum cascade lasers with metallic gratings. *Appl. Phys. Lett.* **87**, 181101 (2005).
16. Kumar, S., Williams, B. S., Qin, Q., Lee, A. W. M. & Hu, Q. Surface-emitting distributed feedback terahertz quantum-cascade lasers in metal-metal waveguides. *Opt. Express* **15**, 113–128 (2007).
17. Yu, N. *et al.* Small-divergence semiconductor lasers by plasmonic collimation. *Nature Photon.* **2**, 564–570 (2008).
18. Bahriz, M., Moreau, V., Colombelli, R., Crisafulli, O. & Painter, O. Design of mid-IR and THz quantum cascade laser cavities with complete TM photonic bandgap. *Opt. Express* **15**, 5948–5965 (2007).
19. Sirigu, L. *et al.* Terahertz quantum cascade lasers based on two-dimensional photonic crystal resonators. *Opt. Express* **16**, 5206–5217 (2008).
20. Barbieri, S. *et al.* 2.9 THz quantum cascade lasers operating up to 70 K in continuous wave. *Appl. Phys. Lett.* **85**, 1674–1676 (2004).
21. Painter, O. *et al.* Two-dimensional photonic band-gap defect mode laser. *Science* **284**, 1819–1821 (1999).
22. Sakai, K., Miyai, E. & Noda, S. Two dimensional coupled wave theory for square-lattice photonic-crystal lasers with TM-polarization. *Opt. Express* **15**, 3981–3990 (2007).
23. Kohen, S., Williams, B. S. & Hu, Q. Electromagnetic modeling of terahertz quantum cascade laser waveguides and resonators. *J. Appl. Phys.* **97**, 053106 (2005).
24. Chassagneux, Y. *et al.* Terahertz microcavity lasers with subwavelength mode volumes and thresholds in the milliamper range. *Appl. Phys. Lett.* **90**, 091113 (2007).
25. Wiersig, J. Hexagonal dielectric resonators and microcrystal lasers. *Phys. Rev. A* **67**, 023807 (2003).
26. Kim, S.-H., Kim, S.-K. & Lee, Y.-H. Vertical beaming of wavelength-scale photonic crystal resonators. *Phys. Rev. B* **73**, 235117 (2006).
27. Vuckovic, J., Loncar, M. & Scherer, A. Surface plasmon enhanced light-emitting diode. *IEEE J. Quant. Electron.* **36**, 1131–1144 (2000).
28. Srinivasan, K. & Painter, O. Momentum space design of high-Q photonic crystal optical cavities. *Opt. Express* **10**, 670–684 (2002).
29. Colombelli, R., Ciuti, C., Chassagneux, Y. & Sirtori, C. Quantum cascade intersubband polariton light emitters. *Semicond. Sci. Technol.* **20**, 985–990 (2005).
30. Ciuti, C. & Carusotto, I. On the ultrastrong vacuum Rabi coupling of an intersubband transition in a semiconductor microcavity. *J. Appl. Phys.* **101**, 081709 (2007).

**Supplementary Information** is linked to the online version of the paper at [www.nature.com/nature](http://www.nature.com/nature).

**Acknowledgements** We thank J.-M. Lourtioz, F. Julien, C. Sirtori, L. Sirigu, G. Scalari and V. Moreau for discussions, P. Gellie for technical help, and J. Alton for the Golay cell. Device fabrication was performed at the CTU-IEF-Minerve, which was partially funded by the Conseil Général de l'Essonne. This work was conducted as part of a EURYI scheme award ([www.esf.org/euryi](http://www.esf.org/euryi)).

**Author Information** Reprints and permissions information is available at [www.nature.com/reprints](http://www.nature.com/reprints). Correspondence and requests for materials should be addressed to R.C. ([raffaele.colombelli@u-psud.fr](mailto:raffaele.colombelli@u-psud.fr)).

# Early formation of evolved asteroidal crust

James M. D. Day<sup>1</sup>, Richard D. Ash<sup>1</sup>, Yang Liu<sup>2</sup>, Jeremy J. Bellucci<sup>1</sup>, Douglas Rumble III<sup>3</sup>, William F. McDonough<sup>1</sup>, Richard J. Walker<sup>1</sup> & Lawrence A. Taylor<sup>2</sup>

Mechanisms for the formation of crust on planetary bodies remain poorly understood<sup>1</sup>. It is generally accepted that Earth's andesitic continental crust is the product of plate tectonics<sup>1,2</sup>, whereas the Moon acquired its feldspar-rich crust by way of plagioclase flotation in a magma ocean<sup>3,4</sup>. Basaltic meteorites provide evidence that, like the terrestrial planets, some asteroids generated crust and underwent large-scale differentiation processes<sup>5</sup>. Until now, however, no evolved felsic asteroidal crust has been sampled or observed. Here we report age and compositional data for the newly discovered, paired and differentiated meteorites Graves Nunatak (GRA) 06128 and GRA 06129. These meteorites are feldspar-rich, with andesite bulk compositions. Their age of  $4.52 \pm 0.06$  Gyr demonstrates formation early in Solar System history. The isotopic and elemental compositions, degree of metamorphic re-equilibration and sulphide-rich nature of the meteorites are most consistent with an origin as partial melts from a volatile-rich, oxidized asteroid. GRA 06128 and 06129 are the result of a newly recognized style of evolved crust formation, bearing witness to incomplete differentiation of their parent asteroid and to previously unrecognized diversity of early-formed materials in the Solar System.

Formation of crust, the outermost solid shell of a planet, is a fundamental process and its chemical nature is a reflection of the formation, differentiation and cooling history of its parent body. Thus, documenting causes of lithological diversity in crustal materials is critical for understanding early Solar System processes and planetary evolution. Knowledge regarding initial formation of planetary crust is largely based on data gleaned from the oldest preserved crustal rock and mineral remnants from Earth ( $<4.4$  Gyr; refs 6, 7), the Moon ( $\sim 4.4$  Gyr; ref. 8), Mars ( $>4.0$  Gyr; ref. 9) and achondrite meteorites ( $\leq 4.56$  Gyr; ref. 10). These materials record crustal formation processes that were demonstrably diverse among these bodies.

GRA 06128 and 06129 (hereafter referred to as GRA 06128/9) are paired achondritic meteorites recovered from the same Antarctic ice-field. The meteorites consist largely of sodium-rich plagioclase ( $>75\%$ ), with olivine, two pyroxenes, phosphates and sulphides. They have andesite to trachy-andesite bulk compositions (Fig. 1a; see Methods and Supplementary Information). Major- and trace-element compositions of silicate minerals are uniform within and between the two meteorites. Minerals are compositionally unzoned and major silicate phases have variable ranges of grain size (diameter  $<0.1$  to  $>0.5$  mm). Co-existing augite and orthopyroxene yield equilibration temperatures of  $\sim 800^\circ\text{C}$ . Oligoclase crystals have large positive Eu anomalies, and merrillite and chlorapatite have elevated rare-earth element (REE) abundances, relative to other minerals in the meteorites. Consequently, the estimated bulk REE composition of GRA 06128/9, determined by modal recombination, is dominated by feldspar for Eu and phosphates for the other REEs (Fig. 1b). The meteorites are enriched to only moderately depleted in volatile elements (for example

K, Na, S, Rb, Cl, Pb) relative to chondrites, and were formed at an oxygen fugacity close to the iron-wüstite +2 buffer (ref. 11).

Although GRA 06128/9 had an igneous origin, they have also been thermally metamorphosed and partially brecciated. Both meteorites possess granoblastic textures,  $120^\circ$  triple junctions between coexisting silicates, polysynthetic twinning in plagioclase and pentlandite-troilite exsolution from a monosulphide solid solution. These features are consistent with slow cooling and partial re-equilibration. Using pyroxene exsolution lamellae, it has been estimated that GRA 06128/9 formed close to the surface (at depths of 15–20 m) of their

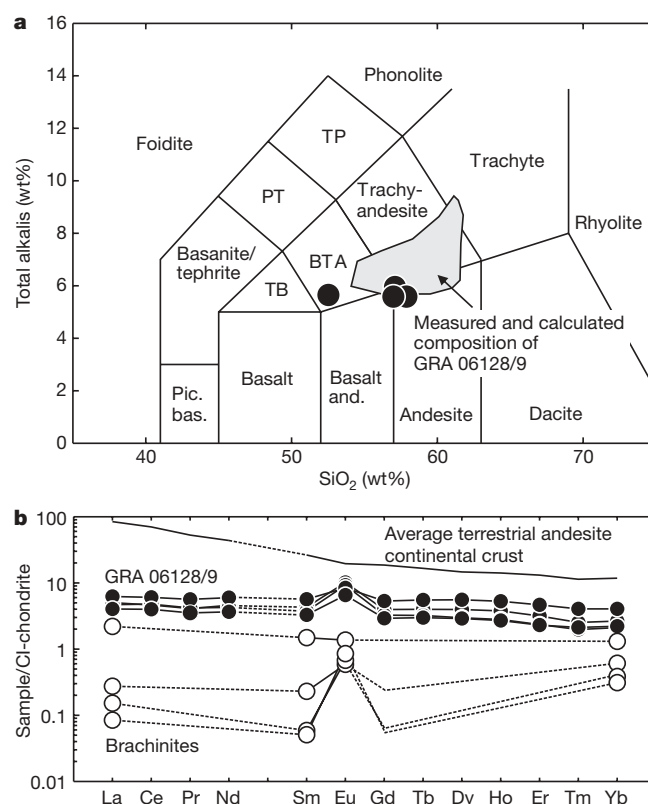


**Figure 1 | Bulk composition of the GRA 06128/9 achondrite meteorites.** **a**, Plot of total alkalis ( $\text{Na}_2\text{O}$  and  $\text{K}_2\text{O}$ ) versus silica, showing multiple measurements (filled circles) and calculated compositions (grey area) of the GRA 06128/9 achondrite meteorites. Calculated compositions are based on the variability in modal mineralogy and mineral major element compositions (Supplementary Information). Abbreviations: TP, trachy-phonolite; PT, phono-tephrite; TB, trachy-basalt; BTA, basaltic trachy-andesite; Pic. bas., picro-basalt; Basalt and., basaltic andesite. **b**, Measured REE patterns for the GRA 06128/9 meteorites. Shown are data for the average terrestrial continental crust<sup>1</sup> and for the brachinites, Brachina, ALH 84025 and EET 99402/407 (ref. 26).

<sup>1</sup>Department of Geology, University of Maryland, College Park, Maryland 20742, USA. <sup>2</sup>Department of Earth and Planetary Sciences, Planetary Geosciences Institute, University of Tennessee, Knoxville, Tennessee 37996, USA. <sup>3</sup>Geophysical Laboratory, Carnegie Institution for Science, Washington DC 20015, USA.



**Table 1 | Three oxygen isotope data for GRA 06128 and GRA 06129**

Sample, specific number	$\delta^{17}\text{O}$ (‰)	$\delta^{18}\text{O}$ (‰)	$\Delta^{17}\text{O}$ (‰)
GRA 06128, 22	2.457	5.052	−0.200
GRA 06128, 22	2.330	4.822	−0.207
GRA 06128 average	$2.394 \pm 0.090$	$4.937 \pm 0.162$	$-0.204 \pm 0.005$
GRA 06129, 9	2.421	4.968	−0.192
GRA 06129, 9	2.334	4.777	−0.179
GRA 06129 average	$2.378 \pm 0.062$	$4.873 \pm 0.135$	$-0.186 \pm 0.009$

parent body<sup>12</sup>. This conclusion is consistent with an origin as evolved crustal material.

Oxygen isotopes (as  $\Delta^{17}\text{O}$  values) provide a means to genetically link Solar System materials (ref. 13;  $\Delta^{17}\text{O}$  notation is defined in Methods). The  $\Delta^{17}\text{O}$  values for multiple pieces of GRA 06128/9 average  $-0.195 \pm 0.012\text{‰}$  (Fig. 2; Table 1). This isotopic composition is different from most known differentiated bodies, including the Earth, Moon and Mars.

The mean  $^{207}\text{Pb}$ – $^{206}\text{Pb}$  age determined for chlorapatite in GRA 06128/9 is  $4.517 \pm 0.060$  Gyr (2 $\sigma$ ; Supplementary Methods). The mean age for merrillite crystals is identical within the greater uncertainty. Since  $^{207}\text{Pb}$ – $^{206}\text{Pb}$  ages reflect the time of cessation of Pb diffusion (ref. 14), the measured phosphate ages probably reflect closure temperatures subsequent to the metamorphic event recorded from pyroxene thermometry ( $\leq 800^\circ\text{C}$ ). Assuming that diffusion characteristics are similar to those of terrestrial phosphates, the closure temperature of Pb in merrillite and chlorapatite in GRA 06128/9 is  $\sim 500^\circ\text{C}$  (ref. 14). Thus, the phosphate age of GRA 06128/9 demonstrates that crystallization, thermal metamorphism and cooling below  $500^\circ\text{C}$  occurred within  $\sim 100$  Myr of the formation of the Solar System at  $\sim 4.567$  Gyr ago<sup>15</sup>. These ages can be used to argue against an origin on any major planetary body, including Venus or Mercury. The average age of the crust on Venus is estimated to be  $< 1$  Gyr (ref. 16), and present knowledge of Mercury suggests it is highly reduced, with a crust that is younger than 4.4 Gyr (ref. 17).

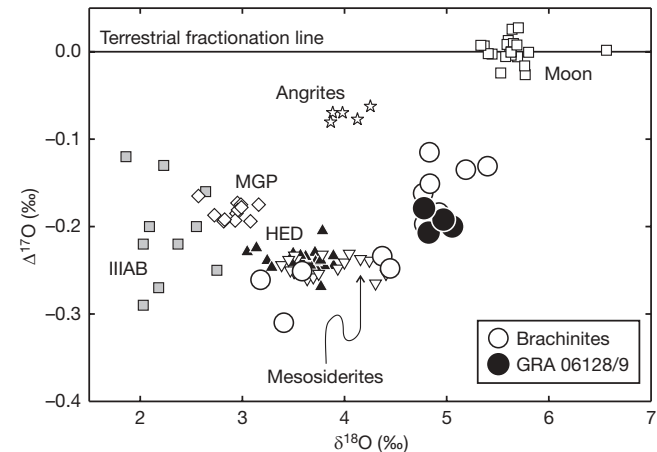


**Figure 2 |  $\delta^{18}\text{O}$ – $\Delta^{17}\text{O}$  plot for GRA 06128/9 versus achondrite meteorites and lunar and terrestrial materials.** MGP, main group pallasites (open diamonds); IIIAB, IIIAB iron meteorites (filled grey squares); HED, howardite-eucrite-diogenite meteorites (filled triangles). The GRA 06128/9 meteorites have oxygen isotope compositions most similar to brachinites. Published data are from refs 5, 32 and references therein. Error bars for data are smaller than symbols.

Taken with the oxygen isotope evidence, we conclude that GRA 06128/9 originated on an asteroid.

Owing to their tendency to strongly partition into metal relative to silicate, the highly siderophile elements (HSE; including Re, Os, Ir, Ru, Pt and Pd) are important recorders of primary planetary differentiation. Concentrations of the HSE in bulk samples of GRA 06128/9 are elevated, in some cases within a factor of two or three of chondritic abundances (Table 2; Fig. 3). These results demonstrate that a metallic core had not segregated before generation of the GRA 06128/9 parental melts. Some of the HSE are fractionated relative to one another in GRA 06128/9. These fractionated HSE compositions could not have been incorporated into the rock via the impact of any known chondritic or metal-rich meteorite material. Nor can they be explained through terrestrial weathering processes. Although the meteorites are weathered (Supplementary Information), laser ablation inductively coupled plasma-mass spectrometry analysis of unaltered sulphides and FeNi metal in the meteorites reveals that the HSE are hosted almost entirely within these primary magmatic phases (Fig. 3). Furthermore, the calculated initial  $^{187}\text{Os}/^{188}\text{Os}$  ratio for the GRA 06128/9 meteorites ( $0.096 \pm 0.001$ ) is within error of the initial Solar System value, inconsistent with disturbance of the  $^{187}\text{Re}$ – $^{187}\text{Os}$  system and consistent with formation via early partial melting of an undifferentiated parent body.

The formation mechanism for GRA 06128/9 was evidently unique among known achondrites. Plagioclase-rich lunar ferroan anorthosites are considered to represent flotation cumulates from a large-scale magma ocean melting event<sup>3,4</sup>. The elevated abundances of the HSE, however, argue against this mode of origin for the GRA 06128/9 meteorites, as  $> 50\%$  melting of the silicate fraction of an asteroid would lead to formation of a gravitationally separated metal–liquid core (ref. 18). Consequently, large-scale differentiation leads to marked depletion of HSE in the silicate portion of the body. For example, lunar and terrestrial crustal rocks respectively contain less than  $\sim 0.02 \text{ ng g}^{-1}$  and  $\sim 0.04 \text{ ng g}^{-1}$  Os (refs 1, 19), as compared with  $\sim 200 \text{ ng g}^{-1}$  Os for GRA 06128/9. Furthermore, HED meteorites, which are considered to derive from the asteroid 4 Vesta (mean diameter  $\sim 530$  km) and are probably the result of a large-scale magma ocean melting event<sup>5</sup>, also have very low abundances of the HSE<sup>20</sup>—compositions at odds with those of GRA 06128/9.

It has been demonstrated that quartz-normative andesite compositions like that of GRA 06128/9 can be generated by partial melting of volatile-rich chondritic precursors (see, for example, ref. 21). These studies have shown that partial melting of an olivine-rich lithology in the forsterite-anorthite-quartz system occurs at the peritectic point, resulting in a melt that contains  $> 50\%$  plagioclase<sup>22</sup>. Furthermore, Na-rich compositions lower liquidus temperatures by up to  $100^\circ\text{C}$  and shift the initial melt compositions to even higher abundances of feldspar<sup>23,24</sup>. These experimental constraints, together with the major-, trace-element and mineralogical data for GRA 06128/9, indicate that they most probably crystallized from magma generated by partial melting of a primitive chondritic source.

The formation of GRA 06128/9 by partial melting and melt segregation of a largely undifferentiated body implies the possibility of a complementary ultramafic residue or cumulate. There are numerous mafic and ultramafic achondrite meteorites in the terrestrial collection, of which the brachinites possess the most complementary characteristics to the GRA 06128/9 meteorites, including overlapping  $\Delta^{17}\text{O}$  values (Fig. 2; ref. 25). The significant O isotope variability present in brachinites ( $\Delta^{17}\text{O} = -0.15$  to  $-0.31\text{‰}$ ) has been attributed to partial or incomplete melting of their primitive

**Table 2 | Whole-rock highly siderophile element data with initial Os isotopic compositions at 4.52 Gyr**

Sample	Specific number	Mass (g)	Os (p.p.b.)	Ir (p.p.b.)	Ru (p.p.b.)	Pt (p.p.b.)	Pd (p.p.b.)	Re (p.p.b.)	$^{187}\text{Os}/^{188}\text{Os}_m$	2s.e.	$^{187}\text{Re}/^{188}\text{Os}$	2s.e.	$^{187}\text{Os}/^{188}\text{Os}_i$	2s.e.
GRA 06128	22	0.21	175.1	78.58	301.4	125.9	53.55	16.06	0.13100	0.00009	0.442	0.007	0.0964	0.0015
GRA 06129	9	0.26	265.0	95.56	378.1	143.0	54.93	24.30	0.13117	0.00005	0.442	0.007	0.0966	0.0015
Brachina	USNM 535L	0.06	156.0	142.6	228.9	110.6	67.45	10.12	0.12041	0.00014	0.312	0.005	0.0960	0.0011

m, measured; i, initial; s.e., standard error.

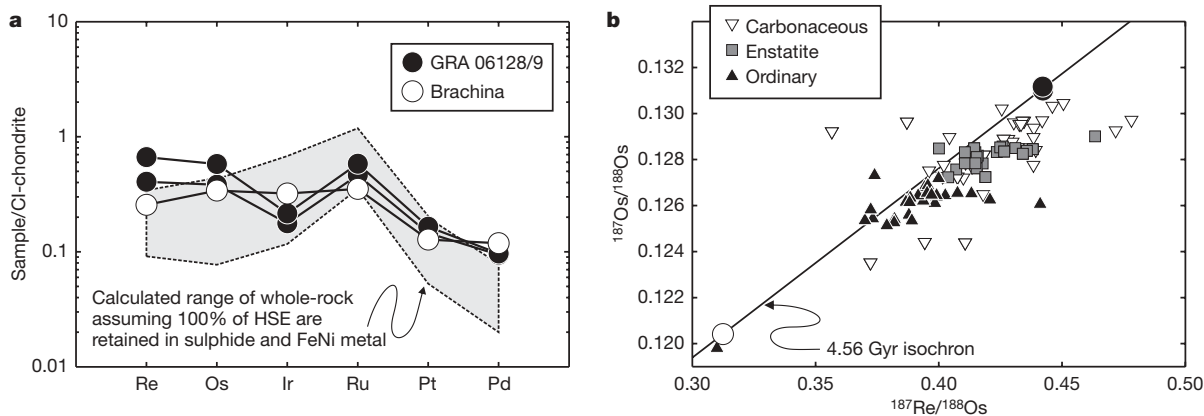


**Figure 3 | Highly siderophile element and Re–Os isotope systematics of GRA 06128/9 and Brachina.** **a**, Measured HSE patterns for GRA 06128/9 and Brachina showing significant fractionation of Ir, Pt and Pd from Re, Os and Ru in the meteorites relative to CI chondrite (Orgueil). Also shown is the calculated whole-rock compositional field (shaded) for GRA 06128/9 using measured modal abundances and HSE compositions of pentlandite/FeNi metal and FeS in the meteorites (Supplementary Information). These calculated estimates are in broad agreement with measured whole-rock values, indicating that HSE are dominantly hosted within sulphide and FeNi

metal. **b**,  $^{187}\text{Re}/^{188}\text{Os}$ – $^{187}\text{Os}/^{188}\text{Os}$  diagram for GRA 06128/9 and Brachina versus chondritic meteorites. GRA 06128/9 plot to elevated values relative to all chondrite groups in  $^{187}\text{Re}/^{188}\text{Os}$ – $^{187}\text{Os}/^{188}\text{Os}$  space. Brachina (open circle) has present-day sub-chondritic  $^{187}\text{Os}/^{188}\text{Os}$ . GRA 06128/9 (filled circles) and Brachina plot along a  $\sim 4.56$  Gyr isochron, with an  $^{187}\text{Os}/^{188}\text{Os}$  value close to the Solar System initial value, which passes through the field of chondritic meteorite data. Normalization and chondrite data are from ref. 33. Error bars for GRA 06128/9 and Brachina data are smaller than symbols.

parent body<sup>26,27</sup>, consistent with the projected parent body for GRA 06128/9. Further, Brachina (the ‘type’ for brachinites) has fractionated HSE, sub-chondritic measured  $^{187}\text{Os}/^{188}\text{Os}$  (0.1204; versus 0.1311 for GRA 06128/9) and a depleted REE pattern, features that are complementary if brachinites represent melt residues to the GRA 06128/9 meteorites (Figs 1 and 3). These characteristics are consistent with an origin as rocks that did not experience metal–silicate equilibration, but underwent partial melting processes broadly complementary to those required for GRA 06128/9. All of these characteristics provide possible evidence that GRA 06128/9 are either genetically related to the brachinites or derive from a parent body with a similar melting history.

Fractionation of the HSE in GRA 06128/9 can be potentially explained by sulphide segregation. The HSE can be fractionated via removal of a sulphide melt from a crystalline monosulphide solid solution in the terrestrial mantle<sup>28</sup>. Similar styles of fractionation of the HSE between GRA 06128/9 and terrestrial ores may implicate this type of process as acting during generation of the GRA 06128/9 parental melts (see Supplementary Discussion).

It has been previously demonstrated that melting and metamorphism of asteroid parent bodies were unlikely to have occurred through impact-related heating, which has been shown to be a highly inefficient process<sup>29</sup>. This conclusion is supported by the lack of evidence for significant impactor contributions to the HSE inventories of the GRA 06128/9 meteorites; energy released from initial accretion of the parent body, or through decay of short-lived radionuclides (for example,  $^{26}\text{Al}$ ), represent more viable heat sources. Constraints on the size of the parent body of the GRA 06128/9 meteorites can only be loosely applied. On asteroids  $<100$  km in radius, it is likely that volatile-rich, low-density melts such as GRA 06128/9 would exceed escape velocities through explosive pyroclastic volcanism and be lost to space<sup>30</sup>. Thus, GRA 06128/9 could have originated either via extrusion from a large ( $>100$  km radius) asteroid or emplaced intrusively on a body of undetermined size.

Remote sensing of asteroids shows that, where detected, the preponderance of crust is basaltic. This is also true for the terrestrial planets and the asteroid 4 Vesta. Feldspar-rich crust is not uncommon, with the Moon’s crust and Earth’s continental crust being feldspar-rich. Feldspar does not have a strong spectral wavelength absorption in the near-infrared, but its high albedo is a diagnostic feature, and a number of E-type asteroids have been detected in the asteroid belt with this characteristic<sup>31</sup>. These asteroids may also have a

significant sulphide component<sup>31</sup>. The presence of E-type asteroids implies that evolved crust may be extensive on some of these bodies. So far, however, only one planet has been found to have a major andesite crust component, namely Earth. It has been argued that, to generate andesite crust, a significant volatile component is required in the mantle of the parent body<sup>2</sup>. On Earth, this is achieved through recycling of water into subduction zones<sup>1</sup>. The GRA 06128/9 meteorites require early partial melting of primitive, volatile-rich source regions in an asteroidal body that did not suffer extensive planetary differentiation, and thus point to an entirely new mode of generation of andesite crust compositions.

## METHODS SUMMARY

For mineralogical characterization we used an SX50 electron microprobe and New Wave Research UP213 (213 nm) laser-ablation (LA) system coupled to a ThermoFinnigan Element 2 inductively coupled plasma-mass spectrometer (ICP-MS).  $^{207}\text{Pb}$ – $^{206}\text{Pb}$  ages were obtained via LA-ICP-MS and were corrected for mass fractionation using an exponential fractionation law by means of bracketing the phosphate analyses with standard reference materials (SRMs: NIST 610, NIST 612, BCR-2g). Ratios of  $^{207}\text{Pb}/^{206}\text{Pb}$  for each SRM were used to calculate the fractionation factor ( $\alpha$ ). Differences in  $\alpha$  between the three SRMs had a negligible effect on calculated ages. Os isotopic and platinum-group elemental abundance measurements were made using isotope dilution and solvent extraction/anion exchange purification methodologies. Os isotopes and concentrations were measured via thermal ionization mass spectrometry, and Ir, Ru, Pt, Pd and Re abundances were measured using solution ICP-MS. Oxygen isotope analysis was performed via laser fluorination of pre-leached powder whole-rock aliquots stripped of magnetic minerals. Standardization of delta values was achieved by comparison with the Gore Mountain garnet standard, USNM 107144, analysed during every analytical session.

**Full Methods** and any associated references are available in the online version of the paper at [www.nature.com/nature](http://www.nature.com/nature).

Received 26 May; accepted 17 November 2008.

1. Rudnick, R. L. & Gao, S. in *The Crust* (ed. Rudnick, R. L.) Vol. 3, *Treatise on Geochemistry* (eds Holland, H. D. & Turekian, K. K.) 1–64 (Elsevier-Pergamon, 2003).
2. Campbell, I. H. & Taylor, S. R. No water, no granites — no oceans, no continents. *Geophys. Res. Lett.* **10**, 1061–1064 (1985).
3. Wood, J. A., Dickey, J. S., Marvin, U. B. & Powell, B. N. Lunar anorthosites and a geophysical model of the Moon. *Proc. Apollo 11 Lunar Sci. Conf.* 965–988 (1970).
4. Smith, J. A. *et al.* Petrologic history of the Moon inferred from petrography, mineralogy, and petrogenesis of Apollo 11 rocks. *Proc. Apollo 11 Lunar Sci. Conf.* 1149–1162 (1970).



5. Greenwood, R. C., Franchi, I. A., Jambon, A. & Buchanan, P. C. Widespread magma oceans on asteroidal bodies in the early Solar System. *Nature* **435**, 916–918 (2005).
6. Bowring, S. A. & Williams, I. S. Priscoan (4.00–4.03 Ga) orthogneiss from northwestern Canada. *Contrib. Mineral. Petrol.* **134**, 3–16 (1999).
7. Wilde, S. A., Valley, J. W., Peck, W. H. & Graham, C. M. Evidence from detrital zircons for the existence of continental crust and oceans on the Earth 4.4 Gyr ago. *Nature* **409**, 175–178 (2001).
8. Carlson, R. W. & Lugmair, G. The age of ferroan anorthosite 60025: Oldest crust on a young Moon? *Earth Planet. Sci. Lett.* **90**, 119–130 (1988).
9. Ash, R. D., Knott, S. F. & Turner, G. A 4-Gyr shock age for a martian meteorite and implications for the cratering history of Mars. *Nature* **380**, 57–59 (1996).
10. Mittlefehldt, D. W., McCoy, T. J., Goodrich, C. A. & Kracher, A. in *Planetary Materials* (ed. Papike, J. J.) Ch. 4 (Mineralogical Society of America, 1998).
11. Shearer, C. K. et al. GRA 06129: A meteorite from a new asteroidal geochemical reservoir or Venus? *Lunar Planet. Sci. Conf. Abstr. XXXIX*, 1825 (2008).
12. Mikouchi, T. & Miyamoto, M. Mineralogy and pyroxene cooling rate of unique achondrite meteorite GRA 06129. *Lunar Planet. Sci. Conf. Abstr. XXXIX*, 2297 (2008).
13. Clayton, R. N. Oxygen isotopes in meteorites. *Annu. Rev. Earth Planet. Sci.* **21**, 115–149 (1993).
14. Cherniak, D. J., Landord, W. A. & Ryerson, F. J. Lead diffusion in apatite and zircon using ion implantation and Rutherford back-scattering techniques. *Geochim. Cosmochim. Acta* **55**, 1663–1673 (1991).
15. Amelin, Y., Krot, A. N., Hutcheon, I. D. & Ulyanov, A. A. Lead isotopic ages of chondrules and calcium-aluminium-rich inclusions. *Science* **297**, 1678–1683 (2002).
16. Strom, R. G., Schaber, G. G. & Dawson, D. D. The global resurfacing of Venus. *J. Geophys. Res.* **99** (E5), 10899–10926 (1994).
17. Taylor, G. J. & Scott, E. R. D. in *Meteorites, Comets, and Planets* (ed. Davis, A. M.) Vol. 1, *Treatise on Geochemistry* (eds Holland, H. D. & Turekian, K. K.) 477–486 (Elsevier-Pergamon, 2003).
18. Taylor, G. J. Core formation in asteroids. *J. Geophys. Res.* **97**, 717–726 (1992).
19. Day, J. M. D., Pearson, D. G. & Taylor, L. A. Highly siderophile element constraints on accretion and differentiation of the Earth-Moon system. *Science* **315**, 217–219 (2007).
20. Bircck, J.-L. & Allègre, C. J. Contrasting Re/Os magmatic fractionation in planetary basalts. *Earth Planet. Sci. Lett.* **124**, 139–148 (1994).
21. Jurewicz, A. J. G., Mittlefehldt, D. W. & Jones, J. H. Experimental partial melting of the Allende (CV) and Murchison (CM) chondrites and the origin of asteroidal basalt. *Geochim. Cosmochim. Acta* **57**, 2123–2139 (1995).
22. Morse, S. A. *Basalts and Phase Diagrams* (Springer, 1980).
23. Tuttle, O. F. & Bowen, N. L. Origin of granite in the light of experimental studies in the system NaAlSi<sub>3</sub>O<sub>8</sub>–KAlSi<sub>3</sub>O<sub>8</sub>–SiO<sub>2</sub>–H<sub>2</sub>O. *Geol. Soc. Am. Mem.* **74**, 153p (1958).
24. Kushiro, I. On the nature of silicate melt and its significance in magma genesis; regularities in the shift of the liquidus boundaries involving olivine, pyroxene, and silica minerals. *Am. J. Sci.* **275**, 411–431 (1975).
25. Ziegler, R. A. et al. Petrology, geochemistry and likely provenance of unique achondrite Graves Nunatak 06128. *Lunar Planet. Sci. Conf. Abstr. XXXIX*, 2456 (2008).
26. Mittlefehldt, D. W., Bogard, D. D., Berkley, J. L. & Garrison, D. H. Brachinites: Igneous rocks from a differentiated asteroid. *Meteorit. Planet. Sci.* **38**, 1601–1625 (2003).
27. Rumble, D., Irving, A. J., Bunch, T. E., Wittke, J. H. & Kuehner, S. M. Oxygen isotopic and petrological diversity among Brachinites NWA 4872, NWA 4874, NWA 4882 and NWA 4969: How many ancient parent bodies? *Lunar Planet. Sci. Conf. Abstr. XXXIX*, 1974 (2008).
28. Bockrath, C., Ballhaus, C. & Holzheid, A. Fractionation of the platinum-group elements during mantle melting. *Science* **305**, 1951–1953 (2004).
29. Keil, K., Stöffler, D., Love, S. G. & Scott, E. R. D. Constraints on the role of impact heating and melting in asteroids. *Meteorit. Planet. Sci.* **32**, 349–363 (1997).
30. Wilson, L. & Keil, K. Consequences of explosive eruptions on small solar system bodies: The case of the missing basalts on the aubrite parent body. *Earth Planet. Sci. Lett.* **140**, 191–200 (1991).
31. Clark, B.-E. et al. E-type asteroid spectroscopy and compositional modelling. *J. Geophys. Res.* **109**, doi:10.1029/2003JE002200 (2004).
32. Spicuzza, M. J., Day, J. M. D., Taylor, L. A. & Valley, J. W. Oxygen isotope constraints on the origin and differentiation of the Moon. *Earth Planet. Sci. Lett.* **253**, 254–265 (2007).
33. Horan, M. F., Walker, R. J., Morgan, J. W., Grossman, J. N. & Rubin, A. E. Highly siderophile elements in chondrites. *Chem. Geol.* **196**, 27–42 (2003).

**Supplementary Information** is linked to the online version of the paper at [www.nature.com/nature](http://www.nature.com/nature).

**Acknowledgements** We thank the ANSMET 2006/2007 field team, the Meteorite Working Group and the Smithsonian Institution of Washington for collection and provision of the GRA 06128/9 and Brachina meteorites. D. Mittlefehldt and R. Greenwood provided reviews that improved the quality of this paper. A. Patchen and P. Piccoli provided assistance with electron microprobe analysis. Portions of this study were supported by the NASA Cosmochemistry Program: NNX07AM29G (R.J.W.), NNX08AH76G (W.F.M.), NNG05GG03G (L.A.T.).

**Author Contributions** All authors participated in data collection and interpretation and commented on the manuscript. J.M.D.D. led the project and wrote the paper.

**Author Information** Reprints and permissions information is available at [www.nature.com/reprints](http://www.nature.com/reprints). Correspondence and requests for materials should be addressed to J.M.D.D. ([jamesday@umd.edu](mailto:jamesday@umd.edu)).

## METHODS

Mineralogical investigations of polished thick and thin sections of GRA 06128 (sub-sections 42 and 51) and GRA 06129 (22 and 25) were performed using a Cameca SX50 electron microprobe analyser<sup>34</sup> (EMPA; University of Tennessee). Concentrations of minor and trace elements were determined in minerals using a New Wave Research UP213 (213 nm) laser-ablation system coupled to a ThermoFinnigan Element 2 ICP-MS (University of Maryland). Minerals were analysed using individual spots with a 15–80 µm diameter, a laser repetition rate of 7 Hz and a photon fluence of 2–2.5 J cm<sup>-2</sup>. Th/ThO production was ~0.07% for all analytical sessions. Backgrounds on the ICP-MS sample gas were collected for ~20 s followed by ~40 s of laser ablation of the sample. Washout time between analyses was >2 min. Data were collected in time-resolved mode so that effects of inclusions, mineral zoning and laser beam penetration could be evaluated. The NIST 610 glass standard was used for calibration of relative element sensitivities. Replicate LA-ICP-MS analyses of the BIR-1g glass standard run at intervals during analytical sessions yielded an external precision of better than 3% (1σ relative standard deviation) for all measured element compositions of silicates and phosphates. Replicate LA-ICP-MS analyses of the University of Toronto JB Sulphide standard run at intervals during analysis of sulphides yielded an external precision of better than 1% (1σ relative standard deviation) for highly siderophile element abundances.

<sup>207</sup>Pb–<sup>206</sup>Pb ages were obtained using the same laser and mass spectrometer settings as those for minerals and glasses analysed by LA-ICP-MS. Chlorapatite and merrillite were measured because the high concentrations of U (0.1–3 p.p.m.) make them suitable for LA-ICP-MS <sup>207</sup>Pb–<sup>206</sup>Pb dating. All data reduction was made offline using Microsoft Excel. Background Pb signals were taken on mass, and subtracted from each isotopic measurement during ablation. Each ratio was determined using the background corrected Pb isotopic measurements. The average and 2σ<sub>mean</sub> of the background corrected ratios, after ratios outside 3σ were discarded, were used to determine the age and error for each phosphate. An exponential fractionation law was used to correct for mass fractionation by means of bracketing the phosphate analyses with standard reference materials (SRM: NIST 610, NIST 612, BCR-2g). Ratios of <sup>207</sup>Pb/<sup>206</sup>Pb for each SRM were used to calculate the fractionation factor (α; ref. 35). Differences in α between the three SRMs had a negligible effect on calculated ages. The <sup>207</sup>Pb–<sup>206</sup>Pb ages were calculated using Isoplot/Ex (ref. 36).

Fused-bead major element concentrations were analysed using the CAMECA SX-50 EMPA and protocols for glass analyses outlined in ref. 34. Minor- and trace-element concentrations were measured on the same beads using LA-ICP-MS protocols outlined above, with 150-µm raster paths and obtaining 20 s of background and ~60 s of analysis. Os isotopic and platinum-group elemental analyses were performed at the University of Maryland using protocols outlined in Supplementary Information. Isotopic compositions of Os were measured in negative ion mode by thermal ionization mass spectrometry. Re, Pd, Pt, Ru and

Ir were measured using an Aridus desolvating nebuliser coupled to an Element 2 ICP-MS in low-resolution mode. External precision for <sup>187</sup>Os/<sup>188</sup>Os, determined via measurement of standards bracketed with the meteorite samples, was 2.5‰ (2σ). External reproducibility on PGE analyses using the Element 2 was better than 0.5% for 0.1 p.p.b. solutions and 0.3% for 1 p.p.b. solutions. Total procedural blanks run with the samples had an average <sup>187</sup>Os/<sup>188</sup>Os isotope composition of 0.1448 ± 0.0024, with average concentrations of 1.5 pg (Re), 37 pg (Pd), 20 pg (Pt), 5 pg (Ru), 2 pg (Ir) and <1 pg (Os); blank corrections were negligible.

Oxygen isotope analyses were performed at the Geophysical Laboratory, Carnegie Institution for Science and are reported in δ<sup>18</sup>O, δ<sup>17</sup>O (δ<sup>X</sup>O<sub>n</sub> is the per mil (‰) deviation of <sup>X</sup>O/<sup>16</sup>O in *n* from the international standard (std) V-SMOW given by the relationship: δ<sup>X</sup>O<sub>n</sub> = 1,000 × ((<sup>X</sup>O/<sup>16</sup>O)<sub>n</sub> / (<sup>X</sup>O/<sup>16</sup>O)<sub>std</sub>) – 1), where *X* is either 17 or 18 and *n* represents the unknown) and Δ<sup>17</sup>O notation, which represents deviations from the terrestrial fractionation line (λ = 0.526 (ref. 37); Δ<sup>17</sup>O = 1,000ln((δ<sup>17</sup>O/1,000) + 1) – 0.526 × 1,000ln((δ<sup>18</sup>O/1,000) + 1)) (after ref. 38). The value of 0.526 was obtained by linear regression of linearized values for δ<sup>17</sup>O and δ<sup>18</sup>O of terrestrial silicate minerals<sup>37,39</sup>. Samples were loaded in a Sharp reaction chamber (ref. 40). Successive, repeated blanks with BrF<sub>5</sub> and vacuum pumping were carried out for 12 h until there was less than 150 µm of non-condensable gas pressure remaining after a blank run. Quantitative release of oxygen by fluorination reaction was performed by heating samples individually with a CO<sub>2</sub> laser in the presence of BrF<sub>5</sub>. Standardization of delta values was achieved by comparison with the Gore Mountain garnet standard, USNM 107144, analysed during every analytical session.

34. Day, J. M. D. *et al.* Comparative petrology, geochemistry, and petrogenesis of evolved, low-Ti mare basalt meteorites from the LaPaz Icefield, Antarctica. *Geochim. Cosmochim. Acta* **70**, 1581–1600 (2006).
35. Baker, J., Peate, D., Waight, T. & Meyzen, C. Pb isotopic analysis of standards and samples using a <sup>207</sup>Pb–<sup>204</sup>Pb double spike and thallium to correct for mass bias with a double-focusing MC-ICP-MS. *Chem. Geol.* **211**, 275–303 (2004).
36. Ludwig, K. R. Isoplot. Program and documentation, version 2.95. (Revised edition of US Open-File report, 91-445, 2003).
37. Rumble, D., Miller, M. F., Franchi, I. A. & Greenwood, R. C. Oxygen three-isotope fractionation lines in terrestrial silicate minerals: An inter-laboratory comparison of hydrothermal quartz and eclogitic garnet. *Geochim. Cosmochim. Acta* **71**, 3592–3600 (2007).
38. Clayton, R. N. & Mayeda, T. K. Oxygen isotope studies of achondrites. *Geochim. Cosmochim. Acta* **60**, 1999–2017 (1996).
39. Miller, M. F. Isotopic fractionation and the quantification of <sup>17</sup>O anomalies in the oxygen three-isotope system: an appraisal and geochemical significance. *Geochim. Cosmochim. Acta* **66**, 1881–1889 (2002).
40. Sharp, Z. D. A laser-based microanalytical method for the *in situ* determination of oxygen isotope ratios of silicates and oxides. *Geochim. Cosmochim. Acta* **54**, 1353–1357 (1990).



# Diversity dynamics of marine planktonic diatoms across the Cenozoic

Daniel L. Rabosky<sup>1,2</sup> & Ulf Sorhannus<sup>3</sup>

Diatoms are the dominant group of phytoplankton in the modern ocean. They account for approximately 40% of oceanic primary productivity and over 50% of organic carbon burial in marine sediments<sup>1</sup>. Owing to their role as a biological carbon pump<sup>2</sup> and effects on atmospheric CO<sub>2</sub> levels<sup>3–5</sup>, there is great interest in elucidating factors that influenced the rapid rise in diatom diversity during the past 40 million years<sup>6,7</sup>. Two biotic controls on diversification have been proposed to explain this diversity increase: (1) geochemical coupling between terrestrial grasslands and marine ecosystems through the global silicon cycle; and (2) competitive displacement of other phytoplankton lineages. However, these hypotheses have not been tested using sampling-standardized fossil data. Here we show that reconstructions of species diversity in marine phytoplankton reject these proposed controls and suggest a new pattern for oceanic diatom diversity across the Cenozoic. Peak species diversity in marine planktonic diatoms occurred at the Eocene–Oligocene boundary and was followed by a pronounced decline, from which diversity has not recovered. Although the roles of abiotic and biotic drivers of diversification remain unclear, major features of oceanic diatom evolution are decoupled from both grassland expansion and competition among phytoplankton groups.

Because diatoms have an absolute requirement for silicon, their diversity and ecological prominence in the contemporary ocean is thought to have been catalysed by processes that increased the flux of soluble silicon into marine ecosystems<sup>1,8</sup>. The rise of grassland ecosystems during the middle to late Miocene would have served as such a macroevolutionary trigger by greatly accelerating the silicon weathering cycle and increasing availability of soluble silicon<sup>8,9</sup>. Grasses contain substantial silicon in the form of phytoliths and are believed to increase silicon mobilization from soils, thus contributing to the reservoir of biogenic silicon in marine systems<sup>10</sup>. This coupling of evolutionary dynamics in terrestrial and marine ecosystems is supported by the apparent synchrony between diatom diversification and the expansion of grasslands<sup>1,6</sup>.

We tested the relation between diatom diversification and grassland ecosystem expansion by reconstructing temporal patterns of species diversity from the Neptune database, a record of Cenozoic microfossil occurrence collected from a globally dispersed network of 165 drilling sites<sup>11</sup>. The number of occurrences, samples and drilling cores included in the database increases towards the present (Supplementary Fig. 1), suggesting that counts of standing taxonomic diversity per temporal interval may reflect differential sampling and preservation through time<sup>12,13</sup>. Although temporal increases in the number of occurrences could in principle reflect a real increase in diversity and abundance through time, the rapid rise in the available number of samples and cores almost certainly indicates an artefactual increase in fossil availability towards the present.

To address these biases in sampling and preservation, we generated sampling-standardized data sets by drawing fixed amounts of data per 1 million year (Myr) temporal bin from the Neptune database. Diversity was estimated as a function of the sampled in-bin (SIB) diversity, the per-bin sampling probability and the overall sampling probability<sup>14</sup> (see Methods). Different subsampling algorithms can generate dissimilar diversity curves<sup>12</sup>, as these methods make different assumptions about the relation between total fossil specimens and the presence or absence of species in a sample as well as the independence of occurrences and samples. We therefore used three methods of subsampling that could accommodate a wide range of assumptions (see Methods): rarefaction of individual taxonomic occurrences per million years<sup>15</sup>; by-lists unweighted (UW), which draws a fixed number of samples per million years<sup>16,17</sup>; and by-lists occurrences-squared weighted (O2W), which scales each list by the square of its occurrence count. The last method draws a fixed number of samples until a quota of occurrences-squared is reached<sup>17</sup>.

Sampling-standardized diversity curves do not support the traditional view that diatom diversity has increased rapidly between the Eocene and the present<sup>1</sup> (Fig. 1a). Rather, we find a dramatic increase in diversity in the late Eocene, with peak diversity at the Eocene–Oligocene transition (Fig. 1b, c). During the Oligocene, diatom diversity plummeted to approximately 50% of the maximum and approached levels observed during the three Palaeocene intervals for which estimates are available (Supplementary Fig. 3). Rarefaction and UW indicate partial recovery from the Oligocene diversity crash, whereas O2W suggests minimal change in diversity across the Neogene (Fig. 1 and Supplementary Fig. 3).

The earliest plausible dates for the expansion of grassland ecosystems<sup>18</sup> all occur after the massive diversity pulse at the Eocene–Oligocene boundary (Fig. 1d). Phytolith<sup>18</sup> and palaeosol data<sup>19</sup> indicate that grassland expansion in North America could not have occurred before the mid-Oligocene, and the expansion occurred much later in Africa and Asia<sup>19</sup>. Furthermore, ecomorphological indices of fossil mammals, particularly horses, show trends associated with adaptation to open savannah/grassland habitats in the middle Miocene<sup>20</sup>. This temporal mismatch between the timing of grassland expansion and reconstructed diatom diversity argues strongly against the view that these processes are related.

We then tested whether trends in diatom diversity could be explained in part by interspecific competition with other phytoplankton lineages. Diversity dynamics among the three major groups of eukaryotic phytoplankton with red plastid symbionts—diatoms, coccolithophorids and dinoflagellates—are thought to be regulated by interspecific competition in relation to oceanic turbulence and nutrient supply over ecological<sup>21,22</sup> and evolutionary timescales<sup>1,6</sup>. In contrast to other phytoplankton, diatoms have a storage vacuole, which allows them to hoard nutrients under conditions of dynamic

<sup>1</sup>Department of Ecology and Evolutionary Biology, Cornell University, Ithaca, New York 14853, USA. <sup>2</sup>Fuller Evolutionary Biology Program, Cornell Laboratory of Ornithology, Ithaca, New York 14850, USA. <sup>3</sup>Department of Biology and Health Services, Edinboro University of Pennsylvania, Edinboro, Pennsylvania 16444, USA.

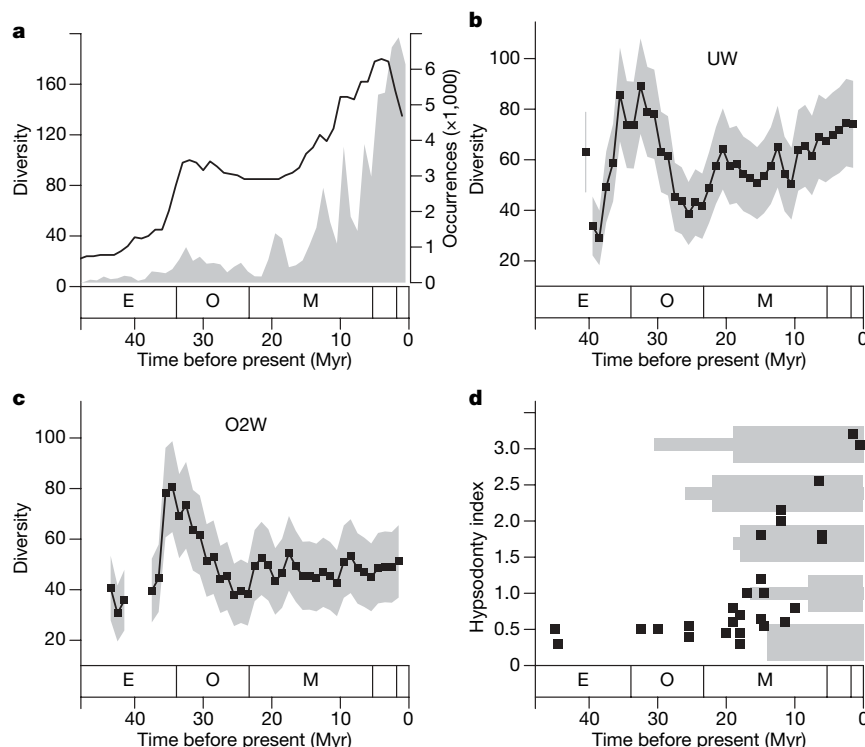


**Figure 1 | Traditional and sampling-standardized diatom diversity curves.** **a**, Traditional view of diatom diversity (line) based on non-standardized data<sup>11</sup> and total diatom occurrences in Neptune (shaded). **b**, **c**, Diatom diversity per million years with 95% confidence envelope after sampling-standardization: UW subsampling (**b**); O2W subsampling (**c**). Results for rarefaction are similar to UW (Supplementary Fig. 3). **d**, Estimated time of expansion of grassland ecosystems in North America (CO, Colorado; NE,

Nebraska; Montana, MT), Pakistan (Pk), and Nigeria (Ni) based on palynological, palaeosol and phytolith data<sup>18,19</sup>. Wide bars indicate period of grassland prominence; narrow bars indicate plausible temporal interval for transition from woodland to grassland. Ecomorphological indices such as hypsodonty in fossil horses (points) suggest that adaptation to grassland/savannah ecosystems did not occur until the mid-Miocene<sup>20</sup>. E, Eocene; O, Oligocene; M, Miocene.

resource availability<sup>1</sup>. Models suggest that this facilitates competitive displacement of other phytoplankton groups by diatoms when ocean conditions shift towards low stratification with high mixing<sup>23</sup>. The rise in diatom diversity and the associated decline in coccolithophorid diversity during the Cenozoic is often interpreted as the evolutionary outcome of interspecific competition under a regime of progressively more turbulent ocean conditions that began at the Eocene–Oligocene boundary<sup>23,24</sup>.

We obtained coccolithophorid data from the Neptune database (comparable data are not available for dinoflagellates) and reconstructed diversity across the Cenozoic using the rarefaction, UW and O2W subsampling methods (Fig. 2 and Supplementary Fig. 5). The UW curve closely matches the traditional view of coccolithophorid diversity through time (Fig. 2b), even though the traditional curve is not based on Neptune data<sup>25</sup> and is not corrected for differential sampling through time. The rarefaction curve is qualitatively similar but shows a dampening of diversity fluctuations through time. The contrast between O2W and traditional curves is striking, as the O2W curve would suggest that coccolithophorid diversity has not changed between the Palaeocene and the present. We note that the UW reconstruction for coccolithophorids is largely concordant with the traditional view, even though these curves are based on different data and methodology.

We then tested for inverse relations between de-trended diversity time series for diatoms and coccolithophorids (see Methods), as expected if competitive interactions mediate macroevolutionary dynamics in these major phytoplankton lineages<sup>23–25</sup>. There is no significant relation between de-trended diversity series for diatoms and coccolithophorids under rarefaction (Fig. 3; Pearson  $r = -0.08$ ,  $P = 0.35$ ; Spearman  $r = -0.06$ ,  $P = 0.32$ ; one-tailed  $P$  values;  $n = 39$ ) and UW subsampling (Pearson  $r = 0.05$ ,  $P = 0.61$ ; Spearman  $r = 0.04$ ,  $P = 0.60$ ). Although there is a negative correlation under O2W

subsampling (Pearson  $r = -0.20$ ,  $P = 0.12$ ; Spearman  $r = -0.36$ ;  $P = 0.012$ ), this cannot explain broad-scale trends in diatom diversity, because the O2W reconstructions imply that coccolithophorid

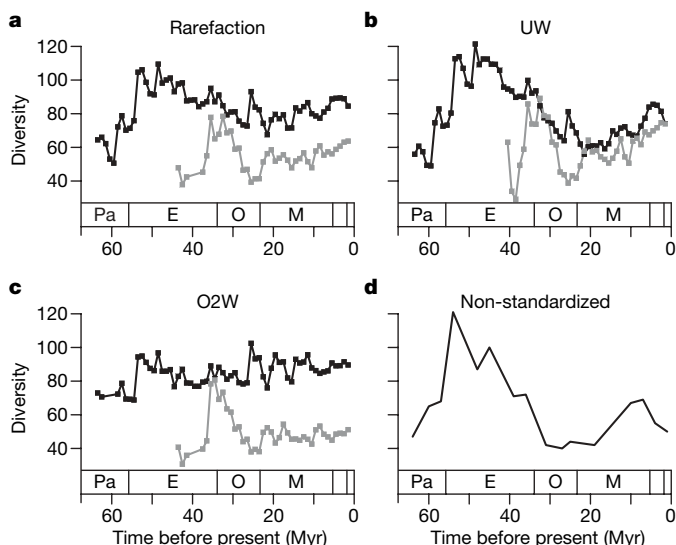


**Figure 2 | Coccolithophorid diversity through time based on sampling-standardized analysis of the Neptune database.** Coccolithophorid diversity (black) was estimated per million year temporal bin; shown are means from 1,000 replicate data sets. Diatom diversity through time curves are shown for comparison (grey). **a**, Rarefaction; **b**, UW; **c**, O2W. **d**, Non-standardized, traditional view of coccolithophorid diversity across the Cenozoic<sup>11,26</sup>. Note that range of the x axis (0–65 Myr) differs from that in Fig. 1. Pa, Palaeocene; E, Eocene; O, Oligocene; M, Miocene.

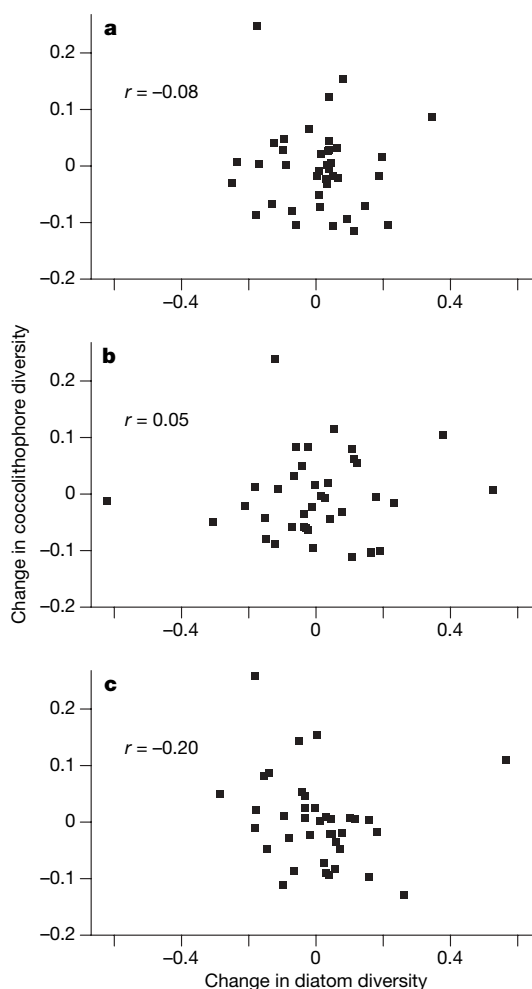


**Figure 3 | Correlations between de-trended diatom and coccolithophorid diversity between the mid-Eocene and the Pleistocene.** Diversity curves across  $n = 39$  temporal bins were estimated under **a**, rarefaction; **b**, UW subsampling; **c**, O2W subsampling. Pearson correlation coefficients are shown. Only O2W subsampling results in a significant negative correlation (Pearson  $r = -0.20$ ,  $P = 0.12$ ; Spearman  $r = -0.36$ ,  $P = 0.012$ , one-tailed).

diversity scarcely changed across the entire Cenozoic (Fig. 2c). Accepting these negative correlations based on O2W reconstructions requires a radical reinterpretation of Cenozoic coccolithophorid diversity. Moreover, there is no evidence that the abrupt rise in diatom diversity before the Eocene–Oligocene boundary was accompanied by a corresponding drop in coccolithophorid diversity (Fig. 2). Taken together, these results indicate decoupled macroevolutionary dynamics in these groups.

These reconstructions of marine phytoplankton diversity reject the prominent role for direct and indirect biotic interactions discussed in recent studies<sup>6,26</sup>. The most striking features of diatom diversity through time are unrelated to both grassland expansion and interspecific competition with coccolithophorids. Although we cannot discount weak feedback between terrestrial ecosystems and diatom macroevolution, grassland expansion is unable to account for major fluctuations in diatom diversity through time. Moreover, although interspecific competition and ecological replacement among phytoplankton groups may be an important feature of the modern ocean<sup>21</sup>, there is little evidence for contrasting patterns of diversity in diatoms and coccolithophorids as suggested by previous studies<sup>25,26</sup>. It is possible that future studies may reveal an inverse relation between diatom and coccolithophorid diversities across shorter timescales, but there is clearly no signal of competition on the long-term trajectory of these groups.

We recognize that our diversity reconstructions may be influenced by problematic age models, unequal geographic coverage and other limitations associated with the Neptune database<sup>11</sup>; moreover, other potential biases, including latitudinal diversity gradients, should be explored by future work. However, most recent studies have taken diversity estimates based on non-standardized Neptune data to represent an accurate depiction of diatom diversity across the Cenozoic<sup>1,25</sup>. Our curves and those of previous studies are based on the same underlying data and are subject to identical biases, differing only in that we applied methods to correct for differential sampling through time. We thus consider it unlikely that traditional curves for marine planktonic diatoms are more accurate than sampling-standardized curves, which address a known and pervasive bias in the fossil record<sup>12,13</sup>.

To the extent that these diversity curves are not strongly influenced by other, yet-unaccounted-for sampling biases, our results suggest that the Eocene–Oligocene transition was an event of profound significance for diatom evolution: marine planktonic diatom diversity reached its highest level at or immediately before the boundary, perhaps reflecting increased speciation or declining extinction rates. Rather than a continuous rise in diatom diversity during the Cenozoic, we find evidence for a pronounced drop in diversity during the Oligocene, possibly followed by partial recovery during the Neogene (Fig. 1). Although many groups declined in conjunction with global cooling at the Eocene–Oligocene boundary<sup>27</sup>, this result is surprising for diatoms because increased thermohaline circulation and oceanic turbulence during the Oligocene are thought to have contributed to both diatom diversity and their replacement of coccolithophorids<sup>23–25</sup>. During the Eocene–Oligocene transition, global temperatures plummeted, resulting in a rapid shift from global ‘greenhouse’ to ‘icehouse’ conditions<sup>28</sup>; this transition was associated with a large drop in atmospheric  $\text{CO}_2$  concentrations<sup>29</sup>. Diatoms have been linked to climate change through their prominent role in the export of organic carbon to the ocean interior<sup>5,26</sup>. To the extent that diatom diversity is correlated with primary productivity, our results suggest the possibility that the explosive rise of diatoms immediately before the Eocene–Oligocene transition contributed to a drawdown in atmospheric  $\text{CO}_2$  and facilitated rapid global cooling.

## METHODS SUMMARY

**Data and analyses.** Neptune data for diatoms and coccolithophorids were downloaded on 26 October 2007 from <http://services.chronos.org/databases/neptune/index.html>. The data consist of lists of taxonomic occurrences associated with a particular horizon of a drilling core (or ‘hole’). We refer to the list of occurrences from a single horizon within a single core as a sample.

Traditional views of diatom diversity through time<sup>1,25</sup> are based on total taxonomic diversity per temporal bin from the Neptune database<sup>11</sup> without regard for differential sampling through time, whereas the traditional coccolithophorid curve is based on total species diversity as inferred from published stratigraphic range data<sup>25</sup>. The subsampling methods used here draw fixed quotas of occurrences, samples and occurrences-squared without replacement using algorithms described in Methods. We constructed replicate data sets of standardized sampling intensity using each subsampling method; for each replicate, total diversity for the  $i$ th temporal bin was estimated as  $(N_{s,i}P_s/P_{s,i})$ , where  $N_{s,i}$  is the count of species actually sampled in bin  $i$  (SIB diversity),  $P_{s,i}$  is the sampling probability for the  $i$ th bin, and  $P_s$  is the overall sampling probability<sup>14</sup>. Results shown are mean diversities from 1,000 replicate data sets. Diatom and coccolithophorid diversity time series were de-trended by computing interval-to-interval differences in log-transformed diversity estimates before correlation analysis.

**Full Methods** and any associated references are available in the online version of the paper at [www.nature.com/nature](http://www.nature.com/nature).

Received 7 February; accepted 16 September 2008.

1. Falkowski, P. G. *et al.* The evolution of modern eukaryotic phytoplankton. *Science* 305, 354–360 (2004).
2. Treguer, P. & Pondaven, P. Global change – silica control of carbon dioxide. *Nature* 406, 358–359 (2000).



3. Falkowski, P. G., Barber, R. T. & Smetacek, V. Biogeochemical controls and feedbacks on ocean primary production. *Science* **281**, 200–206 (1998).
4. Milligan, A. J. & Morel, F. M. M. A proton buffering role for silica in diatoms. *Science* **297**, 1848–1850 (2002).
5. Katz, M. E. *et al.* Biological overprint of the geological carbon cycle. *Mar. Geol.* **217**, 323–338 (2005).
6. Falkowski, P. G., Schofield, O., Katz, M. E., Van De Schootbrugge, B. & Knoll, A. H. in *Coccolithophores: From Molecular Processes to Global Impact* (eds Therstein, H. R. & Young, J. R.) 429–454 (Springer, 2004).
7. Finkel, Z. V., Katz, M. E., Wright, J. D., Schofield, O. M. E. & Falkowski, P. G. Climatically driven macroevolutionary patterns in the size of marine diatoms over the Cenozoic. *Proc. Natl Acad. Sci. USA* **201**, 8927–8932 (2005).
8. Kidder, D. L. & Gierlowski-Kordesch, E. H. Impact of grassland radiation on the nonmarine silica cycle and Miocene diatomite. *Palaios* **20**, 198–206 (2005).
9. Kidder, D. L. & Erwin, D. H. Secular distribution of biogenic silica through the Phanerozoic: comparison of silica-replaced fossils and bedded cherts at the series level. *J. Geol.* **109**, 509–522 (2001).
10. Blecker, S. W., McCulley, R. L., Chadwick, O. A. & Kelly, E. F. Biologic cycling of silica across a grassland bioclimosequence. *Glob. Biogeochem. Cycles* **20**, GB3023 (2006).
11. Spencer-Cervato, C. The Cenozoic deep-sea microfossil record: explorations of the DSDP/ODP sample set using the Neptune database. *Palaeontol. Electron.* **2**, 1–268 (1999).
12. Alroy, J. *et al.* Effects of sampling standardization on estimates of Phanerozoic marine diversification. *Proc. Natl Acad. Sci. USA* **98**, 6261–6266 (2001).
13. Raup, D. M. Taxonomic diversity during the Phanerozoic. *Science* **177**, 1065–1071 (1972).
14. Alroy, J. The dynamics of origination and extinction in the marine fossil record. *Proc. Natl Acad. Sci. USA* **105**, 11536–11542 (2008).
15. Miller, A. I. & Foote, M. Calibrating the Ordovician radiation of marine life: implications for Phanerozoic diversity trends. *Paleobiology* **22**, 304–309 (1996).
16. Smith, E. P., Stewart, P. M. & Cairns, J. Similarities between rarefaction methods. *Hydrobiologia* **120**, 167–170 (1985).
17. Alroy, J. New methods for quantifying macroevolutionary patterns and processes. *Paleobiology* **26**, 707–733 (2000).
18. Stromberg, C. A. E. Decoupled taxonomic radiation and ecological expansion of open-habitat grasses in the Cenozoic of North America. *Proc. Natl Acad. Sci. USA* **102**, 11980–11984 (2005).
19. Retallack, G. J. Cenozoic expansion of grasslands and climatic cooling. *J. Geol.* **109**, 407–426 (2001).
20. MacFadden, B. J. *Fossil Horses* (Cambridge Univ. Press, 1992).
21. Margalef, R. *Our Biosphere* (Ecology Institute, 1997).
22. Sellner, K. G., Sellner, S. G., Lacouture, R. V. & Magnien, R. E. Excessive nutrients select for dinoflagellates in the stratified Patapsco River estuary: Margalef reigns. *Mar. Ecol. Prog. Ser.* **220**, 93–102 (2001).
23. Tozzi, S., Schofield, O. & Falkowski, P. Historical climate change and ocean turbulence as selective agents for two key phytoplankton functional groups. *Mar. Ecol. Prog. Ser.* **274**, 123–132 (2004).
24. Iglesias-Rodriguez, M. D. *et al.* Representing key phytoplankton functional groups in ocean carbon cycle models: coccolithophorids. *Glob. Biogeochem. Cycles* **16**, 1100 (2002).
25. Bown, P. R. Calcareous nannoplankton evolution: a tale of two oceans. *Micropaleontology* **51**, 299–308 (2005).
26. Katz, M. E., Finkel, Z. V., Grzebyk, D., Knoll, A. H. & Falkowski, P. G. Evolutionary trajectories and biogeochemical impacts of marine eukaryotic phytoplankton. *Annu. Rev. Ecol. Syst.* **35**, 523–556 (2004).
27. Prothero, D. R., Ivany, L. C. & Nesbitt, E. A. (eds) *From Greenhouse to Icehouse: The Marine Eocene–Oligocene Transition* (Columbia Univ. Press, 2003).
28. Zanzani, A., Kohn, M. J., MacFadden, B. J. & Terry, D. O. Large temperature drop across the Eocene–Oligocene transition in central North. *Am. Nat.* **445**, 639–642 (2007).
29. Pagani, M., Zachos, J. C., Freeman, K. H., Tipler, B. & Bohaty, S. Marked decline in atmospheric carbon dioxide concentrations during the Paleogene. *Science* **309**, 600–603 (2005).

**Supplementary Information** is linked to the online version of the paper at [www.nature.com/nature](http://www.nature.com/nature).

**Acknowledgements** We thank J. Alroy for comments on our statistical analyses and for suggesting the binomial approximation for confidence limits on diversity; and M. Foote, I. Lovette, A. McCune, A. Agrawal, N. Hairston and the BK Discussion Group for comments on the manuscript. This research was supported in part by NSF-OSIEE-0612855. Part of this work used the resources of the Computational Biology Service Unit from Cornell University, which is partly funded by the Microsoft Corporation.

**Author Contributions** Both authors contributed to study design and the interpretation of results. D.L.R. conducted the analyses and drafted the manuscript.

**Author Information** Reprints and permissions information is available at [www.nature.com/reprints](http://www.nature.com/reprints). Correspondence and requests for materials should be addressed to D.L.R. (DLR32@cornell.edu).

## METHODS

**Data.** All taxon records identified as questionable or with questionable age estimates were eliminated. The final diatom data set contained 66,941 occurrences and 1,024 species. The coccolithophorid data contained 130,261 Cenozoic occurrences and 895 species.

**Subsampling methods.** The diversity analyses we used were developed to correct for biases in sampling intensity through time and can be contrasted with traditional taxon enumeration. In the latter approach, total stratigraphic ranges are inferred by tabulating first and last occurrences of each taxon in a group of interest. Diversity curves are then generated by counting the number of taxa with overlapping stratigraphic ranges at any point in time<sup>30</sup>. Three subsampling methods were used in the main analyses: rarefaction, by-lists unweighted (UW) and by-lists occurrences-squared weighted (O2W). We performed algorithmic rarefaction on the Neptune data by drawing a fixed quota of occurrences per million years<sup>15</sup>. Rarefaction weights each taxonomic occurrence equally and assumes that the number of occurrences in a sample is proportional to the total number of specimens examined<sup>12</sup>. The method further assumes that occurrences can be drawn independently of the samples (or lists) in which they occur; the remaining methods require that entire samples be drawn simultaneously. UW draws a fixed quota of samples and effectively assumes that the number of specimens examined per sample is constant<sup>16,17</sup>. If the number of occurrences within samples is proportional to the true diversity of a particular horizon, then UW will closely track the actual diversity curve. However, if there are temporal trends in the number of occurrences within samples that are independent of the true diversity (for example, if a greater number of specimens were examined for successively younger samples), then UW diversity curves will reflect this bias.

O2W draws samples until a fixed quota of occurrences-squared is reached and thus assumes that the number of occurrences within a sample can be approximated by the square root of the total number of specimens examined<sup>17</sup>. In the Supplementary Information, we include results from a variant of O2W that weights the probability of drawing a particular sample from the  $k$ th drilling core by the inverse of the number of samples from core  $k$ . This inverse weighting method<sup>14</sup>, which we refer to as O2W-CW (occurrences-squared weighted with core weights), equalizes the number of drilling cores contributing to a diversity estimate. Thus, if core 1 contains five samples and core 2 contains 20 samples, the probability of drawing a sample from core 1 will be 0.20 and the probability of drawing a sample from core 2 will be 0.05. Both cores will thus—on average—contribute the same number of samples to a diversity estimate. In principle, this should increase the spatial dispersion of samples selected for a particular temporal bin. Results obtained for O2W-CW subsampling are similar to O2W (Supplementary Figs 2–6). We note that a recent study has advocated empirical tuning of the exponent in ‘occurrences-squared’-type approaches, such that samples are weighted by  $O^x$ , where  $O$  is the number of occurrences in the sample (for example,  $x=2$  for O2W)<sup>31</sup>. However, this is unlikely to change our primary conclusions, as our results are robust across even more disparate subsampling methods.

Subsampling quotas for diatoms were 96 occurrences (rarefaction), 9 samples (UW) and 969 occurrences-squared (O2W). Quotas for coccolithophorids were 400 occurrences, 31 samples and 6,121 occurrences-squared. Diversity and sampling parameters were tabulated from 1,000 pseudo-random data sets generated under each of the subsampling routines discussed above.

**Sampling probability and diversity estimates.** Our diversity estimates (see Methods Summary) are a function of the SIB diversity for a particular bin, the sampling probability for the bin and the overall sampling probability. The SIB diversity is simply the total number of taxa occurring in bin  $i$  and is denoted by

$N_{S,i}$  (uncorrected SIB counts are shown in Supplementary Figs 7 and 9). The sampling probability estimates rely on two additional counts<sup>14</sup>. The first is the number of ‘three timers’, or taxa sampled consecutively in bins  $i-1$ ,  $i$  and  $i+1$ . The second count is referred to as ‘part timers’, or taxa sampled in bins  $i-1$  and  $i+1$  but not in bin  $i$  itself. These counts are abbreviated as  ${}^3T$  and  ${}^PT$ , respectively. The sampling probability for bin  $i$  is simply  $P_{S,i} = {}^3T_i / ({}^3T_i + {}^PT_i)$ , and the overall sampling probability is  $P_S = {}^3T / ({}^3T + {}^PT)$ , where  ${}^3T$  and  ${}^PT$  are summed across all intervals<sup>14,32</sup>. Sampling probabilities through time are shown in Supplementary Figs 4 and 6. This method of diversity counting entirely eliminates edge effects, which result in the underestimation of diversity near the ends of time series under ‘range-through’ methods<sup>12</sup> of diversity counting<sup>14</sup>. Despite severe edge effects, our conclusions are supported by total (range-through) diversity counts that include both SIB diversity as well as taxa ranging across but not sampled within the focal bin (for example ‘Lazarus taxa’<sup>33</sup>; Supplementary Figs 8 and 10).

Because  $P_{S,i}$  requires that the sampling quota be met for three adjacent intervals, we could not estimate diversity for the first or last intervals in the time series. In addition, we lack diversity estimates for diatoms between 38 and 41 Myr for rarefaction and O2W, because a single temporal bin (39–40 Myr) did not meet the sampling quota for these methods. The lack of diversity estimates from 45 to 55 Myr reflects a lack of samples for all methods. We were able to estimate diversity between 58 and 60 Myr under O2W and rarefaction (Supplementary Fig. 3), but these estimates are attributable to just a single drilling core.

**Confidence intervals.** One method of computing confidence intervals on diversity estimates would entail tabulating the 2.5% and 97.5% quantiles of the distribution of diversity estimates for a particular temporal bin from the set of sampling-standardized pseudo-replicate data sets. However, these confidence intervals are excessively narrow for bins whose sample or occurrence total barely reached the subsampling quota, because it is necessarily the case that virtually all data will have been drawn for those intervals. Thus, narrow confidence intervals in such a case reflect only a lack of data to be sampled, not true confidence in the diversity estimates. To avoid this problem, we used the binomial variance to approximate the standard deviation of diversity estimates<sup>15,32,34</sup>. Diversity sampling is modelled with a binomial distribution, where  $N$  is the true number of species occurring within an interval and  $P$  is the probability of sampling each one. It follows that the standard deviation in the number of sampled species  $S$  is  $\sqrt{NP(1-P)}$ . Although  $P$  and  $N$  are unknown, the expected value of  $NP$  is  $S$ . Because  $P$  must decline as the true diversity  $N$  increases (as the observed SIB count  $S$  is a fixed observation), the limit is  $NP$  and the standard deviation can be approximated by  $\sqrt{S}$ . This is a conservative estimate, as it is almost certain that  $S < N$ . We computed confidence intervals using  $\sqrt{S}$  to approximate the standard deviation of a normal distribution with  $\mu = S$ . This method assumes that sampling probabilities are equal among species.

30. Sepkoski, J. J. A factor analytic description of the Phanerozoic marine fossil record. *Paleobiology* **7**, 36–53 (1981).
31. Bush, A. M., Markey, M. J. & Marshall, C. R. Removing bias from diversity curves: the effects of spatially organized biodiversity on sampling-standardization. *Paleobiology* **30**, 666–686 (2004).
32. Alroy, J. et al. Phanerozoic trends in the diversity of marine invertebrates. *Science* **321**, 97–100 (2008).
33. Paul, C. R. C. in *The Adequacy of the Fossil Record* (eds Donovan, S. K. & Paul, C. R. C.) 1–22 (Wiley, 1982).
34. Foote, M. Morphological disparity in Ordovician–Devonian crinoids and the early saturation of morphological space. *Paleobiology* **20**, 320–344 (1994).

# Neural processing of auditory feedback during vocal practice in a songbird

Georg B. Keller<sup>1</sup> & Richard H. R. Hahnloser<sup>1</sup>

Songbirds are capable of vocal learning and communication<sup>1,2</sup> and are ideally suited to the study of neural mechanisms of complex sensory and motor processing. Vocal communication in a noisy bird colony and vocal learning of a specific song template both require the ability to monitor auditory feedback<sup>3,4</sup> to distinguish self-generated vocalizations from external sounds and to identify mismatches between the developing song and a memorized template acquired from a tutor<sup>5</sup>. However, neurons that respond to auditory feedback from vocal output have not been found in song-control areas despite intensive searching<sup>6–8</sup>. Here we investigate feedback processing outside the traditional song system, in single auditory forebrain neurons of juvenile zebra finches that were in a late developmental stage of song learning. Overall, we found similarity of spike responses during singing and during playback of the bird's own song, with song responses commonly leading by a few milliseconds. However, brief time-locked acoustic perturbations of auditory feedback revealed complex sensitivity that could not be predicted from passive playback responses. Some neurons that responded to playback perturbations did not respond to song perturbations, which is reminiscent of sensory-motor mirror neurons<sup>8,9</sup>. By contrast, some neurons were highly feedback sensitive in that they responded vigorously to song perturbations, but not to unperturbed songs or perturbed playback. These findings suggest that a computational function of forebrain auditory areas may be to detect errors between actual feedback and mirrored feedback deriving from an internal model of the bird's own song or that of its tutor. Such feedback-sensitive spikes could constitute the key signals that trigger adaptive motor responses to song disruptions<sup>10,11</sup> or reinforce exploratory motor gestures for vocal learning<sup>12</sup>.

The field L region and the caudolateral mesopallium (CLM) are interconnected brain areas not part of the traditional song-control system and are analogous to the auditory cortex in mammals in that they receive the main stream of auditory input from the thalamus, as well as feedback from motor-related areas<sup>13–17</sup>. Neurons in field L and CLM of awake and anaesthetized animals respond robustly to a large variety of auditory stimuli such as white noise, the bird's own song (BOS), and conspecific songs<sup>18–21</sup>. These features make field L and CLM potential substrates for the integration of self-generated and external sounds and for monitoring singing-related auditory feedback. To explore this hypothesis, we made extracellular recordings from CLM and field L neurons in juvenile male zebra finches using chronically implanted miniature motorized microdrives (Supplementary Fig. 1). Our strategy was first to probe singing-related firing in these neurons for evidence of motor-specific processing beyond passive auditory responses elicited by playback of the BOS, and then to investigate the feedback sensitivity of singing-related spikes by delivering brief acoustic stimuli during singing.

Singing and playback-related firing was similar in most cells (Fig. 1a), despite the large differences in sound amplitudes in vocal

and playback conditions and despite the variable direction of the playback source relative to the bird's head. Average firing rates in vocal and playback conditions were typically above baseline rates (Fig. 1b) and were highly correlated ( $r = 0.77$ ,  $P < 10^{-10}$ ,  $n = 92$ ; Supplementary Figs 2 and 3). Firing rates were also well matched

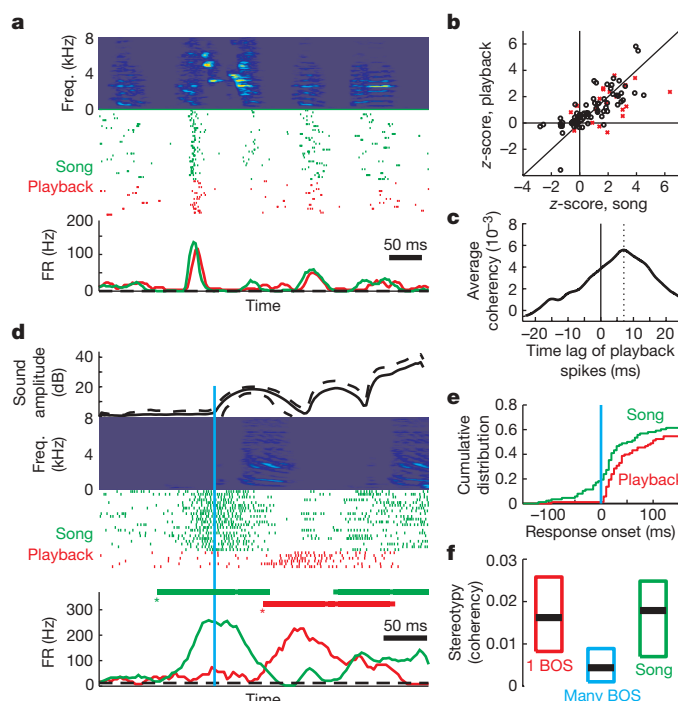


**Figure 1 | Comparison of active responses with passive responses.** Active responses were similar to passive responses, but were more stereotyped and slightly anticipatory. **a**, Activity during song (green rasters) leads activity during BOS playback (red rasters) in this example neuron. Top: spectrogram of an example song motif (high sound amplitudes in red and low amplitudes in blue). Bottom: average firing rate (FR) curves. **b**, Scatter plot of firing rates (z-scores) in individual cells. Cells were stimulated with one version (black circles) or many versions (red crosses) of the BOS. **c**, The mean coherency function between singing- and playback-related spike trains peaked 6.8 ms (dotted line) after singing-related spikes. **d**, The spike rasters in this neuron are anticipatory to song onset (blue line) and delayed relative to playback onset. Significant deviations from baseline firing are marked by green and red horizontal bars, and onset times are indicated by asterisks. Top: mean sound amplitude (solid line) plus/minus standard deviation (dashed line). **e**, Cumulative distribution of response onset times. **f**, Median firing stereotypy (black bars) during song ( $n = 92$ ) is similar to stereotypy during playback of a single BOS ( $n = 24$ ) but higher than stereotypy during playback of many versions of the BOS ( $n = 68$ ). Second and third quartiles are shown by coloured boxes.

<sup>1</sup>Institute of Neuroinformatics, University of Zurich/ETH Zurich, Winterthurerstrasse 190, 8057 Zurich, Switzerland.



on a finer timescale. In 69 of 92 cells, the spike-coherency function<sup>22,23</sup> averaged over all pairings of song and playback trials displayed a significant peak ( $>2$  jackknife standard deviations above zero) within  $\pm 20$  ms. The peak of the mean coherency function (averaged over 92 cells) was significant and occurred 6.8 ms after singing-related spikes (Fig. 1c), indicating that, overall, singing-related activity slightly preceded playback-evoked responses (only 0.5 ms of this lag can be explained by the closer proximity of the sound source to the bird's ears during singing). This anticipatory behaviour of singing-related activity suggests that in addition to auditory inputs, cells in field L and CLM also received inputs from a vocal-related, non-auditory source. Consistent with this view, in roughly one-fifth of the cells we observed firing increases before onset of the first introductory note of a song bout (Fig. 1d, e and Supplementary Fig. 4), which demonstrates a source of non-auditory drive in these cells during singing. Hence, some neurons seemed to integrate auditory with non-auditory signals, of which the latter may have reflected information about song-motor activity, for example as part of a motor estimate of auditory feedback.

Motor-specific processing was also evident by analysis of firing stereotypy, which was higher during singing than during playback of different versions of the BOS (Wilcoxon rank-sum (WRS) test,  $P < 10^{-8}$ ; Fig. 1f). This stereotypy difference could be attributed neither to intrinsic differences between song and playback stimuli (because the latter were copies of the former) nor to differences in average firing rates (Supplementary Fig. 3). By contrast, the firing stereotypy during singing did not differ significantly from the stereotypy during playback of one unique BOS stimulus (WRS test,

$P = 0.42$ ). Thus, singing-related firing stereotypy was higher than predicted by passive responses, but was commensurate with intrinsic synaptic noise, suggesting that auditory responses may be partly subsumed during singing by a motor-specific source of stereotyped synaptic input.

Brief acoustic stimuli delivered during singing provide an effective means of operant conditioning of song features<sup>11</sup>. Such stimuli are thus ideally suited to probing auditory feedback sensitivity. In 50% of song motifs (randomly selected) we applied a brief perturbing stimulus through a second loudspeaker that was time locked to a given syllable (see Methods, Fig. 2a and Supplementary Figs 5 and 6). In agreement with previous reports on adult birds<sup>6</sup>, we found that feedback perturbations did not induce immediate spectral or temporal changes in vocal output (all analyses were restricted to song motifs with conserved syllable sequences; see Supplementary Figs 7–9 and Methods).

We quantified the propensity of cells to respond to perturbations either in the vocal or the playback condition in terms of a response bias  $b$  confined to values between  $b = -1$  (no perturbation response during song) and  $b = 1$  (no perturbation response during playback). Similarly, we quantified the sensitivity of responses to perturbed feedback in terms of a selectivity  $s$  that was normalized to  $s = 0$  if the firing did not change during feedback perturbations and to  $s = 1$  if the firing doubled during perturbations (see Methods). Overall, 66 of 67 cells significantly responded to feedback or playback perturbations (54 of 67 to feedback, and 53 of 67 to playback; see Methods). Many cells responded robustly to perturbations in both conditions (Fig. 2b). However, almost 20% of cells had a strong playback bias

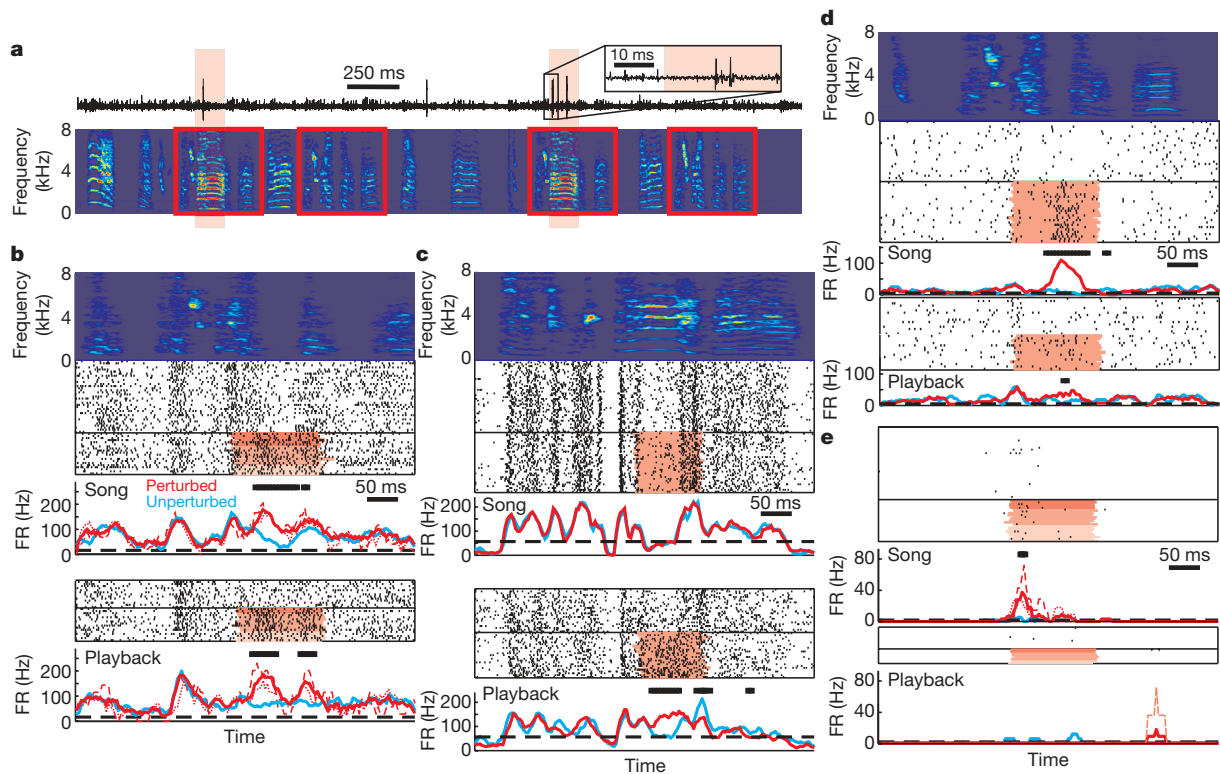


**Figure 2 | Example perturbation responses.** **a**, Bottom: spectrogram of a song that was twice perturbed by a long-call stimulus (red shading). Song motifs are delimited by red boxes. Top: extracellular voltage trace of a simultaneously recorded neuron (inset, spike burst). **b**, Neuron with increased firing during perturbation of song (top) and of BOS playback (bottom). Perturbing stimuli are indicated by red shaded areas; lighter shading corresponds to lower sound amplitudes. Average firing rate curves are shown for cases without perturbation (blue line) and with perturbation (solid red line; dashed and dotted red lines are averages over trials with high

and low perturbation amplitudes, respectively). Also shown are average spontaneous firing rate (dashed horizontal lines) and the times of significant perturbation responses (black horizontal bars).  $b = 0.0$ ,  $s = 0.42$ . **c**, As in **b**, but for a neuron that responds to perturbations only in the playback, but not the vocal condition.  $b = -0.95$ ,  $s = 0.0$ . **d**, **e**, Two feedback-sensitive neurons in the same bird with selective ( $b = 0.38$ ,  $s = 1.38$ ; **d**) and highly selective ( $b = 0.38$ ,  $s = 7.11$ ; **e**) responses for song perturbations (**e** shows the same cell as in **a**).

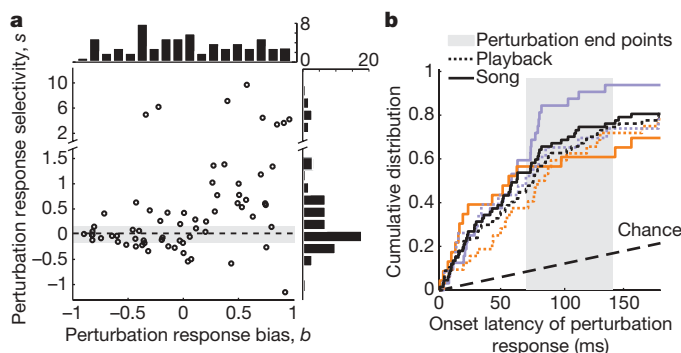


**Figure 3 | Summary of perturbation selectivity.** **a**, Scatter plot of bias,  $b$ , versus selectivity,  $s$  ( $n = 67$  cells, circles), the marginal distributions (histograms, showing number of cells), and the median chance selectivity (dashed line) with first and third quartiles (grey shading; see Methods). **b**, Cumulative distributions of perturbation-response onset latencies during song (solid lines) and playback (dotted lines). Latencies were widely distributed, both across all birds (black lines) and in two individual birds (orange and purple lines). The estimated contribution caused by random fluctuations is shown by the dashed line (labelled 'Chance'; see Methods), and the range of perturbation end points by the grey shaded area.

and small selectivity for distorted feedback ( $b < -0.5$  and  $|s| < 0.5$ ,  $n = 12$ ); these cells responded to playback perturbation, but did not respond to even high-intensity song perturbation (Fig. 2c). About 10% of cells showed very high selectivity for distorted feedback ( $s > 3$ ,  $n = 8$ ), and many of them tended to be quite unresponsive to perturbed playback (Fig. 2d, e and Supplementary Fig. 10a). Feedback perturbations predominantly induced firing increases ( $s > 0$ ), although we observed firing suppression in a few cells (Fig. 3a and Supplementary Fig. 10b, c). In both conditions, sound amplitudes during perturbation responses were significantly lower than average (Student's  $t$ -test,  $P < 10^{-10}$ ), in agreement with a monotonic relation between perturbation amplitude and response selectivity  $s$  (Supplementary Fig. 11). However, onset times of perturbation responses were widely distributed across cells (Fig. 3b), revealing a cell-specific temporal modulation of perturbation sensitivity.

In six of eight cells with selectivity  $s > 3$ , peak firing rates during perturbed song were more than three times higher than peak firing rates during unperturbed song (in the remaining two cells, peak firing rates were more than 40% higher). Thus, responses to perturbed feedback could largely exceed all of unperturbed singing-related activity, suggesting that high selectivity for distorted auditory feedback derives from a precisely timed and strongly coherent synaptic drive.

We also explored whether high selectivity was associated with suppression of neural activity during self-initiated vocalizations, because such suppression is a common gain-control mechanism found in the auditory brain areas of animals as diverse as crickets<sup>24</sup>, bats<sup>1</sup> and marmosets<sup>25</sup>. The baseline firing in highly selective cells ( $s > 3$ ) was lower than for all other cells (5.7 Hz versus 19.5 Hz,  $P = 0.028$ ; Supplementary Fig. 12a); nevertheless, highly selective cells were relatively more suppressed during singing (WRS test of equal median  $z$ -scores,  $P = 0.005$ ; Supplementary Fig. 12b).

In conclusion, field L and CLM responses equally reflect processing of self-generated and external auditory inputs, as made evident by the similarity of average firing rates in active and passive conditions (Fig. 1b and Supplementary Fig. 3), by the uniformly distributed bias index (Fig. 3a) and by similarity of onset-latency curves (Fig. 3b). Hence, the auditory forebrain seems to form an invariant representation of actively and passively perceived songs for integrating and comparing auditory feedback with the songs of other birds. Dissimilarities between active and passive sound processing were evident in terms of a motor-specific drive. Consequently, some neurons showed singing-related activity that resembled playback-evoked

activity but was insensitive to perturbed feedback. Such behaviour is reminiscent of auditory-vocal mirroring reported in HVC<sup>8</sup> neurons and could arise from corollary discharges elicited by an efference copy of motor commands. On the other hand, neurons that were largely quiescent during singing, except when the auditory signal was perturbed, are reminiscent of some neurons in primate auditory cortex that strongly respond to frequency-shifted auditory feedback<sup>26</sup>. Vocal-mirror spikes could contribute to the generation of highly perturbation-selective responses, provided that such spikes are able to precisely counterbalance the excitatory drive elicited by sensory feedback. We find some evidence for such counterbalancing in perturbation-selective neurons in terms of their relatively strong firing suppression during song, even though suppression was rare overall, unlike in monkey auditory cortex<sup>25</sup> and in an auditory ganglion of crickets<sup>24</sup> (note that in crickets, responses are not perturbation-selective, despite this suppression).

Relatively few cells specialized into highly selective perturbation detectors, yet their mere existence suggests that auditory feedback is analysed in the auditory forebrain with reference to an internal model (Supplementary Fig. 13). For example, vocal mirror responses could represent predicted auditory feedback, which helps the bird to generate a stable perception of its song in the midst of a noisy colony. Accordingly, highly feedback-sensitive responses would reflect prediction errors of auditory feedback; such errors could signal song disruptions or simplify vocal learning, according to some forward-model theories<sup>27</sup>. Alternatively, given that the birds in our study were in the process of learning a tutor song, vocal mirroring could constitute online replay of the tutor memory, as evidenced by similar firing stereotypies during song and during playback of a single song template (Fig. 1f). Similarity of vocal and playback-related firing could thus be a reflection of a good match between the actual song and the memorized auditory template, of which the latter may feed into CLM and field L through the caudomedial nidopallium<sup>28,29</sup>. According to such a template-replay interpretation, responses in highly perturbation-selective neurons represent performance errors signalling the dissimilarity between the perturbed song and the tutor memory, a property with obvious benefits for song learning<sup>12,27</sup>. The ability of birds to correlate perturbations with subtle motor variability<sup>11</sup> suggests a functional connection between perturbation-selective neurons and premotor neurons, although a direct link between perturbation selectivity and song learning remains to be observed.

## METHODS SUMMARY

**Subjects and electrophysiology.** All experiments were carried out in accordance with protocols approved by the Veterinary Office of the Canton of Zurich, Switzerland. Data were collected from six juvenile male zebra finches (60–92 days old). Microdrives with three independent electrodes were implanted 1.1–2.1 mm anterior and 1.5–2.0 mm lateral of the midsagittal sinus (under a fixed head angle of 70° or 90°) using methods previously described<sup>30</sup>. After each experiment, the brain was removed for histological examination of unstained slices to verify the location of reference lesions. Neurons were classified as putative CLM or putative field L based on anatomical location<sup>15</sup>.

**Data analysis.** Differences between average firing rates in unperturbed and perturbed trials were assessed using a WRS test ( $P = 0.05$ ) on the number of spikes in 30-ms time windows. Windows were shifted in 5-ms steps and only sequences of at least two subsequent windows with  $P < 0.05$  were considered significantly different.

We defined the response bias as  $b = (|d_t| - |d_p|) / (|d_t| + |d_p|)$ , where  $d_t$  is the feedback perturbation response and  $d_p$  is the playback perturbation response, each defined as the difference in average firing rates between perturbed and unperturbed conditions in a time window extending from the time of onset of perturbation up to 50 ms after perturbation ends. We defined the response selectivity as  $s = d_t / r_s$ , where  $r_s$  is the average firing rate during unperturbed song motifs.

The stereotypies of singing and playback-related spike patterns were assessed using the average coherency of spike rasters at zero time lag (sound traces were aligned by the amplitude onset of the detected syllable). Differences between singing and playback-related firing stereotypies were detected using a WRS test (same BOS,  $P = 0.3$ ; different BOS,  $P < 10^{-7}$ ).

**Full Methods** and any associated references are available in the online version of the paper at [www.nature.com/nature](http://www.nature.com/nature).

**Received 13 May; accepted 29 September 2008.**

**Published online 12 November 2008.**

1. Marler, P. & Tamura, M. Culturally transmitted patterns of vocal behavior in sparrows. *Science* **146**, 1483–1486 (1964).
2. Thorpe, W. H. The biological significance of duetting and antiphonal song. *Acta Neurobiol. Exp. (Wars.)* **35**, 517–528 (1975).
3. Konishi, M. The role of auditory feedback in the control of vocalization in the white-crowned sparrow. *Z. Tierpsychol.* **22**, 770–783 (1965).
4. Brainard, M. S. & Doupe, A. J. Auditory feedback in learning and maintenance of vocal behaviour. *Nature Rev. Neurosci.* **1**, 31–40 (2000).
5. Immelman, K. in *Bird Vocalizations* (ed. Hinde, R. A.) 61–74 (Cambridge Univ. Press, 1969).
6. Leonardo, A. Experimental test of the birdsong error-correction model. *Proc. Natl Acad. Sci. USA* **101**, 16935–16940 (2004).
7. Kozhevnikov, A. A. & Fee, M. S. Singing-related activity of identified HVC neurons in the zebra finch. *J. Neurophysiol.* **97**, 4271–4283 (2007).
8. Prather, J. F., Peters, S., Nowicki, S. & Mooney, R. Precise auditory–vocal mirroring in neurons for learned vocal communication. *Nature* **451**, 305–310 (2008).
9. Rizzolatti, G. & Craighero, L. The mirror-neuron system. *Annu. Rev. Neurosci.* **27**, 169–192 (2004).
10. Leonardo, A. & Konishi, M. Decrystallization of adult birdsong by perturbation of auditory feedback. *Nature* **399**, 466–470 (1999).
11. Tumer, E. C. & Brainard, M. S. Performance variability enables adaptive plasticity of ‘crystallized’ adult birdsong. *Nature* **450**, 1240–1244 (2007).
12. Fiete, I. R., Fee, M. S. & Seung, H. S. Model of birdsong learning based on gradient estimation by dynamic perturbation of neural conductances. *J. Neurophysiol.* **98**, 2038–2057 (2007).
13. Karten, H. J. The ascending auditory pathway in the pigeon (*Columba livia*). II. Telencephalic projections of the nucleus ovoidalis thalami. *Brain Res.* **11**, 134–153 (1968).
14. Nottebohm, F., Kelley, D. B. & Paton, J. A. Connections of vocal control nuclei in the canary telencephalon. *J. Comp. Neurol.* **207**, 344–357 (1982).
15. Vates, G. E., Broome, B. M., Mello, C. V. & Nottebohm, F. Auditory pathways of caudal telencephalon and their relation to the song system of adult male zebra finches. *J. Comp. Neurol.* **366**, 613–642 (1996).
16. Foster, E. F. & Bottjer, S. W. Axonal connections of the high vocal center and surrounding cortical regions in juvenile and adult male zebra finches. *J. Comp. Neurol.* **397**, 118–138 (1998).
17. Zeng, S., Zhang, X., Peng, W. & Zuo, M. Immunohistochemistry and neural connectivity of the Ov shell in the songbird and their evolutionary implications. *J. Comp. Neurol.* **470**, 192–209 (2004).
18. Cardin, J. A. & Schmidt, M. F. Song system auditory responses are stable and highly tuned during sedation, rapidly modulated and unselective during wakefulness, and suppressed by arousal. *J. Neurophysiol.* **90**, 2884–2899 (2003).
19. Bauer, E. E. *et al.* A synaptic basis for auditory–vocal integration in the songbird. *J. Neurosci.* **28**, 1509–1522 (2008).
20. Janata, P. & Margoliash, D. Gradual emergence of song selectivity in sensorimotor structures of the male zebra finch song system. *J. Neurosci.* **19**, 5108–5118 (1999).
21. Amin, N., Grace, J. A. & Theunissen, F. E. Neural response to bird’s own song and tutor song in the zebra finch field L and caudal mesopallium. *J. Comp. Physiol. A* **190**, 469–489 (2004).
22. Kimpo, R. R., Theunissen, F. E. & Doupe, A. J. Propagation of correlated activity through multiple stages of a neural circuit. *J. Neurosci.* **23**, 5750–5761 (2003).
23. Hahnloser, R. H., Kozhevnikov, A. A. & Fee, M. S. Sleep-related neural activity in a premotor and a basal-ganglia pathway of the songbird. *J. Neurophysiol.* **96**, 794–812 (2006).
24. Poulet, J. F. & Hedwig, B. The cellular basis of a corollary discharge. *Science* **311**, 518–522 (2006).
25. Eliades, S. J. & Wang, X. Sensory–motor interaction in the primate auditory cortex during self-initiated vocalizations. *J. Neurophysiol.* **89**, 2194–2207 (2003).
26. Eliades, S. J. & Wang, X. Neural substrates of vocalization feedback monitoring in primate auditory cortex. *Nature* **453**, 1102–1106 (2008).
27. Jordan, M. I. & Rumelhart, D. E. Forward models: Supervised learning with a distal teacher. *Cogn. Sci.* **16**, 307–354 (1992).
28. Phan, M. L., Pytte, C. L. & Vicario, D. S. Early auditory experience generates long-lasting memories that may subserve vocal learning in songbirds. *Proc. Natl Acad. Sci. USA* **103**, 1088–1093 (2006).
29. London, S. E. & Clayton, D. F. Functional identification of sensory mechanisms required for developmental song learning. *Nature Neurosci.* **11**, 579–586 (2008).
30. Fee, M. S. & Leonardo, A. Miniature motorized microdrive and commutator system for chronic neural recording in small animals. *J. Neurosci. Methods* **112**, 83–94 (2001).

**Supplementary Information** is linked to the online version of the paper at [www.nature.com/nature](http://www.nature.com/nature).

**Acknowledgements** This work was supported by a Swiss National Science Foundation Professorship Grant to R.H.R.H. We thank K. Martin, R. Mooney and R. Douglas for comments on the manuscript.

**Author Contributions** G.B.K. performed the experiments and analysed the data. Both authors wrote the manuscript.

**Author Information** Reprints and permissions information is available at [www.nature.com/reprints](http://www.nature.com/reprints). Correspondence and requests for materials should be addressed to R.H.R.H. ([rich@ini.phys.ethz.ch](mailto:rich@ini.phys.ethz.ch)).



## METHODS

**Electrophysiology.** To maximize the experimental yield, microdrives were equipped with a lateral positioner that allowed for electrode displacement parallel to the brain surface. We recorded from 92 cells during song and playback of the BOS at physiological sound levels at which birds hear each other's songs; in 67 of these we also performed perturbation experiments.

**Experimental design.** During recording sessions, birds were housed in a sound isolation chamber equipped with a microphone and two loudspeakers (for playback of the BOS and perturbing stimuli) in a triangular arrangement around the centre of the experimental cage (distance, 25 cm). For each bird, the sound amplitudes of BOS stimuli as recorded with the microphone were matched to those of songs.

Sound amplitudes of perturbations were 6 dB above the maximum sound amplitude of BOS stimuli (both measured at the microphone). For each cell, we first determined the perturbing stimulus that elicited the largest response when presented in isolation and then used this stimulus for the rest of the experiment. If none of the stimuli triggered any noticeable response, we used the long-call stimulus. Perturbing stimuli were white noise (3 out of 67 cells), an introductory note (5 out of 67 cells) or a long call (59 out of 67 cells) (Supplementary Fig. 5). The microphone signal was fed to a custom-made, real-time song recognizer that detected the first stereotypic syllable of song motifs using a two-layer neural network trained on spectrotemporal song data. In 50% of detections, a perturbation was delivered. Offline analysis revealed that perturbation onsets had a standard deviation of 4.3 ms relative to syllable onset (aligned by threshold crossing of sound amplitude). Because our subjects were juvenile birds with developing songs, we recorded BOS stimuli less than one day before each experimental session. A set of 10–20 songs was used for BOS playback experiments. Perturbations were confined to recording sessions only (lasting roughly 0.5–2 hours each) to minimize possible effects of song deterioration. BOS playbacks were interspersed with songs as much as possible; we ignored all data in which birds countersang with song playback.

**Data analysis.** Extracellular voltage traces were digitized at 33 kHz and recorded for offline spike sorting. Firing rates were calculated in 5-ms bins and averaged over multiple renditions or playbacks of the motif. In addition, firing rate curves in Figs 1a, d, 2b–e and Supplementary Figs 4 and 10 were smoothed with a 10-ms Gaussian kernel.

In the plot of cumulative distributions of response-onset times in Fig. 3b, we depicted the estimated chance-related distribution with a dashed black line. The slope of this distribution corresponded to the fraction of neurons with significant firing rate differences between perturbed and unperturbed trials in intervals 50–150 ms prior to perturbation.

To examine dependences of the response bias,  $b$ , and selectivity,  $s$ , on perturbation (sound) amplitudes, we occasionally presented the perturbing stimulus at sound pressure levels differing by  $\pm 6$  dB from normal levels ( $n = 40$  cells; Fig. 2a and Supplementary Fig. 11). Excluding either the high- or low-intensity trials led to only small changes in  $b$  and  $s$  (median absolute change in  $b$ , 0.16; median absolute change in  $s$ , 0.16).

To estimate the fraction of the response selectivity that was caused by small sample sizes but not by perturbations, we computed a chance response selectivity  $s_c = d_c/r_s$ , where  $d_c$  is the difference in average firing rates between perturbed and unperturbed conditions in a time window preceding the perturbation window. The median, as well as the second and third quartiles of  $s_c$  are shown in Fig. 3a by the dashed line and the grey shaded surface, respectively.

To assess changes from background firing, we calculated the  $z$ -score of song/playback responses as

$$z = \frac{\mu_s - \mu_b}{\sqrt{\sigma_s^2 + \sigma_b^2 - 2\text{cov}(S, B)}}$$

where  $\mu_s$  is the average firing rate during song/playback,  $\mu_b$  is the average baseline firing rate assessed in 1–3-s silent intervals interleaved between playbacks and songs, and  $\sigma_s$  and  $\sigma_b$  are the respective standard deviations. Owing to a lack of pairing of vocal and playback conditions, we set the covariance term  $\text{cov}(S, B)$  to 0. We considered cells with a  $z$ -score higher than 0.75 to be significantly excited, and cells with a  $z$ -score less than  $-0.75$  to be significantly inhibited (the criterion  $|z\text{-score}| > 0.75$  corresponds to  $P < 0.05$  if the number of trials is larger than five, which was the case for all our cells).

The dashed lines in the scatter plot of average firing rates in song and playback conditions (Supplementary Fig. 3) are linear regressions (passing through the origin) for two sets of neurons: (1) neurons recorded during multiple playbacks of one unique song bout consisting of two motifs (red); (2) neurons recorded during playback of a set of 20 different song bouts (black).

# Myelomonocytic cell recruitment causes fatal CNS vascular injury during acute viral meningitis

Jiyun V. Kim<sup>1\*</sup>, Silvia S. Kang<sup>2\*</sup>, Michael L. Dustin<sup>1</sup> & Dorian B. McGavern<sup>2</sup>

**Lymphocytic choriomeningitis virus<sup>1</sup> infection of the mouse central nervous system (CNS) elicits fatal immunopathology through blood–brain barrier breakdown<sup>2</sup> and convulsive seizures<sup>3</sup>. Although lymphocytic-choriomeningitis-virus-specific cytotoxic T lymphocytes (CTLs) are essential for disease<sup>4</sup>, their mechanism of action is not known. To gain insights into disease pathogenesis, we observed the dynamics of immune cells in the meninges by two-photon microscopy. Here we report visualization of motile CTLs and massive secondary recruitment of pathogenic monocytes and neutrophils that were required for vascular leakage and acute lethality. CTLs expressed multiple chemoattractants capable of recruiting myelomonocytic cells. We conclude that a CD8<sup>+</sup> T-cell-dependent disorder can proceed in the absence of direct T-cell effector mechanisms and rely instead on CTL-recruited myelomonocytic cells.**

To examine the dynamics of lymphocytic choriomeningitis virus (LCMV)-specific CTLs, we transferred  $1 \times 10^5$  naive green fluorescent protein (GFP)-tagged T-cell receptor (TCR) transgenic CD8<sup>+</sup> T cells (GFP<sup>+</sup> P14 cells) into B6 mice one day before intracerebral (i.c.) inoculation with LCMV Armstrong. Naive CD8<sup>+</sup> T cells obtained from GFP<sup>+</sup> P14 transgenic mice express GFP under the  $\beta$ -actin promoter and express a TCR that recognizes the LCMV glycoprotein (amino acids 33–41) presented in H-2D<sup>b</sup>. Two-photon microscopy (TPM) was performed through a thinned skull window to visualize the meninges overlying the visual cortex in asymptomatic (day 5) and symptomatic (day 6) mice (Fig. 1 and Supplementary Movie 1). In contrast to the few P14 cells observed on day 5 (Fig. 1a), the number of GFP<sup>+</sup> P14 cells was notably increased in the meninges and perivascular regions on day 6 (Fig. 1b, c). To determine whether GFP<sup>+</sup> P14 cells were engaging in antigen-specific interactions, we analysed their motion in the presence of control antibody (immunoglobulin G, IgG) or a blocking monoclonal antibody to D<sup>b</sup> (anti-class I) introduced into the subarachnoid space through a small craniotomy (Fig. 1d–i). P14 speed averaged  $3.41 \pm 0.27 \mu\text{m min}^{-1}$  (mean  $\pm$  s.e.m.) in the absence of the craniotomy and  $3.04 \pm 0.33 \mu\text{m min}^{-1}$  in the presence of the craniotomy and IgG (Fig. 1j). The anti-class I antibody significantly increased ( $*P < 0.0001$ ) the speed of P14 cells to  $5.16 \pm 0.46 \mu\text{m min}^{-1}$  (Fig. 1j, k) and decreased the arrest coefficient (Fig. 1l), but did not influence the speed of CTLs specific for an irrelevant antigen (Supplementary Fig. 1). This significant change in P14 cell speed and arrest after anti-class I treatment was observed in all mice examined and did not depend on CTL abundance (Supplementary Fig. 2). GFP<sup>+</sup> P14 CTL migration appeared random (Supplementary Fig. 3), with confined motion at longer times that was reversed by anti-class I antibodies. Comparison of the speed distributions showed that the entire population shifts after anti-class I treatment (Fig. 1k), suggesting that all GFP<sup>+</sup> P14 cells encountered antigen. Despite this high frequency of antigen encounter, CTLs rarely

synapsed with any one target for  $>10$  min (Fig. 1g, m). These intravital observations raised questions about the infected target population and the CTL effector mechanisms used during fatal meningitis.

We identified the LCMV-infected cells through immunohistochemical studies (Fig. 2, Supplementary Fig. 4 and Supplementary Movie 2). The main LCMV-infected population in the meninges and around meningeal vasculature was ER-TR7<sup>+</sup> stromal cells. LCMV infection was occasionally observed in CD45<sup>+</sup> infiltrating leukocytes and astrocytic foot processes that comprise the glial limitans (Supplementary Fig. 4). Infection of endothelium, smooth muscle cells and pericytes was never observed (Supplementary Fig. 4). ER-TR7<sup>+</sup> stromal cells support rapid migration of CD8<sup>+</sup> and CD4<sup>+</sup> T cells in lymph nodes<sup>5</sup> and may provide strong chemokinetic signals that can overwhelm synapse forming stop signals<sup>6</sup>. This might explain the paucity of antigen-specific arrest (Fig. 1).

Because CD8<sup>+</sup> T cells are essential for pathology<sup>4</sup>, we evaluated several CTL effector mechanisms using genetic knockout and mutant mice (Fig. 3a). Surprisingly, mice with single deficiencies in all major CTL effector pathways—interferon- $\gamma$  receptor, tumour necrosis factor- $\alpha$ , Fas, granzymes, perforin and the degranulation pathway (*Jinx*, also known as *Unc13d*, mutant)—succumbed to the convulsive seizures observed after LCMV infection of wild-type mice. The delay in disease onset observed in perforin-knockout mice was recently attributed to slower CTL recruitment into the central nervous system (CNS)<sup>7</sup>. These data supported the imaging studies in suggesting that CTL effector functions might not be responsible for rapid-onset disease.

To investigate other effectors, we temporally examined the composition of the CNS infiltrate after i.c. LCMV infection (Fig. 3b and Supplementary Fig. 5). Baseline populations prevailed until day 6, at which point monocytes and macrophages were massively recruited into the CNS. A low number of these cells preceded the arrival of CTLs by 2 days. At day 6 a small increase in the number of neutrophils, CD4<sup>+</sup> T cells and B cells was also observed; however, the latter two populations are not required for disease<sup>8,9</sup>. It should be noted that our methodology accounts primarily for extravasated leukocytes, because cells arrested in the vasculature (for example, neutrophils) are expunged during intracardiac saline perfusions. Nevertheless, our results demonstrate a minimal innate cellular response to the virus alone and massive recruitment of myelomonocytic cells that coincided with the arrival of CTLs at day 6.

We next asked whether monocytes and/or neutrophils were required for the seizure-induced death on day 6 (Fig. 3c–f). Neutrophil depletion with low-dose anti-Gr-1 (also known as anti-Ly6g) antibody<sup>10</sup> (Fig. 3c, d) or monocyte infiltration blockade using chemokine receptor 2 (CCR2)-deficient mice<sup>11</sup> (Fig. 3e, f) had no effect on the nature or kinetics of death. Therefore, we hypothesized that both populations might have the potential to induce CNS injury. To test this hypothesis, we depleted monocytes and neutrophils

<sup>1</sup>Program in Molecular Pathogenesis, Helen L. and Martin S. Kimmel Center for Biology and Medicine, Skirball Institute of Biomolecular Medicine, New York University School of Medicine, New York, New York 10016, USA. <sup>2</sup>Department of Immunology and Microbial Sciences, The Scripps Research Institute, La Jolla, California 92037, USA.

\*These authors contributed equally to this work.

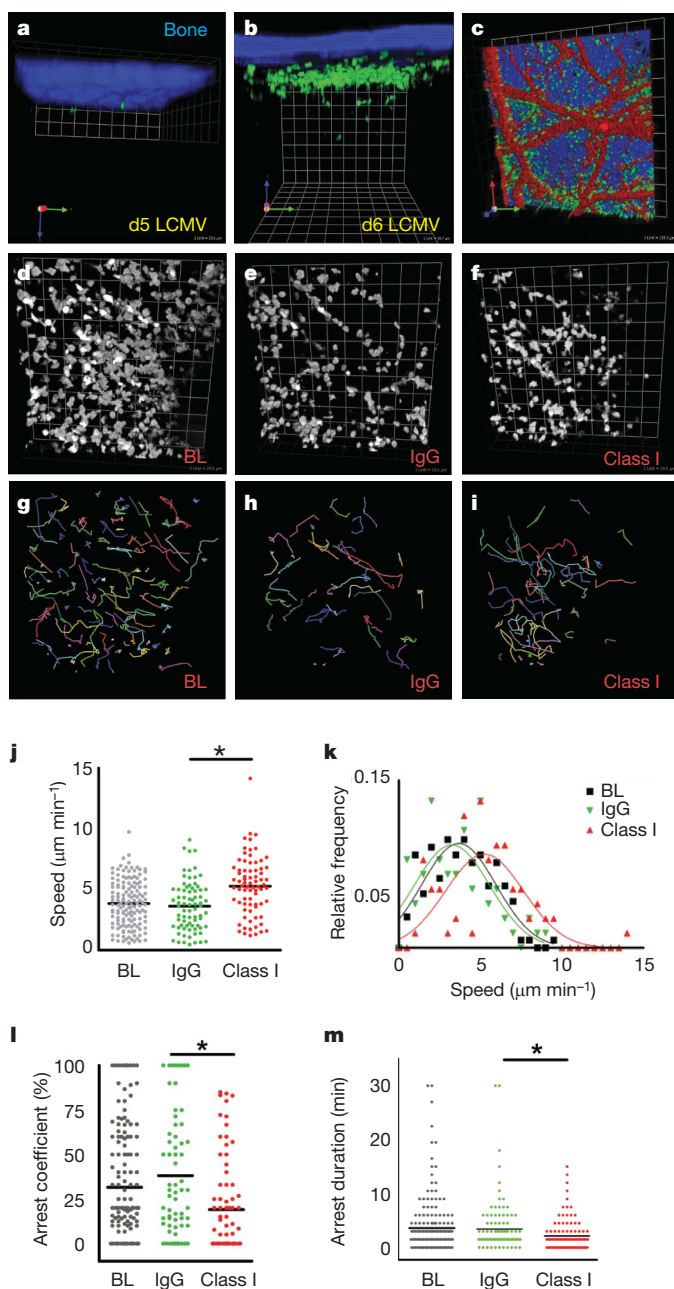


**Figure 1** | CTL localization and dynamics in the meninges of LCMV-infected mice. **a, b**, A representative three-dimensional reconstruction of an intravital two-photon z-stack viewed through a thinned skull is shown for representative mice at day 5 (**a**) and day 6 (**b**) post-infection. Few GFP<sup>+</sup> P14 CTLs (green) were observed in the meninges at day 5 post-infection. At day 6 post-infection, GFP<sup>+</sup> P14 CTLs were confined to a 50- $\mu$ m meningeal space between the undersurface of the skull bone (blue) and the pial surface. Very few CTLs entered the parenchyma. Grid scale is 19.7  $\mu$ m. **c**, A representative three-dimensional reconstruction shows that GFP<sup>+</sup> P14 CTLs (green) localized preferentially along meningeal vasculature (red) at day 6. Skull bone is blue. Grid scale is 119  $\mu$ m. **d–i**, Representative xy-plane thinned skull images of GFP<sup>+</sup> P14 cells at day 6 post-infection (grey scale; **d–f**); corresponding 30-min time-lapse cell tracks (coloured lines; **g–i**) are shown below each image. (Representative xz-plane images are shown in Supplementary Fig. 1.) Note the highly dynamic motion of the CTLs in the meningeal surface at baseline (BL; **d, g**) and after injection of 10  $\mu$ g ml<sup>-1</sup> IgG isotype control (IgG; **e, h**) or anti-H-2D<sup>b</sup> antibody (Class I; **f, i**). Grid scale is 29.6  $\mu$ m. **j–m**, Compared with baseline and IgG isotype control, class I inhibition induced a statistically significant ( $P < 0.0001$ ) change in average speed (**j**), arrest coefficient (**l**) and arrest duration (**m**) for GFP<sup>+</sup> P14 CTLs. Primary velocity data shown in **j** are plotted as histograms using 0.5  $\mu$ m min<sup>-1</sup> bins and a Gaussian curve fit (**k**). See corresponding Supplementary Movie 1 and Supplementary Fig. 1.

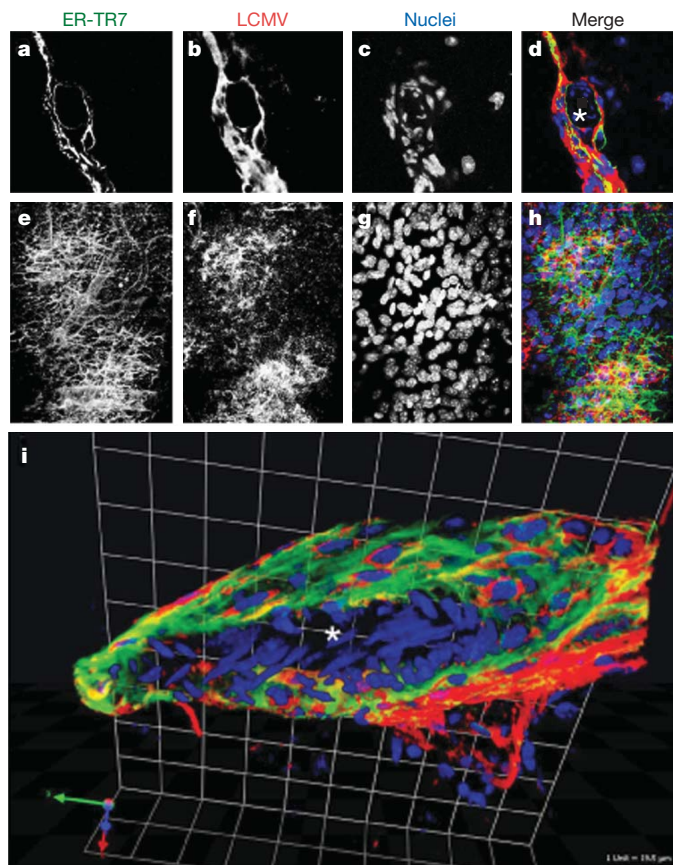


**Figure 2** | LCMV infection of ER-TR7<sup>+</sup> stromal cells in the meninges. **a–d**, A representative two-dimensional image (**a–d**) and a maximal projection of a three-dimensional z-stack (**e–h**) are shown for a mouse at day 6 post-infection. Both images were captured using a one-photon confocal microscope. Note the localization of LCMV (red) to ER-TR7<sup>+</sup> fibroblast-like cells (green) that line the meninges and meningeal vasculature. A cross section of a meningeal blood vessel is denoted with a white asterisk in **d, e–h** depict a top-down view of a large meningeal blood vessel in which the network of fibroblast processes are clearly visible and infected by LCMV. **i**, A three-dimensional reconstruction of a meningeal blood vessel cross section (centre denoted with a white asterisk) is shown to illustrate the degree to which LCMV infects fibroblast-like cells that completely surround meningeal blood vessels. Grid scale is 19.5  $\mu$ m. Cell nuclei are shown in blue in all merged panels. ER-TR7 is shown in green and LCMV in red. See corresponding Supplementary Movie 2 and Supplementary Fig. 3.

simultaneously by administering high-dose anti-Gr-1 to CCR2-knockout mice (Fig. 3e, f). When both cell populations were depleted, seizure-induced death at day 6 was averted and survival was extended by 3 days (Fig. 3e, f), despite a normal frequency of virus-specific CTLs on day 6 (data not shown). These data suggested that myelomonocytic cells were highly pathogenic and were responsible for the rapid-onset seizure-induced death observed at day 6.

During TPM analyses of GFP<sup>+</sup> P14 cells, we often noted that the vasculature appeared ragged and displayed plasma leakage tracked with intravascular-injected quantum dots (Fig. 4a–d and Supplementary Movie 3). We considered that the seizure-induced death at day 6 might be induced by vascular leakage caused by myelomonocytic cells. To test this possibility, we conducted TPM in LCMV-infected lysozyme M (LysM)–GFP mice, in which neutrophils and monocytes were labelled with GFP, to detect the relationship between myelomonocytic extravasation and vascular leakage. There was a tight correlation between locally synchronized LysM–GFP<sup>+</sup> cell extravasation and vascular leakage on day 6 (Fig. 4e–h and Supplementary Movie 4).

To determine the relative contribution of neutrophils versus monocytes to vascular injury, we imaged LysM–GFP mice injected



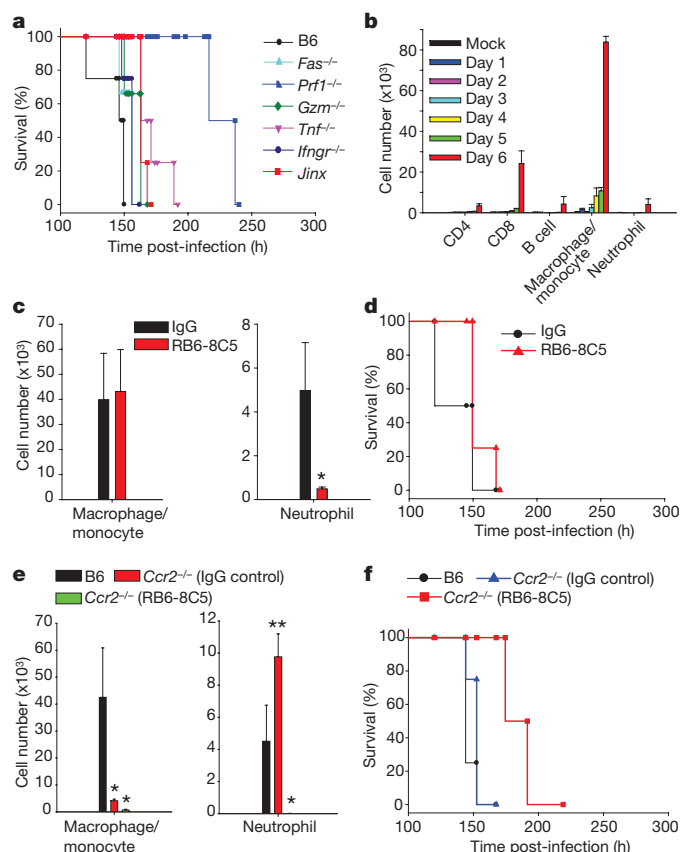


**Figure 3 | Analysis of mononuclear cell infiltrate and effector mechanisms during LCMV-induced meningitis.** **a**, Survival was monitored in mice deficient in all major CTL effector pathways. All infected knockout mice developed convulsive seizures and succumbed to LCMV-induced meningitis. A slight extension (13 h,  $P = 0.029$ ) in survival was observed in tumour necrosis factor- $\alpha$  (*Tnf*) knockout and *Jinx* mice when compared to wild type C57BL/6 (B6) controls. As reported previously, perforin (*Prf1*) deficient mice survived until day 9 ( $P = 0.029$ ). No extension in survival was observed in mice deficient in granzymes (*Gzm*), interferon- $\gamma$  receptor (*Ifng*) and Fas. **b**, The composition of the CNS mononuclear cell infiltrate was examined flow cytometrically at the denoted time points after LCMV infection. A massive influx of CTLs ( $CD45^{+}Thy1.2^{+}CD8^{+}$ ) and peripheral monocytes ( $CD45^{hi}Thy1.2^{-}CD11b^{+}Gr-1^{int}$ ) into the CNS was observed only at day 6 post-infection. Low numbers of neutrophils ( $CD45^{int}Thy1.2^{+}CD11b^{+}Gr-1^{hi}$ ), B cells ( $CD45^{+}Thy1.2^{+}CD19^{+}$ ) and CD4 T cells ( $CD45^{+}Thy1.2^{+}CD4^{+}$ ) were also observed in the CNS at day 6 post-infection. See Supplementary Fig. 5 for examples of flow cytometric data. **c**, **d**, Injection of low-dose anti-Gr-1 antibody (RB6-8C5, 125  $\mu$ g intraperitoneally on day 4) achieved depletion of neutrophils from the CNS (**c**), but did not improve survival (**d**) compared to control mice treated with rat IgG. **e**, **f**, CCR2 deficiency did not improve survival (**f**) after i.c. LCMV infection when compared to wild-type B6 controls; however, flow cytometric studies revealed a compensatory increase in the number of CNS neutrophils (**e**) in CCR2-knockout mice at day 6. Survival was significantly extended ( $P = 0.029$ ) in LCMV-infected CCR2-deficient mice that received high-dose anti-Gr-1 antibody (**f**). The frequency of P14 CTLs gated on  $CD45^{hi}$  cells was not significantly reduced after anti-Gr-1 treatment (data not shown). For all studies described,  $n = 4$  mice per group were used. Asterisks denote statistical significance ( $P < 0.05$ ). Bar graph data are represented as the mean and s.d.

with low-dose anti-Gr-1 antibody, which depletes only neutrophils (Fig. 3c and Supplementary Fig. 6). Interestingly, synchronous extravasation of LysM-GFP<sup>+</sup> cells was not observed in low-dose Gr-1-depleted mice (Fig. 4i–l and Supplementary Movie 5), suggesting that synchronously extravasating LysM-GFP<sup>+</sup> cells are neutrophils. In neutrophil-depleted LysM-GFP mice, we observed perivascular LysM-GFP<sup>+</sup> cells (that is, monocytes and macrophages) in areas of transient vascular leakage. Unlike neutrophils that display

intravascular accumulation followed by explosive extravasation with vascular leakage, the monocytes accumulated more gradually in vascular sites that nonetheless displayed leakage. Statistically, sustained vascular leakage was only correlated ( $r = 0.99$ ;  $P < 0.0001$ ) with neutrophils (Fig. 4m). The presence of intra- or extra-vascular P14 CTLs was not associated with either pattern of vascular leakage (Fig. 4o). Quantum dot leakage was not observed on day 5 post-infection (Fig. 4p), despite low numbers of infiltrating monocytes (Fig. 3b). Vascular injury occurred only at day 6 post-infection and extended into the brain parenchyma (Fig. 4q). Myelomonocytic cells were restricted to the meninges on day 6 (Fig. 4q, r and Supplementary Fig. 10).

The impact of myelomonocytic cells on vascular injury was further assessed by quantifying leakage of Evans blue dye into the brain (Supplementary Fig. 7). Only mice depleted of both monocytes and neutrophils showed significant ( $P < 0.001$ ) preservation of vascular integrity at day 6 post-infection (Supplementary Fig. 7e, f). Depletion of monocytes (Supplementary Fig. 7d, f) or neutrophils (Supplementary Fig. 7c, f) alone failed to prevent Evans blue leakage. Interestingly, in untreated wild-type mice at day 6 post-infection, we observed substantial leakage of Evans blue from meningeal blood vessels into the brain parenchyma (Supplementary Fig. 8), reflecting disrupted blood–brain barrier (BBB) integrity, which has the potential to cause severe seizures<sup>12</sup>.

To examine a potential mechanism by which CTLs attract myelomonocytic cells, we used gene arrays to quantify differentially regulated transcripts in the brains of mock- versus day 6 LCMV-infected mice. Our results revealed a statistically significant increase ( $P < 0.05$ ) in six chemokines (CCL2, 7.3-fold; CCL3, 8.1-fold; CCL4, 1.6-fold; CCL5, 5.6-fold; CCL7, 4.2-fold; CXCL2, 2.8-fold) and two chemokine receptors (CCR1, 2.6-fold; CCR2, 3.6-fold) that can recruit myelomonocytic cells into the CNS. Because it was reported that none of these chemokines were observed in the CNS of T-cell-deficient mice infected i.c. with LCMV<sup>13</sup>, we next used flow cytometry to examine which of these chemokines were produced by virus-specific P14 cells (Supplementary Fig. 9). Our flow cytometric analyses of CNS and splenic P14 CTLs at day 6 revealed that CCL3, CCL4 and CCL5 were all produced at the protein level, which was confirmed using gene arrays<sup>14,15</sup>. Both CCL3 and CCL4 required GP<sub>33–41</sub> peptide stimulation for maximum synthesis, whereas CCL5 was produced on differentiation from naive to effector cells and was not further upregulated on peptide stimulation.

It is well known that CD8<sup>+</sup> T cells are required for LCMV-induced meningitis<sup>4</sup> and vascular leakage<sup>16</sup>. Our results revealed that P14 CTLs produce three of the chemokines with the potential to attract the myelomonocytic cells responsible for vascular injury (Fig. 4 and Supplementary Fig. 7) and rapid-onset seizure-induced death (Fig. 3). To establish a direct link between CD8<sup>+</sup> T cells and CNS myelomonocytic cell recruitment, we infected mice with LCMV and administered anti-CD8 antibody at days 4 and 5 post-infection—after CTL priming. This treatment, which reduced the number of CD8<sup>+</sup> T cells in the CNS by 94%, prevented the rapid onset of seizures at day 6 post-infection (data not shown), and significantly reduced the number of monocytes and neutrophils in the CNS (Supplementary Fig. 10). These data indicate that virus-specific CTLs can contribute to the recruitment of pathogenic myelomonocytic cells either by directly releasing chemoattractants or possibly by inducing other cells to release chemoattractants.

The requirement for CD8<sup>+</sup> T cells in the pathogenesis of LCMV meningitis led to the proposal that CTLs are directly responsible for tissue injury and death<sup>17</sup>. We propose that CTL activation through transient interactions with infected cells leads to massive recruitment of myelomonocytic cells, which compromise vascular integrity and initiate fatal convulsive seizures<sup>3</sup>. It is likely that once seizure-induced death is averted, infected mice ultimately succumb to another pathogenic mechanism possibly mediated by CTLs<sup>18</sup>.

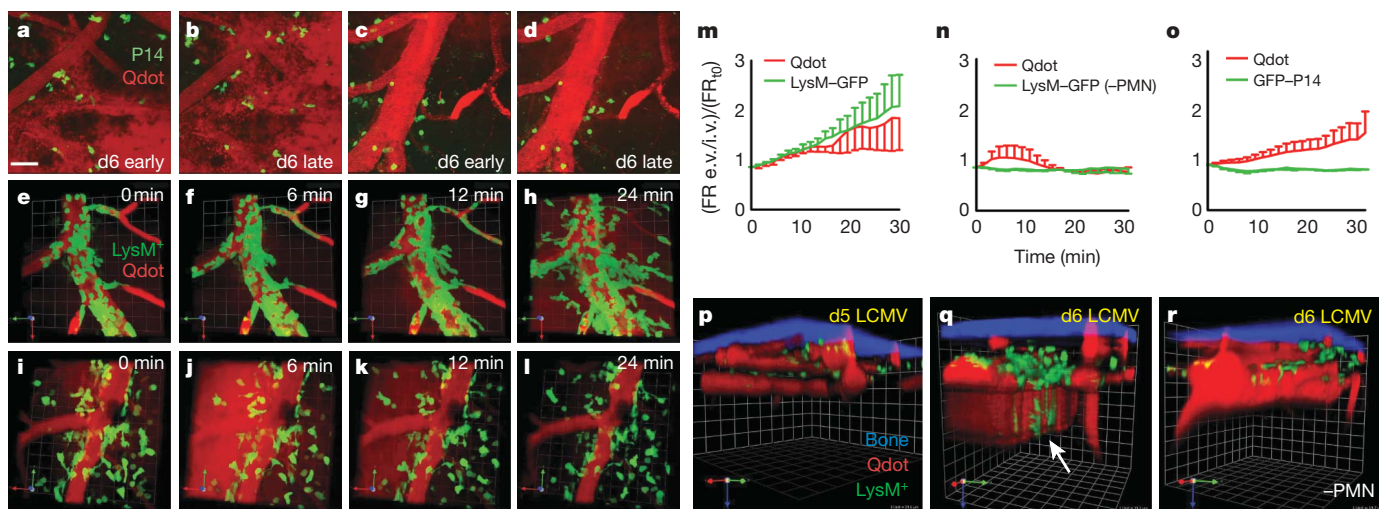


**Figure 4 | Recruitment of myelomonocytic cells into CNS and the relationship to meningeal vascular injury.** **a–d**, Two representative two-photon images at early ( $t = 0$  min; **a**, **c**) and late ( $t = 30$  min; **b**, **d**) points in the time-lapse sequence show the position of GFP<sup>+</sup> P14 CTLs (green) in relation to meningeal vascular changes (red). GFP<sup>+</sup> CTLs were typically found in perivascular regions. Severe disruption of vascular integrity is evidenced by extravascular quantum dot (Qdot) signal (red) is shown in **a** and **b**. Note the ghost outlines of large cells near the ragged vessels that do not correspond to P14 CTLs. In other areas, P14 CTLs remained near perivascular areas that had preserved blood vessel integrity (**c**, **d**). Scale bar, 50  $\mu$ m. See corresponding Supplementary Movie 3. **e–h**, A representative two-photon 30 min time-lapse sequence of vascular leakage of quantum dots (red) and extravasation of LysM–GFP<sup>+</sup> myelomonocytic cells (green) is shown for a symptomatic mouse at day 6 (d6) post-infection. Note that myelomonocytic cells roll and arrest inside the meningeal vessel before penetrating through the vascular wall and extravasating into the meningeal space. The extravasation of myelomonocytic cells is associated with severe vascular injury and quantum dot leakage. Grid scale is 19.7  $\mu$ m. See corresponding Supplementary Movie 4. No similar extravasation events were observed in asymptomatic control mice at day 5 post-infection (data not shown). **i–l**, A representative 30 min time-lapse is shown for a symptomatic LysM–GFP mouse depleted of neutrophils but not monocytes using low-dose anti-Gr-1 antibody. Note that LysM–GFP<sup>+</sup> myelomonocytic

cells (green) in the absence of neutrophils localize perivascularly and are associated with transient vascular leakage (red). Scale, 25  $\mu$ m. See corresponding Supplementary Movie 5. **m–o**, The fluorescent ratio (FR) of extracellular (e.v.) to intracellular (i.v.) GFP and quantum dot fluorescence signal was calculated at each frame, normalized to the baseline ratio at time point 0 ( $FR_{i0}$ ), and plotted against time. Data are represented as mean  $\pm$  s.e.m. P14 CTL extravasation or positioning was not associated with quantum dot leakage (**o**). Myelomonocytic cell extravasation correlated ( $r = 0.99$ ;  $P < 0.0001$ ) with sustained vascular leakage only in the presence of neutrophils (**m**). In neutrophil-depleted LysM–GFP mice, perivascular myelomonocytic cells were associated with transient quantum dot leakage (**n**). **p–r**, Representative three-dimensional reconstructions of two-photon z-stacks depicting skull bone (blue), quantum dot (red) and LysM–GFP<sup>+</sup> myelomonocytic cells (green) are shown for an asymptomatic mouse at day 5 (**p**), a symptomatic LysM–GFP mouse at day 6 (**q**), and a symptomatic LysM–GFP mouse at day 6 depleted of neutrophils (**r**). At day 5, vasculature showed smooth borders, no quantum dot (red) leakage and few LysM–GFP<sup>+</sup> cells (green). In symptomatic mice at day 6, LysM–GFP<sup>+</sup> cells were mostly observed extravasating from meningeal vasculature with some cells accompanying the vascular leakage down into the parenchyma (white arrow). In mice depleted of neutrophils (–PMN), LysM–GFP cells were observed in perivascular meningeal spaces. Grid scale for panels **p–r** is 19.7  $\mu$ m. See corresponding Supplementary Movies 4 and 5.

It is well established that neutrophil extravasation can be linked to vascular leakage<sup>19–21</sup>, and this process usually depends on signalling between leukocytes and endothelial cells<sup>22</sup>. Neutrophil extravasation causes tissue injury in many models including reperfusion injury and sepsis<sup>23,24</sup>. Using TPM we directly visualized this classical process in LCMV meningitis. Monocytes have been associated with atherosclerosis<sup>25</sup> and facilitation of the trafficking of neutrophils<sup>26</sup>. Our results suggest that monocytes also contribute vascular leakage, possibly through a mechanism linked to adherence to the blood vessels<sup>27</sup> and/or chemokine release<sup>28</sup>. Recognizing the complementary pathogenic functions of neutrophils and monocytes is critical for devising therapeutic approaches in CD8<sup>+</sup> T-cell-mediated pathology.

It is not clear why CD8<sup>+</sup> T cells recruit myelomonocytic cells to a site of viral infection. CD4<sup>+</sup> Th17 cells produce interleukin (IL)-17 to coordinate neutrophil recruitment, but anti-viral CD8<sup>+</sup> T cells express transcription factors that suppress this program<sup>29</sup>, and we observed no IL-17 production by peptide-stimulated P14 cells (data not shown). Therapies directed at reducing myelomonocytic activation are obvious treatment candidates to prevent the mode of immunopathology we observed, but are challenging because of their numerous effector mechanisms, fast turnover and acute importance in host defence. A more tractable approach might be to target the chemotactic mechanisms used by CTLs to attract myelomonocytic cells, or, alternatively, to enhance CTL-mediated killing of relevant targets by improving immunological synapse formation or stability<sup>30</sup>. The latter approach might break the feedback to the pathogenic

myelomonocytic arm and improve survival as well as immunity in viral infections of the CNS.

## METHODS SUMMARY

To induce meningitis, mice were infected intracerebrally with the Armstrong strain of LCMV. Immune cells were imaged through a surgically thinned skull using a Bio-Rad multi-photon microscope. Meningeal vasculature was visualized by intravenously injecting quantum dots 10 min before imaging. All imaging data were processed and analysed using Velocity software.

For flow cytometric studies, mice received an intracardiac perfusion with saline. The CNS was then harvested, treated with collagenase D, and mononuclear cells were isolated using a Percoll gradient. Afterwards, mononuclear cells were stained with fluorescently labelled antibodies, and acquired using a Becton Dickinson digital flow cytometer. Data were analysed using FlowJo software.

Low-dose (125  $\mu$ g) anti-Gr-1 antibody (RB6-8C5 clone) was injected once at day 4 post-infection to deplete neutrophils only, whereas high-dose antibody (400  $\mu$ g) was injected daily starting at day 3 post-infection to deplete both monocytes and neutrophils. CD8<sup>+</sup> T cells were depleted by injecting 1,000  $\mu$ g of anti-CD8 (53-6.72 clone) on day 4 and 500  $\mu$ g on day 5 post-LCMV infection.

CNS vascular leakage was evaluated by retroorbitally injecting mice with Evans blue. After 4 h, mice were perfused with saline, and brains were collected. Evans blue was extracted using *N,N*-dimethyl formamide and quantified using a Varioskan Flash fluorometer (620 nm excitation; 695 nm emission). Fluorescence images on vibratome brain sections were captured using a confocal microscope (637 nm excitation). All immunohistochemistry was performed as described in Methods.

To quantify gene expression changes in the LCMV-infected CNS, total RNA was isolated from saline perfused mock- and day 6 LCMV-infected brains and

hybridized to Mouse Exon 1.0 ST Arrays. The analysis was run using XRAY (version 2.3) software; the Excel add-in was from Biotique Systems Inc. Myelomonocytic cell chemoattractants with increased expression at day 6 post-infection were identified, and their expression at the protein level by P14 CTLs was quantified flow cytometrically.

**Full Methods** and any associated references are available in the online version of the paper at [www.nature.com/nature](http://www.nature.com/nature).

**Received 29 August; accepted 30 October 2008.**

**Published online 16 November 2008.**

1. Kang, S. S. & McGavern, D. B. Lymphocytic choriomeningitis infection of the central nervous system. *Front. Biosci.* **13**, 4529–4543 (2008).
2. Marker, O., Nielsen, M. H. & Diemer, N. H. The permeability of the blood–brain barrier in mice suffering from fatal lymphocytic choriomeningitis virus infection. *Acta Neuropathol.* **63**, 229–239 (1984).
3. Camenga, D. L., Walker, D. H. & Murphy, F. A. Anticonvulsant prolongation of survival in adult murine lymphocytic choriomeningitis. I. Drug treatment and virologic studies. *J. Neuropathol. Exp. Neurol.* **36**, 9–20 (1977).
4. Fung-Leung, W. P., Kundig, T. M., Zinkernagel, R. M. & Mak, T. W. Immune response against lymphocytic choriomeningitis virus infection in mice without CD8 expression. *J. Exp. Med.* **174**, 1425–1429 (1991).
5. Bajenoff, M. *et al.* Stromal cell networks regulate lymphocyte entry, migration, and territoriality in lymph nodes. *Immunity* **25**, 989–1001 (2006).
6. Bromley, S. K., Peterson, D. A., Gunn, M. D. & Dustin, M. L. Cutting edge: hierarchy of chemokine receptor and TCR signals regulating T cell migration and proliferation. *J. Immunol.* **165**, 15–19 (2000).
7. Storm, P., Bartholdy, C., Sorensen, M. R., Christensen, J. P. & Thomsen, A. R. Perforin-deficient CD8<sup>+</sup> T cells mediate fatal lymphocytic choriomeningitis despite impaired cytokine production. *J. Virol.* **80**, 1222–1230 (2006).
8. Johnson, E. D., Monjan, A. A. & Morse, H. C. III. Lack of B-cell participation in acute lymphocytic choriomeningitis disease of the central nervous system. *Cell. Immunol.* **36**, 143–150 (1978).
9. Leist, T. P., Cobbold, S. P., Waldmann, H., Aguet, M. & Zinkernagel, R. M. Functional analysis of T lymphocyte subsets in antiviral host defense. *J. Immunol.* **138**, 2278–2281 (1987).
10. Tepper, R. I., Coffman, R. L. & Leder, P. An eosinophil-dependent mechanism for the antitumor effect of interleukin-4. *Science* **257**, 548–551 (1992).
11. Kurihara, T., Warr, G., Loy, J. & Bravo, R. Defects in macrophage recruitment and host defense in mice lacking the CCR2 chemokine receptor. *J. Exp. Med.* **186**, 1757–1762 (1997).
12. Marchi, N. *et al.* Seizure-promoting effect of blood–brain barrier disruption. *Epilepsia* **48**, 732–742 (2007).
13. Asensio, V. C. & Campbell, I. L. Chemokine gene expression in the brains of mice with lymphocytic choriomeningitis. *J. Virol.* **71**, 7832–7840 (1997).
14. Kaech, S. M., Hemby, S., Kersh, E. & Ahmed, R. Molecular and functional profiling of memory CD8 T cell differentiation. *Cell* **111**, 837–851 (2002).
15. Wherry, E. J. *et al.* Molecular signature of CD8<sup>+</sup> T cell exhaustion during chronic viral infection. *Immunity* **27**, 670–684 (2007).
16. Andersen, I. H., Marker, O. & Thomsen, A. R. Breakdown of blood–brain barrier function in the murine lymphocytic choriomeningitis virus infection mediated by virus-specific CD8<sup>+</sup> T cells. *J. Neuroimmunol.* **31**, 155–163 (1991).
17. Doherty, P. C., Allan, J. E., Lynch, F. & Ceredig, R. Dissection of an inflammatory process induced by CD8<sup>+</sup> T cells. *Immunol. Today* **11**, 55–59 (1990).
18. Walker, D. H., Camenga, D. L., Whitfield, S. & Murphy, F. A. Anticonvulsant prolongation of survival in adult murine lymphocytic choriomeningitis. II. Ultrastructural observations of pathogenetic events. *J. Neuropathol. Exp. Neurol.* **36**, 21–40 (1977).
19. Wedmore, C. V. & Williams, T. J. Control of vascular permeability by polymorphonuclear leukocytes in inflammation. *Nature* **289**, 646–650 (1981).
20. Bjork, J. & Arfors, K. E. Oxygen free radicals and leukotriene B<sub>4</sub> induced increase in vascular leakage is mediated by polymorphonuclear leukocytes. *Agents Actions, Suppl.* **11**, 63–72 (1982).
21. Rosengren, S., Ley, K. & Arfors, K. E. Dextran sulfate prevents LTB<sub>4</sub>-induced permeability increase, but not neutrophil emigration, in the hamster cheek pouch. *Microvasc. Res.* **38**, 243–254 (1989).
22. Hixenbaugh, E. A. *et al.* Stimulated neutrophils induce myosin light chain phosphorylation and isometric tension in endothelial cells. *Am. J. Physiol.* **273**, H981–H988 (1997).
23. Sekido, N. *et al.* Prevention of lung reperfusion injury in rabbits by a monoclonal antibody against interleukin-8. *Nature* **365**, 654–657 (1993).
24. Herwald, H. *et al.* M protein, a classical bacterial virulence determinant, forms complexes with fibrinogen that induce vascular leakage. *Cell* **116**, 367–379 (2004).
25. Tacke, F. *et al.* Monocyte subsets differentially employ CCR2, CCR5, and CX3CR1 to accumulate within atherosclerotic plaques. *J. Clin. Invest.* **117**, 185–194 (2007).
26. Maus, U. *et al.* The role of CC chemokine receptor 2 in alveolar monocyte and neutrophil immigration in intact mice. *Am. J. Respir. Crit. Care Med.* **166**, 268–273 (2002).
27. Ancuta, P., Moses, A. & Gabuzda, D. Transendothelial migration of CD16<sup>+</sup> monocytes in response to fractalkine under constitutive and inflammatory conditions. *Immunobiology* **209**, 11–20 (2004).
28. Stamatovic, S. M. *et al.* Monocyte chemoattractant protein-1 regulation of blood–brain barrier permeability. *J. Cereb. Blood Flow Metab.* **25**, 593–606 (2005).
29. Intlekofer, A. M. *et al.* Anomalous type 17 response to viral infection by CD8<sup>+</sup> T cells lacking T-bet and eomesodermin. *Science* **321**, 408–411 (2008).
30. Beal, A. M. *et al.* Protein kinase C $\theta$  regulates stability of the peripheral adhesion ring junction and contributes to the sensitivity of target cell lysis by CTL. *J. Immunol.* **181**, 4815–4824 (2008).

**Supplementary Information** is linked to the online version of the paper at [www.nature.com/nature](http://www.nature.com/nature).

**Acknowledgements** This work was supported by National Institutes of Health grants AI070967-01 (D.B.M.), AI055037 (M.L.D.), a grant from The Burroughs Wellcome Fund (D.B.M.) and the Dana Foundation (M.L.D.). S.S.K. was supported by a National Institutes of Health training grant NS041219-06 and is presently supported by a National Research Service Award (NS061447-01), and J.V.K. is supported by a Multiple Sclerosis Society Center Grant. We thank C. Yau for technical support and the Scripps DNA Array core for their assistance with the gene array experiment.

**Author Information** Reprints and permissions information is available at [www.nature.com/reprints](http://www.nature.com/reprints). Correspondence and requests for materials should be addressed to M.L.D. ([dustin@saturn.med.nyu.edu](mailto:dustin@saturn.med.nyu.edu)) and D.B.M. ([mcgad@scripps.edu](mailto:mcgad@scripps.edu)).



## METHODS

**Transgenic mice.** C57BL/6 (B6), B6 GFP<sup>+</sup>D<sup>b</sup>GP<sub>33–41</sub> TCR-transgenic (tg) (GFP<sup>+</sup> P14)<sup>31</sup>, B6 Thy1.1<sup>+</sup>D<sup>b</sup>GP<sub>33–41</sub> TCR-tg (Thy1.1<sup>+</sup> P14), B6 OT-I TCR-tg, B6 perforin<sup>−/−</sup> (*Prfl*<sup>−/−</sup>), B6 *Tnf*<sup>−/−</sup>, and B6 *Ifngr*<sup>−/−</sup> mice were bred and maintained in a closed breeding facility at The Scripps Research Institute. B6, B6 *Ccr2*<sup>−/−</sup> and B6 *Fas*<sup>−/−</sup> mice were obtained from The Jackson Laboratories. The following mice were gifts from other investigators: B6 LysM–GFP heterozygous knock-in mice (LysM<sup>GFP/+</sup>; T. Graf)<sup>32</sup>, B6 *Jinx* mice (B. Beutler)<sup>33</sup>, and 129 granzyme a × b cluster knockout mice (deficient in granzymes a, b, c and f; T. Ley)<sup>34</sup>. All mice were housed in specific-pathogen-free conditions and treated in accordance with Institutional Animal Care and Use Committee protocols of The Scripps Research Institute and New York University School of Medicine.

**Virus.** To induce meningitis, adult mice at 6–8 weeks of age were infected intracerebrally (i.c.) with  $1 \times 10^5$  plaque-forming units of LCMV Armstrong clone 53b. Survival was monitored daily. Stocks were prepared by a single passage on BHK-21 cells, and viral titres were determined by plaque formation on Vero cells.

**Mononuclear cell isolations and tissue processing.** To obtain cell suspensions for flow cytometric analysis, the brain and spinal cord were harvested from mice after an intracardiac perfusion with 25 ml of 0.9% saline solution to remove the contaminating blood lymphocytes. The CNS was then incubated with 1 ml collagenase D ( $1 \text{ mg ml}^{-1}$ ; Roche) at 37 °C for 30 min. Single-cell suspensions were prepared by mechanical disruption through a 100- $\mu\text{m}$  filter. Brain-infiltrating leukocytes were isolated and counted as described previously<sup>35</sup>. For immunohistochemical analyses, fresh, unfixed brain tissue was either frozen on dry ice in optimal cutting temperature compound (OCT, Tissue-Tek, for frozen sectioning) or incubated overnight (~15 h) with 4% paraformaldehyde (PFA, for vibratome sectioning).

**GFP<sup>+</sup> P14 cell transfer.** CD8<sup>+</sup> T cells were purified from GFP<sup>+</sup> P14 mouse splenocytes by negative selection (Stem Cell Technologies). The purity after enrichment was determined to be greater than 98%. For imaging studies,  $1 \times 10^5$  purified GFP<sup>+</sup> P14 CD8<sup>+</sup> T cells were injected i.v. into naive mice. One day later the mice were challenged i.c. with LCMV Armstrong.

**OT-I cell transfer.** Splenocytes were isolated from OT-I mice and expanded *in vitro* for 7 days in RPMI 1640 containing 10% FBS, 1% L-glutamine, 1% penicillin/streptomycin, 500 units ml<sup>−1</sup> IL-2, and  $1 \mu\text{g ml}^{-1}$  ovalbumin (OVA)<sub>257–264</sub> (SIINFEKL) peptide. The cells were then labelled with 5  $\mu\text{M}$  CFSE in PBS (Invitrogen) at 37 °C for 5 min and washed three times in PBS.  $1 \times 10^7$  CFSE-labelled OT-I cells were transferred into each day 6 LCMV-infected B6 mouse, and intravital imaging was performed 6–12 h after the transfer.

**CD8 T-cell depletion.** To deplete CD8<sup>+</sup> T cells from LCMV-infected B6 mice, 1,000  $\mu\text{g}$  of purified, endotoxin-free anti-CD8 (53-6.72 clone) was injected on day 4 and 500  $\mu\text{g}$  was injected on day 5 post-LCMV infection. This resulted in a 94% reduction in CNS-infiltrating CD8<sup>+</sup> T cells. The control group for these experiments was injected with polyclonal rat IgG (Jackson ImmunoResearch Laboratories).

**Neutrophil depletion.** To deplete myelomonocytic cells from B6 and B6 *Ccr2*<sup>−/−</sup> mice, 125  $\mu\text{g}$  (low dose) or 400  $\mu\text{g}$  (high dose) of purified, endotoxin-free anti-Gr-1 (RB6-8C5 clone) antibody was injected intraperitoneally. The RB6-8C5 hybridoma was provided by P. Allen. Low-dose antibody was injected once at day 4 post-infection to deplete neutrophils only. This resulted in an 87% reduction of neutrophils in the CNS and 98% reduction in the blood. High-dose antibody was injected daily starting at day 3 post-infection to deplete both neutrophils and monocytes. Injection of polyclonal rat IgG (Jackson ImmunoResearch Laboratories) was used as a control.

**Gene array.** Total RNA from mock- and day 6 LCMV-infected brains ( $n = 3$  mice per group) was isolated using a Qiagen RNeasy Midi prep kit and then quantified using Nanodrop ND-1000. Sample quality was checked using an Agilent 2100 Bioanalyser. To remove most of the ribosomal RNA from the RNA, 2.5  $\mu\text{g}$  of each sample was taken through RiboMinus (Invitrogen). After RiboMinus treatment, samples were amplified and labelled using the GeneChip whole-transcript sense target labelling assay (Affymetrix). Samples were checked by gel-shift assay to assess labelling efficiency as described in the GeneChip whole-transcript sense target labelling assay manual. Samples were hybridized overnight to the Mouse Exon 1.0 ST Array. Hybridization and scanning of samples to arrays was performed using standard Affymetrix protocols and reagents from the GeneChip hybridization, wash and stain kit. Chips were scanned using the Affymetrix GeneChip Scanner 3000 7G with default settings. To identify genes with differential gene expression or alternative splicing between the two groups, we studied three hybridizations each on the Mouse Exon 1.0 ST array using mixed model ANOVA. The analysis was run using XRAY (version 2.3) software, with the Excel add-in from Biotique Systems Inc.

**Analysis of BBB integrity.** To quantify BBB permeability, Evans blue leakage in the brains of mock-infected or LCMV i.c. infected mice was assessed. On the

indicated day, mice were injected retroorbitally with 20 mg Evans blue per kg body weight (Sigma). After 4 h, the brains were extracted after a PBS perfusion, which was used to eliminate circulating Evans blue. The tissue was homogenized in 600  $\mu\text{l}$  of *N,N*-dimethyl formamide (Sigma). The homogenate was transferred to new tubes, centrifuged at 16,000g for 20 min at 4 °C and the supernatant was plated in triplicate wells in a 96-well flat-bottom plate. For quantification, an Evans blue standard was diluted in the supernatant of a PBS-perfused uninfected brain that received no Evans blue, but was homogenized in *N,N*-dimethyl formamide. All samples plated in triplicate were read using a Varioskan Flash fluorometer (620 nm excitation; 695 nm emission; Thermo Scientific). The excitation and emission wavelengths were determined by spectral scanning to be optimal for Evans blue. Representative qualitative images of Evans blue permeability from PBS perfused brains were taken using a digital camera.

**Flow cytometry.** Brain-infiltrating leukocytes were collected and blocked with 3.3  $\mu\text{g ml}^{-1}$  anti-mouse CD16/CD32 (Fc block; BD Biosciences) in PBS containing 1% FBS and 0.1% sodium azide for 15 min on ice. After Fc block, cells were stained with the following conjugated antibodies: CD45.2 fluorescein isothiocyanate (FITC) (104), Thy1.2 phycoerythrin (PE) (53-2.1), CD19 peridinin-chlorophyll–protein complex (PerCP) cyanin (CY)5.5 (1D3), Gr-1 allophycocyanin (APC) (RB6-8C5), CD4 APC Cy7 (GK1.5; BD Biosciences), CD8 Pacific Blue (Caltag), MCA771 PE (7/4; Serotec), and anti-CD11b PE/Cy7 (M1/70; eBioscience). Cells were acquired using a digital flow cytometer (Digital LSR II; Becton Dickinson) and flow cytometric data were analysed with FlowJo software (Tree Star, Inc.).

**Intracellular chemokine staining.** Mice seeded with  $10^4$  P14 Thy1.1 cells on day −1 were infected with  $10^3$  plaque-forming units of LCMV Armstrong i.c. on day 0. On day 6 post-infection, brain-infiltrating leukocytes and splenocytes from infected mice and splenocytes from naive P14 Thy1.1 mice were collected and stimulated with 50 U ml<sup>−1</sup> IL-2 (Roche),  $1 \mu\text{g ml}^{-1}$  brefeldin A (Sigma-Aldrich) and  $1 \mu\text{g ml}^{-1}$  GP<sub>33–41</sub> peptide for 5 h at 37 °C. Cells were centrifuged and then blocked with 3.3  $\mu\text{g ml}^{-1}$  anti-mouse CD16/CD32 (Fc block; BD Biosciences) in PBS containing 1% FBS and 0.1% sodium azide for 15 min on ice. After Fc block, cells were stained with the following conjugated antibodies: CD45.2 FITC (104), Thy1.1 PerCP (53-2.1; BD Biosciences) and CD8 APC/Cy7 (53-6.7; BioLegend) for 30 min on ice. Cells were washed and fixed for 10 min at room temperature (~26 °C) in PBS containing 1% FBS, 0.1% sodium azide, 1% PFA and 0.1% saponin. Intracellular staining and washes for all intracellular steps were conducted in PBS containing 1% FBS, 0.1% sodium azide and 0.1% saponin. Cells were stained with PE-conjugated antibodies against CCL-2 (1:100, BioLegend) and CCL3 (1:100, R&D Systems), biotinylated antibodies against CCL5 and CXCL2 (1:100, R&D Systems) or purified antibodies against CCL4 (1:200, BD Bioscience) and CCL7 (1:100, R&D Systems) for 30 min on ice. Secondary and tertiary incubations with biotinylated anti-rat IgG1 (1:100, BioLegend), PE-conjugated donkey anti-goat (1:100, Jackson ImmunoResearch Laboratories) or SA-APC (1:100, Invitrogen) were used in subsequent steps. After the final wash, cells were resuspended in PBS containing 1% FBS and 0.1% sodium azide and acquired using a digital flow cytometer.

**Immunohistochemistry.** To examine LCMV localization, 6- $\mu\text{m}$  frozen sections were cut, fixed with 4% PFA for 15 min, blocked with an avidin/biotin-blocking kit (Vector Laboratories), and stained for 1 h at room temperature with primary guinea pig antibodies against LCMV (1:500). Secondary and tertiary incubations with biotinylated donkey anti-guinea pig (1:200; Jackson ImmunoResearch Laboratories) and streptavidin Rhod-X (1:250; Jackson ImmunoResearch Laboratories), respectively, were performed to detect LCMV antigen. Co-labelling of fibroblasts (anti-ER-TR7; 1:100; Abcam), astrocytes (anti-GFAP; 1:800; DakoCytomation), infiltrates (anti-CD45.2; 1:100, BD Biosciences), endothelium (anti-CD31; 1:200; Chemicon) or smooth muscle actin (anti-SMA; 1:100; Abcam) was also conducted in conjunction with anti-LCMV staining. The cell-marker-specific antibodies were detected with secondary antibodies conjugated to FITC (1:200; Jackson ImmunoResearch Laboratories). All working stocks of primary and secondary reagents were diluted in PBS containing 2% fetal bovine serum (FBS). To generate three-dimensional renderings of LCMV-infected fibroblasts, 100- $\mu\text{m}$  vibratome sections were cut using a Leica VT1000S (Leica) and blocked with PBS containing 10% FBS and 0.1% saponin for 1 h at room temperature. Staining for LCMV and fibroblasts was conducted as indicated above, with the exception that the antibodies were diluted in PBS containing 2% FBS supplemented with 0.1% saponin. To obtain images of Evans blue leakage, 100- $\mu\text{m}$  vibratome sections from PBS-perfused mice injected with Evans blue (as described previously) were stained with anti-CD31 (1:200; Chemicon) diluted in PBS containing 2% FBS supplemented with 0.5% Triton-X (Sigma-Aldrich). CD31 was detected and amplified with a FITC-conjugated goat anti-hamster antibody (1:200; Jackson ImmunoResearch Laboratories), a rabbit anti-FITC antibody (1:200; Zymed) and a FITC-conjugated anti-rabbit antibody (1:200; Jackson ImmunoResearch Laboratories). All sections described above were further stained

with  $1 \mu\text{g ml}^{-1}$  4,6-diamidino-2-phenylindole (DAPI; Sigma-Aldrich) for 3 min at room temperature to visualize cell nuclei.

**One-photon microscopy.** Two-dimensional co-localization images to determine whether LCMV-infected fibroblasts, leukocytes, astrocytes, endothelium, smooth muscle cells or pericytes (Fig. 2 and Supplementary Fig. 3) were captured from 6- $\mu\text{m}$  frozen sections using a MRC2100 confocal microscope (Bio-Rad Laboratories) fitted with  $\times 40$ ,  $\times 63$ , and  $\times 100$  oil objectives and seven laser lines that excite at 405 nm, 457 nm, 477 nm, 488 nm, 514 nm, 543 nm and 637 nm (Carl Zeiss MicroImaging, Inc.). Three-dimensional z-stacks were captured with from 100- $\mu\text{m}$  vibratome sections using a step size of 0.1  $\mu\text{m}$ . Maximal projections and three-dimensional reconstructions (Fig. 2) were generated using Volocity software (Improvision).

**Intravital two-photon microscopy.** Mice were anaesthetized and maintained at core temperature of  $37^\circ\text{C}$ . Thinned-skull and open-skull surgery were performed and imaged using Bio-Rad Radiance multi-photon microscope (Zeiss) powered by Tsunami pulsed laser (Spectraphysics) tuned to 920 nm as described previously<sup>36</sup>. Bone (second harmonic signal), GFP-labelled cells (GFP P14 or LysM-GFP) and intravascular quantum dots were visualized using band-pass filters 400/10, 480/30 and 540/30, respectively. To visualize meningeal vasculature, mice were injected i.v. 10 min before imaging with 50  $\mu\text{l}$  Qtracker 655 nm non-targeted quantum dots (0.2  $\mu\text{M}$ ; Invitrogen). For MHC-class-I-blocking studies, H-2D<sup>b</sup> monoclonal antibody and isotype control (10  $\mu\text{g ml}^{-1}$ ) in 200  $\mu\text{l}$  of artificial cerebral spinal fluid (119 mM NaCl, 26.2 mM NaHCO<sub>3</sub>, 2.5 mM KCl, 1 mM NaH<sub>2</sub>PO<sub>4</sub>, 1.3 mM MgCl<sub>2</sub>, 1.2 mM CaCl<sub>2</sub>, 0.4% glucose, pH 7.4) were administered through a partial open skull adjacent to the thinned skull viewing area. Antibodies were incubated for 15–30 min to permit adequate local tissue diffusion. CTL dynamics were imaged through the adjacent thinned skull. For all imaging studies, stacks of images were acquired using step sizes of 1–3  $\mu\text{m}$  to a depth of 200  $\mu\text{m}$  below the skull using  $\times 20$ ,  $\times 40$  or  $\times 60$  water dipping objectives. Time-lapse movies were acquired with 1- to 1.5-min intervals between three-dimensional stacks. Image analysis was performed and cell movements were tracked using Volocity software and graphs were determined using Graph Prism4. The average speed ( $\mu\text{m min}^{-1}$ ) of CTLs and myelomonocytic cells was quantified manually from 30-min time lapses with 20 intervals. Arrest duration (min) is the total time that a CTL slowed to  $<2 \mu\text{m min}^{-1}$  interval instantaneous speed during a 30-min time lapse. The arrest coefficient is the percentage of total elapsed time that a CTL spent moving  $<2 \mu\text{m min}^{-1}$ . The confinement index was calculated by dividing the displacement (or distance a cell travelled) by the speed. The motility coefficient was calculated as (mean

displacement)<sup>2</sup>/(4  $\times$  time). Histograms showing the relative frequency of CTL velocities under different conditions were generated using a bin size of  $2 \mu\text{m min}^{-1}$  and Gaussian curve fitting. The fluorescence ratio (FR) of extravascular (e.v.) to intravascular (i.v.) Qdot and GFP signal was calculated by first quantifying the mean fluorescence intensity in defined extra- and intra-vascular regions. Mean extravascular fluorescence was then divided by mean intravascular fluorescence for each channel (FR e.v./i.v.) and normalized to the ratio at time 0 (FR<sub>0</sub>) by division ((FR e.v./i.v.)/(FR<sub>0</sub>)). All imaging data are representative of at least three independent experiments.

**Sagittal brain reconstructions.** Two-colour organ reconstructions to visualize the distribution of LysM-GFP<sup>+</sup> cells on 6- $\mu\text{m}$  frozen sections (Supplementary Fig. 10) were obtained using an immunofluorescence microscope (Axiovert S100; Carl Zeiss MicroImaging, Inc.) fitted with an automated xy stage, a colour digital camera (Axiocam, Carl Zeiss MicroImaging, Inc.), and a  $\times 5$  objective. Registered images were captured for each field on the tissue section, and reconstructions were performed using the MosaicX function in KS300 image analysis software (Carl Zeiss MicroImaging, Inc.).

**Statistical analysis.** Statistical significance ( $P < 0.05$ ) was determined using a Student's *t*-test, a Mann-Whitney rank sum test for populations with non-Gaussian distributions, or a one-way ANOVA for experiments containing more than two groups. Correlations were evaluated using a Pearson product moment correlation test.

31. McGavern, D. B., Christen, U. & Oldstone, M. B. Molecular anatomy of antigen-specific CD8<sup>+</sup> T cell engagement and synapse formation in vivo. *Nature Immunol.* **3**, 918–925 (2002).
32. Faust, N., Varas, F., Kelly, L. M., Heck, S. & Graf, T. Insertion of enhanced green fluorescent protein into the lysozyme gene creates mice with green fluorescent granulocytes and macrophages. *Blood* **96**, 719–726 (2000).
33. Crozat, K. *et al.* Jinx, an MCMV susceptibility phenotype caused by disruption of Unc13d: a mouse model of type 3 familial hemophagocytic lymphohistiocytosis. *J. Exp. Med.* **204**, 853–863 (2007).
34. Revell, P. A. *et al.* Granzyme B and the downstream granzymes C and/or F are important for cytotoxic lymphocyte functions. *J. Immunol.* **174**, 2124–2131 (2005).
35. Lauterbach, H., Zuniga, E. I., Truong, P., Oldstone, M. B. A. & McGavern, D. B. Adoptive immunotherapy induces CNS dendritic cell recruitment and antigen presentation during clearance of a persistent viral infection. *J. Exp. Med.* **203**, 1963–1975 (2006).
36. Kim, J. V. & Dustin, M. L. Innate response to focal necrotic injury inside the blood–brain barrier. *J. Immunol.* **177**, 5269–5277 (2006).

## LETTERS

# Memory CD8 T-cell compartment grows in size with immunological experience

Vaiva Vezys<sup>1,2\*</sup>, Andrew Yates<sup>3\*</sup>, Kerry A. Casey<sup>1</sup>, Gibson Lanier<sup>2</sup>, Rafi Ahmed<sup>2</sup>, Rustom Antia<sup>3</sup> & David Masopust<sup>1,2</sup>

Memory CD8 T cells, generated by natural pathogen exposure or intentional vaccination, protect the host against specific viral infections<sup>1</sup>. It has long been proposed that the number of memory CD8 T cells in the host is inflexible, and that individual cells are constantly competing for limited space<sup>2,3</sup>. Consequently, vaccines that introduce over-abundant quantities of memory CD8 T cells specific for an agent of interest could have catastrophic consequences for the host by displacing memory CD8 T cells specific for all previous infections<sup>4–6</sup>. To test this paradigm, we developed a vaccination regimen in mice that introduced as many new long-lived memory CD8 T cells specific for a single vaccine antigen as there were memory CD8 T cells in the host before vaccination. Here we show that, in contrast to expectations, the size of the memory CD8 T-cell compartment doubled to accommodate these new cells, a change due solely to the addition of effector memory CD8 T cells. This increase did not affect the number of CD4 T cells, B cells or naive CD8 T cells, and pre-existing memory CD8 T cells specific for a previously encountered infection were largely preserved. Thus, the number of effector memory CD8 T cells in the mammalian host adapts according to immunological experience. Developing vaccines that abundantly introduce new memory CD8 T cells should not necessarily ablate pre-existing immunity to other infections.

Conventional knowledge dictates that the size and composition of the adaptive immune system, including the number of memory CD8 T cells, is invariable. This paradigm serves as the basis for theories regarding the regulation of immune memory and stipulates that new infections and vaccines erode pre-existing immunity. However, because of variability between mice and the fact that single infections result in the addition of relatively small new memory populations, it is actually quite challenging to enumerate changes in the composition and size of different lymphocyte compartments induced by the addition of new memory CD8 T cells. We overcame this difficulty by developing a unique heterologous prime–boost vaccination strategy designed to introduce enormous numbers of memory CD8 T cells specific for a single antigen<sup>7</sup>, equal in number to the entire population of memory CD8 T cells specific for all previously encountered infections in unvaccinated mice. This event could reflect what occurs naturally on repeated exposure to serological variants of pathogens that express shared CD8 T-cell epitopes, or more probably, such a response could be intentionally induced to test the potential of memory CD8 T cells to protect against pathogens for which antibody-based vaccines have consistently failed<sup>8</sup>. Most importantly, in this context, it provides a more stringent test of the impact of introducing new memory CD8 T cells on the size of the naive and memory CD8 T-cell compartments, the size of the B and CD4 T-cell compartments, and the number of pre-existing memory CD8 T cells specific for a different pathogen.

To establish a defined and easily detectable population of pre-existing memory CD8 T cells, we transferred naive P14 cells, which are CD8 T cells specific for an immunodominant epitope of lymphocytic choriomeningitis virus (LCMV), into C57Bl/6J mice, and then infected recipient mice with LCMV (Armstrong strain)<sup>9</sup>. This allowed us to track precisely a population of non-cross-reactive monoclonal memory CD8 T cells. After LCMV-specific memory was established, mice were subjected to three heterologous prime–boost immunizations, which resulted in a large addition of memory CD8 T cells specific for the ‘N’ peptide of vesicular stomatitis virus (Fig. 1a–c)<sup>7</sup>. Control mice received phosphate buffered saline (PBS) instead of three heterologous prime–boost immunizations, which did not result in an N-peptide-specific response (Fig. 1b).

Consistent with previous reports<sup>10,11</sup>, new immune challenges caused a substantial reduction in the percentage of CD8 T cells specific for LCMV, suggesting profound attrition of pre-existing memory CD8 T cells (Fig. 1b, c). However, we noted that the proportion of CD8<sup>+</sup> lymphocytes in blood unexpectedly increased permanently, from  $11.1 \pm 0.8\%$  ( $\pm$  s.e.m.) in control mice to  $25.4 \pm 1.1\%$  in boosted mice ( $P < 0.0001$ , measured 94 days after final immunization or PBS inoculation, Fig. 1d). If the size of the CD8 T-cell compartment is malleable, it confounds interpretation based on percentages alone (Fig. 1e).

For this reason, we counted the numbers of CD8 T, CD4 T, and B cells in various tissues between 80 and 160 days after the final immunization. We found that heterologous prime–boost immunizations induced a permanent increase in the number of CD8 T cells in almost all tissues, with no significant affect on the number of CD4 T or B cells. For example, the number of CD8 T cells in the spleen increased by 54.9% relative to control mice (Fig. 2), and similar, or even greater, increases were noted in liver, bone marrow (data not shown) and lung (94.5% increase, Supplementary Fig. 1a). The one exception was lymph node, in which there was no change in the number or composition of lymphocytes (Supplementary Fig. 1b). In addition, no changes were seen among any subset of CD4 T cells in any tissue (Supplementary Figs 1 and 2).

We then determined whether the increase in CD8 T cells reflected changes in the numbers of naive CD8 T cells, memory CD8 T cells or both by staining cells for CD44 and CD62L. We found that heterologous prime–boost immunization induced no change among naive (CD44<sup>lo</sup>) CD8 T cells (Fig. 3). Consistent with these data, prime–boost immunized mice mounted primary CD8 T-cell responses that were equivalent to age-matched controls when challenged with a new infection (Supplementary Fig. 3), suggesting no defect in immuno-competence or reduction in naive CD8 T-cell responsiveness.

The increase in CD8 T cells in heterologous prime–boost immunized mice was entirely due to a large increase in the number of

<sup>1</sup>Department of Microbiology and Center for Immunology, University of Minnesota, Minneapolis, Minnesota 55455, USA. <sup>2</sup>Emory Vaccine Center, Emory University School of Medicine, and <sup>3</sup>Department of Biology, Emory University, Atlanta, Georgia 30322, USA.

\*These authors contributed equally to this work.



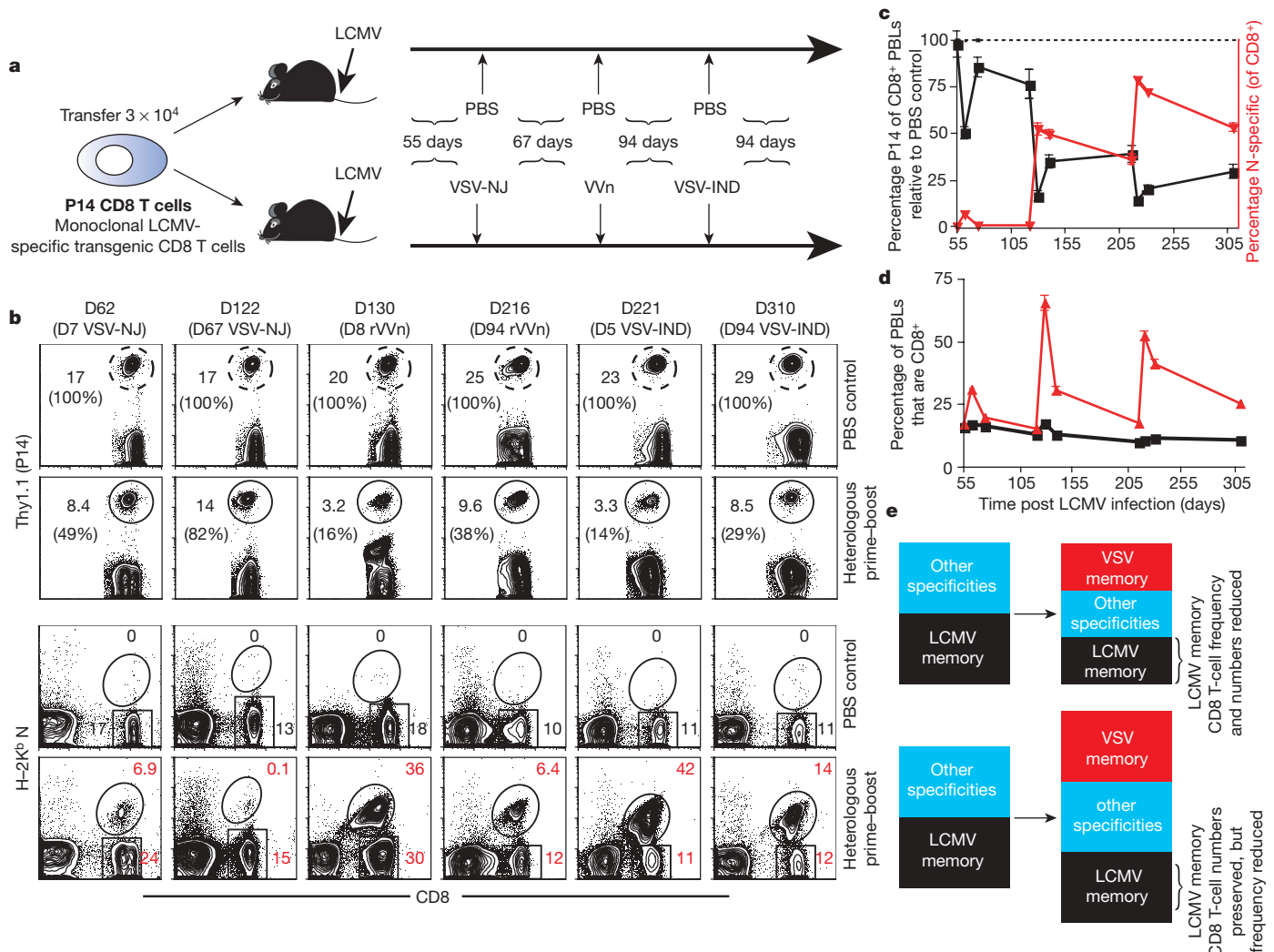


**Figure 1 | Heterologous prime-boost vaccination induces a huge addition of memory CD8 T cells and a permanent increase in the proportion of CD8<sup>+</sup> lymphocytes.** **a**, A monoclonal population of memory CD8 T cells was generated by transferring naive P14 CD8 T cells to naive mice and immunizing with  $2 \times 10^5$  p.f.u. LCMV. After 55 days, mice were subjected to the heterologous prime-boost regimen (as described in ref. 7 and Methods) or three inoculations of PBS (controls). **b**, **c**, Analysis of virus-specific CD8 T cells in blood. In **b**, representative flow cytometry data indicate the percentage of P14 among CD8 T cells (top two rows). The numbers in parentheses indicate the percentage of P14 CD8 T cells in the heterologous prime-boosted group relative to control mice. The bottom two rows indicate the percentage of N-antigen-specific CD8 T cells (as visualized by H-2K<sup>b</sup> N tetramer staining) and the percentage of other CD8 T cells among total

lymphocytes on various days (D) after infection. In **c**, black squares indicate the percentage of P14 among CD8 T cells, normalized to control mice. Red triangles indicate the percentage among total CD8 T cells that are specific for N antigen. **d**, Percentage of CD8<sup>+</sup> cells among all PBLs from control (black) or boosted (red) mice. Error bars indicate s.e.m. and  $n = 16-18$ .

**e**, Interpretation of memory CD8 T-cell homeostasis depends on whether the size of the compartment is fixed or flexible. The upper panels represent a model of fixed homeostasis in which total cell numbers are constant and introduction of new memory specificities erodes the absolute number of memory cells for other pathogens. In contrast, in the flexible memory compartment model (lower panels), addition of new memory cells is accommodated without attrition of other clones, but the frequency of unrelated pre-existing memory CD8 T cells declines nevertheless.

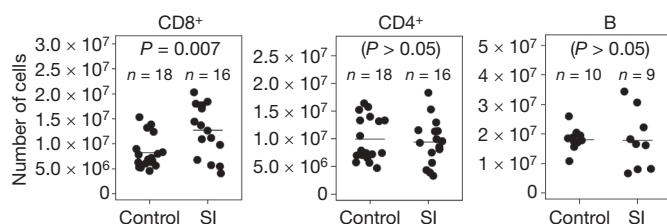


**Figure 2 | Total numbers of CD8 T, CD4 T, and B lymphocytes in the spleen of control mice and mice that have been sequentially immunized with VSV-NJ, VVn and VSV-IND.** Between 80 and 160 days post final immunization, the numbers of CD8 T, CD4 T, and B cells were counted in the spleen of sequentially immunized mice (SI), and compared to that of control mice. Statistics were determined by unpaired two-tailed *t*-test.

memory (CD44<sup>hi</sup>) CD8 T cells (Fig. 3). In fact, this increase occurred almost exclusively in the CD62L<sup>lo</sup> subset of memory CD8 T cells that are often referred to as non-lymphoid effector memory T cells. These data demonstrate that the size of the memory CD8 T-cell compartment is not fixed, and grows with immunological experience.

We then counted the number of new N-peptide-specific memory CD8 T cells, as well as the number of pre-existing memory (P14) CD8 T cells specific for LCMV (Fig. 4). As expected, no N-peptide-specific memory CD8 T cells were detected in control mice. The heterologous prime-boost regimen resulted in so many memory CD8 T cells specific for N, that the population was equivalent in size to the entire CD44<sup>hi</sup> (memory) CD8 T-cell population in control mice. If the size of the memory CD8 T-cell compartment was fixed, one would predict that almost 100% of pre-existing memory CD8 T cells would be ablated. In contrast, memory P14 CD8 T cells specific for LCMV only

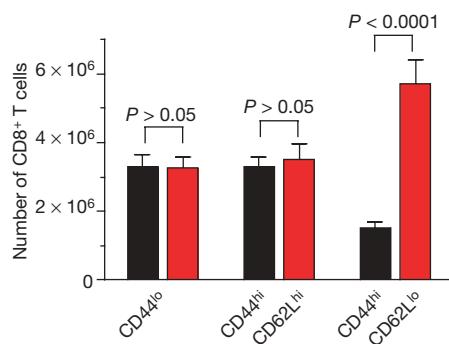


**Figure 3 | Increase among CD8 T cells is due solely to an increase in CD62L<sup>lo</sup> CD44<sup>hi</sup> memory CD8 T cells.** Between 80 and 160 days post final immunization, splenocytes were stained with anti-CD8, -CD44 and -CD62L, and the number of CD8 T cells in each subset were determined ( $n = 16-18$ ). Black bars indicate control mice and red bars indicate heterologous prime-boosted mice. Statistics were determined by unpaired two-tailed  $t$ -test; error bars are s.e.m.

underwent a modest reduction (from  $1.38 \pm 0.17 \times 10^6$  to  $9.15 \pm 1.36 \times 10^5$ , or a 33.6% reduction,  $P = 0.0484$ ,  $n = 16-18$  per group). Modest reductions in memory P14 CD8 T cells were also seen in other tissues (25.6% reduction in lung,  $P = 0.485$ , and 33.4% reduction in lymph node,  $P = 0.390$ ,  $n = 13-15$  per group). These data demonstrate that when very large numbers of new memory CD8 T cells are introduced, the erosion of pre-existing memory CD8 T cells is far less than predicted by a model of fixed homeostasis.

In other experiments, polyclonal endogenous LCMV-specific memory CD8 T cells in C57Bl/6J and/or Balb/c mice did not undergo attrition in response to infections with vaccinia (a virus that elicits a large CD8 T cell response), *Listeria monocytogenes* (an intracellular bacteria) or *Plasmodium yoelii* (a parasite that causes spleens of mice to increase to  $\sim 900 \times 10^6$  lymphocytes), as shown in Supplementary Fig. 4. Although these results do not exclude that certain infections could result in memory T-cell loss—as a result of infection-associated pathology, destruction of lymphoid tissue or direct infection of lymphocytes—we found little evidence of attrition in all models tested.

In conclusion, the memory CD8 T-cell compartment is not fixed in size, as previously thought. Instead, the size and proportion of different subsets of the adaptive immune system are flexible and reflect adaptation to the immunological experience of the individual. These results seem to contradict earlier work describing profound attrition of memory CD8 T cells on exposure to new pathogens<sup>10,11</sup>. However, it should be noted that previous studies quantified this decline as a percentage of CD8 T cells. We also observed a substantial

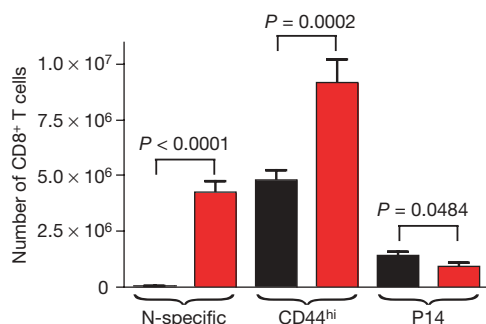


**Figure 4 | Addition of very large numbers of memory CD8 T cells induces only modest attrition of pre-existing memory CD8 T cells.** Total CD44<sup>hi</sup>, P14 and N-specific CD8 T cells were counted between 80 and 160 days post final immunization and compared to control mice ( $n = 16-18$ ). Black bars indicate control mice and red bars indicate heterologous prime-boosted mice. Statistics were determined by unpaired two-tailed  $t$ -test; error bars are s.e.m.

reduction in the frequency of pre-existing memory CD8 T cells specific for LCMV (Fig. 1). However, because the number of CD8 T cells increased in the organism, the erosion of pre-existing memory CD8 T cells was much less than predicted by frequency measurements alone. It should also be noted that previous studies restricted analysis to secondary lymphoid tissue after primary infections that result predominantly in the generation of central memory CD8 T cells. Heterologous prime-boost vaccination preferentially generates effector memory CD8 T cells that are enriched within non-lymphoid tissues (Supplementary Fig. 5 and ref. 7). Indeed, we found no evidence of an increase in total memory CD8 T cells within lymph node, nor an increase in CD62L<sup>+</sup> memory CD8 T cells in any tissue (Fig. 3 and Supplementary Fig. 1). Thus, our study does not reject the hypothesis that central memory CD8 T cells, which are enriched in lymph nodes and depend on interleukin (IL)-15 for survival<sup>12</sup>, may be fixed in number. However, it does suggest that effector memory CD8 T cells, which express low levels of IL-15R and undergo very little 'homeostatic' division<sup>9,13,14</sup>, may not be subject to the same regulation. It should also be noted that the pathological response to certain infections, or situations in which pathogens directly infect memory lymphocytes, could result in the attrition of memory CD8 T cells.

Our data help to explain observed phenomena, and have practical implications. According to the fixed homeostasis model, it is predicted that the number of total memory CD8 T cells remains stable, regardless of exposure to additional pathogens<sup>15</sup>. Two observations cast doubt on this hypothesis. First, effector memory CD8 T cells steadily increase in blood through the first several decades of life<sup>16,17</sup>. Although the number of cells in tissues has not been quantified, and other physiological changes accompany ageing, this supports the hypothesis that the memory CD8 T-cell compartment might enlarge as one is exposed to additional infections. The fixed homeostasis model also predicts that pre-existing CD8 T-cell memory erodes significantly with successive infections. However, the longevity of CD8 T-cell memory after smallpox vaccination was recently shown to be remarkably long-lived ( $t_{1/2} = 8-16$  years)<sup>18</sup>, which also favours a model of a flexible memory CD8 T-cell compartment.

The fact that the adaptive immune system has the capacity to accommodate increased numbers of memory CD8 T cells outside of lymph nodes could be exploited for vaccination. Most successful vaccines elicit protection by means of antibodies. This approach has not rendered a protective HIV vaccine, prompting many to consider vaccines that elicit effector memory CD8 T cells, for which the recognition mechanism is less vulnerable to viral mutations<sup>19</sup>. However, CD8 T cells only eliminate viruses after co-localizing with cells that are already infected, suggesting that low frequencies of CD8 T cells might not act rapidly enough to prevent chronic infection. So far, clinical vaccine trials using CD8 T cells have failed to protect against HIV<sup>20,21</sup>. However, we show that aggressive heterologous prime-boost vaccination with live replicating vectors has the potential to generate  $\sim 100$ -fold larger memory CD8 T-cell frequencies than what is achieved with current approaches (Fig. 1)<sup>22</sup>. Crucially, we show that this only caused very modest attrition of pre-existing cellular immunity to other pathogens (Fig. 4). With this major caveat removed, perhaps the time has come to examine the potential of massive numbers of memory CD8 T cells to mediate very rapid clearance of viral infections.

## METHODS SUMMARY

**Mice and infections.** C57Bl/6J mice were purchased from The Jackson Laboratory. Thy1.1<sup>+</sup> P14 mice bearing the H-2D<sup>b</sup> gp33-specific T-cell receptor were fully backcrossed to C57Bl/6J mice and maintained in our animal colony. We generated P14 chimaeras by transferring  $3 \times 10^4$  naive transgenic Thy1.1<sup>+</sup> P14 T cells into naive C57Bl/6J mice. The next day, mice were infected intraperitoneally (i.p.) with  $2 \times 10^5$  plaque-forming units (p.f.u.) LCMV (Armstrong strain). Fifty-five days later, mice were infected with  $5 \times 10^5$  p.f.u. vesicular stomatitis virus (New Jersey strain, VSV-NJ) intravenously (i.v.), rested for 67 days, infected with  $2 \times 10^6$  p.f.u. recombinant vaccinia virus expressing the

VSV nucleoprotein (VNV) i.v., rested for 94 days, and then infected with  $1 \times 10^6$  p.f.u. VSV (Indiana strain, VSV-IND) i.v. Control mice received PBS i.v. in lieu of VSV and VNV infections.  $n = 16$ – $18$  mice per group. All mice were used in accordance with National Institutes of Health and the University of Minnesota or Emory University Institutional Animal Care and Use Committee guidelines.

**Isolation of lymphocytes and immunofluorescence.** Blood was obtained by disruption of the retro-orbital plexus, and peripheral blood lymphocytes (PBLs) were purified by underlaying Histopaque (Sigma-Aldrich) and performing density centrifugation (800g at 20 °C for 20 min). Lymphocytes were isolated from spleen, lung and inguinal lymph nodes as previously described<sup>7</sup>. Single-cell suspensions were surface-stained with anti-CD8, -Thy1.1, -CD44, -CD62L, -CD4, -B220, -CD3 and -IgD (BD Pharmingen). VSV-nucleoprotein-specific CD8 T cells were identified by staining with H-2K<sup>b</sup> tetramers constructed with the N<sub>52–59</sub> peptide, as previously described<sup>23</sup>. Endogenous LCMV-specific CD8 T cells (Supplementary Fig. 4) were identified by staining with H-2D<sup>b</sup> np<sub>396–404</sub>, H-2D<sup>b</sup> gp<sub>33–41</sub>, H-2D<sup>b</sup> gp<sub>276–286</sub> and H-2L<sup>d</sup> np<sub>118–126</sub> tetramers, constructed as previously described (np and gp refer to LCMV nucleoprotein and glycoprotein, respectively)<sup>24</sup>. Samples were acquired on a FACSCalibur flow cytometer (BD Biosciences).

**Full Methods** and any associated references are available in the online version of the paper at [www.nature.com/nature](http://www.nature.com/nature).

**Received 17 July; accepted 29 September 2008.**

**Published online 12 November 2008.**

- Christensen, J. P., Doherty, P. C., Branum, K. C. & Riberdy, J. M. Profound protection against respiratory challenge with a lethal H7N7 influenza A virus by increasing the magnitude of CD8<sup>+</sup> T-cell memory. *J. Virol.* **74**, 11690–11696 (2000).
- Freitas, A. A. & Rocha, B. Population biology of lymphocytes: the flight for survival. *Annu. Rev. Immunol.* **18**, 83–111 (2000).
- Goldrath, A. W. Maintaining the status quo: T-cell homeostasis. *Microbes Infect.* **4**, 539–545 (2002).
- Welsh, R. M., Selin, L. K. & Szomolanyi-Tsuda, E. Immunological memory to viral infections. *Annu. Rev. Immunol.* **22**, 711–743 (2004).
- Surh, C. D., Boyman, O., Purton, J. F. & Sprent, J. Homeostasis of memory T cells. *Immunol. Rev.* **211**, 154–163 (2006).
- Sad, S. & Krishnan, L. Maintenance and attrition of T-cell memory. *Crit. Rev. Immunol.* **23**, 129–147 (2003).
- Masopust, D., Ha, S. J., Vezys, V. & Ahmed, R. Stimulation history dictates memory CD8 T cell phenotype: implications for prime–boost vaccination. *J. Immunol.* **177**, 831–839 (2006).
- Woodland, D. L. Jump-starting the immune system: prime–boosting comes of age. *Trends Immunol.* **25**, 98–104 (2004).
- Wherry, E. J. et al. Lineage relationship and protective immunity of memory CD8 T cell subsets. *Nature Immunol.* **4**, 225–234 (2003).
- Selin, L. K., Vergilis, K., Welsh, R. M. & Nahill, S. R. Reduction of otherwise remarkably stable virus-specific cytotoxic T lymphocyte memory by heterologous viral infections. *J. Exp. Med.* **183**, 2489–2499 (1996).
- Selin, L. K. et al. Attrition of T cell memory: selective loss of LCMV epitope-specific memory CD8 T cells following infections with heterologous viruses. *Immunity* **11**, 733–742 (1999).
- Schluns, K. S. & Lefrançois, L. Cytokine control of memory T-cell development and survival. *Nature Rev. Immunol.* **3**, 269–279 (2003).
- Masopust, D., Vezys, V., Wherry, E. J., Barber, D. L. & Ahmed, R. Cutting edge: gut microenvironment promotes differentiation of a unique memory CD8 T cell population. *J. Immunol.* **176**, 2079–2083 (2006).
- Jabbari, A. & Harty, J. T. Secondary memory CD8<sup>+</sup> T cells are more protective but slower to acquire a central-memory phenotype. *J. Exp. Med.* **203**, 919–932 (2006).
- Antia, R., Ganusov, V. V. & Ahmed, R. The role of models in understanding CD8<sup>+</sup> T-cell memory. *Nature Rev. Immunol.* **5**, 101–111 (2005).
- Jackola, D. R. & Hallgren, H. M. Dynamic phenotypic restructuring of the CD4 and CD8 T-cell subsets with age in healthy humans: a compartmental model analysis. *Mech. Ageing Dev.* **105**, 241–264 (1998).
- Czesnikiewicz-Guzik, M. et al. T cell subset-specific susceptibility to aging. *Clin. Immunol.* **127**, 107–118 (2008).
- Hammarlund, E. et al. Duration of antiviral immunity after smallpox vaccination. *Nature Med.* **9**, 1131–1137 (2003).
- Pantaleo, G. & Koup, R. A. Correlates of immune protection in HIV-1 infection: what we know, what we don't know, what we should know. *Nature Med.* **10**, 806–810 (2004).
- Sekaly, R. P. The failed HIV Merck vaccine study: a step back or a launching point for future vaccine development? *J. Exp. Med.* **205**, 7–12 (2008).
- Kaiser, J. AIDS research. Review of vaccine failure prompts a return to basics. *Science* **320**, 30–31 (2008).
- Shiver, J. W. & Emini, E. A. Recent advances in the development of HIV-1 vaccines using replication-incompetent adenovirus vectors. *Annu. Rev. Med.* **55**, 355–372 (2004).
- Lefrançois, L., Olson, S. & Masopust, D. A critical role for CD40–CD40 ligand interactions in amplification of the mucosal CD8 T cell response. *J. Exp. Med.* **190**, 1275–1284 (1999).
- Murali-Krishna, K. et al. Counting antigen-specific CD8 T cells: a reevaluation of bystander activation during viral infection. *Immunity* **8**, 177–187 (1998).

**Supplementary Information** is linked to the online version of the paper at [www.nature.com/nature](http://www.nature.com/nature).

**Acknowledgements** We thank S. Jameson, E. J. Wherry and A. Haase for critical discussions and reading of the manuscript, and J. W. Yewdell for recombinant vaccinia virus. This research was supported by start-up funds from the University of Minnesota Medical School (V.V. and D.M.) and NIH grant AI30048 (R. Ahmed).

**Author Information** Reprints and permissions information is available at [www.nature.com/reprints](http://www.nature.com/reprints). Correspondence and requests for materials should be addressed to D.M. (masopust@umn.edu).



## METHODS

**Mice and infections.** To test the impact of large numbers of pre-existing memory CD8 T cells on responses to new infections (Supplementary Fig. 3), naive C57Bl/6J mice were subjected to the heterologous prime–boost regimen as follows: mice were infected with  $5 \times 10^5$  p.f.u. VSV-NJ i.v., rested for 70 days, infected with  $2 \times 10^6$  p.f.u. VVn i.v., rested for 140 days, and then infected with  $1 \times 10^6$  p.f.u. VSV-IND i.v. and rested for 146 days. Age-matched control mice were rested without receiving the heterologous prime–boost regimen. Both groups were then challenged with  $2 \times 10^5$  p.f.u. LCMV Armstrong strain i.p. and analysed 43 days later.

For the experiments described in Supplementary Fig. 4, C57Bl/6J or Balb/c mice were infected with  $2 \times 10^5$  p.f.u. LCMV Armstrong strain. 45–60 days later, mice were challenged with  $2 \times 10^6$  p.f.u. vaccinia virus i.p.,  $2 \times 10^4$  colony-forming units *Listeria monocytogenes* i.v. or  $1 \times 10^6$  red blood cells parasitized with *Plasmodium yoelii*<sup>25</sup> i.p., as indicated.

**Quantification of antibody-secreting cells.** Using a modification of the enzyme-linked immunospot (ELISPOT) technique, 96-well nitrocellulose plates were coated with LCMV-infected BHK cell lysate for approximately 16 h<sup>26</sup>. After washing off unbound antigen, splenocytes from immune and immune-challenged mice were plated and incubated for 5 h at 37 °C. Mouse immunoglobulin G was detected by means of an HRP-conjugated antibody and visualized with aminoethyl carbazole as the chromagen substrate. Spots were enumerated by means of a stereomicroscope and total numbers of antibody-secreting cells per spleen were calculated by multiplying total spleen cell numbers with numbers of spots per well.

25. Hunter, R. L., Kidd, M. R., Olsen, M. R., Patterson, P. S. & Lal, A. A. Induction of long-lasting immunity to *Plasmodium yoelii* malaria with whole blood-stage antigens and copolymer adjuvants. *J. Immunol.* **154**, 1762–1769 (1995).
26. Slifka, M. K., Matloubian, M. & Ahmed, R. Bone marrow is a major site of long-term antibody production after acute viral infection. *J. Virol.* **69**, 1895–1902 (1995).

## LETTERS

# Frequent in-frame somatic deletions activate gp130 in inflammatory hepatocellular tumours

Sandra Rebouissou<sup>1,2</sup>, Mohamed Amessou<sup>1,2</sup>, Gabrielle Couchy<sup>1,2</sup>, Karine Poussin<sup>1,2</sup>, Sandrine Imbeaud<sup>3,4</sup>, Camilla Pilati<sup>1,2</sup>, Tina Izard<sup>5</sup>, Charles Balabaud<sup>6,7</sup>, Paulette Bioulac-Sage<sup>6,8</sup> & Jessica Zucman-Rossi<sup>1,2</sup>

Inflammatory hepatocellular adenomas are benign liver tumours defined by the presence of inflammatory infiltrates and by the increased expression of inflammatory proteins in tumour hepatocytes<sup>1,2</sup>. Here we show a marked activation of the interleukin (IL)-6 signalling pathway in this tumour type; sequencing candidate genes pinpointed this response to somatic gain-of-function mutations in the *IL6ST* gene, which encodes the signalling co-receptor gp130. Indeed, 60% of inflammatory hepatocellular adenomas harbour small in-frame deletions that target the binding site of gp130 for IL-6, and expression of four different gp130 mutants in hepatocellular cells activates signal transducer and activator of transcription 3 (STAT3) in the absence of ligand. Furthermore, analysis of hepatocellular carcinomas revealed that rare gp130 alterations are always accompanied by  $\beta$ -catenin-activating mutations, suggesting a cooperative effect of these signalling pathways in the malignant conversion of hepatocytes. The recurrent gain-of-function gp130 mutations in these human hepatocellular adenomas fully explains activation of the acute inflammatory phase observed in tumorous hepatocytes, and suggests that similar alterations may occur in other inflammatory epithelial tumours with STAT3 activation.

Several recent studies have shown STAT3 activation in epithelial tumours, underscoring the importance of IL-6 signalling and the inflammatory response in tumorigenesis and providing an opportunity for therapeutic intervention<sup>3</sup>. However, the mechanisms that provoke sustained STAT3 activation in tumours are largely unresolved. To define the interaction between the inflammatory response and carcinogenesis in liver tumours, we assessed inflammatory hepatocellular adenomas (IHCA), benign tumours predominately found in women and frequently associated with obesity and alcohol use<sup>1,2</sup>. Tumour hepatocytes of these adenomas express increased levels of serum amyloid A (SAA) and C-reactive proteins (CRP), two members of the acute-phase inflammatory response, whereas SAA and CRP are not expressed in inflammatory cells, Kupffer cells or other sinusoidal cells in IHCA (Fig. 1a, Supplementary Fig. 1 and ref. 1). Inflammatory infiltrates were largely localized to arterial vessels, but were also found within the sinusoidal lumens of IHCA. Here, CD45<sup>+</sup>CD3<sup>+</sup> T lymphocytes (CD4:CD8, 2:1) were intermingled with less numerous CD20<sup>+</sup>CD79A<sup>+</sup> B cells, some plasma cells and a few polymorphonuclear cells; no CD30<sup>+</sup> lymphocytes nor CD56<sup>+</sup> or CD57<sup>+</sup> natural killer cells were observed. In addition, CD68<sup>+</sup> histiocytes were present in infiltrates, and prominent Kupffer cells were present in sinusoidal lumens (Supplementary Fig. 1). Overall, inflammatory infiltrates observed in IHCA were highly polymorphous.

To resolve the underlying pathogenesis of these inflammatory lesions, a genome-wide transcriptome analysis of four IHCA was compared to four normal liver tissue samples. Among the 285 genes significantly overexpressed in IHCA (Supplementary Table 1), gene ontology analysis identified a strong enrichment for genes associated with inflammation and the immune response, accounting for 40% of the overall ontology terms significantly enriched (Supplementary Table 2). High levels of significance were found for genes involved in 'antigen processing and presentation of peptide antigen' ( $P = 2.10^{-11}$ ) and 'regulation of the Janus kinase (JAK)–STAT cascade' ( $P = 10^{-5}$ ; Supplementary Table 2). We confirmed this inflammatory signature in an additional 14 IHCA with a clear activation of the acute-phase inflammatory response affecting both type-1 and type-2 acute-phase genes (Fig. 1b, c and Supplementary Table 3). Consistent with the known roles of IL-6 and JAK–STAT signalling in the acute-phase response<sup>4,5</sup>, STAT3 messenger RNA and protein were significantly increased in IHCA (Fig. 1b, c). IHCA also overexpressed several effectors of type-1 and type-2 interferon signalling pathways (for example JAK2, STAT1 and STAT2) and their downstream targets (Fig. 1b, c). Collectively, these data suggest that IL-6 and interferon signalling are the main inflammatory pathways activated in IHCA (Fig. 1d).

Because IL-6 was not overexpressed in IHCA and the inflammatory response was restricted to tumour hepatocytes (Fig. 1a), we reasoned that somatic genetic mutation(s) might account for activation of IL-6 receptor signalling in IHCA. We selected *IL6ST* as a candidate gene because it encoded the cell surface signalling receptor gp130 shared by at least six different cytokines including IL-6, IL-11, LIF, OSM, CNTF and CT-1 (also known as CTF1; refs 4, 6). We sequenced the entire gp130 coding region in 43 IHCA and 33 non-inflammatory hepatocellular adenomas. Twenty-six mutations in gp130 were identified specifically in 60% (26 out of 43) of IHCA, including 16 unique, small in-frame deletions and one 33-base-pair in-frame duplication in exon 6 (Fig. 2a and Table 1). Notably, all *IL6ST* mutations were found in IHCA and all were of somatic origin, because they were not observed in adjacent normal liver tissues. In all cases, *IL6ST* mutations were monoallelic, and IHCA with these mutations expressed both the wild-type and mutated alleles at comparable levels, as judged by sequencing polymerase chain reaction with reverse transcription (RT–PCR) products of *IL6ST* mRNA (Supplementary Fig. 2).

Binding of IL-6 to its cognate receptor gp80 (encoded by *IL6R*) induces formation of a high-affinity ternary hexameric complex consisting of two molecules each of IL-6, IL-6R and gp130 (refs 7, 8). gp130 engagement then activates JAK–Tyk tyrosine kinases and the

<sup>1</sup>Inserm, U674, Génomique fonctionnelle des tumeurs solides, Paris F-75010, France. <sup>2</sup>Université Paris Diderot, Paris 7, Institut Universitaire d'Hématologie, Paris F-75010, France. <sup>3</sup>Array s/IMAGE, Genexpress, Functional Genomics and Systems Biology for Health, UMR 7091 CNRS; Université Paris 6 Pierre et Marie Curie, Villejuif F-94801, France. <sup>4</sup>Gif/Orsay DNA Microarray Platform (GODMAP), Centre de Génétique Moléculaire, UPR 2167 CNRS; Université Paris-Sud 11, Gif-sur-Yvette F-91198, France. <sup>5</sup>Department of Cancer Biology, The Scripps Research Institute, Jupiter, Florida 33458, USA. <sup>6</sup>Inserm, U889; Université Victor Segalen Bordeaux 2, IFR66, Bordeaux F-33076, France. <sup>7</sup>CHU de Bordeaux, Hôpital Saint-André, Service d'hépatologie, Bordeaux F-33076, France. <sup>8</sup>CHU de Bordeaux, Hôpital Pellegrin, Service d'Anatomie Pathologique, Bordeaux F-33076, France.

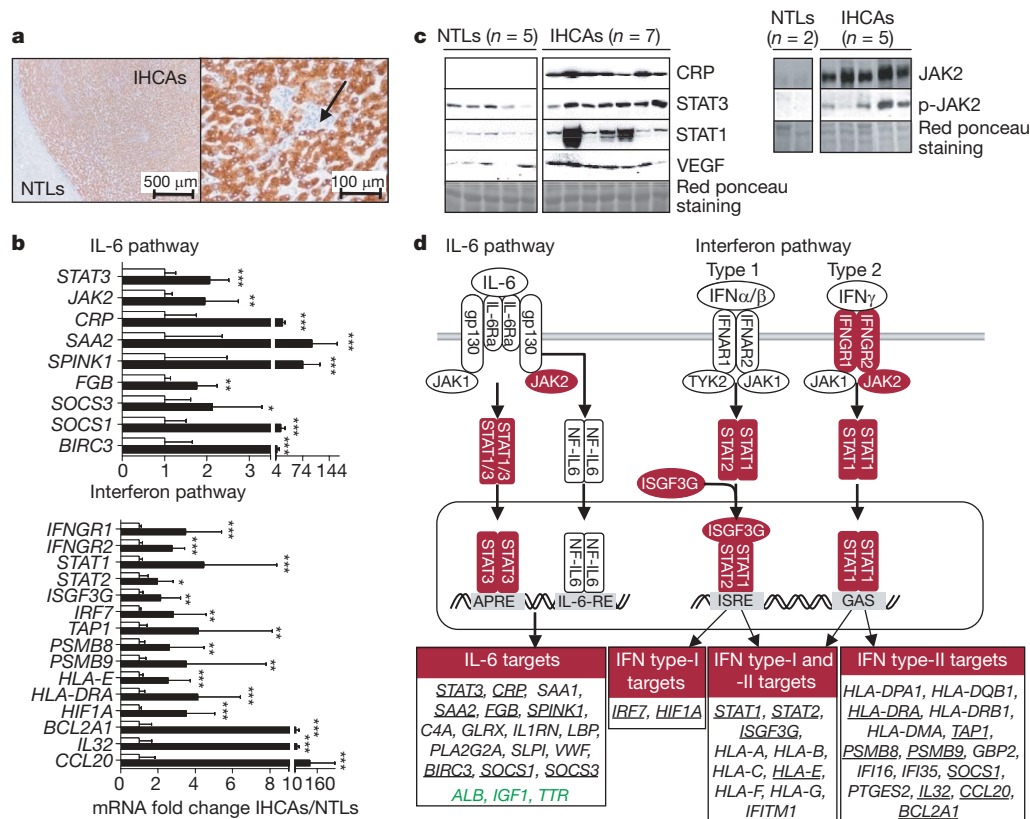


**Figure 1 | Activation of the IL-6 and interferon pathways in IHCA.**

**a**, Immunohistochemical analysis of CRP expression. There is a high level of expression in tumour hepatocytes (IHCA); adjacent normal non-tumour liver hepatocytes (NTL) and inflammatory cells located in the tumour (arrow) are negative. **b**, qRT-PCR validation of gene array expression data comparing IHCA (n = 14, black) with NTLs (n = 6, white). Mean and s.d. are shown; \*, \*\* and \*\*\* indicate the difference between groups at  $P < 0.05$ ,  $P < 0.01$  and  $P < 0.001$ , respectively (two-tailed Mann-Whitney test).

**c**, Western-blot analysis comparing expression levels of STAT1 (84 kDa) and

STAT3 (79, 86 kDa), CRP (24 kDa), VEGF (22 kDa), JAK2 and phospho-JAK2 (p-JAK2, 125 kDa) between IHCA and NTL. **d**, Schematic representation of the IL-6 and interferon pathways showing all genes overexpressed (red) or suppressed (green) in IHCA compared with NTL. Genes validated by qRT-PCR are underlined (IHCA, n = 14; NTL, n = 6); others were extracted from the microarray analysis (IHCA, n = 4; NTL, n = 4). APRE (acute phase response element), GAS (interferon- $\gamma$ -activated site), IL-6Ra (also known as gp80 or IL-6R), IL-6-RE (interleukin 6 response element), ISRE (interferon-sensitive response element).

STAT family of transcription factors<sup>9–11</sup>. The consequences of the IL6ST in-frame deletions observed in IHCA included the removal of 1 to 26 amino acids neighbouring the IL-6/IL-6R binding site (also known as cytokine-receptor homology region, CHR, E-F loop) located in D2 domain of gp130 (Fig. 2a). We modelled the different deletions and the duplication in the known crystal structure of the wild-type IL-6–IL-6R–gp130 ternary complex (Protein Data Bank, PDB: 1P9M)<sup>7</sup>. All of these mutations are predicted to disrupt key residues involved in the gp130–IL-6 interface. Specifically, the most frequent alterations target residues 186–191, which direct the gp130–IL-6 interaction, whereas the remaining deletions and duplication affect the other two loops that contribute to gp130–IL-6 interactions (Fig. 2b). Therefore, the gp130–IL-6 interface is targeted in IHCA.

To investigate possible functional consequences of these gp130 mutations, we tested the effects of enforced expression of two frequent deletions (S187–Y190del and Y186–Y190del) and two infrequent mutants (V184–Y186del, S187A and K173–D177del) in Hep3B cells, a hepatocellular carcinoma line that activates the acute inflammatory phase after IL-6 treatment<sup>12</sup>. In the absence of IL-6 ligand and serum, overexpression of wild-type gp130 alone was not sufficient to activate STAT3 and the downstream acute-phase inflammatory genes (Fig. 3 and refs 7, 13). In contrast, all gp130 IHCA mutants activated an acute-phase inflammatory response and induced typical targets of this response, including CRP, SAA2, SPINK1 and FBG (Fig. 3a, c). Furthermore, as observed in IHCA, all of these gp130 mutants induced the expression of SOCS3, which normally serves to harness cytokine signalling (Fig. 3a). Mutant gp130 S187–Y190del was

constitutively tyrosine phosphorylated and the activity of STAT3 was clearly increased in gp130 S187–Y190del-expressing Hep3B cells (Fig. 3b). Similarly, immunohistochemical analyses of IHCA demonstrated marked increases in nuclear STAT3 phosphorylated at Tyr 705 (Supplementary Fig. 4e, f). Finally, IL-6 augmented the induction of CRP in gp130 S187–Y190del-expressing cells, but mutant receptors were not hypersensitive to low doses of IL-6 (Fig. 3d). Therefore, gp130 mutants are constitutively active, and they activate STAT3 and inflammatory response genes in the absence of IL-6.

A critical step in the activation of intracellular signalling after IL-6 binding on gp130 is the formation of a hexameric structure that juxtaposes the membrane-proximal domains of two gp130 molecules at the cell surface<sup>7,14,15</sup>. Using co-immunoprecipitation, we showed that the gp130 S187–Y190del IHCA mutant was able to homodimerize or heterodimerize with wild-type gp130 independently of IL-6, whereas wild-type gp130 cannot homodimerize (Fig. 3f). Homodimerization of gp130 in the absence of ligand has also been described previously for two other gp130 mutants, Y190FV-to-AAA and Y190A (ref. 16). Moreover, overexpression of wild-type gp130 impaired the activity of the mutant gp130 S187–Y190del in a dose-dependent manner (Fig. 3e); therefore, mutant gp130 activity seems to be driven by its homodimerization, which can be competed for by the wild-type protein. Interestingly, it has recently been shown using a reverse genetic approach in mice that IL-11 promotes chronic gastric inflammation and associated tumorigenesis mediated by gp130 and STAT3 activation<sup>17</sup>. In IHCA, we also found significant increases



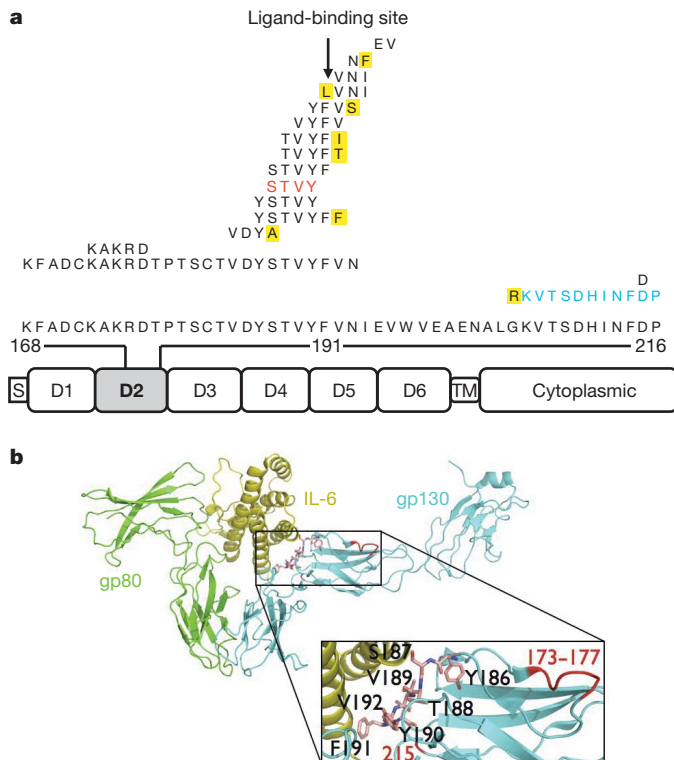


**Figure 2 | gp130 mutations in inflammatory hepatocellular tumours.** **a**, The spectrum of mutations in gp130 detected in IHCAs (S, signal peptide; TM, transmembrane domain). The location of the 16 deletions, the duplication (in blue) and the resulting amino acid substitutions (in yellow) identified in the D2 domain of gp130 are indicated above the wild-type sequence. The most frequent mutation is indicated in red. **b**, Residues 186–192 (shown in pink stick presentation) of the D2 domain of gp130 that are deleted in IHCAs are intimately involved in interactions with IL-6, as shown in the crystal structure of the IL-6R–IL-6–gp130 complex (PDB: 1P9M)<sup>7</sup>. IHCA deletions 173–177 and 215 (labelled in red) are also predicted to disrupt the IL-6–gp130 interface. The numbering of residues corresponds to the *IL6ST* complementary DNA, which has 22 additional amino-terminal residues compared with the polypeptide chain due to the peptide signal.

(sixfold) in the levels of *IL11* mRNA ( $P < 0.01$ ), which may serve to amplify gp130–IL-6 signalling, despite a modest decrease in the expression of its specific receptor (*IL11RA*; Supplementary Fig. 5a). However, in mutant gp130-expressing Hep3B cells *IL11* was not

**Table 1 | gp130 somatic mutations identified in inflammatory hepatocellular tumours**

Number of mutated tumours	Nucleotide change	Amino acid change
6*	560–571del	S187–Y190del
4*	557–571del	Y186–Y190del
3	565–576del	V189–V192del
2	563–574del	T188–F191del, V192I
1	503–580del	K168–N192del
1*	518–532del	K173–D177del
1*	551–559del	V184–Y186del, S187A
1	557–574del	Y186–F191del, V192F
1	559–573del	S187–F191del
1	564–575del	T188–F191del, V192T
1**	569–577del, 578A > C	Y190–V192del, N193S
1	573T > G, 574–582del	F191L, V192–I194del
1	575–583del	V192–I194del
1**	577–579del, 580A > T	N193del, I194F
1	583–588del	E195–V196del
1	614–646dup	K206–P216dup, G205R
1	643–645del	D215del

Codons and mutated nucleotides are numbered according to *IL6ST* cDNA open reading frame. \*gp130 mutants analysed in Hep3B cells. \*\*Mutations identified in HCC.

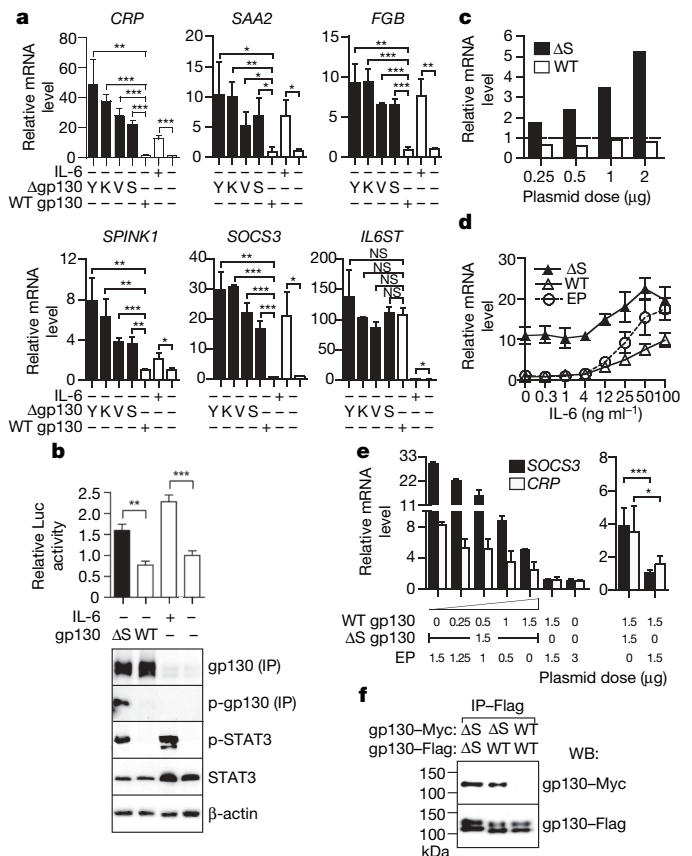


**Figure 3 | Gain-of-function mutations of gp130.** **a**, gp130 mutants ( $\Delta$ ) including S187–Y190del (S), Y186–Y190del (Y), V184–Y186del, S187A (V) and K173–D177del (K) or controls including gp130 wild type (WT) and empty plasmid were transfected in Hep3B cells. Graphs plot qRT–PCR results relative to empty-plasmid-transfected unstimulated cells; mean and s.d. (transfections in triplicate). NS, not significant. **b**, Shown is the luciferase (Luc) activity (mean) measured in triplicate transfections (plus s.d.) with pSTAT3-luc alone or together with WT or the S187–Y190del ( $\Delta$ S) gp130. Expression of total and phosphorylated (p-STAT3 and p-gp130) proteins were analysed using western blotting, after immunoprecipitation (IP) for gp130. **c**, *CRP* mRNA expression after transfection with increasing amounts of plasmids expressing WT or  $\Delta$ S gp130 (baseline, mock-transfected cells). **d**, Hep3B cells were transfected with empty plasmid (EP), WT or  $\Delta$ S gp130 and exposed to increasing concentrations of IL-6. The graph plots mean *CRP* expression value relative to cells transfected with EP (plus s.d.; transfections in triplicate). **e**, Effect of increasing amounts of WT gp130 on the  $\Delta$ S gp130 mutant activity, without IL-6. The graph plots the mean level of expression of SOCS3 and *CRP* relative to cells transfected with EP (plus s.d.) in duplicate (left) or in five independent transfections (right). **f**, Flag- and Myc-tagged constructs expressing either the WT or the mutant  $\Delta$ S gp130 were co-transfected (1:1) into Hep3B cells. gp130 dimer formation was detected after immunoprecipitation using the anti-flag antibody, followed by western blot (WB) analysis with the anti-Myc and anti-Flag antibodies. Shown is one representative of three independent experiments. \*, \*\* and \*\*\* indicate differences between groups at  $P < 0.05$ ,  $P < 0.01$  and  $P < 0.001$ , respectively (two-tailed *t*-test).

induced (Supplementary Fig. 5b), suggesting that an increase of *IL11* in IHCAs *in vivo* may occur through secondary effects.

Relationships between activation of IL-6 signalling and hepatic tumorigenesis have also been suggested from studies in mice, in which transgenic animals that overexpress both IL-6 and IL-6R in hepatocytes develop large liver adenomas<sup>18</sup>. Furthermore, in knock-in mice expressing gp130(Y757) mutant, gastric inflammation and subsequent carcinoma development result from STAT3 activation<sup>19–21</sup>. The IL-6 pathway is also known to activate SHP-2–RAS–ERK signalling<sup>22</sup>. However, in humans, STAT3 activation is a clear hallmark of gp130-mutated IHCAs, phosphorylated ERK1 and ERK2

(phospho-ERK1/2) was only detected in 50% of these tumours (Supplementary Fig. 6a), and phospho-ERK1/2 was not observed in Hep3B cells overexpressing mutant gp130 (Supplementary Fig. 6b). Thus, in contrast to STAT3 activation, activation of the SHP-2–RAS–ERK pathway does not seem to contribute to all IHCA.

Surprisingly, type-1 and type-2 interferon targets are overexpressed in gp130-mutated IHCA. Their aberrant activation here might be due to gp130-mediated STAT1 and STAT2 activation and inefficient negative feedback by SOCS3, which is thought to prevent activation of type-2 interferon genes under physiological conditions<sup>23</sup>. Interestingly, the targets in gp130-mutated IHCA include *HIF1A* (encoding hypoxia-inducible factor-1 $\alpha$ ), which may contribute to vascular endothelial growth factor (VEGF) overexpression and the 'telangiectatic' phenotype of IHCA (Fig. 1b, c)<sup>1,2,24</sup>. Furthermore, the inflammatory infiltrate that is a hallmark of IHCA may reflect the robust induction (~110-fold) of *CCL20* observed in all IHCA (Fig. 1b). Specifically, *CCL20* is a chemokine that interacts with CCR6 and that directs chemoattraction of a wide spectrum of immune cells including dendritic cells and B and T lymphocytes<sup>25</sup>, and such a scenario could direct or augment the inflammatory response seen in IHCA.

To investigate the possible interaction and cooperation of gp130 activation with other pathways altered in hepatocellular adenoma, we searched in the same series of 76 adenomas for *CTNNB1* (encoding  $\beta$ -catenin) and *HNF1A* (encoding hepatocyte nuclear factor 1 $\alpha$ ) mutations, two genetic alterations frequently associated with hepatocellular adenomas (HCA)<sup>2,26,27</sup>. *HNF1 $\alpha$*  inactivation (22 cases) and gp130 activation (26 cases) were mutually exclusive in HCA ( $P < 10^{-4}$ , Fisher exact test; Supplementary Table 4). In contrast,  $\beta$ -catenin-activating mutations were found in 12 adenomas, and half of these had associated gp130 mutations. For two IHCA associated with a malignant transformation to carcinoma, both activating gp130 and  $\beta$ -catenin mutations were found (cases 469 and 786; Supplementary Table 4). In one of these cases we were able to genotype the hepatocellular carcinoma (HCC), and this harboured the same mutations in *CTNNB1* and *IL6ST* as the corresponding IHCA. In contrast, no cases of malignant transformation were observed in gp130-mutated IHCA without a  $\beta$ -catenin mutation ( $P = 0.05$ , two-tailed Fisher exact test). When we sequenced *IL6ST* exon 6 in 111 HCCs lacking a known history of IHCA<sup>28</sup>, only two cases were mutated. Interestingly, these tumours were compatible with a malignant transformation of a non-diagnosed IHCA because both mutated HCCs had inflammatory infiltrates; they harboured  $\beta$ -catenin-activating mutations and developed in non-cirrhotic liver (Supplementary Table 4). Collectively, these findings suggest cooperation between the IL-6 and  $\beta$ -catenin pathways in the malignant transformation of IHCA.

*IL6ST* mutations were identified in 60% of IHCA. The remaining IHCA were, however, similar in their expression profiles to *IL6ST*-mutated IHCA (Supplementary Fig. 3) and, accordingly, activated nuclear phospho-STAT3 was also found in all non-mutated IHCA tested (Supplementary Fig. 4f). Sequencing of the functional domains of three gp130 co-receptors (*IL6R*, *LIFR* and *OSMR*), of the functional domains of three transducing proteins (*JAK2*, *JAK1* and *TYK2*) and of the coding sequence of *SOCS3* failed to identify mutations in gp130-non-mutated IHCA. Moreover, these tumours lacked mutations in the exons or intron–exon boundaries of *IL6ST*, and *IL6ST* mRNA levels were comparable to those expressed in normal hepatocytes (Supplementary Fig. 4a). Finally, no gain of chromosome 5q copy number at the *IL6ST* locus was observed using comparative genomic hybridization using single nucleotide polymorphism genotyping (CGH-SNP) experiments in gp130-mutated and -non-mutated IHCA (data not shown). However, by western blotting and immunohistochemistry we found that most IHCA cases overexpressed gp130 protein (Supplementary Fig. 4b–d), suggesting that the translation or turnover of gp130 is affected in both gp130-non-mutated and -mutated tumours. Therefore, gp130 overexpression and STAT3

activation are related to gp130 activating mutation in 60% of the IHCA, whereas, in the non-mutated cases, the mechanism of STAT3 activation remains to be defined. Here, for example, activation may reflect mutations in a regulatory protein(s) that controls gp130 stabilization, or may be due to alterations in factors that control its translation.

The present findings reveal that STAT3 activation and the inflammatory phenotype in benign liver tumours can occur through gain-of-function somatic mutations in gp130. To our knowledge, this is the first identification of somatic mutation of gp130 in tumours, and our findings define gp130 as an oncogene with involvement in benign human tumours. Our findings also underscore the important role of inflammatory response in hepatocellular tumorigenesis and are in accordance with a recent study demonstrating that IL-6 promotes liver tumour onset in mice<sup>29</sup>. Importantly, our studies also suggest that cooperating mutations of the WNT– $\beta$ -catenin and IL-6–STAT pathways in human liver tumours contribute to the occurrence of inflammatory hepatocellular carcinomas that develop in the absence of cirrhosis. More broadly, these findings indicate that this novel mechanism for activation of the IL-6 signalling pathway should be interrogated in other human tumours, particularly those with an inflammatory phenotype and STAT3 activation, a hallmark of many epithelial tumours.

## METHODS SUMMARY

All tumours and corresponding non-tumour liver tissues were frozen after surgical resection. These tumours were clinically and genetically characterized; they were previously included in genetic and phenotypic studies (Supplementary Table 4 and refs 1, 2, 28). The study was approved by the local Ethics Committee (Paris Saint-Louis), and informed consent was obtained in accordance with French legislation. Transcriptional profiling experiments were performed using Affymetrix oligonucleotide GeneChips HG-U133A. Quantitative (q)RT–PCR was performed as described<sup>30</sup> using pre-designed primers and probe sets from Applied Biosystems (provided in Supplementary Table 5). In all cases the somatic origin of the mutation found in a tumour was verified by sequencing the corresponding adjacent, normal liver sample. In Hep3B cell experiments, all qRT–PCRs, luciferase assays and western blotting experiments were performed two days after transfection and after 6 h of serum starvation.

**Full Methods** and any associated references are available in the online version of the paper at [www.nature.com/nature](http://www.nature.com/nature).

Received 7 April; accepted 26 September 2008.

Published online 19 November 2008.

1. Bioulac-Sage, P. *et al.* Hepatocellular adenoma subtype classification using molecular markers and immunohistochemistry. *Hepatology* **46**, 740–748 (2007).
2. Zucman-Rossi, J. *et al.* Genotype–phenotype correlation in hepatocellular adenoma: new classification and relationship with HCC. *Hepatology* **43**, 515–524 (2006).
3. Grivennikov, S. & Karin, M. Autocrine IL-6 signaling: a key event in tumorigenesis? *Cancer Cell* **13**, 7–9 (2008).
4. Akira, S. *et al.* Molecular cloning of APRF, a novel IFN-stimulated gene factor 3 p91-related transcription factor involved in the gp130-mediated signaling pathway. *Cell* **77**, 63–71 (1994).
5. Wegenka, U. M., Buschmann, J., Luttkien, C., Heinrich, P. C. & Horn, F. Acute-phase response factor, a nuclear factor binding to acute-phase response elements, is rapidly activated by interleukin-6 at the posttranslational level. *Mol. Cell. Biol.* **13**, 276–288 (1993).
6. Hibi, M. *et al.* Molecular cloning and expression of an IL-6 signal transducer, gp130. *Cell* **63**, 1149–1157 (1990).
7. Boulanger, M. J., Chow, D. C., Brevnova, E. E. & Garcia, K. C. Hexameric structure and assembly of the interleukin-6/IL-6 $\alpha$ -receptor/gp130 complex. *Science* **300**, 2101–2104 (2003).
8. Ward, L. D. *et al.* High affinity interleukin-6 receptor is a hexameric complex consisting of two molecules each of interleukin-6, interleukin-6 receptor, and gp130. *J. Biol. Chem.* **269**, 23286–23289 (1994).
9. Luttkien, C. *et al.* Association of transcription factor APRF and protein kinase Jak1 with the interleukin-6 signal transducer gp130. *Science* **263**, 89–92 (1994).
10. Murakami, M. *et al.* IL-6-induced homodimerization of gp130 and associated activation of a tyrosine kinase. *Science* **260**, 1808–1810 (1993).
11. Stahl, N. *et al.* Association and activation of Jak–Tyk kinases by CNTF–LIF–OSM–IL-6 $\beta$  receptor components. *Science* **263**, 92–95 (1994).

12. Coulouarn, C. *et al.* Genome-wide response of the human Hep3B hepatoma cell to proinflammatory cytokines, from transcription to translation. *Hepatology* **42**, 946–955 (2005).
13. Kishimoto, T., Akira, S., Narazaki, M. & Taga, T. Interleukin-6 family of cytokines and gp130. *Blood* **86**, 1243–1254 (1995).
14. Chow, D., He, X., Snow, A. L., Rose-John, S. & Garcia, K. C. Structure of an extracellular gp130 cytokine receptor signaling complex. *Science* **291**, 2150–2155 (2001).
15. Skiniotis, G., Boulanger, M. J., Garcia, K. C. & Walz, T. Signaling conformations of the tall cytokine receptor gp130 when in complex with IL-6 and IL-6 receptor. *Nature Struct. Mol. Biol.* **12**, 545–551 (2005).
16. Li, H. & Nicholas, J. Identification of amino acid residues of gp130 signal transducer and gp80 $\alpha$  receptor subunit that are involved in ligand binding and signaling by human herpesvirus 8-encoded interleukin-6. *J. Virol.* **76**, 5627–5636 (2002).
17. Ernst, M. *et al.* STAT3 and STAT1 mediate IL-11-dependent and inflammation-associated gastric tumorigenesis in gp130 receptor mutant mice. *J. Clin. Invest.* **118**, 1727–1738 (2008).
18. Maione, D. *et al.* Coexpression of IL-6 and soluble IL-6R causes nodular regenerative hyperplasia and adenomas of the liver. *EMBO J.* **17**, 5588–5597 (1998).
19. Judd, L. M. *et al.* Gastric cancer development in mice lacking the SHP2 binding site on the IL-6 family co-receptor gp130. *Gastroenterology* **126**, 196–207 (2004).
20. Judd, L. M. *et al.* STAT3 activation regulates growth, inflammation, and vascularization in a mouse model of gastric tumorigenesis. *Gastroenterology* **131**, 1073–1085 (2006).
21. Tebbutt, N. C. *et al.* Reciprocal regulation of gastrointestinal homeostasis by SHP2 and STAT-mediated trefoil gene activation in gp130 mutant mice. *Nature Med.* **8**, 1089–1097 (2002).
22. Boulton, T. G., Stahl, N. & Yancopoulos, G. D. Ciliary neurotrophic factor/leukemia inhibitory factor/interleukin 6/oncostatin M family of cytokines induces tyrosine phosphorylation of a common set of proteins overlapping those induced by other cytokines and growth factors. *J. Biol. Chem.* **269**, 11648–11655 (1994).
23. Croker, B. A. *et al.* SOCS3 negatively regulates IL-6 signaling *in vivo*. *Nature Immunol.* **4**, 540–545 (2003).
24. Bioulac-Sage, P. *et al.* Clinical, morphologic, and molecular features defining so-called telangiectatic focal nodular hyperplasias of the liver. *Gastroenterology* **128**, 1211–1218 (2005).
25. Schutyser, E., Struyf, S. & Van Damme, J. The CC chemokine CCL20 and its receptor CCR6. *Cytokine Growth Factor Rev.* **14**, 409–426 (2003).
26. Bluteau, O. *et al.* Bi-allelic inactivation of TCF1 in hepatic adenomas. *Nature Genet.* **32**, 312–315 (2002).
27. Chen, Y. W., Jeng, Y. M., Yeh, S. H. & Chen, P. J. P53 gene and Wnt signaling in benign neoplasms:  $\beta$ -catenin mutations in hepatic adenoma but not in focal nodular hyperplasia. *Hepatology* **36**, 927–935 (2002).
28. Boyault, S. *et al.* Transcriptome classification of HCC is related to gene alterations and to new therapeutic targets. *Hepatology* **45**, 42–52 (2007).
29. Naugler, W. E. *et al.* Gender disparity in liver cancer due to sex differences in MyD88-dependent IL-6 production. *Science* **317**, 121–124 (2007).
30. Rebouissou, S. *et al.* HNF1 $\alpha$  inactivation promotes lipogenesis in human hepatocellular adenoma independently of SREBP-1 and carbohydrate-response element-binding protein (ChREBP) activation. *J. Biol. Chem.* **282**, 14437–14446 (2007).

**Supplementary Information** is linked to the online version of the paper at [www.nature.com/nature](http://www.nature.com/nature).

**Acknowledgements** We are indebted to P. Bois and O. Bernard for scientific discussion and critical reading of this manuscript. We thank C. Thomas and G. Cubel for their participation to this work. We also thank J. Saric, C. Laurent, A. Sa Cunha, B. Le Bail and A. Rullier for contributing to the tissue collection (CHU Bordeaux). This work was supported by Inserm (Réseaux de Recherche Clinique et Réseaux de Recherche en Santé des Populations), the Ligue Nationale Contre le Cancer ("Cartes d'Identité des Tumeurs" program), ARC (grant 5158), and the Fondation de France. S.R. and M.A. are supported by a fellowship from la Ligue Nationale Contre le Cancer and the Inca, respectively. J.Z.-R. is supported by an interface contract between Inserm and Bordeaux hospital. T.I. is supported by the National Institutes of Health grants GM071596, AI055894 and AI067949.

**Author Information** The microarray data have been deposited in Gene Expression Omnibus (GEO) under accession number GSE11819. Reprints and permissions information is available at [www.nature.com/reprints](http://www.nature.com/reprints). Correspondence and requests for materials should be addressed to J.Z.-R. ([zucman@cephb.fr](mailto:zucman@cephb.fr)).



## METHODS

A series of 76 HCAs was analysed. All samples were collected in Bordeaux hospital. They were extensively characterized and included in previous studies<sup>1,2</sup>. All of the 111 HCCs were included and described previously<sup>28</sup>. For each tumour, a corresponding frozen non-tumour liver sample was available for analyses.

**Transcriptome analyses.** Transcriptional profiling of four IHCAs and four normal liver tissues were performed using Affymetrix oligonucleotide GeneChips HG-U133A (GEO accession number GSE11819). In each case 5 µg of total RNA was labelled, and hybridization was performed using 20 µg of cRNA per hybridization (GeneChip Fluidics Station 400), according to the manufacturer's instructions (Affymetrix). Array images were digitized by using Microarray Suite 5.0 (MAS5) software, embedded in the Affymetrix GeneChip Operating Software (Affymetrix). Gene intensity derivation was carried out from the raw numerical data (CEL files) by using the R package *affy*<sup>31</sup>, available as part of the Bioconductor project<sup>32</sup>, and the DNA-Chip analyser (dChip) program<sup>33</sup>. Probe sets corresponding to control genes or having a 'x\_at' annotation were masked, yielding a total of 19,787 probe sets available for further analyses. Background subtraction, normalization and expression summaries for every probe set were calculated with the log-scale robust multi-array analysis (RMA) algorithm using a background adjusted PM (perfect match) intensities model<sup>34</sup>, and with the model-based expression indexes (MBEI) calculation following a PM/MM (mismatch intensities) difference model<sup>33</sup>. The log-transformed normalized data was considered for further analysis, and a gene annotation was adjoined using the Unigene cluster identifier as a common primary key (Unigene Build184-June05).

Differential analyses were performed using multiple testing procedures to evaluate statistical significance for differentially expressed genes. The biological groups were compared as independent conditions. A pooled curve-fit error method was used for random error estimation; a range of 3.0 to 4.0 median absolute deviations (MADs) established outlier-detection thresholds automatically. Data were subjected to iterative normalization by centring to the median across biological groups. Statistical analyses were computed using both *z*- and *t*-statistics including a *P*-value ranking. Considering respective tests, a false-discovery-rate adjustment of the *P* values was used for multiple testing corrections, and permutation tests (*n* > 1,000) were computed to control the proportion of false discoveries (that is, false positives, >90% confidence). Only genes for which expression significantly differed between IHCA versus normal liver tissues (considering absolute fold change >1.5 and *P*-values ≤0.01) were selected.

Gene ontology categories that were significantly over-represented in genes significantly upregulated or suppressed in IHCA were determined by the hypergeometric test using the web-based tool GOTree Machine (GOTM) (<http://bioinfo.vanderbilt.edu/gotm/>) by comparison with the distribution of the over-all genes included in the HG-U133A Affymetrix array.

**qRT-PCR.** qRT-PCR was performed in duplicate as described<sup>30</sup>. Ribosomal 18S RNA was used to normalize expression data and the  $2^{-\Delta\Delta CT}$  method was applied. Final results were expressed as the *n*-fold differences in target gene expression in tested samples compared with the mean expression value of non-tumour tissues (for tumour analysis) or with the control cell line.

**DNA sequencing.** DNA sequencing was performed as described<sup>26</sup> using primers provided in Supplementary Table 6. All mutations were validated by sequencing a second independent PCR product on both strands.

**Cell culture.** Hep3B cells (ATCC) were grown in DMEM supplemented with 10% FCS. For transfections, cells were plated 16 h before transfection to produce monolayers that were 60% confluent, and these were transfected by using

Lipofectamine LTX according to the manufacturer's instructions (Invitrogen). Transfection efficiency was monitored by measuring the level of either wild-type and mutated gp130 mRNA using qRT-PCR and western blot analysis. The same gp130 expression level was observed in wild-type and in mutant transfected cells. Forty-eight hours after transfection, cells were maintained in serum-free medium, and then cells were either left untreated or stimulated with recombinant human IL-6 (100 ng ml<sup>-1</sup>) in a serum-free medium for 3 h, just before cell collection and protein and RNA extraction. For the luciferase assay, Hep3B cells were co-transfected with STAT3 luciferase reporter vector (pSTAT3-luc, 0.5 µg, Panomics) and the expression plasmid for wild-type or S187-Y190del mutant gp130 (1 µg). Two days after transfection, the cells were lysed and the luciferase activity was measured according to the manufacturer's recommendations (Promega). The activities were normalized to protein in each cell lysate.

**Generation of gp130 mutants.** A full-length gp130 open reading frame (ORF) cloned in the pORF9 vector was purchased from Invivogen (pORF9-hIL6ST). Mutagenesis reactions were performed using the QuickChange site-directed mutagenesis kit (Stratagen). All constructs were verified by sequencing. Using the same method, we also introduced two different epitope tags (Myc and Flag) at the C-terminal end in the wild-type and S187-Y190del constructs.

**Western blot analysis and immunoprecipitation.** Western blot analyses were performed as described<sup>30</sup> using the antibodies specific for STAT3, phospho-STAT3 Tyr 705, STAT1, phospho-JAK2 Tyr 1007/1008 (Cell Signaling Technology, diluted 1:500), JAK2 (Santa Cruz Biotechnology, 1:500), CRP (Sigma, 1:500), gp130 (C-20 Santa Cruz Biotechnology, 1:200) and VEGF (Novus Biologicals, 1:100). The phosphorylated form of gp130 (p-gp130) was analysed by SDS-PAGE after immunoprecipitation from cell lysates containing 750 µg of proteins using 5 µg of the C-20 anti-gp130 antibody. The membrane was then probed with antibodies directed against phosphotyrosine (clone 4G10, Upstate Biotechnology) and gp130 (C20). For dimerization assays, cell lysates were incubated with Protein G agarose (Pierce) and anti-Flag antibody (Cell Signaling Technology, 1:50), at 4 °C for 16 h. The immune complexes were sedimented, washed, separated by SDS-PAGE and analysed by western blot using anti-Flag (1:1,000) and anti-Myc (1:1,000) antibodies. In the western blot, red ponceau staining or actin (Sigma, 1:3,000) expression was analysed to appreciate protein loading.

**Immunohistochemistry.** Immunohistochemistry was performed using a Dako autostainer, on paraffin sections of 10% fixed tumour tissue using two monoclonal antibodies against inflammatory proteins: anti-CRP (Abcam, 1:1,500), anti-SAA (Dako, 1:50), anti-phospho-STAT3 Tyr 705 (Cell Signaling Technology, 1:50) and anti-gp130 (C-20 Santa Cruz Biotechnology, 1:200). For inflammatory cells immunotyping, the following antibodies (Dako) were used: CD45 (clone EB11+PD7/26, 1:300), CD3 (polyclonal, 1:100), CD4 (clone OPD4, 1:100), CD8 (clone C8/144B, 1:20), CD20 (clone L26, 1:100) and CD68 (clone PG-M1, 1:50). For each immunohistochemical procedure, antigen retrieval was performed in citrate buffer, and detection was amplified by the Dako Envision system.

31. Gautier, L., Cope, L., Bolstad, B. M. & Irizarry, R. A. Affy-analysis of Affymetrix GeneChip data at the probe level. *Bioinformatics* **20**, 307–315 (2004).
32. Gentleman, R. C. *et al.* Bioconductor: open software development for computational biology and bioinformatics. *Genome Biol.* **5**, R80 (2004).
33. Li, C. & Hung Wong, W. Model-based analysis of oligonucleotide arrays: model validation, design issues and standard error application. *Genome Biol.* **2**, Research0032 (2001).
34. Irizarry, R. A. *et al.* Summaries of Affymetrix GeneChip probe level data. *Nucleic Acids Res.* **31**, e15 (2003).

# The dynein regulatory complex is required for ciliary motility and otolith biogenesis in the inner ear

Jessica R. Colantonio<sup>1\*</sup>, Julien Vermot<sup>4\*</sup>, David Wu<sup>4</sup>, Adam D. Langenbacher<sup>2</sup>, Scott Fraser<sup>4</sup>, Jau-Nian Chen<sup>2,3</sup> & Kent L. Hill<sup>1,3</sup>

In teleosts, proper balance and hearing depend on mechanical sensors in the inner ear. These sensors include actin-based microvilli and microtubule-based cilia that extend from the surface of sensory hair cells and attach to biomineralized 'ear stones' (or otoliths)<sup>1</sup>. Otolith number, size and placement are under strict developmental control, but the mechanisms that ensure otolith assembly atop specific cells of the sensory epithelium are unclear. Here we demonstrate that cilia motility is required for normal otolith assembly and localization. Using *in vivo* video microscopy, we show that motile tether cilia at opposite poles of the otic vesicle create fluid vortices that attract otolith precursor particles, thereby biasing an otherwise random distribution to direct localized otolith seeding on tether cilia. Independent knockdown of subunits for the dynein regulatory complex and outer-arm dynein disrupt cilia motility, leading to defective otolith biogenesis. These results demonstrate a requirement for the dynein regulatory complex in vertebrates and show that cilia-driven flow is a key epigenetic factor in controlling otolith biomineralization.

Cilia are evolutionarily conserved organelles that perform motility, sensory and transport functions and are required for normal vertebrate development and physiology<sup>2–5</sup>. As such, cilium defects underlie a broad spectrum of human diseases<sup>4,5</sup>. Among the roles of ciliated organs in vertebrate embryogenesis, the contribution of cilia to inner-ear development remains poorly understood. In the zebrafish, *Danio rerio*, it has been proposed that beating cilia participate in the biogenesis of otoliths<sup>6</sup>, which are analogous to otoconia in the otolithic membrane of human ears. These biomineralized particles provide an inertial mass that facilitates deflection of underlying microvilli and cilia, thereby initiating signalling events that allow the brain to detect sound, gravity and linear acceleration<sup>1,7–9</sup>. During early development, nascent otoliths are formed from a pool of precursor particles and tethered to cilia in the otic vesicle<sup>6</sup>. So far, direct evidence for the necessity of ciliary motility in this process is lacking.

In protists, ciliary motility is controlled by the Dynein Regulatory Complex (DRC), which regulates axonemal dynein activity in response to signals from the radial spokes and central pair apparatus<sup>10–15</sup>. The DRC subunit trypanin is conserved across diverse phyla<sup>15–18</sup> and the vertebrate (human) trypanin homologue, growth arrest-specific 8 (here called GAS8, in line with the HUGO database, but also, and originally, designated GAS11) is a microtubule-binding protein localized to regions of dynein regulation in mammalian cells<sup>19–21</sup>. So far, however, a requirement for GAS8 and the DRC in vertebrates has not been established. We identified a single *trypanin* homologue in zebrafish encoding a protein that is 63.8% identical to the human GAS8 protein and 32.0% identical to trypanin from

*Trypanosoma brucei* (Fig. 1). The sequence identity and conserved genomic structure (Fig. 2a)<sup>15,22</sup> indicate that this zebrafish protein, designated Gas8, is indeed a member of this conserved family of dynein regulatory proteins<sup>13,15</sup>. Maternal *gas8* transcripts are ubiquitous throughout the embryo during early development (Fig. 1b, c). By the 12-somite stage, however, expression becomes concentrated in the developing ears (Fig. 1d, arrow) and this persists through the 18- to 20-somite stage (Fig. 1e, Supplementary Fig. 1). Transcripts are also clearly present in the brain, neural tube and pronephric ducts (Fig. 1f–h). Therefore, *gas8* is expressed in ciliated tissues during zebrafish organogenesis.

To determine how loss of *gas8* expression affects zebrafish development we employed antisense morpholino oligonucleotides (Fig. 2). Hydrocephaly, neural tube cell death and left–right axis defects are common in ciliary morphants and mutants<sup>3</sup> and were evident in *gas8* morphants (Fig. 2, Supplementary Fig. 2). Given the high expression of *gas8* in the otic vesicle, we examined ear development more closely. By two days post-fertilization, inner-ear atrophy was evident *gas8* morphants. The length along the antero-posterior axis was 30% less than in control embryos (morphants,  $52 \pm 6 \mu\text{m}$ ,  $n = 15$ ; control,  $73 \pm 7 \mu\text{m}$ ,  $n = 8$ ; 24–27 hours post-fertilization (h.p.f.); see, for example, Figs 2e, f, 3a, b). By three days post-fertilization, exactly two otoliths were present in control zebrafish, one at the anterior end and one at the posterior end of the otic vesicle, positioned ventrally to a semicircular canal<sup>6</sup>. By contrast, *gas8* morphants had abnormal numbers of otoliths, fused otoliths, abnormally positioned otoliths and small otoliths (Fig. 2g–m). Examination of 24-h.p.f. and 27-h.p.f. embryos showed that the same spectrum of defects is evident during nascent otolith formation (Fig. 2n–p). The otolith phenotype is 95–100% penetrant and co-injection of *in-vitro*-transcribed *gas8* messenger RNA carrying five base-pair mismatch mutations to prevent morpholino hybridization rescued the defect in a majority of embryos (Fig. 2g). Because inner ear patterning is tightly linked with neuraxis patterning<sup>23</sup>, we analysed markers for the hindbrain (*egr2b*), midbrain (*eng2a*), forebrain (*otx2*), inner-ear anterior-ventral area (*fgf8a*)<sup>24</sup> and inner-ear anterior/posterior extremity (*bmp4*)<sup>25</sup>. We did not detect differences between controls and *gas8* morphants (data not shown). Therefore, otolith defects are not due to abnormal neuraxis or inner-ear patterning.

We next asked whether otolith defects were due to improper formation or placement of cilia in the otic vesicle. By 24 h.p.f., two classes of cilia were visible in the otic vesicle<sup>6</sup> (Fig. 3a, Supplementary Movie 1). Numerous short cilia were dispersed throughout the otic vesicle, and small patches of longer, 'tether' cilia were found exclusively at the anterior and posterior poles. Between 19 and 27 h.p.f., small precursor particles coalesced on tether cilia to form anterior

<sup>1</sup>Department of Microbiology, Immunology and Molecular Genetics, <sup>2</sup>Department of Molecular, Cell, and Developmental Biology, <sup>3</sup>Molecular Biology Institute, University of California, Los Angeles, California 90095, USA. <sup>4</sup>Biological Imaging Center, Beckman Institute, California Institute of Technology, Pasadena, California 91125, USA.

\*These authors contributed equally to this work.

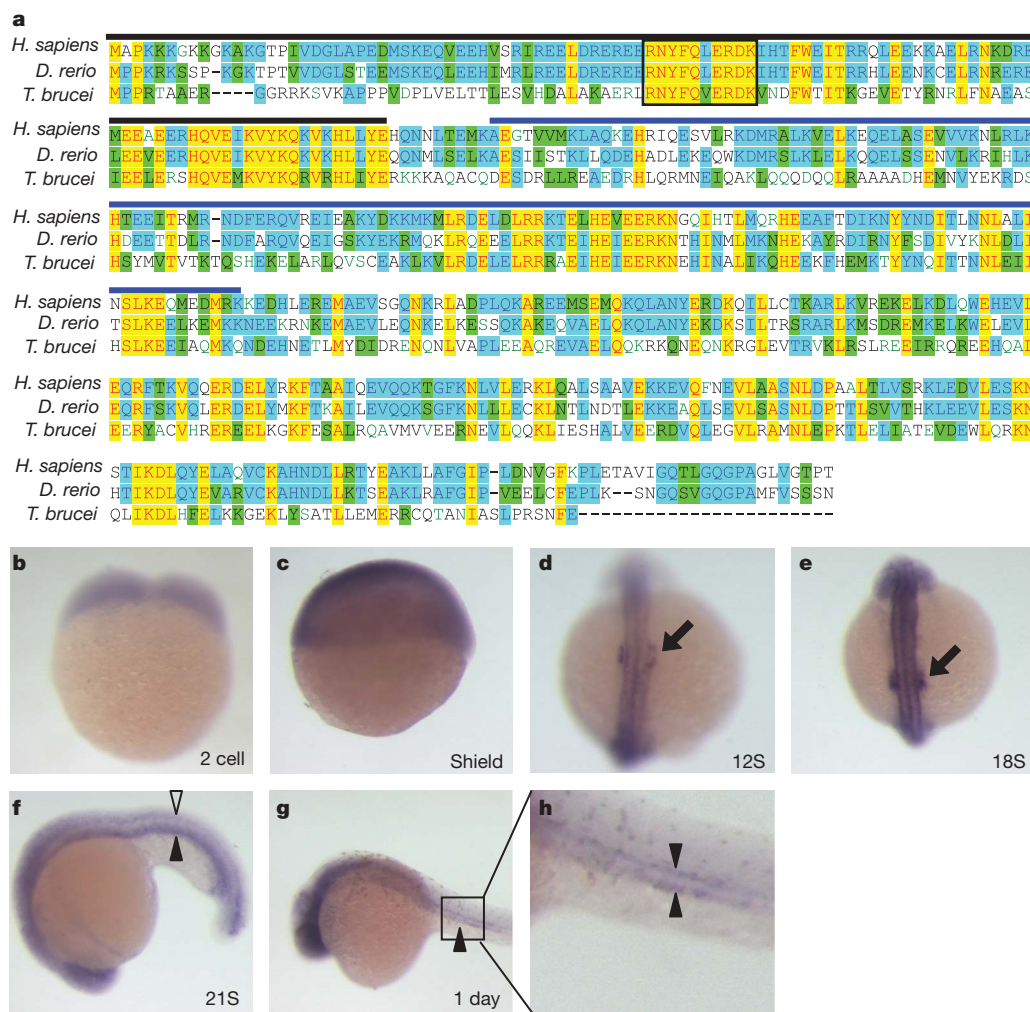


**Figure 1 | *gas8* is expressed in ciliated tissues.** **a**, Protein sequence alignment of trypanin/GAS8 from *Homo sapiens*, *Danio rerio* and *Trypanosoma brucei*. Yellow highlighting indicates absolutely conserved residues, blue indicates residues conserved in two homologues and green indicates residues that are conservative substitutions. The boxed region indicates a conserved RNYFQERDK stretch that is found in every known trypanin/GAS8 homologue<sup>17</sup>. The conserved microtubule binding domain

'GMAD' and the regulatory domain 'IMAD'<sup>19</sup> are indicated with blue and black overlines, respectively. **b–h**, *In situ* hybridizations show the *gas8* expression pattern during the first 24 h of embryonic development. Developing ears (black arrows), neural tube (open arrowhead) and pronephric ducts (filled arrowheads) are shown. Developmental stages are indicated in each panel; S, somite. **h** is an enlargement of the boxed region in **g**.

and posterior otoliths<sup>6</sup>. We examined cilia distribution and size in morphant embryos during the critical developmental window of 19–27 h.p.f., when cilia are postulated to function in otolith assembly. At the 20-somite stage (corresponding to ~19 h.p.f. in wild type), control and morphant embryos had cilia in the developing otic vesicle (data not shown). *gas8* morphants were slightly developmentally delayed, a common feature of morphant fish. Hence, we staged embryos based on developmental progression defined in ref. 26. By 24 h.p.f., both short cilia and tether cilia were distinguishable at the correct locations in control and *gas8* morphant embryos (Fig. 3b, Supplementary Movie 2). Otic vesicle size was reduced as noted above, but we did not detect major length differences of cilia between control (tether,  $5.9 \pm 0.2 \mu\text{m}$ ; short,  $1.4 \pm 0.1 \mu\text{m}$ ;  $n = 5$  embryos) and morphant (tether,  $5.9 \pm 0.4 \mu\text{m}$ ; short,  $1.2 \pm 0.2 \mu\text{m}$ ;  $n = 7$  embryos) embryos. At later stages, tether cilia persisted whereas short cilia began to disappear as expected<sup>6</sup> in both control and morphant embryos (data not shown). Cilia were also observed in the pronephric ducts and neural tube in *gas8* morphants (data not shown). Therefore, loss of *gas8* expression did not prevent formation, maintenance or correct positioning of cilia.

Because protist GAS8 homologues, trypanin in *T. brucei* and paralyzed flagella 2 in *Chlamydomonas reinhardtii*, are specifically

involved in controlling ciliary beat<sup>13–15</sup>, we examined cilia motility directly using *in vivo*, high-speed video microscopy. In all control embryos, one to three beating tether cilia were detected near each nascent otolith (Fig. 3, Supplementary Fig. 3, Supplementary Movies 3–5). Beating cilia directly bore the forming otolith or were located nearby (5–10  $\mu\text{m}$  distant), often causing the otolith itself to oscillate (Supplementary Movies 3, 5). These cilia beat with a frequency of  $34 \pm 6 \text{ Hz}$  ( $n = 20$ ) at 24 h.p.f. Short cilia were not motile (Supplementary Movie 6). This contrasts with a previous report suggesting that tether cilia are immotile whereas short cilia distributed throughout the ear are motile<sup>6</sup>. The reason for this discrepancy is not clear, but it is probably due to technical challenges associated with imaging cilia motility, which was inferred indirectly in the earlier work and imaged directly here. In *gas8* morphants at every stage examined (19–27 h.p.f.), a majority of embryos displayed immotile tether cilia (60%,  $n = 30$ ; Fig. 3, Supplementary Fig. 3, Supplementary Movies 7–8). Commonly, *gas8* morphants displayed ectopic otoliths located at the base of non-motile tether cilia (Fig. 2o). In some cases, morphants harboured ectopic beating cilia (23%,  $n = 30$ ). To confirm that the ear phenotype was due to cilia immotility and not loss of another, unknown *gas8* function, we knocked down two genes directly involved in cilia motility: the gene for



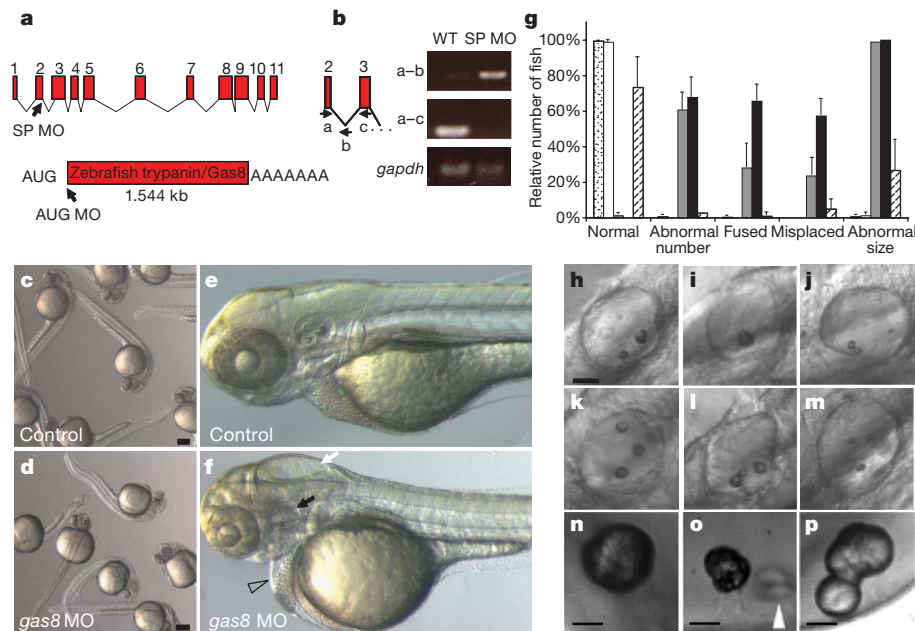


**Figure 2 | *gas8* morphants exhibit developmental defects.** **a**, Intron/exon structure of the *gas8* locus, which encodes a predicted 1.54-kb transcript. The positions of splice blocking (SP MO) and translation blocking (AUG MO) morpholino oligonucleotides are shown. **b**, RNA from wild-type (WT) and *gas8* splice morphant embryos was analysed by PCR with reverse transcription (RT-PCR) using a forward primer (a) in the second exon and a reverse primer in either the second intron (b) or the third exon (c). In the morphant, blocking of the exon-2 splice donor site leads to a 315-bp RT-PCR product with the first primer set and no product with the second primer set. Controls for RT-PCR were provided by amplification of a 95-bp fragment of *gapdh*. **c–f**, *gas8* morphants have a variety of defects: overall morphology of controls (**c**) and *gas8* morphants (**d**) at 24 h.p.f.; detail of control (**e**) and morphant (**f**) embryos at 3 days post-fertilization (d.p.f.) showing hydrocephaly (white arrow), pericardial oedema (open arrowhead), disorganized somites and otolith abnormalities (black arrow).

**g**, Quantitative analysis of otolith defects at 3 d.p.f. The relative number of fish having the indicated defect is shown for uninjected embryos (stippled bars;  $n = 324$ , five experiments), embryos injected with control MO (white bars;  $n = 167$ , two experiments), SP MO (grey bars;  $n = 89$ , two experiments), AUG MO (black bars;  $n = 96$ , two experiments) or co-injected with AUG MO and 250 pg *in-vitro*-transcribed *gas8* mRNA (hatched bars;  $n = 225$ , two experiments). Error bars, s.d. **h–p**, Panels show the spectrum of otolith defects observed in *gas8* morphants at 3 d.p.f. (**h–m**) and earlier times (**n–p**): normal otoliths (**h**); a single otolith (**i**); ectopic, fused and small otoliths (**j–m**); and nascent otoliths in control (**n**, 27 h.p.f.) and *gas8* morphant (**o**, 24 h.p.f.; **p**, 27 h.p.f.) embryos. Scale bars, 30  $\mu$ m (**h–m**); 20  $\mu$ m (**n–p**). White arrowhead indicates ectopic and fused otoliths in the *gas8* morphant. Embryos were injected with 6 ng (AUG MO), 4 or 5 ng (SP MO), 6 ng (standard control MO) or 6 ng (mismatch AUG MO) morpholinos.

leucine-rich repeat-containing 50 protein, *lrcc50*, an outer-arm dynein subunit shown previously to be required for cilia motility<sup>27,28</sup>;

and the left-right dynein gene *dnah9*, a well-characterized motor protein involved in cilia motility<sup>29</sup>. The same results were obtained upon knockdown of *lrcc50* (Supplementary Figs 4, 5). Furthermore, simultaneous knockdown of *lrcc50* and *dnah9* had a synergistic effect, causing more significant motility and otolith defects than either single knockdown alone. These treatments neither affected brain development nor triggered neural tube cell death and pericardial oedema. In all cases, abnormal otolith size, number and positioning were directly correlated with defective ciliary motility in morphants (Supplementary Fig. 4).

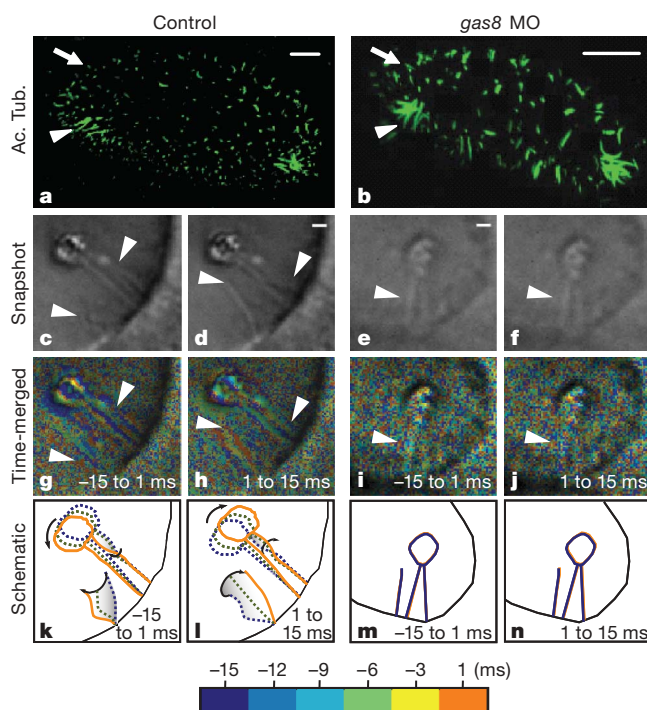


**Figure 3 | *Gas8* is required for tether cilia motility.** **a, b**, Cilia in control (**a**) and *gas8* morphant (**b**) embryos at 24 h.p.f., visualized by immunofluorescence labelling with anti-acetylated tubulin antibodies (Ac. Tub.). Arrowheads indicate the location of the tether cilia and arrows indicate short cilia. Scale bars, 10  $\mu$ m. **c–n**, Tether cilia are motile in control embryos, but not in *gas8* morphants. Bright-field snapshot images from high-speed videos of cilia in controls (**c, d**) and *gas8* morphants (**e, f**), showing two steps of the cilia beat cycle with a 15-ms interval (half the period of a beat). **g–j**, Time-to-colour merge of six frames encompassing 15 ms of the cilia motion immediately preceding the still images shown in **c–f**, respectively. Cilia position in time is marked by different colours following the colour bar. When merged, moving objects are visible in the corresponding colours, whereas immobile objects only show background and noise. **k–n**, Diagrams showing cilia and otolith motion in control (**k, l**) and immotility in *gas8* morphant (**m, n**) embryos with three time points along half the period (15 ms) of the cilia beat cycle (see colour bar). Still images from control (**c, d**) and *gas8* morphant (**e, f**) embryos are taken from Supplementary Movies 3 and 5, respectively. Scale bars, 1  $\mu$ m (**c–f**). Arrowheads point to tether cilia.

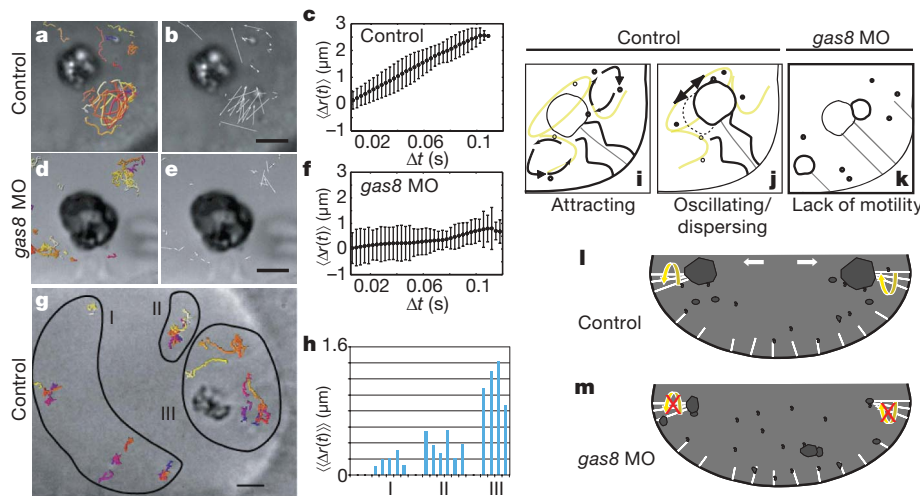


**Figure 4 | Tether cilia motility drives otolith biogenesis.** **a–h**, Particle tracking analysis demonstrates that cilium-dependent fluid dynamics drive precursor particle movement near the otolith. In control embryos, particle tracks (**a**) and displacements (**b**) show that particles near the otolith move by non-Brownian motion. Each track has a different colour. **d, e**, In *gas8* morphants, particle tracks (**d**) and displacements (**e**) show decreased particle displacements in comparison with control. **c, f**, Mean particle displacement,  $\langle \Delta r(t) \rangle$ , plotted as a function of time. In control embryos, mean particle displacement is large and non-random, indicating diffusive transport. In *gas8* morphants, mean particle displacement is small and random, indicating Brownian motion only. Error bars indicate the variance in the calculation of  $\langle \Delta r(t) \rangle$ . **g, h**, Particle tracking in control embryos shows that particle displacement is directly correlated with position relative to the otolith. **g**, particle tracks. **h**, Displacements of particles in regions I, II and III of

**g** were calculated as a function of time and the average of the mean displacement,  $\langle \langle \Delta r(t) \rangle \rangle$ , for each particle is shown. Net particle displacement decreases with increasing distance from tether cilia, indicating the reduction of the influence of ciliary beating. **i–k**, Diagrams depicting cilium-dependent otolith biogenesis. **i**, Tether cilia motility creates vortices that attract precursor particles. **j**, Cilia motility further serves to disperse particles locally and causes oscillation of the otolith, together facilitating uniform otolith growth. **k**, In *gas8* morphants, absence of ciliary motility limits particles to Brownian motion. **l**, In wild-type embryos, the net consequence of tether cilia motility is that precursor particles are concentrated near the tethers, preferentially seeding otoliths at two poles of the otic vesicle. **m**, In *gas8* morphants, loss of normal ciliary motility leads to formation of ectopic aggregates, non-uniform otolith growth and small particles that fail to coalesce into full-sized otoliths. Scale bars, 5 μm.

Otoliths are composite crystals assembled from a common pool of small, precursor particles. We hypothesized that otolith defects in cilia morphants arise as a consequence of abnormal fluid flow and the concomitant failure to properly direct precursor particle movements. To test this hypothesis, we examined fluid flow patterns in the otic vesicle by tracking otolith precursors at high temporal resolution. A direct correlation between cilia beat and fluid flow was observed (Fig. 4, Supplementary Movies 9–11). In control embryos, the motion of precursor particles near the otolith was non-random, whereas those further away from the otolith exhibited Brownian motion (Fig. 4g, h, Supplementary Movies 9–10), consistent with a previous report<sup>6</sup>. Cilia beating triggers a local flow in the vicinity of the otolith, attracting precursors at the base of tether cilia and propelling them towards the otolith (Supplementary Fig. 6, Supplementary Movies 9–10). By contrast, in *gas8* morphants, particles near tether cilia exhibited purely diffusive behaviour (Fig. 4, Supplementary Movie 11). Therefore, the absence of ciliary beating limits particles to random motion, leading to formation of ectopic aggregates.

Our results demonstrate that *Gas8* is required for normal motility of cilia in the otic vesicle and that ciliary motility is essential for normal ear development. The otic vesicle is a closed epithelial organ and fluid flow within this vesicle has been suggested to contribute to otolith formation<sup>6</sup>. Our study provides direct experimental evidence in support of this hypothesis. On the basis of high-speed video microscopy of cilia motility and quantitative analysis of precursor particle movements in wild-type and *gas8* morphant embryos, we propose a new, cilium-dependent hydrodynamic mechanism for otolith biogenesis (Fig. 4). In this model, motility of tether cilia at the poles of the otic vesicle establishes a vortex that attracts otolith precursors (Fig. 4i, l), thereby biasing an otherwise random distribution of precursor particles and concentrating them near the two patches of tether cilia. This ensures preferential otolith seeding at the poles of the otic vesicle. At the otic vesicle poles, tether cilia motility further serves to disperse precursor particles locally and oscillation of the

otolith increases effective contact area with precursors (Fig. 4j). Together, this prevents particles from sedimenting to form ectopic aggregates and promotes efficient uniform otolith growth. This model explains the different features of the otolith phenotype observed in *gas8* morphants (Fig. 4k, m).

Our findings add to a growing list of developmental processes requiring fluid dynamic inputs for proper growth and patterning, further showing that epigenetic cues are part of the embryonic developmental program. In humans, hearing and balance defects are common among the elderly and are the most frequent sensory hereditary defects in newborns<sup>30</sup>. Although human patients with ciliopathies have not generally been observed to have obvious hearing loss<sup>4</sup>, our results should stimulate investigations to look for more subtle inner-ear changes. To conclude, our studies demonstrate a requirement for motile cilia in vertebrate ear development and suggest that DRC subunits should be considered as candidates for disease genes contributing to ciliopathies in humans.

## METHODS SUMMARY

**Zebrafish lines.** Wild-type AB zebrafish were maintained and raised as described in Methods.

**Riboprobe generation and *in situ* hybridization.** Details of the whole-mount *in situ* hybridization protocol and probes used in this study are given in Methods.

**Morpholino antisense oligonucleotides.** Morpholino antisense oligonucleotides against *gas8*, *lrrc50* and *dnah9* were designed and used as described in Methods.

**High-speed video microscopy.** Bright-field images were taken with a Basler A602f CMOS camera running in area-of-interest mode for fast acquisition in a custom Matlab script. The camera was mounted on a home built microscope equipped with an Olympus UPlanAPO water immersion objective (numerical aperture 1.2,  $\times 60$ ) coupled with a tube lens of focal length 300 mm. Frame rates ranged from 100 to 322 frames per second. Further details are provided in Methods.

**Other methods.** Details of immunofluorescence and flow analyses are provided in Methods.

**Full Methods** and any associated references are available in the online version of the paper at [www.nature.com/nature](http://www.nature.com/nature).

**Received 16 July; accepted 30 September 2008.**

**Published online 30 November 2008.**

1. Sollner, C. & Nicolson, T. in *Biomimicry: From Biology to Biotechnology and Medical Application* 2nd edn (ed. Bauerlein, E.) 229–242 (Wiley-VCH, 2004).
2. Satir, P. & Christensen, S. T. Overview of structure and function of mammalian cilia. *Annu. Rev. Physiol.* **69**, 377–400 (2007).
3. Bisgrove, B. W. & Yost, H. J. The roles of cilia in developmental disorders and disease. *Development* **133**, 4131–4143 (2006).
4. Badano, J. L., Mitsuma, N., Beales, P. L. & Katsanis, N. The ciliopathies: an emerging class of human genetic disorders. *Annu. Rev. Genomics Hum. Genet.* **7**, 125–148 (2006).
5. Fliegauf, M., Benzing, T. & Omran, H. When cilia go bad: cilia defects and ciliopathies. *Nature Rev. Mol. Cell Biol.* **8**, 880–893 (2007).
6. Riley, B. B., Zhu, C., Janetopoulos, C. & Aufferdeide, K. J. A critical period of ear development controlled by distinct populations of ciliated cells in the zebrafish. *Dev. Biol.* **191**, 191–201 (1997).
7. Haddon, C. & Lewis, J. Early ear development in the embryo of the zebrafish, *Danio rerio*. *J. Comp. Neurol.* **365**, 113–128 (1996).
8. Hughes, I., Thalmann, I., Thalmann, R. & Ornitz, D. M. Mixing model systems: using zebrafish and mouse inner ear mutants and other organ systems to unravel the mystery of otocorial development. *Brain Res.* **1091**, 58–74 (2006).
9. Nicolson, T. The genetics of hearing and balance in zebrafish. *Annu. Rev. Genet.* **39**, 9–22 (2005).
10. Huang, B., Ramanis, Z. & Luck, D. J. Suppressor mutations in *Chlamydomonas* reveal a regulatory mechanism for flagellar function. *Cell* **28**, 115–124 (1982).
11. Piperno, G., Mead, K. & Shestak, W. The inner dynein arms I2 interact with a “dynein regulatory complex” in *Chlamydomonas* flagella. *J. Cell Biol.* **118**, 1455–1463 (1992).
12. Gardner, L. C., O’Toole, E., Perrone, C. A., Giddings, T. & Porter, M. E. Components of a “dynein regulatory complex” are located at the junction between the radial spokes and the dynein arms in *Chlamydomonas* flagella. *J. Cell Biol.* **127**, 1311–1325 (1994).
13. Ralston, K. S., Lerner, A. G., Diener, D. R. & Hill, K. L. Flagellar motility contributes to cytokinesis in *Trypanosoma brucei* and is modulated by an evolutionarily conserved dynein regulatory system. *Eukaryot. Cell* **5**, 696–711 (2006).
14. Hutchings, N. R., Donelson, J. E. & Hill, K. L. Trypanin is a cytoskeletal linker protein and is required for cell motility in African trypanosomes. *J. Cell Biol.* **156**, 867–877 (2002).
15. Rupp, G. & Porter, M. E. A subunit of the dynein regulatory complex in *Chlamydomonas* is a homologue of a growth arrest-specific gene product. *J. Cell Biol.* **162**, 47–57 (2003).
16. Baron, D. M., Ralston, K. S., Kabututu, Z. P. & Hill, K. L. Functional genomics in *Trypanosoma brucei* identifies evolutionarily conserved components of motile flagella. *J. Cell Sci.* **120**, 478–491 (2007).
17. Hill, K. L., Hutchings, N. R., Grandgenett, P. M. & Donelson, J. E. T lymphocyte triggering factor of African trypanosomes is associated with the flagellar fraction of the cytoskeleton and represents a new family of proteins that are present in several divergent eukaryotes. *J. Biol. Chem.* **275**, 39369–39378 (2000).
18. Ralston, K. S. & Hill, K. L. Trypanin, a component of the flagellar dynein regulatory complex, is essential in bloodstream form African trypanosomes. *PLoS Pathogens* **2**, doi:10.1371/journal.ppat.0020101 (2006).
19. Bekker, J. M. et al. Direct interaction of Gas11 with microtubules: Implications for the dynein regulatory complex. *Cell Motil. Cytoskeleton* **64**, 461–473 (2007).
20. Colantonio, J. R. et al. Expanding the role of the dynein regulatory complex to non-axonemal functions: association of GAS11 with the golgi apparatus. *Traffic* **7**, 538–548 (2006).
21. Yeh, S. D. et al. Isolation and properties of Gas8, a growth arrest-specific gene regulated during male gametogenesis to produce a protein associated with the sperm motility apparatus. *J. Biol. Chem.* **277**, 6311–6317 (2002).
22. Whitmore, S. A. et al. Characterization and screening for mutations of the growth arrest-specific 11 (GAS11) and C16orf3 genes at 16q24.3 in breast cancer. *Genomics* **52**, 325–331 (1998).
23. Bok, J., Brunet, L. J., Howard, O., Burton, Q. & Wu, D. K. Role of hindbrain in inner ear morphogenesis: analysis of Noggin knockout mice. *Dev. Biol.* **311**, 69–78 (2007).
24. Leger, S. & Brand, M. Fgf8 and Fgf3 are required for zebrafish ear placode induction, maintenance and inner ear patterning. *Mech. Dev.* **119**, 91–108 (2002).
25. Mowbray, C., Hammerschmidt, M. & Whitfield, T. T. Expression of BMP signalling pathway members in the developing zebrafish inner ear and lateral line. *Mech. Dev.* **108**, 179–184 (2001).
26. Kimmel, C. B., Ballard, W. W., Kimmel, S. R., Ullman, B. & Schilling, T. F. Stages of embryonic development of the zebrafish. *Dev. Dyn.* **203**, 253–310 (1995).
27. Sullivan-Brown, J. et al. Zebrafish mutations affecting cilia motility share similar cystic phenotypes and suggest a mechanism of cyst formation that differs from pkd2 morphants. *Dev. Biol.* **314**, 261–275 (2008).
28. van Rooijen, E. et al. LRRC50, a conserved ciliary protein implicated in polycystic kidney disease. *J. Am. Soc. Nephrol.* **19**, 1128–1138 (2008).
29. Kawakami, Y., Raya, A., Raya, R. M., Rodriguez-Esteban, C. & Belmonte, J. C. Retinoic acid signalling links left–right asymmetric patterning and bilaterally symmetric somitogenesis in the zebrafish embryo. *Nature* **435**, 165–171 (2005).
30. Shastri, B. S. Mammalian cochlear genes and hereditary deafness. *Microb. Comp. Genomics* **5**, 61–69 (2000).

**Supplementary Information** is linked to the online version of the paper at [www.nature.com/nature](http://www.nature.com/nature).

**Acknowledgements** We are grateful to R. Crosbie for discussions and encouragement throughout the course of the project. We thank I. Drummond and C. Nguyen for discussions and comments on the work. We are grateful to L. Trinh, O. Bricaud and A. Collazo for sharing reagents and for providing probes, as well as to all the members of the Fraser laboratory for discussions, in particular M. Liebling and W. Supatto for sharing Matlab scripts and comments. We are grateful to Z. P. Kabututu for performing the *lrrc50* reverse transcriptase PCR experiments. J.V. was supported by a fellowship from the Human Frontier Science Program, D.W. was supported by the NIH Medical Scientist Training Program at UCLA/ Caltech. J.R.C. was supported by NIH RSDA training grant no. M07185 and a Warsaw Fellowship from the MIMG Department at UCLA. A.D.L. is supported by an NSF fellowship. This work was supported by NIH grant R01 HL081799 (J.C.), NIH grant R01AI52348 and Beckman Young Investigator Award (K.L.H.).

**Author Contributions** J.R.C., J.V., D.W. and K.L.H. designed the experiments and interpreted the results. J.R.C., J.V. and D.W. conducted the experiments. J.V. and D.W. developed the equipment and systems for and performed *in vivo* video imaging for the quantitative flow study and analyzed the data with J.R.C., S.F. and K.L.H. A.D.L. assisted with *in situ* hybridization. A.D.L. and J.C. provided guidance on *gas8* morpholino injections. The manuscript was written by J.R.C., J.V., D.W. and K.L.H. All authors discussed the results and commented on the manuscript.

**Author Information** Reprints and permissions information is available at [www.nature.com/reprints](http://www.nature.com/reprints). Correspondence and requests for materials should be addressed to K.L.H. ([kenthill@mednet.ucla.edu](mailto:kenthill@mednet.ucla.edu)).



## METHODS

**Zebrafish lines.** Wild-type AB zebrafish were maintained and raised as described previously<sup>31</sup>. Dechorionated embryos were kept at 28.5 °C in E3 solution with or without 0.003% 1-phenyl-2-thiourea (PTU, Sigma) to suppress pigmentation. Embryos were staged according to somite number (S) or hours post-fertilization<sup>31</sup>. ***gas8* riboprobe generation and *in situ* hybridization.** The predicted *gas8* gene transcript of zebrafish, *Danio rerio* (Ensembl Gene ID #ENS DARG00000040871), was obtained from the annotated Ensembl automatic analysis pipeline and predicted exon/intron boundaries, transcript size and predicted protein size were obtained as described previously<sup>32</sup>. *D. rerio gas8* complementary DNA in pME18S-FL3 (clone IMAGE:5410961) was subcloned into the expression vector pcGlobin2 by PCR amplification of *gas8* from pME18S-FL3 using SacII and XhoI flanked primers (5' primer, CCCCGCGGGTGAACAATTCAATGCATT; 3' primer, CCGCTCGAGATTGAAGAAGAAACAAACA). *gas8*-pcGlobin2 was linearized using BamHI and the antisense digoxigenin-labelled full length riboprobe was transcribed using SP6 RNA polymerase (Promega). Whole-mount *in situ* hybridization was carried out essentially as described in ref. 33 using either the *gas8* probe or one of the following probes: *spaw*, *eng2a*, *otx2*, *egr2b*, *bmp4*, *fgf8a* (provided by L. Trinh). Embryos were fixed with 4% paraformaldehyde, digested with proteinase K, and hybridized with the probe at 67 °C. Alkaline-phosphatase-conjugated anti-digoxigenin antibody (Roche) was used to detect the *gas8* signals. After staining with NBT/X-phosphate (Roche), embryos were refixed with 4% paraformaldehyde and stored in PBS buffer. For imaging, embryos were mounted in 3.5% methyl cellulose and photographed on a Zeiss Axioplan microscope equipped with a Zeiss AxioCam digital camera.

**Morpholino antisense oligonucleotides.** Morpholino antisense oligonucleotides were designed to either target the translation start site of the *gas8* mRNA (AUG MO) or to target the splice donor site of the second coding exon (SP MO) and were obtained from Gene Tools. *gas8* AUG MO: GCGACGATTTCT-TTTTGGTGGCAT; *gas8* SP MO: CGTTACCGACAAAATACCTGCTCTT; *gas8* 5-bp mismatch AUG MO, used for rescue experiments: GCCACCATTTT-GTTTTTGCTGGGAT; standard control MO: CCTCTTACCTCAGTTACAA-TTATA. *lrrc50* SP MO: AATGTAGACACTAAAGTTACCTGCT; *lrrc50* 5-bp mismatch MO: AATcTAGACAgTAAAcTTAgCTcCT; *dnah9* AUG MO: CGGTCCTGCTCCTCCATCGCGCCG. The morpholinos were diluted in 5 mM HEPES buffer, pH 7.6. Embryos were injected at the one- to four-cell stage with either 6 ng AUG MO, 4 or 5 ng SP MO, or 6 ng standard control MO or mismatch AUG MO. For morpholino amounts used in *lrrc50* and *dnah9* injections, see Supplementary Fig. 5. The first MO (SP MO) targets the splice junction between exons 2 and 3, causing abnormal RNA processing and yielding a predicted transcript with an early stop codon (Fig. 2a). The second MO (AUG MO) targets the translational start site (Fig. 2a). Splice interference by the SP MO was demonstrated by RT-PCR (Fig. 2b).

Microinjection of either MO consistently produced hydrocephaly, brain and neural tube cell death, pericardial oedema, curved body axis and otolith defects (Fig. 2 and data not shown). Left-right axis determination was also affected, as demonstrated by *in situ* hybridization with the *southpaw* protein, a nodal-related protein that is normally expressed in the left lateral plate mesoderm<sup>34</sup> (Supplementary Fig. 1).

**RT-PCR.** Primer pairs used in RT-PCR to investigate the knockdown efficiency of *gas8* SP MO are 5'-AATCGTCGCCGAAGGGCAAAAC-3' (forward in exon 2) and 5'-CTGCATTGTTGTGGCTGCAG-3' (reverse in intron 2-3) or 5'-CTTG-GTGGCGTTCCTCTACTTC-3' (reverse in exon 3); these pairs yield no product (normal splicing) or 315 bp (abnormal splicing with intron 1 retained), and 258 bp (normal splicing) or 1,957 bp (abnormal splicing with intron 1 retained; too large to be amplified under conditions used), respectively. Primers used for *lrrc50* were (1) 5'-GATCGTATCCACATCGATGAAC-3' ('*lrrc50*-Forward'), (2) 5'-CTCCATTAGGCATTTACATG-3' ('*lrrc50*-Intron 1'), and (3) 5'-CTGGGGCCTGAAGGCTTTATG-3' ('*lrrc50*-Exon 2'). Control primer pairs for amplification of *gapdh* transcripts were also used to amplify a 95-bp region: 5'-TGTGATGGGAGTCAACCAGGACAA-3' (forward); 5'-TTAGCCAGAGG-AGCCAAGCAGTTA-3' (reverse).

**Immunofluorescence.** Embryos were fixed in 4% formaldehyde in PBS buffer for a minimum of 2 h, rinsed in methanol, permeabilized by proteinase K treatment, blocked in 10% goat serum in PBS buffer containing 1% DMSO and 0.1% Tween 20 for at least 1 h, and incubated with a 1:500 dilution of anti-acetylated alpha tubulin antibody (Sigma) overnight. Secondary antibody, anti-mouse IgG Alexa-Fluor 488 (Molecular Probes), was used at 1:200 dilution. Embryos were then embedded in 1% low melting agarose and imaged on a Zeiss LSM 510 confocal microscope using a water immersion objective with numerical aperture 1.1 and magnification either  $\times 40$  or  $\times 63$ . Confocal images were collected using Zeiss LSM 510 software. Images were processed using Imaris (Bitplane AG).

**High-speed video microscopy.** For video microscopy, fish were anaesthetized with 0.0175% tricaine and embedded in agarose wells using 0.7% low-melt agarose. As a test, imaging of embryos without anaesthetic did not affect cilia beating relative to anaesthetized animals. Particle tracking was performed using Imaris (Bitplane AG). Data were further analysed using Matlab scripts. One hallmark of purely diffusive systems is a non-zero mean displacement  $\langle \Delta r(t) \rangle$  over extended periods of time. Thus, a marker for non-diffusive transport is a changing mean displacement over time. We measured  $\langle \Delta r(t) \rangle$  over a range of elapsed times  $t$ . To determine with a single parameter whether the mean displacement changes over time, we calculated the average of this quantity,  $\langle \langle \Delta r(t) \rangle \rangle$ . If the particle is freely diffusing then  $\langle \langle \Delta r(t) \rangle \rangle \approx 0$ ; if it is driven then  $\langle \langle \Delta r(t) \rangle \rangle > 0$ . Cilia motion displayed in Fig. 3g-j was obtained using the time-to-colour Matlab script (provided by M. Liebling). Time-to-colour visualizes moving objects by assigning a colour according to the point in the cycle from which the image was taken. The resulting coloured images are obtained by superimposing six frames of the image sequence plus a greyscale frame. The first frame is assigned blue and the last frame, which corresponds to the still frame, is assigned orange. Non-moving objects, therefore, look like noise whereas moving objects display coherent patterns.

- Westerfield, M. *The Zebrafish Book: A Guide for the Laboratory Use of Zebrafish (Danio rerio)* (Univ. Oregon Press, 1993).
- Curwen, V. *et al.* The Ensembl automatic gene annotation system. *Genome Res.* **14**, 942-950 (2004).
- Chen, J. N. & Fishman, M. C. Zebrafish tinman homolog demarcates the heart field and initiates myocardial differentiation. *Development* **122**, 3809-3816 (1996).
- Drees, B. L. *et al.* A protein interaction map for cell polarity development. *J. Cell Biol.* **154**, 549-576 (2001).

## LETTERS

# Caenorhabditis elegans dauers need LKB1/AMPK to ration lipid reserves and ensure long-term survival

Patrick Narbonne<sup>1</sup> & Richard Roy<sup>1</sup>

Many organisms can enter a dormant state or diapause to survive harsh environmental conditions for extended durations. When *Caenorhabditis elegans* larvae enter dauer they arrest feeding but remain active and motile, yet become stress-resistant, extremely long-lived and non-ageing<sup>1</sup>. Entry into dauer is associated with a reduction in insulin-like signalling, the accumulation of nutritive resources and a concomitant global change in metabolism<sup>2–5</sup>, yet the precise molecular and physiological processes that enable long-term survival in the absence of caloric intake remain largely unknown. We show here that *C. elegans* larvae that lack LKB1/AMPK (AMP-activated protein kinase) signalling enter dauer normally, but then rapidly consume their stored energy and prematurely expire following vital organ failure. We found that this signalling pathway acts in adipose-like tissues to downregulate triglyceride hydrolysis so that these lipid reserves are rationed to last the entire duration of the arrest. Indeed, the downregulation of adipose triglyceride lipase (ATGL-1) activity suppresses both the rapid depletion of stored lipids and reduced life span of AMPK mutant dauers, while AMPK directly phosphorylates ATGL-1. Finally, we show that the slow release of energy during dauer is critical for appropriate long-term osmoregulation, which fails as triglyceride resources become depleted. These mechanisms may be essential for survival through diapause, hibernation, or long-term fasting in diverse organisms and may also underlie AMPK-dependent life span extension.

*C. elegans* larvae with compromised insulin-like signalling (ILS) constitutively enter the 'enduring' dauer stage, while mutant adults are very long-lived<sup>3,6</sup>. Hence, it is proposed that the changes that confer life span extension in ILS pathway mutants result from the inappropriate expression of a plethora of dauer-specific genes during adulthood. *aak-2* (the *C. elegans* AMP-activated kinase  $\alpha 2$  catalytic subunit) mutants form morphologically normal dauer larvae under reduced ILS, but do not demonstrate long-term survival<sup>7</sup>. Indeed, both their maximal and mean life span are below 1/3 that of control larvae, whether they are induced by crowding/starvation, or by reduced insulin-like or TGF- $\beta$  signalling (Table 1; Fig. 1b). Here we take advantage of this phenotype of *aak-2* mutant dauers to better understand the basis of the extended 'non-ageing' life span of dauer larvae.

AMPK functions as a hetero-trimeric complex composed of one catalytic ( $\alpha$ ) and two regulatory subunits ( $\beta$  and  $\gamma$ ), for each of which two or more isoforms exist. In addition to being activated allosterically by AMP, this kinase complex also requires phosphorylation for optimal activity, predominantly by LKB1 (ref. 8). Consistent with this, loss of *par-4* activity (the *C. elegans* LKB1 orthologue) reproduces the phenotypes of *aak-2*/AMPK mutants<sup>7,9</sup>. It was also found that the ability of LKB1 to phosphorylate its targets is greatly enhanced by its association with two co-factors, STRAD, a Ste-20 related adaptor pseudokinase, and MO25 (ref. 8), yet the significance of each of these components *in vivo* remains elusive.

To better understand how *aak-2* mediates the long-term survival of dauer larvae, we tested whether mutations in other conserved components of the *C. elegans* LKB1/AMPK cascade similarly reduce dauer life span. Strikingly, a null mutation in the second AMPK catalytic subunit (*aak-1*) shows no such phenotype, while it only marginally enhances the phenotype of an *aak-2* null mutant (Table 1), suggesting that the  $\alpha 2$  catalytic subunit of AMPK contributes predominantly to dauer survival. In contrast, *aak-2* can function with either of the two  $\beta$  regulatory subunits to fulfil this role, since neither *aakb-1* nor *aakb-2* mutations alone phenocopied *aak-2*, while the dauer life span of double *aakb-1*; *aakb-2* mutants was severely affected (Table 1). The survival of *par-4*/LKB1; *strd-1*/STRAD double mutant dauers was also severely compromised (Table 1), indicating that *aak-2*/AMPK requires activating phosphorylation by LKB1-STRAD for long-term dauer survival (Fig. 1a).

AMPK has been intensively studied in unicellular systems, where it acts as a metabolic master switch to restore energy balance during periods of energetic stress<sup>8</sup>. This cell autonomous function of AMPK could ensure the long-term survival of multi-cellular animals facing similar stresses. Consistent with this, *aak-2* is widely and strongly expressed during dauer (Supplementary Fig. 1). To determine the tissue(s) wherein LKB1/AMPK signalling is required, we attempted to rescue the long-term dauer survival of *aak-2* mutants using tissue-specific *aak-2*(WT) transgenes (here WT indicates wild type), the expression of which was verified by semiquantitative RT-PCR (Supplementary Fig. 2). The maximal, but not the average, dauer life span of *aak-2* mutants can be fully rescued with a transgene containing a genomic copy of the *aak-2* gene (Fig. 1c). We cloned the *aak-2* cDNA to better control for tissue-specific expression and were able to rescue dauer life span using the *sur-5* promoter (*sur-5p*) as a positive control for ubiquitous somatic *aak-2* cDNA expression, albeit to a

**Table 1 | Life span of *C. elegans* dauer larvae**

Identifier	Genotype*	Mean dauer life span†
A	Control	29.6 (230)
B	<i>aak-1(tm1944)</i>	>15 (80)
C	<i>aak-2(ok524)</i>	8.1 (200)‡
D	<i>aak-2(rr48)</i>	10.5 (108)‡
E	<i>aak-1(tm1944); aak-2(ok524)</i>	7.5 (213)‡ ( $P < 0.005$ vs C)
F	<i>aakb-1(tm2658)</i>	>15 (109)
G	<i>aakb-2(rr88)</i>	>15 (161)
H	<i>aakb-1(tm2658); aakb-2(rr88)</i>	11.6 (60)‡
I	<i>par-4(it57)</i>	>15 (50)
J	<i>strd-1(rr91)</i>	>15 (100)
K	<i>strd-1(rr92)</i>	>15 (59)
L	<i>strd-1(ok2283)</i>	>15 (50)
M	<i>strd-1(rr92); par-4(it57)</i>	9.0 (100)‡
N	<i>aak-1(tm1944); par-4(it57); aak-2(ok524)</i>	7.7 (80)‡ ( $P = 0.85$ vs E)

\* All strains carry the *daf-2(e1370)* mutation.

† Days at 25 °C; sample size, *n*, is given in parentheses; '>15' indicates that more than 85% of the animals survived over 15 days.

‡ Indicates statistical significance using the log-rank test ( $P < 0.005$ ) versus Control.

<sup>1</sup>Department of Biology, McGill University, Montréal, Québec H3A 1B1, Canada.

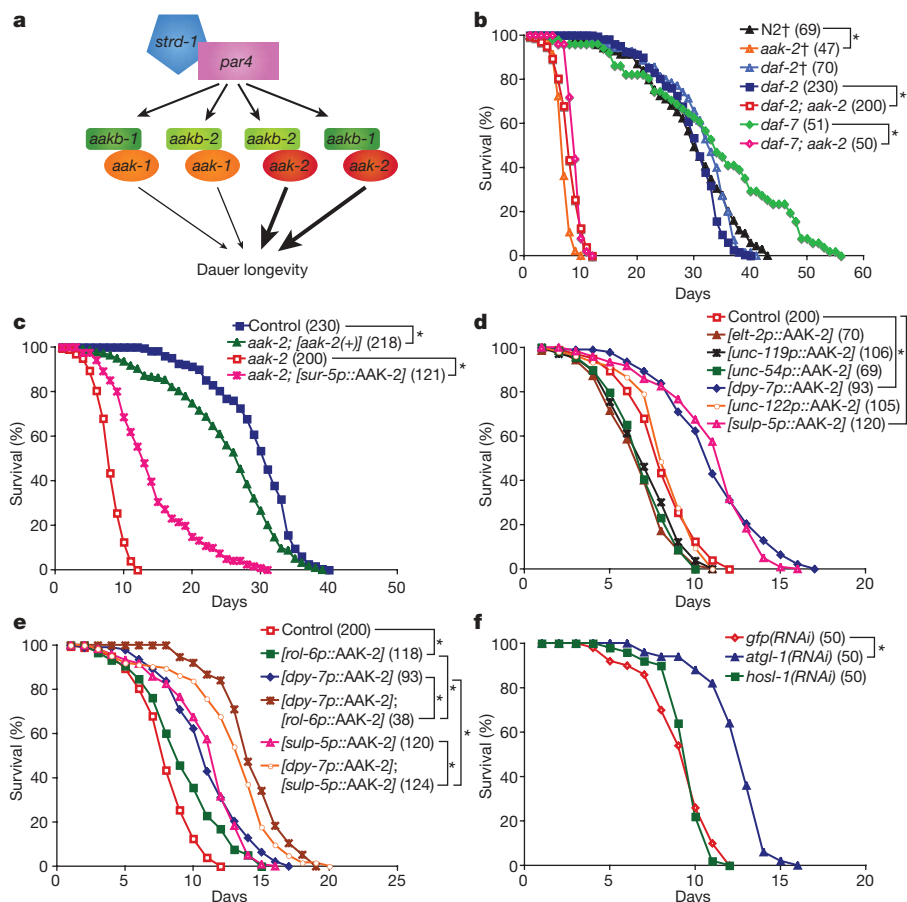


**Figure 1** | *aak-2* functions in the hypodermis and excretory system to regulate dauer survival. **a**, An *aak-2*-specific *strd-1*/*par-4*-dependent signalling cascade is required for long-term dauer survival. Arrows represent genetic activation. **b–f**, The life span (25 °C) of dauer larvae in double distilled H<sub>2</sub>O was scored using the dauer trap<sup>7</sup>. The sample size for each genotype is shown in parentheses. For transgenics, represented by square brackets, 1 to 4 lines were tested in two or more experiments not performed in parallel and the data were added (for details, see Supplementary Table 1).

lesser extent than the genomic sequence (Fig. 1c; Supplementary Note 1). We used intestinal (*elt-2*)<sup>10</sup>, neuronal (*unc-119*)<sup>11</sup>, muscle (*unc-54*)<sup>12,13</sup> and hypodermal (*dpy-7*)<sup>14</sup>-specific promoters to restore *aak-2* function in the major *C. elegans* tissues. We also used the *sulp-5* and *unc-122* promoters to drive *aak-2* expression in the excretory cell<sup>15,16</sup> and in the coelomocytes<sup>17</sup>, respectively. Strikingly, only hypodermal- and excretory cell-specific expression of the *aak-2* cDNA significantly rescued dauer life span (Fig. 1d). Thus, AMPK can function in specific cells/tissues to cell non-autonomously regulate the survival of a multi-cellular animal.

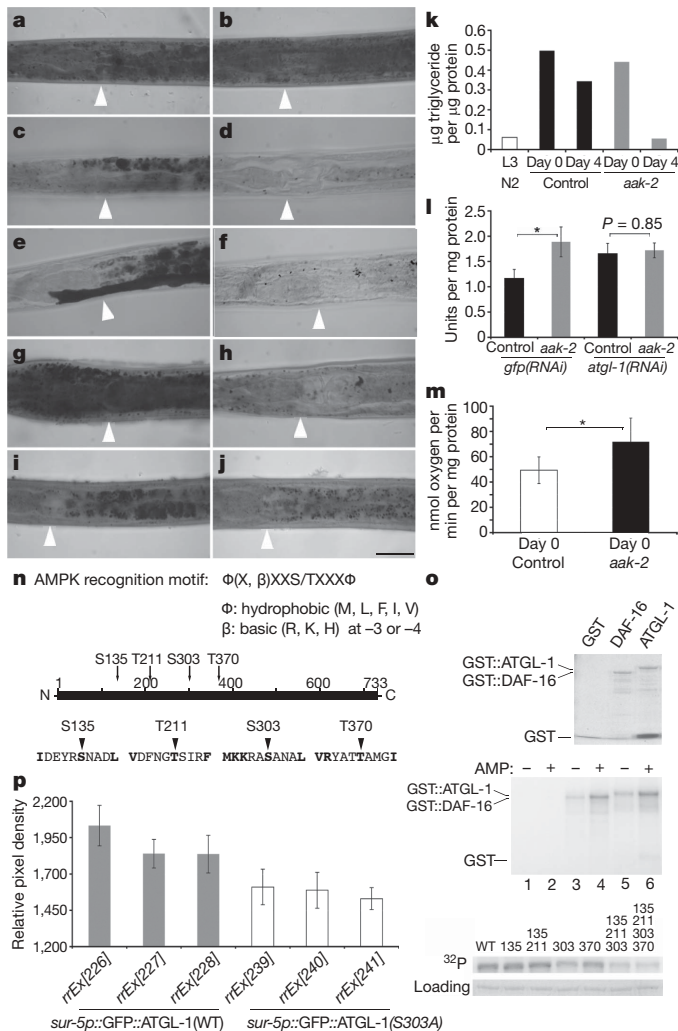
In each case however, the rescue of dauer life span was only partial, and although additive, expression in these two tissues together did not fully rescue the dauer life span of *aak-2* mutants (Fig. 1e). This could be due to insufficient expression levels from these promoters during dauer and/or from additional simultaneous expression requirements in other tissues, while alternative scenarios regarding tissue specificity and cell autonomy cannot be formally excluded. To confirm that hypodermal-specific *aak-2* expression rescues the premature lethality of *aak-2* mutant dauers, we tested the promoter of a second hypodermal-specific gene, *rol-6* (refs 18, 19). This significantly restored the dauer life span of *aak-2* mutants (Fig. 1e). Furthermore, animals that carried both hypodermal *aak-2* transgenes together showed significantly enhanced rescue compared to animals that possessed either individual transgene (Fig. 1e), suggesting that long-term dauer survival is linked to the level of hypodermal *aak-2* expression, and thus of LKB1/AMPK signalling in this tissue.

The *daf-2(e1370)*, *aak-2(ok524)* and *daf-7(e1372)* alleles were used throughout. †Indicates that dauer formation was induced at 15 °C by crowding/starvation. **c**, All strains carry the *daf-2(e1370)* mutation. **d–f**, All strains carry both the *daf-2(e1370)* and the *aak-2(ok524)* mutations. **f**, Shown is one of three replicate trials with similar outcomes. \*Indicates that dauer life span was significantly less or greater than (**b**, **c**) or greater than (**d–f**) that of the control strain ( $P < 0.005$ ), using the log-rank test.

The hypodermis of *C. elegans* acts like our skin and contributes to the basic body form of the animal. In addition, it acts in energy storage, much like the adipose tissue of higher organisms. During preparation for dauer, larvae accumulate fat reserves in their intestinal and hypodermal cells<sup>2</sup>. This is particularly obvious in dauer constitutive mutants that become very dark when they form dauer in the presence of abundant food, largely due to the accumulation of fat droplets<sup>3,20</sup>. *daf-2*; *aak-2* dauers initially look dark, like *daf-2* single mutants, but then rapidly become clear (data not shown). The requirement for *aak-2* in adipose-like tissue prompted us to determine whether this dauer-dependent ‘clear’ phenotype could be due to a problem in maintaining fat stores during dauer, so we stained *aak-2* mutants using Sudan black to reveal their lipid content<sup>20</sup>. We also quantified triglyceride content, and found that unlike *daf-2* dauer larvae, which maintain relatively high lipid levels for a long duration, the stored lipids were rapidly lost in *daf-2*; *aak-2* mutant dauers (Fig. 2a–d, k). Consistent with this, *daf-2*; *aak-2* mutant dauers had increased lipase activity compared to control *daf-2* animals (Fig. 2l). The rapid lipid depletion was rescued by hypodermal-specific expression of the *aak-2* cDNA (Fig. 2g, h), suggesting that *aak-2* functions cell autonomously to maintain lipid stores during dauer.

AMPK could therefore function to downregulate lipolysis in the hypodermis during dauer to ensure a slow release of the stored energy so that it could be sustained for the duration of the diapause. Therefore, *aak-2* mutant dauers may die prematurely following the depletion of their energy stores. Animals store fat in adipose tissue





primarily in the form of triglycerides<sup>21,22</sup>. To mobilize the stored energy, triglycerides must be hydrolysed, and the initial step in this reaction requires adipose triglyceride lipase (ATGL) both in mice<sup>22</sup> and in *Drosophila*<sup>23</sup>, while hormone sensitive lipase (HSL) has also been implicated in this process<sup>21</sup>. To test whether the inhibition of the rapid triglyceride hydrolysis that occurs in *aak-2* mutant dauers could delay their death, we impaired the function of the *C. elegans* orthologues of HSL and ATGL: *hosl-1* (C46C11.1) and *atgl-1* (C05D11.7), respectively. In addition to blocking the abnormal lipid hydrolysis (Fig. 2e), *atgl-1*(RNAi) significantly rescued the dauer life span of *aak-2* mutants (Fig. 1f). In contrast, the depletion of *hosl-1* activity had no effect on either process (Figs 1f, 2f; data not shown). Like *aak-2*, *atgl-1* is expressed in the hypodermis<sup>15</sup> and interestingly, we found several sites in ATGL-1 that match some of the criteria of the AMPK consensus phosphorylation motif<sup>24</sup> (Fig. 2n). Kinase assays indicated that AMPK phosphorylates ATGL-1 at multiple sites, where S303 is the predominant phosphoacceptor (Fig. 2o), suggesting that ATGL-1 may be a direct inhibitory target of AMPK. Due to the absence of AMPK-dependent inhibitory phosphorylation, increased ATGL-1 activity could account for the elevated triglyceride lipase activity observed in *daf-2*; *aak-2* mutant dauers. We therefore tested whether reducing ATGL-1 levels could suppress the increased lipase activity that results from impaired AMPK signalling. Consistent with this, the difference in lipase activity between *daf-2* and *daf-2*; *aak-2* dauers was greatly reduced by *atgl-1*(RNAi) (Fig. 2l; Supplementary Note 2).

To verify the *in vivo* significance of AMPK-dependent phosphorylation at S303, we ubiquitously expressed ATGL-1(WT) or a non-phosphorylatable ATGL-1(S303A) variant in *daf-2* animals. Misexpression

**Figure 2 | *aak-2* blocks ATGL-1-mediated triglyceride hydrolysis to ensure long-term dauer survival.** Shortly after the dauer moult, both *daf-2*(*e1370*) (**a**) and *daf-2*(*e1370*); *aak-2*(*ok524*) (**b**) animals stain intensely with Sudan black in their intestine and hypodermis. Four days after the dauer moult, *daf-2*(*e1370*) (**c**) still stain quite strongly with Sudan black, while *daf-2*(*e1370*); *aak-2*(*ok524*) animals (**d**) grown in parallel are almost completely devoid of lipids (little Sudan black staining). Under similar conditions, four days after their dauer moult, Sudan black staining is restored in *daf-2*(*e1370*); *aak-2*(*ok524*); *atgl-1*(RNAi) animals (**e**), but not in *daf-2*(*e1370*); *aak-2*(*ok524*); *hosl-1*(RNAi) (**f**) animals. **g**, Expression of the *aak-2* cDNA in the hypodermis using the *dpy-7* promoter suppressed the rapid loss of lipids that occurs in *aak-2* mutant dauers. A Sudan black-stained 4-day-old *daf-2*(*e1370*); *aak-2*(*ok524*); [*dpy-7p::AAK-2*] dauer is shown. Some *daf-2*(*e1370*); *aak-2*(*ok524*); [*dpy-7p::AAK-2*] animals were Dpy, probably due to titration of promoter binding factors, as GFP-expressing animals from [*dpy-7p::GFP*] lines were Dpy. To show that the lack of *dpy-7* gene product does not suppress *aak-2* (**h**), we also stained 4-day-old *daf-2*(*e1370*); *dpy-7*(*e88*) *aak-2*(*ok524*) dauer larvae. **k**, Triglyceride content (L3-stage N2 larvae were well-fed). **l**, Lipase activity (1 unit catalyses the cleavage of 1  $\mu\text{mol}$  of substrate per minute), and **m**, oxygen consumption were determined in control *daf-2*(*e1370*) and *daf-2*(*e1370*); *aak-2*(*ok524*) dauers. **n**, The ATGL-1 sequence has 16 potential ( $\Phi$ XXXXS/TXXX $\Phi$ ) AMPK consensus recognition motifs<sup>24</sup>. Amongst these, only S303 and T370 also had a basic residue at -3 or -4, while only S135 and T211 are phylogenetically conserved (data not shown). **o**, AMPK directly phosphorylates ATGL-1 in an AMP-dependent manner at multiple sites. The first panel shows the protein loaded on a Coomassie-stained gel. In the second panel, AMPK was incubated with GST (lanes 1, 2), GST::DAF-16 (lanes 3, 4), GST::ATGL-1 (lanes 5, 6) in the absence or presence of AMP (GST::DAF-16 was used as a positive control<sup>28</sup>). The third panel shows phosphorylation of ATGL-1 variants where the indicated S/T were mutated to A. **i–j**, **p**, The ubiquitous expression of a non-phosphorylatable mutant version of ATGL-1[S303A] increases lipid loss during dauer. Sudan black staining of a 4-day-old *daf-2*(*e1370*); *rrEx226*[*sur-5p::GFP::ATGL-1*(WT)] and *daf-2*(*e1370*); *rrEx239*[*sur-5p::GFP::ATGL-1*(S303A)] dauer larvae are shown in (**i**) and (**j**), respectively. **p**, Three different transgenic lines (15–20 animals per line) were analysed for staining intensity for each construct (pixel density was inverted to represent lipid content). Every WT line was significantly different from every S303A line ( $P < 0.005$ ; ANOVA followed by Tukey HSD tests). \*Indicates statistical significance ( $P < 0.005$ ) using ANOVA followed by a Tukey HSD test in **i**, or the one-tailed *t*-test in **m**. **l**, **m**, **p**, Error bars represent s.d. **a–j**, Arrowhead indicates the junction between the pharynx (left) and the intestine (right). Scale bar, 20  $\mu\text{m}$ .

of the S303A variant significantly increased lipid loss during dauer compared to misexpression of WT ATGL-1 (Fig. 2 i, j, p), suggesting that, in the presence of AMPK, ATGL-1(S303A) demonstrates elevated lipase activity compared to ATGL-1(WT). Our data therefore reveal that a high level of LKB1/AMPK signalling is required in the hypodermis to downregulate triglyceride hydrolysis during dauer through direct inhibitory ATGL-1 phosphorylation by AMPK. This ensures that the stored lipids are hydrolysed progressively to slowly release the stored energy, thereby allowing dauer larvae to survive for an extended duration in the absence of caloric intake.

To gain insight into whether the hydrolysed lipids are converted through the respiratory pathway, we determined the rate at which *aak-2* mutant dauers consume oxygen. Oxygen consumption is reduced in dauers compared to non-dauer animals<sup>2,5</sup> (data not shown). In *aak-2* mutant dauers, however, oxygen consumption is significantly higher than in control dauers (Fig. 2m). Therefore, during the dauer stage, in the absence of LKB1/AMPK signalling, animals rapidly consume their energy reserves and consequently exhibit abnormally high rates of respiration.

Energy is required for living organisms to maintain homeostasis, and metazoans have evolved specialized organs to fulfil this role. The excretory system of *C. elegans* functions primarily in osmoregulation, somewhat like a kidney<sup>25</sup>. Mutant adults in which ILS is compromised have increased hypertonic stress resistance<sup>26</sup>, and dauer larvae are even more resistant to this stress (Fig. 3a). Thus, *aak-2* could function in the excretory system to improve osmotic stress resistance in ILS mutants and/or in dauer larvae, and this would in turn

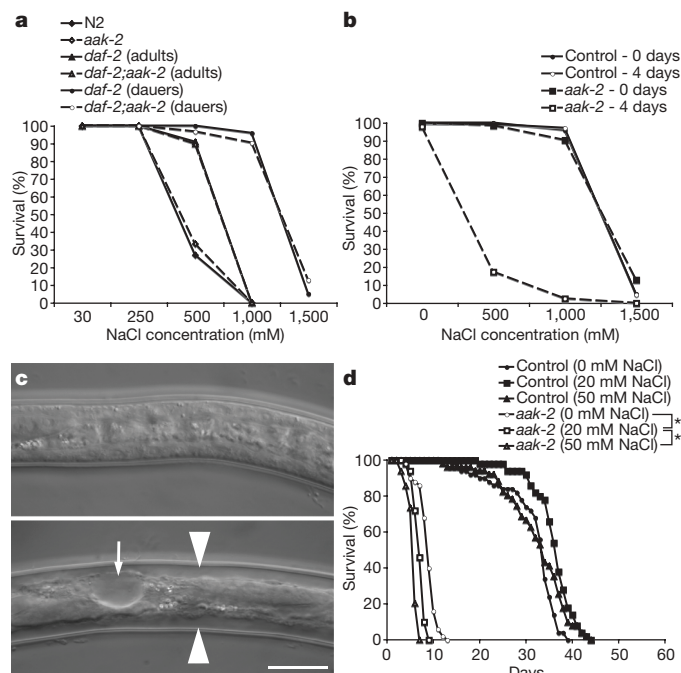


**Figure 3** | *aak-2* is required for proper osmoregulation during dauer. **a**, *daf-2(e1370)* mutant adults are osmoreistant compared to wild type (N2), while these mutants are even more resistant as dauer larvae, and this is independent of *aak-2*. **b**, *daf-2(e1370); aak-2(ok524)* mutant dauers however become osmosensitive after four days, and **(c)** (bottom) accumulated fluid in their body cavity (arrowheads) and/or in vesicles (arrow) 8 days after their dauer moult. This was not observed in control *daf-2(e1370)* dauers of the same age (top). Scale bar, 20  $\mu$ m. **d**, The life span of *daf-2(e1370); aak-2(ok524)* mutant dauers is reduced in NaCl-supplemented cultures while these variations have no negative effect on control *daf-2(e1370)* dauers. \*Indicates that dauer life span was significantly reduced compared to the control strain ( $P < 0.005$ ), using the log-rank test. This experiment was repeated twice ( $n \approx 50$  per assay), yielding similar results. Sample size was between 100 and 1,000 for each point in **a**, **b**. Genotype includes *daf-2(e1370)* in **b**, **d**.

contribute to the resilience and long-term survival of the dauer larva. However, *aak-2* mutant adults are not hypersensitive to osmotic stress, nor is *aak-2* required for the increased resistance observed in *daf-2* mutants (Fig. 3a). Furthermore, young *aak-2* mutant dauers showed no obvious difference in their resistance to hypertonic stress compared to control dauers (Fig. 3a). Although *aak-2* mutant dauers initially osmoregulate properly, we suspected that the rapid energy depletion that occurs in these mutants could later render animals osmosensitive. In this scenario, after their lipid stores are depleted, the excretory system of *aak-2* mutant dauers would begin to falter, causing animals to eventually expire due to improper osmoregulation. We found that the majority (75%;  $n = 51$ ) of living, 8-day-old *aak-2* mutant dauers had accumulated fluid in their body cavity, while 12% also contained fluid-filled vesicles (Fig. 3c), similar to those that form in animals following excretory cell ablation<sup>25</sup>. In contrast, this was never observed in control dauers ( $n = 34$ ). Further tests showed that older, lipid-depleted, *aak-2* dauers are hypersensitive to osmotic stress (Fig. 3b). Moreover, the dauer life span of *aak-2* mutants is further reduced if the animals are cultured in media lightly supplemented with salt, while this treatment had no negative effect on the life span of control dauers (Fig. 3d). These data therefore suggest that the final cause of lethality in *aak-2* mutant dauers is a failure in osmoregulation, secondary to the premature depletion of the stored energy. AMPK activity in the excretory system thus is likely to enhance excretory function during energetic stress, perhaps due to its long-known cell-autonomous role in energy balance, thereby allowing the animal to survive longer.

In summary, LKB1/AMPK signalling appears to execute dual functions: it cell non-autonomously regulates survival of the dauer larva by ensuring a slow release of the triglycerides stored in the hypodermis over a prolonged duration, while also enhancing osmoregulation in the excretory system during periods of nutrient depletion. Obesity, on the other hand, results from excessive storage of lipids in adipose tissues, much like in animals that prepare for diapause. If these mechanisms are indeed conserved, our work suggests that the specific impairment of LKB1/AMPK signalling could potentially affect the hydrolysis of stored fat in obese individuals. Finally, AMPK is required for *C. elegans* adult life span extension induced by reduced ILS, certain types of dietary restriction, and altered mitochondrial or protein deacetylase function, while the mechanisms through which this is accomplished remain enigmatic<sup>9,27–29</sup>. Our work shows that LKB1/AMPK signalling affects lipid metabolism and vital organ function during periods of energetic stress, two processes that could influence life span.

## METHODS SUMMARY

Nematodes were cultured on MYOB plates with *Escherichia coli* (HB101) and maintained at 15 °C unless otherwise stated. The Bristol isolate (N2) was used as wild type. The following alleles were used: LGIII: *daf-7(e1372)*, *daf-2(e1370)*, *strd-1(ok2283, rr91, rr92)*, *aakb-2(rr88)*, *aak-1(tm1944)*. LGV: *par-4(it57)*. LGX: *dpy-7(e88)*, *aak-2(ok524, rr48)*, *hosl-1(tm2369)*, *aakb-1(tm2658)*. Details on alleles, transgenic lines, plasmid constructions, and semiquantitative RT-PCR can be found in Methods.

Dauers were stained with Sudan black as previously described<sup>20</sup>. For Fig. 2p, mean pixel density was determined using Openlab, and inverted in order to quantitatively score lipid content.

For the lipase assay, dauers (day 0) were homogenized in a 20% glycerol, 0.1 M KCl, 20 mM HEPES (pH 7.6) buffer essentially as previously described<sup>29</sup>. Lipase activity was quantified with a commercially-available QuantiChrom kit from BioAssay Systems according to the manufacturer's recommendations.

For *in vitro* kinase assays, purified rat liver AMPK (Millipore) was incubated with the various substrates ( $\sim 2 \mu$ g) as previously described<sup>28</sup> and <sup>32</sup>P incorporation was quantified using a STORM phospho-imager.

Adult osmotic resistance was assayed as previously described on plates at 20 °C (ref. 26). For dauer larvae, synchronized L1 larvae were grown on regular plates at 25 °C until they formed dauer. They were then (or four days later) gathered in a drop of double-distilled H<sub>2</sub>O and transferred to solutions of varying NaCl concentrations for 24 h at 25 °C, after which animals were transferred back to regular plates, allowed to recover for one hour, and scored for survival (response to prodding).

RNAi, microscopy and analysis of dauer life span<sup>7</sup>, oxygen consumption assay<sup>30</sup>, and triglyceride content determination<sup>29</sup> were performed as described elsewhere.

**Full Methods** and any associated references are available in the online version of the paper at [www.nature.com/nature](http://www.nature.com/nature).

Received 14 November 2007; accepted 13 October 2008.

Published online 3 December 2008.

- Klass, M. & Hirsh, D. Non-ageing developmental variant of *Caenorhabditis elegans*. *Nature* **260**, 523–525 (1976).
- Burnell, A. M., Houthoofd, K., O'Hanlon, K. & Vanfleteren, J. R. Alternate metabolism during the dauer stage of the nematode *Caenorhabditis elegans*. *Exp. Gerontol.* **40**, 850–856 (2005).
- Kimura, K. D., Tissenbaum, H. A., Liu, Y. & Ruvkun, G. *daf-2*, an insulin receptor-like gene that regulates longevity and diapause in *Caenorhabditis elegans*. *Science* **277**, 942–946 (1997).
- McElwee, J., Bubb, K. & Thomas, J. H. Transcriptional outputs of the *Caenorhabditis elegans* forkhead protein DAF-16. *Aging Cell* **2**, 111–121 (2003).
- McElwee, J. J., Schuster, E., Blanc, E., Thornton, J. & Gems, D. Diapause-associated metabolic traits reiterated in long-lived *daf-2* mutants in the nematode *Caenorhabditis elegans*. *Mech. Ageing Dev.* **127**, 458–472 (2006).
- Kenyon, C., Chang, J., Gensch, E., Rudner, A. & Tabtiang, R. A. *C. elegans* mutant that lives twice as long as wild type. *Nature* **366**, 461–464 (1993).
- Narbonne, P. & Roy, R. Inhibition of germline proliferation during *C. elegans* dauer development requires PTEN, LKB1 and AMPK signalling. *Development* **133**, 611–619 (2006).
- Hardie, D. G. AMP-activated/SNF1 protein kinases: Conserved guardians of cellular energy. *Nature Rev. Mol. Cell Biol.* **8**, 774–785 (2007).
- Apfeld, J., O'Connor, G., McDonagh, T., DiStefano, P. S. & Curtis, R. The AMP-activated protein kinase AAK-2 links energy levels and insulin-like signals to lifespan in *C. elegans*. *Genes Dev.* **18**, 3004–3009 (2004).

10. Fukushige, T., Hendzel, M. J., Bazett-Jones, D. P. & McGhee, J. D. Direct visualization of the *elt-2* gut-specific GATA factor binding to a target promoter inside the living *Caenorhabditis elegans* embryo. *Proc. Natl Acad. Sci. USA* **96**, 11883–11888 (1999).
11. Maduro, M. & Pilgrim, D. Identification and cloning of *unc-119*, a gene expressed in the *Caenorhabditis elegans* nervous system. *Genetics* **141**, 977–988 (1995).
12. Masse, I., Molin, L., Billaud, M. & Solari, F. Lifespan and dauer regulation by tissue-specific activities of *Caenorhabditis elegans* DAF-18. *Dev. Biol.* **286**, 91–101 (2005).
13. Okkema, P. G., Harrison, S. W., Plunger, V., Aryana, A. & Fire, A. Sequence requirements for myosin gene expression and regulation in *Caenorhabditis elegans*. *Genetics* **135**, 385–404 (1993).
14. Myers, T. R. & Greenwald, I. *lin-35* Rb acts in the major hypodermis to oppose ras-mediated vulval induction in *C. elegans*. *Dev. Cell* **8**, 117–123 (2005).
15. McKay, S. J. *et al.* Gene expression profiling of cells, tissues, and developmental stages of the nematode *C. elegans*. *Cold Spring Harb. Symp. Quant. Biol.* **68**, 159–169 (2003).
16. Sherman, T. *et al.* The abts and sulp families of anion transporters from *Caenorhabditis elegans*. *Am. J. Physiol. Cell Physiol.* **289**, C341–C351 (2005).
17. Loria, P. M., Hodgkin, J. & Hobert, O. A conserved postsynaptic transmembrane protein affecting neuromuscular signaling in *Caenorhabditis elegans*. *J. Neurosci.* **24**, 2191–2201 (2004).
18. Huang, P. & Stern, M. J. FGF signaling functions in the hypodermis to regulate fluid balance in *C. elegans*. *Development* **131**, 2595–2604 (2004).
19. Mello, C. C., Kramer, J. M., Stinchcomb, D. & Ambros, V. Efficient gene transfer in *C. elegans*: Extrachromosomal maintenance and integration of transforming sequences. *EMBO J.* **10**, 3959–3970 (1991).
20. Ogg, S. & Ruvkun, G. The *C. elegans* PTEN homolog, DAF-18, acts in the insulin receptor-like metabolic signaling pathway. *Mol. Cell* **2**, 887–893 (1998).
21. Schweiger, M. *et al.* Adipose triglyceride lipase and hormone-sensitive lipase are the major enzymes in adipose tissue triacylglycerol catabolism. *J. Biol. Chem.* **281**, 40236–40241 (2006).
22. Zimmermann, R. *et al.* Fat mobilization in adipose tissue is promoted by adipose triglyceride lipase. *Science* **306**, 1383–1386 (2004).
23. Gronke, S. *et al.* Brummer lipase is an evolutionary conserved fat storage regulator in *Drosophila*. *Cell Metab.* **1**, 323–330 (2005).
24. Gwinn, D. M. *et al.* AMPK phosphorylation of raptor mediates a metabolic checkpoint. *Mol. Cell* **30**, 214–226 (2008).
25. Nelson, F. K. & Riddle, D. L. Functional study of the *Caenorhabditis elegans* secretory-excretory system using laser microsurgery. *J. Exp. Zool.* **231**, 45–56 (1984).
26. Lamitina, S. T. & Strange, K. Transcriptional targets of DAF-16 insulin signaling pathway protect *C. elegans* from extreme hypertonic stress. *Am. J. Physiol. Cell Physiol.* **288**, C467–C474 (2005).
27. Curtis, R., O'Connor, G. & DiStefano, P. S. Aging networks in *Caenorhabditis elegans*: AMP-activated protein kinase (*aak-2*) links multiple aging and metabolism pathways. *Aging Cell* **5**, 119–126 (2006).
28. Greer, E. L. *et al.* An AMPK-FOXO pathway mediates longevity induced by a novel method of dietary restriction in *C. elegans*. *Curr. Biol.* **17**, 1646–1656 (2007).
29. Schulz, T. J. *et al.* Glucose restriction extends *Caenorhabditis elegans* life span by inducing mitochondrial respiration and increasing oxidative stress. *Cell Metab.* **6**, 280–293 (2007).
30. Feng, J., Bussiere, F. & Hekimi, S. Mitochondrial electron transport is a key determinant of life span in *Caenorhabditis elegans*. *Dev. Cell* **1**, 633–644 (2001).

**Supplementary Information** is linked to the online version of the paper at [www.nature.com/nature](http://www.nature.com/nature).

**Acknowledgements** We thank A. Fire, O. Hobert, I. Greenwald, D. Baillie, K. Nehrke, J. McGhee, M. Han, S. Li, E. Colella, M. Hebeisen, J. Ouellet, A. Shingina, M. Maduro, F. Solari, E. Greer, J. Lapointe, W. Yang and S. Hekimi for reagents, strains, constructs, help, advice and support. Some of the strains that were used in this analysis came from the *Caenorhabditis* Genetic Center (CGC), the *C. elegans* Gene Knockout Consortium, the Japan National Bioresource Project, and the Genome BC *C. elegans* Gene Expression Consortium. This work was supported by research grants from the Canadian Cancer Society and the Canadian Institutes of Health Research (CIHR) to R.R. P.N. is a recipient of an NSERC studentship. R.R. is a CIHR New Investigator.

**Author Contributions** P.N. designed and conducted all the experiments, except the kinase assays, which were performed by R.R.. The manuscript was written by P.N. and edited by R.R.

**Author Information** Reprints and permissions information is available at [www.nature.com/reprints](http://www.nature.com/reprints). Correspondence and requests for materials should be addressed to R.R. ([richard.roy@mcgill.ca](mailto:richard.roy@mcgill.ca)).



## METHODS

**Allele details.** *aak-1(tm1944)* is a predicted null allele that deletes part of the catalytic domain and introduces a frameshift and a premature stop codon thereafter. *strd-1(rr91)* is a [C964T] transition that introduces a premature stop codon. *strd-1(rr92)* is a [G727A] transition that causes a single amino acid substitution. *strd-1(ok2283)* deletes exon 4 and is predicted to cause a frameshift and a premature stop codon thereafter. *aakb-1(tm2658)* is a small in-frame deletion that removes part of the glycogen-binding domain. *aakb-2(rr88)* is a [C262T] transition which introduces a premature stop codon.

**Transgenic lines and plasmid constructions.** *daf-2(e1370)* or *daf-2(e1370); aak-2(ok524)* animals were micro-injected with various constructs (see Supplementary Table 1 for concentrations used and lines tested), using either pRF4: *rol-6(su1006)gf* at 50–100 ng  $\mu\text{l}^{-1}$ , pMR352: *myo-2p::GFP* (*PstI-MscI* digested *myo-2* promoter from pPD30.69, inserted into *PstI-SmaI* pPD95.75) at 50 ng  $\mu\text{l}^{-1}$  or pTG96: *sur-5p::GFP* at 20–50 ng  $\mu\text{l}^{-1}$  as a co-transformation marker. The *aak-2* genomic rescuing fragment (pMR701) has previously been described<sup>7</sup>. pMR701 was digested with *Sall* and the resulting ~6 kb fragment was cloned into *Sall*-digested pPD95.75 (gift from A. Fire) to generate pMR705, an early-truncated *aak-2p::AAK-2N::GFP* translational fusion protein that contains ~3.1 kb of promoter sequence, in addition to the first intron. *aak-2* cDNA was obtained from an RT–PCR reaction performed on wild type worm RNA extracts using the following primers: 5'-ATGTTTTCTCATCAAGATCGAG-3' and 5'-CTTAACGAGCCAGTGTTCC-3', and cloned into pGEMt (Promega) to generate pMR702 (the insert being oriented such that the start codon is downstream of the *SpeI* site in the vector). pMR702 was then cut using *PstI-SacII*, and the resulting fragment (*aak-2* cDNA) was blunted and transferred into pPD49.26 (gift from A. Fire) at the *EcoRV* site, upstream of the *unc-54* 3' UTR, to generate pMR725. The *sur-5* ubiquitous promoter was PCR-amplified from pTG96 (gift from M. Han) using the following primers: 5'-ATATCTGCAGTGCTAAATTGCAACCCCGTG-3' and 5'-AAGTGCGGCCGCCATTCTGAAAACAAAATGTAAAG-3', digested with *PstI-NotI* and inserted at the corresponding sites into pMR725 to generate *sur-5p::AAK-2* (pMR732). The GFP sequence was amplified from pPD95.75 with the following primers: 5'-ATATGCGGCCGCTATGAGTAAAGGAGAAGAAC-3' and 5'-ATATGCGGCCGCTTTGTATAGTTCA-TCCATG-3', digested with *NotI* and cloned into *NotI*-digested pMR732 to generate *sur-5p::GFP::AAK-2* (pMR747). The *unc-119* neuronal promoter was PCR-amplified from MM0051<sup>11</sup> using the following primers: 5'-ATATCTGCAGCTCGAGGTGACGGTATCG-3' and 5'-TAGTGCGGCCGCTTCATATATGCTGTTGTAGC-3', digested with *PstI-NotI* and inserted at the corresponding sites into pMR725 to generate *unc-119p::AAK-2* (pMR729). The *unc-54* muscle promoter was digested from *PEunc-54::gfp*<sup>12,13</sup> using *HindIII* and *KpnI*, blunted and inserted into *XmaI*-digested, blunted pMR725 to generate *unc-54p::AAK-2* (pMR731). The *elt-2* intestinal promoter was digested from pJM67<sup>10</sup> using *HaeIII* (4.3 kb fragment) and inserted into *XmaI*-digested, blunted pMR725 to generate *elt-2p::AAK-2* (pMR736). The *dpy-7* hypodermal promoter was digested from *dpy-7p::lin-35(+)*<sup>14</sup> using

*PmeI-SmaI* and cloned into *SmaI*-digested pMR725 or pPD95.67 to generate *dpy-7p::AAK-2* (pMR737) and *dpy-7p::GFP* (pMR743), respectively. The *rol-6* hypodermal promoter<sup>18</sup> was PCR-amplified using pRF4 as a template<sup>19</sup> and the following primers: 5'-ATATCTGCAGAGAAAAACGATGGATTGAG-3' and 5'-TATAGCGGCCGCCATCTGGAAATTTTCAGTTAG-3', digested with *PstI-NotI* and inserted at the corresponding sites into pMR725 to generate *rol-6p::AAK-2* (pMR742). The *unc-122* coelomocyte promoter was PCR-amplified from a *unc-122p::GFP* reporter as a template<sup>17</sup> with the following primers: 5'-CATGCCTGCAGGTTTCCC-3' and 5'-ATATGCGGCCGCCGTTGTGA-GCCCAATGAAG-3', digested with *PstI-NotI* and inserted at the corresponding sites into pMR725 to generate *unc-122p::AAK-2* (pMR744). The *sulp-5* excretory cell promoter was PCR-amplified from a *sulp-5p::GFP* reporter<sup>15,16</sup> using the following primers: 5'-ATATCTGCAGAACAAATTTGCATTGAATTGGG-3' and 5'-ATATGCGGCCGCAATCGTAGGAGTTGATGGTG-3', digested with *PstI-NotI* and inserted at the corresponding sites into pMR725 to generate *sulp-5p::AAK-2* (pMR746).

*atgl-1* cDNA was obtained from an RT–PCR reaction performed on wild type worm RNA extracts using the following primers: 5'-ATGACTATGAT-AAATAGTCGGC-3' and 5'-AGAGTAGATGGGTACAGG-3', and cloned into a pKSII variant to generate pMR749 (the insert being oriented such that the start codon is downstream of the *SmaI* site in the vector). pMR749 was then cut using *XmaI-NotI*, and the resulting fragment (*atgl-1* cDNA) was transferred into pGEX-6P-2 (GE Healthcare) at the corresponding sites, to generate pMR750. The diverse S/T to A variants were generated by site-directed mutagenesis using the GeneTailor kit (Invitrogen) according to the manufacturer's protocol. pMR749 was also cut using *SmaI-SpeI*, blunted, and the resulting fragment was transferred into pPD49.26 at the *EcoRV* site, to generate pMR751. Two PCR reactions were performed using this plasmid as a template; one with rr1087-rr1088 and one with rr1089-rr1090 primers (sequence available upon request). Each resulting fragment was digested with *SacI-NotI* and they were ligated together to generate an ATGL-1::HA construct (pMR753). The *sur-5* promoter was PCR-amplified from pTG96 using the following primers: 5'-ATATCCCGGGTGCTAAATTGCAACCCCGTG-3' and 5'-AAGTGCGGC-CGCCATTCTGAAAACAAAATGTAAAG-3', digested with *XmaI-NotI* and inserted at the corresponding sites into pMR753 to generate *sur-5p::ATGL-1::HA* (pMR754). The GFP sequence was amplified from pPD95.75 with the following primers: 5'-ATATGCGGCCGCTATGAGTAAAGGAGAAGAAC-3' and 5'-ATATGCGGCCGCTTTGTATAGTTTCATCCATG-3', digested with *NotI* and cloned into *NotI* digested pMR754 to generate *sur-5p::GFP::ATGL-1::HA* (pMR758). The S303A variant (pMR767) was generated by site-directed mutagenesis of pMR758 using the GeneTailor kit (Invitrogen).

**Semi-quantitative RT–PCR.** Total RNA was isolated from 100 dauer larvae for each of the tested genotypes using Trizol. RT reactions were performed with 130 ng RNA in 20  $\mu\text{l}$  total volume using *act-1* and *aak-2*-specific reverse primers. 43 PCR cycles were performed on 5  $\mu\text{l}$  of the RT reaction in 50  $\mu\text{l}$  total volume (14  $\mu\text{l}$  loaded per lane). Details of primer sequences are available upon request.

# Analysis of combinatorial *cis*-regulation in synthetic and genomic promoters

Jason Gertz<sup>1</sup>, Eric D. Siggia<sup>2</sup> & Barak A. Cohen<sup>1</sup>

Transcription factor binding sites are being discovered at a rapid pace<sup>1,2</sup>. It is now necessary to turn attention towards understanding how these sites work in combination to influence gene expression. Quantitative models that accurately predict gene expression from promoter sequence<sup>3–5</sup> will be a crucial part of solving this problem. Here we present such a model, based on the analysis of synthetic promoter libraries in yeast (*Saccharomyces cerevisiae*). Thermodynamic models based only on the equilibrium binding of transcription factors to DNA and to each other captured a large fraction of the variation in expression in every library. Thermodynamic analysis of these libraries uncovered several phenomena in our system, including cooperativity and the effects of weak binding sites. When applied to the *S. cerevisiae* genome, a model of repression by Mig1 (which was trained on synthetic promoters) predicts a number of Mig1-regulated genes that lack significant Mig1-binding sites in their promoters. The success of the thermodynamic approach suggests that the information encoded by combinations of *cis*-regulatory sites is interpreted primarily through simple protein–DNA and protein–protein interactions, with complicated biochemical reactions—such as nucleosome modifications—being downstream events. Quantitative analyses of synthetic promoter libraries will be an important tool in unravelling the rules underlying combinatorial *cis*-regulation.

Thermodynamic models of gene regulation have shown promising results in eukaryotic systems<sup>6,7</sup> when applied to small gene sets. Owing to limitations in studying genomic promoters, the number of observations in these studies is small compared to the number of molecular events that are modelled, and over-fitting is therefore a serious concern. An approach that circumvents this limitation is to model the expression of synthetic promoters<sup>8–10</sup>. As conceivably any promoter sequence can be created and analysed, a large portion of possible regulatory element combinations can be evaluated.

We constructed synthetic promoter libraries consisting of random combinations of three to four transcription factor binding sites (TFBS), or building blocks (Table 1 and Supplementary Information). In total, we analysed 2,807 promoters among 7 libraries using 18 different building blocks. All promoters were placed upstream of a medium strength basal promoter driving yellow fluorescent protein (YFP; Supplementary Fig. 1) and integrated into the yeast genome at

the *TRP1* locus. The level of gene expression directed by each synthetic promoter was quantified by flow cytometry of 25,000 individual cells per promoter (Fig. 1a, b).

Figure 1c shows the expression levels of 429 synthetic promoters from the L1 library (see Supplementary Tables 1–7 for expression and sequence of all promoters). Basal promoter only controls (Fig. 1c, shown in red) were used to estimate the technical variance of our expression measurements, which is 1.3% of the total variance of the L1 library; the average technical variance for all libraries is 0.8% of the total variance. The biological replicate variance, which refers to the gene expression differences between independent transformants that have the same synthetic promoter by chance, is 35% of the total variance in the L1 library and 17% on average. Therefore, a perfect model relating promoter sequence to our expression data would explain 65% of the variance in expression driven by the different promoters in the L1 library.

We constructed a thermodynamic model of the relationship between promoter sequence and expression. The purpose of the model was to provide a formal mathematical framework for predicting the activity of novel combinations of *cis*-regulatory sites, and to gain insight into the mechanisms that generate diverse expression levels from different arrangements of the same *cis*-regulatory sites. We used a model first proposed in ref. 11, and later modified in ref. 12. The main assumption of this model is that gene regulation is controlled completely by the equilibrium binding of proteins to DNA and to each other. Enzymatic events, such as chromatin modifications and polymerase phosphorylation, are not taken into account. The model consists of parameters that describe the changes in free energy of particular DNA–protein and protein–protein interactions that can occur on the promoters. These parameters are used to calculate the probability of RNA polymerase (RNAP) being bound to each promoter in the library (see Supplementary Information). We then assume that the probability of RNAP being bound to a given promoter is directly proportional to the intensity of YFP fluorescence measured for that promoter.

In every library, thermodynamic models explained 44–59% of the variance in expression (Table 1), which is more than double the amount of variance explained by the best models of genome-wide expression data<sup>4,5</sup>. The thermodynamic model for the L1 library

**Table 1 | Summary of synthetic promoter libraries**

Library	Building blocks	Number of promoters	Number of parameters fitted	Fraction of variance explained ( $R^2$ )
L1	Mig1, Gcr1, Spacer	429	5	0.49
L1-test	Same as L1	83	0	0.44
L1-weak	Same as L1 plus a weak Mig1 site	266	1	0.44
L2	Mig1, Reb1, Rap1, Gcr1 (different from L1)	471	4	0.59
L3	Adr1, Hap2/3/4/5, CSRE, Rgt1	596	6	0.47
L4	Cbf1, Gcn4, Met31/32, Nrg1	381	10	0.54
L5	Msn2/4, Smp1, Xpb1	581	4	0.57

<sup>1</sup>Center for Genome Sciences, Department of Genetics, Washington University in Saint Louis School of Medicine, 4444 Forest Park Avenue, St Louis, Missouri 63108, USA. <sup>2</sup>Center for Studies in Physics and Biology, The Rockefeller University, New York, New York 10021, USA.

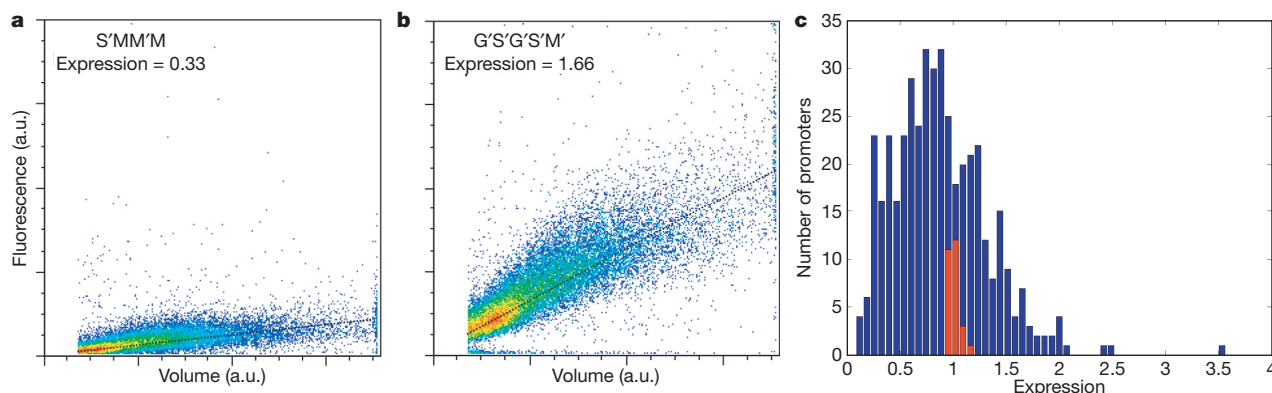


**Figure 1 | Gene expression measurements.** **a, b,** Graphs of cell volume versus fluorescence for 25,000 individual cells containing the promoters S'MM'M (**a**) and G'S'G'S'M' (**b**). Here S = Spacer, G = Gcr1 site, M = Mig1 site and prime indicates a site in the reverse orientation.

captured 49% of the variance in expression (Supplementary Fig. 2; 75% of the available variance). The overall success of the thermodynamic approach indicates that expression driven by combinations of binding sites can be generally and accurately modelled by simply considering protein–DNA and protein–protein binding events.

To determine the predictive power of our model for the L1 library, we constructed the L1-test library, which consists of novel combinations of the L1 building blocks. With the same parameter values from the L1 library, the model still captures 44% of the variance in expression, implying that the model is not over-fitted. This lack of over-fitting is not surprising, considering that each model contains about 6 parameters fitted to an average of over 400 promoters. The Mig1 parameter values found in the L1 library were held constant among thermodynamic models for three other libraries (L1-test, L1-weak and L2) that all exhibited high predictive power (see Supplementary Table 8 for all parameter values). Our model for the L1 library predicts that the 'Spacer' building block, which we designed to contain no known or predicted regulatory sequence elements, can recruit RNAP to promoters. As about half of the DNA-binding proteins in yeast do not yet have an associated *cis*-regulatory motif<sup>1</sup>, it is likely that the Spacer site is actually an unidentified *cis*-regulatory element. The ability of the model to incorporate an unknown sequence element and accurately predict its behaviour points to a strength of the approach.

Analysis of the model for the L1 library suggests that Mig1 binds cooperatively to the synthetic promoters. Because nothing in the previous literature suggested cooperativity between Mig1 monomers, we decided to analyse Mig1 cooperativity independent of the model. We fitted a Hill equation relating percentage repression to the number of Mig1 sites, with the assumption that 100% repression occurs with five Mig1-binding sites. We found that a Hill coefficient of  $3.4 \pm 0.25$  and  $K = 1.8$  (where  $K$  is the number of Mig1 sites that causes half maximal repression) gives the best fit, suggesting cooperativity. Figure 2a shows that the observed data fit well to the Hill equation and that without cooperativity the fit is substantially worse. These results are consistent with the thermodynamic model and suggest that Mig1 acts cooperatively to repress transcription in our system, which led us to examine the influence of low affinity TFBS on expression.

Low affinity, or weak, TFBS are known to play important roles in prokaryotic promoters<sup>13</sup> and have been postulated to be important in eukaryotic gene regulation<sup>14</sup>. However, their quantitative effect on gene expression is difficult to determine. To study the effects of weak TFBS, we constructed a library (L1-weak) incorporating a building block matching a Mig1-binding site that was shown to have low affinity for Mig1 *in vitro*<sup>15</sup>. The sequence of this weak site scores below any reasonable cut-off in a genome scan for Mig1 sites based on a

**c,** Histogram of expression values for all L1 library members. Expression values were computed as the average fluorescence/volume ratio for 25,000 individual cells, and then normalized to plate controls. Control promoters with no library insert are shown in red. a.u., arbitrary units.

weight matrix derived from known Mig1 sites<sup>16,17</sup>. In our system, the low affinity Mig1 site behaved as a weaker repressor than the strong site (Fig. 2b). However, when there are strong Mig1 sites present in a promoter, the weak sites behave as strong sites. When comparing promoters with the same building block content except for the

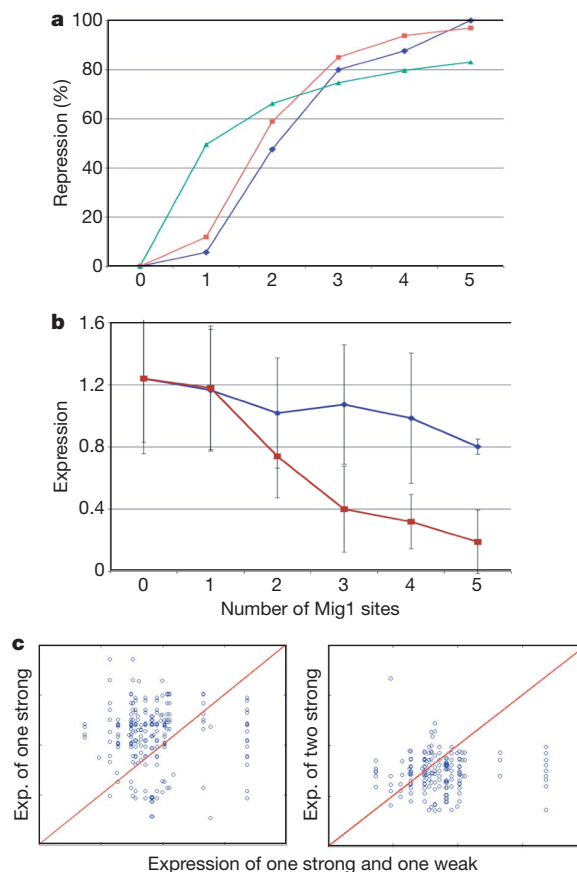


**Figure 2 | Mig1-binding sites act cooperatively, and a weak Mig1 site represses weakly.** **a,** Hill equation with a Hill coefficient of 3.4 and  $K = 1.8$  (red) fits the observed data (blue) well, compared to a Hill equation with a Hill coefficient of 1 (green). **b,** Plot of average expression versus the number of weak sites (blue) without strong sites, and versus the number of strong sites (red) without weak sites. Error bars,  $\pm 1$  s.d. **c,** Plots of expression for pairs of promoters that are almost identical except that either one strong Mig1 site or two strong Mig1 sites replace one strong and one weak Mig1 site. A blue circle represents one promoter pair and the red line represents equal expression.



number of Mig1 sites, promoters with one weak and one strong Mig1 site exhibit lower expression compared to promoters with one strong Mig1 site (Fig. 2c;  $P < 10^{-8}$ , sign test,  $n = 211$ ) and the same expression as promoters with two strong Mig1 sites (Fig. 2c;  $P > 10^{-2}$ , sign test,  $n = 177$ ). This behaviour suggests that strong and weak Mig1 sites interact cooperatively to repress transcription in our system. This interaction produces complex patterns of expression in the L1-weak library.

The thermodynamic model of transcriptional regulation accurately captures many of the complexities of expression in the L1-weak library by adding only one adjustable parameter to the L1 library model parameters—namely, the relative affinity of Mig1 for the weak site. The optimal value of the new parameter corresponds to a 6.7-fold lower relative affinity for Mig1 than the stronger Mig1 site. This value is in good agreement (and within a 95% confidence interval) with an independent computational analysis of a position specific weight matrix for Mig1, which predicted a 9.0-fold lower affinity of the weak site for Mig1 (refs 16, 18). The similarity of the  $R^2$  of this model with that of the L1 library model demonstrates that we are capturing the additional complexities caused by the effect of weak Mig1 sites on expression.

We next examined the possibility that weak sites contribute to Mig1 repression of genomic promoters. Weak Mig1-binding sites are over-represented in *S. cerevisiae* promoters compared to shuffled *S. cerevisiae* promoters ( $P < 10^{-3}$ , simulation,  $n = 1,000$ ; Supplementary Fig. 3). Weak sites are found in 24% of all promoters, while 39% of promoters containing a significant match to a Mig1 weight matrix also contain a weak site ( $P < 10^{-12}$ , hypergeometric test), indicating that strong and weak sites tend to co-occur. Of 33 genes that are known to be regulated by Mig1 (refs 19, 20), and whose promoters contain a significant match to a Mig1 weight matrix, 20 also contain a weaker Mig1 site in their promoters compared to 8 genes expected by chance. According to our model of gene regulation, promoters with one strong and one weak site are more sensitive to changes in Mig1 concentrations than are promoters with either two strong or two weak sites; promoters with one strong and one weak site therefore may be best suited to respond to changes in available carbon sources (Supplementary Fig. 4). These results suggest that combinations of strong and weak Mig1-binding sites are commonly found together in genomic promoters, and may provide a sensitive strategy for glucose repression.

We sought to determine if the properties of Mig1 repression found in the synthetic promoter libraries were informative when studying genomic promoters. In the *S. cerevisiae* genome, 359 promoters have a significant match to a Mig1 weight matrix and 33 of these promoters correspond to one of 136 documented Mig1-regulated genes. To compare these results directly to our model, we applied the thermodynamic model of Mig1 repression to genomic promoters (see Methods). Out of the top 359 promoters ranked by the thermodynamic model for the strength of Mig1 repression, 41 correspond to one of the 136 documented Mig1-regulated genes. Using the regulatory

rules encoded in our thermodynamic model, we explain eight (24%) more known Mig1-regulated genes (*HXT9*, *HXT12*, *HXT13*, *GSY1*, *SOR1*, *ICS2*, *YIL172C*, *YOL153C*) than by simply looking for promoters with a significant match to a Mig1 weight matrix. For example, the *SOR1* promoter does not harbour a significant match to a Mig1 site but contains a number of weak sites that cluster together (Fig. 3a). As cooperativity between Mig1 sites is an important part of our quantitative model, we correctly predicted that *SOR1* is Mig1 regulated and also identified the likely binding sites of Mig1 in this promoter.

Using the thermodynamic model, we also predicted a number of Mig1-regulated genes that were not previously known to be Mig1 targets (Supplementary Table 9). *MIG2*, a paralogue of *MIG1* that represses and binds the same site as Mig1 (ref. 15), was predicted by the model to be auto-regulated on the basis of its promoter sequence (Fig. 3b). To validate this prediction, we measured *MIG2* promoter activity (see Methods) in strains deleted for both *MIG1* and *MIG2*. *MIG2* promoter activity increased significantly in the *mig1Δ mig2Δ* strain as compared to wild type ( $P < 10^{-3}$ ,  $t$ -test,  $n = 24$ ), showing that *MIG2* is auto-regulated by Mig1/Mig2 (Fig. 3c). The prediction from the model was that *MIG2* expression would increase 1.8-fold in a *mig1Δ mig2Δ* strain, and we observed a 1.5-fold change. The regulation of *MIG2* by Mig1/Mig2 represents a previously unreported negative feedback loop in the glucose repression network that was identified on the basis of our analysis of synthetic promoters.

Using a simple system, we have succeeded in constructing an accurate model of the relationship between promoter sequence and gene expression. In part this was because we sampled a much larger fraction of promoter space using our library than we could by sampling genomic promoters. Thus, we were able to fit models containing a small number of parameters to data containing large numbers of observations. We found that a completely thermodynamic model based on the equilibrium binding of the transcription factors and RNAP to each other, and to their *cis*-regulatory sites, was a reasonable way to capture the relationship between promoter sequence and gene expression in our system for all of the libraries examined. This does not imply that kinetic processes, such as histone or RNAP modification, are unimportant in gene regulation; however, it does suggest that the information encoded in a promoter is decoded primarily by the sequence-specific binding of transcription factors. Our results support the idea that the complexity and variation in gene regulation could stem from very simple rules describing the binding of proteins to DNA and to each other<sup>12,13,21</sup>.

## METHODS SUMMARY

To create the building blocks that make up the synthetic promoters, oligonucleotide pairs (each with a 5' phosphate) were annealed by being boiled and then slowly cooled to room temperature (see Supplementary Information for building block sequences). 15  $\mu$ l of 50  $\mu$ M double-stranded building blocks were then ligated with 200 U of T4 DNA ligase (New England Biolabs) for 2 hours at 16 °C. The ligation products were then purified using a Microcon YM-100 column (Millipore) to reduce the number of short promoters. 15 ng of purified ligation

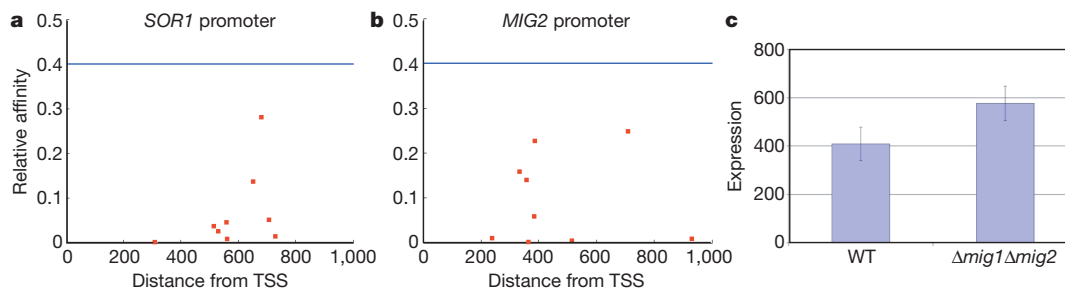


**Figure 3 | Thermodynamic model explains Mig1 repression in the genome.** **a, b**, Mig1-binding sites in the promoters of *SOR1* (**a**) and *MIG2* (**b**). The affinity of Mig1 for the site based on a position weight matrix score relative to the strong site is plotted versus the location upstream of the translation start

site (TSS). The horizontal line represents the significance threshold for the weight matrix and each square represents a Mig1 site. **c**, *MIG2* promoter activity in a wild-type (WT) strain and a *mig1Δ mig2Δ* strain. Error bars,  $\pm 1$  s.d.

product were then ligated into the BamHI site of the integrating reporter plasmid pJG102 (20 ng) and transformed into *Escherichia coli*. Transformants were scraped into Luria broth plus carbenicillin, grown overnight and then DNA was extracted using the GenElute HP Plasmid Maxiprep kit (Sigma). 130 µg of library DNA was digested with BglI, BamHI, SalI and EcoRI (200 U each) and transformed into yeast as described<sup>22</sup>. Colonies growing on medium lacking uracil were picked into 96-well plates and Trp<sup>-</sup> colonies were then identified by replica plating onto medium lacking tryptophan. We observed that some building blocks were represented slightly more than others, even though they were added at equal molar concentrations. The relative abundance of each building block in each library scaled similarly to the melting temperature of the building block.

**Full Methods** and any associated references are available in the online version of the paper at [www.nature.com/nature](http://www.nature.com/nature).

**Received 16 July; accepted 1 October 2008.**

**Published online 23 November 2008.**

1. Harbison, C. T. *et al.* Transcriptional regulatory code of a eukaryotic genome. *Nature* **431**, 99–104 (2004).
2. Hu, Z., Killian, P. J. & Iyer, V. R. Genetic reconstruction of a functional transcriptional regulatory network. *Nature Genet.* **39**, 683–687 (2007).
3. Beer, M. A. & Tavazoie, S. Predicting gene expression from sequence. *Cell* **117**, 185–198 (2004).
4. Bussemaker, H. J., Li, H. & Siggia, E. D. Regulatory element detection using correlation with expression. *Nature Genet.* **27**, 167–171 (2001).
5. Das, D., Banerjee, N. & Zhang, M. Q. Interacting models of cooperative gene regulation. *Proc. Natl Acad. Sci. USA* **101**, 16234–16239 (2004).
6. Segal, E., Raveh-Sadka, T., Schroeder, M., Unnerstall, U. & Gaul, U. Predicting expression patterns from regulatory sequence in *Drosophila* segmentation. *Nature* **451**, 535–540 (2008).
7. Zinzen, R. P., Senger, K., Levine, M. & Papatsenko, D. Computational models for neurogenic gene expression in the *Drosophila* embryo. *Curr. Biol.* **16**, 1358–1365 (2006).
8. Murphy, K. F., Balazsi, G. & Collins, J. J. Combinatorial promoter design for engineering noisy gene expression. *Proc. Natl Acad. Sci. USA* **104**, 12726–12731 (2007).
9. Ligr, M., Siddharthan, R., Cross, F. R. & Siggia, E. D. Gene expression from random libraries of yeast promoters. *Genetics* **172**, 2113–2122 (2006).
10. Cox, R. S. III, Surette, M. G. & Elowitz, M. B. Programming gene expression with combinatorial promoters. *Mol. Syst. Biol.* **3**, 145 (2007).
11. Shea, M. A. & Ackers, G. K. The OR control system of bacteriophage lambda. A physical-chemical model for gene regulation. *J. Mol. Biol.* **181**, 211–230 (1985).
12. Buchler, N. E., Gerland, U. & Hwa, T. On schemes of combinatorial transcription logic. *Proc. Natl Acad. Sci. USA* **100**, 5136–5141 (2003).
13. Ptashne, M. & Gann, A. *Genes and Signals* (Cold Spring Harbor Laboratory Press, 2002).
14. Tanay, A. Extensive low-affinity transcriptional interactions in the yeast genome. *Genome Res.* **16**, 962–972 (2006).
15. Lutfiyya, L. L. *et al.* Characterization of three related glucose repressors and genes they regulate in *Saccharomyces cerevisiae*. *Genetics* **150**, 1377–1391 (1998).
16. Hertz, G. Z. & Stormo, G. D. Identifying DNA and protein patterns with statistically significant alignments of multiple sequences. *Bioinformatics* **15**, 563–577 (1999).
17. Matys, V. *et al.* TRANSFAC: transcriptional regulation, from patterns to profiles. *Nucleic Acids Res.* **31**, 374–378 (2003).
18. Nehlin, J. O. & Ronne, H. Yeast MIG1 repressor is related to the mammalian early growth response and Wilms' tumour finger proteins. *EMBO J.* **9**, 2891–2898 (1990).
19. Monteiro, P. T. *et al.* YEASTRACT-DISCOVERER: new tools to improve the analysis of transcriptional regulatory associations in *Saccharomyces cerevisiae*. *Nucleic Acids Res.* **36**, D132–D136 (2008).
20. Teixeira, M. C. *et al.* The YEASTRACT database: a tool for the analysis of transcription regulatory associations in *Saccharomyces cerevisiae*. *Nucleic Acids Res.* **34**, D446–D451 (2006).
21. Ptashne, M. & Gann, A. Transcriptional activation by recruitment. *Nature* **386**, 569–577 (1997).
22. Gietz, R. D. & Schiestl, R. H. Large-scale high-efficiency yeast transformation using the LiAc/SS carrier DNA/PEG method. *Nature Protocols* **2**, 38–41 (2007).

**Supplementary Information** is linked to the online version of the paper at [www.nature.com/nature](http://www.nature.com/nature).

**Acknowledgements** We thank R. Mitra, G. Stormo, M. Johnston, K. Varley, S. Doniger and members of the Cohen laboratory for discussions and suggestions, and J. Sabina for technical help with LacZ experiments. B.A.C. and J.G. were supported by the NIH (R01 GM078222) and E.D.S. was supported by the NSF (DMR0129848). J.G. was also supported by an NSF Graduate Research Fellowship (DGE-0202737).

**Author Contributions** J.G. performed all experiments and analyses. B.A.C. and J.G. designed the experiments and wrote the paper. E.D.S. conceived the idea of applying the thermodynamic model to the synthetic promoter libraries, and contributed to its development.

**Author Information** Reprints and permissions information is available at [www.nature.com/reprints](http://www.nature.com/reprints). Correspondence and requests for materials should be addressed to B.A.C. ([cohen@genetics.wustl.edu](mailto:cohen@genetics.wustl.edu)).

## METHODS

**Strains and plasmids.** The strain harbouring the synthetic promoter library was derived from the haploid strain BY4742 (*MATa his3Δ1 leu2Δ0 lys2Δ0 ura3Δ0*) as described<sup>23</sup>. The library of promoters was constructed in plasmid pJG102. pJG102 was created by amplifying the *TSA1* promoter from genomic DNA using the following primers: forward, 5'-CGCGGATCCGGCTCGGGTTGGCAAA-GTCGGC-3'; reverse, 5'-CGCGGATCCACTAGTGTGTATGTATGTGTATGT-AGTTGTGG-3'. The amplification product was digested with BamHI and ligated into the BglII and BamHI sites of pJG100 (GenBank accession number FJ175377) to create pJG102. To measure *MIG2* promoter activity we used the plasmid pBM4346 described in ref. 24 and the strains BY4743 and YM6682 described in refs 23 and 24 respectively, which were provided by M. Johnston (Washington Univ.).

**Expression analysis.** Cultures were grown to log phase in 2 ml 96-well plates in 500 μl of synthetic complete media with 2% glucose and lacking uracil. The fluorescence intensities and electronic volumes of 25,000 events from each well were measured on a Beckman Coulter Cell Lab Quanta SC with a multi-plate loader. For each well, the mean of fluorescence divided by electronic volume for 25,000 events was taken as the expression value for that well. On each plate the expression value of the four no-insert controls were averaged to calculate a plate effect to account for changes in laser intensity or growth differences. Each expression value on the plate was then divided by the plate effect.

**Sequencing.** Synthetic promoters were sequenced directly from library members. First colony-PCR was used to amplify the synthetic promoter using the following primers: forward, 5'-GAGTTGATGAATCTCGGTGTG-3'; reverse, 5'-GAACTGGCAATTTACCAGTAGTAC-3'. The PCR reactions were treated with ExoI and shrimp alkaline phosphatase. The PCR products were then sequenced using the forward primer with Big Dye mix v3.1 from Applied Biosystems. Promoter sequences were called only if sequence matched both ends of the PCR product and the number of building blocks found by WU-BLAST<sup>25</sup> matched the expected number of building blocks based on the length of the read.

**Thermodynamic model.** For details about the thermodynamic framework and parameter fitting, see Supplementary Information.

**Genome analysis of thermodynamic model.** We used a thermodynamic model of Mig1 repression on genomic promoters. The promoter sequences used were

obtained from ref. 26. First each sequence was scanned using Patser<sup>27</sup> with an experimentally derived Mig1 position weight matrix<sup>28</sup>, with a cut-off of 2, which is well below the significance cut-off of 7.11. The relative affinity of the weak and strong Mig1 sites predicted by the model was consistent with the difference in weight matrix scores between the weak site and the strong site. We therefore calculated the natural log of relative affinities ( $q$  in Supplementary Information) for each site found by Patser by subtracting 8.01 (the score of the strong site) from the score calculated by Patser. Cooperativity between Mig1 sites in the model was only between Mig1 proteins bound next to each other without any interfering factors. As it is impossible to know what other transcription factors are bound at every promoter, we made the simplifying assumption that Mig1 proteins can only interact with each other when the sites are within 40 base pairs. The thermodynamic model only involving Mig1 sites was then run using the Mig1 parameters described in the manuscript.

**MIG2 expression analysis.** Strains carrying the plasmid containing the *MIG2* promoter upstream of LacZ were grown to mid-log phase in synthetic complete media with 2% glucose and lacking leucine. The cells were disrupted with YPER (Pierce) and then β-galactosidase was monitored using Novagen's Betafluor β-Galactosidase Assay Kit measured on a BioTek Synergy HT. The velocity of the reaction was divided by the OD<sub>600</sub> of each sample to calculate expression. Six replicates were performed for each strain.

23. Brachmann, C. B. *et al.* Designer deletion strains derived from *Saccharomyces cerevisiae* S288C: a useful set of strains and plasmids for PCR-mediated gene disruption and other applications. *Yeast* **14**, 115–132 (1998).
24. Kaniak, A., Xue, Z., Macool, D., Kim, J. H. & Johnston, M. Regulatory network connecting two glucose signal transduction pathways in *Saccharomyces cerevisiae*. *Eukaryot. Cell* **3**, 221–231 (2004).
25. Gish, W. WU BLAST. (<http://blast.wustl.edu>) (1995–, 2008).
26. Cliften, P. *et al.* Finding functional features in *Saccharomyces* genomes by phylogenetic footprinting. *Science* **301**, 71–76 (2003).
27. Hertz, G. Z. & Stormo, G. D. Identifying DNA and protein patterns with statistically significant alignments of multiple sequences. *Bioinformatics* **15**, 563–577 (1999).
28. Nehlin, J. O. & Ronne, H. Yeast MIG1 repressor is related to the mammalian early growth response and Wilms' tumour finger proteins. *EMBO J.* **9**, 2891–2898 (1990).



# Structural basis for androgen specificity and oestrogen synthesis in human aromatase

Debashis Ghosh<sup>1,2</sup>, Jennifer Griswold<sup>1</sup>, Mary Erman<sup>1</sup> & Walter Pangborn<sup>1</sup>

Aromatase cytochrome P450 is the only enzyme in vertebrates known to catalyse the biosynthesis of all oestrogens from androgens<sup>1–3</sup>. Aromatase inhibitors therefore constitute a front-line therapy for oestrogen-dependent breast cancer<sup>3,4</sup>. In a three-step process, each step requiring 1 mol of O<sub>2</sub>, 1 mol of NADPH, and coupling with its redox partner cytochrome P450 reductase, aromatase converts androstenedione, testosterone and 16 $\alpha$ -hydroxytestosterone to oestrone, 17 $\beta$ -oestradiol and 17 $\beta$ ,16 $\alpha$ -oestrinol, respectively<sup>1–3</sup>. The first two steps are C19-methyl hydroxylation steps, and the third involves the aromatization of the steroid A-ring, unique to aromatase. Whereas most P450s are not highly substrate selective, it is the hallmark androgenic specificity that sets aromatase apart. The structure of this enzyme of the endoplasmic reticulum membrane has remained unknown for decades, hindering elucidation of the biochemical mechanism. Here we present the crystal structure of human placental aromatase, the only natural mammalian, full-length P450 and P450 in hormone biosynthetic pathways to be crystallized so far. Unlike the active sites of many microsomal P450s that metabolize drugs and xenobiotics, aromatase has an androgen-specific cleft that binds the androstenedione molecule snugly. Hydrophobic and polar residues exquisitely complement the steroid backbone. The locations of catalytically important residues shed light on the reaction mechanism. The relative juxtaposition of the hydrophobic amino-terminal region and the opening to the catalytic cleft shows why membrane anchoring is necessary for the lipophilic substrates to gain access to the active site. The molecular basis for the enzyme's androgenic specificity and unique catalytic mechanism can be used for developing next-generation aromatase inhibitors.

Human aromatase is the product of the *CYP19A1* gene on chromosome 15q21.1 and consists of a haem group and a polypeptide chain of 503 amino-acid residues. Although aromatase has been extensively studied for more than 35 years<sup>1–3,5–19</sup>, the mechanism of the aromatization step remains poorly understood. Many soluble bacterial P450s, such as P450cam<sup>20</sup> and P450eryF<sup>21</sup>, as well as recombinant human microsomal P450s, such as 3A4 (ref. 22), 2D6 (ref. 23) and 2A6 (ref. 24), that metabolize drug/xenobiotics, have been crystallized and studied by X-ray crystallography. Several laboratories have reported the purification of aromatase from human placenta<sup>7,8</sup> and recombinant expression systems<sup>14,18</sup>. Nevertheless, attempts to crystallize either the placental or a recombinant or modified aromatase have been unsuccessful and an experimental aromatase structure has remained unknown. Numerous mechanistic and homology models based on known P450 structures and site-directed mutagenesis data have been proposed<sup>5,6,9–13,15–18</sup>, leading to the identification of catalytically important residues and possible substrate-binding modes.

The 2.90-Å resolution crystal structure of aromatase purified from term human placenta<sup>19</sup> in complex with its natural substrate androstenedione (androst-4-ene-3,17-dione) exhibits the characteristic cytochrome P450 fold (Fig. 1a; see Methods, Supplementary Fig. 1 and Supplementary Table 1). Androstenedione binds with its  $\beta$ -face oriented towards the haem group and C19 4.0 Å from the Fe atom (Fig. 1b and Supplementary Fig. 2). To test the catalytic viability of the substrate-binding mode, the haem Fe is modelled as a hypothetical oxyferryl Fe(IV)=O moiety (Fig. 1c). The resulting binding geometry of the C19 methyl hydrogens closely resembles that of the reactants for hydroxylation by P450cam<sup>25</sup>. The residues comprising the catalytic cleft are Ile 305, Ala 306, Asp 309 and Thr 310 from the I-helix, Phe 221 and Trp 224 from the F-helix, Ile 133 and Phe 134 from the B-C loop, Val 370, Leu 372 and Val 373 from the K-helix- $\beta$ 3 loop, Met 374 from  $\beta$ 3, and Leu 477 and Ser 478 from the  $\beta$ 8- $\beta$ 9 loop (Fig. 1b). The 17-keto oxygen of the substrate makes a hydrogen bond (2.8 Å) with the backbone amide of Met 374 and a weak contact (3.4 Å) with NH1 of Arg 115 (Fig. 1b). The 3-keto oxygen is 2.6 Å from the carboxylate O<sub>82</sub> of the Asp 309 side chain (Figs 1b and 2a, b), indicating that the carboxylate moiety may be protonated. The hydrophobic residues and porphyrin rings of haem pack tightly against the steroid backbone, forming a cavity complementary in shape to the bound steroid (Fig. 2a). The side chains of residues Arg 115, Ile 133, Phe 134, Phe 221, Trp 224, Ala 306, Thr 310, Val 370, Val 373, Met 374 and Leu 477 make direct van der Waals contacts with the bound androstenedione. Ile 133, Phe 134, Phe 221, Trp 224 and Leu 477 approach the substrate from the  $\alpha$ -face and follow the contour and puckering of the steroid backbone, while the side chains of Arg 115, Ala 306 and Met 374 make contacts at its edge, and Thr 310, Val 370 and Val 373 on the  $\beta$ -face. The combined surface creates a pocket that encloses the bound androstenedione snugly. The volume of the binding pocket is no more than 400 Å<sup>3</sup>, considerably smaller than the volume of about 530 Å<sup>3</sup> of the active sites in 3A4 (ref. 22) and 2D6 (ref. 23), the two drug/xenobiotic-metabolizing human P450s with highest sequence identities (14–18%) to human aromatase.

A distortion in the I-helix backbone resulting in a roughly 3.5-Å displacement of the helix axis is crucial for creating the androgen-specific binding pocket at the active site. This shift in the helix axis caused by Pro 308, a residue unique to aromatase among all P450s, is stabilized by a strong Ala 306CO $\cdots$ HOThr 310 (2.8 Å) hydrogen bond, as well as by an Asp 309 peptide CO $\cdots$ water (3.4 Å) interaction (Fig. 2b). Although an irregularity in the I-helix backbone at this region is observed in other P450s<sup>20–24,26</sup>, this Pro 308-mediated axis shift precisely accommodates the 3-keto end of androstenedione near the fifth turn of the helix (Met 303 to Ala 307), allowing the Asp 309 side chain to hydrogen-bond to the 3-keto oxygen (Fig. 2b). Superposition of the aromatase backbone with bacterial P450cam and P450eryF (Supplementary Fig. 3) as well as with human P450

<sup>1</sup>Structural Biology, Hauptman-Woodward Medical Research Institute, 700 Ellicott Street, Buffalo, New York 14203, USA. <sup>2</sup>Pharmacology and Therapeutics, Roswell Park Cancer Institute, Elm and Carlton Streets, Buffalo, New York 14263, USA.

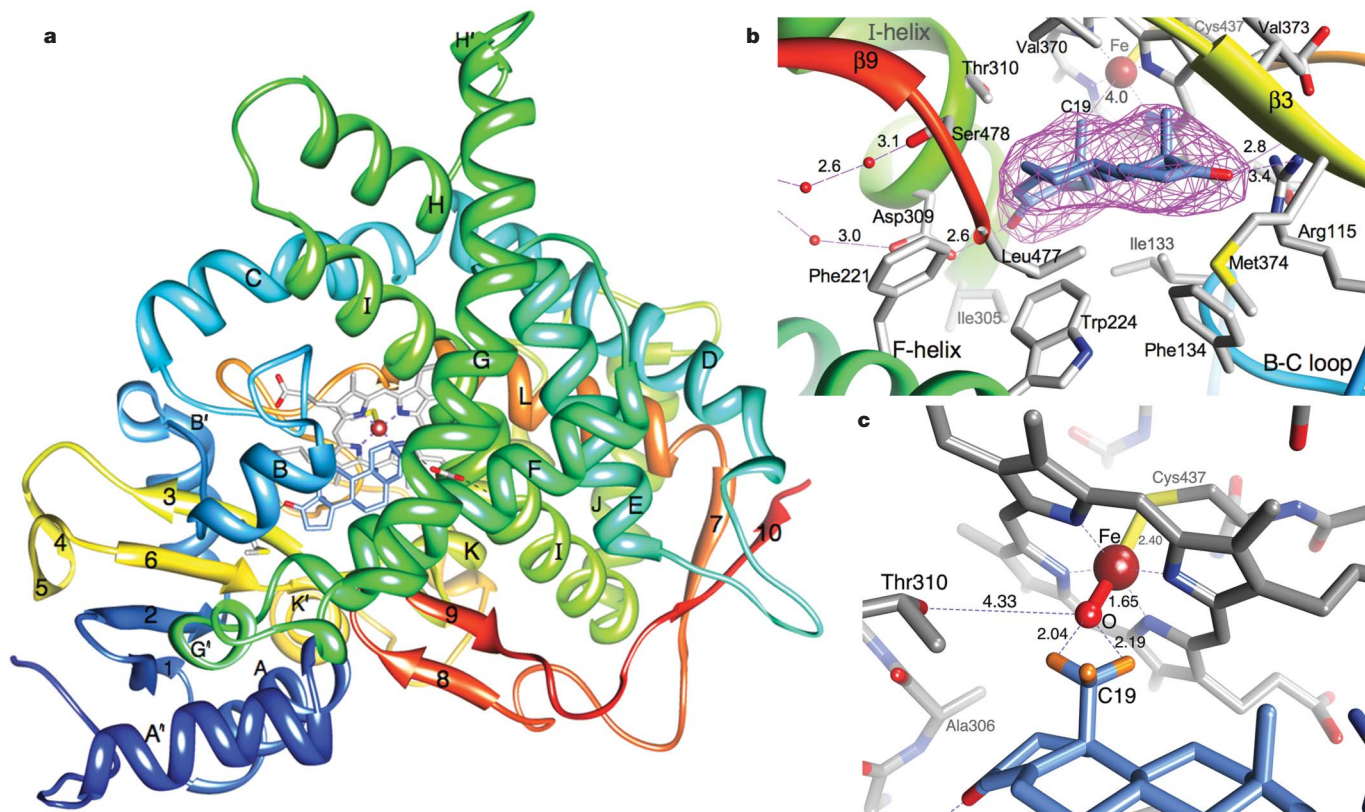


**Figure 1 | The structure of aromatase.** **a**, A ribbon diagram showing the overall structure. The N terminus, starting at residue 45, is coloured dark blue and the C terminus ending at residue 496 is coloured red. The  $\alpha$ -helices are labelled from A to L and  $\beta$ -strands are numbered from 1 to 10. The haem group, the bound androstenedione molecule at the active site and its polar interactions are shown. **b**, A close-up view of the active site showing the bound androstenedione molecule in unbiased difference ( $F_{\text{obs}} - F_{\text{cal}}$ ) electron density contoured at 4.5 times the standard deviation. **c**, Modelling

of Fe(III) as an oxyferryl Fe(IV)=O moiety. The C19-methyl hydrogen atoms are shown at the calculated ideal positions. Important side chains, haem and water molecules are depicted in element colours: grey, C; blue, N; red, O; yellow, S; firebrick, Fe; orange, H. The C atoms of androstenedione are coloured cornflower blue. This colour code is used in all figures. Distances are in ångströms. The directions of view into the active site are roughly similar in all panels. Unless otherwise noted, all three-dimensional illustrations were prepared with Chimera<sup>28</sup>.

3A4 and P450 2D6 (Supplementary Fig. 4) shows that without this shift, the 3-keto end of the substrate would clash with the I-helices of P450cam, P450eryF, P450 2D6 and P450 3A4. The structure therefore confirms the critical roles of Pro 308 and Asp 309 predicted by mutagenesis and modelling<sup>9,10,15</sup>.

The Asp 309 side chain also forms a hydrogen bond with a water molecule 3.0 Å from O<sub>δ1</sub> (Figs 1b and 2a and Supplementary Fig. 5). The geometries of these two hydrogen bonds place the 3-keto oxygen and the water oxygen atom roughly in the carboxylate plane (Fig. 2b). Furthermore, this water molecule is situated at 3.6 Å from the guanidinium group of the Arg 192 side chain (Fig. 2b), which forms a salt bridge with Glu 483. An elongated electron density adjacent to the Ser 478 side chain (Supplementary Fig. 5) was modelled as two water molecules, hydrogen-bonded to each other and to the Ser 478 side chain OH, which in turn donates a hydrogen bond to His 480 N<sub>δ1</sub> farther from the active site. The Ser 478 side chain is linked through these two water molecules to Arg 192 by a weak hydrogen bond (3.4 Å; Fig. 2b and Supplementary Fig. 5). It is probably as a result of being linked to this network of proton donors on one side, and the keto group of a large hydrophobic substrate on the other, that the Asp 309 side chain remains protonated and engaged in the substrate-binding interaction. This network could also serve as the proton source for the proposed participation of the Asp 309 carboxylate moiety in the enolization process, as discussed below.

H2 $\beta$  of the A-ring of the bound androstenedione (Fig. 3a) that gets abstracted in the aromatization step is close to the Ala 306CO $\cdots$ HO $\gamma$ Thr 310 pair (C=O $\cdots$ H2 $\beta$ -C2: 3.7 Å and C2-H2 $\beta$  $\cdots$ O $\gamma$ H: 3.8 Å). Thr 310, highly conserved in P450s, has been implicated in the P450 hydroxylation steps. The mechanism of P450

hydroxylation has been studied extensively for two bacterial enzymes, P450cam<sup>20</sup> and P450eryF<sup>21</sup>. In the dioxygen complex of P450cam, the residue pair Thr 252–Gly 248 carbonyl, and two catalytic water molecules, are involved in the activation of ferrous dioxygen to the hydroxylating Fe(IV)=O species by providing two protons<sup>20</sup>. A similar hydroxylation mechanism involving the corresponding Thr 310–Ala 306 carbonyl pair, and catalytic water molecules (the binding of which could be promoted by dioxygen binding as in P450cam), is probably at work for each of the first two steps catalysed by aromatase, yielding the C19-aldehyde derivative of androstenedione through 19,19-*gem*-diol formation and retention of the *pro-S* hydrogen<sup>1–3,5,6</sup>. The same catalytic residues could also be responsible for the H2 $\beta$  abstraction of the 2,3-enolization processes in the aromatization step. To accomplish this, a nucleophilic attack on H2 $\beta$ -C by the Ala 306CO $\cdots$ HO $\gamma$ Thr 310 moiety (perhaps along with a water) and a concerted electrophilic attack on the C3-keto oxygen by a protonated Asp 309 side chain could promote the H2 $\beta$  abstraction and 2,3-enolization, akin to  $\text{H}_2\text{C}=\text{C}3\text{-keto}$  to  $\text{HC}=\text{C}3\text{-enol}$  tautomerization (Fig. 3b). A bound water molecule (perhaps linked to the proton relay network) between Thr 310-O $\gamma$  and the iron-peroxy/hydroperoxy intermediate could lower the pK<sub>a</sub> of Thr 310-O $\gamma$ H, rendering Ala 306C=O a more potent nucleophile; alternatively, it could itself act as a nucleophile, as shown in Fig. 3b. Asp 309 thus seems to have a direct participation in enolization, unlike the indirect roles of Asp 251 and Glu 244 in hydroxylation by P450cam and P450eryF, respectively<sup>20,21</sup>. A density-function-theory calculation for the final catalytic step of aromatase suggests a strikingly low energy barrier (less than 7 kcal mol<sup>-1</sup>) for H1 $\beta$  abstraction when steroids are 2,3-enolized<sup>27</sup>. However, the 1 $\beta$



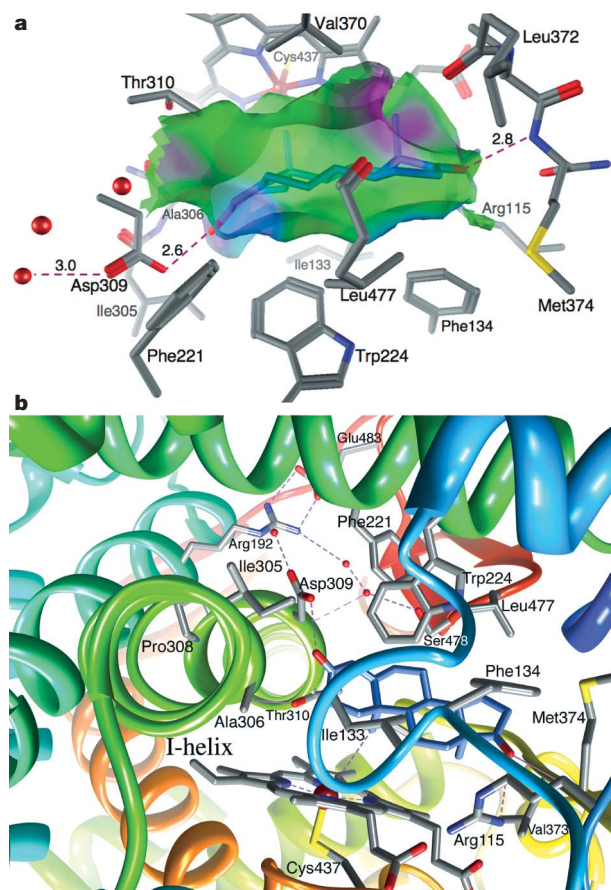


**Figure 2 | Views of the active site of aromatase.** **a**, A van der Waals interaction surface cast by the protein and haem atoms at the active site. The semi-transparent surface, coloured green for hydrophobic interactions and magenta for polar interactions, closely resembles the shape, size and puckering of the steroid backbone. This figure was prepared with MOE. **b**, A view along the I-helix axis from its N-terminal end. The disruption to the helicity of the backbone at residues Pro 308–Thr 310 causes the helix axis to displace by about 3.5 Å, allowing the side chain of Asp 309 to interact with the 3-keto oxygen of the steroid. The deviation from helicity could be stabilized by a strong Ala 306CO···HOThr 310 (2.8 Å) hydrogen bond, as well as by Asp 309 peptide CO···water (3.4 Å) interaction as indicated.

hydrogen is too far from this carbonyl (6.2 Å) to be abstracted in such a manner. It points at and is close to the haem Fe (4.2 Å), and is probably removed after the Fe-peroxy nucleophilic attack on the 19-aldehyde (Fig. 3b) as previously proposed<sup>3,5,6</sup>.

To examine how a mechanism-based steroidal inhibitor could interfere with the aromatization process, an exemestane (Aromasin; one of the three aromatase inhibitors approved by the US Food and Drug Administration) molecule was built into the active site (Fig. 3c) by using the androstenedione backbone. The two steroids superimpose quite well (root mean square (r.m.s.) deviation about 0.2 Å), except for differences in puckering of the A-rings. The extra C6-methylidene group in exemestane is accommodated in a shallow hydrophobic crevice surrounded by the side-chain C atoms Thr 310–C $\gamma$ , Val 370–C $\gamma$ 2 and Ser 478–C $\beta$ , at the mouth of the active-site access channel (described below). The distance between the methylidene C and C $\gamma$ –Thr 310 is 3 Å, shorter than the van der Waals contact distance. Indeed, a slight adjustment of these side chains on the binding of exemestane is highly likely. The clamping of C6-methylidene in a hydrophobic surrounding, resulting in entropic gain and a lowering of the free energy and the dissociation constant, could greatly reduce the mobility of the Thr 310 side chain and/or interfere with its ability to interact with the catalytic waters for the creation of the active oxyferryl moiety. Exemestane would thus remain tightly bound in the pocket without being hydroxylated at C19.

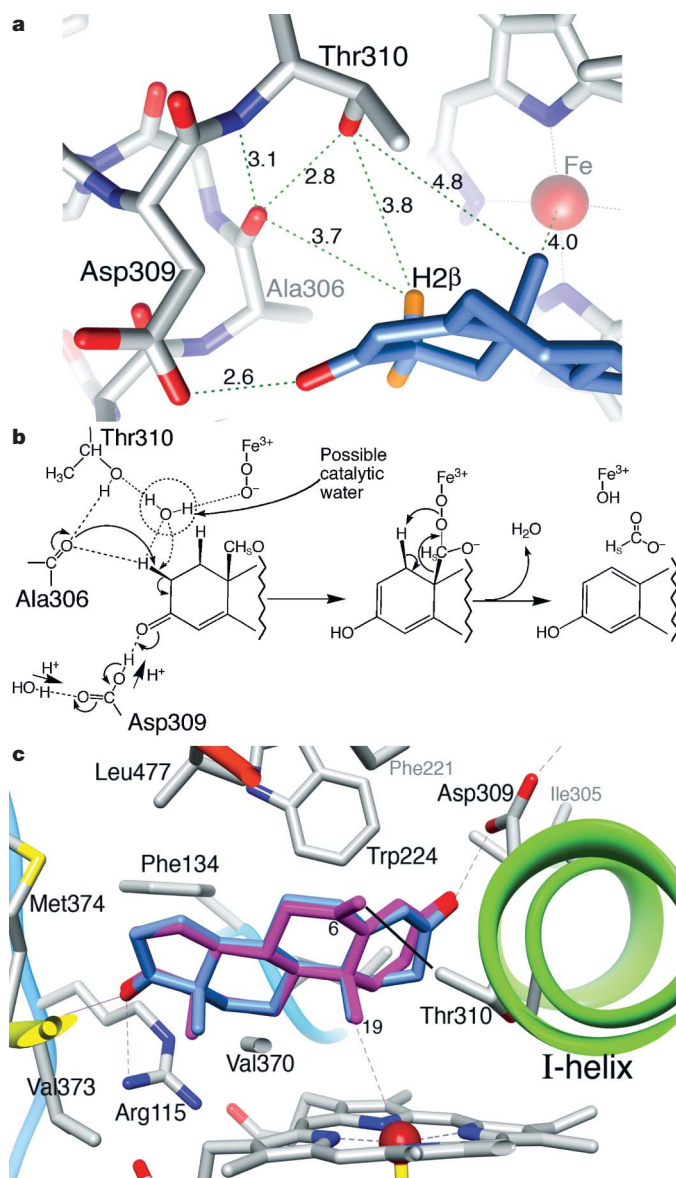


**Figure 3 | Steroid–protein interactions and mechanistic implications.** **a**, A close-up view of the Ala 306CO···HOThr 310 pair that may function in the aromatization of the A-ring of androstenedione. Calculated hydrogen-atom positions of C2 of the bound androstenedione are shown. Distances are in ångströms. **b**, A possible mechanism for H2 $\beta$  abstraction and 2,3-enolization that could be initiated by a nucleophilic attack on C2–H2 $\beta$  by the Ala 306CO···HOThr 310 pair, along with an electrophilic attack on the C3 carbonyl by a protonated Asp 309 side chain. The direction of proton flow from the proton relay network through Asp 309 carboxylate to the substrate is indicated by arrows. Involvement of a catalytic water in H2 $\beta$  abstraction is a possibility. The backbone carbonyl of the Ala 306CO···HOThr 310 pair aided by a potential catalytic water molecule, or the water oxygen itself (as indicated by dotted arrow) could act as the nucleophile. H1 $\beta$  abstraction is drawn as proposed previously<sup>6</sup>. **c**, Modelling of an exemestane molecule (C atoms in magenta) after the experimental positioning of androstenedione. The short van der Waals contact distance (3 Å) between the C6-methylidene carbon and C $\gamma$  of Thr 310 is indicated by a black line.

An access channel links the active site to the outer surface. Figure 4a is a view of the interior of a semi-transparent solvent-excluded surface<sup>28</sup> that also excludes the active-site region, consisting of the steroid-binding pocket and haem, from the protein interior by forming a ‘pouch’-like cleft that opens only to the exterior through the channel, at the arrowhead. The inset shows a view along this channel, revealing the locations of three water molecules within the channel and a glimpse of the opening to the active-site cavity. The salt-bridging



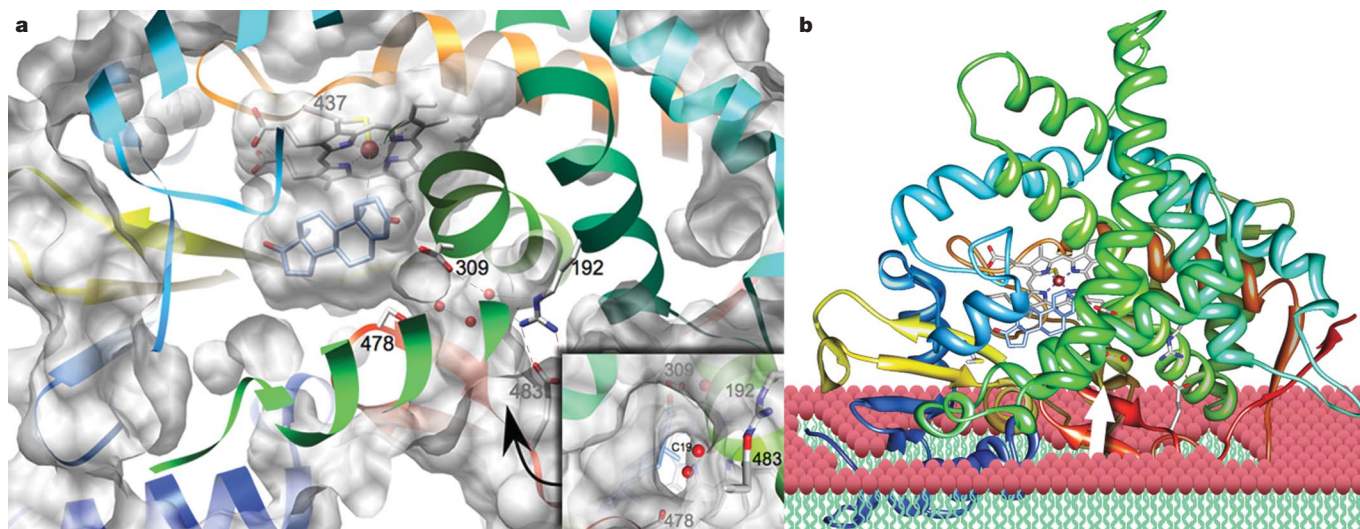


**Figure 4 | A putative active-site access channel from within the lipid bilayer.** **a**, The solvent-excluded surface<sup>28</sup> of aromatase excludes the steroid-binding pocket and haem from the protein interior by forming a 'pouch'-like cleft that has the only opening to the protein exterior through a channel, roughly at the arrowhead. The course of the polypeptide chain is shown in rainbow colour. Residues Arg 192, Asp 309, Ser 478 and Glu 483 border this channel from the protein interior; three water molecules, part of the proton relay network, are within the channel. The inset is a view along this channel

Arg 192–Glu 483 pair as well as Asp 309 and Ser 478 line the channel that hosts the putative proton relay network and is also probably the major transport route to and from the active site for water, oxygen and steroid molecules. This channel seems to be a confluence of what was previously described as channels 2a, 2ac and 2c for other P450s<sup>29</sup>. Although it becomes narrower at points, the channel is probably flexible to permit the passage of molecules such as steroids.

Having seven cysteines in the reduced form, the bulk of aromatase probably resides in the reducing environment of the cytoplasm. A hydrophobicity plot of the aromatase sequence suggests lipid integration for residues 21–42 and 49–71, thereby placing the N terminus with glycosylation at Asn 12 on the opposite side; that is, the lumen<sup>30</sup>. It is possible that the transmembrane segment of residues 21–42, which is too short to traverse the bilayer as a regular  $\alpha$ -helix, is at least partly an extended polypeptide devoid of secondary structure. This is consistent with the observed weak electron density for the polypeptide chain beyond residue 45 towards the N terminus. It is also likely that the hydrophobic helix A' (residues 57–68) and part of helix A (residues 69–80) are embedded in the membrane. This arrangement positions several arginine (Arg 64, Arg 79 and Arg 86) and tryptophan (Trp 67 and Trp 88; Trp 239 from the F–G loop) residues at the lipid/protein interface, a telltale sign of lipid integration. Besides, electron densities for at least two detergent molecules were identified near Trp 67 of helix A'. We therefore propose that lipid integration of aromatase begins with these helices as the N terminus traverses farther into the bilayer towards the lumen side. A model (Fig. 4b) based on these concepts places the entrance to the active-site access channel (Fig. 4a) on the membrane surface. Although other possible entry and exit routes cannot be excluded, this arrangement allows the lipophilic substrate to enter the aromatase active site directly from within the membrane, travelling between and across the F–G loop and the  $\beta$ 8– $\beta$ 9 loop, roughly along the path indicated by the white arrow in Fig. 4b. The structure of aromatase therefore provides a rationale for its crucial membrane integration.

The crystal structure of human aromatase reveals a finely tuned molecular machine that makes oestrogens from androgens. Use of the molecular basis for enzyme–substrate and enzyme–drug interactions could lead to more efficacious intervention of oestrogen production.

at the arrowhead, showing the locations of water molecules and opening to the active site. **b**, In a proposed membrane integration model, the opening to the active-site access channel rests on the lipid bilayer surface, allowing the steroids to enter the aromatase active site directly from within the bilayer, roughly along the arrow shown. The model suggests lipid integration/association of the N terminus up to helix A, and other loops near the C terminus. The orientation of aromatase is roughly the same in both panels.

## METHODS SUMMARY

Aromatase was purified from term human placenta by immuno-affinity chromatography in a highly active form. It was complexed with androstenedione and crystallized at 4 °C in the oxidized high-spin ferric state of the haem iron with poly(ethylene glycol) 4000 as the precipitant. The space group was  $P3_221$  and the unit cell parameters are  $a = b = 140.2$  Å,  $c = 119.3$  Å,  $\alpha = \beta = 90^\circ$ ,  $\gamma = 120^\circ$ , having one aromatase molecule in the asymmetric unit. Diffraction data at about 100 K were collected initially at the Cornell High Energy Synchrotron Source (CHESS) and then to 2.90 Å resolution at the Advanced Photon Source, Argonne National Laboratory, with glycerol as a cryoprotectant. Two data sets at the Fe absorption edge were also collected at the CHESS. The structure was solved by the molecular replacement method coupled with Bijvoet difference Fourier synthesis for identifying the correct solution. Model building and refinement were performed with Coot and Refmac5, respectively. The final model contained 452 amino acid residues; 44 N-terminal and 7 C-terminal residues could not be built because of weakness of their electron densities. The final  $R$  factor for all reflections between 38 and 2.90 Å resolution was 0.214, and the  $R$ -free value was 0.244. The r.m.s. deviations of bond lengths and angles from ideal values were 0.009 Å and  $1.32^\circ$ , respectively. The average isotropic thermal factor for all atoms was  $77.3$  Å<sup>2</sup>. There were only two violations in the backbone torsion angle Ramachandran plot, both in the loop regions. The oxyferryl Fe(IV)=O moiety was generated by adding an oxygen atom to Fe with the modelling software MOE (Chemical Computing Group). The exemestane molecule was built into the active site by superimposing it on the experimentally derived androstenedione atomic positions with MOE.

**Full Methods** and any associated references are available in the online version of the paper at [www.nature.com/nature](http://www.nature.com/nature).

Received 21 June; accepted 6 November 2008.

- Thompson, E. A. & Siiteri, P. K. Utilization of oxygen and reduced nicotinamide adenine dinucleotide phosphate by human placental microsomes during aromatization of androstenedione. *J. Biol. Chem.* **249**, 5364–5372 (1974).
- Simpson, E. R. *et al.* Aromatase cytochrome P450, the enzyme responsible for estrogen biosynthesis. *Endocr. Rev.* **15**, 342–355 (1994).
- O'Neal Johnston, J. Aromatase inhibitors. *Crit. Rev. Biochem. Mol. Biol.* **33**, 375–405 (1998).
- Eisen, A., Trudeau, M., Shelley, W., Messersmith, H. & Pritchard, K. I. Aromatase inhibitors in adjuvant therapy for hormone receptor positive breast cancer: A systematic review. *Cancer Treat. Rev.* **34**, 157–174 (2008).
- Akhtar, M., Calder, D. L., Corina, D. L. & Wright, J. N. Mechanistic studies on C19-demethylation in oestrogen biosynthesis. *Biochem. J.* **201**, 569–580 (1982).
- Akhtar, M., Njar, V. C. & Wright, J. N. Mechanistic studies on aromatase and related C–C bond cleaving P-450 enzymes. *J. Steroid Biochem. Mol. Biol.* **44**, 375–387 (1993).

7. Nakajin, S., Shinoda, M. & Hall, P. F. Purification to homogeneity of aromatase from human placenta. *Biochem. Biophys. Res. Commun.* **134**, 704–710 (1986).
8. Kellis, J. T. & Vickery, L. E. Purification and characterization of human placental aromatase cytochrome P-450. *J. Biol. Chem.* **262**, 4413–4420 (1987).
9. Zhou, D., Pompon, D. & Chen, S. Structure–function studies of human aromatase by site-directed mutagenesis: kinetic properties of mutants Pro-308–Phe, Tyr-361–Phe, Tyr-361–Leu, and Phe-406–Arg. *Proc. Natl Acad. Sci. USA* **88**, 410–414 (1991).
10. Kadohama, N., Yarborough, C., Zhou, D., Chen, S. & Osawa, Y. Kinetic properties of aromatase mutants Pro 308Phe, Asp 309Asn, and Asp 309Ala and their interactions with aromatase inhibitors. *J. Steroid Biochem. Mol. Biol.* **43**, 693–701 (1992).
11. Chen, S. *et al.* Structure–function studies of human aromatase. *J. Steroid Biochem. Mol. Biol.* **44**, 347–356 (1993).
12. Laughton, C. A., Zvelebil, M. J. & Neidle, S. A detailed molecular model for human aromatase. *J. Steroid Biochem. Mol. Biol.* **44**, 399–407 (1993).
13. Oh, S. S. & Robinson, C. H. Mechanism of human placental aromatase: a new active site model. *J. Steroid Biochem. Mol. Biol.* **44**, 389–397 (1993).
14. Amarneh, B. & Simpson, E. R. Expression of a recombinant derivative of human aromatase P450 in insect cells utilizing the baculovirus vector system. *Mol. Cell. Endocrinol.* **109**, R1–R5 (1995).
15. Graham-Lorence, S., Amarneh, B., White, R. E., Peterson, J. A. & Simpson, E. R. A three-dimensional model of aromatase cytochrome P450. *Protein Sci.* **4**, 1065–1080 (1995).
16. Kao, Y. C., Korzekwa, K. R., Laughton, C. A. & Chen, S. Evaluation of the mechanism of aromatase cytochrome P450. A site-directed mutagenesis study. *Eur. J. Biochem.* **268**, 243–251 (2001).
17. Chen, S. *et al.* Structure–function studies of aromatase and its inhibitors: a progress report. *J. Steroid Biochem. Mol. Biol.* **86**, 231–237 (2003).
18. Hong, Y., Cho, M., Yuan, Y. C. & Chen, S. Molecular basis for the interaction of four different classes of substrates and inhibitors with human aromatase. *Biochem. Pharmacol.* **75**, 1161–1169 (2008).
19. Lala, P. *et al.* Suppression of human cytochrome P450 aromatase activity by monoclonal and recombinant antibody fragments and identification of their stable antigenic complex. *J. Steroid Biochem. Mol. Biol.* **88**, 235–245 (2004).
20. Nagano, S. & Poulos, T. L. Crystallographic study on the dioxygen complex of wild-type and mutant cytochrome P450cam. Implications for the dioxygen activation mechanism. *J. Biol. Chem.* **280**, 31659–31663 (2005).
21. Nagano, S., Cupp-Vickery, J. R. & Poulos, T. L. Crystal structures of the ferrous dioxygen complex of wild-type cytochrome P450eryF and its mutants, A245S and A245T: investigation of the proton transfer system in P450eryF. *J. Biol. Chem.* **280**, 22102–22107 (2005).
22. Williams, P. A. *et al.* Crystal structures of human cytochrome P450 3A4 bound to metyrapone and progesterone. *Science* **305**, 683–686 (2004).
23. Rowland, P. *et al.* Crystal structure of human cytochrome P450 2D6. *J. Biol. Chem.* **281**, 7614–7622 (2006).
24. Sansen, S., Hsu, M. H., Stout, C. D. & Johnson, E. F. Structural insight into the altered substrate specificity of human cytochrome P450 2A6 mutants. *Arch. Biochem. Biophys.* **464**, 197–206 (2007).
25. Guallar, V., Baik, M. H., Lippard, S. J. & Friesner, R. A. Peripheral heme substituents control the hydrogen-atom abstraction chemistry in cytochromes P450. *Proc. Natl Acad. Sci. USA* **100**, 6998–7002 (2003).
26. Podust, L. M., Poulos, T. L. & Waterman, M. R. Crystal structure of cytochrome P450 14 $\alpha$ -sterol demethylase (CYP51) from *Mycobacterium tuberculosis* in complex with azole inhibitors. *Proc. Natl Acad. Sci. USA* **98**, 3068–3073 (2001).
27. Hackett, J. C., Brueggemeier, R. W. & Hadad, C. M. The final catalytic step of cytochrome p450 aromatase: a density functional theory study. *J. Am. Chem. Soc.* **127**, 5224–5237 (2005).
28. Pettersen, E. F. *et al.* UCSF Chimera—a visualization system for exploratory research and analysis. *J. Comput. Chem.* **25**, 1605–1612 (2004).
29. Cojocaru, V., Winn, P. J. & Wade, R. C. The ins and outs of cytochrome P450s. *Biochim. Biophys. Acta* **1770**, 390–401 (2007).
30. Shimozawa, O. *et al.* Core glycosylation of cytochrome P-450(arom). Evidence for localization of N terminus of microsomal cytochrome P-450 in the lumen. *J. Biol. Chem.* **268**, 21399–21402 (1993).

**Supplementary Information** is linked to the online version of the paper at [www.nature.com/nature](http://www.nature.com/nature).

**Acknowledgements** We thank Y. Osawa, who pioneered aromatase research and its purification from human placenta at the institute, for many discussions and encouragement; past graduate students, postdoctoral scientists and research associates for contributions to the initial purification and crystallization efforts; H. Davies for discussions; D. Gewirth, V. Cody, G. DeTitta and J. Griffin for critically reading the manuscript; staff at the Women's and Children's Hospital of Buffalo for providing the placenta used in this work; and staffs of the Cornell High Energy Synchrotron Source and the Advanced Photon Source, Argonne National Laboratory, for helping with the synchrotron X-ray data collection. The research is supported in part by grants GM62794 and GM59450 (to D.G.) from the National Institutes of Health.

**Author Contributions** J.G. and M.E. performed the purification and crystallization of aromatase. W.P. and J.G. contributed to diffraction data collection. D.G. was involved in diffraction data collection and processing. D.G. solved the structure, wrote the manuscript and was responsible for overall planning and supervision of the project.

**Author Information** Atomic coordinates and structure factor files have been deposited with the Protein Data Bank under the accession code 3EQM. Reprints and permissions information is available at [www.nature.com/reprints](http://www.nature.com/reprints). Correspondence and requests for materials should be addressed to D.G. ([ghosh@hwi.buffalo.edu](mailto:ghosh@hwi.buffalo.edu)).

## METHODS

**Purification and crystallization.** The enzyme was purified to homogeneity from the microsomal fraction of homogenized fresh human placenta by immunoaffinity chromatography (Supplementary Fig. 1a). The purified enzyme was highly active: the specific activity with androstenedione as the substrate ranged between about 10 and about 100 nmol min<sup>-1</sup> mg<sup>-1</sup> over a large number of purification experiments. Details of this procedure have been described previously<sup>19,31</sup>. The absorption spectrum of the androstenedione complex had a Soret band at 394 nm (Supplementary Fig. 1b), which is characteristic of the oxidized high-spin ferric (Fe<sup>3+</sup>) state of the haem iron and is suggestive of the formation of the androstenedione complex<sup>32</sup>. Freshly purified aromatase in 100 mM potassium phosphate buffer pH 7.4 containing 20% glycerol, 20 mM dithiothreitol, 0.1 mM androstenedione and 1 mM n-dodecyl- $\beta$ -D-maltopyranoside (BDM) was mixed with reservoir cocktails of 24–30% poly(ethylene glycol) 4000 and 0.5 M NaCl in 0.05 M Tris-HCl buffer pH 8.5 and vapour-diffused in sealed 24-well sitting-drop plates against corresponding reservoir solution. The purification and crystallization experiments were all conducted at 4 °C. Reddish-brown hexagonal rod-shaped crystals appeared in 7–10 days and continued to grow up to 14–16 days. Typically, the crystals were about 0.05–0.50 mm in length, with a hexagonal cross-section of about 0.01–0.12 mm (Supplementary Fig. 1c).

**Data collection.** Initially, diffraction data sets to about 3.3 Å resolution were collected at the A-1 station of the Cornell High Energy Synchrotron Source (CHESS). The crystal was flash-cooled in a stream of liquid nitrogen with about 40% glycerol as the cryoprotectant, and maintained at about 100 K during data collection. Additionally, two data sets, each to 4.2 Å resolution, were measured at the CHESS F-2 station by tuning the beam to the peak and the inflection point of the iron absorption edge (inflection (1.7433 Å): total 31,833, unique 9,814, completion 97%,  $I/\sigma I$  highest 4.1,  $R_{\text{merge}}$  0.159; remote (1.7284 Å): total 32,671, unique 9,903, completion 98%,  $I/\sigma I$  highest 4.6,  $R_{\text{merge}}$  0.126). Finally, a 2.9-Å diffraction data set used for solution and refinement of the structure was gathered at cryogenic temperature at beamline 19-ID-D (0.979 Å) of the Advanced Photon Source, Argonne National Laboratory. The data were recorded on an ADSC Q315 CCD detector and processed with the HKL3000 software package<sup>33</sup>. The space group was  $P3_121$  and the unit cell parameters were  $a = b = 140.2$  Å,  $c = 119.3$  Å,  $\alpha = \beta = 90^\circ$ ,  $\gamma = 120^\circ$ . There was one aromatase molecule in the asymmetric unit, with a solvent content of about 79%. A total of 184,295 diffraction intensities were measured, yielding 30,371 unique reflections. The diffraction data were 99.4% complete to 2.90 Å resolution with an overall intensity to sigma ratio of 31.1 and an  $R_{\text{merge}}$  of 0.067. The intensity to sigma ratio was 2.8 in the highest-resolution shell. Supplementary Table 1 summarizes the diffraction data statistics.

**Structure solution and refinement.** The structure was solved by the molecular replacement method (at 3.3 Å), coupled with Bijvoet difference Fourier synthesis with the Fe-absorption edge data sets (at 4.5 Å). The latter helped in identifying the correct molecular replacement solution, at the same time confirming that there was one molecule in the asymmetric unit. Extensive rotation and translation function searches were conducted with a large number of P450 coordinates from the Protein Data Bank (PDB ID codes: 1PQ2, 1R90, 1TQN, 1Z10, 1W0E, 1Z11, 1ZO4, 1ZOA, 2F9Q, 2FDV, 2FDY, 2FDU, 2FDW, 2HI4, 2JOC, 2JOD, 2OJD and 2P85) with the AMORE and MOLREP routines in the CCP4 software package<sup>34</sup>. Only two search models yielded the correct molecular replacement solution: 2F9Q (human P450 2D6; ref. 23) and 1W0E (human P450 3A4; ref. 22), the two human cytochrome P450s with highest sequence identities with aromatase (14–18%). Model building and refinement were performed with Coot<sup>35</sup> and Refmac5 (ref. 36) routines, respectively, running on

either a dual-CPU G5 or a Powerbook G4 with the Mac OS 10.4 operating system. The final model contained 452 amino-acid residues, a haem group, one androstenedione molecule, 35 solvent waters and 2 phosphate ions (3,767 total atoms). Models for 44 N-terminal and 7 C-terminal residues could not be built because of weakness of the their electron densities. Apart from these residues, the electron density for the rest of the molecule was mostly well defined, except for two short loop/turn regions. The fit between the experimental electron density of side chains and the corresponding sequence was excellent except for a few exposed charged amino acids, such as lysines. In the space of missing N-terminal residues, an isolated patch of weak electron density was identifiable and could be fitted to a four-turn helix. However, because of the lack of side-chain identities, the helix could not be modelled unequivocally. Additionally, electron densities for two detergent molecules were located near the Trp 67 side chain, the presumed transmembrane region of the enzyme, but were not included in the final refinement because of the possibility of multiple orientations of the sugar moiety or the alkyl chain. The final  $R$  factor for all reflections between 37.8 and 2.90 Å resolutions was 0.214, and the  $R$ -free value was 0.244. The r.m.s. deviations of bond lengths and angles from ideal values were 0.009 Å and 1.32°, respectively. The average isotropic thermal factor ( $B$ ) for all atoms was 77.3 Å<sup>2</sup>, whereas the Wilson plot  $B$ -value was 94.5 Å<sup>2</sup>. Of 407 non-glycine and non-proline residues, there were two violations in the backbone torsion angle Ramachandran plot, all in weaker loop regions. Overall random coordinate errors were 0.33 Å (based on  $R$ -working), 0.26 Å (on  $R$ -free) and 0.19 Å (on maximum likelihood). A summary of all numbers from refinement is provided in Supplementary Table 1.

**The overall structure of aromatase.** The structure of aromatase consists of 12 major  $\alpha$ -helices (A to L) and 10  $\beta$ -strands (1 to 10) distributed into one major and three minor sheets, and follows the characteristic cytochrome P450 fold (Fig. 1a). The major  $\beta$ -sheet is a mixed four-stranded sheet that begins near the N terminus ( $\beta$ 1:83–88 and  $\beta$ 2:93–97) but ends in two strands from the C-terminal half of the polypeptide chain ( $\beta$ 3:373–376 and  $\beta$ 6:393–396). The N-terminal residues 47–50 make one backbone hydrogen bond with  $\beta$ 1 and add an extra  $\beta$ -strand-like element to this sheet in aromatase. Each of the three minor sheets consists of two antiparallel strands scattered over the polypeptide chain (sheet2:  $\beta$ 4:381–383 and  $\beta$ 5:386–388; sheet3:  $\beta$ 8:473–475 and  $\beta$ 9:479–481; sheet4:  $\beta$ 7:458–461 and  $\beta$ 10:491–494). Of the 12 major helices, I (293–324), F (210–227), G (242–267), H (278–287), C (138–152), D (155–174), E (187–205), J (326–341), K (354–366) and L (440–455) are similar to those found in most of the cytochrome P450s. Helices A' (57–68), A (69–80), B' (100–109), B (119–126), G' (232–236), H' (271–274), J' (346–349), K' (398–404) and K'' (414–418) are one to four turns long and have more variability among P450s. The residues in aromatase involved in haem coordination are Arg 115, Trp 141, Arg 145, Arg 375 and Arg 435.

31. Yoshida, N. & Osawa, Y. Purification of human placental aromatase cytochrome P-450 with monoclonal antibody and its characterization. *Biochemistry* **30**, 3003–3010 (1991).
32. Sato, R. & Omura, T. *Cytochrome P-450* (Kodansha/Academic, 1978).
33. Otwinowski, Z. & Minor, W. *HKL Manual* (Yale University, 1995).
34. Collaborative Computational Project Number 4. The CCP4 suite: programs for protein crystallography. *Acta Crystallogr. D* **50**, 760–763 (1994).
35. Emsley, P. & Cowtan, K. Coot: model building tools for molecular graphics. *Acta Crystallogr. D* **60**, 2126–2132 (2004).
36. Murshudov, G. N., Vagin, A. A. & Dodson, E. J. Refinement of macromolecular structures by the maximum-likelihood method. *Acta Crystallogr. D* **53**, 240–255 (1997).



# naturejobs

**THE CAREERS  
MAGAZINE FOR  
SCIENTISTS**

**Y**ou have probably noticed some big changes at our website, [www.naturejobs.com](http://www.naturejobs.com). It's undergone a major redesign. With the help of a hard-working web-development crew, we hope we've created a strong, navigable, user-friendly, aesthetically pleasing online presence. We expect the site not only to provide useful content and job-search resources, but also to act as a portal to the careers and workforce news found elsewhere in *Nature*.

First, we reorganized content and added some new sections. Our online careers editorial content is in a section called News & comment. Latest stories are easier to find and the archive is easier to navigate, using keywords and categories such as sector (academia, government, industry, nonprofit or private). Towards the bottom of News & comment, we list career-related articles appearing elsewhere in *Nature*.

Career toolkit is a new page with sections on mentoring, networking, salaries, presentation, interview skills and 'ask the expert'. The content, some still in development, will include both past and new *Naturejobs* articles. It will also include practical tips, such as how to deliver an outstanding science presentation.

Our World map has improved significantly; we've made it easier to zoom in on and explore career content by region of choice.

Care to share your thoughts on science careers? Our new homepage poll asks readers to weigh in on timely career-related issues, and instantly displays the results. Although, of course, it's non-scientific, we hope this feature may provide some insight — or at least a bit of fun. Please feel free to suggest questions, whether serious or light-hearted. And we've made our interactive careers-advice forum more accessible. Postings appear simultaneously in a box on the *Naturejobs* homepage as well as on Nature Network, where the forum first started. Join in and offer your own perspectives at <http://tinyurl.com/4slo5n>.

We hope you can more easily find the job, the advice and the analysis you're looking for. But as with any large web project, there are, no doubt, tweaks and improvements to be made. As always, we welcome your feedback.

**Gene Russo is editor of *Naturejobs*.**

## CONTACTS

**Editor:** Gene Russo

**Assistant editor:** Karen Kaplan  
e-mail: [naturejobseditor@nature.com](mailto:naturejobseditor@nature.com)

**European Head Office, London**  
The Macmillan Building,  
4 Crinan Street, London N1 9XW, UK  
Tel: +44 (0) 20 7843 4961  
Fax: +44 (0) 20 7843 4996  
e-mail: [naturejobs@nature.com](mailto:naturejobs@nature.com)

**European Sales Manager:**  
Andy Douglas (4975)  
e-mail: [a.douglas@nature.com](mailto:a.douglas@nature.com)  
**Assistant European Manager:**  
Nils Moeller (4953)

**Natureevents:**  
Ghizlaine Ababou (+44 (0) 20 7014 4015)  
e-mail: [g.ababou@nature.com](mailto:g.ababou@nature.com)

**Southwest UK/RoW:**  
Alexander Ranken (4944)

## Northeast UK/Ireland:

Matthew Ward (+44 (0) 20 7014 4059)

**France/Switzerland/Belgium:**  
Muriel Lestringuez (4994)

**Scandinavia/Spain/Portugal/Italy:**  
Evelina Rubio-Hakansson (4973)

**North Germany/The Netherlands/Eastern**

**Europe:** Kerstin Vincze (4970)

**South Germany/Austria:**

Hildi Rowland (+44 (0) 20 7014 4084)

**Advertising Production Manager:**

Stephen Russell

To send materials use London address above.

Tel: +44 (0) 20 7843 4816

Fax: +44 (0) 20 7843 4996

e-mail: [naturejobs@nature.com](mailto:naturejobs@nature.com)

**Naturejobs web development:** Tom Hancock

**Naturejobs online production:** Dennis Chu

**US Head Office, New York**

75 Varick Street, 9th Floor,  
New York, NY 10013-1917

Tel: +1 800 989 7718

Fax: +1 800 989 7103

e-mail: [naturejobs@nature.com](mailto:naturejobs@nature.com)

**US Sales Manager:** Ken Finnegan

**India**

Vikas Chawla (+91 1242881057)

e-mail: [v.chawla@nature.com](mailto:v.chawla@nature.com)

**Japan Head Office, Tokyo**

Chiyoda Building, 2-37 Ichigayatamachi,  
Shinjuku-ku, Tokyo 162-0843

Tel: +81 3 3267 8751

Fax: +81 3 3267 8746

**Asia-Pacific Sales Manager:**

Ayako Watanabe (+81 3 3267 8765)

e-mail: [a.watanabe@natureasia.com](mailto:a.watanabe@natureasia.com)

**Business Development Manager, Greater**

**China/Singapore:**

Gloria To (+852 2811 7191)

e-mail: [g.to@natureasia.com](mailto:g.to@natureasia.com)

# Survival

A life-changing experience.

**Graeme Wistow**

He survived the crash.

It was almost a miracle. After the engines blew, the escape pod had missed safe orbit and took a barely controlled plunge into the atmosphere. Down to Lem.

It had come to rest wedged in a hillside at the end of the long scar it had carved in the landscape, a scar that was already healing. The pod itself was in bad shape. Air tanks were ruptured, coms were out, power draining away. He could tell something was broken in his leg and he could feel sticky wetness inside his suit. It was already hard to breathe. Rescue would be on the way, but it wouldn't get there in time. There was an oxygen atmosphere out there, but it might as well have been chlorine. He knew he mustn't emerge, but if he didn't he was going to die very soon, suffocating in the metal coffin.

The planet Lem contained, or perhaps was contained by, the only biosphere discovered outside the Solar System. This was Gaia to the *n*th degree: a mass of reproducing, recombining single-celled organisms like living nanobots, infinitely adaptable polyps that assembled and exchanged in complex forms, filling the air, the sea, even the planetary crust. Sealed unmanned landing probes from the orbiting starship had been infiltrated and absorbed in hours. Snatched samples had been studied in orbit but rapidly died like severed body parts cut off from the bloodstream.

A manned landing was out of the question, but now it had happened anyway.

He knew they wouldn't abandon him. A rescue ship could attempt to hover, grab the pod and haul it back to space. It was probably already on the way, but it would take time. He was choking and bleeding now. Just a few lungfuls of air and maybe he would survive long enough to be rescued.

He opened the hatch.

The scenery blazed with colour and movement. The horizon heaved slowly and the hills in which he had landed rippled gently like waves in a viscous ocean. Rainbow clouds drifted over forests of purple and red trees with writhing sea-anemone arms. Something like a huge dragonfly

hummingbird zipped past, stopped and splintered into a swarm of bright iridescent motes that swirled away over a bank of 'flowers' darting in and out of their rippling patterns.

The air in his lungs was metallically bad, stale, hot and bubbled ominously with each, increasingly painful, breath. He cracked the seal and removed his helmet. He had to breathe; he had to take the gamble, to stay alive until help came, he had to survive.

distance, still watching. It didn't seem dangerous.

He winced as he opened his suit to check the damage. Amazingly, the gash in his side was healing before his eyes, just like the scar in the landscape. He should have been alarmed at this decidedly mixed blessing, but he felt fine, better than fine in fact, and he was still alive. He was going to survive.

All at once he realized that the sounds of the biosphere were actually songs, ranging in scale from humpback whale to night-ingale and beyond. They called and answered. The forests sang to the moving hills that responded with variations on the same theme in their own timbre. Even the clouds murmured to the flowers. It was beautiful, natural.

A sonic boom cracked across the sky, a harsh dissonance clashing with the music of Lem.

A blunt cone descended towards him on a tail of fire. He knew it was rescue, but something felt terribly wrong. The cone nearly touched down, an amazingly risky manoeuvre, as his colleagues tried to reach him. The fire of the landing jets burned away the encroaching biosphere. Revulsion washed through him at the sight. He rotated away from the pod and the fire and noise of the spacecraft.

A hatch opened and a hideous, stiff but oddly familiar figure emerged waving frantically and directing waldos that reached out towards the already dissolving escape pod.

A speaker boomed urgently. "Blurg!" said the man.

Frightened, he flinched away on bright new limbs. The decapod came closer and extruded a helping pseudopod.

"Come," it said, a word orchestrated with fugues and arpeggios of information and reassurance. As the wrecked pod disintegrated and was absorbed into the ground, the ugly cone and its jarring inhabitants gave up and roared away, briefly marring the sky. As the echoes faded, the two Lemoids smiled in relief and cart-wheeled away together across the rippling meadows and blended with the forest.

**Graeme Wistow is a scientist who adapts to survive in the Washington suburbs.**



JACEY